UNIVERSITAT DE
BARCELONA

CERKL as a modulator gene of mitochondrial dynamics and stress response in the retina

Rocío García Arroyo

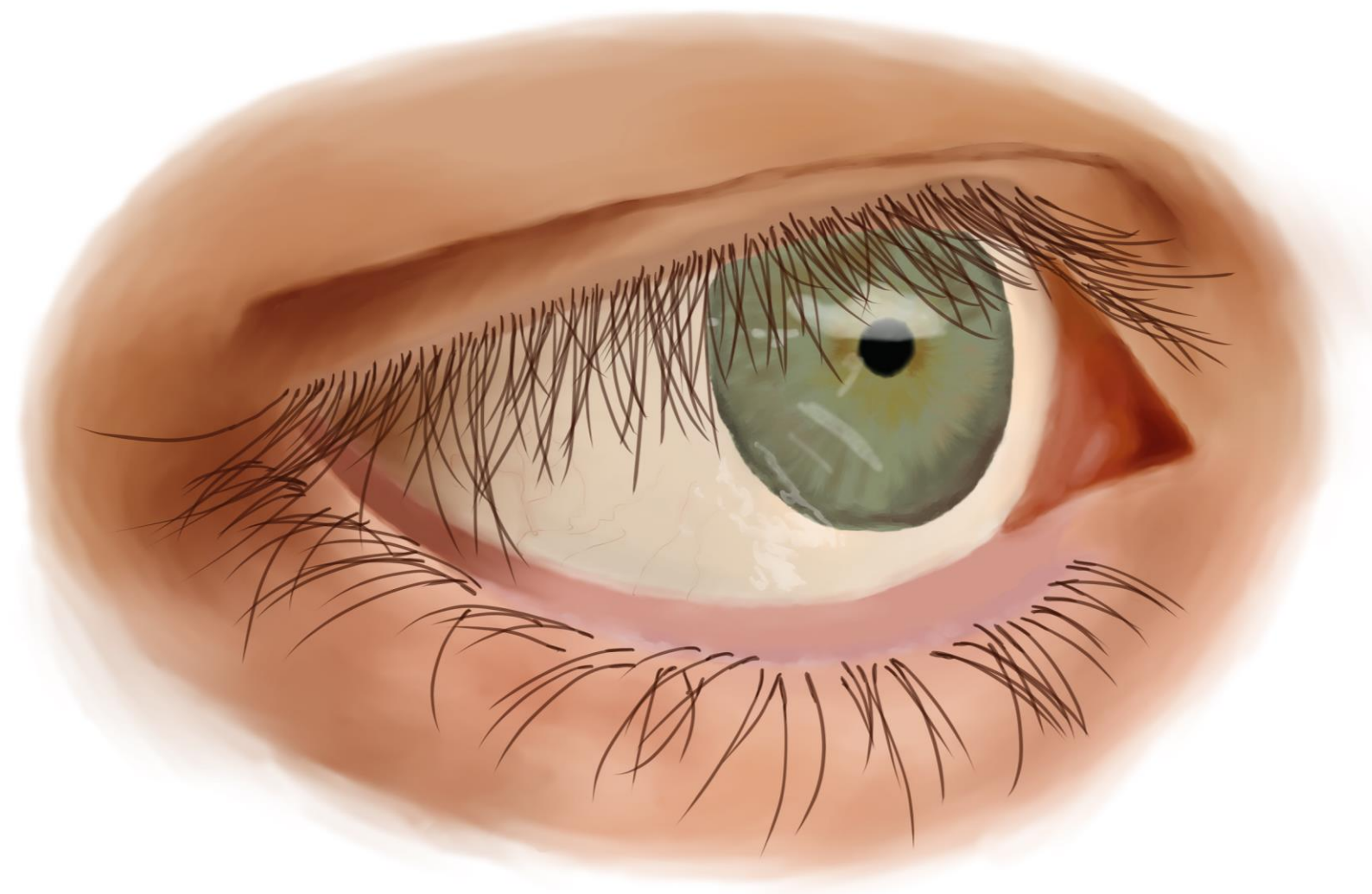# *CERKL* AS A MODULATOR GENE OF MITOCHONDRIAL DYNAMICS AND STRESS RESPONSE IN THE RETINA

ROCÍO GARCÍA ARROYO
DOCTORAL THESIS
2024

Universitat de Barcelona

Tesis Doctoral

CERKL as a modulator gene of mitochondrial dynamics and stress response in the retina

Memoria presentada por **Rocío García Arroyo**

Para optar al grado de

Doctora por la Universitat de Barcelona

Programa de Doctorado "Genética"

Departamento de Genética, Microbiología y Estadística,

Universitat de Barcelona.

Directoras: **Dra. Gemma Marfany Nadal** y **Dra. Serena Mirra**

Tutora: **Dra. Gemma Marfany Nadal**

Doctoranda: **Rocío García Arroyo**

Barcelona, febrero 2024

A mi hermano Dani, papá, mamá y Sergio.

Sois la luz de mi vida.

INDEX

ABBREVIATIONS

- aa: amino acid
- AAV: adeno-associated virus
- ABCR: ATP-binding cassette transporter
- Ad: adenovirus
- AEC: Ethical Committee for Animal Experimentation
- AGO1/3: argonaut protein 1/3
- AMP: Adenosine monophosphate
- AMPK: AMP-activated protein kinase
- AON: antisense oligonucleotide
- ARVO: Association for Research in Vision and Ophthalmology
- ATF101: activating transcription factor 101
- ATF6: activating transcription factor 6
- ATG: autophagy-related genes
- AuNPs: gold nanoparticles
- BBS: Bardet-Biedl syndrome
- BDNF: brain-derived neurotrophic factor
- BiP: immunoglobulin binding protein
- BMP-4: human bone morphogenetic protein-4
- bp: base pairs
- Caprin: cytoplasmic activation /proliferation-associated protein
- Cas: CRISPR-associated protein
- CBS: cystathionine synthase
- cDNA: copy DNA
- CERK: ceramide kinase
- CERKL: ceramide kinase-like
- cGMP: cyclic guanosine monophosphate
- ChR: channelrhodopsin
- CIB1: calcium and integrin binding 1
- CIPF: Centro de Investigación Príncipe Felipe
- CL: cystathionase
- CNS: central nervous system
- CNTF: ciliary neurotrophic factor
- CPEB1: Cytoplasmic polyadenylation element-binding protein 1
- CRD: cone-rod dystrophy
- CRISPR: clustered regularly interspaced short palindromic repeats
- crRNA: CRISPR RNA
- CSNB: congenital stationary night blindness
- DAGK: diacylglycerol kinase
- DAPI: 4',6-diamidino-2-phenylindole
- DCP2: mRNA-decapping enzyme 2
- DMEM: Dulbecco's Modified Eagle's Medium
- DNA: desoxyribonucleic acid
- DRP1: dynamin-related protein 1
- *E. coli*: *Escherichia coli*
- E6: essential 6 medium
- EDC3: Enhancer of mRNA-decapping protein 3
- EEA1: Early Endosomal Antigen 1

- eIF2A: eukaryotic translation initiation factor 2A
- eIF3: eukaryotic initiation factor 3
- eIF4A/B: eukaryotic initiation factor 4-A/B
- eIF4E: eukaryotic initiation factor 4-E
- EIF4E-T: 4E-transporter
- eIF4G: eukaryotic initiation factor 4-G
- EMA: European Medicines Agency
- ER: endoplasmic reticulum
- FBS: foetal bovine serum
- FDA: Food and Drug Administration (U. S.)
- FIS1: mitochondrial fission protein 1
- FMR1: fragile X messenger ribonucleoprotein 1
- G3BP1/2: G3BP stress granule assembly factor 1/2
- GCAP1/2: guanylate cyclase activating protein 1 and 2
- GCL: ganglion cell layer
- GCS: γ-glutamylcysteine synthase
- GDP: guanosine diphosphate
- GFAP: glial fibrillary acidic protein
- GFP: green fluorescence protein
- GO: gene ontology
- GPX: glutathione peroxidases
- GR: glutathione reductase
- gRNA: guide RNA
- GRP78: glucose-related protein 78
- GS: glutathione synthase
- GSH: glutathione
- GSSG: disulfide-oxidized GSH
- GTP: guanosine triphosphate
- h*CERKL*: human *CERKL* gene
- HDR: homology-directed repair
- hiPSCs: human induced pluripotent stem cells
- HNRNPM: heterogeneous nuclear ribonucleoprotein M
- IMPDH-1: inosine monophosphate dehydrogenase
- INL: inner nuclear layer
- IPL: inner plexiform layer
- iPSC: induced pluripotent stem cell
- IRBP: Interphotoreceptor retinoid-binding protein
- IRDs: inherited retinal dystrophies
- IRE1: inositol requiring enzyme 1
- iRNA: interference RNA
- IS: inner segment
- ITGA4: integrin subunit alpha 4
- JBS: Joubert syndrome
- kb: kilobases
- KD: knockdown
- kDa: kilodalton
- KEAP1: Kelch-like ECH-associated protein 1
- KO: knockout
- LAMP1: lysosome-associated membrane glycoprotein 1
- LAP: LC3-associated phagocytosis
- LB: lysogeny broth

- LB: Lysogeny broth
- LC3: light chain 3 protein
- LCA: Leber congenital amaurosis
- L-OPA1: long OPA1
- LoxP: locus of x-over, P1
- LRAT: lecithin retinol acyltransferase
- LV: lentivirus
- MAT: methionine adenosyl-transferase
- m*Cerkl*: mouse *Cerkl* gene
- MFF: mitochondrial fission factor
- MFN1: mitofusin 1
- MFN2: mitofusin 2
- MiD49: mitochondrial dynamics protein 49
- MiD54: mitochondrial dynamics protein 54
- miRNA: microRNA
- MIRO1: mitochondrial Rho GTPase 1
- MIRO2: mitochondrial Rho GTPase 1
- MO: morpholino
- MOI: multiplicity of infection
- mRNA: messenger RNA
- MT: methyltransferase
- mTOR: mammalian target of rapamycin
- NCS: neuronal sensor calcium
- NES: nuclear export signal
- NeuroD1: neurogenic differentiation 1
- NHEJ: non-homologous end joining
- NIM: neural induction medium
- NLS: nuclear localization signal
- NPs: nanoparticles
- NRF2: Nuclear factor erythroid 2-related factor 2
- NRVs: neuroretinal vesicles
- ON: optic nerve
- ONL: outer nuclear layer
- OPA1: optic atrophy 1
- OPL: outer plexiform layer
- OS: outer segment
- OXPHOS: oxidative phosphorylation
- PAB/PABP: polyadenylate-binding protein
- PAM: protospacer-adjacent motive
- P-bodies: processing-bodies
- PCR: polymerase chain reaction
- PDE: phosphodiesterase
- PE: phosphatidyl-ethanolamine
- PERK: PKR-like endoplasmic reticulum kinase
- PFA: paraformaldehyde
- PH: pleckstrin-homology
- PI3K: phosphatidylinositol 3-kinase
- PI3P: phosphatidylinositol 3-phosphate
- PINK1: PTEN Induced Kinase 1
- pRPE: primary RPE
- pVHL: von Hippel–Lindau protein
- RA: retinoic acid
- Rab7: Ras-related protein-7
- RB1CC1 (or FIP200): RB1-inducible coiled-coil 1

- RDH: retinol dehydrogenase
- RDM: retinal differentiation medium
- rep: replication-associated protein
- RGCs: retinal ganglion cells
- RHO: rhodopsin
- RMM: retinal maturation medium
- RNA: ribonucleic acid
- RNA-Seq: RNA-sequencing
- RNP: ribonucleoprotein
- RNS: reactive nitrogen species
- ROI: region of interest
- ROS: reactive oxygen species
- RP: retinitis pigmentosa
- RPE: retinal pigment epithelium
- RT-PCR: reverse transcription PCR
- SAHH: S-adenosylhomocysteine hydrolase
- sgRNA: single guide RNA
- SIRT-1: SIRTUIN-1
- SLS/NPHP: Senior-Loken syndrome
- S-OPA1: short OPA1
- ssODN: single-stranded donor oligonucleotide
- SVCV P: spring viremia of carp virus phosphoprotein
- TALEN: Transcription Activator-Like Effector Nuclease
- TBK1: TANK-binding kinase 1

- TDP-43: TAR DNA-binding protein 43
- TIGEM: Telethon Institute of Genetics and Medicine
- tracrRNA: trans-activating CRISPR RNA
- TRAK1: trafficking kinesin protein 1
- TRAK2: trafficking kinesin protein 1
- TRX2: thioredoxin 2
- TSS: transcription start site
- UAB: Universitat Autònoma de Barcelona
- ULK1: Unc-51 Like Autophagy Activating Kinase 1
- UPR: Unfolded Protein Response
- US: Usher syndrome
- UTR: untranslated region
- UV: ultraviolet
- WT: wild-type
- XRN4: exoribonuclease 4
- ZF*cerkl*: zebrafish *cerkl* gene
- λH: Lambda DNA/HindIII
- λHE: Lambda DNA/HindIII+EcoRI

ABSTRACT

Inherited Retinal Dystrophies (IRDs) are a clinically and genetically highly heterogeneous group of genetic pathologies characterized by progressive attrition of photoreceptor cells and other retinal neurons, which eventually leads to vision loss. The retina, the most affected tissue in IRDs, is the specialized region of the central nervous system capable of transducing light into neural signals. This neurosensory tissue is particularly susceptible to genetic and environmental alterations due to its highly active metabolism, external location, and daily light irradiation. Therefore, the disturbance of the balance between retinal resilience systems and endogenous and exogenous stress factors eventually leads to several alterations that underlie the pathogenesis of many IRDs, such as mitochondrial dysfunction, misregulated autophagy, and activation of cell death pathways.

CERKL (*CERamide Kinase-Like*) mutations cause two different IRDs in humans: Retinitis Pigmentosa and Cone-Rod Dystrophy. While the precise role of CERKL remains unclear, numerous studies have proposed *CERKL* as a resilience gene against oxidative stress, by participating in the formation of stress granules, regulation of the antioxidant protein TRX2 and inhibition of oxidative stress-induced apoptosis, among other functions. Previous work from our research group led to the generation of the *Cerkl*$^{KD/KO}$ mouse model, characterised by a strong deficiency in the expression of *Cerkl*. This model mimics the disease progression of *CERKL*-associated Retinitis Pigmentosa-affected patients, showing a slow and progressive loss of photoreceptors and, ultimately, vision impairment.

Taking advantage of the *Cerkl*$^{KD/KO}$ mouse model, we aimed to dissect CERKL function in mitochondrial metabolism and dynamics. Our findings describe a pool of CERKL isoforms colocalizing with mitochondria. In addition, we observed accumulation of fragmented mitochondria and mitochondrial bioenergetics dysfunction in *Cerkl*$^{KD/KO}$ retinas. Moreover, mitochondrial distribution and trafficking were reduced in retinal and hippocampal neurons upon *Cerkl* depletion, reflecting the important role of CERKL in the regulation of mitochondrial network morphology and energy production.

Furthermore, we sought to analyse the impact of CERKL downregulation on stress response and activation of photoreceptor death mechanisms upon light/oxidative

stress. Data collected from *CERKL* silencing and overexpression experiments in ARPE-19 cells (derived from retinal pigment epithelium) revealed that CERKL exerts a protective role maintaining the mitochondrial network morphology against oxidative damage. Additionally, using *Cerkl*^{KD/KO} albino mouse models, we assessed immediate (early) or after two weeks (late) retinal stress response to light injury, using data from transcriptomics, metabolomics, and immunohistochemistry images. Our results showed that *Cerkl* depletion causes an exacerbated response to stress in basal conditions, through alterations in glutathione metabolism and stress granule production. Consequently, upon light-stress exposure, *Cerkl*^{KD/KO} retinas cannot cope with additional stress factors, resulting in increased ROS levels and the subsequent activation of several cell death mechanisms.

To sum up, our studies indicate that *Cerkl* gene is a novel player in regulating mitochondrial organization and metabolism, together with light-challenged retinal homeostasis, thus suggesting that *CERKL* mutations cause blindness by impairing the mitochondrial homeostasis and oxidative stress response in the retina. These findings contributed to determine early phenotypic biomarkers of the *Cerkl*-depleted mouse retina, which will be compared and confirmed with those observed in retinal organoids derived from *CERKL*^{R257X} patient-derived hiPSCs (currently under differentiation). Altogether, these studies will allow us to test the feasibility of genetic rescue using a proof-of-principle AAV-based gene augmentation therapy for *CERKL*-associated IRDs, as well as novel gene delivery systems using gold nanoparticles as vectors.

The principal area of cooperation of this Thesis in the Sustainable Development Goals (SDGs) is related to the SDG 3: "Good health and well-being" according to the point 3.8: "Achieve universal health coverage, including financial risk protection, access to quality essential health-care services and access to safe, effective, quality and affordable essential medicines and vaccines for all". Moreover, an important part of our findings was result of fruitful collaborations with groups with high expertise in other areas. Therefore, the objectives of this work are also related to SDG 17: "Partnerships for the goals" according to the point 17.6: "Knowledge sharing and cooperation for access to science, technology and innovation". Finally, this PhD Thesis has been directed, supervised and tutorized by women, Dr Gemma Marfany and Dr Serena Mirra, and our research group has also been mostly composed of female scientists during many years, contributing to SDG 5: "Gender equity and empowering of girls and women" according to the point 5.5: "Assure effective and full participation of women and equity in leadership opportunities at all deciding levels in politic, economic and public life".

RESUMEN

La retina, el tejido neurosensorial que transduce luz en señales nerviosas, es particularmente susceptible a alteraciones genéticas y ambientales, las cuales pueden sobrepasar los sistemas de resiliencia celular, provocando alteraciones patogénicas causantes de distrofias hereditarias de retina (IRDs). En humanos, mutaciones en el gen *CERKL* (*CERamide Kinase-Like*) causan Retinosis Pigmentaria y Distrofia de Conos y Bastones, dos IRDs caracterizadas por la muerte progresiva de fotorreceptores y pérdida de visión. Aunque su función exacta es desconocida, se ha propuesto que *CERKL* es un gen de resiliencia a estrés oxidativo.

Usando el modelo *Cerkl^{KD/KO}*, que expresa menos del 10% de *Cerkl* –y sufre la muerte progresiva de fotorreceptores con la consiguiente pérdida de visión–, nuestro objetivo ha sido la disección de la función de CERKL en el metabolismo y dinámica mitocondriales, tanto en condiciones basales como en respuesta al estrés oxidativo/lumínico. Hemos descrito la localización de un conjunto de isoformas de CERKL en mitocondria, además de la acumulación de mitocondrias fragmentadas y disfuncionales en retinas *Cerkl^{KD/KO}*. Asimismo, las neuronas *Cerkl^{KD/KO}* presentan alteraciones en la distribución y tráfico mitocondriales. Además, la sobreexpresión de CERKL *in vitro* protege la red mitocondrial del estrés oxidativo, reflejando la importancia de CERKL en la regulación de la morfología y bioenergética mitocondriales. También hemos evaluado la respuesta a estrés lumínico en ratones albinos *Cerkl^{KD/KO}*, observando una respuesta exacerbada en condiciones basales, con alteraciones en el metabolismo del glutatión y producción de gránulos de estrés. Consecuentemente, ante estrés lumínico, las retinas *Cerkl^{KD/KO}* no pueden sobrellevar un daño adicional, causando un incremento en especies reactivas de oxígeno y activación de mecanismos de muerte celular.

En conclusión, nuestros estudios postulan el gen *CERKL* como un nuevo regulador de la organización y metabolismo mitocondriales, así como de la homeostasis retinal frente a estrés lumínico, indicando que las mutaciones en *CERKL* causan ceguera al desestabilizar estos sistemas en la retina. Estos resultados han contribuido a determinar biomarcadores tempranos en las retinas *Cerkl^{KD/KO}*, que serán comparados y confirmados con los observados en organoides de retina derivados

de hiPSCs de pacientes. Así podremos evaluar el potencial rescate fenotípico tras aplicar terapia basada en AAV-CERKL.

1. The retina

Vision plays a dominant and crucial role in human perception, contributing to about 90 % of the sensory information that is integrated in the brain. Additionally, almost one third of the cortical surface is dedicated to process visual information, underscoring the importance of the intricate work of the retina and associated tissues in this complex process (1).

1.1. Structure and cell types

The retina is the specialized tissue of the central nervous system (CNS) that transduces light stimuli into neural signals. This neurosensitive tissue is located in the posterior part of the eye, between the choroid and the vitreous chamber, and is a layered structure composed of six major classes of neurons alternatively arranged in cell somas and plexiform layers. In the most posterior part of the retina, the retinal pigment epithelium (RPE), a monolayer of pigmented epithelial cells, lays in intimate contact with the tips of photoreceptors –rods and cones–, whose somas are in the outer nuclear layer (ONL). Synaptic contacts between photoreceptors and postsynaptic neurons –horizontal, bipolar and amacrine cells–, found in the inner nuclear layer (INL), occur in the outer plexiform layer (OPL). Ganglion cells are the innermost neuronal cell type of the retina, located in the ganglion cell layer (GCL), and ultimately receive information from synapses in the inner plexiform layer (IPL) (Figure 1) (2,3).

Vision begins with the light entering the eye and passing through all the retinal layers to eventually reach cone and rod photoreceptors cells, where photoreception occurs. Photoreceptor cells convert light energy into membrane potential changes to finally release neurotransmitters into the second order postsynaptic neurons, the bipolar cells, in the OPL. Synaptic contacts between photoreceptors and bipolar cells are modulated by horizontal cells. Bipolar cells then contact with amacrine and retinal ganglion cells within the IPL to integrate and process visual information. Finally, retinal ganglion cells, which render the sole output of the visual information, project their axons forming the optic nerve (ON) to higher visual centres in the brain (4,5).
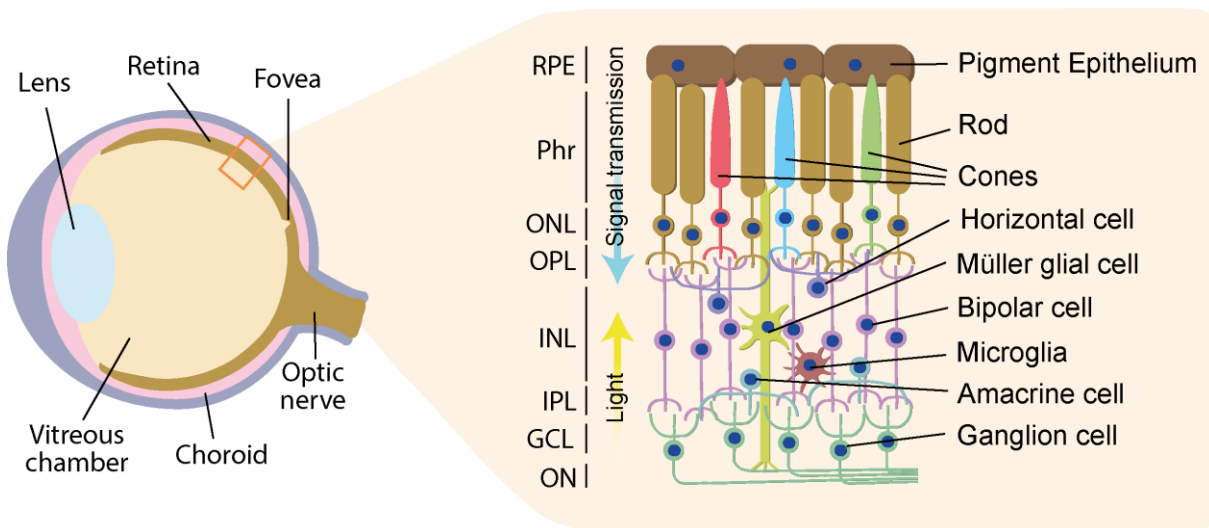
Figure 1. Architectural arrangement of the eye and the retina. On the left side, simplified diagram of the eye indicating some elements (lens, vitreous chamber, retina, fovea, choroid, and optic nerve). On the right side, a high-magnified scheme of the retina with its layers and cell types, e.g. pigment epithelium, rods, cones, horizontal, bipolar, amacrine and ganglion cells, Müller glia and microglia. RPE: retinal pigment epithelium; Phr: photoreceptor layer; ONL: outer nuclear layer; OPL: outer plexiform layer; INL: inner nuclear layer; IPL: inner plexiform layer; GCL: ganglion cell layer; ON: optic nerve fiber.

Apart from neuronal cells, glial cells are also crucial for retinal function. Within the retina, macroglia (Müller cells and astrocytes) and microglia (resident retinal macrophages) (Figure 1) play a crucial role in maintaining retinal homeostasis and conferring neuroprotection against transient pathophysiological situations via different intra- and intercellular changes, as well as morphological responses (6–8).

1.2.   Photoreceptor cells: rods and cones

Photoreceptor cells, the principal photo-sensitive neurons of the retina, provide visual perception owing to the expression of opsins, the specialized visual pigments capable of detecting photons. There are two classes of photoreceptors: rods and cones, which differ in shape, structure, type of expressed opsin, light sensitivity, prevalence, and distribution, thus reflecting a high level of specialization. Remarkably, both types of photoreceptors are highly polarized cells and share common architectural regions, namely the outer (OS) and the inner (IS) segments, the cell body, and the synaptic terminal (Figure 2) (9).

Figure 2. Structural organization of photoreceptor cells: rods and cones. They mainly differ in the structure and disk organization of the outer segment (OS).
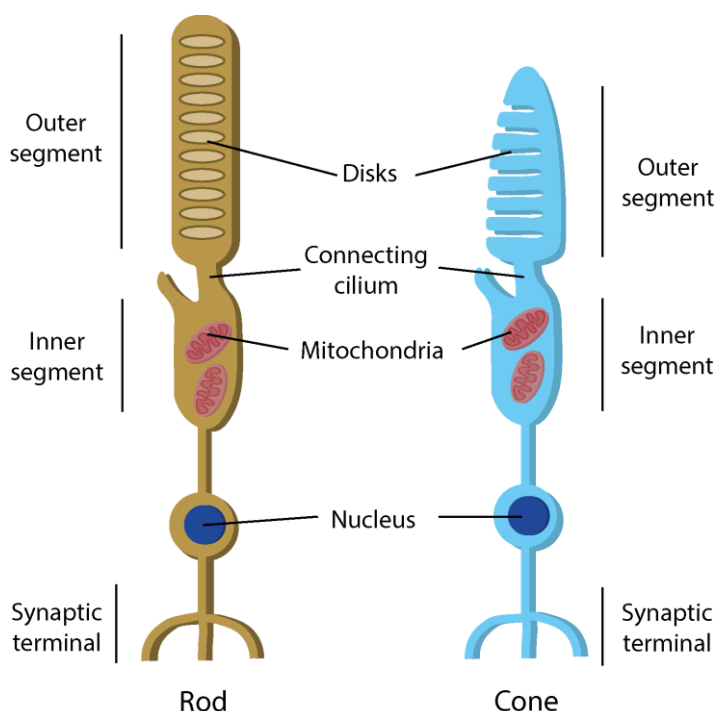
Interestingly, rods and cones are named after their characteristic shape. Despite sharing common structural elements, the principal difference between rods and cones lies in their OS, a highly specialized sensory cilium that houses the phototransduction machinery. In rods, the OS is longer, more rigid, and fully packed with closed membranous disks, while cones present a shorter OS with membrane invaginations instead of intracellular disks. On the other hand, cell body and synaptic terminal are quite similar in both types of photoreceptor cells. The IS contains different organelles responsible for protein production, including endoplasmic reticulum, Golgi, and mitochondria. Proteins produced in the IS are transported to the OS through the connecting cilium (10).

The specific photopigment of photoreceptors is found in the OS membranous disks or invaginations. Rods solely express rhodopsin, whereas cones express different opsins with distinct peaks of light sensitivity, for instance: S-opsin detects short (blue) wavelengths, M-opsin responds to medium (green) wavelengths, and L-opsin is stimulated by long (red) wavelengths. The expression of each different opsin in cones gives rise to three classes of cones in humans: S-cones, M-cones, and L-cones, while mice and other mammals only present the first two types of opsins. In contrast, zebrafish possesses a fourth opsin sensitive to ultraviolet (UV) light (11).

Because of these structural and enzymatic differences, rods are highly sensitive to dim light but display limited spatial resolution, contributing to scotopic vision. On the other hand, cones are responsible for photopic vision as they respond to increased levels of light, have high spatial resolution, and also detect different colours (12,13).

Regarding prevalence and distribution across the retina, rods are the most abundant photoreceptor cells (around 95 % in humans and 97 % in mice) and are distributed almost ubiquitously throughout the retina. Conversely, cones are much less prevalent than rods and are organized in a mosaic-like pattern. However, in the macula and, particularly in the fovea, a highly specialized region of the central retina, the cone-rod ratio is dramatically shifted due to an important enrichment of cones, which grants high visual acuity. Among mammals, the fovea is present in humans and other primates (14).

1.3. Retinal ganglion cells

Retinal ganglion cells (RGCs) are the last input and solely output neurons of the retina that encode, integrate, and finally relay visual information through the projection of their very thin (0.5-1 μm) and long (50 mm) axons to the lateral geniculate nucleus in the thalamus and the superior colliculus in the midbrain. To execute this process, specific subcellular compartmented structures are needed: dendrites, soma, non-myelinated axon, and myelinated axon (15).

After the reception of visual inputs from photoreceptor cells, bipolar and amacrine cells synapse with RGCs dendrites in the IPL. RGCs somas, located in the GCL, receive electrical signals from the dendrites and convey them through their axons to higher visual centres. Remarkably, these projection neurons do not present myelin in the first but long region of their axons (intraocular and optic nerve head portions) to preserve retinal transparency. High energy production requirements are needed to assure efficient and functional transmission of potential actions through non-myelinated axon regions, making RGCs particularly susceptible to metabolic alterations (16,17).

Despite sharing the mentioned common structural domains, RGCs can be classified into several subtypes by their anatomical, functional, and molecular signature. Santiago Ramón y Cajal was a pioneer at describing in detail

morphologically different subclasses of RGCs. In the last years, functional and molecular analyses have complemented morphological studies, giving rise to up to 40 classes of RGCs (18–21).

1.4. Retinal Pigment Epithelium

The retinal pigment epithelium (RPE) consists of a monolayer of pigmented epithelial cells strategically situated between the tips of photoreceptor cells and the choriocapillaris, a dense network of highly permeable capillaries that directly nourishes the RPE and outermost neuroretina. Although it does not participate in light detection and signal integration and transmission, the RPE plays essential roles for retinal function and homeostasis (22).

The RPE transports nutrients and ions between the choriocapillaris and photoreceptors. Therefore, the RPE contributes to the nourishment of photoreceptors by taking up nutrients such as glucose, retinol, and fatty acids from the blood and delivering them to photoreceptor cells. The RPE also handles removal of photoreceptors waste products through the trafficking of water, electrolytes, and metabolic end products from the subretinal space to the choroid. The continuous stabilization of ion composition in the retinal surface enables correct photoreceptor excitability (23).

RPE cells exhibit a polarized basal-apical structure. In the apical surface, RPE cells extend microvilli to envelop the OS tips of rod and cone photoreceptor cells, while the basal surface presents complex infoldings, a typical specialization of cells involved in transport. The interaction between the RPE and the tips of photoreceptors is of special relevance to ensure retinal function. Photoreceptor cells are daily exposed to intense levels of light, which leads to accumulation of photo-damaged lipids and proteins. As light transduction in photoreceptors depends on the correct structure and function of multiple proteins and lipids, the OS undergoes a constant renewal process to maintain the excitability of photoreceptors. In this process, the RPE phagocytes the shed membranes from the tips of photoreceptors OSs, which contain the highest concentration of radicals and photo-damaged proteins and lipids, whereas at the cilium base, the OS is newly built. In the RPE, phagosomes containing OSs are fusioned with endosomes and later with lysosomes, which contain

the enzymes necessary to digest the phagocyted content (Figure 3). In this process, some relevant molecules, such as retinal, are returned to photoreceptors, completing the visual cycle (explained in more detail in Introduction Section 1.5.) among others (24).
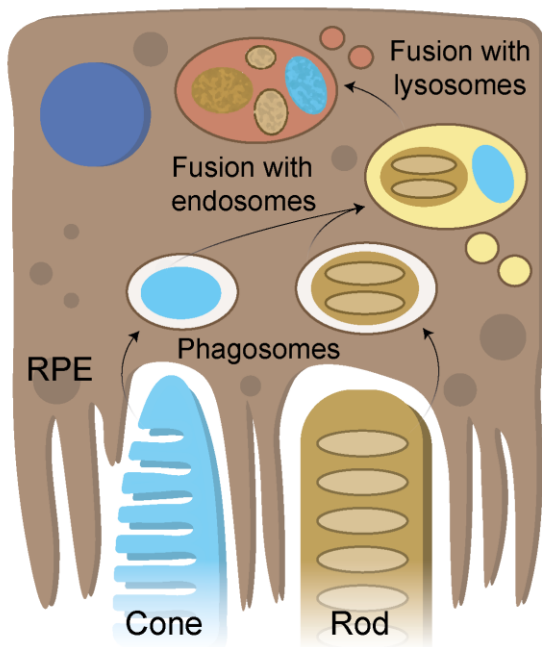
Figure 3. Phagocytosis of rod and cone photoreceptors OSs by RPE cells. The tip of the OS is phagocyted, then the phagosome is fusioned with endosomes and, later, with lysosomes to digest its content.

Furthermore, the RPE secretes a variety of growth factors that help to preserve the structural integrity of photoreceptors and choriocapillaris endothelium. Secretion of immunosuppressive factors by the RPE also provides immunoprivilege to the eye. Finally, the presence of pigments in the RPE, such as melanin and lipofuscin, contributes to increase optical quality by absorption of scattered light focused onto the retina by the lens, thereby helping to reduce the oxidative damage of the neuroretina (25).

RPE-photoreceptors relationship requires an intricate balance and the failure of any of the RPE numerous functions can lead to retinal loss of function, degeneration, and eventually blindness (23).

1.5.   Phototransduction and visual cycle

When light enters through the eye, the lens focuses it onto the retina where it is detected by photo-sensitive proteins (rhodopsin in rods and opsins in cones), embedded into the membrane of the disks or invaginations of photoreceptor OSs. These photo-sensitive proteins initiate a cascade of events that finally regulates the

release of neurotransmitter into postsynaptic neurons –bipolar and horizontal cells (26,27).

Both rhodopsin and cone opsins display the common chromophore 11-*cis*-retinal, which is isomerized into all-*trans*-retinal by light, inducing a conformational change in the photoreceptive molecule necessary for initiation of phototransduction. Then, the activated form of the visual pigment carries out the exchange of GDP for GTP on the α-subunit of transducin, a trimeric G-protein. The transducin α-subunit bound to GTP dissociates from the β and γ-subunits to activate a phosphodiesterase (PDE), that catalyses the hydrolysis of cGMP. The decreasing levels of cGMP results in the closure of cyclic nucleotide-gated channels and, consequently, the cessation of Na^+ and Ca^{2+} influx. This eventually provokes the hyperpolarization of the photoreceptor cell and the consequent inhibition of neurotransmitter release at the synapse (26–29).

To maintain the phototransduction cascade and photoreceptor excitability, as well as to keep the continuity of vision, clearance of all-*trans*-retinal and replacement with fresh 11-*cis*-retinal is mandatory. Interestingly, photoreceptor cells are unable to reisomerize all-*trans*-retinal back into 11-*cis*-retinal, whereas RPE cells possess the ability to perform this conversion. Therefore, the constant exchange of retinal between photoreceptor cells and the RPE, known as the visual cycle of retinal, is absolutely required for retinal function (22,23).

The visual cycle of retinal consists of several steps catalysed or facilitated by enzymes, transporters and retinoid-binding proteins situated both in the RPE and photoreceptor cells. Firstly, all-*trans*-retinal is released from bleached visual pigments inside OS disks and transported to the cytoplasm by the specific ATP binding cassette transporter (ABCR). Next, it is reduced by retinol dehydrogenase 8 (RDH8), among other all-*trans*-RDHs, within photoreceptor OS and further trafficked to the RPE bound to the interphotoreceptor retinoid binding protein (IRBP). Inside RPE cells, all-*trans*-retinol is esterified by lecithin:retinol acyltransferase (LRAT). The resulting all-*trans*-retinyl esters are then hydrolysed and isomerised by the isomerohydrolase RPE65, generating 11-*cis*-retinol. The 11-*cis*-retinol is subsequently oxidized by 11-*cis*-retinol dehydrogenase enzymes (RDH5 and other 11-*cis*-RDHs) in the RPE and

shuttled back to the OS of photoreceptors to regenerate visual pigments, thus completing the visual cycle (Figure 4) (30,31).
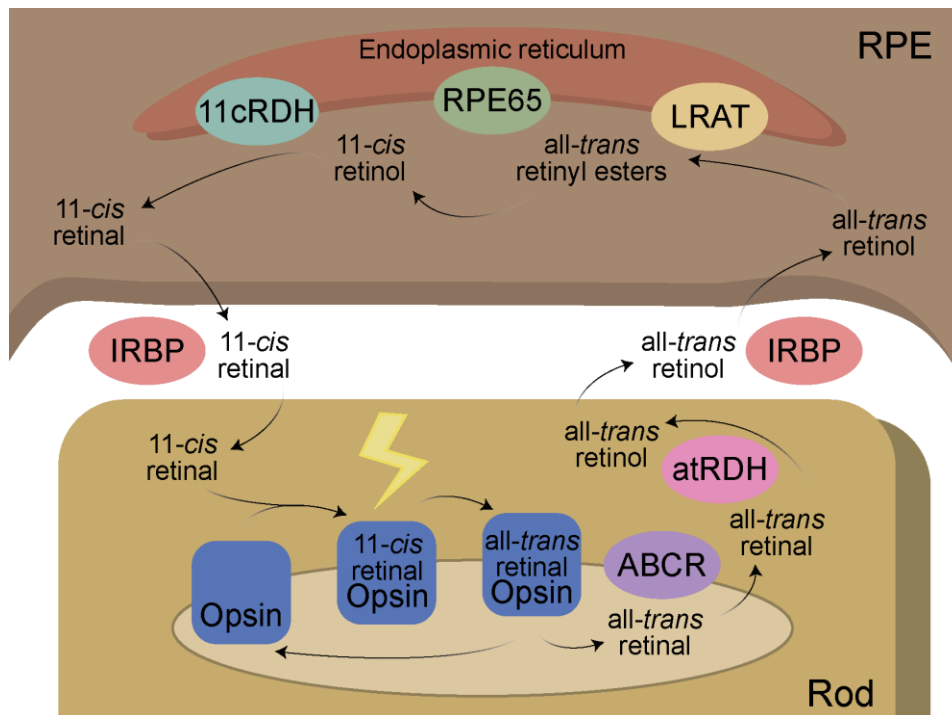
Figure 4. Graphic representation of the visual cycle of retinal. Light excites the 11-*cis*-retinal bound to opsin, producing its isomerization into all-*trans*-retinal opsin. Then, all-*trans*-retinal is liberated inside the OS disk and transported to the cytoplasm through ABCR. There, all-*trans*-retinal is reduced to all-*trans*-retinol by atRDH and trafficked to RPE cells bound to IRBP. In RPE, all-*trans*-retinol is esterified by LRAT. All-*trans*-retinyl esters are catalysed into 11-*cis*-retinol thanks to RPE65. Finally, 11-*cis*-retinol is reduced to 11-*cis*-retinal by 11cRDH and returned to photoreceptor cells via IRBP to regenerate bleached opsins. atRDH: all-*trans*-RDH, 11cRDH: 11-*cis*-RDH.

The photoreceptor-RPE visual cycle is the best-known canonical mechanism of regenerating 11-*cis*-retinal. Nonetheless, there are other alternative pathways such as that which involves cones and Müller cells. To ensure the rapid renewal of 11-*cis*-retinal in daylight conditions, Müller cells recycle the chromophore and selectively supply it to cones (32).

1.6.   Retinal dystrophies

Inherited retinal dystrophies (IRDs) are a clinically and genetically heterogeneous group of genetic disorders characterized by progressive and irreversible degeneration of photoreceptor cells, RPE and other retinal neurons, which eventually causes loss of vision and blindness. IRDs have a prevalence of 1:3,000 people and

represent the leading cause of blindness across all age groups worldwide (33). To date, there are over 300 genes and *loci* known to be responsible of IRDs (Figure 5) (RetNet, the Retinal Information Network, 1996-2023, https://web.sph.uth.edu/RetNet/home.htm). IRD-causative genes perform different roles within the retina, including photoreceptor differentiation (e.g. *NRL*, *NR2E3*), specific structural roles (e.g. *CEP290*, *PROM1*), phototransduction and visual cycle (e.g. *Rhodopsin*, *PDE6B*, *RPE65*), and protective antioxidant systems. Notably, most IRD-related proteins are expressed in the same cell types and are located in the same organelles and intracellular structures in mice as they are in humans, which makes mouse a suitable model for studying IRDs (further explained in Introduction Section 3.3) (34). Depending on the gene and the specific mutation, the inheritance pattern may vary (including autosomal dominant, autosomal recessive, mitochondrial, and X-linked inheritance) as well as the age of onset, disease progression, and associated phenotypic traits (35).

Clinical classification of IRDs is based on disease progression and the primarily affected retinal cell type, although there is an overlap between these phenotypic categories (Figure 5). Considering the progression of the pathology, IRDs can be stationary —as it happens in most patients with congenital stationary night blindness (CSNB)— or progressive —such as in retinitis pigmentosa (RP) or cone-rod dystrophy (CRD). Based on the cell type that is primarily involved in the pathogenesis (rod or cone photoreceptors), IRDs can be categorized into rod-cone dystrophies and cone-rod dystrophies, respectively. In rod-cone dystrophies, e.g. RP and Leber congenital amaurosis (LCA), rods are affected first, leading to night blindness and tunnel vision as initial symptoms. On the contrary, cone photoreceptor cells are primarily affected in cone-rod dystrophies, initially giving rise to central vision loss defects that expand towards the mid-periphery. Late in the IRD disease progression, both cones and rods are affected, making it difficult to obtain a clear diagnosis. Although photoreceptor cell survival is predominantly affected in IRDs, many causative genes are not expressed by photoreceptor cells. In fact, RPE dysfunction —affecting visual chromophore recycling and its reincorporation into photoreceptor cells— is a major cause of IRDs, for instance in patients with LCA or RP caused by mutations in *RPE65*. Furthermore, some IRDs affect only the retina, while others present systemic features,

e.g. Alström syndrome (hearing loss, obesity, cardiomyopathy), Bardet-Biedl syndrome (BBS) (polydactyly, obesity, reduced renal function), Joubert syndrome (JBS) (Cerebellar hypoplasia), Senior-Loken syndrome (SLS/NPHP) (nephronophthisis), and Usher syndrome (US) (sensorineural hearing loss) (Figure 5) (36,37).
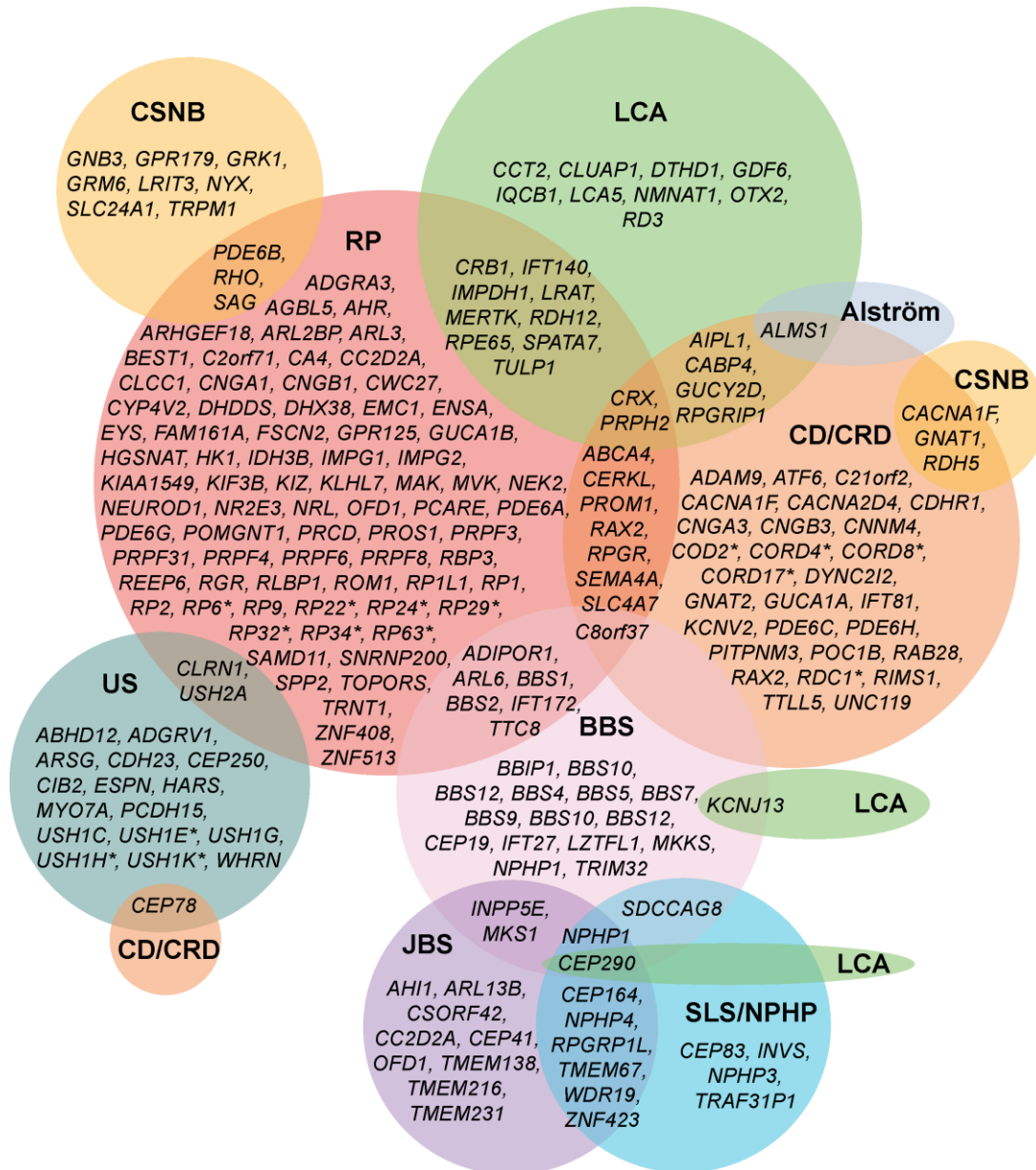
Figure 5. Schematic representation of IRDs and their causative genes. Genes implicated in diverse IRDs, including retinitis pigmentosa (RP), congenital stationary night blindness (CSNB), Leber congenital amaurosis (LCA), Alström syndrome, cone/cone-rod dystrophy (CD/CRD), Bardet-Biedl syndrome (BBS), Joubert syndrome (JBS), Senior-Loken syndrome/nephronophthisis (SLS/NPHP), and Usher syndrome (US). Asterisks (*) indicate mapped genetic *loci* without an identified gene. Information retrieved from RetNet, the Retinal Information Network (https://web.sph.uth.edu/RetNet/home.htm) in January 2024.

Among the numerous retinal disorders included in IRDs, retinitis pigmentosa (RP) is the most common, affecting approximately between 1:3,000 and 1:5,000 live births, and is caused by mutations in more than 70 genes and *loci* (34).

The extreme diversity of genes/*loci* and mutations that are causative of IRDs complicates the genetic diagnosis and further development of specific gene-therapeutic approaches. Nevertheless, other treatment possibilities are being explored as a proof-of-concept to try to slow down or even halt the disease progression regardless of the affected gene (further explained in Introduction Section 4.3) (38,39).

1.7. Retina and brain: two elements of the CNS

"The retina is a window to the brain" is a widely known statement in the scientific community. This idea comes from the fact that, despite of its peripheral location, the neuroretina belongs to the CNS and its accessibility makes it amenable to manipulation and studies in order to dissect the deeper mysteries of the brain (40).

Known as an extension of the brain, the retina consists of different neurons with strong resemblance to neurons from other parts of the CNS, such as cortical and hippocampal neurons. Particularly RGCs present typical neuronal morphological structures, including dendrites, a soma, and an axon. Therefore, extensively studied regions of the brain, e.g. hippocampus, can be utilized as neuronal models for retinal dystrophies affecting RGCs. While RGC primary culture and transfection is a difficult and not fully optimized technique, hippocampal neuron primary culture and transfection procedures are broadly used, enabling the handily addition of reporter genes, such as GFP, thus making live imaging techniques feasible (40–43).

Among other similarities between the retina and the brain, the inner blood-retinal barrier, constituted by nonfenestrated endothelial cells connected by tight junctions and enclosed by Müller and astroglial cells endfeet, highly resembles the blood-brain barrier. Moreover, both regions of the CNS host specialized immune responses. Given the common features shared by the eye and the rest of the CNS, much information obtained from the retina could be applicable to the brain and spinal cord, and vice versa. Many neurological disorders, such as stroke, multiple sclerosis,

INTRODUCTION

spinocerebellar ataxia, Parkinson disease and Alzheimer disease, present ocular manifestations that often precede symptoms in the brain. In addition, several retinal diseases display characteristics of neurodegenerative disorders. Therefore, ocular imaging techniques assessing the functional and structural state of the retina can offer noninvasive diagnosis and prognosis of CNS disorders. Indeed, this also suggests that treatments that are beneficial in brain diseases might be also applicable to retinal disorders, and vice versa (44–46).

2. Stressors and antioxidant responses in the retina

The retina is constantly subjected to environmental insults and stressors, such as light and pollution, as a direct consequence of its peripheral location and specialized function. These external stressors, together with the high retinal energy-demanding metabolism, inherited genetic mutations plus age-associated alterations, promote the formation of reactive oxygen species (ROS). Accumulation of ROS impairs retinal function and increases the vulnerability of photoreceptors, RPE and retinal neurons to cell death. Therefore, efficient resilience mechanisms for maintenance of the retinal homeostasis and regulation of antioxidant responses are key to ensure retinal cells survival and proper function (47).

2.1. Stress agents

In all living cells, free radicals are generated as metabolic byproducts of oxidation-reduction reactions. Free radicals can be divided into oxygen and nonoxygen radicals, which respectively are reactive oxygen species (ROS) and reactive nitrogen species (RNS). ROS/RNS include hydrogen peroxide (H_2O_2), hydroxyl radicals ($^{\bullet}OH$), superoxide anions ($O_2^{\bullet-}$), nitric oxide ($NO^{\bullet}$), and peroxynitrite ($ONOO^-$). ROS conform the predominant category, giving rise to around 95 % of all free radicals (48). Free radicals can be produced via multiple pathways, including endogenous and exogenous stimuli, e.g. intensive metabolism, pollution, light radiation, chemical drugs, and smoking. Free radicals are extremely reactive and short-lived intermediates containing one or more unpaired electrons, which react with different biomolecules, such as nucleic acids, proteins, and lipids, leading to cell damage or functional impairment. At normal conditions, production of low levels of free radicals is involved in maintaining homeostasis, as well as in the regulation of gene expression, transcription factors, and epigenetic pathways (49). Nevertheless, accumulation of ROS or deficiency in antioxidant mechanisms results in an oxidation-reduction unbalance and oxidative stress. Continuous oxidative stress may eventually damage cells and contribute to the progression of many neurodegenerative diseases (50).

The retina is particularly susceptible to the production and further accumulation of ROS due to its neuronal complexity, high quantity of polyunsaturated fatty acids,

external location, elevated metabolic demand, and daily light irradiation. Particularly, photoreceptor cells are constantly exposed to light, which can cause toxicity and oxidative stress, but they also demand high energetic production and constant protein turnover, which makes them especially vulnerable to mitochondrial and endoplasmic reticulum perturbations. Thus, a wide range of sophisticated retinal oxidative defence mechanisms (including enzymatic and non-enzymatic processes) are required, which need to be not only accurately regulated, but also extremely effective and efficient to cope with stress conditions, in order to mitigate and prevent potential damages. Under pathological conditions, the dynamic redox balance between free radicals' production and antioxidant responses is disrupted, triggering multiple stress-related mechanisms that finally jeopardize retinal integrity, such as excessive oxidative stress, inflammatory responses, defects in autophagy and immune responses, mitochondrial dysfunction, endoplasmic stress, alterations in apoptotic cascades, and microglial activation and gliosis, among others (47,51–53). Further development of therapeutic interventions to promote the maintenance of redox balance may decelerate or even prevent the progression of ocular neurodegenerative diseases (54).

2.2. Autophagy

In all living cells, a finely regulated equilibrium between anabolism and catabolism is required to ensure cellular homeostasis. Autophagy is one of the principal catabolic pathways of all tissues and cells and is mediated by autophagy-related genes (ATG). This process facilitates the degradation of damaged cell components through the lysosomal pathway to provide energy as well as to preserve intracellular quality control. According to how the material to be degraded reaches the lysosome, autophagy can be classified into three main types. Microautophagy consists of the invagination of the endosomal or lysosomal membrane to surround the material destined for degradation (55). In chaperone-mediated autophagy, exclusive of mammalian cells, proteins harbouring a specific targeting amino acid sequence are specifically recognized and degraded (56). Finally, macroautophagy (often called general autophagy) is the best described class, which involves the engulfment of cytoplasmic material (encompassing lipids, proteins, whole organelles and even

parts of the nucleus) thanks to a double-membrane structure to form the autophagosome. Then, autophagosomes fuse with lysosomes in which acidic hydrolases degrade the engulfed material. Lysosomes ultimately release the resulting products of this process, which include amino acids, nucleotides, and lipids, to generate ATP and new "building blocks" for anabolic reactions, thus sustaining cell homeostasis and survival. Therefore, a basal level of autophagy is necessary to maintain cells free of damaged material, but the autophagic process can also be induced in response to environmental stimuli, such as starvation or oxidative stress (57,58).
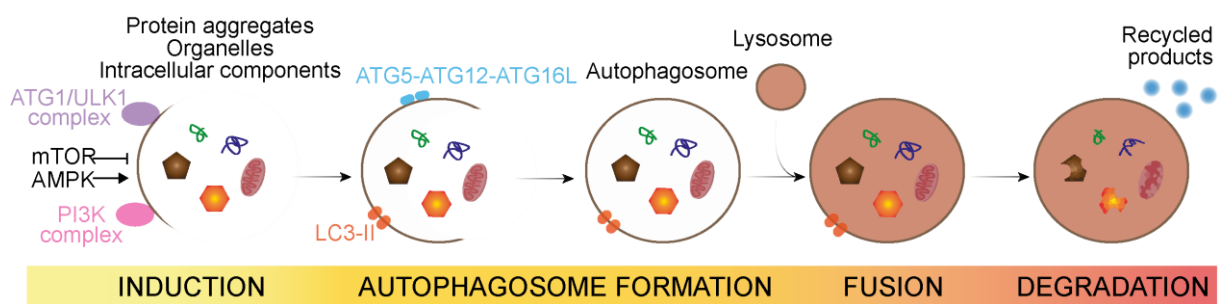
Figure 6. **Macroautophagic process.** In the induction step, inhibition of mTOR or activation of AMPK promotes the formation of ATG1/ULK1 and PI3K complexes to start engulfing protein aggregates, organelles, and intracellular component. Then, the autophagosome is formed after conjugation of ATG5-ATG12-ATG16L and LC3-II. Next, the autophagosome is fused with the lysosome to degrade its content and provide recycled products.

Macroautophagy occurs following a series of subsequent steps. In response to mTOR inhibition or activation of AMPK signalling, the kinase ATG1/ULK1 forms a complex with the proteins ATG13, ATF101, and FIP200 (also named RB1CC1), resulting in the induction phase. Then, the ULK1 kinase forms the phosphatidylinositol 3-kinase (PI3K) complex, formed by VPS34, BECLIN1, VPS14, and VPS15, and facilitates the generation of phosphatidylinositol 3-phosphate (PI3P) at phagophore initiation sites. Next, ATG7 catalyses two reactions: the conjugation of ATG12, ATG5, and ATG16L, and also the conjugation of phosphatidyl-ethanolamine (PE) to LC3 (light chain 3 protein), to form LC3-II (the autophagosome-bound form of LC3). ATG9 enables the elongation of the autophagosome through assembly of protein-protein and protein-lipid complexes as well as delivery of lipids. The final phases of macroautophagy are mediated by proteins and other molecules involved

in the maturation of the autophagosome, but also fusion with endosomes and lysosomes for degradation and recycling of the engulfed material (Figure 6) (57,58).

In the retina, autophagy plays a fundamental role to sustain intracellular quality control specially considering the influence of metabolic and environmental stress to this tissue. In fact, photoreceptor OS phagocytosis in RPE cells occurs via non-canonical autophagy pathway, also known as LC3-associated phagocytosis (LAP). In this process, ATG5 and LC3 trigger the degradation of extracellular cargo, which is, in this specific case, the photoreceptor OS. LAP is not strictly considered autophagy because the degraded material is not derived from the cell itself. Nonetheless, after the formation of the phagosome, the consequent steps and involved proteins are common between LAP and the macroautophagic process (59).

The impairment of autophagy in the retina leads to increased oxidative stress and contribute to photoreceptor cells damage and dysfunction, thus supporting the relevance of the autophagic pathway in the retina. On the other hand, several studies have described an overactivation of autophagy in different IRD mouse models, contributing to the loss of photoreceptor homeostasis. Therefore, the proper regulation of the autophagic pathway is considered indispensable to maintain visual function, since deficient autophagy affects the structure and function of photoreceptors. Importantly, enhanced autophagic process also leads to photoreceptor degeneration (59,60).

2.3.   Retinal metabolism: mitochondrial dynamics and homeostasis

Over a century ago, the German scientist Otto Warburg postulated the retina as the most energy-demanding tissue of the body, even exceeding the energetic necessities of the brain, in order to maintain neuronal excitation and ensure phototransduction, neurotransmission, and normal cellular function (61). Interestingly, the retina displays two different anabolic mechanisms to produce energy depending on the cell type and the cell compartment. In photoreceptors, mitochondria are mainly located in the IS. Although they are the essential organelles involved in energy production, aerobic glycolysis is the main mechanism to fulfil the high metabolic demands in the OS. This process, also known as Warburg effect, may occur because of the absence of mitochondria in this subcellular compartment.

Additionally, this phenomenon serves as a mechanism to ensure membrane biosynthesis for the constant renewal of photoreceptor OS membranous disks (59,62).

Mitochondria are crucial organelles for all eukaryotic cells and represent the major source for cellular energy production via oxidative phosphorylation (OXPHOS). These organelles are composed of an outer and inner membrane, which define two compartments, the intermembrane space, and the internal matrix space. Apart from OXPHOS, which resides in the inner mitochondrial membrane, mitochondria fulfil other relevant critical functions to preserve cell integrity and survival, including scavenging ROS, regulation of calcium homeostasis, biosynthesis of amino acids, cholesterol and phospholipids, nucleotide metabolism, and apoptotic signalling. Approximately 1-5 % of ROS are estimated to be generated by mitochondrial activity in physiological conditions. Malfunctioning of mitochondria leads to loss of mitochondrial membrane potential, decreased OXPHOS, damage of mitochondrial DNA, and ROS-induced ROS vicious circle, causing severe alterations in cell and tissue homeostasis, which places mitochondrial dysfunction at the basis of many neurodegenerative disorders, including retinal pathologies (63–66).

Mitochondria are very dynamic organelles that constantly change their size, morphology, and intracellular location in response to endogenous and exogenous cues. Mitochondrial membrane dynamics, including fusion and fission, are indispensable processes for mitochondrial homeostasis and distribution. Mitochondrial fusion, which involves the physical merge of two mitochondria, allows intermixing and exchanging proteins, respiratory complexes, and mitochondrial DNA for functional complementation between different mitochondria. On the other hand, mitochondrial fission is necessary for the appropriate distribution of mitochondria along the cells, as well as for quality control and clearance of damaged mitochondria through mitophagy, the specific form of autophagy that targets mitochondria for degradation. The coordinated interplay between fusion, fission, transport and mitophagy constantly remodels the mitochondrial network to preserve proper energy production (67).

INTRODUCTION

Mitochondrial fusion and fission are specifically orchestrated by four dynamin-related GTPases: mitofusins 1 and 2 (MFN1 and MFN2), optic atrophy 1 (OPA1), and dynamin-related protein 1 (DRP1). MFN1 and MFN2, together with OPA1, mediate mitochondrial fusion. In mitochondrial fusion, OPA1, embedded in the inner mitochondrial membrane, interacts with MFN1 and MFN2, in the outer mitochondrial membrane, to couple the fusion between the inner and outer mitochondrial membranes. OPA1 presents eight isoforms comprising long and cleaved versions. Preserving the balance between long (L-OPA1) and short OPA1 (S-OPA1) isoforms —maintaining the pull of L-OPA1 isoform— is required for fusion to occur (68). Mitochondrial fission is mostly mediated by DRP1, which is mainly located in the cytoplasm. DRP1 is recruited to the outer mitochondrial membrane by the adaptors FIS1, MFF, MiD49 and MiD54 —situated in the outer mitochondrial membrane— to promote the phosphorylation and assemblance of DRP1 into spiral filaments around mitochondria to cause mitochondrial fission (69).

Mitochondrial trafficking through microtubules, which is necessary to fulfil the energetic demands in the most requiring intracellular compartments, is controlled by the motor proteins kinesin and dynein, involved in anterograde and retrograde transport respectively. In mammalian cells, mitochondria are linked to the motor proteins by the molecular adaptors TRAK1 and TRAK2, which contact the GTPases MIRO1 and MIRO2 (70). Finally, mitophagy mediates the degradation of depolarized and damaged mitochondria via the PINK1-PARKIN pathway. When mitochondrial membrane potential is lost, PINK1 —in the outer mitochondrial membrane— recruits the cytosolic E3 ubiquitin ligase PARKIN to dysfunctional and damaged mitochondria to target them for proteasomal degradation and/or mitophagy (Figure 7) (71).

Mitochondria are abundantly represented in the retina and optic nerve, because of their substantial metabolic needs. Indeed, within the retina, these organelles are particularly relevant in RPE, photoreceptor cells, RGCs, and Müller glia. Dysfunctional mitochondria in photoreceptor cells and RPE are widely known to underlie outer retinal pathologies. Therefore, alterations in RPE energetic metabolism profoundly influence photoreceptor viability. Conversely, mitochondrial dysfunction in Müller

glial cells and RGCs, as well as altered mitochondrial trafficking in the latter, have been suggested to relevantly contribute to inner retinal disorders (59,65,72,73).
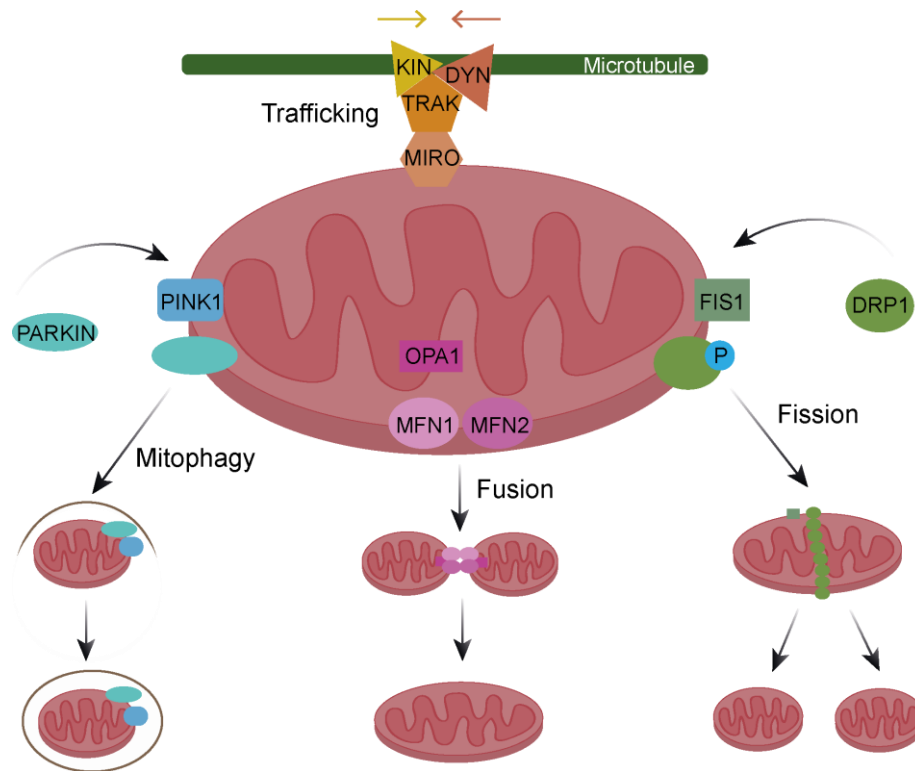
Figure 7. **Mitochondrial dynamics.** Mitochondria can undergo fusion, fission, transport and mitophagy events. MFN1, MFN2 and OPA1 are involved in fusion. FIS1 and phosphorylated (P) DRP1 mediate fission. Dynamin (DYN), kinesin (KIN), TRAK and MIRO control mitochondrial trafficking along microtubules. PINK1-PARKIN coordinate mitophagy.

2.4. Endoplasmic reticulum stress and unfolded protein response

The endoplasmic reticulum (ER), together with mitochondria, are central hubs governing protein and metabolism homeostasis. The ER is the subcellular compartment responsible for biosynthesis, post-translational modification, folding, and trafficking of proteins, as well as for storage of calcium. Therefore, in the ER there resides the stringent quality control of all plasma and secreted proteins folding, allowing only properly folded proteins to be released from the ER. Misfolded proteins are retained in the ER to be consequently degraded in order to prevent the accumulation of dysfunctional or potentially toxic proteins. If the ER protein quality control is disrupted and protein misfolding ensues chronically, cell death mechanisms are triggered. To detect protein misfolding within the ER, cells possess the Unfolded Protein Response (UPR), which consists of several intracellular signalling

pathways that eventually yield protective and proapoptotic processes in response to ER stress (74,75).

The UPR is a primary cellular stress response that attempts to restore the protein homeostasis in the ER through different mechanisms, including reduction of protein translation, increased protein-folding capacity, and promotion of misfolded protein degradation. Moreover, a novel function of the UPR has been recently identified in the modulation of cell metabolism, redox regulation, autophagy, and mitochondrial function, whose overall disturbance also contributes to neuronal degeneration and dysfunction. Under stress conditions, excessive unfolded or misfolded proteins are accumulated in the ER, causing ER stress, and activating the UPR. Then, to alleviate ER stress, glucose-related protein 78 (GRP78, also named immunoglobulin binding protein, BiP), an ER resident chaperone, dissociates from different trans-ER proteins, such as activating transcription factor 6 (ATF6), inositol requiring enzyme 1 (IRE1), and PKR-like endoplasmic reticulum kinase (PERK). Subsequently, GRP78 recognizes and binds to unfolded and misfolded proteins to promote their correct folding and prevent protein aggregation. ATF6, IRE1 and PERK activate downstream cascades that work synergically to recuperate ER homeostasis through increasing protein degradation, attenuating protein translation and enhancing the production of chaperone proteins that facilitate proper protein folding. Nevertheless, if the UPR fails to restore ER homeostasis, cell death mechanisms are activated to eliminate damaged and stressed cells. Unresolved ER stress then activates pathological signalling pathways implicated in many neurodegenerative diseases, including retinal dystrophies (76,77).

Importantly, photoreceptor cells present a continuous protein turnover to preserve the membranous disks of their OS and maintain their specific function, thus needing proper production and accurate folding of proteins. Many mutations associated with IRDs lead to the generation of misfolded proteins in the retina, activating the UPR (78,79). The best-known example of UPR-related IRD is observed in the most common mutation of rhodopsin, RHO^{P23H}, a missense mutation that replaces a proline with a histidine in the position 23 of the protein, thereby impairing its binding with 11-*cis*-retinal (80,81). This specific mutation leads to misfolding of rhodopsin and the

accumulation of the protein in the ER, located in the IS of photoreceptor cells, because only properly folded rhodopsin is efficiently trafficked to the membranous disks of the OS, where it is usually located to perform its function (82). As a consequence, ER stress and UPR are activated and eventually lead to apoptosis of photoreceptor cells (83). Therefore, targeting the UPR pathways may be an interesting therapeutic approach for protecting retinal integrity in early stages of retinal dystrophies by improving metabolic regulation and protein homeostasis.

2.5. Glutathione metabolism

Glutathione (GSH) and the related enzymes conform a pivotal antioxidant system to protect the retina against chemical and oxidative stress. Glutathione exists in its reduced (GSH) and disulfide-oxidized (GSSG) forms, although it is found mostly in the reduced state. GSH is predominantly present in the cytoplasm (80-85 %) and mitochondria (10-15 %). Among other functions, GSH is implicated in scavenging free radicals, regulating DNA and protein synthesis, signal transduction, proteolysis, and regulation of the immune response. Upon oxidative stress, GSH protects proteins by the reversible glutathionylation of active thiols. In addition, GSH helps to maintain the reduced state of antioxidant enzymes and eliminate damaging free radicals, such as hydrogen peroxide, using its own GSH-GSSG redox cycle (84,85).

The biosynthesis of GSH is a multi-step process that requires the combination of three precursor amino acids —cysteine, glutamate, and glycine— to form the tripeptide GSH. This pathway is initiated with the transsulfuration of methionine into cysteine via several enzymatic steps. Successive demethylation and removal of the adenosyl moiety, catalysed by methionine adenosyltransferase (MAT), methyltransferase (MT), and S-adenosylhomocysteine hydrolase (SAHH), results in homocysteine. Then, cystathionine synthase (CBS) catalyses the condensation between homocysteine and serine to generate cystathionine. Next, cystathionase (CL) catalyses the cleavage of cystathionine, releasing free cysteine. The steps of this pathway between methionine and homocysteine are readily interconvertible, whereas the formation of cystathionine is irreversible. The subsequent step, catalysed by γ-glutamylcysteine synthase (GCS), involves the formation of γ-glutamylcysteine using cysteine and glutamate as precursors. Finally, glutathione synthase (GS) catalyses the reaction

between γ-glutamylcysteine and glycine to produce GSH. In the redox cycle of glutathione, the reduced form (GSH) can be oxidized by glutathione peroxidases (GPX) into its oxidized state (GSSG), which, in turn, can also be reduced to GSH using glutathione reductase (GR) enzymes (Figure 8) (86,87).
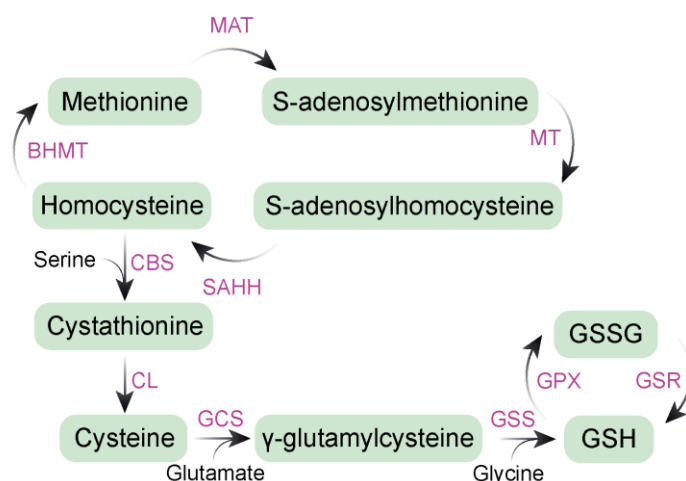
Figure 8. Glutathione biosynthesis pathway. Metabolites (in green) and enzymes (in purple) involved in methionine transsulfuration, glutathione synthesis, and GSH redox cycle.

Effective GSH metabolism, including GSH-related enzymes, is extremely relevant for the retina as protection against continuous oxidative stress exposure. It is particularly abundant in RPE, photoreceptors, Müller glia, and astrocytes. Alterations in the balance between GSH and GSSG, as well as in the enzymes involved in GSH redox cycle, such as GPX4, are associated with IRDs in both patients and mouse models. In contrast, addition of antioxidant molecules to preserve GSH levels or overactivation of GPX enzymes counteract oxidative damage protecting retinal structure and function (85,88–91).

2.6.   mRNA stress granules

As a protective mechanism against adverse environmental conditions, such as oxidative stress, membraneless stress assemblies are rapidly and reversibly formed by aggregation of non-translating messenger ribonucleoproteins to protect messenger RNAs (mRNAs) encoding housekeeping genes. Stress assemblies play pivotal roles in cell survival upon stress damage, as well as in thriving of cells upon stress relief through their pleiotropic cytoprotective effects. The two best characterized stress assemblies are stress granules and the RNA-based processing-

bodies (P-bodies), which are formed in response to stress events, including oxidative, endoplasmic reticulum, osmotic and nutrient stress, among many others. Of interest, both stress assemblies —stress granules and P-bodies— are heterogeneous with respect their formation pathways and their RNA and protein content, although they share common features and may interexchange material (92,93).

On the one hand, P-bodies are composed of translationally inactive mRNAs and proteins associated with translation repression and mRNA turnover. They are usually composed of the proteins AGO1/3, DCP2, XRN4, EDC3, EIF4E-T, LSM1-7, SMG7, HNRNPM and CPEB1. Considering their concentration in RNA decay factors, P-bodies have been proposed as sites of mRNA turnover and degradation. However, recent studies showed that mRNA degradation might not occur exclusively in P-bodies and propose these structures as storage sites for repressed mRNAs that are released and subsequently translated at the appropriate time. Thus, P-bodies contradictorily present intact mRNAs and RNA decay factors, reflecting the possible protection of mRNAs by inhibiting degradation thanks to the presence of specific RNA-binding proteins and translational repressors (92,93).

On the other hand, stress granules, which are reversibly formed upon the inhibition of RNA translation and polysome disassembly after stress damage, consist of polyadenylated mRNAs, the eukaryotic translation initiation factors eIF2A, eIF3, eIF4A/B, eIF4E and eIF4G, the RNA-binding proteins PAB1, Caprin, FMR1, TDP-43, Tia1 and G3BP1/2, as well as 40S ribosomes. These structures reverse the vulnerability of cells to different stress factors because they temporarily sequester crucial components for cell fate and survival inside their chamber structure, blocking the interactions of proteins with their substrates and altering their physiological localization too, thus promoting cell survival. Additionally, stress granules can plug holes in punctured organelles, such as damaged lysosomes, avoiding the leakage of their content into the cytoplasm. Nonetheless, recent advances indicate that, under persistent stress conditions, stress granules can trigger the formation of pathological proteins that eventually cause neurodegeneration. Therefore, impairment in stress granules dynamics exacerbates the susceptibility of neuron cells to stress in neurodegenerative disorders (94,95).

2.7. Microglial activation and gliosis

The proper retinal function demands an exquisitely regulated cellular network, whose homeostasis is maintained thanks to microglial and macroglial cells, including astrocytes and Müller cells (7).

The retinal microglia, considered the resident phagocytes of the retina, is responsible for immune surveillance and defence, playing a key role in the fate of photoreceptors in IRDs. In healthy conditions, microglia display a ramified morphology and constantly scan the surrounding area to clear metabolic products and tissue debris (96). Additionally, microglial cells secrete a wide range of antioxidants, anti-inflammatory cytokines, and growth factors, such as brain-derived neurotrophic factor (BDNF) and ciliary neurotrophic factor (CNTF), to nurse and protect photoreceptor cells (97).

Astrocytes and Müller cells conform the retinal macroglia. Müller cells are in close contact with all retinal cells owing to their large size and distribution. Among their functions, Müller cells secrete neurotrophic factors, regulate the ion balance and pH, and uptake and clear neurotransmitters to preserve retinal homeostasis (98). Astrocytes are located in the most inner part of the retina and display a star-like shape with long processes to interact with both neurons and blood vessels. Astrocytes contribute to ionic homeostasis, modulation of synaptic transmission and formation, and neurotransmitter clearance (99).

In a scenario of retinal injury or alteration, as observed in IRDs, both microglia and macroglia are activated. Microglial activation consists of a change of morphology from ramified to ameboid form that allows them to move toward the damaged region and proliferate to exert enhanced phagocytic activity. In this context, activated microglia secrete several pro-inflammatory cytokines, such as TFN-α, IL-1β and IL-6, as well as ROS and RNS (100). Astrocytes and Müller cells undergo gliosis, increasing the expression of gliosis-related genes. Müller cells are extremely sensitive to damage and can undergo gliosis before retinal neuronal cell death is detected. In response to damage, both Müller cells and astrocytes induce the expression of intermediate filament proteins, including vimentin, nestin, and glial fibrillary acidic

protein (GFAP). In addition, they suffer from hypertrophy, migration, and proliferation to protect neuronal cells (98,101–103).

It is generally assumed that activation of microglia and macroglial gliosis aim to protect retinal neurons to restore homeostasis. Nevertheless, under persistent injury, this process can become a chronic condition that eventually results in deleterious effects for the retinal integrity. Therefore, the precise function of activated microglia and macroglia remains controversial (104).

3. *CERKL*

This PhD thesis focuses on the gene *CERKL*, whose mutations are causative of two different IRDs: autosomal recessive retinitis pigmentosa (RP) and autosomal recessive cone-rod dystrophy (CRD). The study took advantage of a mouse model where *Cerkl* is depleted to dissect the specific role of CERKL in the retina and other neural tissues through molecular, cellular, and functional analyses.

3.1.   Discovery, mutations, and gene structure

Paradoxically, the gene *CERKL* (*CERamide Kinase-Like*) was discovered in two different groups almost at the same time but using dissimilar procedures to pursue distinct aims (105,106). Nonetheless, the group led by Dr Roser González was the first to publish the identification of the gene in 2004 by genetic diagnosis of Spanish families suffering IRDs and identification of the causative gene by linkage analysis and positional cloning (105). In this linkage study, the locus 2q31-q33 was shown to cosegregate in the analysed families (105,107). Afterwards, this autosomic recessive RP locus, named RP26, was finely mapped and refined until a previously unannotated gene, *CERKL*, was identified. *CERKL*, located between the *ITGA4* and the *NEUROD1* genes, was named *CERKL* because its cDNA, which spans 1,596 nucleotides and 13 exons, showed homology with several eukaryotic ceramide, sphingosine, and diacylglycerol kinases, but particularly with the human ceramide kinase (CERK) (29 % amino acid identity and 50 % similarity) (105). In addition to the identification of the *CERKL* gene in 2004, the IRD-causative homozygous nonsense mutation *CERKL*[R257X] —also known as *CERKL*[R283X]— was determined in the consanguineous analysed patients. This mutation results in a premature stop codon in exon 5 (105). Up to the present time, several studies have described more than 40 IRD-causative mutations in the *CERKL* gene yielding nonsense and missense alterations, as well as aberrant splicing and small and gross insertions and deletions (Table 1). Notably, these mutations are present in homozygous or compound heterozygous patients. Hence, mutations in *CERKL* are responsible for autosomal recessive IRDs.

Table 1. Classification of IRD-causative identified mutations in the gene *CERKL*. Information retrieved from The Human Gene Mutation Database (https://www.hgmd.cf.ac.uk/ac/index.php) in November 2023.

Nonsense and missense mutations				
Codon change	Localization	Amino acid change	Phenotype	Reference
GAG-TAG	c.193G>T	p.E65*	Retinal degeneration	(108,109)
CGT-AGT	c.316C>T	p.R106C	Retinal degeneration	(110)
CGT-TGT	c.316C>A	p.R106S	Retinitis Pigmentosa, autosomal recessive	(109)
GGT-GAT	c.356G>A	p.G119D	Cone-rod dystrophy	(111,112)
CTC-CGC	c.365T>G	p.L122R	Retinitis Pigmentosa	(113)
TGC-TGG	c.375C>G	p.C125W	Cone-rod dystrophy	(114)
CTA-CCA	c.398T>C	p.L133P	Retinitis Pigmentosa	(115)
TGG-GGG	c.451T>G	p.W151G	Retinal dystrophy	(116)
CCG-CTG	c.497C>T	p.P166L	Macular degeneration	(117)
AAA-TAA	c.598A>T	p.K200*	Retinitis pigmentosa	(118)
CAG-TAG	c.664C>T	p.Q222*	Retinitis Pigmentosa, autosomal recessive	(119)
GAT-GTT	c.674A>T	p.D225V	Retinitis pigmentosa	(120)
GGA-AGA	c.772G>A	p.G258R	Cone-rod dystrophy	(121)
CTG-CCG	c.812T>C	p.L271P	Retinitis pigmentosa	(122)
CGA-TGA	c.847C>T	p.R283*	Retinitis pigmentosa	(105)
ATA-ACA	c.890T>C	p.I297T	Retinitis pigmentosa and rod-cone dystrophy	(123)
TGC-TGA	c.999C>A	p.C333*	Cone-rod dystrophy	(124)
CGA-TGA	c.1090C>T	p.R364*	Cone/cone-rod dystrophy	(125)
TGT-TGA	c.1164T>A	p.C388*	Retinal degeneration, pericentral	(126)
CAG-TAG	c.1270C>T	p.Q424*	Retinitis pigmentosa	(127)
CGA-TGA	c.1381C>T	p.R461*	Retinitis pigmentosa	(128)
AGC-TGC	c.1651A>T	p.S551C	Macular and cone/cone-rod dystrophy	(129)

Continuation Table 1

Splicing mutations			
Splicing mutation	Localization	Phenotype	Reference
IVS1 ds +1 G-A	c.238+1G>A	Retinal degeneration	(130)
IVS1 ds +2 T-C	c.238+2T>C	Retinitis pigmentosa, cone-rod dystrophy	(131)
IVS2 ds +2 T-G	c.481+2T>G	Cone-rod dystrophy	(127)
IVS9 as -3 T-A	c.1212-3T>A	Retinitis pigmentosa	(132)
IVS11 as -3 C-G	c.1347-3C>G	Retinal dystrophy	(133)

Small deletions				
Mutation	Localization	Amino acid change	Phenotype	Reference
CACTT^139 GATCTtATTAATTTAA	c.420delT	p.(Ile141 Leufs*3)	Retinitis pigmentosa	(118)
ACTGT^149 GACATatGGTTTAGACA	c.450_451 delAT	p.(Ile150 Metfs*3)	Cone-rod dystrophy	(134)
GTA^204ACAA_EI_ GTAagTAATTTTCAG	c.613+4_613+5 delAG		Retinitis pigmentosa	(133)
TA^204ACAA_EI_ GTAAgtaaTTTTCAGAAT	c.613+5_613+8 delGTAA		Retinitis pigmentosa	(135)
TTTTCTAG_IE_ TGtT^254GTCTGTGTT	c.759delT	p.(Val254 Serfs*12)	Retinal dystrophy	(116)
AATGCT^278 GGGAtGGAAACAGAC	c.836delT	p.(Met279 Argfs*7)	Retinitis pigmentosa	(136)
GAATC^285 CTGACtCCTGTCAGAG	c.858delT	p.(Pro287 Leufs*10)	Retinitis pigmentosa	(118)
ATTGCAC^322 ATTatAATGG_EI_GTAAG	c.968_969 delTA	p.(Ile323 Asnfs*46)		(137)
GTTCTCA^348 GCCatGTTTGGCTTT	c.1045_1046 delAT	p.(Met349 Valfs*20)	Retinal dystrophy	(108)
AAA^383CTTAA_EI_ GTaagtCTTTTTCTTA	c.1151+3_1151+6 delAAGT		Retinitis pigmentosa	(133)
GCAGAA^387 GACTgtGAAATATCAT	c.1164_1165 delTG	p.(Cys388*)		(138)
CTGTT^493 GAGGAaGTAAAAGTTC	c.1482delA	p.(Val495*)	Retinal dystrophy	(139)

Continuation Table 1

Small insertions				
Mutation	Localization	Amino acid change	Phenotype	Reference
GGGCATC^52 TTCtGAGATCGGGA	c.156_157 insT	p.(Glu53*)	Retinitis pigmentosa	(136)
GCGAG^66CGAGC gagcACTGCGGTGG	c.197_200 dupGAGC	p.(Leu68 Serfs*15)	Macular degeneration, cone/cone-rod dystrophy	(132)
TGAGACT^490 TACttacACTGTTGAGG	c.1467_1470 dupTTAC	p.(Thr491 Leufs*4)	Retinitis pigmentosa	(140)
ATCAGT^547 CTTTctttATGGAGGAAG	c.1639_1642 dupCTTT	p.(Tyr548 Serfs*19)	Retinitis pigmentosa	(115)

Gross deletions			
Mutation	Localization	Phenotype	Reference
gDNA	Exon 1-2	Retinal degeneration	(141)
gDNA	Exon 2	Retinitis pigmentosa	(132)
gDNA	Exon 2	Macular degeneration, cone/cone-rod dystrophy	(133)
gDNA	Exon 1	Retinitis pigmentosa, cone-rod dystrophy	(131)
gDNA	Exon 2	Retinitis pigmentosa, cone-rod dystrophy	(131)

The human *CERKL* (h*CERKL*) gene, and its ortholog in mouse (m*Cerkl*), display a highly complex regulation in the retina, with several transcription start sites, alternative splicing events and translation start sites, thus yielding more than 20 different transcripts in the retina of both mouse and human. These variety of transcripts rises from the presence of differential transcription start sites (TSS): the commonly reported TSS at 5'UTR of h*CERKL*/m*Cerkl*, the TSS of the adjacent upstream gene h*NEUROD1*/m*NeuroD1*, an internal TSS in exon 1 (in human), and another internal TSS in exon 3 (142). Apart from the reported 13 exons that code for h*CERKL*, there is an extra exon between exons 4 and 5, named 4b, unique to the primate genomes (Figure 9A). Given that, in the human retina four main isoforms were first determined: the full-length isoform, CERKLa, which spans the described 13 exons (GenBank accession number AY357073); the longest isoform, CERKLb, which harbours the 4b exon (GenBank accession number AY690329); CERKLc isoform,

which results from an alternative splicing event that excludes exons 3, 4, 4b and 5 (GenBank accession number AY690330); and CERKLd isoform, which is the outcome of alternative splicing from exon 3 to exon 6 (GenBank accession number AY690331) (Figure 9B) (143). Nevertheless, many additional isoforms are also generated using alternative translation initiation sites located downstream, with potential initiating methionines within exons 5, 6 (in mouse), 7, 10 and 13 (in human) (142). On the contrary, the ortholog gene in zebrafish (ZF*cerkl*) only gives rise to three transcripts (144).
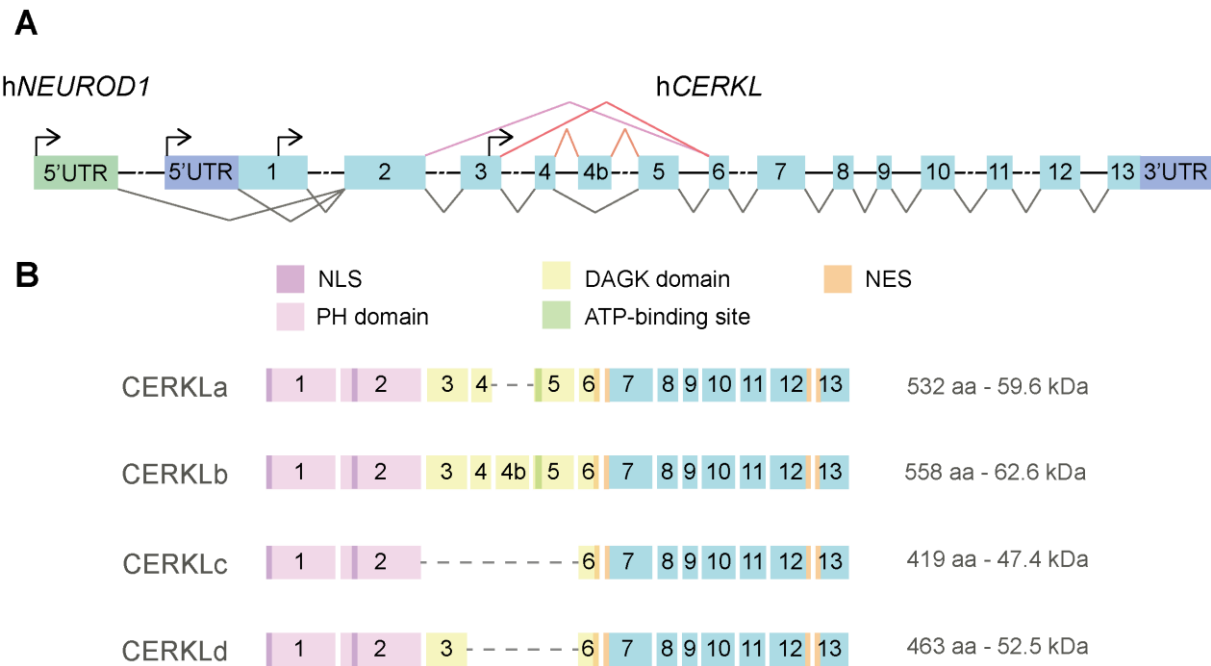
Figure 9. Gene structure and reported isoforms of human *CERKL* (h*CERKL*). (A) Structure of human *CERKL* showing all the exons (light blue squares) and UTRs (dark blue squares), as well as human *NEUROD1* (h*NEUROD1*) 5'UTR (green square). Black arrows indicate differential transcription start sites. Splicing events are indicated in grey, while alternative splicing events leading to CERKLb (orange), CERKLc (pink) or CERKLd (red) are represented in colour. (B) Representation of the principal isoforms of CERKL including the protein domains encoded and the approximate molecular weight size. NLS: nuclear localization signal; PH domain: pleckstrin homology domain; DAGK domain: diacylglycerol kinase domain; NES: nuclear export signal; aa: amino acid; kDa: kilodalton.

The estimated peptidic sequence of the CERKLa isoform codes for a 532-amino acid protein, with a molecular weight of 59.6 kDa. Various investigations predicted a putative pleckstrin homology (PH) domain and diacylglycerol kinase (DAGK) signatures, including an ATP-binding site, in the CERKLa protein isoform via sequence

homology studies (106,143,145). Furthermore, other functional analysis deducted two nuclear localization signals (NLS), one located at the beginning of exon 1 and other in the exon 2 (146); in addition to two nuclear export signals (NES) in the terminal part of the DAGK domain (145). The protein isoforms yielded from alternative splicing events display differential protein domains depending on the included or excluded exons. The CERKLb isoform incorporates 26 additional amino acids in-frame within the DAGK catalytic domain, whereas CERKLc and CERKLd isoforms are devoid of most of the DAGK domain (Figure 9B) (143).

3.2. Basic research: tissue expression, subcellular localization, and functions

h*CERKL*, m*Cerkl* and ZF*cerkl* mRNAs have been primarily detected in the human, mouse and zebrafish retinas at different developmental stages (147,148), as well as in other tissues, including brain, kidney, liver, lung, ovary, spleen, and testis (105,106,142,144). m*Cerkl* and ZF*cerkl* mRNAs are predominantly expressed in the ganglion cell layer of mouse and zebrafish retinas respectively, although it can also be faintly detected in the inner nuclear and photoreceptor cell layers (105,144). In more exhaustive studies, CERKL protein was immunodetected in mouse and zebrafish retinal cryosections localizing intensely in the OSs of cones, as well as faintly detected in rods. Additionally, CERKL was situated perinuclearly in some cells of the ONL, as well as in RPE, amacrine, bipolar, and retinal ganglion cells (142,147–149).

CERKL subcellular location presents a highly dynamic pattern. Overexpression of tagged CERKLa, CERKLb, CERKLc and CERKLd isoforms in COS cells (fibroblast-like cell lines derived from monkey kidney tissue) showed similar subcellular distribution for all isoforms, localizing at the cytoplasm, endoplasmic reticulum, Golgi, mitochondria, nucleus, and nucleolus. In contrast, the *CERKL^{R257X}* mutant was retained in the nucleus but did not localize at the nucleolus, and the *CERKL^{R106S}* mutant (missense mutation affecting the second NLS) was accumulated in the cytoplasm (106,143,146,149). Consistently, immunodetection of endogenous CERKL protein in ARPE-19 (a cell line of human RPE cells) and 661W (an immortalized mouse photoreceptor cell line) cells revealed variable distribution between the cytoplasm, perinuclear region, and nucleus, although the nucleolar localization was not detectable (147).

INTRODUCTION

Given its homology with CERK, CERKL was predicted as a lipid kinase enzyme. Nonetheless, numerous studies led by different research groups were not able to detect any lipid-binding capacity or lipid-phosphorylation activity of CERKL. Consequently, it has not been demonstrated yet that CERKL functions as a lipid kinase (106,143,146,150).

Several studies have proposed CERKL as a stress-response protein, as it is able to protect cells from oxidative stress-induced damage and apoptosis (143,148,149). Interestingly, as many antioxidant proteins, *CERKL* expression is boosted in response to stress injury. Additionally, CERKL protein levels are enriched upon hypoxia due to deubiquitination and inhibition of pVHL-mediated proteasomal degradation (148,149). In fact, overexpression of CERKL provides protection against oxidative stress, while CERKL downregulation promotes higher susceptibility to damage in cell culture (143,149). Although the exact stress-protective mechanism of CERKL remains elusive, various investigations reported that, in response to light/oxidative stress *in vitro* and *in vivo*, CERKL protein shifts its diffuse cytoplasmic location to form punctuated aggregates in the cytoplasm (148,149,151). *In vitro* analysis described colocalization of overexpressed CERKLa isoform with stress assemblies, including stress granules and P-bodies, upon oxidative stress conditions, while the *CERKL^{C125W}* mutant (missense mutation in the PH domain) did not localize to stress assemblies or the nucleus. Furthermore, in the absence of stress, CERKLa isoform was also observed to interact with mRNAs, translation machinery, and microtubules (151). Moreover, CERKL protein interacts with the mitochondrial antioxidant enzyme TRX2 —via PH domain— and maintains it in its reduced form (149). Beyond that, CERKL regulates autophagy through the regulation of the stability and function of SIRTUIN-1 (SIRT1), a deacetylase of ATG proteins. Therefore, autophagy is downregulated in *CERKL*-depleted ARPE-19 cells (152).

CERKL also interacts with several neuronal sensor calcium (NCS) proteins, including guanylate cyclase activating protein 1 and 2 (GCAP1 and GCAP2), RECOVERIN, and calcium and integrin binding 1 (CIB1). The interaction between CERKL and GCAP1 or GCAP2 is specifically mediated by the PH domain of CERKL. Notably, this interaction is not essential to localize CERKL at the OS of cone

photoreceptor cells, although it might be indicative of the implication of CERKL in the regulation of light transduction and calcium signalling pathways, thus affecting photoreceptor cells survival (150).

Besides CERKL function in the retina, recent studies have shown that CERKL contributes to antioxidant activities in other tissues. In cutaneous squamous cell carcinoma, CERKL is upregulated to maintain cellular sphingolipids and protect cancer cells from oxidative damage (153). Moreover, overexpression of CERKL in a mouse model of cerebral ischemia reperfusion relieved the induced oxidative damage and apoptosis (154). Recently, it has also been reported an unknown function of CERKL in association with antiviral response in zebrafish. The authors described that CERKL interacts with and regulates the ubiquitin-mediated degradation of the host-immune-response protein TBK1 (TANK-binding kinase 1) and the viral protein SVCV P (spring viremia of carp virus phosphoprotein). So that CERKL increases the stability and levels of TBK1 and directs SVCV P protein for degradation, thereby enhancing the fish immune response and declining viral activity (155).

3.3.   Animal models: mouse and zebrafish

In pursuit of unveiling the role of CERKL in the retina and the pathogenic mechanisms in which it is involved, several knockdown (KD) and knockout (KO) animal models generated by deletion of different regions of the *Cerkl* gene have been characterized.

In a first approach to generate a *Cerkl* KO mouse model, the exon 5 of *Cerkl* was deleted to produce a mutated and inactive CERKL protein, which lacks part of the DAGK domain and the putative ATP-binding site (156). Exon 5-directed deletion was performed using Cre/LoxP technology. It involved flanking the target region –exon 5– with LoxP sequences (locus of x-over, P1) that were then recognized by Cre recombinase. This process generated a recombination between LoxP sequences, effectively eliminating the region in-between (157). However, this mouse model did not show any sign of retinal degeneration or impact in the levels of ceramide and ceramide-1-phosphate (Figure 10) (156).
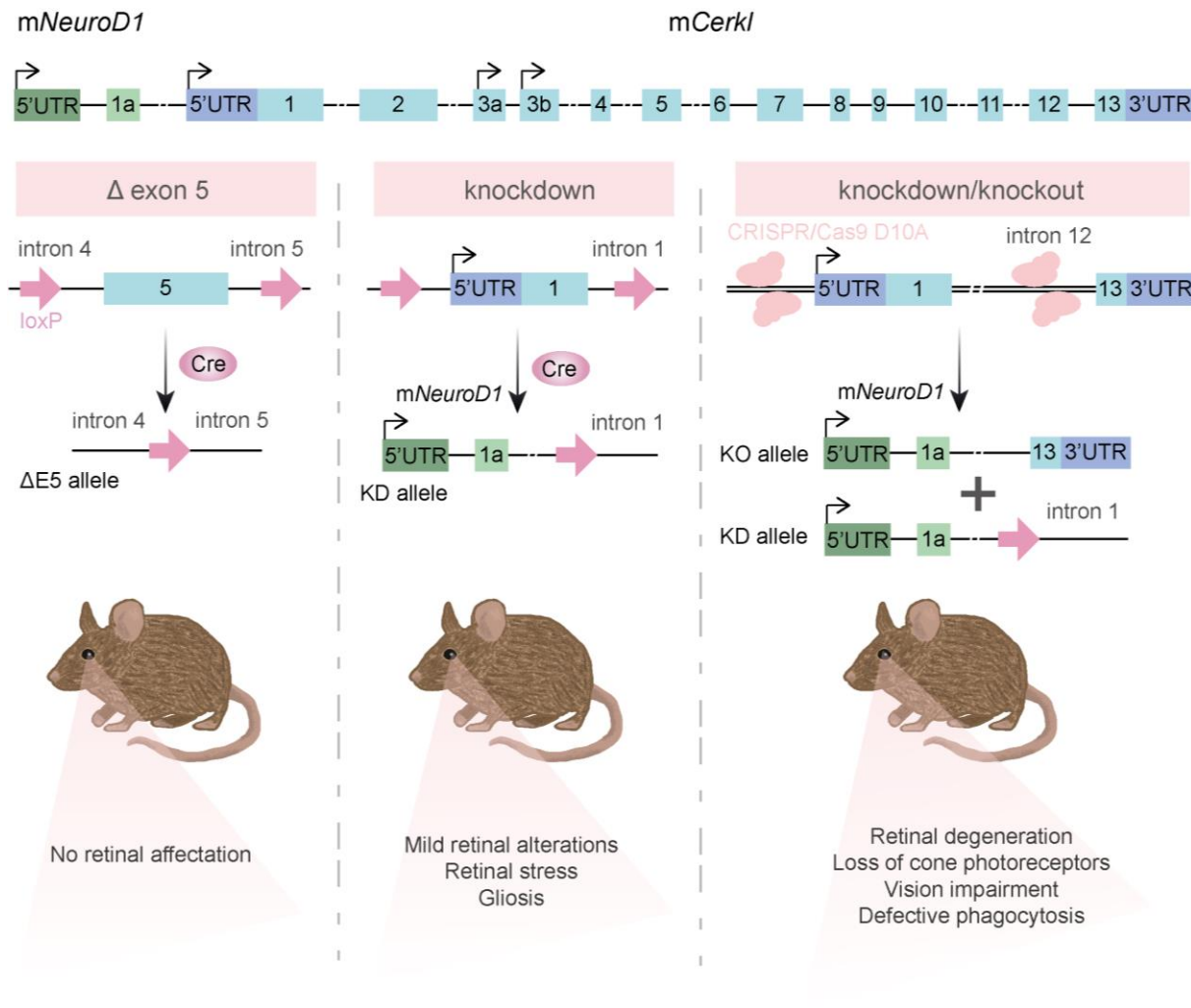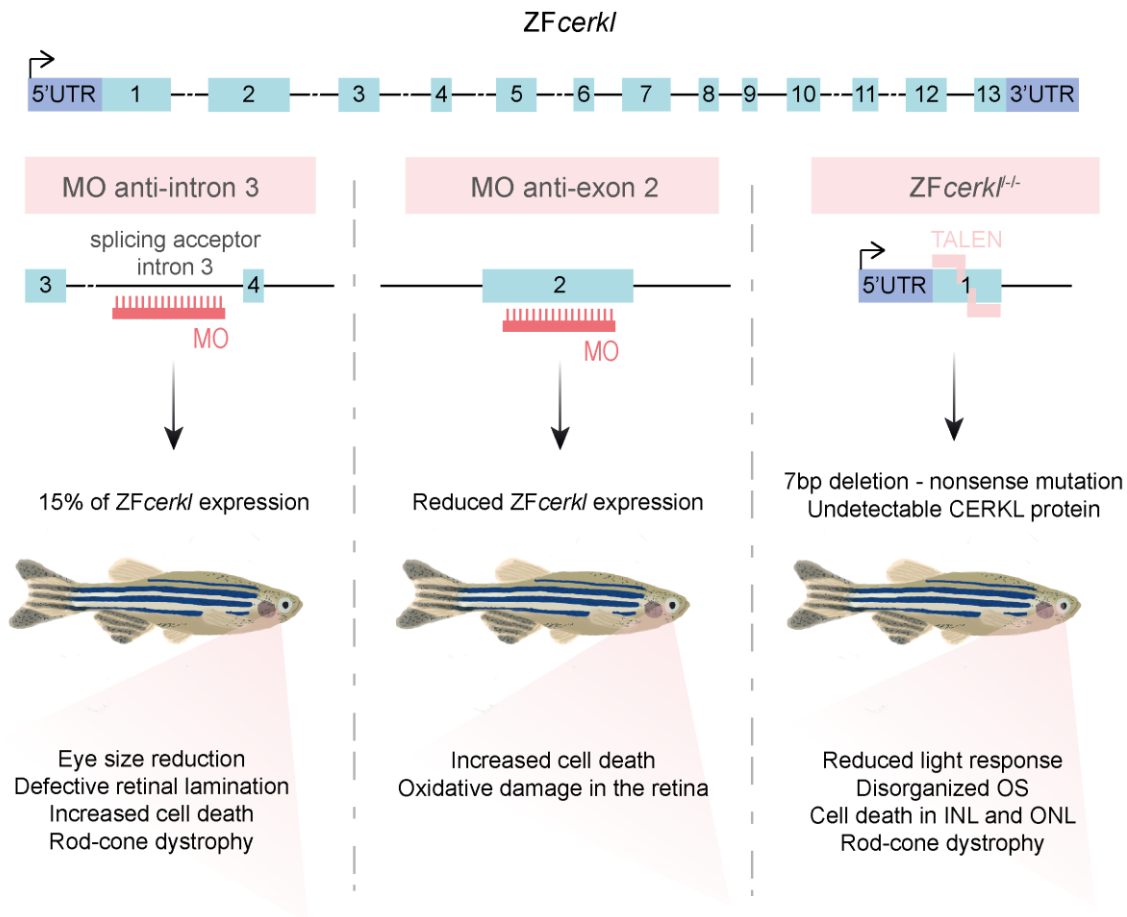
Figure 10. Mouse models of *Cerkl* generated using gene-editing techniques. Representation of mouse *Cerkl* gene (m*Cerkl*) including its exons (light blue) and UTRs (dark blue), as well as the mouse *NeuroD1* (m*NeuroD1*) represented in green, in the upper part of the image. In the lower part of the image, graphical representation of the generation and alterations of the different mouse models to study CERKL. Left panel: deletion of exon 5 using Cre/LoxP technology generated a mouse model without retinal affectation (156). Middle panel: deletion of proximal promoter and exon 1 yielded a knockdown mouse model with mild retinal alteration (158). Right panel: knockout allele was generated using CRISPR/Cas9 D10A tool. *KD/KO* mouse model suffers from retinal degeneration and vision impairment (159).

Later, in our research group, the proximal promoter and exon 1 (2.3 kb) were excised using Cre/LoxP system with the aim of generating a *Cerkl* KO mouse model. Nonetheless, this targeted deletion resulted in a KD more than a KO model because of the presence of functional alternative promoters (unreported at that time) directing up to 35 % of *Cerkl* expression. The homozygous *Cerkl* KD model did not present any gross morphological or structural alteration in the retina, although clear and

consistent signals of retinal stress, gliosis and apoptosis were detected. Functional impairment at the GCL was also observed in this mouse model (Figure 10) (158). In addition, lipidomic analysis of *Cerkl* KD retinas yielded a decrease in specific sphingolipid content, particularly of the glucosyl/galactosyl ceramide species while the phospholipid and neutral lipid content stood unaffected (159).

Finally, the complete locus of *Cerkl* was eliminated using CRISPR/Cas9 in our group (159). CRISPR/Cas9 editing technology has been widely applied to generate disease models, gene therapies, transcriptional modulation, and diagnostics. The CRISPR system (clustered regularly interspaced short palindromic repeats) consists of a single guide RNA (sgRNA) that recognizes a specific region of the target DNA and directs the Cas9 protein (CRISPR-associated protein), an endonuclease, to promote a DNA double-strand break at the target site. Then, the DNA can be repaired by the cell by either non-homologous end joining (NHEJ) or using a template of single-stranded donor oligonucleotides (ssODNs) by homology directed repair (HDR) (160,161). In this study, in order to diminish the frequency of off-target effects, the D10A Cas9 nickase was used. This nickase produces DNA single-strand breaks, thus needing two sgRNAs to eventually generate a DNA double-strand break. So, four sgRNAs were needed, two located upstream the proximal promoter and two in the intron 12, as well as ssODNs to facilitate the generation of the recombinant deletion allele lacking 97 kb. Mating of heterozygous *Cerkl*$^{WT/KO}$ mice did not generate any pup homozygous for the *Cerkl* deletion, suggesting developmental lethality. Therefore, turning to account the previously generated *Cerkl* KD mouse model and this new complete deletion, a novel animal model was obtained by combining the two recombinant alleles: the double heterozygote *Cerkl*$^{KD/KO}$ (henceforth referred as *KD/KO*) mouse model, in which the expression of *Cerkl* is drastically reduced to less than 10 %. *KD/KO* retinas presented decreased number of cones and progressive loss of photoreceptor cells. Moreover, different morphological alterations were observed in the OS of photoreceptor cells, including poorly stacked membranous disks and longer OSs, suggesting defective RPE phagocytosis. Finally, electrophysiological recordings showed progressive vision impairment, closely mimicking the disease progression in human patients carrying mutations in *CERKL* (Figure 10) (159).

Figure 11. Zebrafish models of *Cerkl* generated using gene-editing techniques. Representation of zebrafish *cerkl* (ZF*cerkl*) including its exons (light blue) and UTRs (dark blue) in the upper part of the image. In the lower part, graphical representation of the generation and alterations described in the different zebrafish models to study CERKL. Left panel: knockdown model using morpholino (MO) against the splicing acceptor site in intron 3-exon 4 (144). Middle panel: knockdown model generated through MO against exon 2 (149). Right panel: ZF*cerkl*⁻/⁻ model produced through TALEN system (163).

Besides mouse models, several zebrafish models have been generated and studied. Given that m*Cerkl* presents an elevated transcriptional complexity and ZF*cerkl* only generates three transcripts, zebrafish seemed a suitable and easy tool to generate *cerkl* KO models. Morpholinos (MOs) represent a simple manner of generating KD models in zebrafish. MOs are antisense oligonucleotides that precisely target translation or splicing of a specific mRNA, thus abolishing gene expression (162). Two different studies analysed ZF*cerkl* KD MO-zebrafish models and observed retinal cell death (144,149). Morphological analysis revealed defective lamination in all retinal layers, as well as reduced eye size (Figure 11) (144).

Furthermore, KD of ZF*cerkl* resulted in an augmentation of different oxidative damage biomarkers, such as 4-hydroxy-nonenal (Figure 11) (149).

Ultimately, a KO zebrafish model was generated by using TALEN machinery (Transcription Activator-Like Effector Nuclease). TALENs are custom-designed endonucleases that target DNA sequences with high specificity and bind there to induce a DNA double-strand break at that precise location. Then, the cell can repair the double-strand break through NHEJ or HDR (164). By means of TALEN technology, the target-cut sites were located at the first exon of ZF*cerkl* to generate mutations by NHEJ and inactivate the entire protein. A 7-bp deletion producing a frame-shift alteration was generated and homozygous zebrafish carrying this mutation, ZF*cerkl*$^{-/-}$, exhibited complete abolition of CERKL expression. ZF*cerkl*$^{-/-}$ animals showed reduced light response and retinal degeneration, being the rod photoreceptors affected first, and later, the cone photoreceptors. Additionally, the OS of photoreceptors displayed different alterations, including disorganized disks and detachment from RPE, suggesting a defect in RPE phagocytosis (Figure 11) (163). Besides, autophagy was impaired in ZF*cerkl*$^{-/-}$ retinas before degeneration (152).

3.4. 2D and 3D iPSC-derived retinal models

Aside from the clear advantages derived from the use of animal models in expanding the knowledge about developmental, physiological, and functional attributes of the retina, there are noticeable disadvantages, such as the physiologically differences between rodents and human, including the absence of fovea in rodents and differences in colour vision. Consequently, the scientific community is increasingly moving towards the use of *in vitro* induced pluripotent stem cell (iPSC)-derived 2D and 3D retinal models as an unlimited and ethically acceptable alternative. Hence, in less than a decade, 3D retinal organoids have been largely employed to study the pathogenic mechanisms of many IRDs and have also facilitated the development of novel therapies (165).

The discovery of embryonic stem cells and the posterior generation of iPSCs from somatic cells has brought about a revolution in the scientific community to boost biomedical stem-cell research and production of stem cell-derived somatic cells or tissues (166). As pluripotent cells, iPSCs can give rise to all cell types of cell lineages

—comprising retinal cell types— when cultured and incubated with precise and appropriate fate-specification factors in an *in vitro* environment (167). Notably, human iPSCs (hiPSCs) derived from somatic cells conserve the genome of the donor individual, therefore, they maintain the same genetic background and cellular context to characterize the disease mechanisms of genetic disorders (168). This provides an excellent opportunity to perform a personalized characterization of patients, as well as to generate or correct concrete mutations using gene-editing techniques (169).

In the retinal context, iPSCs can be differentiated into several retinal cell types to analyse the specific features and phenotypic traits in IRD-models. Therefore, the obtention of iPSC-derived 2D cultures of RGCs, photoreceptor precursor cells and RPE cells has meant a great progress in the field (170–172). However, iPSC-derived 2D cultures do not completely mimic the structural, physiological, and functional features of the entire retina. Therefore, to address this limitation and recreate the natural cell interactions and signalling processes, 3D retinal organoids offer a reliable and effective model for studying and analysing retinal disorders (165).
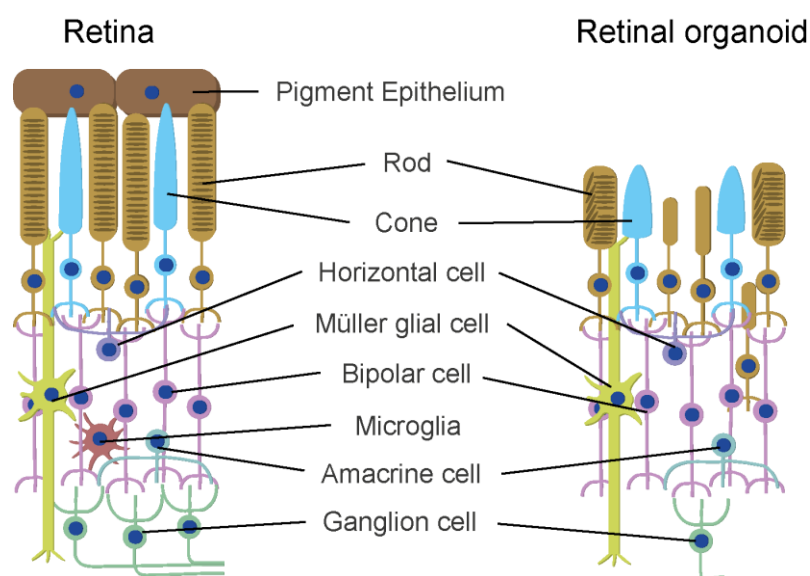
Figure 12. Comparison between the retina and retinal organoids. Both structures contain layer-organized cell types, although retinal organoids lack some cell types, such as microglia and RPE cells. Moreover, photoreceptors in retinal organoids present shorter OSs with disorganized membranous disks. Image inspired in (173).

Retinal organoids require a prolonged culture to fully differentiate into a tissue that structurally, physiologically, and functionally highly resembles the natural retina

(further explained in Results Chapter 3). Retinal organoids present a laminar structure containing different cell types, including rod and cone photoreceptor cells, RPE cells, bipolar cells, amacrine cells, RGCs and Müller glia. However, the OSs are shorter, and the membranous disks are not properly stacked in photoreceptor cells from retinal organoids. When present, the RPE is juxtaposed to photoreceptor cells forming a clump, instead of a monolayer (Figure 12) (173). Nonetheless, retinal organoids represent an amenable and suitable tool to study retinal development, characterize retinal diseases and test the impact of novel therapies in human tissues (174). Thus, many authors have developed retinal organoid models of several IRD-causative genes, including mutations in *CEP290*, *PDE6B*, *RPGR*, *RPE65* and *ABCA4* (175–179).

4. Therapeutic approaches for inherited retinal dystrophies

IRDs are the leading cause of blindness in the Western world and, until recently, they were considered untreatable. However, the retina is an exceptional model for developing therapies for hereditary rare diseases, thanks to its immunoprivilege and easy access for delivery of therapeutic agents. In addition, the efficacy of the treatment can be simply evaluated using non-invasive structural and functional assays (180).

The heterogeneous nature of IRD-causative mutations requires different therapeutic approaches, including gene replacement/augmentation, gene silencing/editing of the mutated gene, or altering the expression of a modifier gene that improves cellular function by affecting the upstream or downstream pathways in which the causative gene is involved. In addition, several vectors, and routes of administration appropriate to target the affected region or specific cell type of interest have been and are still being developed (181).

Gene augmentation therapies consist in supplying a "healthy" or functional copy of the damaged/dysfunctional gene of interest to increase the production of the functional protein and restore its normal function. This approach is the usual choice in loss-of-function mutations in recessive patterns of inheritance, such as the addition of *RPE65* gene in LCA patients (182). In contrast, to address the effects of dominant mutations, where the produced altered protein interferes with the normal function of the wild-type protein, gene silencing strategies involving interference RNA (iRNA), microRNA (miRNA) or antisense oligonucleotides (AONs) are usually preferred. These strategies aim to repair or silence the mutated gene and mitigate the adverse effects of the mutant protein, e.g. AON-based therapy to correct splicing defects in *ABCA4* gene (183,184).

Gene-therapy systems can be delivered using several routes of administration, either systemic or localized. Localized routes are usually preferred to avoid unspecific effects in non-ocular tissues and reduce the risk of immunogenicity. Depending on the nature of the selected vector and therapy, invasive and non-invasive routes can be used. Nevertheless, invasive ocular delivery routes, such as subretinal injection, provide a more restricted delivery, increasing the bioavailability of the therapeutic

product in the target tissue. However, these methods typically need skilled and experienced surgeons and present higher risk of complications, including retinal detachment, infections, and haemorrhage (185).

In this section, two leading vectors for gene-augmentation therapies will be discussed in detail: viral- and nanoparticle-mediated systems. Besides, other therapeutic strategies aside from gene-augmentation tools will be introduced briefly.

4.1. Viral-based therapies

In the last years, several viral and nonviral vectors have been analysed for their transduction efficacy in the retinal cells most affected in IRDs, namely, RPE and photoreceptor cells. To do so, gene transfer vectors usually display cellular specificity —tropism—, thus transducing only target cells. As IRDs require permanent correction, the transgene expression is usually needed to be long-lasting. Additionally, non-integrative vectors are preferred in order to avoid the adverse effects of integration following insertional mutagenesis. Various recombinant viral vectors that are replication deficient and exhibit different cargo limits, integration capacities, cellular tropism, transduction efficiency, and risk of immune responses, have been extensively employed for delivering the healthy gene into diseased retinas (gene replacement therapy). These vectors include adenoviruses (Ads), lentiviruses (LVs), and mostly, adeno-associated viruses (AAVs) (Figure 13) (181).
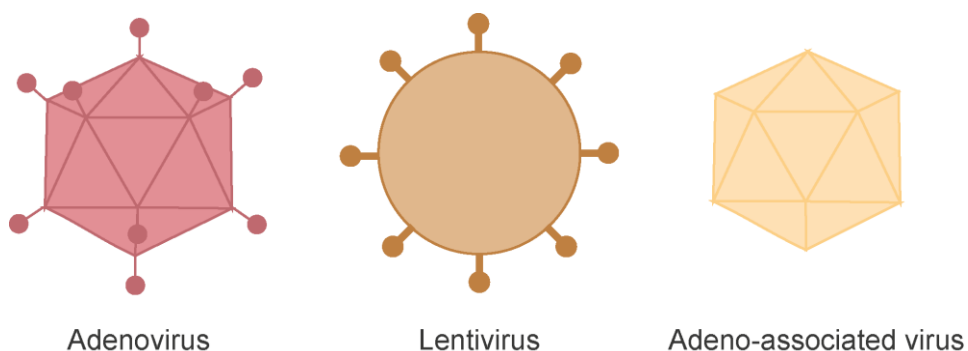
Figure 13. Illustration of the viral vectors used in gene therapy. From left to right, adenovirus, lentivirus, and adeno-associated virus.

Ads are DNA viruses that can infect cells regardless of their replication state. They replicate in the nucleus without integrating in the host genome. Adenoviral vectors present a large cargo capacity (up to 36 kb) and transduce many different cell types.

INTRODUCTION

Vectors derived from human Ad2 and Ad5 serotypes were tested as some of the first viral delivery systems for retinal gene therapies. However, the presence of neutralizing pre-existing antibodies in the host usually leads to the clearance of these vectors (186,187).

LVs are retroviruses with a packaging capacity of 8 kb. Nevertheless, they exhibit two main drawbacks. First, LVs integrate into the host genome, carrying the risk of insertional mutagenesis. This limitation can be overcome with the use of integration-deficient LVs, which have been successfully tested in mice (188). Second, LVs do not effectively transduce photoreceptor cells, yielding infection percentages that are insufficient for therapeutic purposes, although they are capable of transducing RPE cells (189).

AAVs are single-strand DNA parvoviruses with a cargo capacity of 4.7 kb. They have been extensively used in gene therapy approaches for IRDs, due to their negligible pathogenicity, positive immunogenic profile, non-integrating nature without the rep protein, stable transgene expression and expansive retinal tropism. There are 13 different serotypes of AAVs isolated from primates (AAV1-AAV13) displaying differences in the capsid conformation and other features, particularly concerning tropism. Furthermore, AAVs can be modified by pseudotyping of cross-packaging, a process in which the viral genome of an AAV serotype with a transgene is packaged into the capsid of a different serotype, e.g. AAV2/8 is a pseudotype containing the genome of AAV2 serotype into the AAV8 capsid. The choice of the serotype and pseudotype is relevant for the optimal design of the therapeutic strategy (190). Up to now, the serotypes or pseudotypes AAV2/5, AAV2/8, and AAV8 have been used in dozens of clinical trials to treat IRDs (Table 2). Interestingly, the first approved gene therapy, under the name of Luxturna, used AAV2 system to treat autosomal recessive *RPE65*-associated LCA and proved that gene-augmentation and viral-delivery could be safe and effective (182,191,192). Recently, the pseudotype AAV2/7m8 has been reported to have superior transduction in retinal organoids (193). Moreover, different approaches have been developed to overcome the limited packaging capacity of AAVs, such as dual AAV vectors or intein technology, in which the final RNA or protein —respectively— are "fragmented" and delivered by different vectors administered at

the same time to achieve an *in vivo* "reconstruction" of the therapeutic molecule (194–196).

Table 2. Currently active clinical trials using AAV delivery system for IRDs, indicating the number of the clinical trial (NCT number), as well as the treated condition, causative gene and intervention. Information retrieved from ClinicalTrials.gov (https://clinicaltrials.gov/) in November 2023.
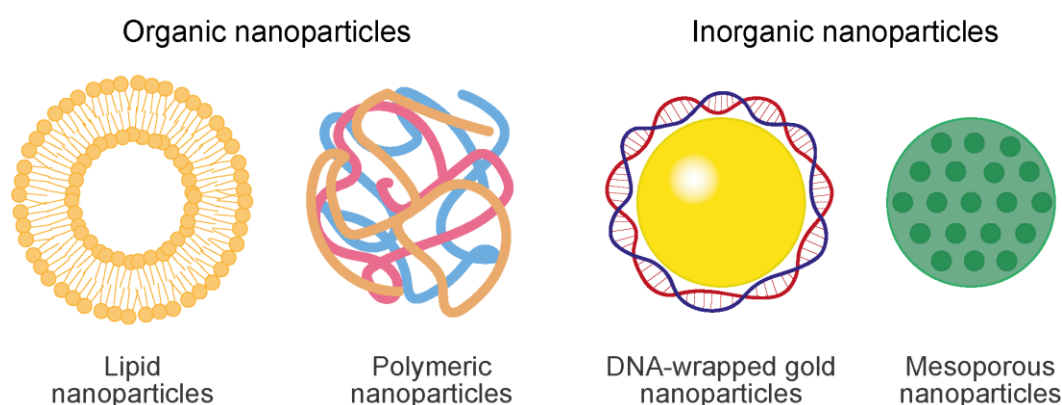
NCT Number	Conditions	Causative gene	Interventions
NCT04517149	X-Linked Retinitis Pigmentosa	*RPGR*	BIOLOGICAL: 4D-125
NCT00999609	Leber Congenital Amaurosis	*RPE65*	BIOLOGICAL: AAV2-hRPE65v2, voretigene neparvovec-rzyl
NCT05748873	Retinitis Pigmentosa	*RHO*, *PDE6A*, or *PDE6B*	DRUG: SPVN06
NCT03584165	Choroideremia X-Linked Retinitis Pigmentosa	*RPGR*	GENETIC: BIIB111 GENETIC: BIIB112
NCT03328130	Retinitis Pigmentosa	*PDE6B*	BIOLOGICAL: AAV2/5-hPDE6B
NCT04945772	Retinitis Pigmentosa		BIOLOGICAL: Gene Therapy Product-MCO-010
NCT03316560	X-Linked Retinitis Pigmentosa	*RPGR*	BIOLOGICAL: rAAV2tYF-GRK1-RPGR
NCT03326336	Non-syndromic Retinitis Pigmentosa		COMBINATION_PRODUCT: Gene therapy: GS030-DP AND Medical device: GS030-MD
NCT04850118	X-Linked Retinitis Pigmentosa	*RPGR*	BIOLOGICAL: rAAV2tYF-GRK1-hRPGRco
NCT05694598	Bietti Crystalline Dystrophy	*CYP4V2*	GENETIC: VGR-R01

4.2. Nanoparticle-mediated delivery

To overcome the hurdles of the limited capacity in AAVs and associated immunogenic responses, nanoparticles (NPs) offer a promising prospect as a nonviral system for delivery of therapeutic molecules to the retinal cells (197). According to their nature, NPs can be classified into organic and inorganic NPs. Organic NPs include lipid-based and polymeric NPs, whereas DNA-gold NPs, quantum dots, nanotubes and mesoporous NPs are considered inorganic NPs (Figure 14) (198). The different types of NPs allow the personalized optimization of delivery platforms, as

they possess the potential to enhance the solubility and stability of the cargos, elevate secure transport through biological membranes, and extend the circulation and tissue-specific expression of the therapeutic reagent, thus increasing the safety and efficacy of the delivered treatment (199). To date, several NP-based therapies and diagnostics have been clinically approved by the FDA (U. S. Food and Drug Administration) (200).

Organic nanoparticles   **Inorganic nanoparticles**

Lipid
nanoparticles

Polymeric
nanoparticles

DNA-wrapped gold
nanoparticles

Mesoporous
nanoparticles

Figure 14. Graphical representation of the different nanoparticles used as vectors in gene therapy. Lipid and polymeric nanoparticles are organic, whereas DNA-wrapped gold and mesoporous nanoparticles are inorganic.

Lipid-based NPs are spherical structures formed by a lipid bilayer surrounding an internal aqueous compartment (201). Liposomes, a subtype of lipid-based NPs, have several clinical applications as they can carry hydrophilic, hydrophobic, and lipophilic drugs due to their flexible biophysical properties (200). Indeed, a clinically approved treatment for macular degeneration, vorteporfin, efficiently uses liposomes as delivery system (202). Lipid NPs, another subclass of lipid-based NPs, are extremely manipulable and modifiable structures and are generally used for nucleic acid delivery. However, their clinical applications are hindered by the difficulty to control their properties –size, uniformity, and stability– *in vivo* (203,204).

Polymeric NPs are a heterogeneous group of structures synthesized from monomers and polymers of natural or synthetic sources. They are biocompatible, simple, water soluble, and stable, which makes them ideal delivery vehicles for gene therapy, although some risk of particle aggregation toxicity still remains. Therapeutic reagents can be encapsulated within polymeric NPs core, but they can also be

chemically conjugated or bound to the polymeric NP surface, enabling the delivery of hydrophilic and hydrophobic substances (205).

Inorganic NPs are constituted of inorganic materials, including gold, silica, and iron, and can be formulated into various sizes, geometries, and structures. Inorganic NPs display unique optical, physical, electrical, and magnetic features depending on the base material, which offers a bright future for gene- and drug-therapy delivery applications (206). For example, gold NPs present free electrons on their surface in a constant oscillation state at a given frequency, which confers photothermal and plasmonic properties. As a result, gold NPs can be temporarily activated using light to penetrate the plasma membrane of the cells without disturbing it. In addition, they are non-toxic and offer a great flexibility in cargo packaging and tissue- or cell-specificity (207). As another example of inorganic NPs, mesoporous silica NPs are porous structures made of silica with unique physicochemical characteristics. Their surface area, pore sizes, and volumes can be easily modified, conferring versatility in terms of therapeutic substance encapsulation. Additionally, they seem to exhibit low toxicity and biocompatibility (208).

4.3.   Other therapeutic strategies

Besides the great advances in gene-augmentation therapies, the extensive genetic heterogeneity of IRDs necessitates progress in alternative therapeutical approaches. In this context, promising therapeutic strategies for IRDs encompass antisense oligonucleotides (AONs), CRISPR/Cas9, neuroprotection and optogenetic mechanisms.

AONs are synthetic short single-stranded nucleic acids that complementary bind a mRNA to modify its translation, promote its degradation by RNase-H cleavage, alter splicing or promote exon skipping or insertion. In this manner, AONs change the final gene product before the pathogenic protein is produced. Despite of the gene-silencing function of AONs, the most recent applications are focused on splicing activity to promote exon skipping and block splicing integration to avoid the disturbance of downstream reading frames and correct mutations that introduce a pseudoexon (209). Various preclinical and clinical studies have yielded favourable results of the use of AONs to correct splicing mutations in IRDs (184,210,211).

INTRODUCTION

Although the backbone of AONs can be easily degraded within cells, several structural modifications have been developed to prolong AONs half-life and promote its function. In fact, recent work has shown that when the protein has an extremely low turnover, the therapeutic effect of AONs can least *in vivo* more than a year after the delivery (211).

The continuous and expansive advancements in gene-editing tools offer a remarkable potential system for correcting mutations causing IRDs. In recent years, base and prime editing tools have emerged from CRISPR/Cas9 system. These new technologies not only have the capability to address all types of point mutations, but also to introduce insertions and deletions. However, the existence of off-target effects remains a challenge to be addressed (212). The application of this system to reverse IRD-causative mutations in hiPSC has demonstrated positive results (169,177).

Irrespective of the causative mutation and gene, most IRDs share common pathogenic mechanisms and outcomes, namely the death of photoreceptor cells that eventually leads to sight loss. Personalized medicine is usually difficult to develop and only a few patients can exploit its benefits. Therefore, the development of mutation-independent therapeutic approaches represents a valid alternative and/or complementary approach to gene-specific treatments. In this regard, therapies based on neuroprotection systems aim to minimize or delay cell attrition in diseased retinas by targeting common dysregulated pathways that cause retinal damage. Neurotrophic and antioxidant factors generally have short half-lives and require from frequent administration to preserve the appropriate therapeutic levels (213). To overcome this problem, several studies have taken advantage of the use of AAVs to overexpress a specific neurotrophic or antioxidant factor and their results indicate that neuroprotective therapies promote cell survival and retinal homeostasis in different IRD-related mouse models (214–216).

Finally, for patients at advanced stages of the disease, where severe loss of photoreceptors has already occurred, the optogenetic approach renders a significant opportunity to restore some degree of vision irrespective of the causative mutation and affected gene. Optogenetics involves the ectopic expression of light-gate microbial channelrhodopsin proteins (ChRs) into surviving second- and third-order

retinal neurons, making them light-sensitive neurons (217,218). This therapeutic platform has already advanced into early clinical trials and have yielded beneficial results in many treated patients (219).

In the recent years, the development of a comprehensive compendium of therapies for IRDs has significantly contributed to the evolution and cure of these diseases once considered incurable conditions. Despite these advancements, IRDs are a genetically and clinically heterogeneous group of pathologies, limiting the efficacy of precision medicine to a subset of patients. However, the field of therapeutic strategies is still in its infancy, and in the near future, an increasing number of novel therapies, using innovative vectors, are expected to be developed. This holds the promise of providing hope to a broader spectrum of patients.

Several years and intensive efforts have been dedicated to the understanding and dissection of CERKL function in the retina in health and disease. However, a substantial amount of information remains to be determined. Considering the collective background knowledge and previous results, the principal objective of this PhD thesis has been to assess the involvement of CERKL in the response to stress, focusing on mitochondrial dynamics and metabolism, as well as to obtain reliable phenotypic biomarkers of the disease progression in the $Cerkl^{KD/KO}$ mouse model to finally design gene addition therapeutic approaches aimed to rescue or ameliorate the phenotypic alterations associated to CERKL depletion. Therefore, the specific aims of this work are:

1. Dissection of the role of CERKL in mitochondrial dynamics and metabolism.

    1.1. Analysis of mitochondrial dynamics and function in $Cerkl^{KD/KO}$ mouse retinas.

    1.2. Study of mitochondrial dynamics, trafficking, and function in $Cerkl^{KD/KO}$ hippocampal cells.

    1.3. Assessment of phagocytosis, ciliogenesis and mitochondrial morphology $Cerkl^{KD/KO}$ mouse primary RPE cells.

2. To elucidate CERKL function in the oxidative stress response.

    2.1. Evaluation of mitochondrial homeostasis *in vitro*, in *CERKL*-depleted RPE cells subjected to oxidative stress.

    2.2. Examination of antioxidant responses and cell death mechanisms *in vivo*, in $Cerkl^{KD/KO}$ retinas after acute light stress.

3. Differentiation of hiPSCs carrying mutations in *CERKL* into retinal organoids.

    3.1. Generation of an isogenic line of hiPSC carrying the $CERKL^{R257X/R257X}$ mutation via CRISPR/Cas9.

    3.2. Differentiation of $CERKL^{R257X/R257X}$ patient's and CRISPR-derived hiPSCs into 3D retinal organoids.
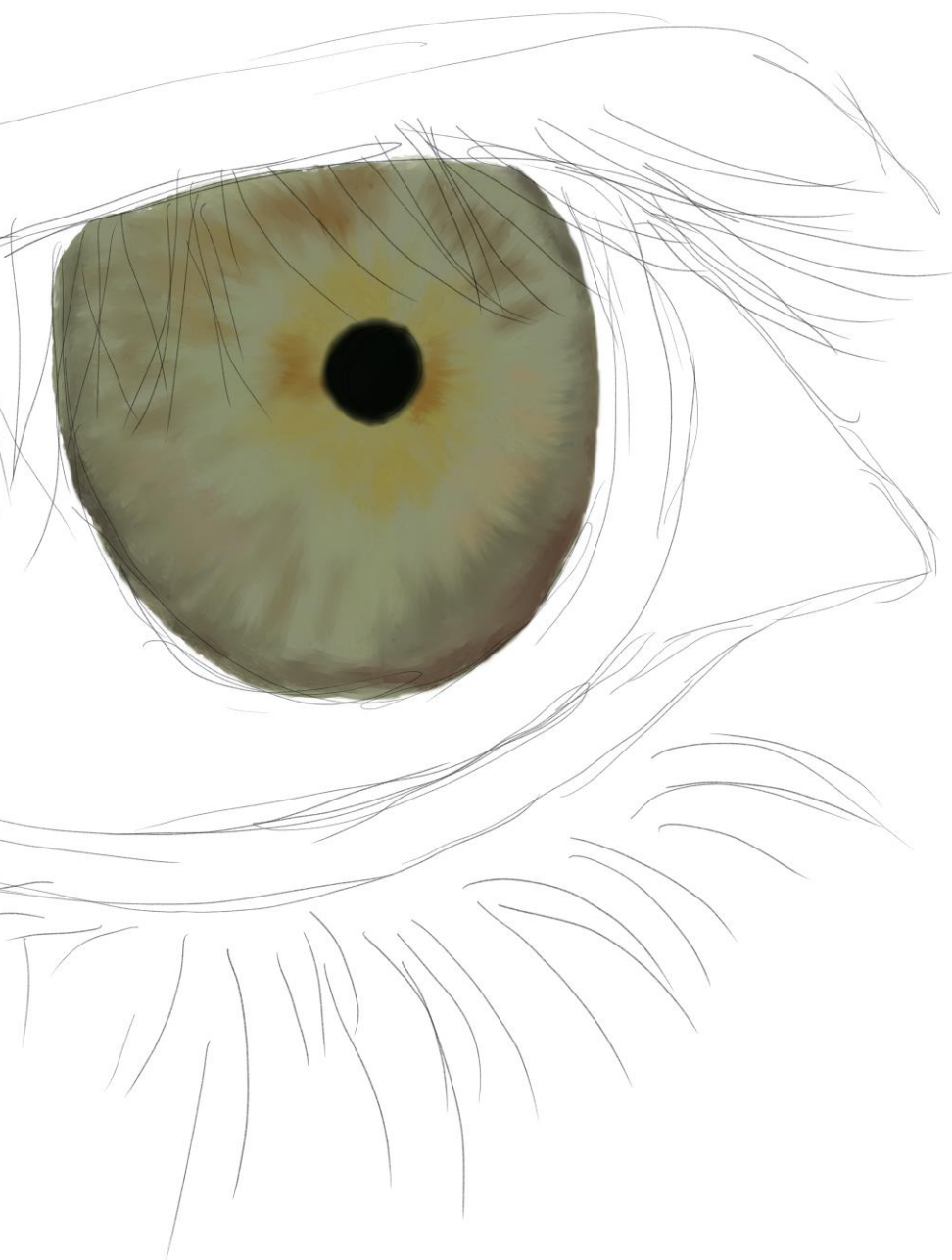
4. To design and test a therapeutic approach based on gene therapy.

    4.1. Designing and optimization of AAV-mediated gene therapy *in vitro* and *in vivo*.

    4.2. Testing nanosome-mediated gene therapy in retinal explants as a proof of concept for nonviral gene-addition therapies.

Report of the Thesis directors

The Thesis entitled: "*CERKL* as a modulator gene of mitochondrial dynamics and stress response in the retina", presented by Rocío García Arroyo to opt for the PhD in Genetics has been supervised by us (Drs Marfany and Mirra) and performed in the Dept. de Genètica, Microbiologia i Estadística (Universitat de Barcelona). This Thesis is presented as a compendium of 3 completely original publications where Rocío figures as a first author and 1 more where she is second author (after one of the directors of her Thesis), all of them already published and available in Open Access. Additionally, Rocío has contributed to 2 other publications to different extents (see the Annex for a list of articles and details). During her PhD, Rocío has been granted different fellowships: the "Beca d'iniciació a la recerca" from the Institut de Biomedicina de la Universitat de Barcelona (IBUB), and the FI-DGR from the Generalitat de Catalunya. Besides, Rocío has attended several specific courses of specialization and has presented her work (both orally and as a poster) to several national and international congresses. Notably, she was selected for an oral presentation in the European Society for Human Genetics Congress, 2023.

Concerning the articles presented as the main core of her Thesis, we can attest the relevant contribution of Rocío to:

Publication 1

Mirra S, **García-Arroyo R**, B Domènech E, Gavaldà-Navarro A, Herrera-Úbeda C, Oliva C, Garcia-Fernàndez J, Artuch R, Villarroya F, Marfany G. *CERKL*, a retinal dystrophy gene, regulates mitochondrial function and dynamics in the mammalian retina. Neurobiology of Disease, 2021 Aug; 156:105405.

doi: 10.1016/j.nbd.2021.105405.   PMID: 34048907.

Impact factor: 5.332

Category: Neurosciences (Position 48/272, Quartile 1)

During the experiments required for this publication, Rocío learnt most of the cell biology techniques that she used later in her PhD Thesis, particularly Western blotting, and the studies of mitochondrial fragmentation in axons of primary cell

cultures of retinal neurons. Her contributions are relevant in the generation of Figures 3, 4 and some supplementary figures.

Publication 2

García-Arroyo R, Marfany G, Mirra S. *CERKL*, a Retinal Dystrophy Gene, Regulates Mitochondrial Transport and Dynamics in Hippocampal Neurons. International Journal of Molecular Sciences, 2022 Sep 30; 23(19):11593.

doi: 10.3390/ijms231911593.   PMID: 36232896

Impact factor: 6.208

Category: Biochemistry & Molecular Biology (Position 69/297, Quartile 1)

This publication, in which Rocío signs as a unique predoctoral student with us as PhD directors, shows the skills acquired by Rocío during her PhD, and the quality of her work in live imaging and other types of image analyses. She not only prepared all the figures and analysed the data, but also wrote the first draft of the manuscript and draw the model.

Publication 3

García-Arroyo R, Gavaldà-Navarro A, Villarroya F, Marfany G, Mirra S. Overexpression of CERKL Protects Retinal Pigment Epithelium Mitochondria from Oxidative Stress Effects. Antioxidants (Basel). 2021 Dec 19;10(12):2018.

doi: 10.3390/antiox10122018.   PMID: 34943121

Impact factor: 6.313

Category: Biochemistry & Molecular Biology (Position 60/295, Quartile 1)

Again, most of the work in this manuscript was performed by Rocío. We collaborated with a group specialized in mitochondria respiration analyses that contributed to a specific Figure, but all the images and data produced were

interpreted by her. Rocío also draw the first draft of the manuscript and the model for the role of CERKL in the RPE.

Publication 4

García-Arroyo R, Domènech EB, Herrera-Úbeda C, Asensi MA, Núñez de Arenas C, Cuezva JM, Garcia-Fernàndez J, Pallardó FV, Mirra S, Marfany G. Exacerbated response to oxidative stress in the Retinitis Pigmentosa *Cerkl*$^{KD/KO}$ mouse model triggers retinal degeneration pathways upon acute light stress. Redox Biology. 2023 Oct; 66:102862.

doi: 10.1016/j.redox.2023.102862.   PMID: 37660443

Impact factor: 11.4

Category: Biochemistry & Molecular Biology (Position 20/285, Decile 1)

This publication is at the core of our research work on the characterization of *CERKL* role in oxidative stress response and is the culmination of Rocío's Thesis. As it covers many different biochemical and molecular functional aspects, this work was performed in collaboration with other highly specialized groups in transcriptomics and metabolomics. Rocío participated in the design and conception of most experiments required to confirm and assess different transcriptomic results, and therefore, she has contributed to all figures. She also wrote a first draft of the article and participated in the discussion and revision after submission for publication.
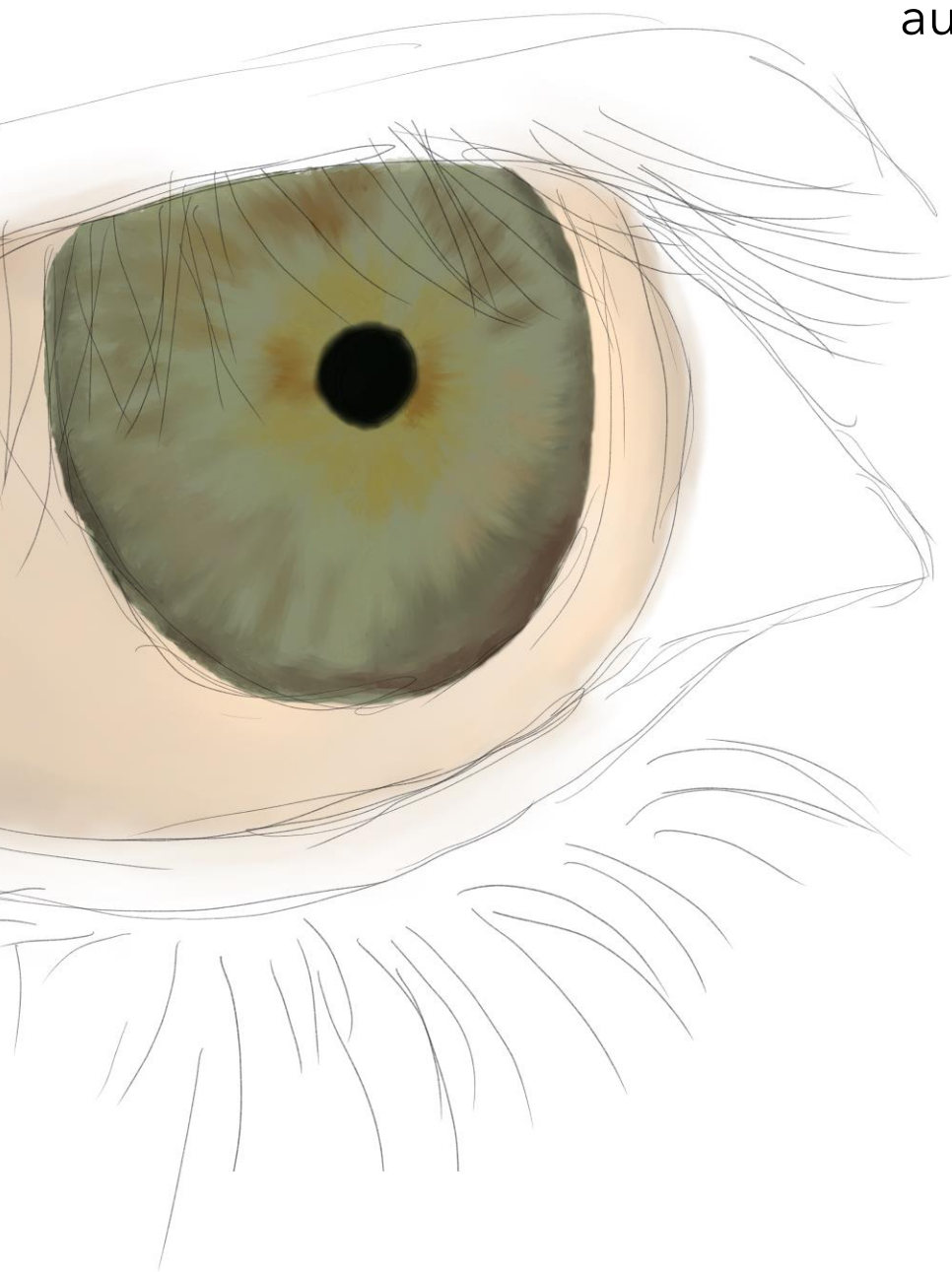
Barcelona, February 2024

Gemma Marfany Nadal   Serena Mirra

Involvement of CERKL in mitochondrial metabolism and autophagy regulation

1.1. CERKL regulates autophagy and mitochondrial dynamics in the mammalian retina

Publication 1

Title

CERKL, a retinal dystrophy gene, regulates mitochondrial function and dynamics in the mammalian retina

Authors

Serena Mirra, Rocío García-Arroyo, Elena B. Domènech, Aleix Gavaldà-Navarro, Carlos Herrera-Úbeda, Clara Oliva, Jordi Garcia-Fernàndez, Rafael Artuch, Francesc Villarroya, Gemma Marfany

Reference

Abstract

The retina is a highly active metabolic organ that displays a particular vulnerability to genetic and environmental factors causing stress and homeostatic imbalance. Mitochondria constitute a bioenergetic hub that coordinates stress response and cellular homeostasis, therefore structural and functional regulation of the mitochondrial dynamic network is essential for the mammalian retina. *CERKL* (*ceramide kinase like*) is a retinal degeneration gene whose mutations cause Retinitis Pigmentosa in humans, a visual disorder characterized by photoreceptors neurodegeneration and progressive vision loss. *CERKL* produces multiple isoforms with a dynamic subcellular localization. Here we show that a pool of CERKL isoforms

localizes at mitochondria in mouse retinal ganglion cells. The depletion of CERKL levels in *Cerkl*[KD/KO] (knockdown/knockout) mouse retinas cause increase of autophagy, mitochondrial fragmentation, alteration of mitochondrial distribution, and dysfunction of mitochondrial- dependent bioenergetics and metabolism. Our results support *CERKL* as a regulator of autophagy and mitochondrial biology in the mammalian retina.

Personal contribution to this work

This work was mainly performed by Dr Serena Mirra, although I actively participated in the development of many experiments and result analysis. My personal contribution to this publication has been: a) analysis of mitochondrial network in the whole retina and retinal ganglion cells (Figure 3C, 3D, 4A, 4B, 4F and Supplementary Figure 5); b) design and creation of the figures (Figure 3C, 3D, 4A, 4B, 4F and Supplementary Figure 5); c) the discussion of the results; and d) critical reading of the manuscript.
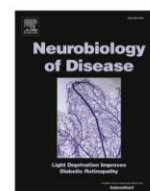
CERKL, a retinal dystrophy gene, regulates mitochondrial function and dynamics in the mammalian retina

Serena Mirra [a,b,c,*], Rocío García-Arroyo [a], Elena B. Domènech [a,b], Aleix Gavaldà-Navarro [c,d,e], Carlos Herrera-Úbeda [a], Clara Oliva [f], Jordi Garcia-Fernàndez [a], Rafael Artuch [b,f], Francesc Villarroya [c,d,e], Gemma Marfany [a,b,c,*]

[a] Department of Genetics, Microbiology and Statistics and Institute of Biomedicine (IBUB), Faculty of Biology, University of Barcelona, Barcelona, Spain
[b] Centro de Investigación Biomédica en Red de Enfermedades Raras (CIBERER), Instituto de Salud Carlos III, Barcelona, Spain
[c] Institut de Biomedicina de la Universitat de Barcelona- Institut de Recerca Hospital Sant Joan de Déu, IBUB-IRSJD, Barcelona, Spain
[d] Department of Biochemistry and Molecular Biomedicine, Barcelona, Spain
[e] CIBEROBN, Instituto de Salud Carlos III, Spain
[f] Clinical Biochemistry Department, Hospital Sant Joan de Déu, Spain

ABSTRACT

The retina is a highly active metabolic organ that displays a particular vulnerability to genetic and environmental factors causing stress and homeostatic imbalance. Mitochondria constitute a bioenergetic hub that coordinates stress response and cellular homeostasis, therefore structural and functional regulation of the mitochondrial dynamic network is essential for the mammalian retina. CERKL (ceramide kinase like) is a retinal degeneration gene whose mutations cause Retinitis Pigmentosa in humans, a visual disorder characterized by photoreceptors neurodegeneration and progressive vision loss. CERKL produces multiple isoforms with a dynamic subcellular localization. Here we show that a pool of CERKL isoforms localizes at mitochondria in mouse retinal ganglion cells. The depletion of CERKL levels in Cerkl$^{KD/KO}$ (knockdown/knockout) mouse retinas cause increase of autophagy, mitochondrial fragmentation, alteration of mitochondrial distribution, and dysfunction of mitochondrial-dependent bioenergetics and metabolism. Our results support CERKL as a regulator of autophagy and mitochondrial biology in the mammalian retina.

1. Introduction

Autophagy is an intracellular catabolic pathway where damaged organelles, toxic aggregates or cell components are engulfed and delivered to lysosomes for degradation and recycling, to produce energy and nutrients that are necessary to maintain metabolic homeostasis, particularly in conditions such as starvation or cellular stress (Boya et al., 2013). Autophagy is finely regulated at the molecular level through a set of Atg proteins, such as Beclin 1, which contribute to the initiation and elongation of autophagosomes, and more downstream factors, such as LC3 or p62 (Gatica et al., 2018). Selective autophagy of

mitochondria, known as mitophagy, represents an important mechanism for organelle quality control. Mitochondria are very dynamic organelles that can fuse and divide, move throughout the cell and undergo regulated turnover through mitophagy (Mandal and Drerup, 2019). They can readily adapt to changes in cellular requirements after physiological or environmental cues. When cells are subjected to mild stresses such as nutrient deprivation, mitochondria fuse and form a branched and interconnected network, as a means to increase ATP production and recover cellular homeostasis. Conversely, in the case of severe stress, mitochondria are fragmented to facilitate mitophagy (Zemirli et al., 2018). Defects in general autophagy, mitophagy and mitochondrial

---

dynamics regulation have been associated with several pathological conditions, such as neurodegenerative disorders, diabetes, age-associated diseases, and lysosomal storage diseases (Yang and Klionsky, 2020; Mizushima and Levine, 2020).

The retina is endowed with an active metabolism and is particularly vulnerable to genetic and environmental alterations that cause mitochondrial dysfunction, such as impaired energy production, mtDNA instability, disturbance of mitochondrial dynamics and mitochondrial quality control (Narayan et al., 2017). These alterations make photoreceptors and retinal ganglion cells (RGCs) more susceptible to cell death and contribute significantly to the onset of retinal neurodegeneration (Eells, 2019; Mirra and Marfany, 2019).

Inherited retinal dystrophies (IRDs) are a broad group of neurodegenerative disorders associated with reduced visual capacities or even complete vision loss, which affect 1:3000 people worldwide. Retinitis Pigmentosa (RP) is the most common IRD and it is characterized by dysfunction and death of photoreceptor cells in the retina.

RP is caused by mutations in more than 70 causative genes. Among them, *CERKL (CERamide Kinase Like)* was first identified in a RP Spanish family (Tuson et al., 2004) and was later also associated to cone-rod dystrophy (CRD) (Aleman et al., 2009). *CERKL* is expressed in several tissues, such as brain, lung and kidney, but the retina is the tissue where *CERKL* expression is the highest. CERKL belongs to the ceramide kinase protein family, even though CERKL has never been shown to exert any kinase activity (Bornancin et al., 2005; Tuson et al., 2009). CERKL contains a diacylglycerol kinase domain (DAGK), a Pleckstrin homology (PH) domain, an ATP-binding domain and two nuclear localization and nuclear export signals implicated in the nucleus-cytoplasm traffic (Bornancin et al., 2005; Ali et al., 2008; Inagaki et al., 2006; Riera et al., 2013).

CERKL expression produces more than 20 transcripts in both human and mouse (Garanto et al., 2011). This transcriptional complexity translates to a wide range of proteins that can localize at different cellular compartments, among them cytosol, nucleus, mitochondria, Golgi vesicles and endoplasmic reticulum.

Previous functional studies performed on zebrafish embryos by knocking down *Cerkl* showed an abnormal eye development, with lamination defects in retina and increased apoptosis (Riera et al., 2013). We also generated a *Cerkl* knockdown mouse model using cre/loxP-mediated deletion of the first exon plus promoter. Notably, the model retained 40% of *Cerkl* expression through the use of an alternative upstream promoter. Concerning the retina, no gross morphological alterations were observed, although the RGCs function was altered in these mice (Garanto et al., 2012).

Later on we generated a complete knockout of the *Cerkl* locus using CRISPR/Cas9 (>97 kb deletion), which resulted to be lethal at embryonic stages in homozygosis (Domenech et al., 2020). Consequently, we generated a new double heterozygote model, *Cerkl*^{KD/KO} (KD/KO) in which the protein expression level is below 10% of that of the wild-type retina (Domenech et al., 2020). This mouse model showed a clear phenotype of progressive retinal neurodegeneration that starts in young mice (2-month-old) and slowly progresses with age. The retinal phenotype of this *KD/KO* model is clearly detectable and includes morphological alterations such as a decreased number of cones, photoreceptor elongation, opsin mislocalization, alterations in the RPE microvilli structure and phagocytosis, and activation of gliosis markers. In young mice, there is not a detectable functional impairment of the retina. However, the electrophysiological response is strongly impaired in 18 month-old mice, thus suggesting a gradual and slow progression of visual impairment, similarly to what occurs in most patients carrying mutations in *CERKL* (Domenech et al., 2020).

CERKL has been described to bind several neuronal calcium sensors (Nevet et al., 2012) and sphingolipids (Garanto et al., 2013), protecting cells from oxidative stress (Tuson et al., 2009), and stabilizing the NAD-deacetylase SIRT1 to regulate general autophagy (Hu et al., 2019). Moreover, CERKL localizes at mitochondria where it interacts with

mitochondrial thioredoxin 2 in NIH3T3 cells (Li et al., 2014). However, the precise cellular and molecular function of CERKL in mammalian retina is yet to be determined.

Here we describe a pool of CERKL isoforms localizing at mitochondria in mouse RGCs primary culture. In addition, taking advantage of *KD/KO* in vivo model, we studied the impact of CERKL expression levels on mitochondrial function and mitochondrial network organization. Our results showed that retinas from *Cerkl*^{KD/KO} model are characterized by increased autophagy that is not concomitant with increased mitophagy. Additionally, depletion of *Cerkl* causes alteration of the mitochondrial size and distribution, and dysregulation of mitochondrial metabolism and other energy-related markers.

Overall, our studies describe *CERKL* as a relevant retinal gene involved in the regulation of mitochondrial biology and metabolism, and provide a solid link between inherited retinal disorders and the alteration of cell metabolism and homeostasis in the mammalian retina.

2. Materials and methods

2.1. Animal experimentation

WT and CERKL transgenic lines in C57BL/6 J or Albino background were genotyped as described previously (Garanto et al., 2012; Domenech et al., 2020). Animal experiments were performed according to the ARVO statement for the use of animals in ophthalmic and vision research, as well as the regulations of the Ethical Committee for Animal Experimentation (AEC) of the Generalitat of Catalonia, according to the European Directive 2010/63/EU and other relevant guidelines.

2.2. Genomic DNA and genotyping by PCR

DNA for genotyping was extracted from ear punches. Primers for genotyping and PCR conditions are described in Domenech et al. (2020).

2.3. Retina isolation

After euthanizing the mice by cervical dislocation, eyes were enucleated and disposed in cold PBS. The neural retina was separated from the sclera, pigment epithelium and finally from the lens under a binocular Leica lens and using a pair of thin tweezers.

2.4. Primary cultures

Primary retinal cultures were obtained from dissection of P0-2 mouse retinas. Single cell suspension was obtained using Neural Tissue Dissociation Kit (Miltenyi Biotec, Bergisch, Gladbach, Germany). 150,000 cells were plated onto poly-D-ornithine-laminin coated coverslips in Neurobasal™-A medium (Thermo Fisher Scientific, Waltham, Massachusetts, USA) supplemented with 0.06% glucose, 0.0045% NaH_2CO_3, 1 mM L-glutamine, B27 $1\times$ (Invitrogen, Carlsbad, CA), penicillin/streptomycin (Invitrogen 1%), forskolin 5 μM (Sigma Aldrich, Saint Louis, Missouri, USA), BDNF 5 ng/ml (Peprotech, 450–02) and rat CNTF 20 ng/ml (Peprotech, 450–25). After 7 days of differentiation in vitro (7DIV), cells were fixed in 4% PFA for 20 min and washed 3 times with PBS $1\times$. If necessary, cells were stored for further experiments in cryoprotector solution (30% Glicerol, 25% Etilenglicol 100% and 0.1 M PBS). Selection of RGCs was performed as described in Domenech et al. (2020). Autophagy flux experiments were performed in vitro by adding hydroxichloroquine (HCQ, 30 μg/ml, Dolquine, Lab. Rubió, Barcelona, Spain) for 6 h to the complete culture medium to block autophagosome-lysosome fusion. To obtain hippocampal cultures E16 mouse brains were dissected in PBS containing 3% glucose and the hippocampi were dissected out. After trypsin (Invitrogen, Carlsbad, CA, USA) and DNAse treatment (Roche Diagnostics), hippocampi were dissociated and cells were seeded onto 0.5 mg/ml poly-L-lysine (Sigma-Aldrich)-coated coverslips in neurobasal medium (Gibco, Grand Island, NY, USA) containing

2 mM glutamax, 120/ml penicillin, 200/ml streptomycin and B27 supplement (Invitrogen). Cells were maintained at 37 °C in the presence of 5% CO_2 and were cultured for between 5 and 6 days.

2.5. 661 W culture and plasmid constructs

CERKL-GFP was obtained by cloning the coding region of hCERKL532 cDNA (NM_201548.4) in pEGFPN2, by using *Xho*I and BamHI restriction sites. Cone progenitor-derived 661 W cells were cultured in DMEM (Invitrogen) supplemented with 10% fetal bovine serum (FBS), 120 μg/ml penicillin and 200 μg/ml streptomycin (Life Technologies), maintained at 37 °C in the presence of 5% CO_2 and split at a ratio of 1:5 once per week. Upon confluence, the cells were trypsinized and 70,000 cells were seeded for each sterile glass coverslip previously coated wiyh poli-L lysine (Sigma-Aldrich). The cells were transfected using Lipofectamin 2000 (Invitrogen) following the manufacturer's instructions and processed 48 h after transfection.

2.6. Immunofluorescence, confocal microscopy, and colocalization analysis

In immunocytochemistry experiments, cells were fixed in pre-chilled methanol at −20 °C for 10 min, washed in PBS (3 × 5 min), permeabilized in 0.2% Triton X-100 (St. Louis, MO, USA) in PBS (20 min at RT), and blocked for 1 h in 10% Normal Goat Serum (Roche Diagnostics) in PBS. Primary antibodies were incubated overnight at 4 °C in blocking solution. The primary antibodies used were the following: LC3 (AB BCN, Genetex; 1:1000), p62 (Abcam, ab56416, 1:500), LAMP1 (Abcam, [1D4B] ab25245, 1:500), CERKL2 and CERKL5 (Domenech et al., 2020). After incubation, coverslips with cells were rinsed in PBS 1× (3 × 5 min), incubated with the corresponding secondary antibodies conjugated to either Alexa Fluor 488, 568 or 647 (Life Technologies, Grand Island, NY, USA) (1:400) at RT (1 h) in blocking solution. Nuclei were stained with DAPI (Roche Diagnostics, Indianapolis, IN, USA) (1:1000), washed again in PBS 1 × (3 × 5 min), mounted in Mowiol 4–88 (Merck, Darmstadt, Germany).

For immunohistochemistry experiment, eyes from adult mice were enucleated, fixed in PFA 4%, and embedded in OCT. Cryosections (12-μm section) were collected and kept frozen at −80 °C until used. Cryosections were air dried for 10 min and rehydrated with 1× PBS (3 × 5 min) and blocked in blocking solution (1× PBS containing 10% Normal Goat Serum and 0.3% Triton X-100 [Sigma-Aldrich]) for 1 h at room temperature. Primary antibody incubation was performed overnight at 4 °C. After three rinses with 1× PBS (10 min each), cryosections were incubated for 1 h at room temperature with the corresponding secondary antibodies conjugated to a fluorophore. Finally, the slides were washed with 1× PBS (3 × 10 min) and coverslipped with Fluoprep (BioMerieux, Marcy-l'Étoile, France). The primary antibodies and dilutions used included: Sestrin2 (Proteintech, I0795-I-AP; 1:500), COXIV (Invitrogen, 459,600; 1:500), LAMP1 (Abcam, [1D4B] ab25245, 1:500).

For whole-mount retina staining, retinas from adult mice were placed on glass slides photoreceptors side up, flattened by cutting the edges, fixed 1 h in 4% paraformaldehyde and rinsed with 1× PBS (3 × 5 min). The retinas were then blocked in blocking solution (1× PBS containing 10% Normal Goat Serum and 2% Triton X-100) for 1 h at room temperature and incubated with COXIV (Invitrogen, 459,600; 1:500) primary antibody overnight. Then they were rinsed with 1× PBS (3 × 5 min) and incubated with Alexa Fluor 568 (Thermo Fisher Scientific, Waltham, MA) for 1 h. Retinas were washed with 1× PBS (3 × 5 min), mounted with Fluoprep (BioMerieux).

All the samples were analyzed by confocal microscopy (Zeiss LSM 880, Thornwood, NY, USA) and images were collected using ZEN-LSM software. For quantitative analysis in both RGCs and 661 W cells, the number of the fluorescent dots (LC3 dots and p62 dots) was counted manually with ImageJ software (National Institutes of Health, Bethesda, MD). Analysis of colocalization was performed with JACoP ImageJ

plugin after images deconvolution, obtained using Huygens Deconvolution Software.

2.7. Transmission electron microscopy

Mice were transcardially perfused with cold fixative solution (2.5% glutaraldehyde, 2% PFA in 0.1 M phosphate buffer). Eyes were removed, retinas were dissected and fragmented in $1mm^3$ pieces. Retinal fragments were immersed in fixative solution (2.5% glutaraldehyde, 2% PFA in 0.1 M phosphate buffer) and incubated at 4 °C overnight. Retinal fragments were post-fixed in 1% osmium tetroxide 2% $K_4Fe(CN)_6$ in the dark for 2 h at 4° temperature, rinsed in double distilled water to remove the osmium. Retinal fragments were dehydrated in ascending concentrations of acetone. Then was infiltrated and embedded in Epon (EMS). Blocs were obtained after polymerisation at 60 °C for 48 h. Ultrathin sections of 60 nm in thickness were obtained using a UC6 ultramicrotome (Leica Microsystems, Austria) and were stained with 2% uranyless and lead citrate. Sections were observed in a Tecnai Spirit 120 Kv TEM, images were acquired with a 1 k × 1 k CCD Megaview camera.

2.8. Quantitative analyses of mitochondrial morphology

Quantitative analyses of immunofluorescence images (mitochondrial morphology in 661 W cells, RGCs cells and mitochondrial length in RGCs axons) was performed using an ImageJ software macro as described in Cherubini et al. (2015). Briefly, a binary image containing black mitochondrial structures on a white background was obtained from confocal images using the ImageJ software. From this binary image, individual mitochondria (particles) were subjected to particle analyses to acquire form factor (FF, $(4\pi \times Am/Pm^2)$ where Pm is the length of mitochondrial outline and Am is the area of mitochondrion) and aspect ratio values (AR, the ratio between the major and minor axis of the ellipse equivalent to the mitochondrion). Mitochondrial Area in 661 W cells was calculated for each cell using the ImageJ software and normalized for the total area of the cell, labeled with citosolic GFP green fluorescence. Quantitative analyses of TEM microphotography were performed in 26,500× images to determine mitochondrial area, mitochondrial length, mitochondrial circularity and mitochondrial aspect ratio, using the ImageJ software. Mitochondrial area represents the area occupied by each single mitochondrion; mitochondrial length represents major axis length of mitochondria; aspect ratio was obtained as major axis/minor axis. 102–123 mitochondria were analyzed from 2 *WT/WT* and 3 *KD/KO*.

2.9. Study of autophagy in ex vivo retinas

After adult retina dissection, half-retina sections were separately processed for study (one-half for each experimental condition, with a total of 4 experimental conditions per animal). Explants were cultured in cell culture inserts (Millipore) under control conditions [Neurobasal medium (Invitrogen) supplemented with 0.06% glucose, 0.0045% NaH_2CO_3, 1 Mm L-glutamine, 1× B27 (Invitrogen, Carlsbad, CA)] and starvation conditions (Earle's Balanced Salt Solution, EBSS) in the presence or absence of HCQ (30 μg/ml, Dolquine, Lab Rubió, Barcelona, Spain). Explants were maintained for 6 h at 37 °C in the presence of 5% CO_2. Successively, retinal explants were processed for western blotting analysis.

2.10. Western blotting

Adult retinas or retinal explants were lysed in RIPA buffer [50 mM Tris, pH 7.4, 150 mM NaCl, 1 mM EDTA, 1% NP-40, 0.25% Na-deoxycholate, protease inhibitors (Complete; Mini Protease Inhibitor Cocktail Tablets; Roche)]. Proteins were analyzed by SDS-PAGE and transferred onto nitrocellulose membranes, which were blocked with 5% non-fat dry milk in Tris-HCl-buffered saline (TBS) containing 0.1%

3

Tween 20, and incubated overnight at 4 °C with primary antibodies. After incubation with horseradish peroxidase-labeled secondary antibodies for 1 h at room temperature, membranes were revealed with the ECL system (Lumi-Light Western Blotting Substrate, Roche). Images were acquired by ImageQuant™ LAS 4000 mini Image Analyzer (Fujifilm) and quantified using ImageJ software. TUBULIN or GAPDH loading controls were used when needed. The primary antibodies used were the following: Beclin1 (Abcam, ab207612; 1:1000), LC3 (AB BCN, Genetex; 1:1000), VDAC (Calbiochem, (Ab-5) (185–197); 1:7000), TUBULIN (Sigma, T5168, 1:1000), GAPDH (Abcam, ab8245, 1:1000), Rodent Total OXPHOS Cocktail (MitoSciences, Eugene, OR, USA, 6 μg/ml), Sestrin2 (Proteintech, I0795-I-AP; 1:1000), MITOFUSIN2 (Abcam, ab56889, 1:1000), OPA1 (Proteintech, 27,733-1-AP; 1:1000), DRP1 (Cell Signaling Technology14647S, 1:1000), P-DRP1 (Cell Signaling Technology, S616:3455S, 1:000). The secondary antibodies used were: HRP-labeled anti-mouse (P447-01, Vector; 1:2000) and anti-rabbit (P217-02, Vector; 1:2000).

2.11. Seahorse analysis

Seahorse analysis of ex vivo retinas was performed on retinal disks as described in Kooragayala et al. (2015). Briefly, adult neural retinas were dissected and two disks with a diameter of 1 mm were obtained from the central region of each retina, arranged onto Cell-Tak (Corning) pre-coated XF24 Islet Fluxpak mesh inserts (photoreceptors side up) and transferred to an islet plate (one disk per well) containing 450 μl of Seahorse XF Assay Medium (Seahorse Bioscience). After 1 h of incubation at 37 °C, plates were loaded into an XFe24 respirometry machine (Seahorse Bioscience). Maximum OCR was assayed with FCCP (2 μM). To inhibit complex I- and III-dependent respiration, rotenone (5 μM) and antimycin A (15 μM) were used, respectively. OCR represents the oxygen tension and ECAR acidification of the medium as a function of time (pmol min^{-1}). 3 animals were used for each experimental condition to obtain 6 retinas and 10 retinal discs. Measurements of OCR from each disc were considered as independent value for statistical analysis.

2.12. DNA isolation and quantification of mtDNA content

Total DNA was isolated from retinal samples by phenol/chloroform extraction. Mitochondrial DNA (mtDNA) was quantified by real-time PCR amplification of 100 ng of total DNA using a cytochrome b (MT-CYTB) primer/probe set (Mm04225271_g1). The results were expressed relative to the quantity of nuclear DNA, which was determined by amplification of the intronless gene CEBPα (Mm00514283_s1) (Villar-roya et al., 2010).

2.13. Determination of D-glucose oxidation

Retinal samples were incubated with DMEM (without D-glucose) for 1 h followed by an incubation with DMEM (without D-glucose) supplemented with 3 mM D-glucose and 1.5 μCi [14C(U)]-D-glucose (Hartmann Analytic GmbH, Braunschweig, Germany) for 3 h at 37 °C in a 5% (v/v) CO$_2$ atmosphere. Labeled ^{14}CO$_2$ was then released from the medium by acidification with 3 M HClO$_4$ and retained in a CO$_2$ trap consisting of Whatman 3MM Chr paper (Whatman, GE Healthcare, Little Chalfont, UK) impregnated with β-phenylethylamine (Sigma) and positioned over the wells inside the sealed plates. After 1 h, CO$_2$ traps were placed in scintillation vials containing 5 ml of scintillation fluid, and the samples were counted using a Packard 2100TR TriCarb Liquid Scintillation Counter (Packard Instrument Company Inc., Meriden, CT).

2.14. RNA isolation from retinas

Retinal samples were homogenized using a Polytron PT1200E homogenizer (Kinematica, AG, Lucerne, Switzerland). Total RNA was isolated using the RNeasy mini kit (Qiagen, Germantown, MD),

following the manufacturer's instructions.

2.15. Adult retinas RNA-seq

Total RNA from *Mus musculus* (Albino) retinas was quantified by Qubit® RNA BR Assay kit (Thermo Fisher Scientific) and the RNA integrity was estimated by using RNA 6000 Nano Bioanalyzer 2100 Assay (Agilent). RNASeq libraries were prepared with KAPA Stranded mRNA-Seq Illumina® Platforms Kit (Roche) following the manufacturer's recommendations. Briefly, 100–300 ng of total RNA was used for the poly-A fraction enrichment with oligo-dT magnetic beads, following the mRNA fragmentation by divalent metal cations at high temperature. The strand specificity was achieved during the second strand synthesis performed in the presence of dUTP instead of dTTP. The blunt-ended double stranded cDNA was 3'adenylated and Illumina platform compatible adaptors with unique dual indexes and unique molecular identifiers (Integrated DNA Technologies) were ligated. The ligation product was enriched with 15 PCR cycles and the final library was validated on an Agilent 2100 Bioanalyzer with the DNA 7500 assay. The libraries were sequenced on HiSeq 4000 (Illumina) with a read length of 2x76bp + 8 bp + 8 bp using HiSeq 4000 SBS kit (Illumina) and HiSeq 4000 PE Cluster kit (Illumina), following the manufacturer's protocol for dual indexing. Image analysis, base calling and quality scoring of the run were processed using the manufacturer's software Real Time Analysis (RTA 2.7.7). The read-count analysis was performed using Gene-Counts option from STAR (v2.7.0d). Analysis of differentially expressed genes (DEGs) used DESeq2 v1.26.0 including principal component analysis to test for outlier samples and batch effects. One *KD/KO* sample grouped distinctly and was excluded from DEG analysis which used 2 mutant and 3 control samples. For a gene to be considered differentially expressed, we required expression change of >0.5 log$_2$ (fold change) and adjusted p value <0.05, plus absolute expression level of >10 counts in the sum of all conditions. Data in Supplementary Table S1 were obtained by extracting relevant genes obtained from a DESeq2 (Love et al., 2014) output of *WT/WT* vs *KD/KO* retinas and automatically annotated using DAVID (v6.8) (Huang et al., 2009).

2.16. cDNA synthesis and RT-PCR

cDNA was synthesized from 500 ng of total RNA using Multiscribe reverse transcriptase and random-hexamer primers (TaqMan Reverse Transcription Reagents from Applied Biosystems/Life Technologies, Foster City, CA). For mRNA expression analyses, TaqMan quantitative real-time PCR (qPCR) was performed on a 7500 Real-Time PCR System (Applied Biosystems) in a final volume of 20 ml using Platinum Quantitative PCR SuperMix-UDG with ROX reagents (Invitrogen/Life Technologies) and the *Ppargc1a* (Mm01208835_m1) and *Nr4a3* specific primer pair/probe sets. The relative levels of target mRNA expression were normalized to that of *Ppia* (Mm02342430_g1), used as an endogenous control.

2.17. Caspase 3/7 activity

Caspase-9 activity was measured in retinal disks with a diameter of 1 mm (9 retinal disks from 3 animals per genotype) using a luminescence-based system (Casapase-Glo 3/7 Assay, Promega). Data were expressed as relative luminescence units (RLU).

2.18. Targeted metabolomic analysis

250 μg of retinas (right and left) were homogenized in 200 uL of PBS and stored at −80 °C until the moment of the analysis. After centrifugation at 1500 xg (10 min and 4 °C), the clear supernatant was used for the analysis. Amino acids were determined by tandem mass spectrometry, as previously reported (Casado et al., 2018). Briefly, amino acids were analyzed on a Waters ACQUITY UPLC H-class instrument with a
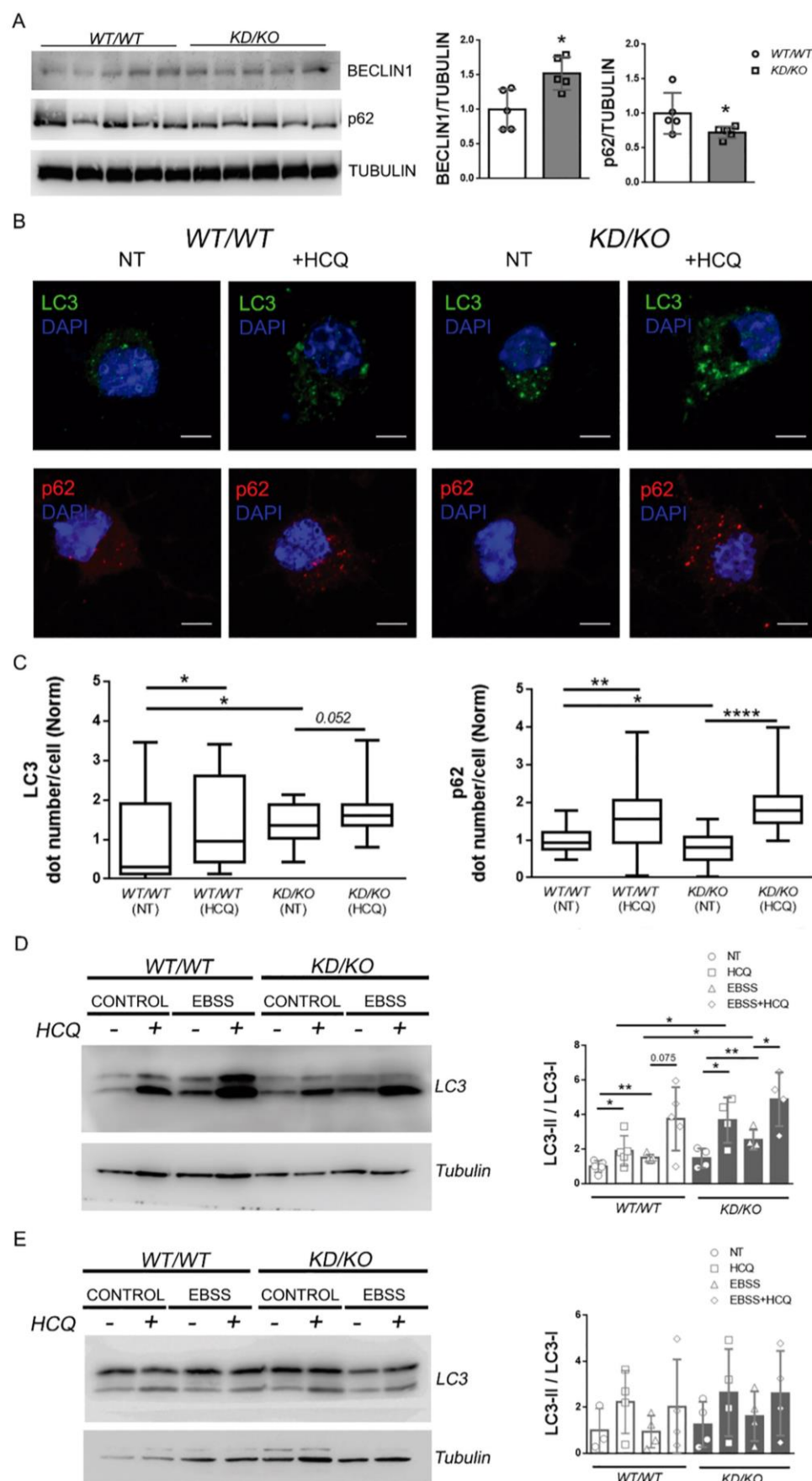
Fig. 1. Autophagy is activated in *KD/KO* retinas. A) Quantification of autophagy markers BECLIN 1 and p62 in *WT/WT* and *KD/KO* retinal lysates. (*n* = 5 animals per genotype). **B,C)** Fluorescence microscopy detection and quantification of LC3-positive and p62-positive dots in *WT/WT* and *KD/KO* RGCs, maintained in control medium or treated with HCQ for 6 h. Scale bar 5 μm. (*n* = 25–33 cells for condition, from 3 to 4 animals per genotype). **D)** Western blot analysis on *WT/WT* or *KD/KO* retinal explants from 3 month-old mice and densitometric quantification of the relative intensity of LC3-II/LC3-I ratio. Retinal explants were cultured in control or starvation (EBSS) media, maintained for 6 h in the presence or absence of HCQ and then processed for LC3 detection. **E)** Western blot analysis on *WT/WT* or *KD/KO* retinal explants from 10 month-old mice (as described in D) and densitometric quantification of the relative intensity of LC3-II/LC3-I ratio. (*n* = 4–5 animals, with 4 explants under different conditions per animal). Data are shown as the mean ± SD. Statistical analysis by Mann-Whitney test. *p-value ≤0,05; **: p-value ≤0,01; ****: p-value ≤0,001.

RESULTS

S. Mirra et al.   Neurobiology of Disease 156 (2021) 105405

reversed-phase C-18 column using water and acetonitrile with 0.1% formic acid as the mobile phases (run time = 9 min). The detection was performed with a Waters Xevo TQD triple-quadrupole mass spectrometer using positive electrospray ionization in the multiple reaction monitoring mode. Organic acids were analyzed by Gas-Chromatography Mass spectrometry of the trimethylsylyl derivatives (BSTFA), as reported (Van Noolen et al., 2020). Briefly, after derivatisation, compounds were separated in a 60-m capillary column and detected by mass spectrometry in scan mode (to verify the nature of the compound compared with the NIST library), and quantitative mode by analyzing the response of the target ion related with that of the internal standard (undecanodioc acid). A table with the analyzed compounds is stated in Supplementary Table S2.

2.19. Statistical analysis

Statistical analyses were performed using the two-tailed unpaired Student's t-test. When data are not normally distributed, non-parametric Mann–Whitney test was used to determine the statistical significance. ROUT test was used to determine statistical outliers (Q = 1%). Calculations were performed with GraphPad Prism statistical software, version 6. N is shown at each Fig legend. Statistical significance was set with a value of $p < 0.05$, (* $p < 0.05$, ** $p < 0.01$, *** $p < 0.005$, **** $p < 0.001$). Data are expressed as standard deviation (SD).

3. Results

3.1. Autophagy is increased in KD/KO in in vitro and ex-vivo systems

To determine the potential role of CERKL in regulating autophagy in the mammalian retina we took advantage of the $Cerkl^{KD/KO}$ mouse model (Domenech et al., 2020). A first analysis was performed by assessing the abundance of the autophagy markers Beclin 1 and p62 by quantitative western blotting in total protein homogenates from WT/WT and KD/KO retinas (Fig. 1A). Compared to the wild-type retinas, extracts of KD/KO retinas showed both a significant increase in Beclin 1 and a decrease of p62 (Fig. 1A). These results indicate that autophagy is increased in KD/KO retinas.

To extend this result we studied autophagic flux in WT/WT and KD/KO primary cultures of retinal ganglion cells (RGCs) (P0-P2 mouse pups) maintained 7 days in vitro (7DIV). Cells were cultured in the absence (not treated, NT) or presence of hydroxychloroquine (+HCQ), a blocker of lysosomal degradation. After immunostaining with LC3 or p62 antibodies the numbers of isolation membranes and autophagosomes in the cytoplasm was measured (Fig. 1B–C). The number of LC3 dots in KD/KO was higher than in WT/WT cells in NT condition, whereas the number of p62 dots in KD/KO was lower than in WT/WT cells, indicating an increased autophagy in KD/KO RGCs, in agreement with our preliminary results (Fig. 1C). Besides, inhibition of lysosomal activity in WT/WT RGC cultures induced a significant increase in LC3 or p62-positive dots, indicating the existence of basal autophagy (Fig. 1C). These changes were similar in KD/KO retinas although with less intra-group variability than in WT/WT (Fig. 1C).

We next investigated autophagy in ex vivo retinal explants from WT/WT and KD/KO 3 month-old mice by monitoring LC3-II levels by western blot. Retinal explants were cultured in control or EBSS medium to induce starvation, and thus autophagy. Additionally, the explants were maintained 6 h in the absence (−) or presence (+) of HCQ prior processing for western blot analysis. As expected, inhibition of lysosomal activity induced an increase in LC3-II/LC3-I ratio, reflecting basal autophagy. Moreover starvation media also induced an increase in LC3-II/LC3-I ratio, an effect augmented by concomitant lysosomal inhibition (Esteban-Martínez et al., 2015). This response was globally higher in KD/KO retinal explants than in WT/WT, pointing out to an increased basal autophagy in KD/KO retinas (Fig. 1D), again in accordance with our previous results. Interestingly, the exacerbation of autophagic

response in KD/KO mice was detected in young retinas but was no longer evident in 10 month-old retinas (Fig. 1E).

In order to investigate the transcriptional changes occurring in KD/KO retinas, we performed RNA-seq analysis of retinal samples extracted from WT/WT and KD/KO mice. Triplicate RNA samples were prepared from the retinas of 3 different mice for genotype. After quality control and normalization of the data, we investigated how the overall expression of protein-coding genes changed in KD/KO retinas. However, PCA (principal component analysis) showed that one out of three KD/KO samples behaved as an outlier and it was excluded from subsequent analyses. We considered the differentially expressed gene when an expression change of >0.5 log_2 (fold change) is found. Hierarchical clustering was performed according to their expression values on the differentially expressed genes (DEGs) involved in autophagy to determine mice with similar DEG expression profiles; samples were clustered according to their genotype group (Fig. 2A). Among the DEG we found genes involved in both autophagy inhibition (such as Decorin, Tspo, Pik3cg) and activation (such as Depp1, Dram1, Dram2, Sesn2). Sesn2 was increased in KD/KO (Log2Fold-Change:0,55,471) retinas. It encodes SESTRIN2, an intracellular sensor involved in a wide range of processes, such as the regulation of antioxidant defenses (by the stimulation of transcription factors such as p53, Nrf2, AP-1, and FoxOs), metabolism (by controlling AMPK and mTOR signaling), autophagy and mitophagy. It regulates autophagy by promoting the autophagic degradation of p62-dependent targets, including KEAP1, thereby up-regulating the transcription of antioxidant genes through NRF2 stabilization (Bae et al., 2013). Moreover, SESTRIN2 physically interacts with ULK1 and p62 and inhibits mTor, thus favoring autophagy initiation (Parmigiani et al., 2014). We observed that in the retina, SESTRIN2 is mostly expressed in photoreceptors (localizing at the inner segment), the inner nuclear layer and the ganglion cell layer. SESTRIN2 expression pattern is maintained in KD/KO retinas (Fig. 2B), although its expression levels were increased in KD/KO (Fig. 2C).

3.2. Different pools of CERKL isoforms localize at mitochondria in retinal ganglion cells and hippocampal neurons.

CERKL has been described to localize at different cellular compartment, among them mitochondria in NIH3T3 cells, where it associates with mitochondrial thioredoxin 2 (Li et al., 2014). Moreover, it is required for autophagy in ARPE-19 cells and zebrafish models (Hu et al., 2019). CERKL can shuttle from cytosol to nucleus in response to oxidative stress conditions (Fathinajafabadi et al., 2014). However, little is known about the subcellular localization of CERKL in mammalian retina. To assess whether endogenous CERKL colocalizes with organelles involved in autophagy, we used immunofluorescence staining. 7 DIV RGCs were distinguished from other cellular populations for the presence of a large axon and the expression of TUBULIN-III-β (Supplementary Fig. S1A). To detect CERKL we used two different in-house antibodies against peptides encoded by either exon 2 (anti-CERKL2) or exon 5 (CERKL5), which detect a different pool of endogenous isoforms (Domenech et al., 2020). CERKL isoforms did not co-localize with the lysosome marker LAMP1 or the autophagosome marker p62 (Supplementary Fig. S1B–C).

On the other hand, we observed partial colocalization with the mitochondrial marker Mitotracker (Fig. 3A). Specifically, anti-CERKL2 signal was detected in both nuclear and somatic compartments, with some colocalization with mitochondria, whereas anti-CERKL5 mainly stained isoforms localized in somatic compartment, strongly colocalizing with mitochondria. To further corroborate these results in a different neuronal system we checked the expression of CERKL in several neural tissues by using the two antibodies against CERKL. We found that each antibody recognizes distinct CERKL isoforms in tissue-dependent fashion in both developing and adult mice (Supplementary Fig. S2A–B). Thus, 3DIV hippocampal neurons from E16 mouse embryos were used to overexpress GFP-tagged CERKL (CERKL-GFP) and stain
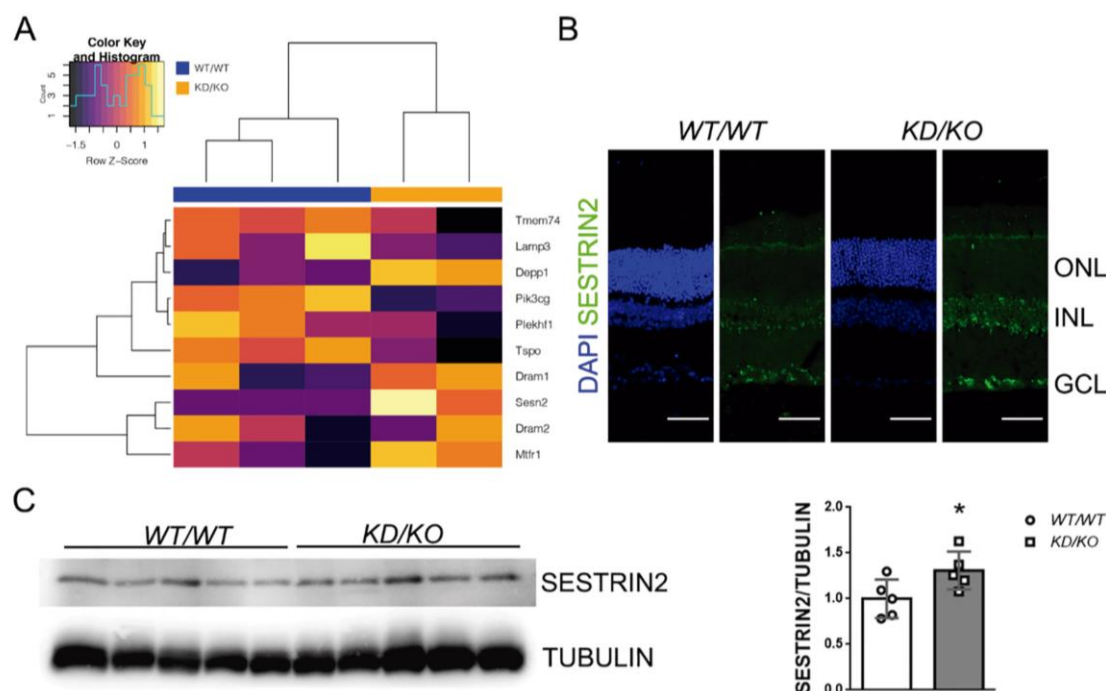
Fig. 2. Differential expressed genes identified by RNAseq compairing *WT/WT* and *KD/KO* retinas include genes involved in autophagy regulation. A) Heatmap with hierachical clustering of differentially expressed autophagy-related genes of *WT/WT* (group in blue) versus *KD/KO* (group in orange) mouse retinas. The heatmap colours reflect the *Z*-score and thus differences in gene expression between samples for each of the genes selected for comparison. **B)** Immunohisto-chemistry of SESTRIN2 in *WT/WT* and *KD/KO* retinas. Scale bar: 50 μm. C) SESTRIN2 is upregulated in *KD/KO* retinas. (*n* = 5 animals per genotype). Data are shown as the mean ± SD. Statistical analysis by Mann-Whitney test. *: *p*-value ≤0,05. (For interpretation of the references to colour in this figure legend, the reader is referred to the web version of this article.)

mitochondria with Mitotracker. We observed that CERKL-GFP associated with moving mitochondria in live axons (Supplementary Fig. S2C–D). Furthermore, we confirmed the strong association of isoforms including the exon 5 epitope with mitochondria in both control and in presence of sodium arsenite to induce oxidative stress (Supplementary Fig. S3). Therefore, different pools of CERKL isoforms are associated to mitochondria undergoing mitochondrial dynamics in primary retinal ganglion cells and hippocampal neurons, with isoforms including exon 5 displaying preferential mitochondrial localization.

3.3. Mitochondrial mass increased in Cerkl^{KD/KO} retinas

Since autophagy is the catabolic pathway able to degrade entire mitochondria, we postulated that CERKL mitochondrial localization could regulate mitochondrial total amount in retina. We first analyzed mitochondrial mass in retinas from *WT/WT* and *KD/KO* adult mice by immunostaining whole mount retinas (photoreceptors side up) for mitochondrial protein COX-IV. We found a significant increase in mitochondrial mass of *KD/KO* photoreceptors (Fig. 3B) and this result was further corroborated by analyzing the mitochondrial protein VDAC by western blot on total retinal homogenates (Fig. 3C). This increase in mitochondrial mass could not be attributed to an increased mitochondrial biogenesis, as the expression levels of *Pgc1a*, the major regulator of mitochondrial biogenesis, were found unaffected at level of both transcript and protein (Fig. 3D,E). Furthermore, the expression of *Nr4a3*, also essential to promote mitochondrial biogenesis was found reduced in *KD/KO* retinas (Fig. 3D). RNAseq analysis did not provide evidence of high differential alterations in the expression of other genes regulating mitochondrial biogenesis, although *Nrf1* and *Nfe2l2* are respectively slightly upregulated and downregulated (Supplementary Table S1).

Consequently, we checked possible changes in mitophagy. Among the different retinal layers, mitophagy has been showed to be highly

localized in vivo in the outer nuclear layer, where the soma of photo-receptors reside (McWilliams et al., 2019). Thus, we immunostained *WT/WT* and *KD/KO* retinal cryosections for COX-IV (mitochondria marker) and LAMP1 (lysosome marker) and assessed mitophagy by analyzing mitochondria-lysosomes colocalization in photoreceptors (Fig. 4A–B). Surprisingly, we did not detect any change in mitophagy by this assay (Fig. 4B).

We also used *WT/WT* and *KD/KO* RGCs cultures to assess colocalization between the mitochondrial marker Mitotracker and LAMP1 in basal conditions and after blocking autophagic flux by HCQ treatment (Supplementary Fig. S4A). We observed that the colocalization coefficient in presence of HCQ was higher than in absence of HCQ, similarly in both *WT/WT* and *KD/KO* RGCs (Supplementary Fig. S4 B). These results indicated that the basal level of mitophagy is not altered when *Cerkl* expression is strongly downregulated in RGCs primary cultures.

Is there any effect of the overexpression of CERKL on mitophagy? To answer this question, we transfected the 661 W photoreceptor-derived cell line with CERKL-GFP or control GFP plasmids (Fig. 4C). We observed that CERKL overexpression induced an increase in mitochondria-lysosomes colocalization (Fig. 4C), indicating that CERKL overexpression promotes mitophagy.

Overall, our data indicate that CERKL may positively regulate mitophagy, but this regulation might not be direct as it is only detected upon CERKL overexpression, whereas a strong depletion of CERKL (*Cerkl^{KD/KO}* model) results in a global increase of general autophagy with mitophagy levels remaining similar to the WT retinas.

### 3.4. CERKL downregulation alters mitochondrial morphology and distribution

Correct mitochondrial metabolism and dynamics are essential for retinal cells and the preservation of mitochondrial function and

S. Mirra et al.
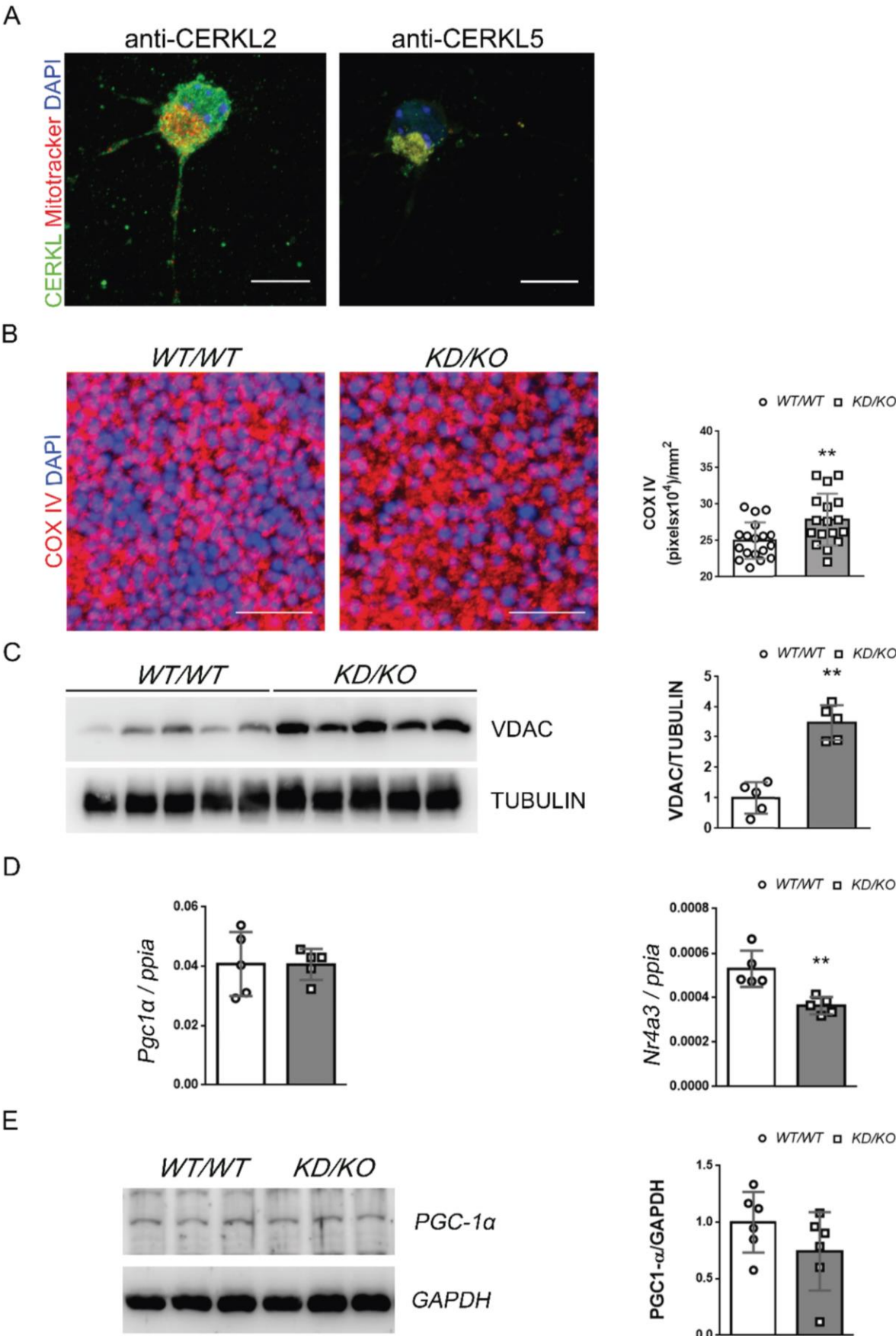
(caption on next page)

Fig. 3. A pool of CERKL co-localizes with mitochondria, whose mass is increased in *KD/KO* retinas despite mitochondrial biogenesis is unaltered. A) Immunofluorescence of RGCs in primary retinal cultures treated with mitochondrial marker Mitotracker and immunostained with anti-CERKL2 (green, left panels) and anti-CERKL5 (green, right panels) antibodies. Scale bar: 10 μm. **B)** Mitochondrial immunostaining and quantification of COX-IV (red) in whole mount retinas (photoreceptors side up). Nuclei were stained with DAPI (blue). Scale bar: 20 μm. (*n* = 18 ROIs, 6 ROIs per animal from 3 animals per genotype). **C)** Western blot analysis and quantification of mitochondrial protein VDAC on *WT/WT* or *KD/KO* retinal homogenates. **D)** Quantitative RT-PCR for *Pgc1a* and *Nr4a3* genes in *WT/WT* or *KD/KO* retinas. **E)** Representative western blot analysis and quantification of PCG1-α protein on *WT/WT* and *KD/KO* retinal homogenates. In C, D and F), *n* = 5 animals per genotype; in E), *n* = 6 retinas fron 3 animals per genotype; data are represented as the means±SD. Statistical analysis by Mann-Whitney test. *: *p*-value ≤0,05; **: *p*-value ≤0,01. (For interpretation of the references to colour in this figure legend, the reader is referred to the web version of this article.)
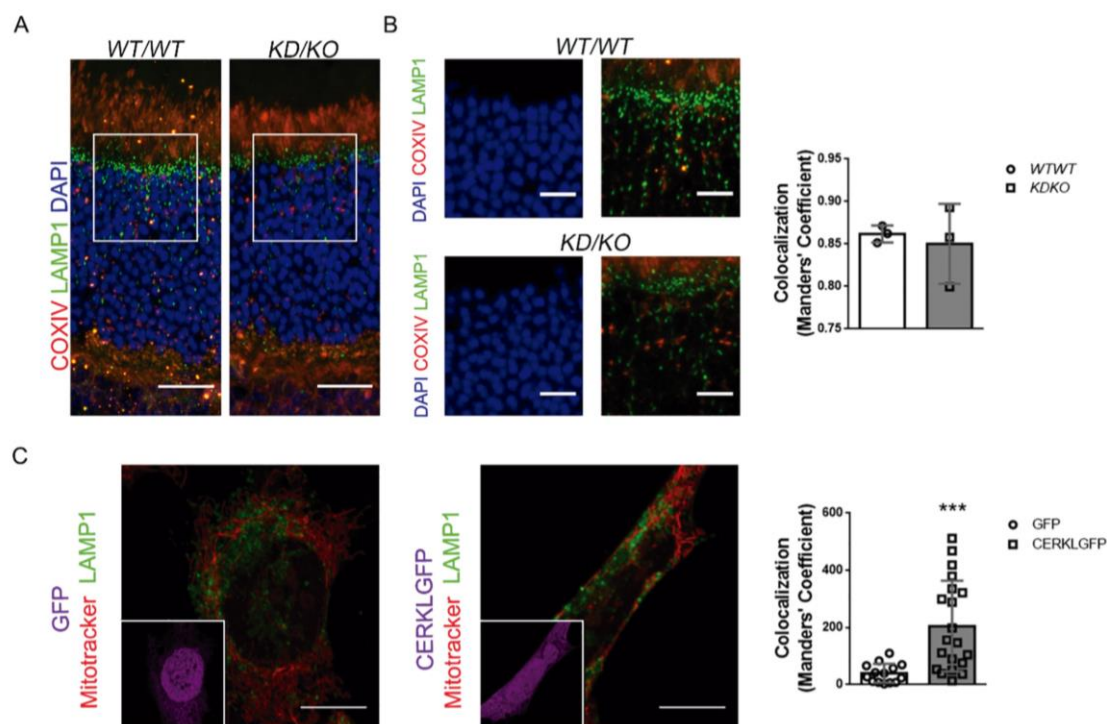
Fig. 4. CERKL overexpression increased mitophagy in photoreceptor cell line. A) Immunostaining of retinal cryosections from *WT/WT* and *KD/KO* mice with COX-IV (red) and LAMP1 (green). Scale bar: 20 μm. **B)** ROIs such as in A) were used to assess mitophagy in photoreceptors by quantifying mitochondria-lysosomes colocalization. Scale bar: 10 μm. (*n* = 3 animals per genotype, 8 ROIs per animal). **C)** 661 W cells transiently expressing control GFP or CERKL-GFP (pseudo-colour in magenta, left bottom frame) were treated with Mitotracker. Scale bar: 10 μm. Mitophagy was analyzed by measuring colocalization between Mitotracker (red) and LAMP1 (pseudo-colour in green). Scale bar: 10 μm. (*n* = 19–21 cells from 2 independent experiments). Statistical analysis by Mann-Whitney test. **: *p*-value ≤0,01; ***: p-value ≤0,001. (For interpretation of the references to colour in this figure legend, the reader is referred to the web version of this article.)

morphology is required to guarantee retinal homeostasis. Since a pool of CERKL colocalizes at mitochondria and CERKL overexpression promotes mitophagy, we also aimed to assess the role of CERKL in regulating mitochondrial morphology.

To analyse the phenotypic traits of mitochondria, 7DIV RGCs from *WT/WT and KD/KO* P0-P1 pups were cultured and analyzed. Mitochondria were stained with Mitotracker and mitochondrial size was analyzed in proximal and distal regions of the axon (Fig. 5A). Mitochondria in *KD/KO* are shorter than in *WT/WT* in distal regions, whereas no differences in size were found in proximal regions. Notably, in *KD/KO* distal regions mitochondria are smaller than in proximal regions, indicating mitochondrial fragmentation in the regions that are farther from the soma (Fig. 5B). Moreover, we found an increased mitochondrial density in both proximal and distal regions of *KD/KO* axons (Fig. 5C). We extended our analysis to somatic mitochondria, but we were not able to detect any change in mitochondrial number and mitochondrial area (Supplementary Fig. S5A–C). Moreover, morphometric analysis revealed that mitochondria in *KD/KO* RGC somas did not display significant differences in morphological parameters such as the Aspect Ratio (AR) and Form factor (FF) in comparison to control cells (Supplementary Fig. S5D–E).

These data are indicative of alterations in mitochondrial dynamics (such as fusion, fission or trafficking) that could prevent a correct distribution of mitochondria from the soma to the more distal regions of the axon. To further study the possible alterations of mitochondrial abundance and morphology in *KD/KO* retinas we analyzed transmission electron microscopy (TEM) microphotographies from *WT/WT and KD/KO* RGCs and photoreceptors. In *KD/KO* RGCs we observed fragmented mitochondria characterized by irregular shapes and cristae. Moreover, autophagic structure and vacuoles were often found in *KD/KO* RGCs (Fig. 5D). From longitudinally orientated retinal samples, the IS mitochondria of *KD/KO* photoreceptors presented an abnormal morphology, with an increased circularity and a decreased maximal length and aspect ratio when compared to *WT/WT* (Fig. 5E).

To gain insight into the molecular mechanisms underlying mitochondrial fragmentation in *KD/KO* retinas, we analyzed the expression of the mitochondrial fusion/fission main regulators MITOFUSIN2, OPA1 and DRP1. The mitochondrial fusion protein MITOFUSIN2 is downregulated in KD/KO retinas (Fig. 5F), suggesting that mitochondrial fusion might be altered upon *Cerkl* depletion.

Overall, our data indicated that *Cerkl* expression levels regulate mitochondrial number, morphology and distribution in different

9
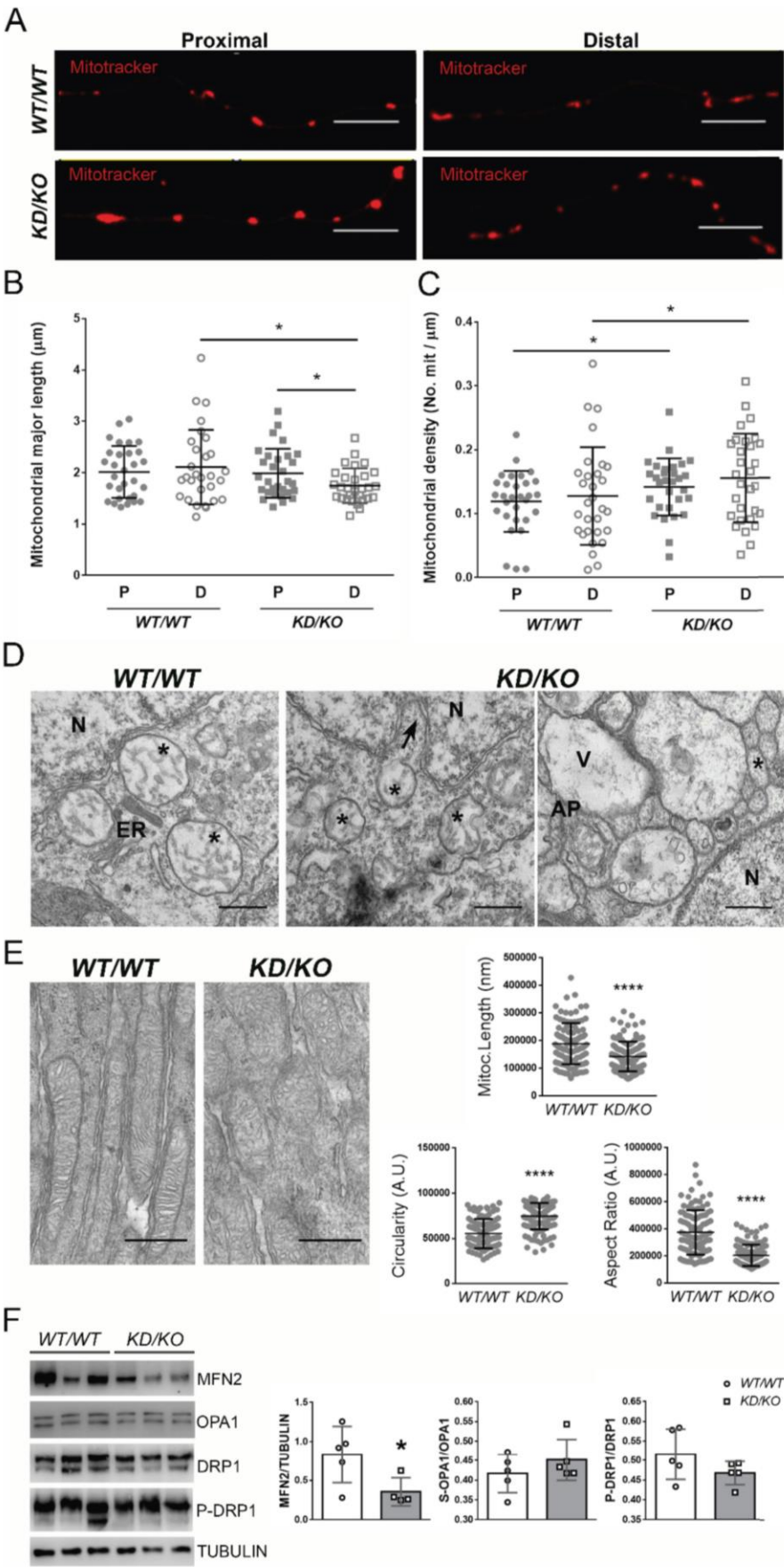
Fig. 5. Differential mitochondrial morphology and distribution of in *Cerkl* KD/KO retinas compared to *WT/WT*. **A)** Representative confocal images of proximal (20 μm from the soma) and distal (100 μm from the soma) axon regions of *WT/WT* and *KD/KO* RGCs. Mitotracker was used to detect mitochondria (red). Scale bar: 10 μm. **B)** Quantification of mitochondrial major length in proximal and distal axon regions of *WT/WT* and *KD/KO* RGCs. **C)** Quantification of mitochondrial density in proximal and distal axon regions of *WT/WT* and *KD/KO* RGCs. ($n = 30$ cells from 4 to 6 animals per genotype). Statistical analysis by Mann-Whitney test. *: *p*-value ≤0,05; **: p-value ≤0,01 **D)** TEM microphotographies from *WT/WT* and *KD/KO* retinas. Control cells displaying normal mitochondria (*) and endoplasmic reticulum (ER). Mitochondria (*) in *KD/KO* RGCs are smaller, with irregular membrane shape cristae; invaginations in nuclear membrane (arrow), large vacuoles (V) and autophagy events (AP) are detected in *KD/KO* RGCs. Scale bar: 1 μm. **E)** TEM microphotographies were used to quantify mitochondrial length, circularity and aspect ratio in the inner segment. Scale bar: 1 μm. Data are represented as the means±SD. ($n = 12$ images with a total of 102–123 mitochondria, from 2 *WT/WT* and 3 *KD/KO*). Statistical analysis by Mann-Whitney test or 2-tailed Ttest ****: p-value ≤0,0001. **F)** Representative western blot analysis and quantification of MITOFUSIN2, OPA1, P-DRP1 and total DRP1 proteins on *WT/WT* and *KD/KO* retinal homogenates. $n = 4$–5 animals per genotype; data are represented as the means±SD. Statistical analysis by Mann-Whitney test. *: p-value ≤0,05. (For interpretation of the references to colour in this figure legend, the reader is referred to the web version of this article.)

cellular population of mammalian retina.

3.5. Oxygen consumption and energy related is impaired in KD/KO retinas

The retina is a highly metabolic tissue, generating adenosine triphosphate (ATP) via glycolysis in the cytosol or via oxidative phosphorylation in mitochondria. Seahorse analysis on *KD/KO* and *WT/WT* retinal explants allowed us to measure changes in oxygen consumption rates (OCR), as an index of mitochondrial respiration, as well as extracellular acidification rates (ECAR), as an index of glycolysis. Our results clearly support that *KD/KO* retinal explants show a strong decrease in OCR when compared with *WT/WT* retinas (Fig. 6A). Indeed, basal respiration, maximal respiration and spare capacity are all compromised in *KD/KO* explants (Fig. 6B). On the other hand, the ECAR remained equivalent between *KD/KO* and *WT/WT* (Fig. 6C). Moreover, we checked if glucose oxidation might be altered in *KD/KO* retinas but no significant differences were found with respect to *WT/WT* retinas (Fig. 6D).

We next wondered whether this decrease in oxygen consumption rates was associated with a decrease in mitochondrial DNA copy number in *Cerkl*-depleted retinas. Retinal extracts from *WT/WT* and *KD/KO* retinas were used to determine mtDNA-encoded *CYTB* copy number, which tended to be higher in *KD/KO* retinas compared with wild type situation, but without reaching statistical significance (Fig. 6E).

In order to explore whether alterations in mitochondrial morphology and respiration may result in apoptotic activation, we measured caspase 3/7 activity in retinal disks from *WT/WT and KD/KO* retinas. Our results clearly indicated a significant increase in apoptosis in *KD/KO*, which could be associated to this decrease in mitochondrial function (Fig. 6F). We next analyzed possible changes in the abundance of total mitochondrial content and to this end, several OXPHOS proteins were immunodetected and quantified in retinal extracts from *WT/WT* and *KD/KO* retinas (Fig. 6G). As previously observed, VDAC protein levels supported an overall increase in mitochondrial content. Additionally, we observed significant increase in CIII-UQCRC2, while CII-SDHB levels tend to decrease. No changes were found in the expression of other OXPHOS proteins (CV-ATP5A, CII-SDHB, CI-NDUFB8) (Fig. 6H), suggesting differential modulation of structural and functional mitochondrial proteins.

3.6. KD/KO retinas display altered metabolism

In order to understand the metabolic changes in *KD/KO* retinas we further analyzed the RNaseq data. We found several downregulated genes involved in lipid metabolism (such as *Abca9* and *Hacd4*) as well energy metabolism related-genes (suchas *Suclg*, *Ndufa4l2*, *Cox8b* or several *Slc* genes) (Fig. 7 A–B). Other mitochondrial-related genes showed a significant adjusted *p* value (<0.05), even though the change of their expression was considered below the stringent theshold levels used for cut-off ('0.5 log$_2$Fc), (Fig. 7C and Supplementary Table S1).

Thus, we applied targeted metabolomic analysis to reveal if such changes may have an impact in energy metabolism related biomarkers analyzed in the retina.

After the quantitative analysis of amino acids, no significant changes were observed when we compared *WT/WT* and *KD/KO* model. Regarding organic acids, after the analysis of a large list of metabolites related with energy metabolism (Supplementary Table S2), succinate was found increased in the *KD/KO* retinas, but no other Krebs cycle metabolites or lactate (Fig. 7C). A second molecule that was significantly different when we compared both populations was pyroglutamic acid, which was significantly higher in the *KD/KO* (Fig. 7C).

4. Discussion

In this work we took advantage of the double heterozygote *Cerkl*$^{KD/}$

^{KO} model to describe for the first time the cellular scenario originated by the impairment of CERKL function in the mammalian retina. The retina, one of the most metabolically active regions of the central nervous system, is continuously subject to light stress and oxidative injury, which are extremely damaging to neurons and compromise retinal function. Photoreceptor and retinal ganglion cells are the retinal cell types most susceptible to apoptosis and their survival depends on the action of cell resilience and anti-apoptotic mechanisms to prevent premature death. We here provide strong evidence of mitochondrial localization of CERKL in the mammalian retina. In particular, CERKL isoforms containing exon 5 strongly localize at mitochondria. Interestingly, the *Cerkl* protein sequence does not include any mitochondrial localization signal. However, exon 5 encodes a domain with an ATP-binding site that is conserved in vertebrates (Riera et al., 2013). Of note, the most prevalent RP mutation (R283X) is in exon 5, highlighting the importance of mitochondrial localization of CERKL. Given the very dynamic nature of CERKL subcellular localization, we postulated that a certain pool of CERKL isoforms (especially those including exon 5) can be recruited at mitochondria at basal level and/or in response to certain stimuli. CERKL had been already reported to interact with TRX2 at mitochondria in NIH3T3 cells, regulating the mitochondrial peroxiredoxin-mediated antioxidant pathway (Li et al., 2014). In view of our results, CERKL may be also recruited to mitochondria by interacting with additional scaffold mitochondrial proteins.

We wondered if *Cerkl* downregulation could have an impact on mitochondrial function. Mitochondria supply energy to the cell through oxidative phosphorylation (OXPHOS), which result to be more advantageous in terms of energetic yield if compared with glycolysis. It has been shown that photoreceptor mitochondria perform at their maximal respiratory capacity, with limited reserve below 25% (Kooragayala et al., 2015). Consequently, photoreceptors are very sensitive to alterations in aerobic energy metabolism and their survival closely depends on metabolic homeostasis. Our data points to the ability of CERKL to functionally impact mitochondrial respiration but not glycolysis or glucose oxidation in retina. In *Cerkl*-depleted retinas, the bioenergetics decrease detected by Seahorse is supported by changes in the levels proteins from different complexes of the OXPHOS system. Moreover, we observed transcriptional changes in several OXPHOS genes (Fig. 7B–C).

Targeted metabolomic analysis revealed that most energy-related metabolites were not different when we compared *WT/WT* and *KD/KO* retinas. It was not a surprise since this observation has been consistently reported in humans with different mitochondrial disorders of genetic origin. Interestingly, succinate was significantly higher in *KD/KO*. Two hypotheses may explain these results: i) the decreased expression of *Suclg2* gene detected in RNASeq analysis; *Suclg2* encodes the succinate-Coenzyme A ligase, which metabolize succinate to succinyl-CoA in a reversible reaction coupled to GDP/GTP; ii) the slight reduction observed in mitochondrial complex II protein. In any case, succinate is a metabolite with pleiotropic properties, since it has been involved in energy metabolism, in regulation of ketone body utilization, ROS homeostasis, tumorigenesis, inflammation or hypoxia, among other conditions (Tretter et al., 2016). Pyroglutamic acid, a precursor of glutathione, was also increased in *KD/KO*. Although no evidences were observed after RNAseq analysis in the genes related with the glutathione cycle, this finding might reflect an increased glutathione biosynthesis to cope with the increased ROS generation in *Cerkl*-mutant retinas.

Our findings point out a state of metabolic stress in *KD/KO* retinas, which could have strong negative effects on photoreceptors homeostasis. Indeed, studies performed in 661 W cells showed that changes in energy metabolism correlates with the amount of subsequent cell death (Perron et al., 2013). Previous work showed that CERKL overexpression protects cells from apoptosis and that its downregulation induce apoptosis-like cell death in zebrafish (Tuson et al., 2009; Riera et al., 2013). Interestingly, we were able to detect retinal cell death through analysis of caspase 3/7 activity, which significantly increased in *KD/KO* retinal explants. The initiation of apoptosis at this stage could be

11
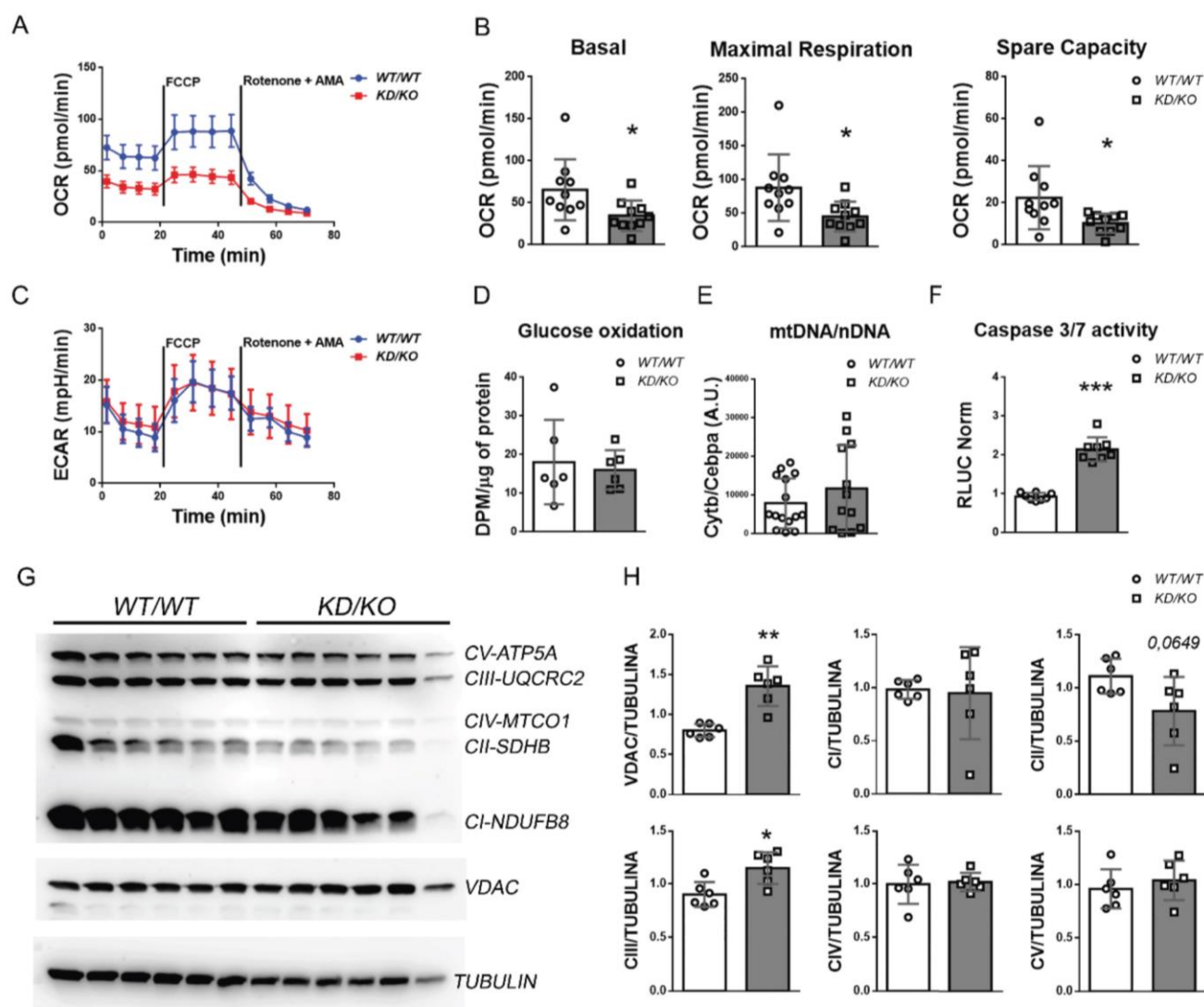
Fig. 6. Oxygen consumption impairment in *KD/KO* retinas. A) Diminished oxygen consumption rate (OCR) in *KD/KO* retinas compared to *WT/WT* as measured by Seahorse XF24 Analyzer. **B)** Basal: initial OCR without treatment; maximal respiration: after addition of FCCP (carbonyl cyanide-4-trifluoromethoxy phenyl-hydrazone); spare capacity: calculated by subtracting basal respiration from maximal respiratory capacity. Treatment with rotenone and antimycin A (AMA) reveals non-mitochondrial respiration. **C)** No differences in extracellular acidification response (ECAR) were detected between genotypes in the same experiment of A). A) to C) ($n = 10$ retinal disks from 3 animals per genotype). **D)** Glucose uptake in *WT/WT* and *KD/KO* retinas were detected by a glucose oxidation assay. ($n = 6$ retinas from 3 animals per genotype). **E)** mtDNA relative abundance in *WT/WT* and *KD/KO* retinas. ($n = 12$–15 retinas from 6 to 8 animals per genotype). Statistical analysis in A) to E) was performed with 2-tailes Student's t-test and represented as the means±SEM. **F)** Caspase 3/ activity in *WT/WT* and *KD/KO* retinal disks. ($n = 9$ retinal disks from 3 animals per genotype). Statistical analysis by Mann-Whitney test. ***: p-value $\leq 0{,}001$ **G)** Western blots of OXPHOS proteins and VDAC in *WT/WT* and *KD/KO* retinas. **H)** Densitometric quantification of mitochondrial proteins. (n = 6 retinas from 3 animals per genotype). Data are represented as the means±SD. Statistical analysis was performed with Mann-Whitney test. *: p-value $\leq 0{,}05$; **: p-value $\leq 0{,}01$.

considered the beginning of the neurodegenerative process that could progress with age, thus inducing neuroinflammation, photoreceptor loss and finally culminating in the visual impairment characterizing *Cerkl*$^{KD/KO}$ aged mice (Domenech et al., 2020).

Energy depletion usually generates oxidative stress conditions, mitochondrial depolarization and mitochondrial damage. Interestingly, mitochondrial dysfunction has been found in retinas of relatively young *KD/KO* mice (3-month old) and could represent a metabolic trigger for the wide set of cellular alteration observed in this study. Indeed, in a global scenario of metabolic dysfunction, the activation of autophagy can be interpreted as a stereotyped response to restore cellular homeostasis by: i) supplying the cell with the nutrients and energy in order to

compensate metabolic imbalance; ii) eliminating cellular components and organelles that are damaged by oxidative stress arising from mitochondrial dysfunction; iii) activating anti-oxidant response by inducing of p62/Keap1/Nrf2 system. Interestingly, RNAseq analysis provided several differentially regulated genes that are involved in the anti-oxidant response through autophagy regulation. Among them, *Depp* is an hypoxia-induced gene involved in autophagy that mediates autophagosome formation (Salcher et al., 2017; Stepp et al., 2014); *Tspo* is an outer-mitochondrial membrane protein that acts as redox regulator of cell mitophagy and lipophagy (Kim et al., 2020; Scaini et al., 2019; Gatliff and Campanella, 2015); *Dram1* is a lysosomal membrane protein that is required for the autophagy induction via inhibition of P3K-AKT-
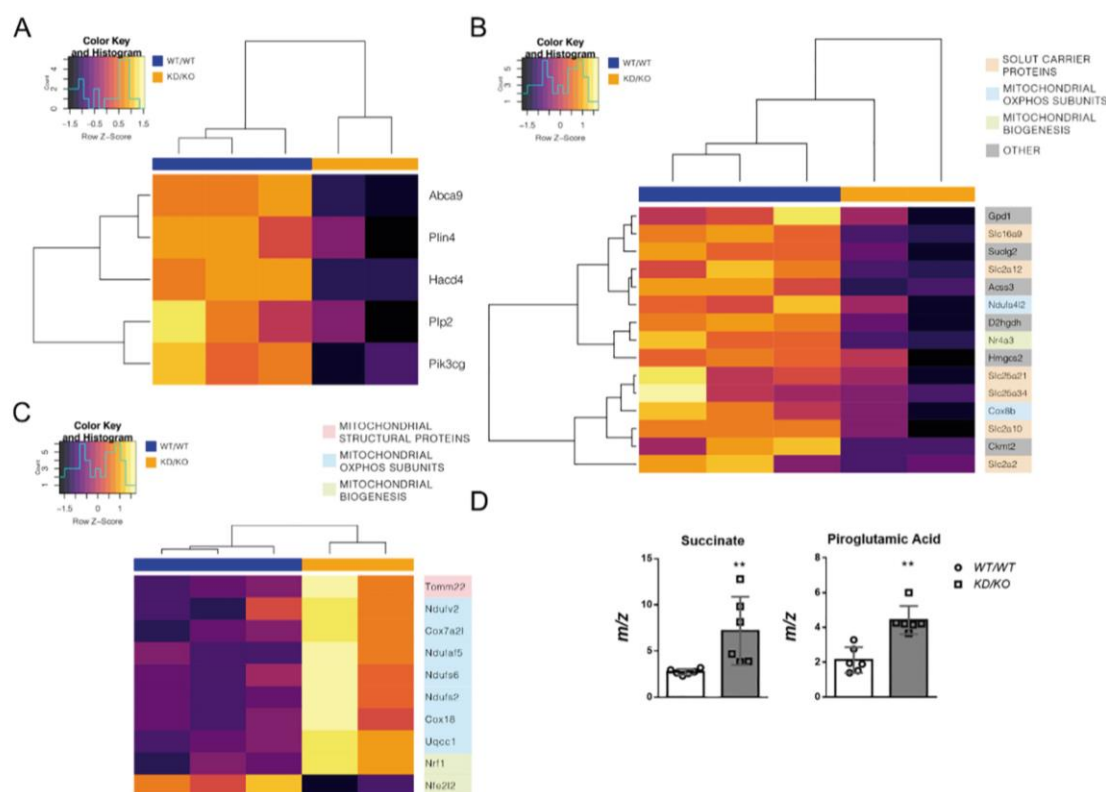
Fig. 7. A–B) Heatmap with hierachical clustering of differentially expressed lipid-related (A) and mitochondrial-energy-related genes (B) of *WT/WT* (group in blue) versus KD/KO (group in orange) mouse retinas. **C)** Graphical representation of mitochondrial biology-related genes with a significant adjusted *p* value (< 0.05) which were not included in B) because of their lower log₂Fc values ('0.5). The heatmap colours reflect differences in gene expression between the group of genes selected for comparison but are not directly related to the global gene expression levels. **D)** Targeted metabolomic analysis revealed changes in succinate and piroglutamic acid in the *KD/KO* retinas. Data are shown as the mean ± SD. Statistical analysis by Mann-Whitney test. **: *p*-value ≤0,01. (For interpretation of the references to colour in this figure legend, the reader is referred to the web version of this article.)

mTOR-S6 pathway among others (Lu et al., 2019; Wu et al., 2018; Nagata et al., 2018); *Dram2* induces autophagy in a p53-dependent manner, and its mutations are causative of autosomal recessive adult-onset cone-rod dystrophy (Abad-Morales et al., 2019; Yoon et al., 2012); and *Sestrin2* is induced upon stressful conditions to sustain NRF2 activation and activates autophagy by both inhibiting mTORC1 and activating AMPK (Bae et al., 2013; Parmigiani et al., 2014; Morsch et al., 2019). Interestingly, SESTRIN2 was expressed in the inner segment of photoreceptors, where mitochondria are mainly localized.

The scarcity of data concerning the molecular function of CERKL includes the notion that CERKL interacts with SIRT1, one of the main regulators of acetylation/deacetylation in autophagy (Hu et al., 2019). In Zebrafish *Cerkl*-depleted retinas SIRT1 was downregulated as they were its targets ATG5 and ATG7 (both showing a higher degree of acetylation); as a consequence, autophagy decreased (Hu et al., 2019). We also observed a decrease in SIRT1 protein levels in in *KD/KO* mouse retinas (Supplementary Fig. S6), suggesting that additional molecular mechanisms contribute to autophagy regulation in mammalian retina. Therefore, further studies are required to outline the role of CERKL-SIRT1 interaction in mammalian retina and the mechanisms of autophagy induction.

In recent years multiple findings have shed light on the important role of autophagy in the maintenance of photoreceptor homeostasis and therefore, of visual function (Boya et al., 2016). Autophagy alterations have been related with RP, but the evidence regarding its role in the disease is controversial, probably due to both the wide heterogeneity of this pathology and the different roles that autophagy may play in the death of rods and cones. Moreover, autophagy is usually beneficial under low levels of stress but may be deleterious when the stress

dramatically increases, thus leading to cell death and degeneration (Chen et al., 2013; Punzo et al., 2009; Zaninello et al., 2020). Our data demonstrate an increased basal autophagy that is also concomitant with cell death, probably at the early stages of neurodegeneration, given the absence of visual impairment at the phenotypic level in young animals (Domenech et al., 2020). It may represent either a residual attempt to restore cellular homeostasis and/or a first manifestation of cell death commitment.

The phenotype of mitochondrial fragmentation in *KD/KO* is indicative of alterations in mitochondrial dynamics, such as an increased fission, a decreased fusion and/or alteration in mitochondrial trafficking along the axons. Alterations in mitochondrial dynamics may cause cytoarchitectural changes previously observed in *KD/KO* RGCs, which included axon shortening and dendritic arbor expansion (Domenech et al., 2020). However, we have not observed transcriptional changes in the more conventional and well characterized molecular pathways regulating mitochondrial morphology (Supplementary Table S1). However, the alteration in mitochondrial morphology may derive from changes in the protein levels or post-translational modification. Consistently, we found that MITOFUSIN2 is downregulated in *KD/KO* retinas. Further work will determine the mechanism of CERKL role in the regulation of mitochondrial morphology.

Global alteration in mitochondrial dynamics could be a consequence of mitochondrial dysfunction. Indeed, a wide set of findings support the model that mitochondrial fission promote the segregation of damaged mitochondria and facilitate their clearance by mitophagy (Twig et al., 2008; Ashrafi and Schwarz, 2012; Buhlman et al., 2014). By using different in vitro and ex vivo approaches, we demonstrated that general autophagy is increased in *KD/KO* retinas. Accumulation of mitochondria

13
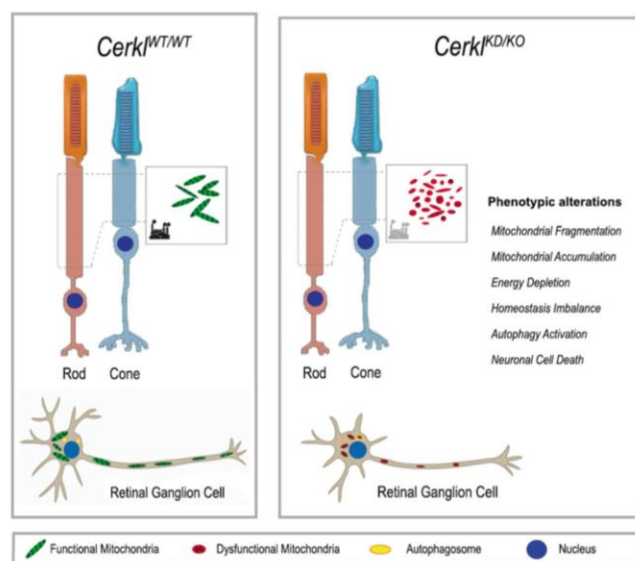
Fig. 8. Model for the altered cellular phenotype observed in *Cerkl*^KD/KO^ photoreceptors and retinal ganglion cells. Depletion of *Cerkl* expression increased mitochondrial content in *Cerkl*^KD/KO^ photoreceptors, concomitant to mitochondrial dysfunction in *Cerkl*^KD/KO^ retina and increased autophagy activation, thus reflecting homeostasis imbalance. Cell death was also increased in *Cerkl*^KD/KO^ retinal explants.

is not accompanied by a massive induction of mitochondrial biogenesis pathways; thus, we hypothesize a loss of the synergic modulation between mitochondrial biogenesis and mitochondrial clearance in *KD/KO* retinas. Nevertheless, this strong response in activating autophagy does not correlate with an increased mitophagy neither in vivo in photoreceptors nor in vitro in RGCs. In spite the recent generation of reliable tools to analyzing mitophagy in vivo, the assessment of mitochondrial selective autophagy in the retina remains changeling (McWilliams et al., 2019; Rosignol et al., 2020). However, data coming from CERKL overexpression in 661 W photoreceptor-derived cell line support that CERKL increases mitophagy and allows to postulate that its depletion could prevent mitophagy. This possibility is supported by the increase in mitochondrial content observed in *KD/KO* retinas. Those mechanisms would be necessary to ensure a neuroprotective effect in a context of strong metabolic dysfunction. Our proposed model for the cellular phenotype observed in *Cerkl*^KD/KD^ photoreceptors and ganglion cells is summarized in Fig. 8. Depletion of *Cerkl* expression induced mitochondrial dysfunction that cannot be compensated by synergic modulation of mitophagy and mitochondrial biogenesis. In this context cellular metabolism and homeostasis are impaired, autophagy increases, and cells start to undergo apoptosis.

Additionally, *Cerkl*^KD/KO^ RGCs showed alterations in axonal mitochondrial morphology and distribution, which probably resulted in the cytoarchitectural changes observed (previous work, (Domenech et al., 2020)), such as increased number of neurites and shortened axons.

An increasing number of studies report novel mechanisms and molecular actors regulating mitochondrial dynamics and function, which are essential in central nervous system in both physiological processes and disease conditions (Khacho and Slack, 2018; Mirra et al., 2016; Yang et al., 2020; Zhang et al., 2020). Consequently, mitochondria represent a promising therapeutic target, and several therapeutical strategies have been reported to act on mitochondrial related retinal diseases. These strategies include gene therapy, microRNA, genome editing, optogenetics, and stem cell-mediated mitochondrial donation (Carrella et al., 2020; Jiang et al., 2019). Moreover, the functional characterizations of metabolic and signaling pathways that are altered by mutations in RP causative genes are essential to face the great challenge of designing

efficient therapeutic strategies. Our results here provide a list of mitochondrial metabolic pathways altered by *CERKL* mutations that are worth exploring. We propose that restoring homeostasis and mitochondrial function in some IRDs may increase photoreceptor resilience and thus slow down, or even halt, the progress of retinal neurodegeneration.

5. Conclusions

In conclusion, our results support that the retinal degeneration *CERKL* gene is a regulator of mitochondrial biology with a retinal resilience role. *Cerkl* downregulation has an impact on mitochondrial morphology, dynamics, and mitochondria-energy-related processes. We propose a model to explain why mutations in this gene leads to severe retinal cell death in Retinitis Pigmentosa and CRD. This study opens novel therapeutic avenues based on a metabolic intervention approach to treat retinal neurodegeneration.

Supplementary data to this article can be found online at https://doi.org/10.1016/j.nbd.2021.105405.

References

Abad-Morales, V., Burés-Jelstrup, A., Navarro, R., Ruiz-Nogales, S., Méndez-Vendrell, P., Corcóstegui, B., Pomares, E., 2019. Characterization of the cone-rod dystrophy retinal phenotype caused by novel homozygous DRAM2 mutations. Exp. Eye Res. 187, 107752. https://doi.org/10.1016/j.exer.2019.107752.

Aleman, T.S., Soumittra, N., Cideciyan, A.V., Sumaroka, A.M., Ramprasad, V.L., Herrera, W., Windsor, E.A.M., Schwartz, S.B., Russell, R.C., Roman, A.J., Inglehearn, C.F., Kumaramanickavel, G., Stone, E.M., Fishman, G.A., Jacobson, S.G., 2009. CERKL mutations cause an autosomal recessive cone-rod dystrophy with inner retinopathy. Investig. Ophthalmol. Vis. Sci. 50, 5944–5954. https://doi.org/10.1167/iovs.09-3982.

Ali, M., Ramprasad, V.L., Soumittra, N., Mohamed, M.D., Jafri, H., Rashid, Y., Danciger, M., McKibbin, M., Kumaramanickavel, G., Inglehearn, C.F., 2008. A missense mutation in the nuclear localization signal sequence of CERKL (p.R106S) causes autosomal recessive retinal degeneration. Mol. Vis. 14, 1960–1964. http://www.ncbi.nlm.nih.gov/pubmed/18978954 (accessed May 1, 2020).

Ashrafi, G., Schwarz, T.L., 2012. The pathways of mitophagy for quality control and clearance of mitochondria. Cell Death Differ. 20, 31–42. https://doi.org/10.1038/cdd.2012.81.

Bae, S.H., Sung, S.H., Oh, S.Y., Lim, J.M., Lee, S.K., Park, Y.N., Lee, H.E., Kang, D., Rhee, S.G., 2013. Sestrins activate Nrf2 by promoting p62-dependent autophagic

degradation of keap1 and prevent oxidative liver damage. Cell Metab. 17, 73–84. https://doi.org/10.1016/j.cmet.2012.12.002.

Bornancin, F., Mechtcheriakova, D., Stora, S., Graf, C., Wlachos, A., Dévay, P., Urtz, N., Baumruker, T., Billich, A., 2005. Characterization of a ceramide kinase-like protein. Biochim. Biophys. Acta Mol. Cell Biol. Lipids 1687, 31–43. https://doi.org/10.1016/j.bbalip.2004.11.012.

Boya, P., Reggiori, F., Codogno, P., 2013. Emerging regulation and functions of autophagy. Nat. Cell Biol. 15, 713–720. https://doi.org/10.1038/ncb2788.

Boya, P., Esteban-Martínez, L., Serrano-Puebla, A., Gómez-Sintes, R., Villarejo-Zori, B., 2016. Autophagy in the eye: development, degeneration, and aging. Prog. Retin. Eye Res. 55, 206–245. https://doi.org/10.1016/j.preteyeres.2016.08.001.

Buhlman, L., Damiano, M., Bertolin, G., Ferrando-Miguel, R., Lombès, A., Brice, A., Corti, O., 2014. Functional interplay between Parkin and Drp1 in mitochondrial fission and clearance. Biochim. Biophys. Acta, Mol. Cell Res. 1843, 2012–2026. https://doi.org/10.1016/j.bbamcr.2014.05.012.

Carrella, S., Indrieri, A., Franco, B., Banfi, S., 2020. Mutation-independent therapies for retinal diseases: focus on gene-based approaches. Front. Neurosci. 14 https://doi.org/10.3389/fnins.2020.588234.

Casado, M., Sierra, C., Batllori, M., Artuch, R., Ormazabal, A., 2018. A targeted metabolomic procedure for amino acid analysis in different biological specimens by ultra-high-performance liquid chromatography-tandem mass spectrometry. Metabolomics 14 (6), 76. https://doi.org/10.1007/s11306-018-1374-4.

Chen, Y., Sawada, O., Kohno, H., Le, Y.Z., Subauste, C., Maeda, T., Maeda, A., 2013. Autophagy protects the retina from light-induced degeneration. J. Biol. Chem. 288, 7506–7518. https://doi.org/10.1074/jbc.M112.439935.

Cherubini, M., Puigdellívol, M., Alberch, J., Ginés, S., 2015. Cdk5-mediated mitochondrial fission: a key player in dopaminergic toxicity in Huntington's disease. Biochim. Biophys. Acta Mol. basis Dis. 1852, 2145–2160. https://doi.org/10.1016/j.bbadis.2015.06.025.

Domenech, E.B., Andres, R., Lopez-Iniesta, Jose, Mirra, S., Arroyo, R.G., Milla, S., Sava, F., Andilla, J., Alvarez, P.L., De La Villa, P., Duarte, R.G., Marfany, G., 2020. A New cerkl mouse model generated by crispr-cas9 shows progressive retinal degeneration and altered morphological and electrophysiological phenotype. Investig. Ophthalmol. Vis. Sci. 61 https://doi.org/10.1167/IOVS.61.8.14.

Eells, J.T., 2019. Mitochondrial dysfunction in the aging retina. Biology (Basel). 8 https://doi.org/10.3390/biology8020031.

Esteban-Martínez, L., Doménech, E., Boya, P., Salazar-Roa, M., Malumbres, M., 2015. Mitophagy in mitosis: more than a myth. Autophagy. 11, 2379–2380. https://doi.org/10.1080/15548627.2015.1108509.

Fathinajafabadi, A., Pérez-Jiménez, E., Riera, M., Knecht, E., Gonzàlez-Duarte, R., 2014. CERKL, a retinal disease gene, encodes an mRNA-binding protein that localizes in compact and untranslated mRNPs associated with microtubules. PLoS One. https://doi.org/10.1371/journal.pone.0087898.

Garanto, A., Riera, M., Pomares, E., Permanyer, J., de Castro-Mir, M., Sava, F., Abril, J.F., Marfany, G., Gonzlez-Duarte, R., 2011. High transcriptional complexity of the retinitis pigmentosa CERKL gene in human and mouse. Investig. Ophthalmol. Vis. Sci. 52, 5202–5214. https://doi.org/10.1167/iovs.10-7101.

Garanto, A., Vicente-Tejedor, J., Riera, M., De la Villa, P., Riera, M., Gonzàlez-Duarte, R., Blanco, R., Marfany, G., 2012. Targeted knockdown of Cerkl, a retinal dystrophy gene, causes mild affectation of the retinal ganglion cell layer. Biochim. Biophys. Acta Mol. basis Dis. 1822, 1258–1269. https://doi.org/10.1016/j.bbadis.2012.04.004.

Garanto, A., Mandal, N.A., Egido-Gabás, M., Marfany, G., Fabriàs, G., Anderson, R.E., Casas, J., Gonzàlez-Duarte, R., 2013. Specific sphingolipid content decrease in Cerkl knockdown mouse retinas. Exp. Eye Res. https://doi.org/10.1016/j.exer.2013.03.003.

Gatica, D., Lahiri, V., Klionsky, D.J., 2018. Cargo recognition and degradation by selective autophagy. Nat. Cell Biol. 20, 233–242. https://doi.org/10.1038/s41556-018-0037-z.

Gatliff, J., Campanella, M., 2015. TSPO is a REDOX regulator of cell mitophagy. Biochem. Soc. Trans. 43, 543–552. https://doi.org/10.1042/BST20150037.

Hu, X., Lu, Z., Yu, S., Reilly, J., Liu, F., Jia, D., Qin, Y., Han, S., Liu, X., Qu, Z., Lv, Y., Li, J., Huang, Y., Jiang, T., Jia, H., Wang, Q., Liu, J., Shu, X., Tang, Z., Liu, M., 2019. CERKL regulates autophagy via the NAD-dependent deacetylase SIRT1. Autophagy. 15, 453–465. https://doi.org/10.1080/15548627.2018.1520548.

Huang, D.W., Sherman, B.T., Lempicki, R.A., 2009. Systematic and integrative analysis of large gene lists using DAVID bioinformatics resources. Nat. Protoc. 4, 44–57. https://doi.org/10.1038/nprot.2008.211.

Inagaki, Y., Mitsutake, S., Igarashi, Y., 2006. Identification of a nuclear localization signal in the retinitis pigmentosa-mutated RP26 protein, ceramide kinase-like protein. Biochem. Biophys. Res. Commun. 343, 982–987. https://doi.org/10.1016/j.bbrc.2006.03.056.

Jiang, D., Xiong, G., Feng, H., Zhang, Z., Chen, P., Yan, B., Chen, L., Gandhervin, K., Ma, C., Li, C., Han, S., Zhang, Y., Liao, C., Lee, T.L., Tse, H.F., Fu, Q.L., Chiu, K., Lian, Q., 2019. Donation of mitochondria by iPSC-derived mesenchymal stem cells protects retinal ganglion cells against mitochondrial complex I defect-induced degeneration. Theranostics. 9, 2395–2410. https://doi.org/10.7150/thno.29422.

Khacho, M., Slack, R.S., 2018. Mitochondrial dynamics in the regulation of neurogenesis: from development to the adult brain. Dev. Dyn. 247, 47–53. https://doi.org/10.1002/dvdy.24538.

Kim, S., Kim, N., Park, S., Jeon, Y., Lee, J., Yoo, S.J., Lee, J.W., Moon, C., Yu, S.W., Kim, E.K., 2020. Tanycytic TSPO inhibition induces lipophagy to regulate lipid metabolism and improve energy balance. Autophagy. 16, 1200–1220. https://doi.org/10.1080/15548627.2019.1659616.

Kooragayala, K., Gotoh, N., Cogliati, T., Nellissery, J., Kaden, T.R., French, S., Balaban, R., Li, W., Covian, R., Swaroop, A., 2015. Quantification of oxygen consumption in retina ex vivo demonstrates limited reserve capacity of photoreceptor mitochondria. Investig. Ophthalmol. Vis. Sci. 56, 8428–8436. https://doi.org/10.1167/iovs.15-17901.

Li, C., Wang, L., Zhang, J., Huang, M., Wong, F., Liu, X., Liu, F., Cui, X., Yang, G., Chen, J., Liu, Y., Wang, J., Liao, S., Gao, M., Hu, X., Shu, X., Wang, Q., Yin, Z., Tang, Z., Liu, M., 2014. CERKL interacts with mitochondrial TRX2 and protects retinal cells from oxidative stress-induced apoptosis. Biochim. Biophys. Acta Mol. basis Dis. https://doi.org/10.1016/j.bbadis.2014.04.009.

Love, M.I., Huber, W., Anders, S., 2014. Moderated estimation of fold change and dispersion for RNA-seq data with DESeq2. Genome Biol. 15 https://doi.org/10.1186/s13059-014-0550-8.

Lu, T., Zhu, Z., Wu, J., She, H., Han, R., Xu, H., Qin, Z.H., 2019. DRAM1 regulates autophagy and cell proliferation via inhibition of the phosphoinositide 3-kinase-Akt-mTOR-ribosomal protein S6 pathway. Cell Commun. Signal. 17 https://doi.org/10.1186/s12964-019-0341-7.

Mandal, A., Drerup, C.M., 2019. Axonal transport and mitochondrial function in neurons. Front. Cell. Neurosci. 13 https://doi.org/10.3389/fncel.2019.00373.

McWilliams, T.G., Prescott, A.R., Villarejo-Zori, B., Ball, G., Boya, P., Ganley, I.G., 2019. A comparative map of macroautophagy and mitophagy in the vertebrate eye. Autophagy. 15, 1296–1308. https://doi.org/10.1080/15548627.2019.1580509.

Mirra, S., Marfany, G., 2019. Mitochondrial gymnastics in retinal cells: a resilience mechanism against oxidative stress and neurodegeneration. In: Adv. Exp. Med. Biol. Springer, pp. 513–517. https://doi.org/10.1007/978-3-030-27378-1_84.

Mirra, S., Ulloa, F., Gutierrez-Vallejo, I., Martì, E., Soriano, E., 2016. Function of Armcx3 and Armc10/SVH genes in the regulation of progenitor proliferation and neural differentiation in the chicken spinal cord. Front. Cell. Neurosci. 10 https://doi.org/10.3389/fncel.2016.00047.

Mizushima, N., Levine, B., 2020. Autophagy in human diseases. N. Engl. J. Med. 383, 1564–1576. https://doi.org/10.1056/nejmra2022774.

Morsch, A.L.B.C., Wisniewski, E., Luciano, T.F., Comin, V.H., de Silveira, G.B., de Marques, S.O., Thirupathi, A., Lock, P.C. Silveira, De Souza, C.T., 2019. Cigarette smoke exposure induces ROS-mediated autophagy by regulating sestrin, AMPK, and mTOR level in mice. Redox Rep. 24, 27–33. https://doi.org/10.1080/13510002.2019.1601448.

Nagata, M., Arakawa, S., Yamaguchi, H., Torii, S., Endo, H., Tsujioka, M., Honda, S., Nishida, Y., Konishi, A., Shimizu, S., 2018. Dram1 regulates DNA damage-induced alternative autophagy. Cell Stress. 2, 55–65. https://doi.org/10.15698/cst2018.03.127.

Narayan, D.S., Chidlow, G., Wood, J.P.M., Casson, R.J., 2017. Glucose metabolism in mammalian photoreceptor inner and outer segments. Clin. Exp. Ophthalmol. 45, 730–741. https://doi.org/10.1111/ceo.12952.

Nevet, M.J., Vekslin, S., Dizhoor, A.M., Olshevskaya, E.V., Tidhar, R., Futerman, A.H., Ben-Yosef, T., 2012. Ceramide kinase-like (CERKL) interacts with neuronal calcium sensor proteins in the retina in a cation-dependent manner. Investig. Ophthalmol. Vis. Sci. 53, 4565–4574. https://doi.org/10.1167/iovs.12-9770.

Parmigiani, A., Nourbakhsh, A., Ding, B., Wang, W., Kim, Y.C., Akopiants, K., Guan, K.L., Karin, M., Budanov, A.V., 2014. Sestrins inhibit mTORC1 kinase activation through the GATOR complex. Cell Rep. 9, 1281–1291. https://doi.org/10.1016/j.celrep.2014.10.019.

Perron, N.R., Beeson, C., Rohrer, B., 2013. Early alterations in mitochondrial reserve capacity; a means to predict subsequent photoreceptor cell death. J. Bioenerg. Biomembr. 45, 101–109. https://doi.org/10.1007/s10863-012-9477-5.

Punzo, C., Kornacker, K., Cepko, C.L., 2009. Stimulation of the insulin/mTOR pathway delays cone death in a mouse model of retinitis pigmentosa. Nat. Neurosci. 12, 44–52. https://doi.org/10.1038/nn.2234.

Riera, M., Burguera, D., Garcia-Fernàndez, J., Gonzàlez-Duarte, R., 2013. CERKL knockdown causes retinal degeneration in Zebrafish. PLoS One. https://doi.org/10.1371/journal.pone.0064048.

Rosignol, I., Villarejo-Zori, B., Teresak, P., Sierra-Filardi, E., Pereiro, X., Rodríguez-Muela, N., Vecino, E., Vieira, H.L.A., Bell, K., Boya, P., 2020. The mito-QC reporter for quantitative mitophagy assessment in primary retinal ganglion cells and experimental glaucoma models. Int. J. Mol. Sci. 21 https://doi.org/10.3390/ijms21051882.

Salcher, S., Hermann, M., Kiechl-Kohlendorfer, U., Ausserlechner, M.J., Obexer, P., 2017. C10ORF10/DEPP-mediated ROS accumulation is a critical modulator of FOXO3-induced autophagy. Mol. Cancer 16. https://doi.org/10.1186/s12943-017-0661-4.

Scaini, G., Barichello, T., Fries, G.R., Kennon, E.A., Andrews, T., Nix, B.R., Zunta-Soares, G., Valvassori, S., Soares, J.C., Quevedo, J., 2019. TSPO upregulation in bipolar disorder and concomitant downregulation of mitophagic proteins and NLRP3 inflammasome activation. Neuropsychopharmacology. 44, 1291–1299. https://doi.org/10.1038/s41386-018-0293-4.

Stepp, M.W., Folz, R.J., Yu, J., Zelko, I.N., 2014. The c10orf10 gene product is a new link between oxidative stress and autophagy. Biochim. Biophys. Acta, Mol. Cell Res. 1843, 1076–1088. https://doi.org/10.1016/j.bbamcr.2014.02.003.

Tretter, L., Patocs, A., Chinopoulos, C., 2016. Succinate, an intermediate in metabolism, signal transduction, ROS, hypoxia, and tumorigenesis. Biochim. Biophys. Acta Bioenerg. 1857, 1086–1101. https://doi.org/10.1016/j.bbabio.2016.03.012.

Tuson, M., Marfany, G., Gonzalez-Duarte, R., 2004. Mutation of CERKL, a novel human ceramide kinase gene, causes autosomal recessive retinitis pigmentosa (RP26). Am. J. Hum. Genet. 74, 128–138. https://doi.org/10.1086/381055.

Tuson, M., Garanto, A., Gonzalez-Duarte, R., Marfany, G., 2009. Overexpression of CERKL, a gene responsible for retinitis pigmentosa in humans, protects cells from apoptosis induced by oxidative stress. Mol.Vis. 15, 168–180.

Twig, G., Elorza, A., Molina, A.J.A., Mohamed, H., Wikstrom, J.D., Walzer, G., Stiles, L., Haigh, S.E., Katz, S., Las, G., Alroy, J., Wu, M., Py, B.F., Yuan, J., Deeney, J.T., Corkey, B.E., Shirihai, O.S., 2008. Fission and selective fusion govern mitochondrial

—113—

segregation and elimination by autophagy. EMBO J. 27, 433–446. https://doi.org/10.1038/sj.emboj.7601963.

Van Noolen, L., Acquaviva-Bourdain, C., Dessein, A.F., Minet-Quinard, R., Nowoczyn, M., Garnotel, R., Corne, C., 2020. Recommendations for urinary organic acids analysis. Ann. Biol. Clin. (Paris). 78, 547–554. https://doi.org/10.1684/ABC.2020.1583.

Villarroya, J., Diaz-Delfin, J., Hyink, D., Domingo, P., Giralt, M., Klotman, P.E., Villarroya, F., 2010. HIV type-1 transgene expression in mice alters adipose tissue and adipokine levels: towards a rodent model of HIV type-1 lipodystrophy. Antivir. Ther. 15, 1021–1028. https://doi.org/10.3851/IMP1669.

Wu, X., Qin, Y., Zhu, X., Liu, D., Chen, F., Xu, S., Zheng, D., Zhou, Y., Luo, J., 2018. Increased expression of DRAM1 confers myocardial protection against ischemia via restoring autophagy flux. J. Mol. Cell. Cardiol. 124, 70–82. https://doi.org/10.1016/j.yjmcc.2018.08.018.

Yang, Y., Klionsky, D.J., 2020. Autophagy and disease: unanswered questions. Cell Death Differ. 27, 858–871. https://doi.org/10.1038/s41418-019-0480-9.

Yang, W., Xiong, G., Lin, B., 2020. Cyclooxygenase-1 mediates neuroinflammation and neurotoxicity in a mouse model of retinitis pigmentosa. J. Neuroinflammation 17. https://doi.org/10.1186/s12974-020-01993-0.

Yoon, J.H., Her, S., Kim, M., Jang, I.S., Park, J., 2012. The expression of damage-regulated autophagy modulator 2 (DRAM2) contributes to autophagy induction. Mol. Biol. Rep. 39, 1087–1093. https://doi.org/10.1007/s11033-011-0835-x.

Zaninello, M., Palikaras, K., Naon, D., Iwata, K., Herkenne, S., Quintana-Cabrera, R., Semenzato, M., Grespi, F., Ross-Cisneros, F.N., Carelli, V., Sadun, A.A., Tavernarakis, N., Scorrano, L., 2020. Inhibition of autophagy curtails visual loss in a model of autosomal dominant optic atrophy. Nat. Commun 11 https://doi.org/10.1038/s41467-020-17821-1.

Zemirli, N., Morel, E., Molino, D., 2018. Mitochondrial dynamics in basal and stressful conditions. Int. J. Mol. Sci. 19 https://doi.org/10.3390/ijms19020564.

Zhang, Z., Yan, B., Gao, F., Li, Q., Meng, X., Chen, P., Zhou, L., Deng, W., Li, C., Xu, W., Han, S., Feng, H., Li, Y., Chen, J., Yin, Z., Liao, C., Tse, H.F., Xu, A., Lian, Q., 2020. PSCs reveal PUFA-provoked mitochondrial stress as a central node potentiating RPE degeneration in Bietti's crystalline dystrophy. Mol. Ther. 28, 2642–2661. https://doi.org/10.1016/j.ymthe.2020.07.024.

114

Supplemental material
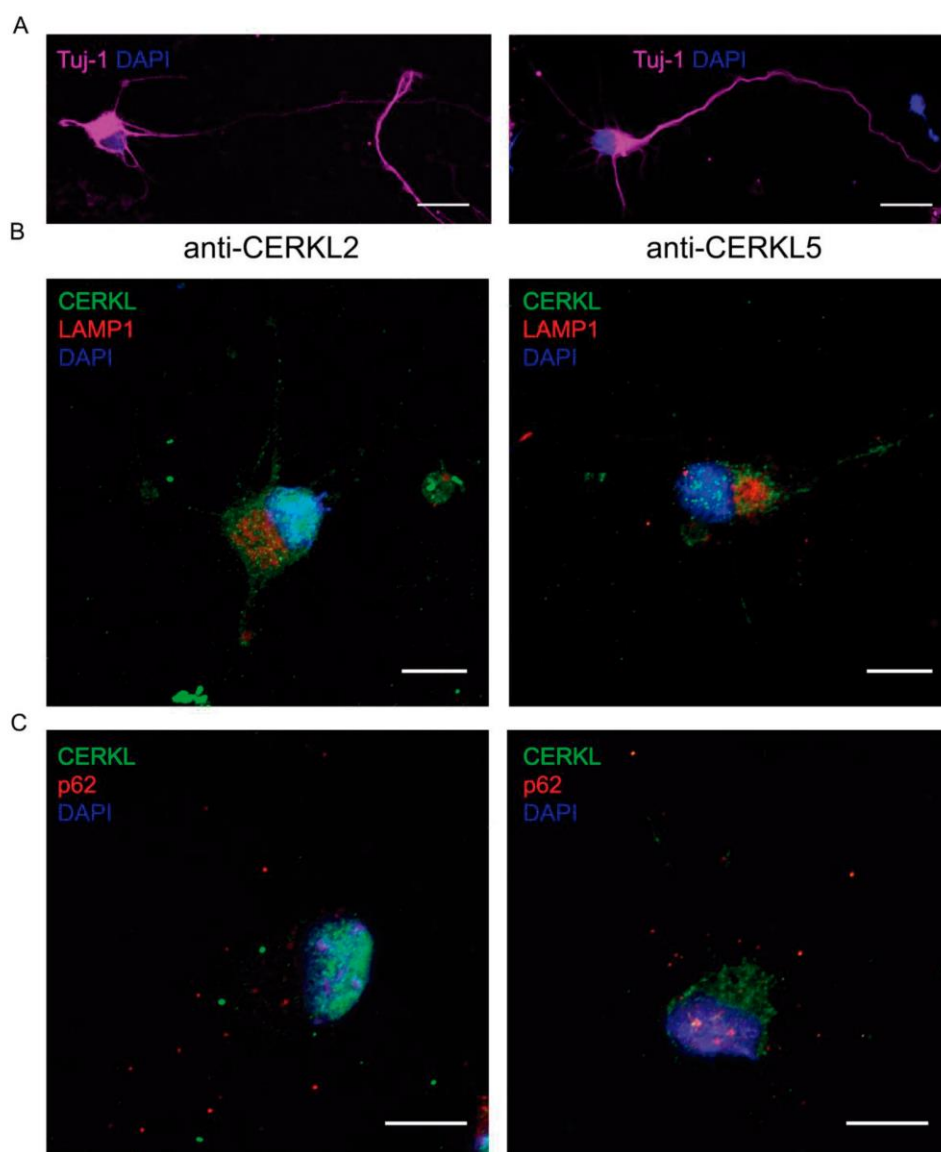
S1 Fig. CERKL does not co-localize with lysosomes or autophagosomes in mouse postnatal RGCs. **A)** Immunofluorescence in primary retinal cultures allowed to distinguish TUBULIN-III-β positive RGCs (magenta), characterized by a typical somatic morphology and a large axon. Scale bar: 20 μm. **B,C)** Immunofluorescence of RGCs in primary retinal cultures with anti-CERKL2 (green, left panels) and anti-CERKL5 (green, right panels) antibodies. Scale bar: 10 μm.
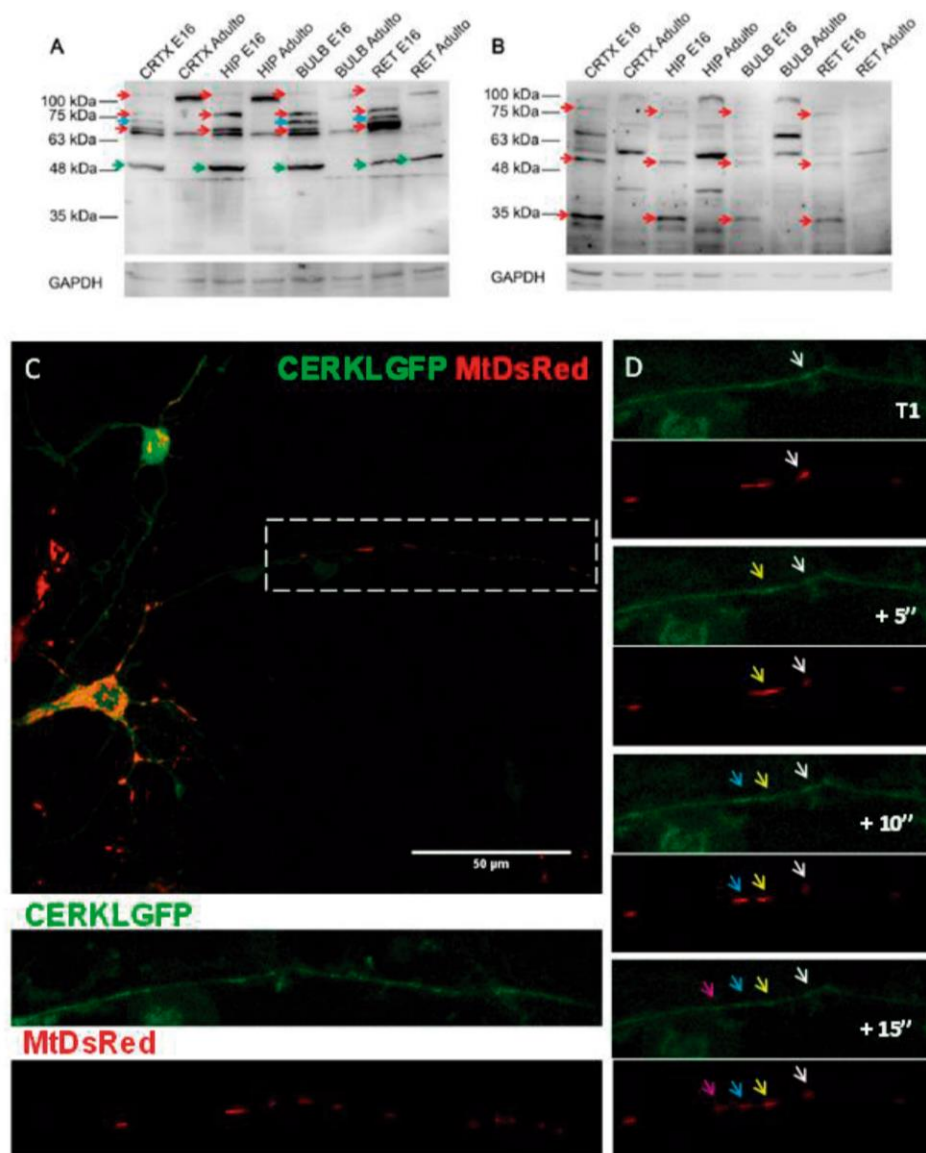
S2 Fig. CERKL is expressed in both developing and adult brain and associates with motile mitochondria in hippocampal cultures. A, B) Western blot analysis of CERKL expression in several neural tissues by using anti-CERKL2 (A) and anti-CERKL5 (B). Red arrows: CERKL isoforms most expressed at embryonic stage E16; green arrows: CERKL isoforms most expressed at embryonic stage E16 in retina and olfactory bulb; blue arrows: CERKL isoforms most expressed at embryonic stage E16 and adult retina. CRTX=cortex, HIP=hippocampus, BULB=olfactive bulb, RET=retina. **C)** Hippocampal mouse neurons overexpressing CERKL-GFP cDNA display normal mitochondrial distribution in cell body, neurites and axon (C, axonal projection in D). Scale bar 50 µm. **D)** Series of four

representative confocal images, taken every 5 seconds, of live axons overexpressing MtDsRed or CERKL-GFP fusion protein.
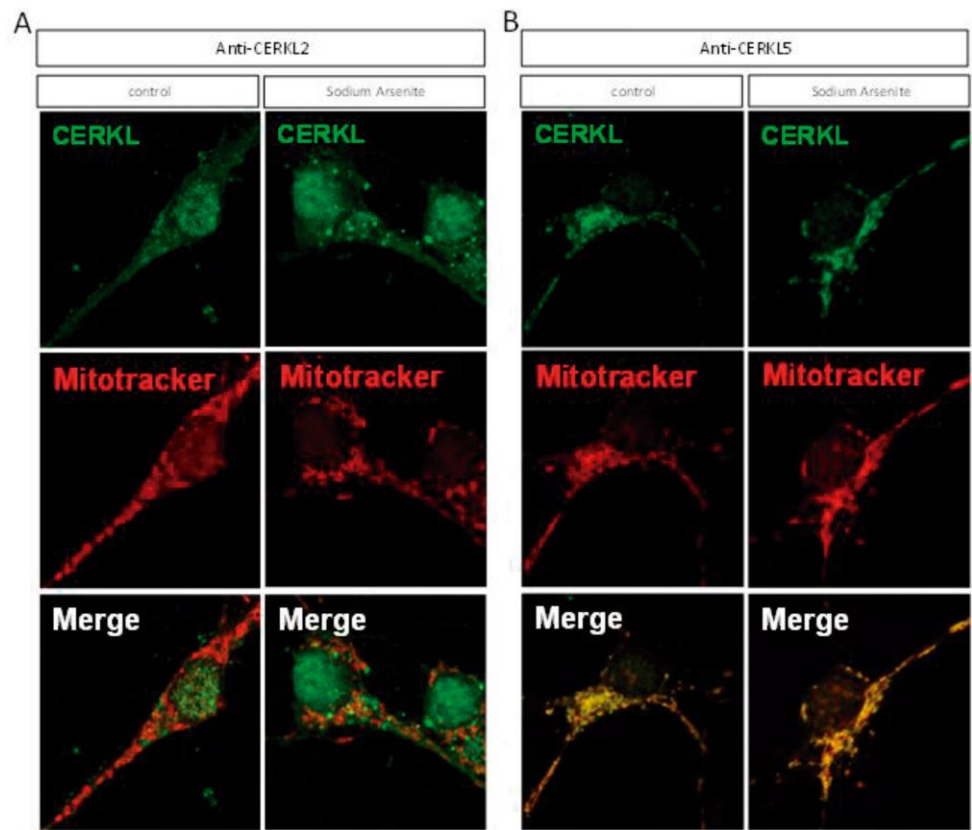
S3 Fig. CERKL expression and localization pattern in 3DIV hippocampal mouse neurons in response to arsenite stress treatment. Immunofluorescence of 3DIV hippocampal cells untreated (control) or exposed to sodium arsenite. Cells were treated with Mitotracker (red) and stained with anti-CERKL2 (**A**) or anti-CERKL5 (**B**) antibodies (green). Images from maximal projection show the strong association of isoforms that include the exon 5 epitope with mitochondria in both control and stressed conditions.
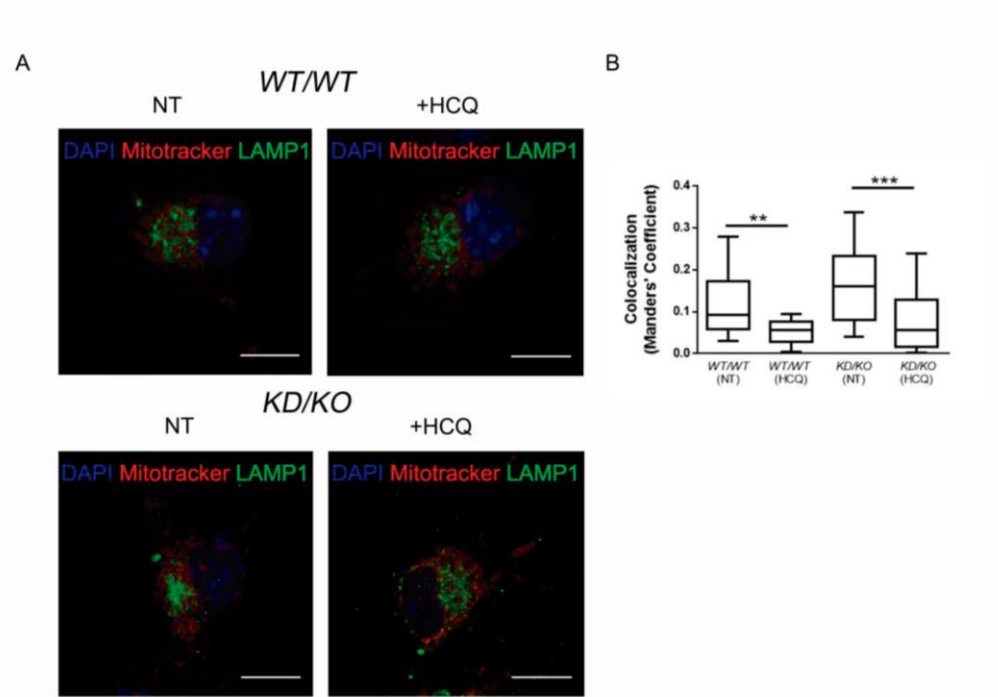
S4 Fig. Mitophagy was found unaffected in *KD/KO* vs WT/WT RGCs. A) Fluorescence microscopy detection of Mitotracker (red) and LAMP1 (green) in *WT/WT* and *KD/KO* RGCs, maintained in control medium or treated with HCQ for 6 h does not show statistically significant differences between genotypes. HCQ treatment inhibits the fusion of auphagosomes to lysosomes (significant decrease in colocalization upon treatment within each genotype). Scale bar: 10 μm. **B)** Quantification of mitochondria/LAMP1 colocalization in *WT/WT* and *KD/KO* RGCs, as shown in A. (n = 15-26 cells for experimental condition from 2-3 animals per genotype). Statistical analysis was performed with Mann-Whitney test.
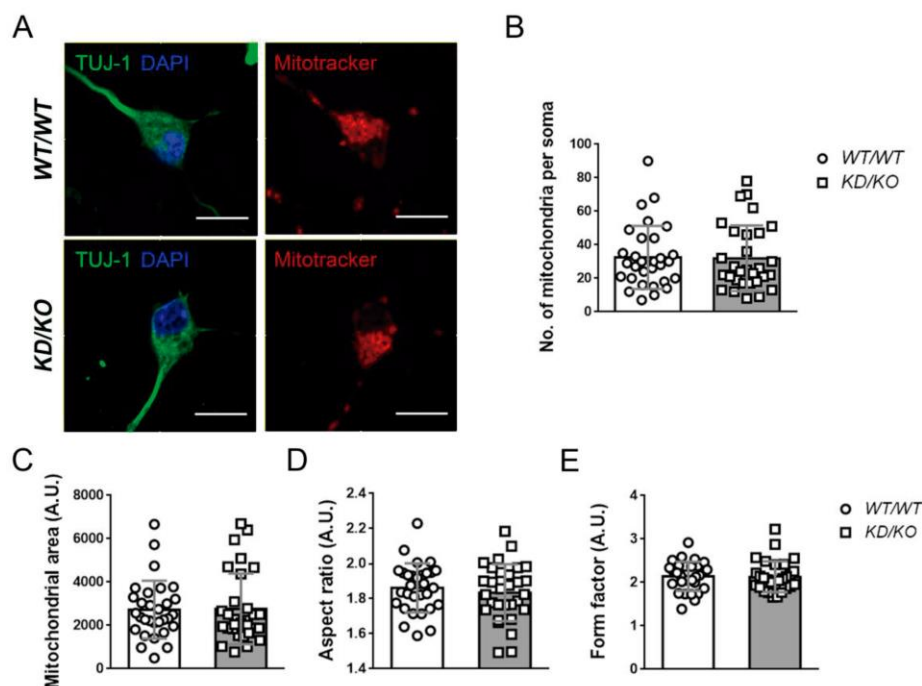
S5 Fig. No differences in number and morphology of somatic mitochondria were observed in *KD/*KO vs *WT/WT* RGCs. A) Representative confocal images of *WT/WT* and *KD/KO* RGCs somas used to analyse differences in mitochondrial number and morphology. TUJ-1 (green) was used to detect neurons and the length of axon and general morphology allowed to identify RGCs. Mitotracker was used to detect mitochondria (red), whereas nuclei were counterstained with DAPI (blue). Scale bar: 10 µm. **B, C)** Quantification of mitochondrial number and mitochondrial area. **C, D)** Morphometric analysis of somatic mitochondria as in A) by evaluation of the morphological parameters Aspect Ratio (AR) and Form factor (FF). Statistical analysis was performed with Mann-Whitney test and data are represented as the means±SD. (n = 30 images per genotype from 4-6 animals).
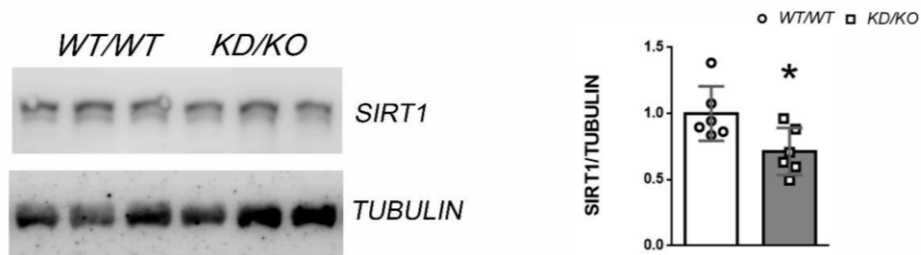
S6

S6 Fig. Representative western blot analysis and quantification of SIRT1 protein on *WT/WT* and *KD/KO* retinal homogenates. n= 6 retinas from 3 animals per genotype; data are represented as the means±SD. Statistical analysis by Mann-Whitney test. *: p-value ≤ 0,05.

S1 Table - Genes identified by RNA-Seq in relevant mitochondrial related-pathways comparing WT/WT vs KD/KO retinas (see accompanying spreadsheet in excel format)

S2 Table. Organic acids analyzed in targeted metabolomic by Gas-Chromatography Mass spectrometry of the trimethylsylyl derivatives (BSTFA).

Organic acids	Target ion	Amino acids and related compounds	Precursor ion (m/z)	Internal standard
Internal standard (undecanedioci acid)	345	Histidine	326,1	Histidine ($^{13}C_6$,$^{15}N_3$)
		4OH-Proline	302,1	Histidine ($^{13}C_6$,$^{15}N_3$)
Lactate	219	Asparagine	303,1	Serine ($^{13}C_3$,^{15}N)
Oxalate	190	Phosphoetanolamine	312	Serine ($^{13}C_3$,^{15}N)
2-hydroxyisovalerate	145	Arginine	345,2	Arginine ($^{13}C_6$,$^{15}N_4$)
Malonate	233	Taurine	296,1	Serine ($^{13}C_3$,^{15}N)
Glycerol	205	Serine	276,1	Serine ($^{13}C_3$,^{15}N)
Ethylmalonate	217	Aspartylglucosamine	506	Serine ($^{13}C_3$,^{15}N)
Succinate	247	Glutamine	317,1	Glutamic acid ($^{13}C_5$, ^{15}N)
Uracil	241	Glycine	246,1	Glycine ($^{13}C_2$, ^{15}N)
Fumarate	245	Aspartic acid	304,1	Aspartic acid ($^{13}C_4$, ^{15}N)
Glutarate	261	Citrulline	346,2	Glutamic acid ($^{13}C_5$, ^{15}N)
Thymine	255	Argininosuccinic acid	461	Glutamic acid ($^{13}C_5$, ^{15}N)
Malate	245	Sarcosine	260,1	Glutamic acid ($^{13}C_5$, ^{15}N)
Adipate	275	Sulfo-cysteine	372	Glutamic acid ($^{13}C_5$, ^{15}N)
Piroglutamate	258	Glutamic acid	318,1	Glutamic acid ($^{13}C_5$, ^{15}N)
2-Ohglutarate	247	β-alanine	260,1	Alanine ($^{13}C_3$, ^{15}N)
2-Ketoglutarate	347	Threonine	290,1	Threonine ($^{13}C_4$, ^{15}N)
Suberate	303	Sacaropine	447	Threonine ($^{13}C_4$, ^{15}N)
Homovanillic acid	326	Alanine	260,1	Alanine ($^{13}C_3$, ^{15}N)
Citrate	273	g-aminobutyric acid	274,1	Alanine ($^{13}C_3$, ^{15}N)
Sebacate	331	Proline	286,1	Proline (**$^{13}C_5$, ^{15}N**)
5-Hydroxyindoleacetic acid	407	β-aminoisobutyric acid	274,1	Proline ($^{13}C_5$, ^{15}N)
		Ornithine	237,1	Glutamic acid ($^{13}C_5$, ^{15}N)
		Homocitrulline	360	Glutamic acid ($^{13}C_5$, ^{15}N)
		Cystationine	282,1	Proline ($^{13}C_5$, ^{15}N)
		OH-Lysine	333,2	Proline ($^{13}C_5$, ^{15}N)
		Cystine	291,1	Cystine ($^{13}C_6$, $^{15}N_2$)
		Anserine	411	Serine ($^{13}C_3$,^{15}N)
		α-aminobutyric acid	274,1	Lysine ($^{13}C_6$, $^{15}N_2$)
		Lysine	244,2	Lysine ($^{13}C_6$, $^{15}N_2$)
		Glycilproline	343	Lysine ($^{13}C_6$, $^{15}N_2$)

		Tyrosine	352,1	Tyrosine ($^{13}C_9$, ^{15}N)
		Metionine	320,1	Methionine ($^{13}C_5$, ^{15}N)
		Pipecolic acid	300	Valine ($^{13}C_5$, ^{15}N)
		Valine	288,1	Valine ($^{13}C_5$, ^{15}N)
		Homocysteine	305	Isoleucine ($^{13}C_6$, ^{15}N)
		Isoleucine	302,1	Isoleucine ($^{13}C_6$, ^{15}N)
		Alloisoleucine	302,1	Isoleucine ($^{13}C_6$, ^{15}N)
		Leucine	302,1	Leucine ($^{13}C_6$, ^{15}N)
		Phenylalanine	336,1	Phenylalanine ($^{13}C_9$, ^{15}N)
		Tryptophan	375,1	Phenylalanine ($^{13}C_9$, ^{15}N)

1.2. CERKL is involved in mitochondrial dynamics and trafficking in the hippocampus

Publication 2

Title

CERKL, a Retinal Dystrophy Gene, Regulates Mitochondrial Transport and Dynamics in Hippocampal Neurons

Authors

Rocío García-Arroyo, Gemma Marfany and Serena Mirra

Reference

García-Arroyo R, Marfany G, Mirra S. *CERKL*, a Retinal Dystrophy Gene, Regulates Mitochondrial Transport and Dynamics in Hippocampal Neurons. International Journal of Molecular Sciences, 2022 Sep 30; 23(19):11593. doi: 10.3390/ijms231911593. PMID: 36232896; PMCID: PMC9570143.

Abstract

Mutations in the *Ceramide Kinase-like* (*CERKL*) gene cause retinal dystrophies, characterized by progressive degeneration of retinal neurons, which eventually lead to vision loss. Among other functions, CERKL is involved in the regulation of autophagy, mitochondrial dynamics, and metabolism in the retina. However, *CERKL* is nearly ubiquitously expressed, and it has been recently described to play a protective role against brain injury. Here we show that *Cerkl* is expressed in the hippocampus, and we use mouse hippocampal neurons to explore the impact of either over- expression or depletion of CERKL on mitochondrial trafficking and dynamics along axons. We describe that a pool of CERKL localizes at mitochondria in hippocampal axons. Importantly, the depletion of CERKL in the *Cerkl*^{KD/KO} mouse model is associated with changes in the expression of fusion/fission molecular regulators, induces mitochondrial fragmentation, and impairs axonal mitochondrial

trafficking. Our findings highlight the role of *CERKL*, a retinal dystrophy gene, in the regulation of mitochondrial health and homeostasis in central nervous system anatomic structures other than the retina.

Personal contribution to this work

This article is part of the main core of my Thesis. My personal contribution to this publication has been: a) analysis of mitochondrial morphology and dynamics in *Cerkl*$^{KD/KO}$ hippocampal neurons (Figure 2 and 6); b) evaluation of mitochondrial trafficking in *Cerkl*$^{KD/KO}$ hippocampal neurons (Figure 4); c) assessment of mitochondrial bioenergetics and cytochrome release in *Cerkl*$^{KD/KO}$ hippocampi (Figure 7); d) design and creation of the figures; e) discussion of the results (Figure 8); and f) draft writing and critical reading of the manuscript.

Article

CERKL, a Retinal Dystrophy Gene, Regulates Mitochondrial Transport and Dynamics in Hippocampal Neurons

Rocío García-Arroyo [1,2,3], Gemma Marfany [1,2,3,4,*] and Serena Mirra [1,2,3,*]

1   Department of Genetics, Microbiology and Statistics, Universitat de Barcelona, Avda. Diagonal 643, 08028 Barcelona, Spain
2   CIBERER, Instituto de Salud Carlos III, 28029 Madrid, Spain
3   Institut de Biomedicina-Institut de Recerca Sant Joan de Déu (IBUB-IRSJD), Universitat de Barcelona, 08028 Barcelona, Spain
4   DBGen Ocular Genomics, 08028 Barcelona, Spain
*   Correspondence: gmarfany@ub.edu (G.M.); serena.mirra@ub.edu (S.M.)

Abstract: Mutations in the *Ceramide Kinase-like* (*CERKL*) gene cause retinal dystrophies, characterized by progressive degeneration of retinal neurons, which eventually lead to vision loss. Among other functions, CERKL is involved in the regulation of autophagy, mitochondrial dynamics, and metabolism in the retina. However, *CERKL* is nearly ubiquitously expressed, and it has been recently described to play a protective role against brain injury. Here we show that *Cerkl* is expressed in the hippocampus, and we use mouse hippocampal neurons to explore the impact of either overexpression or depletion of CERKL on mitochondrial trafficking and dynamics along axons. We describe that a pool of CERKL localizes at mitochondria in hippocampal axons. Importantly, the depletion of CERKL in the *Cerkl*$^{KD/KO}$ mouse model is associated with changes in the expression of fusion/fission molecular regulators, induces mitochondrial fragmentation, and impairs axonal mitochondrial trafficking. Our findings highlight the role of *CERKL*, a retinal dystrophy gene, in the regulation of mitochondrial health and homeostasis in central nervous system anatomic structures other than the retina.

Keywords: *CERKL*; hippocampus; neurons; mitochondria; mitochondrial trafficking; mitochondrial dysfunction

1. Introduction

The central nervous system (CNS) is a high-metabolic-rate system, and its functionality is largely dependent on mitochondria. Mitochondria are the powerhouse of cells and actively participate in the regulation of cell respiratory mechanisms, metabolic processes, and energy homeostasis. Alterations in mitochondrial function can be due to genetic, physiological, or environmental cues and are frequently associated to the mitochondrial network remodeling and the alteration of mitochondrial dynamics, including fusion, fission, transport, interorganellar communication, and mitochondrial quality control [1,2]. Therefore, the failure of mitochondrial function and dynamics eventually leads to cell death and neurodegeneration [3].

The retina is the sensory system responsible for vision and belongs to the CNS, sharing with the brain a common developmental origin, cell-type composition, and anatomic and genetic features. Importantly, several well-defined neurodegenerative conditions originating from mitochondrial dysfunctions and affecting the brain and spinal cord have manifestations in the eye. Furthermore, various retinal pathologies caused by an impaired mitochondrial performance, share characteristics with other CNS pathologies [4].

CERKL is a retinal resilience gene whose mutations underlie retinitis pigmentosa and cone-rod dystrophy, two retinal dystrophies characterized by progressive vision loss due to photoreceptor degeneration [5]. The human *CERKL* gene is composed of 14 exons and

presents an extremely high transcriptional complexity: it generates more than 20 transcripts in both human and mouse because of the use of multiple promoters and transcription start sites as well as alternative splicing events (Figure S1A) [6].

CERKL belongs to the CERK family, where the members share some protein domains, such as the pleckstrin homology domain, the diacylglycerol kinase domain, and the ATP binding site (Figure S1A) [7]. However, assays to show whether CERKL displays any kinase activity have been unsuccessful [8]. CERKL also displays two nuclear localization and two nuclear export signals (Figure S1B) [6]. These signals allow the protein to switch between the nucleus and the cytoplasm—where it localizes with endoplasmic reticulum and the Golgi apparatus [7].

In the human retina, we identified four main CERKL protein isoforms as a result of different alternative splicing events, although other protein isoforms might be also present (Figure S1B). The a isoform consists of 13 exons (532 amino acids); the b isoform contains an extra exon (4b), which is only found in humans (558 amino acids); the c isoform undergoes an alternative splicing event fusing exon 2 to exon 6 (419 amino acids); and the d isoform is the result of a splicing event fusing exon 3 to exon 6 (463 amino acids). Such a repertoire of protein isoforms displaying different domains suggests distinct cellular roles (Figure S1B) [7]. At the functional level, CERKL has been described as binding several neuronal calcium sensors [9] and sphingolipids [8], regulating general autophagy [10,11] and localizing at mitochondria in both immortalized and primary cell lines [11–13]. Moreover, *Cerkl* depletion is associated with alterations in mitochondrial size and distribution, and dysregulation of mitochondrial metabolism in the mammal retina [11].

CERKL is expressed in several tissues other than retina, such as neural tissues, kidney, lung, and testis. It has been recently proposed that CERKL can exercise a protective role against oxidative stress in a variety of contexts. Indeed, overexpression of CERKL protects retinal pigment epithelium from oxidative stress through the regulation of mitochondrial dynamics [13]. Moreover, CERKL enhances the survival of cutaneous squamous cell carcinoma challenged by oxidative stress [14]. CERKL overexpression has been also recently shown to alleviate the ischemia reperfusion induced nervous system injury by regulating SIRT1/PINK1/Parkin pathway [15]. Interestingly, the complete knockout of the *Cerkl* locus has been shown to be lethal at embryonic stages in homozygosis [16], highlighting the importance of *Cerkl* expression in vital organs or systems.

In this study, we explored the function of CERKL in regulating mitochondrial trafficking and dynamics in primary hippocampal neurons. We took advantages from the double heterozygote knockdown/knockout mouse model, *Cerkl*$^{KD/KO}$ (KD/KO), in which the *Cerkl* expression levels are highly reduced [16]. This mouse model showed a clear phenotype of progressive retinal neurodegeneration, but the effects of *Cerkl* depletion have not been yet studied in tissues other than the retina.

Our findings shed new insights into the molecular mechanisms regulating mitochondrial dynamics in neurons and may provide relevant information to develop prevention and treatment strategies to ameliorate not only retinal dystrophies but also neural pathologies, which frequently involve alteration of the oxidative stress response, and dysfunction of mitochondrial dynamics and bioenergetic homeostasis.

2. Results

2.1. CERKL Is Expressed in Hippocampal Neurons

It is well known that CERKL is highly expressed in the neuroretina where it plays an important role regulating stress response and mitochondrial dynamics and function [7,11,12]. Nevertheless, knowledge about CERKL function in other nervous tissues besides the retina has been growing lately [15]. Therefore, in this study we aimed to shed light on the function of CERKL related to mitochondrial dynamics in the brain.

Hippocampi was selected as the source of brain neurons because it can be easily recognized and dissected from the mouse embryo brain, and the protocol for primary cell

culture is well established. We first assessed whether *Cerkl* is expressed in hippocampal cells of the adult mouse brain through immunohistochemistry using an in-house antibody [16]. CERKL is detected in cornu ammonis 1–3 and the dentate gyrus (Figure S2). To further study the intracellular function of CERKL in hippocampal neurons, primary cell cultures from E16 embryos were analysed through immunocytochemistry using two different antibodies that recognize specific protein epitopes encoded in either exon 2 (ex2) or exon 5 (ex5) of the mouse *Cerkl* gene, as well as Mitotracker to stain mitochondria. We detected a differential CERKL subcellular localization with the two antibodies: while CERKL isoforms containing exon 2 were distributed diffusely within the neuron, including nucleus and cytoplasm, CERKL isoforms containing exon 5 showed higher localization at mitochondria (Figure 1A). In addition, we also transfected primary hippocampal neurons with hCERKLa-GFP (full length 532 aa isoform of human CERKL fused to GFP) and confirmed its expression and scattered localization in the nucleus, cytoplasm, and mitochondria (Figure 1B).
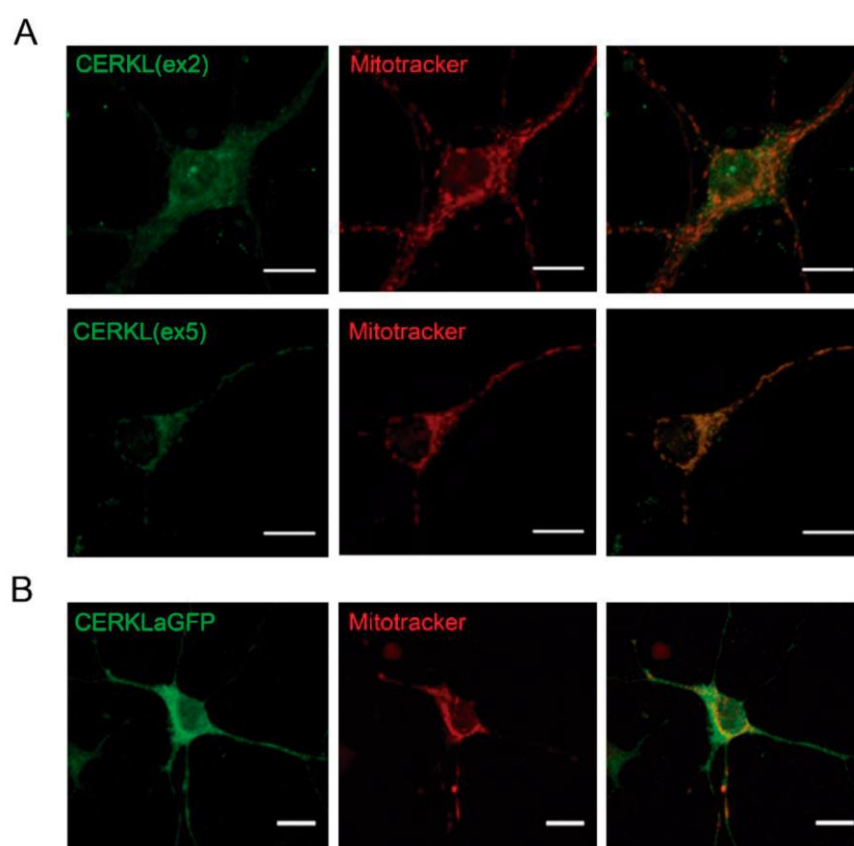
Figure 1. CERKL is expressed in primary hippocampal neurons and partially localizes at mitochondria. (**A**) CERKL is detected in primary hippocampal neurons (E16) by immunostaining with antibodies CERKL(ex2) or CERKL(ex5) (green). Mitotracker (red) is used to stain mitochondria. Note that CERKL isoforms containing exon 5 (detected with CERKL(ex5)) show higher localization at mitochondria. (**B**) Overexpression of CERKLa-GFP in primary hippocampal neurons shows partial localization of CERKLa (green) at mitochondria, which are stained with Mitotracker (red). Scale bars: 10 μm.

To sum up, CERKL is endogenously expressed in E16 and adult mouse hippocampi, suggesting it might play a role in both developing and in adult hippocampi. CERKL protein isoforms that contain the exon 5-encoded peptide show high colocalization with mitochondria.

2.2. Hippocampal Axons from Cerkl^{KD/KO} Mice Display Fragmented Mitochondria

Recent studies showed that the depletion of *CERKL* caused mitochondrial fragmentation in retinal ganglion cells and retinal pigment epithelium [11,13]. As *Cerkl* is expressed in hippocampi, we aimed to assess the effect of *Cerkl* depletion on mitochondrial morphology in this tissue, taking advantage of the double heterozygote knockdown/knockout *Cerkl^{KD/KO}* mouse model (heretofore, *KD/KO*). Thus, *WT/WT* and *KD/KO* primary hippocampal neurons were cultured, and MitoDsRed-labelled individual mitochondria were analysed in their axons (Figure 2A). Analysis of mitochondrial morphological parameters revealed no changes in the number of mitochondria along the axon; instead, a significant decrease in major mitochondrial length of *KD/KO* neurons was detected (Figure 2B).
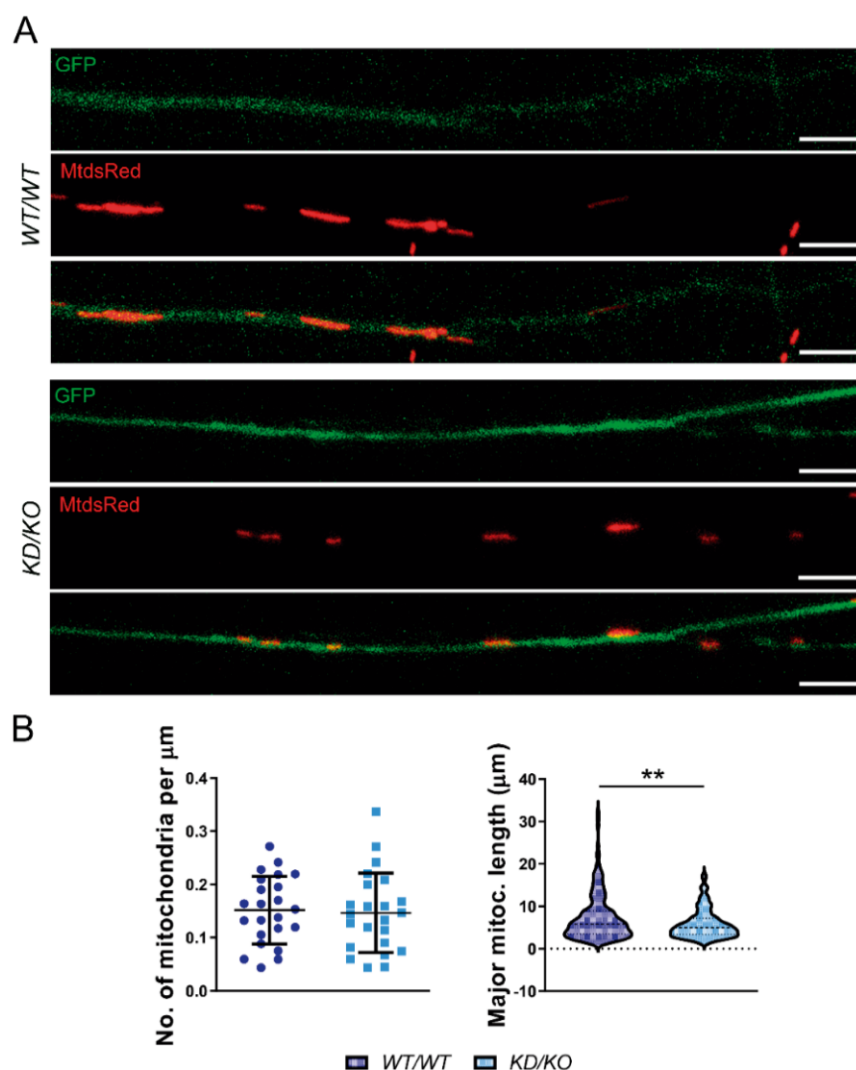
Figure 2. CERKL depletion causes mitochondrial fragmentation in axons of hippocampal neurons. (**A**) Axons from *WT/WT* and *KD/KO* primary hippocampal neurons were used to visualize and (**B**) quantify the mitochondrial density (mitochondria per μm) and mitochondrial length (μm). Hippocampal neurons were transfected with GFP to distinguish the axon (green) and MitoDsRed to stain mitochondria. Scale bars: 5 μm. Statistical analysis by *t*-test. n = 222–227 mitochondria from n = 23 axons per genotype. **: *p*-value $\leq$ 0.01.

Overall, these results indicate that depletion of CERKL levels in *KD/KO* hippocampal axons causes mitochondrial fragmentation although it does not alter mitochondrial number (density).

2.3. Overexpression of CERKLa Does Not Affect Mitochondrial Morphology in Hippocampal Axons

Once the effect of *Cerkl* depletion in mitochondrial morphology was evaluated using the *KD/KO* mouse model, we wondered whether overexpression of CERKL might also alter mitochondrial morphological parameters. To this end, *WT/WT* primary hippocampal neurons were transfected with either control GFP or CERKLa-GFP, as well as MitoDsRed to detect mitochondria. Although most CERKLa-GFP was distributed diffusely within the axon, a pool of the protein also localized at mitochondria (Figure 3A). Nonetheless, the analyses of mitochondrial morphology in the axons of the hippocampal cells overexpressing CERKL showed neither changes in mitochondrial density nor in major mitochondrial length compared to controls (Figure 3B).
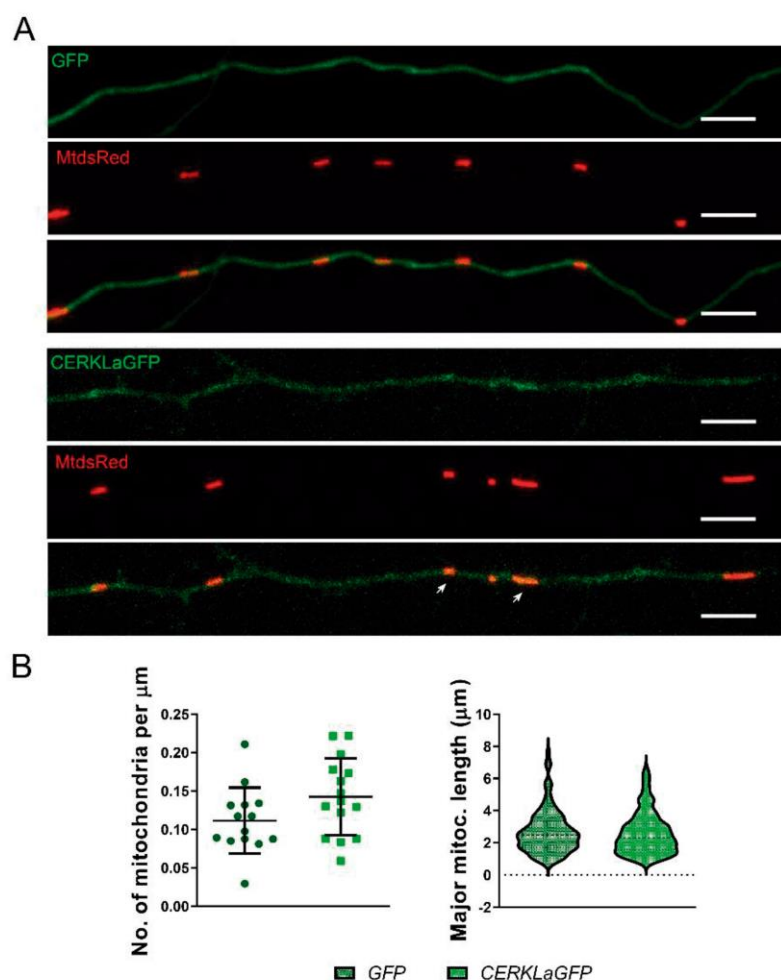
Figure 3. Overexpression of CERKL does not alter mitochondrial morphology or size. (**A**) GFP-(control) or CERKLa-GFP-transfected axons from *WT/WT* primary hippocampal neurons were used to quantify (**B**) the mitochondrial density and mitochondrial length. Mitochondria were detected by transfection with MitoDsRed. A pool of CERKL colocalizes with mitochondria (white arrows). Scale bar: 5 μm. Statistical analysis by *t*-test. *n* = 103–164 mitochondria from *n* = 14–15 axons per condition.

In summary, overexpression of CERKLa-GFP did not alter mitochondrial density or size in hippocampal axons.

2.4. Mitochondrial Trafficking Is Reduced in KD/KO Hippocampal Axons

Neuronal homeostasis is supported by proper mitochondrial transport from cell body to axons and dendrites, where ATP production and calcium buffering are required to guarantee correct neuronal function [17,18]. We aimed to assess whether mitochondrial trafficking was altered in *KD/KO* neurons. GFP and MitoDsRed were transfected to label individual axons and axonal mitochondria, respectively, in both *KD/KO* and *WT/WT* neurons. MitoDsRed transfection allows only a small number of neurons to be labelled, guaranteeing a precise analysis of anterograde and retrograde movements in single axons. Mitochondria from a segment of the axon were recorded over 10 min in live imaging experiments (Figure 4A) and mitochondrial trafficking was analysed through kymographs, which represent each mitochondrion movement through time (Figure 4B).
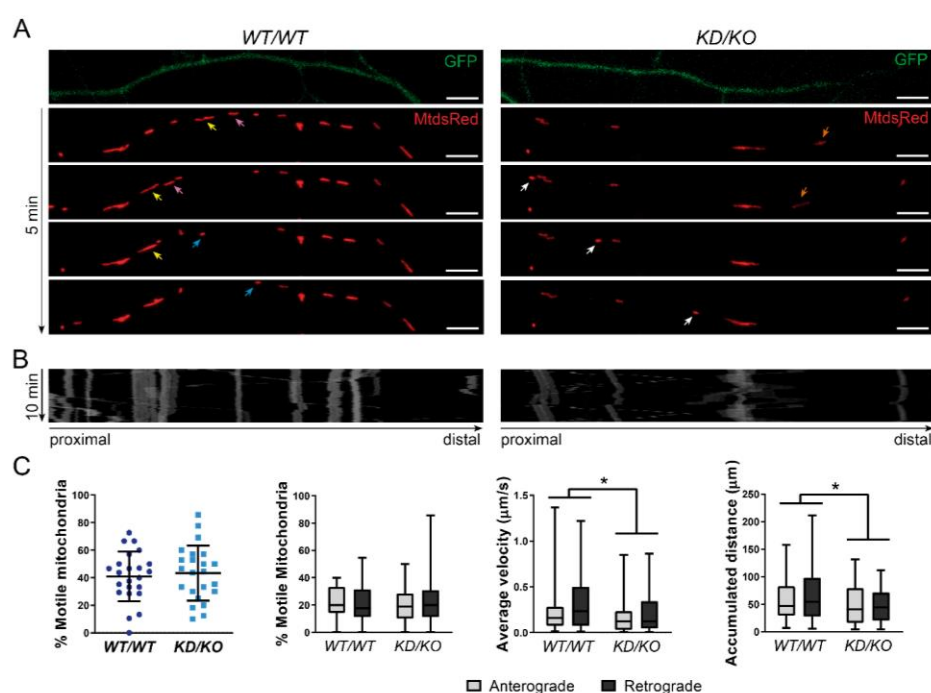
Figure 4. Mitochondrial trafficking is reduced in *KD/KO* hippocampal neuron axons. (**A**) Mitochondrial trafficking live imaging from *WT/WT* and *KD/KO* hippocampal cells (representative images of different timepoints over 5 min). Neurons were transfected with GFP to visualize the axon and MitoDsRed to label mitochondria. Yellow, pink, and orange arrows indicate mitochondria moving in anterograde direction. Blue and white arrows point mitochondria moving in anterograde direction. Scale bars: 5 μm. (**B**) Kymographs showing the path of each mitochondrion along the axons for 10 min. (**C**) CERKL depletion impairs mitochondrial trafficking in hippocampal axons. Percentage of total motile, anterograde, and retrograde mitochondria is not different between genotypes. However, average velocity and accumulated distance are reduced in *KD/KO* axons of hippocampal neurons. Statistical analysis by *t*-test and two-way ANOVA. $n = 50–57$ mitochondria from $n = 23$ axons per genotype. *: *p*-value ≤ 0.5.

No differences between genotypes were found in the percentage of total moving mitochondria nor the percentage of mitochondria moving in anterograde or retrograde directions (Figure 4C). On the other hand, the analysis of the mitochondrial average velocity and accumulated distance per mitochondria showed significant changes between

genotypes, with a clear decrease of both parameters in mitochondria from *KD/KO* axons, independently of the direction of the movement (Figure 4C).

Altogether, these results indicate that depletion of CERKL in *KD/KO* mice alters mitochondrial trafficking in hippocampal axons, resulting in a reduction of velocity and accumulated distance in mitochondria moving in both, anterograde and retrograde directions, while preserving the total number and percentage of moving mitochondria.

2.5. CERKLa-Transfected Hippocampal Axons Do Not Display Mitochondrial Trafficking Alterations

As CERKL depletion led to decreased mitochondrial trafficking in hippocampal axons, we also considered whether CERKL overexpression might also alter mitochondrial movement. To test this hypothesis, we recorded primary hippocampal neurons transfected with CERKLa-GFP and MitoDsRed (Figure 5A). Kymographs were again used to analyse mitochondrial trafficking from live imaging videos (Figure 5B). Notably, we did not observe any change in the percentage of total motile mitochondria in the axons of neurons transfected with CERKLa-GFP, and the balance between anterograde and retrograde mitochondria was maintained unaltered in comparison with control GFP-transfected axons. Moreover, neither average velocity nor accumulated distance in any direction were different in transfected versus control cells (Figure 5C).
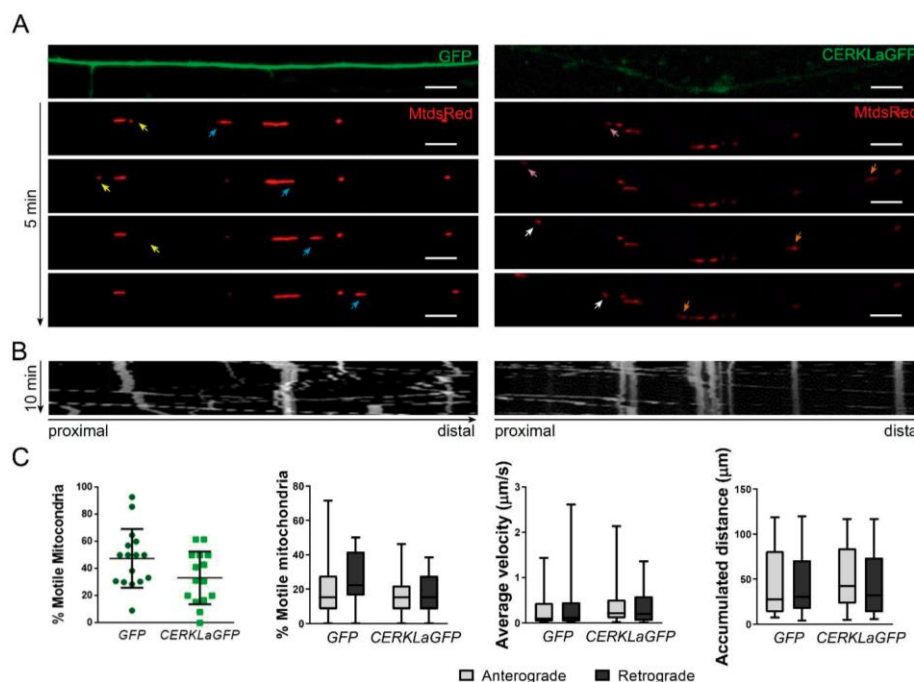
Figure 5. Mitochondrial trafficking is not altered upon CERKL overexpression in hippocampal axons. (**A**) Mitochondrial trafficking live imaging from GFP-(control) and CERKLa-GFP-transfected hippocampal axons (representative images of different timepoints over 5 min). Mitochondria were stained with MitoDsRed. Yellow, pink, and orange arrows indicate mitochondria moving in retrograde direction. Blue and white arrows point to mitochondria moving in anterograde direction. Scale bars: 5 μm. (**B**) Kymographs showing the path of each mitochondrion along the axons for 10 min. (**C**) CERKL overexpression does not alter mitochondrial trafficking in hippocampal axons. Percentage of total motile, anterograde, and retrograde mitochondria is not different between conditions. There are no differences in average velocity and accumulated distance in the axons of CERKLa-GFP-transfected primary hippocampal neurons. Statistical analysis by *t*-test and two-way ANOVA. *n* = 35–47 mitochondria from *n* = 14–15 axons per condition.

Therefore, contrary to what happens with CERKL depletion, overexpression of CERKL does not alter the studied mitochondrial trafficking parameters in hippocampal axons.

2.6. Mitochondrial Fission Is Increased in KD/KO Hippocampi

In our experiments, we observed a reduction of mitochondrial size in *KD/KO* axons, suggesting alterations in mitochondrial fusion and/or fission. By taking advantage of recorded live imaging of *WT/WT* and *KD/KO* axons, we quantified fusion and fission events in each genotype (Figure 6A), as well as in GFP- or CERKL-aGFP-transfected neurons (Figure 6B). Notably, the percentage of fission events was significantly increased in *KD/KO* axons, while no changes were found upon CERKLa-GFP overexpression (Figure 6C), in concordance with the data obtained from mitochondrial morphology analyses (Figures 2 and 3).

To obtain further insight into the molecular mechanisms regulating mitochondrial fission in *KD/KO* axons, we analysed the expression of mitochondrial fusion/fission key regulators in *WT/WT* and *KD/KO* hippocampal lysates. *KD/KO* hippocampi showed an increase in P-DRP1/DRP1 levels, although they did not reach statistical significance (Figure 6D). Notably, the ratio between the long and short OPA1 isoforms was significantly different due to an increase in the short OPA1 isoform in *KD/KO*, as MFN2 levels were also significantly decreased, overall indicating impaired mitochondrial fusion in *KD/KO* hippocampi (Figure 6D).

Overall, the depletion of CERKL induces fragmentation of mitochondria in *KD/KO* axons. This increase in mitochondrial fragmentation may be explained by increased levels of the activated (phosphorylated) form of the fission positive regulator DRP1, as well as by changes in both the ratio between OPA1 isoforms (regulating the inner mitochondrial membrane fusion) and the decreased expression of MFN2 (a positive regulator of the outer mitochondrial membrane).

2.7. Oxidative Phosphorylation Chain Complexes Are Altered in KD/KO Hippocampal Axons

Our results show that upon CERKL depletion, hippocampal neurons displayed aberrant mitochondrial dynamics, including fission, fusion, and trafficking. Such alterations might also affect mitochondrial function [19]. Therefore, we evaluated the expression of the mitochondrial structural membrane protein VDAC and functional proteins of the OXPHOS system in WT/WT and KD/KO hippocampi by Western blot analysis. VDAC levels were significantly increased in KD/KO hippocampi, indicating an increase in mitochondrial mass. Additionally, quantification of OXPHOS complexes showed a significant decrease in the levels of CI-NDUFB8, CIII-UQCRC2 and CIV-MTCO1 per mitochondrial mass in KD/KO, whereas CII-SDHB and CV-ATP5A remained unaltered, suggesting differential regulation of functional and structural mitochondrial proteins (Figure S3). To shed further light on the changes in OXPHOS protein expression/localization at mitochondria, we performed mitochondria/cytosol fractionation experiments and checked the levels of both mitochondrial and cytosolic OXPHOS proteins. As expected, we found almost all the OXPHOS proteins (CI-NDUFB8, CIII-UQCRC2, CIV-MTCO1 and CV-ATP5A) exclusively in the mitochondrial fraction, where their expression is also differentially downregulated in *KD/KO* compared with *WT/WT* samples (Figure 7A). As in whole cell lysates, CV-ATP5A remained unaltered also in the mitochondrial fraction (Figure 7A). CII-SDHB, whose expression was found unaltered in whole cell lysates, was found in both mitochondrial fraction—where its expression tends to decrease in *KD/KO*—and in the cytosolic fraction—where its expression tends to increase in *KD/KO* (Figure 7A). Finally, we analyzed the cytochrome C release from mitochondria to cytosol compartment as a critical event related to mitochondrial integrity and apoptosis triggering. We found a statistically significant increase in the ratio between cytosolic and mitochondrial cytochrome C in *KD/KO* hippocampi (Figure 7B), reinforcing the notion of mitochondrial damage in the *KD/KO* tissue.
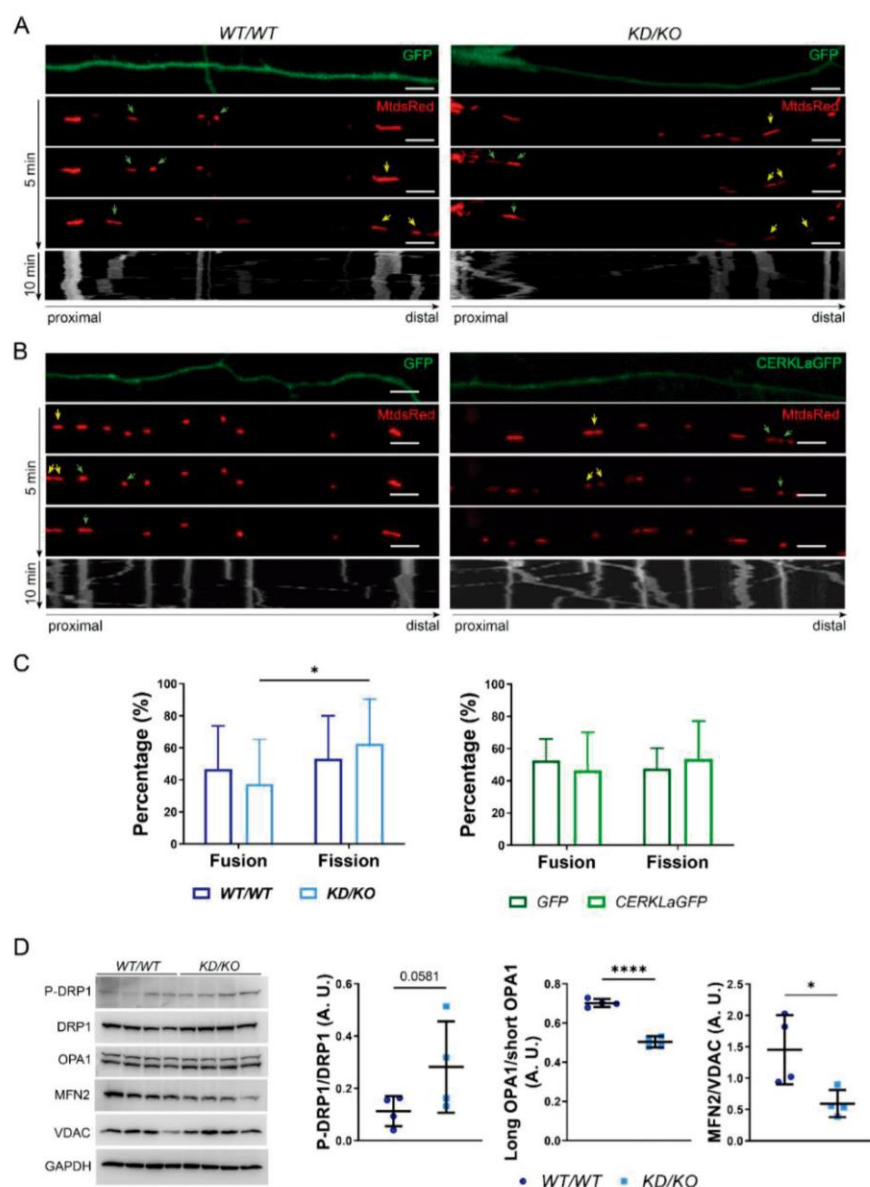
Figure 6. Mitochondrial fission is increased in the axons of *KD/KO* hippocampal neurons. Mitochondrial trafficking live imaging (representative images of different timepoints over 5 min) from axons of primary hippocampal neurons in order to analyse mitochondrial fusion (green arrows) and fission (yellow arrows) events in (**A**) CERKL overexpression conditions, comparing GFP-(control) and CERKLa-GFP-transfected neurons; and (**B**) CERKL depletion conditions, comparing *WT/WT* and *KD/KO* hippocampal axons. Mitochondria were stained with MitoDsRed. Scale bars: 5 μm. Kymographs showing the path of each mitochondrion along the axons for 10 min. (**C**) The percentage of fission events is increased in *KD/KO* hippocampal axons, whereas it remains unchanged in CERKLa-GFP-transfected hippocampal neurons, compared to their respective controls. Statistical analysis by two-way ANOVA. $n = 23$ axons per genotype, $n = 14$–15 axons per condition. (**D**) Mitochondrial fusion/fission proteins are altered in *KD/KO* hippocampi. Western blot analysis and quantification of P-DRP1, total DRP1, OPA1 and MITOFUSIN2 proteins in *WT/WT* and *KD/KO* hippocampi lysates show: an increase of P-DRP1/DRP1, and a decrease in long OPA1/short OPA1 and MFN2 levels in *KD/KO* samples. Statistical analysis by *t*-test. $n = 4$ animals per genotype. *: *p*-value ≤ 0.5; ****: *p*-value ≤ 0.0001.

Figure 7. OXPHOS protein content in mitochondrial fraction and cytochrome C release are differentially altered in *KD/KO* hippocampi. (**A**) Western blot analysis and quantification of OXPHOS proteins in *WT/WT* and *KD/KO* cytosolic (Cyt) or mitochondrial fractions (Mit). VDAC and GAPDH are used as both loading and fraction enrichment controls. (**B**) Western blot analysis of cytochrome °C in mitochondrial and cytosolic fractions. Note that * or ** in both A and B, indicate that the same control has been used for different quantifications because immunodetections have been performed on the same membrane. Statistical analysis by *t*-test. *n* = 4 animals per genotype. *: *p*-value ≤ 0.5.

3. Discussion

To date, mutations in the *CERKL* gene have only been associated with retinal dystrophies, such as retinitis pigmentosa and cone-rod dystrophy [5,20], although recent studies have shown its potential role in other not-related-to-retina tissues and pathologies [14,15]. Although CERKL specific function still remains undetermined, there are several studies with evidence suggesting it plays a crucial role regulating homeostasis and survival of photoreceptors and retinal neurons acting as a resilience gene against apoptosis and regulating mitochondrial health in front of oxidative stress [7,12,13]. Correct mitochondrial function and dynamics are essential to maintain neuronal homeostasis and viability. In fact, in view of the high energy demand of the CNS, mitochondrial dysfunction is associated with the onset and progression of many neurodegenerative disorders [21]. Hence, in this work we aimed to assess CERKL implication on mitochondrial health in CNS tissues expressing *Cerkl* other than the retina, such as hippocampus.

Mitochondrial trafficking is an essential process that underlies the proper subcellular distribution of mitochondria from the soma, where they are produced, to axons and dendrites, to meet subcellular energetic demands and ensure the correct function and survival of neurons [17,22]. Here we describe, for the first time, that depletion of *Cerkl* impairs mitochondrial trafficking in neurons. More specifically, *KD/KO* hippocampal cell axons displayed an unchanged number of motile mitochondria, with a reduction in average velocity and accumulated distance of both anterogradely and retrogradely moving mitochondria (Figure 4C). These data suggest that CERKL is involved in regulating efficiency of mitochondrial trafficking and movement, rather than directional mitochondrial recruitment on microtubules. On the other hand, CERKLa overexpression does not affect these parameters of mitochondrial trafficking, pointing out that the relevant issue is to maintain sufficient functional CERKL protein upon a threshold rather than to maintain CERKL levels within a strict range. In fact, although the overexpression of several mitochondrial trafficking key regulators is known to potentiate mitochondrial trafficking in neurons [23–25], not always does protein overexpression result in a complementary physiological reverse effect from those obtained in down-regulation studies [26,27]. On the other hand, *CERKL* produce several protein isoforms [7], and we cannot discard the situation that the overexpression of distinct isoforms could differentially affect mitochondrial trafficking in neurons. Furthermore, different protein isoforms of CERKL may be expressed in brain due to tissue-specific mechanisms of alternative splicing regulation [28]. In line with this hypothesis, we show that different pools of protein isoforms containing exon 2 or exon 5 may localize at mitochondria in hippocampal neurons, with a strong localization of the isoforms containing the peptide encoded in exon 5 (including isoforms containing both exons). Given that the CERKL protein does not include any mitochondrial localization signal, we believe that the ATP-binding site encoded by exon 5 might promote association to mitochondria at basal level and/or in response to certain stimuli. Importantly, the most prevalent RP mutation (R283X) is located in exon 5, highlighting the importance of mitochondrial localization of CERKL. However, also isoforms including exon 2 presented a partial colocalization with the mitochondrial marker. This colocalization may derive from isoforms including both exons 2 and 5. Indeed, the PH domain encoded by exon 2 might also mediate recruitment of CERKL to mitochondria, since PH domains are involved in recruiting proteins to different membrane compartments. Considering the importance of correct mitochondrial transport for maintaining neuronal function and viability [29], our results provide new insight into the function of CERKL in maintaining neuronal homeostasis in the CNS.

Mitochondrial network is a highly dynamic structure in which mitochondria constantly undergo fusion and fission events to maintain mitochondrial health [19]. In mammalian cells, fission/fusion events are mainly mediated by several large dynamin-related GTPase proteins, including optic dominant atrophy 1 (OPA1), conserved dynamin-related GTPase (DRP1), and conserved dynamin-related GTPase mitofusion (MFN1 and MFN2) [3]. In this study we further characterized the effects of *Cerkl* down-regulation on mitochondrial morphology in hippocampal neurons. Our results showed a significant decrease

in mitochondrial size in *KD/KO* hippocampal axons (Figure 2B), in concordance with previous studies that described mitochondrial fragmentation upon *Cerkl* depletion in different retinal cells, including neurons and retinal pigment epithelium [11,13]. In healthy cells, the frequency of mitochondrial fission and fusion events is equal in order to maintain mitochondrial number and morphology [19,30]. Nevertheless, *KD/KO* hippocampal neurons displayed a higher rate of fission events (Figure 6C). In agreement with that, we found an imbalance of the molecular machinery that regulates fusion and fission, namely down-regulation of MFN2, increase of DRP1 phosphorylation and reduction of long OPA1 isoform (Figure 6D), which prompts to decreased fusion and increased fission. Mitochondrial fusion–fission imbalance compromises mitochondrial health, and it is particularly relevant in environmental or genetic stress conditions [30]. Indeed, fusion rescues stress by allowing functional mitochondria to complement dysfunctional mitochondria by diffusion and sharing of components between organelles [31]. On the other hand, fission can be associated with the segregation of dysfunctional mitochondria that need to be eliminated throughout mitophagy [32]. Our data in hippocampal neurons are in accordance with our previous finding obtained in *KD/KO* retinal cells (photoreceptors, ganglion cells, and retinal pigment epithelium), where mitochondria are fragmented, with a consequent severe dysfunction in mitochondrial respiration and metabolism [11,13]. Then, our data further reinforce the important role of CERKL in mitochondrial network organization in neurons, although further research is recommended to identify the specific molecular mechanisms of the CERKL-mitochondria interaction.

In order to assure correct CNS function and facilitate synaptic transmission, the brain requires up to 25% of the body's total glucose levels, which mainly undergoes mitochondrial oxidative phosphorylation (OXPHOS) [21,33]. We found a reduction in the levels of some OXPHOS chain complexes in *KD/KO* mitochondria (Figures 7A and S3), which may involve mitochondrial dysfunction and neuronal bioenergetic impairment. Overall, our results indicate that *KD/KO* hippocampi display an altered OXPHOS chain structure/composition. Moreover, the protein levels of several OXPHOS subunits at the mitochondria are downregulated in *KD/KO* hippocampi. As for the CII-SDHB subunit, a fraction of which has been found to be retained in the cytosol, this change may be due to an altered transport of the protein at mitochondria. These results are in concordance with the deficiency in mitochondrial oxygen consumption in the retinas of *KD/KO* mice [11]. Notably, mitochondrial mass was increased in *KD/KO* hippocampi, although mitochondrial density in the axon fragments analysed did not appear altered (Figure 2B); probably the mitochondrial trafficking impairment results in decreased transport from the soma to the axons (Figure 4), in accordance with that reported in *KD/KO* retinal ganglion cells, where only smaller and fragmented mitochondria reached distal axonal segments [11]. This suggests an accumulation of dysfunctional mitochondria in the soma due to trafficking alterations and probably to defects in mitophagy [11], which also may explain the cytoarchitectural changes observed in retinal ganglion cells (increased number of neurites and shortened axons) [16]. Moreover, we observed an increased release of mitochondrial cytochrome C in cytosol, again supporting that the mitochondrial integrity is impaired in *KD/KO* hippocampi (Figure 7B). Therefore, all the phenotypic effects on mitochondrial dynamics, content, and metabolism due to *Cerkl* down-regulation are clearly conditioning neuron homeostasis and function. Our proposed model based on these results is summarized in Figure 8.
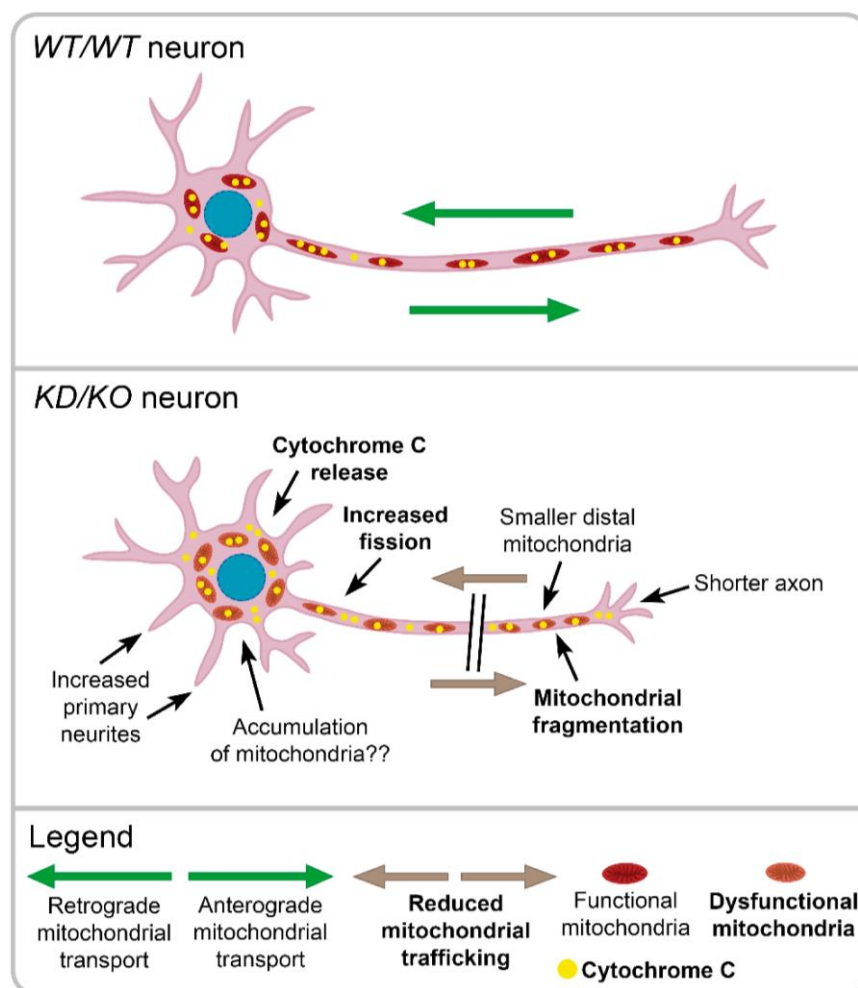
Figure 8. Model recapitulating mitochondrial and morphological alterations in the *KD/KO* mouse retinal and hippocampal neurons. *KD/KO* neurons show cytoarchitectural alterations, with an increased number of primary neurites and reduced axon length, compared to WT [16]. Besides, *KD/KO* neurons show dysfunctional mitochondrial (in orange) with an increase of mitochondrial fragmentation and fission events, a reduction of mitochondrial trafficking (brown arrows) and release of cytochrome C (in yellow) from mitochondria to cytosol. Our model proposes that *Cerkl* depletion causes altered distribution of mitochondria along the neuron, with an accumulation of mitochondria in the soma, an increase of fragmented mitochondria in the distal axon, and release of cytochrome C in the cytosol due to impaired mitochondria integrity (results from [11] and this work [highlighted in bold]).

CERKL has been proposed as a resilience gene against oxidative stress and its protective function is usually triggered by a challenge. In absence of stress conditions, overexpression of CERKL does not alter the mitochondrial network, in contrast, it clearly protects mitochondria from oxidative stress [13]. In this work, cultured neurons were not challenged by oxidative stress conditions, and thus it is not surprising that CERKL overexpression did not alter any of the studied mitochondrial parameters (Figures 3, 5 and 6C). In addition, CERKL overexpression might be contributing to other pathways besides mitochondrial dynamics, such as the formation of RNA stress granules [34], regulation of autophagy [10], and apoptosis prevention [7]. However, CERKL depletion affects the mitochondrial network and makes cells more vulnerable to stress conditions [11,13]. We detected endogenous expression of CERKL in both embryonic and adult hippocampi from *WT/WT*

mice (Figures 1 and S1). Embryonic development is a process that involves multiple changes where mitochondrial proper function is crucial in determining cell fate and maintaining cell growth and survival [33,35]. In this context, the observed effects of *Cerkl* depletion in embryonic hippocampi suggest that CERKL may be playing such an important role in CNS development, that it would provide a rationale for embryonic lethality upon homozygous total deletion of *Cerkl* in mouse [16].

Interestingly, although CERKL plays a protective role against oxidative stress in different tissues such as epidermis and brain [14,15], *CERKL* mutations have been reported to solely affect the retina so far. Each tissue is especially vulnerable to different stress events and relies on distinct resilience molecular mechanisms [36]. In this context, CERKL seems to be a key stress regulator for retinal health whereas it might not be that relevant in other regions of the CNS. Indeed, the contribution of CERKL to different tissue-specific pathways may explain the absence of brain phenotype. Therefore, further studies in tissues other than the retina might shed light on other phenotypic alterations due to *CERKL* mutations.

4. Materials and Methods

4.1. Animal Experimentation

WT and *Cerkl*$^{KD/KO}$ mice (C57BL/6J) were bred and housed in the animal research facilities at the University of Barcelona. Animals were provided with food and water ad libitum and maintained in a temperature-controlled environment in a 12/12 h light–dark cycle. Animal experiments were performed according to the ARVO statement for the use of animals in ophthalmic and vision research, as well as the regulations of the Ethical Committee for Animal Experimentation (AEC) of the Generalitat de Catalunya (protocol C-449/18), according to the European Directive 2010/63/EU and other relevant guidelines.

4.2. Genomic DNA and Genotyping by PCR

DNA for genotyping was extracted from ear punches. Primers for genotyping and PCR conditions are described in [16].

4.3. Cell Culture and Transfections

Hippocampi were carefully dissected from WT and *Cerkl*$^{KD/KO}$ mouse brains (E16 embryos) in PBS containing 3% glucose. Then, the samples were treated with trypsin (Invitrogen, Carlsbad, CA, USA) and DNAse (Roche Diagnostics, Indianapolis, IN, USA) and physically dissociated into single neurons. Neurons were plated on glass coverslips or 35-mm *Fluorodish* plates (World Precision Instruments Inc), coated with 0.5 mg/mL poly-L-lysine (Sigma-Aldrich, St. Louis, MO, USA) and incubated in neurobasal medium (Gibco, Grand Island, NY, USA) containing 2 mM glutamax, 120/mL penicillin, 200/mL streptomycin, and B27 supplement (Invitrogen, Waltham, MA, USA). Cells were maintained at 37 °C in the presence of 5% CO_2 and were cultured for between 5 and 6 days. Hippocampal cultures at 4 DIV were transfected with Lipofectamine 2000 (Life Technologies, Carlsbad, CA, USA) according to the manufacturer's guidelines.

In immunocytochemistry experiments on fixed cells, 1 μM MitoTracker™ Orange CMTMRos (Thermo Fisher Scientific, Rockford, IL, USA) was added to the neurons to stain mitochondria and incubated for 20 min at 37 °C before fixation.

4.4. Plasmid Vectors

CERKLa-GFP was obtained by cloning the coding region of hCERKL532 cDNA (NM_201548.4) in pEGFPN2 (BD Bioscience, NJ, USA), by using XhoI and BamHI restriction sites. Mitochondrial-targeted DsRed (mitoDsRed) was kindly provided by Prof. Eduardo Soriano (University of Barcelona, Barcelona, Spain).

4.5. Immunofluorescence

For immunocytochemistry, primary neurons were fixed in pre-chilled methanol at −20 °C for 10 min, washed in PBS (3 × 5 min), permeabilized in 0.2% Triton X-100

(St. Louis, MO, USA) in 1× PBS (20 min at RT), and blocked for 1 h in 10% Normal Goat Serum (Roche Diagnostics) in 1× PBS. Primary antibodies were incubated overnight at 4 °C in blocking solution. The primary antibodies used were CERKL(ex2) and CERKL(ex5), and were obtained in-house against epitopes encoded in exon 2 or exon 5 of the mouse *Cerkl* gene respectively [16]. After incubation, coverslips with cells were rinsed in 1× PBS (3 × 5 min), incubated with the corresponding secondary antibodies conjugated to Alexa Fluor 488 (Life Technologies, Grand Island, NY, USA) (1:500) at RT (1 h) in blocking solution. Nuclei were stained with DAPI (Roche Diagnostics, Indianapolis, IN, USA) (1:1000), washed again in 1× PBS (3 × 5 min), and mounted in Mowiol 4–88 (Merck, Darmstadt, Germany).

4.6. Tissue Processing and Histology

Adult *WT/WT* mice were anesthetized and perfused with 4% PFA in 0.1 M phosphate buffer (PB). Brains were carefully extracted, post-fixed overnight with 4% PFA in PB, cryoprotected with 30% sucrose in PBS, and frozen at −42 °C in isopentane. Frozen brain samples were sectioned in 30-μm coronal sections using a freezing microtome (Leica, Wetzlar, Germany). Free-floating sections were collected in cryoprotectant solution (85% glycerol, 100% ethylene glycol, 0.1 M PBS) and kept at −20 °C until use. For immunohistochemistry, frozen brain sections were permeabilized and incubated for 2 h at RT with 0.2% Triton-X-100, 1% BSA and 0.2 M glycine in PBS. The same solution was used for CERKL(ex2) primary antibody incubation, performed overnight at 4 °C, and Alexa Fluor 488 secondary antibody incubation, (Life Technologies, Grand Island, NY, USA) (1:500), performed for 2 h at RT. Nuclei were stained using DAPI (Roche Diagnostics, Indianapolis, IN, USA) (1:1000), and sections were mounted in Mowiol 4–88 (Merck, Darmstadt, Germany).

4.7. Western Blot

Hippocampi from adult WT and *Cerkl*$^{KD/KO}$ mice were carefully dissected and lysed in RIPA buffer [50 mM Tris, pH 7.4, 150 mM NaCl, 1 mM EDTA, 1% NP-40, 0.25% Na-deoxycholate, protease inhibitors (Complete Mini Protease Inhibitor Cocktail Tablets; Roche, Indianapolis, IN, USA)]. In mitochondria/cytosol fractioning experiments, we used the Cytochrome c Release Assay Kit (GeneTex, Alton Pkwy, Irvine, CA, USA, GTX85531), following the manufacturer's instructions to obtain mitochondrial and cytosolic fraction. Proteins were separated by SDS-PAGE and transferred onto nitrocellulose membranes, which were blocked with 5% non-fat dry milk in tris-HCl-buffered saline (TBS) containing 0.1% Tween 20 and incubated overnight at 4 °C with primary antibodies. After incubation with horseradish peroxidase-labelled secondary antibodies for 1 h at RT, membranes were revealed with the ECL system (Lumi-Light Western Blotting Substrate, Roche, Indianapolis, IN, USA). Images were acquired by ImageQuant^{TM} LAS 4000 mini Image Analyser (Fujifilm, Tokyo, Japan) and quantified using ImageJ software. TUBULIN or GAPDH loading controls were used when needed. The primary antibodies used were: VDAC (Sigma-Aldrich, St. Louis, MO, USA, (Ab-5) (185–197); 1:7000), TUBULIN (Sigma-Aldrich, St. Louis, MO, USA, T5168, 1:1000), GAPDH (Abcam, Cambridge, UK, ab8245, 1:1000), Rodent Total OXPHOS Cocktail (MitoSciences, Eugene, OR, USA, 6 μg/mL), MITOFUSIN2 (Abcam, Cambridge, UK, ab56889, 1:1000), OPA1 (Proteintech, Rosemont, IL, USA, 27733-1-AP, 1:1000), DRP1 (Cell Signaling Technology, Danvers, MA, USA, 14647S, 1:1000), P-DRP1 (Cell Signaling Technology, Danvers, MA, USA, S616:3455S, 1:000), Anti-Cytochrome C antibody (GeneTex, Alton Pkwy, Irvine, CA, USA, GTX108585, 1:1000).

The secondary antibodies used were: HRP-labelled anti-mouse (Vector Labs, Mowry Ave Newark, CA, USA; P447-01, 1:2000) and anti-rabbit (Vector Labs, Mowry Ave Newark, CA, USA; P217-02, 1:2000).

4.8. Live Cell Imaging and Microscope Image Acquisition

In vivo imaging experiments were performed at 37 °C in an atmosphere of 5% CO$_2$ with an LSM780 confocal microscope (Zeiss, Oberkochen, Germany) equipped with 40x

(NA 1.3) and 63x (NA 1.4) oil objectives. All electronics were controlled through the ZEN software (Zeiss, Oberkochen, Germany). MitoDsRed-labelled mitochondria in axons were live imaged 1–2 days after transfection (5–6 DIV cultures). In mitochondrial tracking experiments, an axonal segment located approximately 90 to 160 μm distal to the soma was selected for live imaging. Z stacks of 7 images from the axonal region were taken every 6 s over 10 min using the mitoDsRed channel with 800 × 100 pixel resolution and an extra 2× digital zoom. Movies were processed using ImageJ software (http://imagej.nih.gov/ij/, accessed on 4 December 2017), and kymographs were generated by tracing axons in their z-projections. In kymographs, straight vertical lines were considered as static mitochondria, and motile mitochondria (non-straight vertical lines) were traced to evaluate their motility and directionality. The percentage of time in motion was calculated as the percentage of time a given mitochondrion (static or motile) spent moving at speed over 0.0083 μm/s towards the anterograde or retrograde direction and represented as an average. The percentage of motile mitochondria represents the relation between the number of motile and static mitochondria for each condition.

4.9. Mitochondrial Number and Length

Live neuronal cultures expressing mitoDsRed were imaged with a LSM780 (Zeiss, Oberkochen, Germany) confocal microscope equipped with a 63x oil objectives. Confocal images of the red (MtDsRed) channel were acquired, then number and length of mitochondria within the axon were quantified using an ImageJ software macro as described in [37] and standardized to the length of the axonal section imaged. Mitochondrial length represents the major axis length of mitochondria. Mitochondrial number and length were determined from axonal proximal segments of 14–23 neurons per condition.

4.10. Analysis of Mitochondrial Fusion and Fission Events

Events of fusion and fission were manually calculated from the same axons recorded in live cell imaging experiments. Both movies and kymographs were used for the quantification. The percentage of fusion or fission represents the relation between the number of fusion or fission events and the total number of fusion and fission events in each single recorded axon.

4.11. Statistical Analyses

Statistical analyses were performed using the two-tailed unpaired Student's *t*-test and two-way ANOVA. When data did not follow a normal distribution, non-parametric Mann–Whitney test was used to determine the statistical significance. ROUT test was used to determine statistical outliers (Q = 1%). Calculations were performed with GraphPad Prism statistical software, version 6 (GraphPad6 Software Inc., San Diego, CA, USA). N is shown at each figure legend. Statistical significance was set with a *p*-value ≤ 0.05, (*: *p*-value ≤ 0.05, **: *p*-value ≤ 0.01, ***: *p*-value ≤ 0.005, ****: *p*-value ≤ 0.001). Data are expressed as standard deviation (SD).

5. Conclusions

Overall, in this work we determined that CERKL is not only involved in mitochondrial morphology and function in neurons, but also in mitochondrial trafficking regulation, contributing to the intricate network that regulates mitochondrial health in neurodegenerative diseases. Therefore, *CERKL* might play an important role as a resilience gene regulating neuronal homeostasis and viability in the brain during embryonic development and adult stages. We propose *CERKL* as a potential candidate gene contributing to neurological pathologies due to its implication in mitochondrial dynamics and resilience to stress in the CNS.

Supplementary Materials: The following supporting information can be downloaded at: https://www.mdpi.com/xxx/s1.

References

1. Muthuraman, A.; Ramesh, M.; Shaikh, S.A.; Aswinprakash, S.; Jagadeesh, D. Physiological and Pathophysiological Role of Cysteine Metabolism in Human Metabolic Syndrome. *Drug Metab. Lett.* **2021**, *14*, 177–192. [CrossRef] [PubMed]
2. Mirra, S.; Marfany, G. Mitochondrial Gymnastics in Retinal Cells: A Resilience Mechanism Against Oxidative Stress and Neurodegeneration. In *Advances in Experimental Medicine and Biology*; Springer: Berlin/Heidelberg, Germany, 2019; Volume 1185, pp. 513–517.
3. Yang, D.; Ying, J.; Wang, X.; Zhao, T.; Yoon, S.; Fang, Y.; Zheng, Q.; Liu, X.; Yu, W.; Hua, F. Mitochondrial Dynamics: A Key Role in Neurodegeneration and a Potential Target for Neurodegenerative Disease. *Front. Neurosci.* **2021**, *15*, 654785. [CrossRef] [PubMed]
4. London, A.; Benhar, I.; Schwartz, M. The retina as a window to the brain—From eye research to CNS disorders. *Nat. Rev. Neurol.* **2013**, *9*, 44–53. [CrossRef]
5. Aleman, T.S.; Soumittra, N.; Cideciyan, A.V.; Sumaroka, A.M.; Ramprasad, V.L.; Herrera, W.; Windsor, E.A.M.; Schwartz, S.B.; Russell, R.C.; Roman, A.J.; et al. CERKL mutations cause an autosomal recessive cone-rod dystrophy with inner retinopathy. *Investig. Ophthalmol. Vis. Sci.* **2009**, *50*, 5944–5954. [CrossRef] [PubMed]
6. Garanto, A.; Riera, M.; Pomares, E.; Permanyer, J.; de Castro-Miro, M.; Sava, F.; Abril, J.F.; Marfany, G.; Gonzalez-Duarte, R. High transcriptional complexity of the retinitis pigmentosa CERKL gene in human and mouse. *Investig. Ophthalmol. Vis. Sci.* **2011**, *52*, 5202–5214. [CrossRef]
7. Tuson, M.; Garanto, A.; Gonzalez-Duarte, R.; Marfany, G. Overexpression of CERKL, a gene responsible for retinitis pigmentosa in humans, protects cells from apoptosis induced by oxidative stress. *Mol.Vis.* **2009**, *15*, 168–180. [PubMed]
8. Garanto, A.; Mandal, N.A.; Egido-Gabás, M.; Marfany, G.; Fabriàs, G.; Anderson, R.E.; Casas, J.; Gonzàlez-Duarte, R. Specific sphingolipid content decrease in Cerkl knockdown mouse retinas. *Exp. Eye Res.* **2013**, *110*, 96–106. [CrossRef] [PubMed]
9. Nevet, M.J.; Vekslin, S.; Dizhoor, A.M.; Olshevskaya, E.V.; Tidhar, R.; Futerman, A.H.; Ben-Yosef, T. Ceramide kinase-like (CERKL) interacts with neuronal calcium sensor proteins in the retina in a cation-dependent manner. *Investig. Ophthalmol. Vis. Sci.* **2012**, *53*, 4565–4574. [CrossRef]
10. Hu, X.; Lu, Z.; Yu, S.; Reilly, J.; Liu, F.; Jia, D.; Qin, Y.; Han, S.; Liu, X.; Qu, Z.; et al. CERKL regulates autophagy via the NAD-dependent deacetylase SIRT1. *Autophagy* **2019**, *15*, 453–465. [CrossRef]
11. Mirra, S.; García-Arroyo, R.; Domènech, E.B.; Gavaldà-Navarro, A.; Herrera-Úbeda, C.; Oliva, C.; Garcia-Fernàndez, J.; Artuch, R.; Villarroya, F.; Marfany, G. CERKL, a retinal dystrophy gene, regulates mitochondrial function and dynamics in the mammalian retina. *Neurobiol. Dis.* **2021**, *156*, 105405. [CrossRef] [PubMed]
12. Li, C.; Wang, L.; Zhang, J.; Huang, M.; Wong, F.; Liu, X.; Liu, F.; Cui, X.; Yang, G.; Chen, J.; et al. CERKL interacts with mitochondrial TRX2 and protects retinal cells from oxidative stress-induced apoptosis. *Biochim. Biophys. Acta-Mol. Basis Dis.* **2014**, *1842*, 1121–1129. [CrossRef] [PubMed]
13. García-Arroyo, R.; Gavaldà, A.; Villarroya, F.; Marfany, G.; Mirra, S. Overexpression of CERKL Protects Retinal Pigment Epithelium Mitochondria from Oxidative Stress Effects. *Antioxidants* **2021**, *10*, 2018. [CrossRef] [PubMed]

14. Meyer, J.M.; Lee, E.; Celli, A.; Park, K.; Cho, R.; Lambert, W.; Pitchford, M.; Gordon, M.; Tsai, K.; Cleaver, J.; et al. CERKL is upregulated in cutaneous squamous cell carcinoma and maintains cellular sphingolipids and resistance to oxidative stress. *Br. J. Dermatol.* **2021**, *185*, 147–152. [CrossRef]

15. Huang, S.; Hong, Z.; Zhang, L.; Guo, J.; Li, Y.; Li, K. CERKL alleviates ischemia reperfusion-induced nervous system injury through modulating the SIRT1/PINK1/Parkin pathway and mitophagy induction. *Biol. Chem.* **2022**, *403*, 691–701. [CrossRef] [PubMed]

16. Domènech, E.B.; Andres, R.; López-Iniesta, M.J.; Mirra, S.; García-Arroyo, R.; Milla, S.; Sava, F.; Andilla, J.; Alvarez, P.L.; De La Villa, P.; et al. A New Cerkl Mouse Model Generated by CRISPR-Cas9 Shows Progressive Retinal Degeneration and Altered Morphological and Electrophysiological Phenotype. *Investig. Ophthalmol. Vis. Sci.* **2020**, *61*, 14. [CrossRef]

17. Sheng, Z.H.; Cai, Q. Mitochondrial transport in neurons: Impact on synaptic homeostasis and neurodegeneration. *Nat. Rev. Neurosci.* **2012**, *13*, 77–93. [CrossRef] [PubMed]

18. Chamberlain, K.A.; Sheng, Z.H. Mechanisms for the maintenance and regulation of axonal energy supply. *J. Neurosci. Res.* **2019**, *97*, 897–913. [CrossRef] [PubMed]

19. Detmer, S.A.; Chan, D.C. Functions and dysfunctions of mitochondrial dynamics. *Nat. Rev. Mol. Cell Biol.* **2007**, *8*, 870–879. [CrossRef]

20. Tuson, M.; Marfany, G.; Gonzàlez-Duarte, R. Mutation of CERKL, a Novel Human Ceramide Kinase Gene, Causes Autosomal Recessive Retinitis Pigmentosa (RP26). *Am. J. Hum. Genet.* **2004**, *74*, 128–138. [CrossRef] [PubMed]

21. Trigo, D.; Avelar, C.; Fernandes, M.; Sá, J.; da Cruz e Silva, O. Mitochondria, energy, and metabolism in neuronal health and disease. *FEBS Lett.* **2022**, *596*, 1095–1110. [CrossRef] [PubMed]

22. Schwarz, T.L. Mitochondrial trafficking in neurons. *Cold Spring Harb. Perspect. Med.* **2013**, *5*, a011304. [CrossRef] [PubMed]

23. MacAskill, A.F.; Kittler, J.T. Control of mitochondrial transport and localization in neurons. *Trends Cell Biol.* **2010**, *20*, 102–112. [CrossRef] [PubMed]

24. Fang, D.; Yan, S.; Yu, Q.; Chen, D.; Yan, S.S. Mfn2 is required for mitochondrial development and synapse formation in human induced pluripotent stem cells/hiPSC derived cortical neurons. *Sci. Rep.* **2016**, *6*, 31462. [CrossRef] [PubMed]

25. Norkett, R.; Modi, S.; Birsa, N.; Atkin, T.A.; Ivankovic, D.; Pathania, M.; Trossbach, S.V.; Korth, C.; Hirst, W.D.; Kittler, J.T. DISC1-dependent regulation of mitochondrial dynamics controls the morphogenesis of complex neuronal dendrites. *J. Biol. Chem.* **2016**, *291*, 613–629. [CrossRef] [PubMed]

26. Wang, W.; Li, L.; Lin, W.L.; Dickson, D.W.; Petrucelli, L.; Zhang, T.; Wang, X. The ALS disease-associated mutant TDP-43 impairs mitochondrial dynamics and function in motor neurons. *Hum. Mol. Genet.* **2013**, *22*, 4706–4719. [CrossRef]

27. Serrat, R.; Mirra, S.; Figueiro-Silva, J.; Navas-Pérez, E.; Quevedo, M.; López-Doménech, G.; Podlesniy, P.; Ulloa, F.; Garcia-Fernàndez, J.; Trullas, R.; et al. The Armc10/SVH gene: Genome context, regulation of mitochondrial dynamics and protection against Aβ-induced mitochondrial fragmentation. *Cell Death Dis.* **2014**, *5*, e1163. [CrossRef]

28. Aísa-Marín, I.; García-Arroyo, R.; Mirra, S.; Marfany, G. The alter retina: Alternative splicing of retinal genes in health and disease. *Int. J. Mol. Sci.* **2021**, *22*, 1855. [CrossRef]

29. Vanhauwaert, R.; Bharat, V.; Wang, X. Surveillance and transportation of mitochondria in neurons. *Curr. Opin. Neurobiol.* **2019**, *57*, 87–93. [CrossRef]

30. Karbowski, M.; Youle, R.J. Dynamics of mitochondrial morphology in healthy cells and during apoptosis. *Cell Death Differ.* **2003**, *10*, 870–880. [CrossRef]

31. Liu, Y.J.; McIntyre, R.L.; Janssens, G.E.; Houtkooper, R.H. Mitochondrial fission and fusion: A dynamic role in aging and potential target for age-related disease. *Mech. Ageing Dev.* **2020**, *186*, 111212. [CrossRef]

32. Sun, N.; Youle, R.J.; Finkel, T. The Mitochondrial Basis of Aging. *Mol. Cell* **2016**, *61*, 654–666. [CrossRef] [PubMed]

33. Pérez, M.J.; Quintanilla, R.A. Development or disease: Duality of the mitochondrial permeability transition pore. *Dev. Biol.* **2017**, *426*, 1–7. [CrossRef] [PubMed]

34. Fathinajafabadi, A.; Pérez-Jiménez, E.; Riera, M.; Knecht, E.; Gonzàlez-Duarte, R. CERKL, a retinal disease gene, encodes an mRNA-binding protein that localizes in compact and untranslated mRNPs associated with microtubules. *PLoS ONE* **2014**, *9*, e87898. [CrossRef] [PubMed]

35. Khacho, M.; Harris, R.; Slack, R.S. Mitochondria as central regulators of neural stem cell fate and cognitive function. *Nat. Rev. Neurosci.* **2019**, *20*, 34–48. [CrossRef]

36. Kim, J.M.; Kim, H.G.; Son, C.G. Tissue-Specific Profiling of Oxidative Stress-Associated Transcriptome in a Healthy Mouse Model. *Int. J. Mol. Sci.* **2018**, *19*, 3174. [CrossRef] [PubMed]

37. Cherubini, M.; Puigdellívol, M.; Alberch, J.; Ginés, S. Cdk5-mediated mitochondrial fission: A key player in dopaminergic toxicity in Huntington's disease. *Biochim. Biophys. Acta-Mol. Basis Dis.* **2015**, *1852*, 2145–2160. [CrossRef] [PubMed]
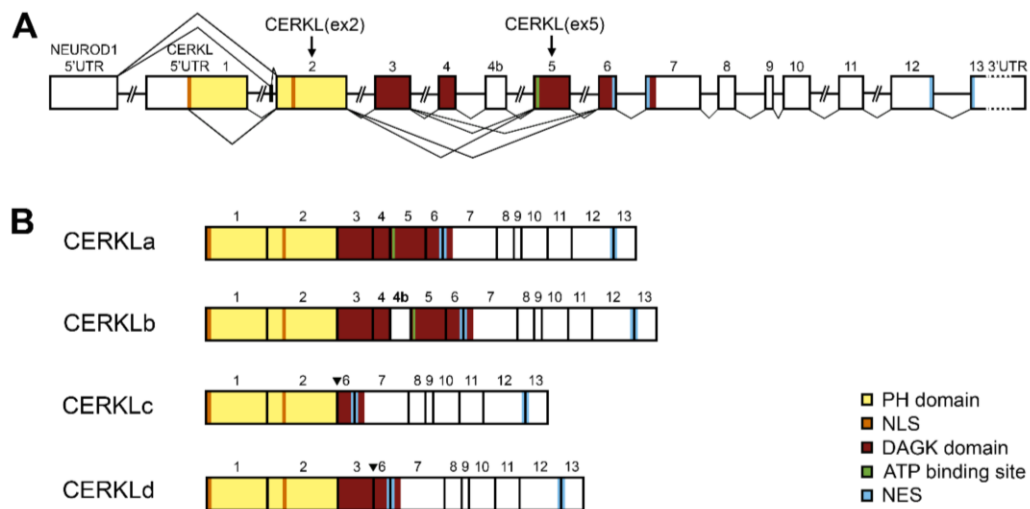
Figure S1. Schematic representation of the genomic structure and transcription of *CERKL* and some encoded protein retinal isoforms. (**A**) The human *CERKL* gene consists of 14 exons, uses multiple transcriptional start sites and undergoes multiple alternative splicing events. The position of the encoded domains in exons 2 and 5 used for antibody production are also indicated. (**B**) In the human retina, *CERKL* generates at least 4 protein isoforms as a result of alternative splicing events. Each of these isoforms displays different domains (PH, pleckstrin; DAGK, diacylglycerol kinase domain; NLS, nuclear localization signals; NES, nuclear export signals). Black triangles in isoforms c and d indicate the position of alternatively spliced exon junctions.
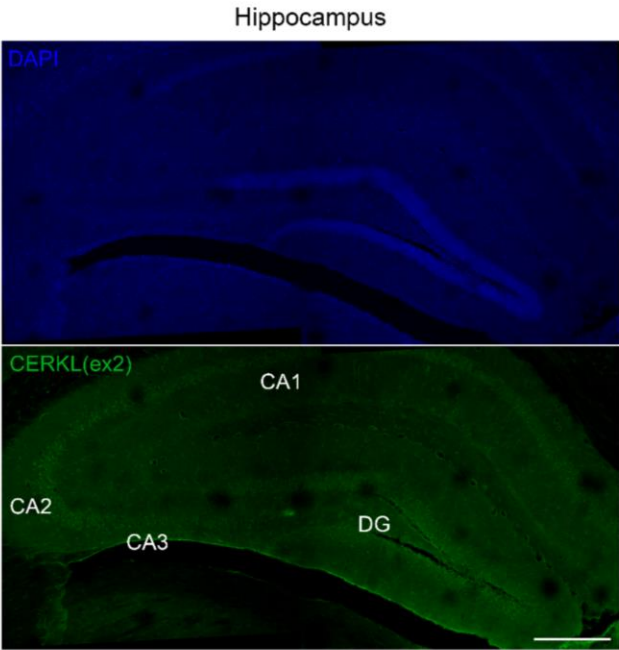
Figure S2. CERKL is expressed in adult mouse hippocampus. Adult mouse hippocampal cryosections immunostained with antibody CERKL(ex2) (green) and DAPI (blue), which stain the nuclei. CA1–CA3: Cornu Ammonis1–3; DG: dentate gyrus. Scale bar: 150 μm.
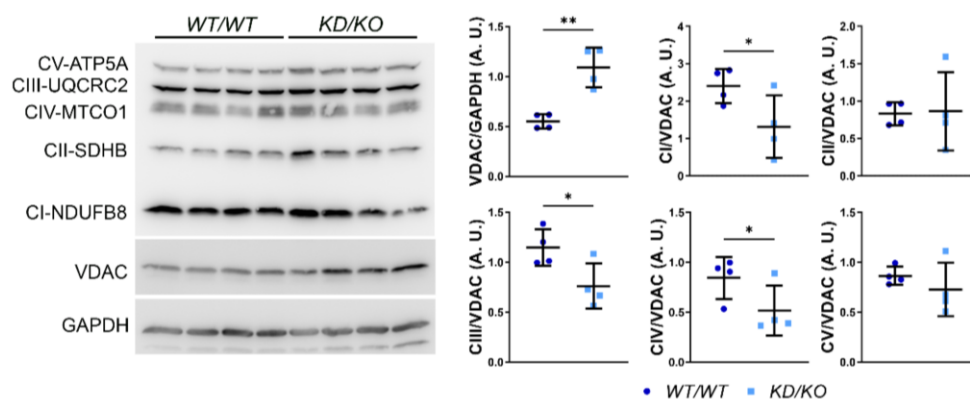
Figure S3. OXPHOS proteins are significantly altered in whole lysates from *KD/KO* hippocampi. Western blot analysis and quantification of OXPHOS proteins, VDAC and GAPDH in *WT/WT* and *KD/KO* hippocampi. VDAC is increased whereas CI-NDUFB8, CIII-UQCRC2 and CIV-MTCOI are decreased in *KD/KO* lysates, indicating shortage of OXPHOS proteins per mitochondria in *KD/KO* tissue. Statistical analysis by T-test. n=4 animals per genotype. *: p-value ≤0.5; **: p-value ≤0.01.

1.3. Characterization of *Cerkl*^{KD/KO} retinal pigment epithelial cells in primary culture

1.3. Characterization of *Cerkl*$^{KD/KO}$ retinal pigment epithelial cells in primary culture

Analysis of mitochondrial network in *KD/KO* primary RPE cells

After carefully assessing the mitochondrial network and dynamics in the neuroretina and hippocampal neurons, we aimed to further characterize the phenotypic alterations caused by *Cerkl* depletion in *KD/KO* primary RPE (pRPE) cells. pRPE cells constitute a valuable tool to handily evaluate several parameters important for the proper retinal function, including mitochondrial network organization, phagocytosis, ciliogenesis and cilium length.

Morphological analyses of the mitochondrial network resulted in a statistically significant slightly increase in mitochondrial major (median *WT/WT* 1.155 µm; *KD/KO* 1.230 µm) and minor length (median *WT/WT* 0.6774 µm; *KD/KO* 0.7068 µm) in *KD/KO* pRPE cells compared to *WT/WT*, although no alterations were observed in regard of mitochondrial area (Figure 15). Nevertheless, these minor differences in mitochondrial size are in the order of nanometres and, in fact, are statistically significant due to the large number of studied mitochondria. Additionally, the used imaging technique has limitations in detecting differences below 250 nanometres.
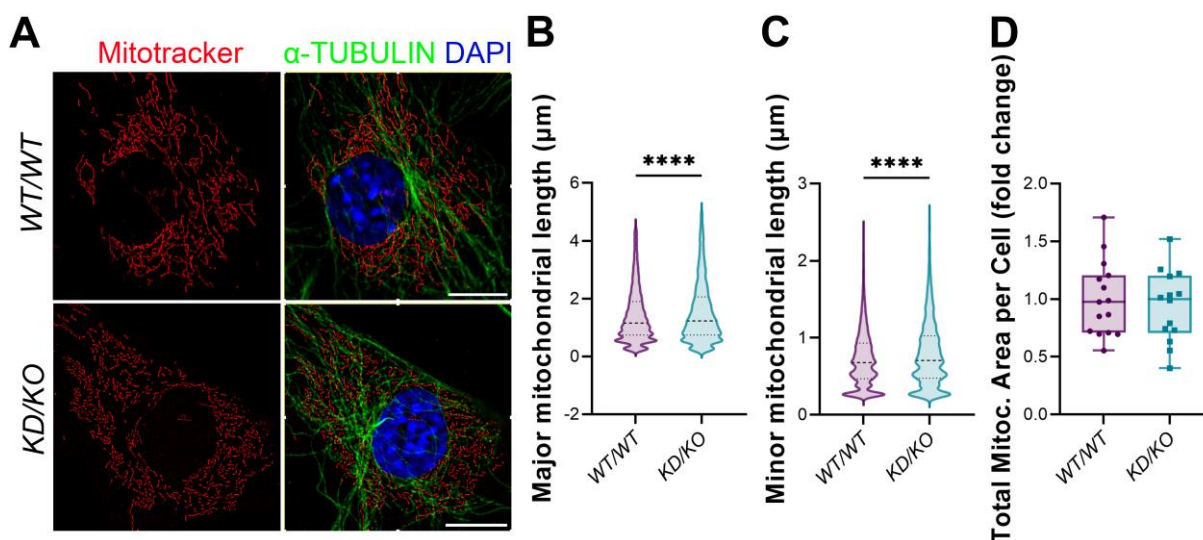
Figure 15. Slight differences in the mitochondrial size in pRPE from *KD/KO* versus *WT/WT* retinas. (A) Representative immunostaining confocal images of *WT/WT* and *KD/KO* pRPE; showing mitochondria (Mitotracker, in red), α-tubulin (green) and nuclei (DAPI, in blue). Scale bar: 10 µm. (B-D) Immunofluorescence images from a single focal plane were used to quantify mitochondrial major (B) and minor length (C), as well as total mitochondrial area per cell (D). n = 6392-10447 mitochondria from 14-15 cells from 3 animals per genotype. **** *p*-value ≤ 0.0001.

Thus, the reported nanometre-scale differences in *KD/KO* pRPE cells may not involve any biological relevance in mitochondrial homeostasis or metabolism.

Study of phagocytosis and endocytic pathway in *KD/KO* primary RPE cells

Previous phenotypic characterization of the *KD/KO* mouse model described an accumulation of phagosomes/lysosomes in the basal region of RPE cells (159). Considering that these results suggest alterations in phagocytosis and the endocytic pathway, we performed a functional phagocytosis assay using fluorescent latex beads on *KD/KO* pRPE cells to evaluate phagosome trafficking and maturation *in vitro*.

Following a 24-hour incubation with the beads, latex spheres were engulfed by *WT/WT* and *KD/KO* pRPE cells. A pool of these engulfed beads followed the endocytic pathway, colocalizing with specific markers of early (EEA1) and late (Rab7) endosomes (Figure 16A). Quantification of the percentage of beads in early endosomes showed no differences between genotypes (Figure 16B). However, the percentage of beads in late endosomes significantly decreased in *KD/KO* pRPE cells, also diminishing the ratio of beads contained in late endosomes versus early endosomes (Figure 16C, 16D). Nonetheless, Western blot analysis of EEA1 and Rab7 from *WT/*WT and *KD/KO* pRPE lysates showed no statistically significant differences in their protein levels between genotypes (Figure 16E).

Therefore, the observed alterations in the early to late endosome maturation after phagocytosis in *KD/KO* pRPE cells cannot be directly attributed to differences in the number of endosomes of each type.

KD/KO primary RPE cells display alterations in cilium length

The cilium has a pivotal role in retinal physiology, particularly in photoreceptor cells, equipped with a highly specialized neurosensory cilium, namely the OS. In the retina, RPE cells also present a primary cilium, which acts as an antenna detecting external cues and triggering cellular responses by activating signal transduction cascades (220). Using pRPE cultures from *WT/WT* and *KD/KO* mice, we assessed ciliogenesis and primary cilium length after 24 and 48 hours of serum deprivation, which induce differentiation and promotes cilium formation (Figure 17A).
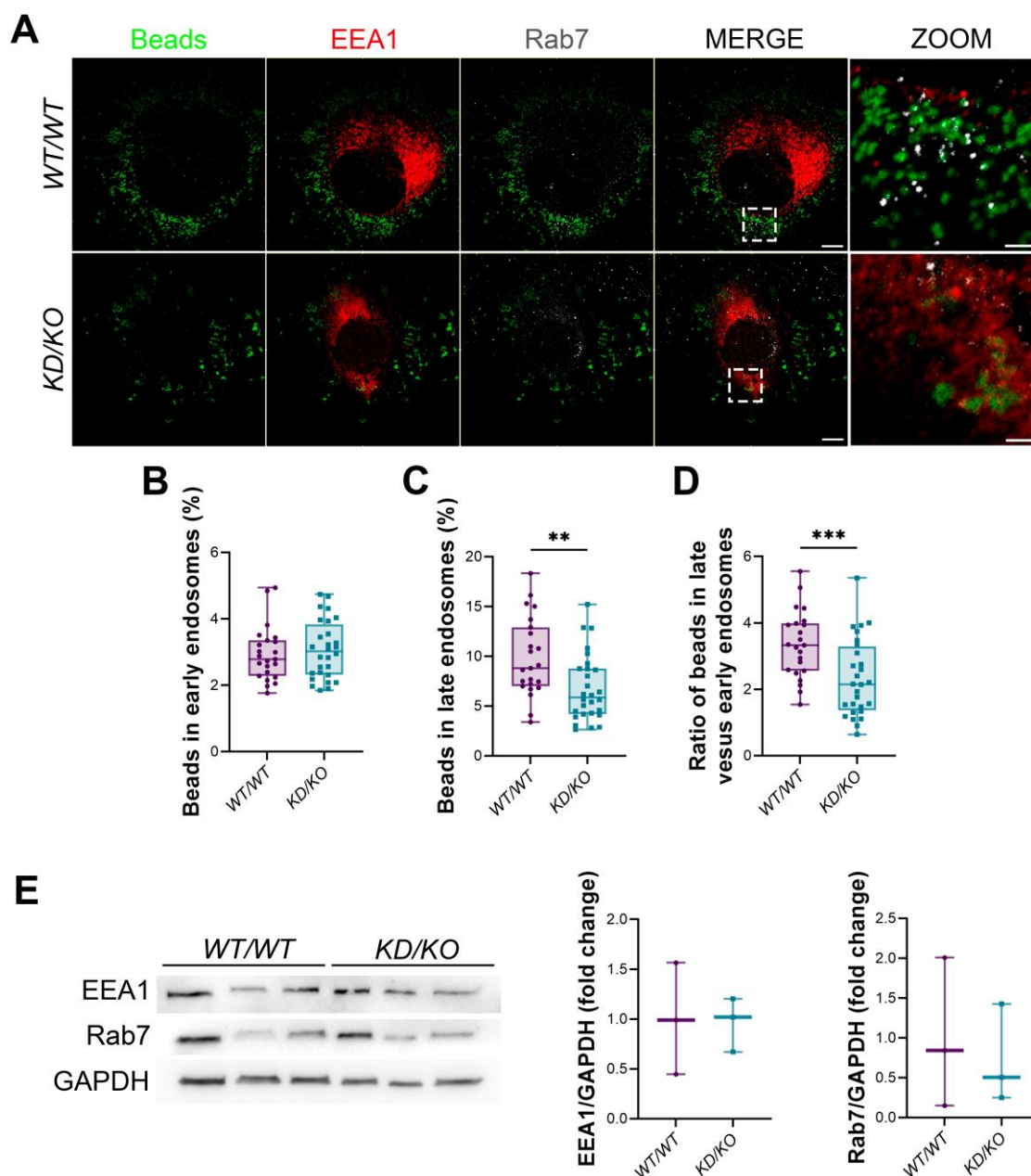
Figure 16. *KD/KO* pRPE cells present altered endosome maturation. (A) Representative confocal images of *WT/WT* and *KD/KO* pRPE cells treated with latex fluorescent beads (green) immunodetecting EEA1 (red) and Rab7 (grey). Scale bar: 10 μm. High magnification images indicate the colocalization between the latex beads and EEA1 or Rab7. Scale bar: 5 μm. (B-D) Percentage of beads in early (B) and late endosomes (C), as well as the ratio between them (D). n = 24-27 pRPE cells from 3 animals per genotype. (E) Western blot, immunodetection and quantification of EEA1, Rab7 and GAPDH in homogenates from *WT/WT* and *KD/KO* pRPE cultures. n = 3 animals per genotype. ** *p*-value ≤ 0.01; *** *p*-value ≤ 0.001.
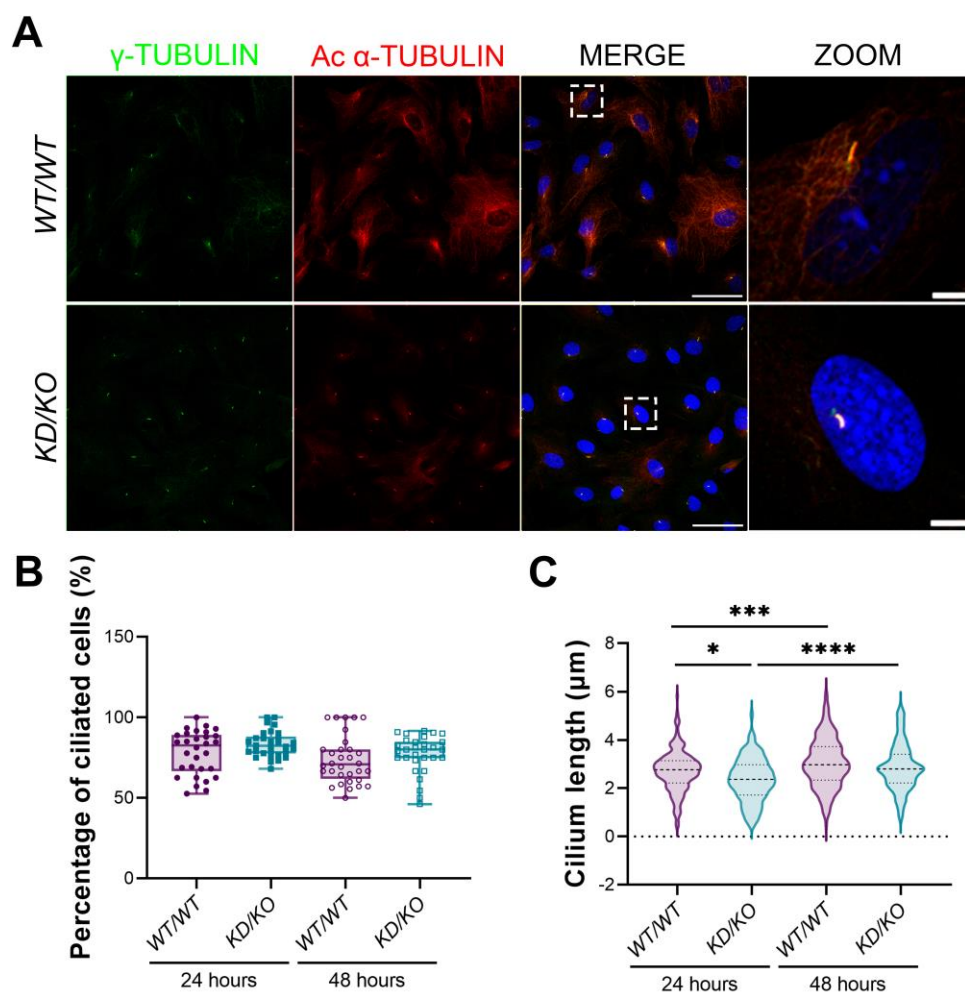
Figure 17. Cilium length is affected in *KD/KO* pRPE cells. (A) Representative confocal images of *WT/WT* and *KD/KO* pRPE cells after 24 hours of serum deprivation. Cilia were immunostained to visualize γ-TUBULIN (green) and acetylated (Ac) α-TUBULIN (red). Scale bar: 50 μm. High magnification images showing cilia with higher detail. Scale bar: 5 μm. (B) The percentage of ciliated cells do not differ between genotypes or conditions. n = 30-32 ROIs from 3 animals per genotype and condition. (C) Cilium length is significantly shorter in *KD/KO* pRPE cells at 24 hours of differentiation, although it reaches the length of that of *WT/WT* at 48 hours of differentiation. n = 192-230 cilia from 3 animals per genotype and condition. * p-value ≤ 0.05; *** p-value ≤ 0.001; **** p-value ≤ 0.0001.

After 24 hours of differentiation, both *WT/WT* and *KD/KO* pRPE cells exhibited a primary cilium, measurable as shown in Figure 17A. The number of ciliated cells was not different between genotypes at 24 and 48 hours of differentiation, indicating that the ability of pRPE cells to produce (24 hours) and maintain (48 hours) a primary cilium remained unaffected by *Cerkl* depletion (Figure 17B). However, at 24-hour differentiation stage, *KD/KO* pRPE cilium length was significantly shorter compared to *WT/WT*. Nevertheless, *KD/KO* cilia demonstrated a subsequent increase in length

at 48-hour differentiation, reaching values similar to those observed in *WT/WT*. Within the same genotype, the length of the cilium increased with longer differentiation times, allowing more time for ciliary growth (Figure 17C).

Overall, these findings indicate that *KD/KO* pRPE cells can indeed form a primary cilium, but the process of ciliary growth appears to be delayed.

MATERIAL AND METHODS

Animal handling

C57BL/6J *Cerkl^{WT/WT}* and *Cerkl^{KD/KO}* mice were bred and housed in the animal research facility of the Faculty of Pharmacy at the University of Barcelona. Animals were provided with food and water *ad libitum* and maintained in a temperature-controlled environment in a 12/12 hours light–dark cycle. All animal handling and assays were performed according to the ARVO statement for the use of animals in ophthalmic and vision research, as well as the regulations of the Ethical Committee for Animal Experimentation (AEC) of the Generalitat de Catalunya (protocol C-449/18), according to the European Directive 2010/63/EU and other relevant national guidelines. Each cohort had equivalent proportion of male and female mice, as autosomal recessive retinitis pigmentosa affects similarly both biological sexes.

Genomic DNA and genotyping by PCR

DNA for genotyping was extracted from ear punches. Primers for genotyping and PCR conditions were previously described in (159).

Primary Retinal Pigment Epithelium culture

The eyeballs from three 6-to-8-weeks-old mice per genotype were collected and stored in ice prior to dissection of the RPE. Each eyecup was rinsed in cold 1× PBS containing 1 % penicillin/streptomycin and 33 μg/mL tobramycin. Next, eyes were transferred into a 0.4 mg/mL collagenase/2 % dispase solution to extract the cornea and flatten the eyecup. Then, the eyecup was rinsed with 1× PBS and Versene (0.48 mM EDTA in 1× PBS) prior to the 10-minutes incubation at room temperature with 2 % dispase. After a rinse with 1× PBS, the retina was detached from the posterior eyecup, and the eyecup was further incubated with 2 % dispase for 10 additional minutes at 37 °C. Subsequently, the RPE was scrapped off from the eyecup in a 6-well plate well (Thermo Fisher Scientific, Waltham, MA, USA; 140675) and 2 mL of complete medium (1 % penicillin/streptomycin (Life Technologies, Carlsbad, CA, USA) and 10 % foetal bovine serum (FBS) (Life Technologies, Carlsbad, CA, USA; 15140-122) in DMEM (ATCC, Manassas, VA, USA; 30-2002)) were added. Media was

changed after 72 hours and the six pRPE cell lines were maintained and grown with complete medium.

For the different experiments, 1.5×10^4 cells were seeded onto 24-well plate wells (Sigma, San Luis, MO, USA; CLS3527-100EA). For differentiation, cells were incubated in serum-deprived medium (1 % penicillin/streptomycin and 0.2 % FBS in DMEM) for 24 or 48 hours prior to fixation.

Phagocytosis assay

After the first 24 hours of differentiation, 5×10^6 0.1 μm-diameter fluorescent latex beads (Sigma, San Luis, MO, USA; L9904) were added to the media in each well for a 24-hour-long incubation at 37 °C.

Immunocytochemistry

After fixation with 4 % PFA for 15 minutes at room temperature, cells were permeabilized during 20 minutes with 0.2 % Triton X-100 (Scharlab, Hamburg, Germany; TR04441000) in 1× PBS and blocked with 1× PBS containing 5 % normal goat serum (Life technologies, Carlsbad, CA, USA; 16210064) for 1 hour at room temperature. Then, cells were incubated with primary antibody (anti-α-TUBULIN (Sigma; T5168; 1:1000), anti-acetylated-α-TUBULIN (Sigma; SAB5600134; 1:1000), anti-γ-TUBULIN (Sigma; T6557; 1:500), anti-EEA1 (Abcam, Plc, Cambridge, UK; ab2900; 1:200) and anti-Rab7 (Abcam; ab50533; 1:200)) in blocking solution overnight at 4 °C and secondary antibody (AlexaFluor 488 anti-Mouse (Thermo Fisher Scientific, Rockford, IL, USA; A11017; 1:500), AlexaFluor 568 anti-Rabbit (Thermo Fisher Scientific; A11011; 1:500), and Alexa Fluor 647 anti-mouse (Thermo Fisher Scientific; A21235; 1:500)) with DAPI (Sigma-Aldrich, St. Louis, MO, USA; 10236276001; 1:1000) for 1 hour at room temperature. Finally, coverslips were mounted using Mowiol 4-88 (Merck, Kenilworth, NJ, USA) and visualized by means of confocal microscopy (Zeiss LSM 880, Thornwood, NY, USA). Confocal images were analysed using ImageJ software.

To stain mitochondria, 1 μM MitoTracker™ Orange CMTMRos (Thermo Fisher Scientific, Rockford, IL, USA; M7510) was added to the cells and incubated for 20 min at 37 °C before fixation.

RESULTS

Image analysis

Quantitative analyses of mitochondrial morphology and area in pRPE cells was performed using an ImageJ software macro as described in (221). Briefly, using ImageJ software, a threshold was established to distinguish mitochondria from the background. Particle analyses from each individual mitochondrion (particle) were performed to determine mitochondrial major and minor lengths, as well as mitochondrial area. The total mitochondrial area in pRPE cells was calculated by adding each mitochondrion area for each cell and normalized using the total area of the cell.

To assess the percentage of ciliated cells, the length from 60-100 cilia was measured in each pRPE line with the segmented line selection tool in ImageJ, accounting up to 192-230 measured cilia per genotype and time point.

In the phagocytosis functional assay, colocalization analysis of the green signal from the beads with endosomes markers was performed in selected areas with ImageJ software.

Western blotting

Cell protein lysates were directly collected by adding 70 µL of 1× Loading Buffer (60 mM TrisHCl pH 6.8, 10 % glycerol, 2 % Sodium Dodecyl Sulphate, 0.1 % Bromophenol blue in Milli®-Q water) and 5 % β-mercaptoethanol, and boiled for 5 minutes at 95 °C. Proteins were analysed by SDS-PAGE and transferred onto nitrocellulose membranes, which were blocked with 5 % non-fat dry milk in 1× PBS containing 0.1 % Tween 20 and incubated overnight at 4 °C with primary antibodies. After incubation with horseradish peroxidase-labelled secondary antibodies for 1 hour at room temperature, immunodetection was developed using the ECL system (Lumi-Light Western Blotting Substrate, Roche, Basilea, Switzerland; 12015200001). Images were acquired by ImageQuant™ LAS 4000 mini Image Analyzer (Fuji-film, Tokio, Japan) and quantified using ImageJ software. GAPDH loading control was used to normalize protein values. The primary antibodies were the following: anti-GAPDH (Sigma; G9545; 1:1000), anti-EEA1 (Abcam; ab2900; 1:1000) and anti-Rab7 (Abcam; ab50533; 1:1000). The secondary antibodies were: HRP-labelled anti-

mouse (Sigma; A5906; 1:2000) and anti-rabbit (GE Healthcare; NA934-100UL; 1:2000).

Statistical analyses

Data were analysed using GraphPad Prism software (GraphPad9 Software Inc., San Diego, CA, USA). Homoscedasticity and normality were verified using Bartlett's test, and D'Agostino and Person's test, respectively. In case homoscedasticity or normality were not fulfilled, logarithm or square root corrections were performed. When data were homoscedastic and followed a normal distribution, data were analysed by t-test, one-way ANOVA, or two-way ANOVA. Mann–Whitney and Kruskal–Wallis tests were used when data did not follow a normal distribution.
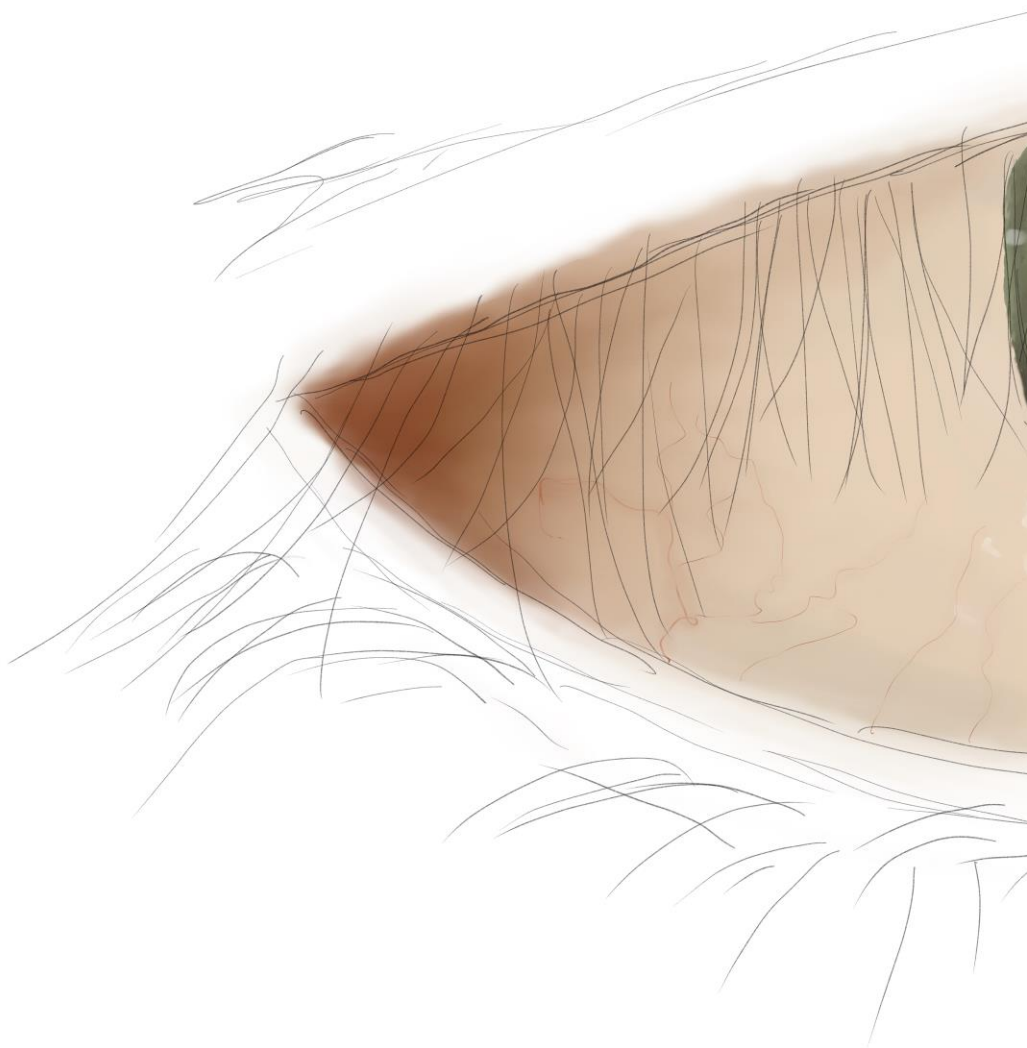
CHAPTER 2

Response to light and oxidative stress in *CERKL*-depleted models
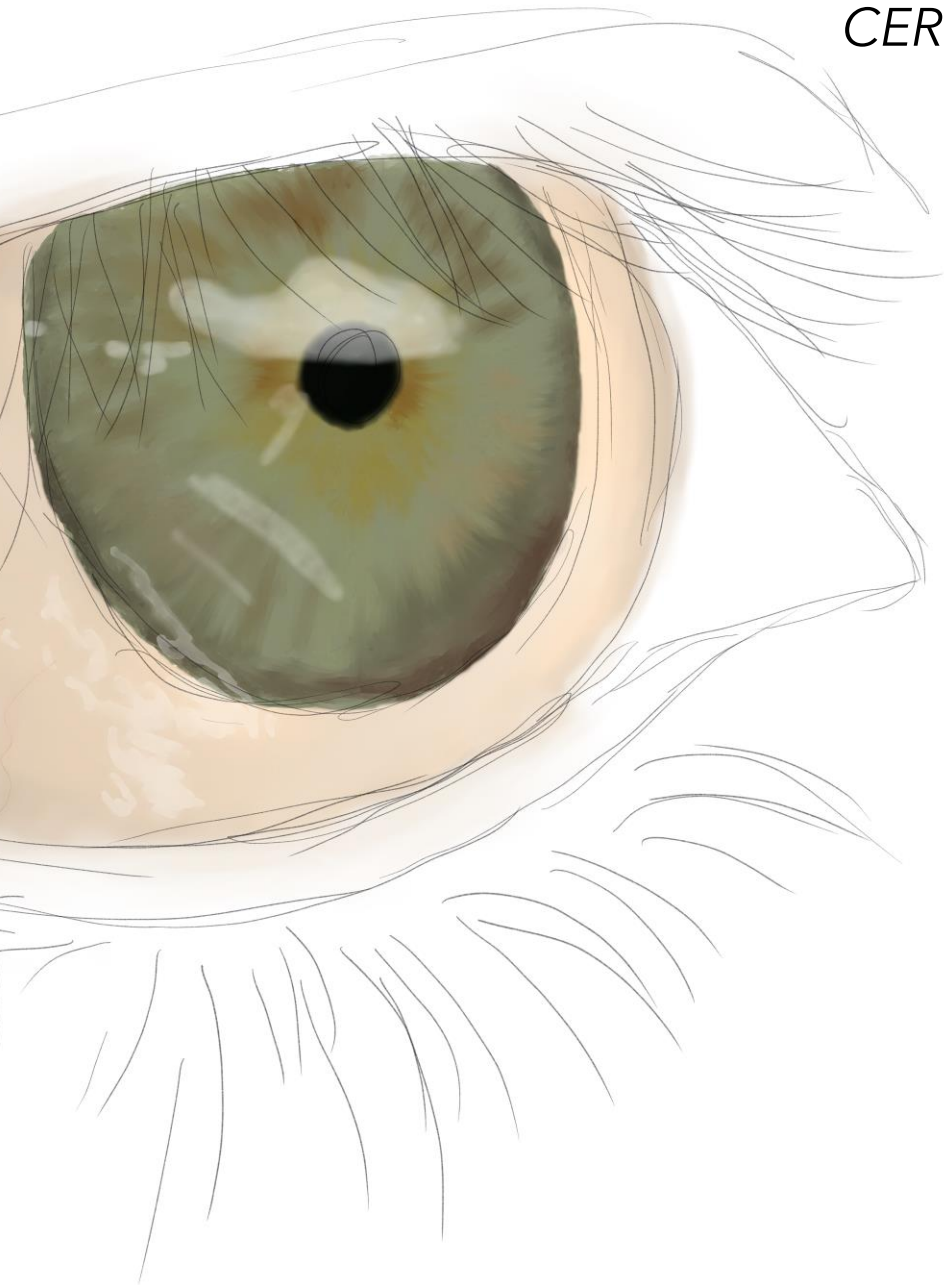
2.1. Overexpression of CERKL protects RPE cells from oxidative stress

Publication 3

Title

Overexpression of CERKL Protects Retinal Pigment Epithelium Mitochondria from Oxidative Stress Effects

Authors

Rocío García-Arroyo, Aleix Gavaldà-Navarro, Francesc Villarroya, Gemma Marfany and Serena Mirra

Reference

Abstract

The precise function of *CERKL*, a Retinitis Pigmentosa (RP) causative gene, is not yet fully understood. There is evidence that *CERKL* is involved in the regulation of autophagy, stress granules, and mitochondrial metabolism, and it is considered a gene that increases resilience against oxidative stress in retinal cells. Mutations in most RP genes affect photoreceptors, but retinal pigment epithelium (RPE) cells may be also altered. Here, we aimed to analyze the effect of *CERKL* overexpression and depletion in vivo and in vitro, focusing on the state of the mitochondrial network under oxidative stress conditions. Our work indicates that the depletion of *CERKL* increases the vulnerability of RPE mitochondria, which show a shorter size and altered shape, particularly upon sodium arsenite treatment. *CERKL*-depleted cells have dysfunctional mitochondrial respiration particularly upon oxidative stress conditions.

The overexpression of two human CERKL isoforms (558 aa and 419 aa), which display different protein domains, shows that a pool of CERKL localizes at mitochondria in RPE cells and that CERKL protects the mitochondrial network—both in size and shape—against oxidative stress. Our results support *CERKL* being a resilience gene that regulates the mitochondrial network in RPE as in retinal neurons and suggest that RPE cell alteration contributes to particular phenotypic traits in patients carrying *CERKL* mutations.

Personal contribution to this work

This is one of the main articles of my Thesis. My personal contribution to this publication has been: a) design and testing of siRNA against *CERKL* (Figure 2A); b) quantitative analysis of mitochondrial morphology and area in ARPE-19 cells upon *CERKL*-depletion and overexpression in control and oxidative stress conditions (Figures 2 and 3); c) evaluation and quantification of mitochondrial superoxide in ARPE-19 cells upon *CERKL*-depletion and overexpression in control and oxidative stress conditions (Figure 4); d) preparation of *CERKL*-depleted ARPE-19 cells for assessment of mitochondrial bioenergetics (Figure 5); e) design and creation of the figures; f) the discussion of the results (Figure 6); and g) draft writing and critical reading of the manuscript.

Article

Overexpression of CERKL Protects Retinal Pigment Epithelium Mitochondria from Oxidative Stress Effects

Rocío García-Arroyo [1,2,3], **Aleix Gavaldà-Navarro** [3,4,5], **Francesc Villarroya** [3,4,5], **Gemma Marfany** [1,2,3,6,*] and **Serena Mirra** [1,2,3,*]

1   Department of Genetics, Microbiology and Statistics, Avda. Diagonal 643, Universitat de Barcelona, 08028 Barcelona, Spain; rociogarciaarroyo@ub.edu
2   CIBERER, Instituto de Salud Carlos III, 28029 Madrid, Spain
3   Institut de Biomedicina-Institut de Recerca Sant Joan de Déu (IBUB-IRSJD), Universitat de Barcelona, 08028 Barcelona, Spain; aleixgavalda@ub.edu (A.G.-N.); fvillarroya@ub.edu (F.V.)
4   Department of Biochemistry and Molecular Biomedicine, Avda. Diagonal 643, Universitat de Barcelona, 08028 Barcelona, Spain
5   CIBEROBN, Instituto de Salud Carlos III, 28029 Madrid, Spain
6   DBGen Ocular Genomics, 08028 Barcelona, Spain
*   Correspondence: gmarfany@ub.edu (G.M.); serena.mirra@ub.edu (S.M.)

Abstract: The precise function of *CERKL*, a Retinitis Pigmentosa (RP) causative gene, is not yet fully understood. There is evidence that *CERKL* is involved in the regulation of autophagy, stress granules, and mitochondrial metabolism, and it is considered a gene that is resilient against oxidative stress in the retina. Mutations in most RP genes affect photoreceptors, but retinal pigment epithelium (RPE) cells may be also altered. Here, we aimed to analyze the effect of *CERKL* overexpression and depletion in vivo and in vitro, focusing on the state of the mitochondrial network under oxidative stress conditions. Our work indicates that the depletion of *CERKL* increases the vulnerability of RPE mitochondria, which show a shorter size and altered shape, particularly upon sodium arsenite treatment. *CERKL*-depleted cells have dysfunctional mitochondrial respiration particularly upon oxidative stress conditions. The overexpression of two human CERKL isoforms (558 aa and 419 aa), which display different protein domains, shows that a pool of CERKL localizes at mitochondria in RPE cells and that CERKL protects the mitochondrial network—both in size and shape—against oxidative stress. Our results support *CERKL* being a resilient gene that regulates the mitochondrial network in RPE as in retinal neurons and suggest that RPE cell alteration contributes to particular phenotypic traits in patients carrying *CERKL* mutations.

Keywords: retinitis pigmentosa; *CERKL*; retinal pigment epithelium; mitochondrial network; oxidative stress

1. Introduction

Retinitis pigmentosa (RP) comprises a genetically heterogenous group of retinal degenerative diseases characterized by night blindness and progressive loss of vision due to photoreceptor degeneration. To date, more than 70 causative genes have been identified [1]. Mutations in *CERKL* (CERamide Kinase Like) have been reported to cause non-syndromic autosomal recessive RP [2] as well as cone-rod dystrophy (CRD) [3]. *CERKL* expression is highly complex, with more than 20 transcripts and several alternative promoters in human and mouse tissues [4,5].

This transcriptional complexity results in at least four CERKL isoforms displaying different protein domains [6]. CERKL isoforms have a dynamic subcellular localization and multiple functions: they act as a shuttle from the cytoplasm to the nucleus; are able to bind sphingolipids [7]; interact with antioxidant enzymes [8]; and regulate autophagy, and mitochondrial dynamics and metabolism [9,10]. Notably, CERKL has been also described as a RNA binding protein that localizes in polysomes, mRNA compact particles, stress granules

(SG), and P-bodies under stress conditions [11]. Altogether, these findings point to *CERKL* being a resilient gene acting in multiple pathways to protect retinal photoreceptors against oxidative stress. Thus, mutations in CERKL most probably increase the sensitivity of retinal tissue to oxidative damage, resulting in cell death and retinal neurodegeneration [12].

Knowledge about *CERKL* function in the neuroretina has been growing during the last years with the obtention of several mouse models. Using CRISPR-Cas9 gene editing, our group generated a double heterozygous knock-down/knock-out, $Cerkl^{KD/KO}$, mouse line, where some *Cerkl* expression was retained to ensure organism survival. Specifically, the $Cerkl^{KD/KO}$ retina expressed less than 20% of *Cerkl* compared with that of wild type [5]. In the retina, CERKL expression has been mostly described in rods, cones, and retinal ganglion cells [5]. Notably, most mutated genes that cause RP are also expressed in retinal pigment epithelium (RPE), and previous data from our lab showed a strong expression of CERKL in mouse RPE [5]. However, very little is known about the function of CERKL in RPE. RPE is a monolayer of post-mitotic cells located between the neuroretina and the choroid, playing an important role in retinal homeostasis. The functions of RPE include (a) helping renew outer segments by phagocytosis and degradation of spent discs of photoreceptor outer segments, (b) ensuring photoreceptor survival by supplying small molecules (amino acids, ascorbic acid, and D-glucose), (c) supporting the recycling of molecules associated with the visual cycle, (d) creating a firm barrier against choroidal blood-borne substances, and (e) protecting the outer retina from excessive high-energy light and light-generated reactive oxygen species (ROS). Consequently, RPE is shown to have an immense metabolic activity. Recent evidence suggests that mitochondrial damage and oxidative stress in the RPE may play important roles in RP pathogenesis [13].

Mitochondria are crucial organelles that provide energy to the cell because of oxidative phosphorylation. In addition, they are important to buffer calcium, to control the cell cycle, and to regulate apoptosis. It is estimated that 1–5% of ROS is generated by mitochondrial activity in physiological conditions [14]. An altered mitochondrial function caused by environmental or physiological changes generates loss of mitochondrial membrane potential, decreases oxidative phosphorylation, causes damage in mitochondrial DNA, and creates a vicious circle of ROS-generated ROS [15]. These perturbations induce reorganization of the mitochondrial network through changes in mitochondrial dynamics that consist of fission, fusion, transport, communication between organelles, and quality control mechanisms [16]. All these alterations can finally lead to programmed cell death. Importantly, RPE experiences a high-oxygen environment, which is exacerbated by the loss of rods in RP, thus creating a hyperoxic environment that is presumably hostile for the remaining cells [17]. One protective strategy in RP and other inherited retinal dystrophies is to augment the oxidative damage defense systems in both retina and RPE [15].

Here, we describe the CERKL-mediated cellular response to oxidative stress in RPE, focusing on mitochondria. By comparing the RPE of wild-type (WT) and $Cerkl^{KD/KO}$ (heretofore *KD/KO*) animals combined with in vitro assays, we study the impact of CERKL expression levels on RPE mitochondrial network organization and dynamics at basal conditions and under oxidative stress.

2. Materials and Methods

2.1. Animal Handling

Mouse tissue from WT and $Cerkl^{KD/KO}$ was obtained according to the ARVO statement for the use of animals in ophthalmic and vision research under the regulations of the Ethical Committee for Animal Experimentation (AEC) of the Generalitat of Catalonia according to the European Directive 2010/63/EU and other national laws. The procedures received institutional approval from the Universitat de Barcelona.

2.2. Transmission Electron Microscopy

Three-month-old C57BL6/J mice or twelve-month-old albino mice were transcardially perfused with cold fixative solution (2.5% glutaraldehyde and 2% PFA (paraformaldehyde) in 0.1 M phosphate buffer). Their eyes were removed, and the retinas were dissected and fragmented in 1 mm^3 pieces. Retinal fragments were immersed in fixative solution (2.5% glutaraldehyde and 2% PFA in 0.1 M phosphate buffer) and incubated at 4 °C overnight. The retinal fragments were post-fixed in 1% osmium tetroxide 2% $K_4Fe(CN)_6$ in the dark for 2 h at 4 °C and rinsed in double-distilled water to remove the osmium. The retinal fragments were dehydrated in ascending concentrations of acetone, then infiltrated, and embedded in Epon (EMS). Blocks were obtained after polymerization at 60 °C for 48 h. Ultrathin sections of 60 nm in thickness were obtained using a UC6 ultramicrotome (Leica Microsystems, Vienna, Austria) and were stained with 2% uranyless and lead citrate. Sections were observed in a Tecnai Spirit 120 Kv TEM (FEI company, Eindhoven, The Netherlands), and images were acquired with a 1 k × 1 k CCD Megaview camera (Olympus Soft Imaging Solutions, Münster, Germany).

2.3. Whole-Mount RPE

For whole-mount RPE staining, RPE from adult mice were obtained as described in [18], placed on glass slides flattened by cutting the edges, fixed for 1 h in 4% paraformaldehyde, and rinsed with 1× PBS (3 × 5 min). The retinas were then incubated with Alexa Fluor 647 Phalloidin (Thermo Fisher Scientific, Rockford, IL, USA; A22287) for 1 h. Retinas were washed with 1X PBS (3 × 5 min) and mounted with Fluoprep (BioMerieux, Marcy-l'Étoile, France). All of the samples were analyzed by confocal microscopy (Zeiss LSM 880, Thornwood, NY, USA), and images were collected using ZEN-LSM software (version 2.3, Zeiss, Thornwood, NY, USA). N = 25–34 ROI from 3 animals per genotype.

2.4. Immunohistochemistry on Mouse Retina Cryosections

For immunohistochemistry, eyes from adult mice were enucleated, fixed in 4% PFA, and embedded in OCT. Cryosections (12 µm section) were collected and kept frozen at −80 °C until use. Cryosections were rehydrated with 1× PBS (3 × 5 min) and blocked in blocking solution (1× PBS containing 10% normal goat serum and 0.3% Triton X-100 (Sigma-Aldrich, St. Louis, MO, USA) for 1 h at room temperature. Incubation with the primary antibodies COXIV (Thermo Fisher Scientific, Rockford, IL, USA; 459600; 1:500), CERKL2, and CERKL5 (both produced in-house [5]) was performed overnight at 4 °C. After three rinses with 1X PBS (10 min each), cryosections were incubated for 1 h at room temperature with the corresponding secondary antibodies (AlexaFluor 568 anti-Mouse (Thermo Fisher Scientific, Rockford, IL, USA; A11004; 1:300) and AlexaFluor 488 anti-Rabbit (Thermo Fisher Scientific, Rockford, IL, USA; A11070; 1:300)) and with 4′,6-diamidino-2-phenylindole (DAPI) (Sigma-Aldrich, St. Louis, MO, USA; 10236276001; 1:1000). Finally, the slides were washed with 1× PBS (3 × 10 min) and coverslipped with Fluoprep (BioMerieux, Durham, NC, USA). Image visualization was performed using confocal laser scanning microscope (Zeiss LSM 880, Thornwood, NY, USA).

2.5. ARPE-19 Cell Culture, Transfection, and siRNA Reverse Transfection

Human ARPE-19 cells (ATCC, Elizabeth City, NC, USA; CRL_2302) were cultured in 10% fetal bovine serum (FBS) and 1% penicillin/streptomycin in 1:1 Dulbecco's Modified Eagle's Medium (DMEM) (ATCC, Manassas, VA, USA) and Ham's F-12 Nutrient Mix (F12) (Life Technologies, Carlsbad, CA, USA) in a 5% CO_2 cell culture humidified incubator at 37 °C. ARPE-19 cells were incubated without FBS for 48 h to induce differentiation.

Cell transfection was performed using Lipotransfectine (Niborlab, Guillena, Spain) (DNA–lipotransfectine ratio 1:2). ARPE-19 cells were seeded in poly-L-lysine pre-treated coverslips in 24-well plates (10^5 cells per well) and incubated for 24 h. pEGFP-N2, CERKLb-GFP, and CERKLc-GFP vectors (1 µg per well) were transfected in non-antibiotic medium. After 5 h, the non-antibiotic medium was replaced with differentiation medium for 48 h.

For siRNA reverse transfection, cells in suspension were transfected using lipofectamine RNAiMAX reagent (Thermo Fisher Scientific, Rockford, IL, USA) and 20 nM scrambled (scr) (scr1: Non-targeting siRNA #1, D-001810-01-05, Dharmacon; and scr2: Silencer™ Negative Control No. 4 siRNA, AM4641, Ambion, Thermo Fisher, Rockford, IL, USA) or anti-CERKL small interfering (si)RNA. Anti-CERKL siRNA were obtained from Ambion (Thermo Fisher, Rockford, IL, USA), and their sequences were si*CERKL*1: 5′-UAAAACACCUGAAAAGAUAtt-3′ and si*CERKL*2: 5′-GCAUCAGAGGUCCAUAUUAtt-3. Then, ARPE-19 cells were seeded in poly-L-lysine pre-treated coverslips in 24-well plates (2×10^5 cells per well) and incubated for 48 h in differentiation conditions.

Finally, in the different assays, to test the effects of oxidative stress in ARPE-19 cells, cells were treated with 100 μM sodium arsenite ($NaAsO_2$) for 4 h.

2.6. Immunocytochemistry

After fixation with 4% PFA for 10 min at room temperature, cells were blocked with 1X PBS containing 0.01% Triton X-100 (Scharlau, Hamburg, Germany) and 10% normal goat serum or 2% sheep serum for 1 h at room temperature. Then, cells were incubated with primary antibody (anti-GFP (Abcam, Plc, Cambridge, UK; ab290; 1:1000) and anti-CERKL (in-house antibody; 1:100)) in blocking solution overnight at 4 °C and secondary antibody (AlexaFluor 488 anti-Mouse (Thermo Fisher Scientific, Rockford, IL, USA; A11017; 1:500), AlexaFluor 488 anti-Rabbit (Thermo Fisher Scientific, Rockford, IL, USA; A11070; 1:500), and Alexa Fluor 647 Phalloidin (Thermo Fisher Scientific, Rockford, IL, USA; A22287; 1:250)) with DAPI (Sigma-Aldrich, St. Louis, MO, USA; 10236276001; 1:1000) for 1 h at room temperature. Finally, coverslips were mounted using Mowiol 4-88 (Merck, Kenilworth, NJ, USA) and visualized by means of confocal microscopy (Zeiss LSM 880, Thornwood, NY, USA). Confocal images were analyzed using ImageJ software. To stain mitochondria, 1 μM MitoTracker™ Orange CMTMRos (Thermo Fisher Scientific, Rockford, IL, USA) was added to the cells and incubated for 20 min at 37 °C before fixation.

2.7. Mitochondrial Superoxide Quantification

MitoSOX™ Red (Thermo Fisher Scientific, Rockford, IL, USA) was used to measure the mitochondrial superoxide levels. ARPE-19 cells were previously treated with 100 μM $NaAsO_2$ for 4 h. Then, cells were incubated with differentiation medium containing 5 μM of MitoSOX Red at 37 °C for 10 min and washed three times with medium. Finally, cells were fixed with 4% PFA for 10 min at room temperature. Fluorescence intensity was determined by confocal microscopy (Zeiss LSM 880, Thornwood, NY, USA) and quantified by means of ImageJ software (version 1.53n, National Institutes of Health, Bethesda, MD, USA) applying CTCF (corrected total cellular fluorescence) normalization formula where cell fluorescence is corrected for the fluorescence of the background multiplied for the cell area.

2.8. Quantitative Analyses of Mitochondrial Morphology

Quantitative analyses of mitochondrial morphology and area in Transmission Electron Microscopy (TEM) microphotography 26,500× images and ARPE-19 cells were performed using an ImageJ software macro as described in [10]. Briefly, using ImageJ software, a threshold was established to distinguish mitochondria from the background. Particle analyses from each individual mitochondrion (particle) were performed to determine aspect ratio (AR, the ratio of the width to the height of the ellipse equal to the mitochondrion) and form factor values (FF, ($4\pi \times Am/Pm^2$), in which Am is the area of the mitochondrion and Pm is the length of the mitochondrial perimeter). The mitochondrial area in ARPE-19 cells was calculated by adding each mitochondrion area for each cell and normalized using the total area of the cell.

For TEM microphotographies, 78–89 mitochondria were analyzed from 3 WT and 3 *KD/KO* (3-month-old mice) and 38–44 mitochondria were analyzed from 3 WT and 3 *KD/KO* (12-month-old mice). Concerning ARPE-19 cells, 223–309 mitochondria were ana-

Chapter 2

Antioxidants **2021**, 10, 2018
5 of 16

lyzed from 15–20 siRNA-treated cells per condition and 404–726 mitochondria were analyzed from 28–30 transfected cells per condition. Three experimental replicates were performed.

2.9. Seahorse Analysis

ARPE-19 cells were reversely transfected with scr1 and si*CERKL*1 in a 24-well plate. After 24 h, *CERKL*-silenced cells were detached and reseeded in a Seahorse 24-well cell culture plate (Agilent, Santa Clara, CA, USA) (2.5×10^5 cells per well). For antioxidant and stress treatments, cells were treated with 4 μM N-acetyl-L-cysteine (NAC) (Merck, Kenilworth, NJ, USA; A9165) for 24 h and 100 μM sodium arsenite for 4 h prior to Seahorse assay. After treatments, cells were incubated with Seahorse XF Assay Medium (Agilent, Santa Clara, CA, USA) for 1 h at 37 °C. Then, plates were loaded into an XFe24 respirometry machine (Agilent, Santa Clara, CA, USA). Complex V was inhibited with 5 μM oligomycin A. Maximum oxygen consumption rate (OCR) was assayed by adding 2 μM carbonyl cyanide-p-trifluoromethoxyphenylhydrazone (FCCP). Rotenone (5 μM) and antimycin A (15 μM) were used to inhibit complex I- and III-dependent respiration, respectively. Five replicates were performed for each experimental condition.

2.10. Statistical Analyses

Data were analyzed using GraphPad Prism software (GraphPad6 Software Inc., San Diego, CA, USA). Homoscedasticity and normality were verified using Bartlett's test, and D'Agostino and Person's test, respectively. In case homoscedasticity or normality were not fulfilled, logarithm or square root corrections were performed. When data were homoscedastic and followed a normal distribution, data were analyzed by *t*-test, one-way ANOVA, and two-way ANOVA. Mann–Whitney and Kruskal–Wallis tests were used when data did not follow a normal distribution.

3. Results

3.1. KD/KO RPE Displays More Polynucleated Cells and Smaller Mitochondria

CERKL localizes at different cellular compartments, e.g., nuclei, Golgi apparatus, and mitochondria, among others, in both immortalized and primary cell lines [8–11]. However, little is known about the subcellular localization of CERKL in mammalian RPE. To assess whether endogenous CERKL colocalizes with mitochondria in murine RPE, we performed immunofluorescence of retinal cryosections from *WT/WT* mice with the mitochondrial marker COX-IV and two different in-house antibodies against peptides encoded by exon 2 (anti-CERKL2) or exon 5 (anti-CERKL5), which detect different pools of endogenous isoforms [5]. In both cases, CERKL partially colocalizes with mitochondria (Figure 1A).

Detrimental factors, such as aging or oxidative stress, may compromise RPE homeostasis. Aging and blinding diseases, including rare retinopathies, are associated with changes to RPE structure, such as the increasing of bi- and multinucleated RPE cells [19,20]. Multinuclear cell formation has been proposed as a mechanism to compensate the apoptotic loss of RPE cells and to maintain the epithelial layered structure under stress conditions [21]. As *CERKL* is proposed as a resilience gene against oxidative stress in mammalian retina, and its depletion in *KD/KO* mice causes retinal degeneration, we investigated if *KD/KO* RPE suffered changes in the percentage of mono- and multinucleated cells. We observed that the ratio of mono- and poly-nucleated cells is shifted in *KD/KO* RPE, with an increase in poly-nucleated cells with a decrease in mono-nucleated cells (Figure 1B).

The preservation of mitochondrial function and morphology is essential to ensure RPE homeostasis and a correct crosstalk with neuroretina. Since a pool of CERKL colocalizes at mitochondria in both RPE and neuroretina, we assessed possible alterations of mitochondrial morphology in *KD/KO* RPE in vivo by transmission electron microscopy (TEM) of *WT/WT* and *KD/KO* RPE from 2-month-old mice. We found a significant decrease in mitochondrial area and length in *KD/KO*, without changes in the morphological parameter aspect ratio (Figure 1C). These findings were further confirmed by performing the same morphological analysis of mitochondria in 8-month-old mice (Figure S1A–C). On the other

hand, no detectable changes in the size of the Bruch's membrane, of which the structure is typically altered in several retinopathies, could be observed (Figure S1A,C).
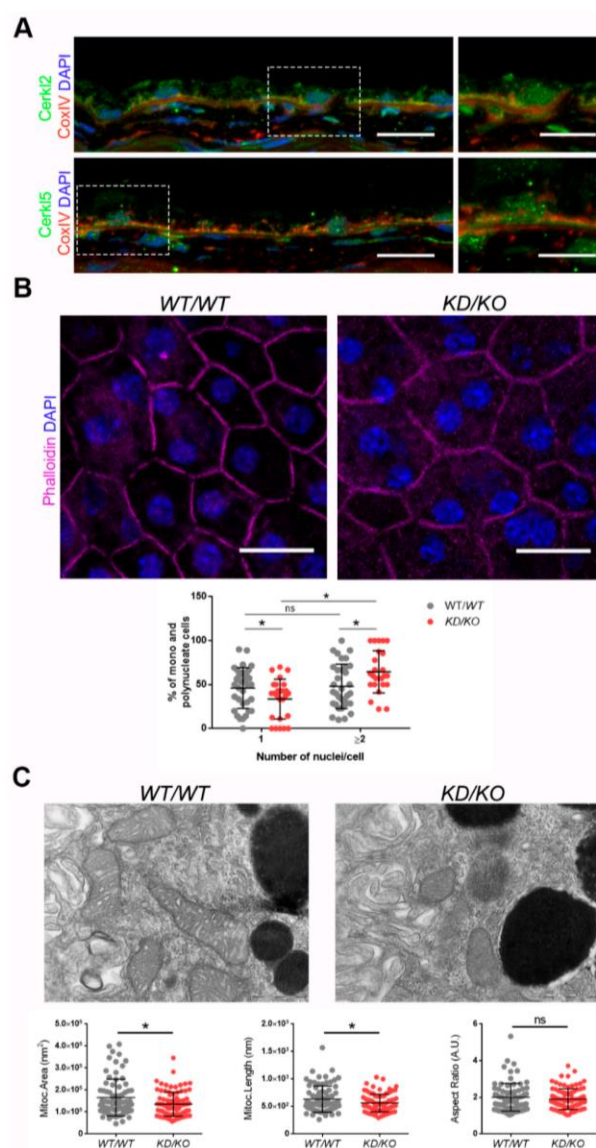
Figure 1. The Retinal Pigment Epithelium (RPE) of *KD/KO* mice shows morphological alterations. (**A**) CERKL is expressed in RPE as detected by immunofluorescence of retinal cryosections from *WT/WT* mice with COX-IV (red) and anti-CERKL2 or anti-CERKL5 (green) antibodies. Regions of interest (ROIs) represent higher magnification from left panels. Scale bar: 20 μm (lower magnification) or 10 μm (higher magnification). (**B**) The RPE from *KD/KO* mice shows an increased number of polynucleated cells. RPE flat mounts from *WT/WT* and *KD/KO* mice stained with phalloidin (for F-actin, magenta) and 4′,6-diamidino-2-phenylindole (DAPI, blue) and imaged by confocal microscopy were used to quantify the percentage of mono and polynucleated cells. Scale bar: 20 μm. (**C**) Mitochondrial fragmentation in *KD/KO* RPE. Transmission electron microscopy (TEM) microphotographies of retinal pigment cells from *WT/WT* and *KD/KO* (2-month-old mice) were used to quantify mitochondrial area, length, and aspect ratio. Scale bar: 500 nm. The data are expressed as the mean $\pm$ SD, *n* = 25–34 ROIs from 3 animals per group in (**B**) and *n* = 78–89 mitochondria from 3 animals per group in (**C**). Statistical analysis by Mann–Whitney test: * *p*-value $\leq$ 0.05.

Overall, our data indicated that the depletion of *Cerkl* expression alters cell structure and mitochondrial morphology in RPE cells in vivo.

3.2. CERKL-Silenced ARPE-19 Cells Show Alterations in Mitochondrial Network

Since depletion of *Cerkl* in *KD/KO* mouse model cause alterations in the mitochondrial network of RPE, we studied the deficiency of *CERKL* in vitro, taking advantage of ARPE-19 cells treated with small interference (si) RNAs against *CERKL*. To evaluate the effect of siRNAs on CERKL expression, we tested two different control siRNAs (scr1 and scr2) and two siRNAs against different regions of *CERKL* (si*CERKL*1 and si*CERKL*2) on ARPE-19 cells through immunofluorescence using an in-house antibody that recognizes most isoforms of the human CERKL protein (anti-CERKL). Phalloidin was used to delimit cell area (Figure 2A).

Quantification of CERKL fluorescence intensity revealed a significant decrease in CERKL expression in both si*CERKL*1 and si*CERKL*2-treated cells. The most significant difference in CERKL expression occurred between scr1 and si*CERKL*1 siRNAs and were thus selected for subsequent experiments (Figure 2A).

Due to genetic and environmental factors, the retina, including RPE, is constantly under stress conditions that may damage mitochondrial network organization if resilience mechanisms do not work properly [15]. To assess CERKL function in regulating the morphology of the mitochondrial network in retinal epithelium cells, we knocked down *CERKL* expression in human ARPE-19 cells using si*CERKL*1 under basal and oxidative stress conditions (100 µM sodium arsenite for 4 h) and studied mitochondrial morphology through the fluorescent mitochondrial tracker Mitotracker (Figure 2B). In accordance with previous studies, a pool of CERKL localizes at the mitochondria. Remarkably, CERKL total expression is significantly induced in ARPE-19 cells under oxidative stress conditions. Notably, this sodium arsenite-dependent boost expression of CERKL is completely impaired when *CERKL* is downregulated by si*CERKL*1 (Figure 2C).

Analyses of mitochondrial morphology revealed a significant decrease in mitochondrial major length, form factor, and aspect ratio in *CERKL*-silenced cells compared with control cells under stress conditions. In addition, these morphological parameters were significantly diminished in *CERKL*-silenced cells when comparing oxidative stress conditions with basal conditions (Figure 2D–F). Moreover, we found a significant increase in aspect ratio between control and *CERKL*-silenced cells both in basal conditions (Figure 2F). *CERKL*-silenced cells showed significantly decreased mitochondrial area in basal conditions compared with controls, and this decrease was more evident under stress conditions (Figure 2G).

To sum up, *CERKL* deficiency alters the mitochondrial network in ARPE-19 cells, particularly in response to oxidative stress conditions.

3.3. CERKLb and CERKLc Overexpression Restores Mitochondrial Network under Oxidative Stress in ARPE-19 Cells

CERKL overexpression has been described as protective against oxidative stress by interacting with antioxidant enzymes [8], regulating autophagy [9], and downregulating apoptosis [6], among others. In the human retina, due to different alternative splicing events, *CERKL* produces at least four different protein isoforms (CERKLa, CERKLb, CERKLc, and CERKLd) [6] that display different protein domains.

In order to test if different isoforms may differentially regulate mitochondrial dynamics, we overexpressed human CERKLb and CERKLc isoforms in ARPE-19 cells. The CERKLb isoform is the longest one (558 aa) and includes a human-specific additional exon (4b), whereas CERKLc is the shortest isoform (419 aa) and lacks the ATP-binding site and the diacylglycerol kinase (DAGK) domain. The two isoforms display a pleckstrin-homology domain (including a mRNA binding domain) and the nuclear localization and export signals. ARPE-19 cells transfected with either CERKLb or CERKLc isoforms were treated with 100 µM sodium arsenite for 4 h, and the morphology of their mitochondrial network was assessed by immunofluorescence using Mitotracker (Figure 3A). CERKLb lo-

calizes more diffusely within the cell, including the nucleus, whereas CERKLc is 10% more concentrated in mitochondria under basal and oxidative stress conditions (Figure 3A,B).
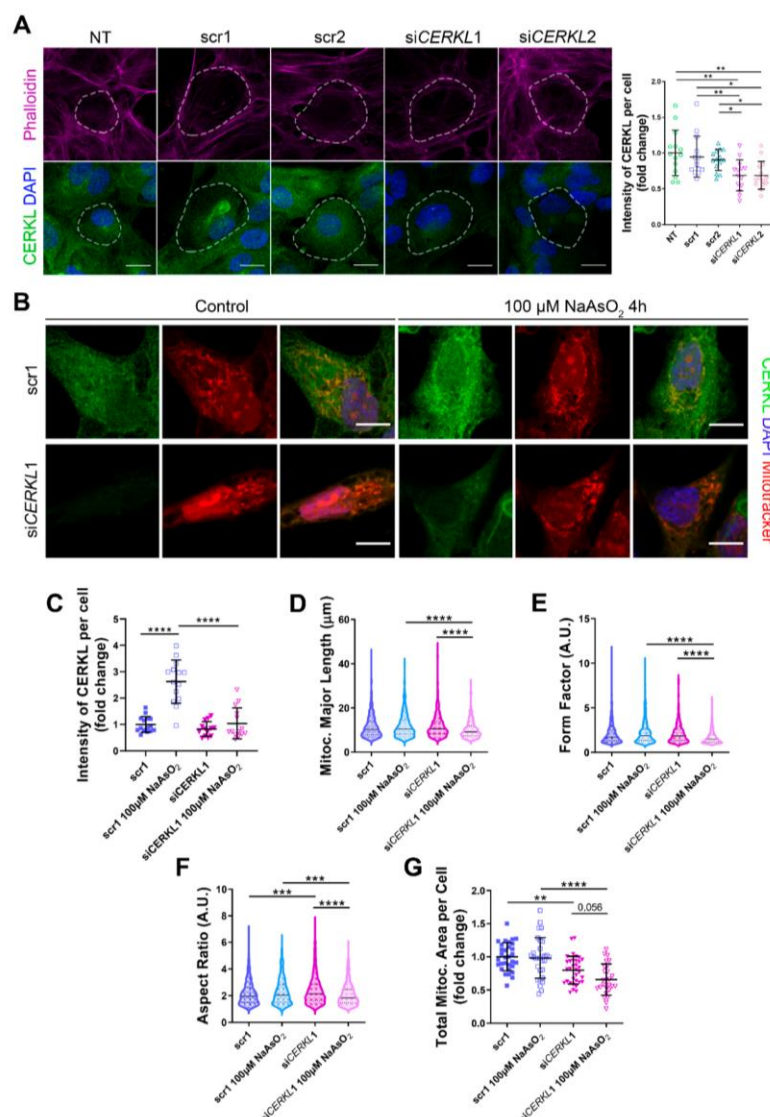
Figure 2. Mitochondrial morphology is altered in *CERKL*-silenced human ARPE-19 cells. (**A**) siRNAs against *CERKL* decrease *CERKL* expression in ARPE-19 cells. Immunofluorescence confocal images of non-transfected, negative control (scr1 and scr2) and *CERKL*-silenced (si*CERKL*1 and si*CERKL*2) differentiated ARPE-19 cells stained with phalloidin (magenta), CERKL (green), and DAPI (blue) were used to quantify CERKL fluorescence intensity per cell. Scale bar: 15 μm. (**B**) Mitochondrial fragmentation in *CERKL*-silenced cells under stress conditions. Immunofluorescence images from a single focal plane of negative control (scr1) and *CERKL*-silenced (si*CERKL*1) differentiated ARPE-19 cells in the control and under oxidative stress conditions were used to quantify CERKL fluorescence intensity (**C**), mitochondrial major length (**D**), form factor (**E**), aspect ratio (**F**), and mitochondrial area (**G**). Cells were stained with CERKL (green) and DAPI (blue), and mitochondria were marked with Mitotracker (red). Scale bar: 10 μm. Data are represented as the mean $\pm$ SD (**A,C,G**) and as violin plots (**D–F**), $n = 15$ cells per condition (**A,C**) and $n = 565$–997 mitochondria (**D–F**) from $n = 26$–33 cells (**G**) per condition. Statistical analysis by one-way ANOVA (**A,C,G**) and Kruskal–Wallis (**D–F**) tests: * p-value ≤ 0.05, ** p-value ≤ 0.01, *** p-value ≤ 0.001, **** p-value ≤ 0.0001.
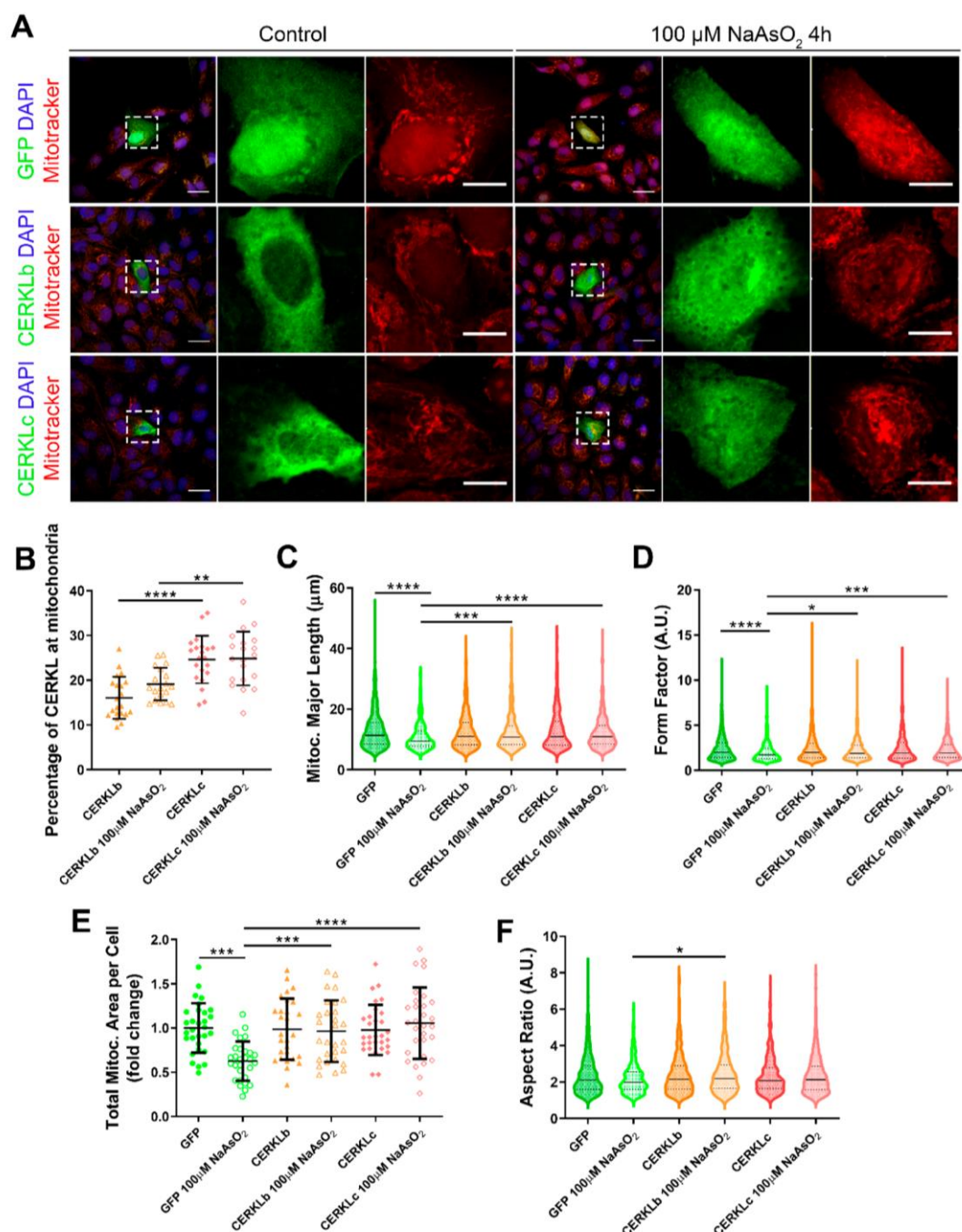
Figure 3. Mitochondrial morphology is restored in ARPE-19 cells under oxidative stress conditions when CERKL isoforms are overexpressed. (**A**) CERKL overexpression protects the mitochondrial network under oxidative stress conditions. Immunofluorescence images from a single focal plane of differentiated ARPE-19 cells transfected with pEGFP-N2, CERKLb-GFP, and CERKLc-GFP in the control and under oxidative stress conditions were used to quantify the percentage of CERKL at mitochondria (**B**), mitochondrial major length (**C**), form factor (**D**), mitochondrial area (**E**), and aspect ratio (**F**). Mitochondria were marked with Mitotracker (red), and nuclei were counterstained with DAPI (blue). Scale bars: 25 μm and 10 μm in higher magnification images. Data are represented as the mean $\pm$ SD (**B**,**F**) and as violin plots (**C**–**E**), n = 20–21 cells (**B**) and n = 404–726 mitochondria (**C**–**E**) from n = 28–30 cells (**F**) per condition. Statistical analysis by one-way ANOVA (**B**,**F**) and Kruskal–Wallis (**C**–**E**) tests: * p-value $\leq$ 0.05, ** p-value $\leq$ 0.01, *** p-value $\leq$ 0.001, and **** p-value $\leq$ 0.0001.

Morphological analyses showed a statistically significant decrease in mitochondrial major length, area, and form factor in GFP-transfected cells (controls) under oxidative stress compared with in the basal condition. However, mitochondria in cells transfected with both CERKLb and CERKLc did not show any significant change in these parameters between basal and oxidative stress conditions. In fact, the mitochondrial length, area, and form factor in CERKLb and CERKLc-transfected cells under stress conditions were not affected in contrast with the decrease in all these measurements in stressed control cells (Figure 3C–F).

Altogether, these results strongly indicated that both CERKLb and CERKLc localized at mitochondria and that CERKL overexpression in ARPE-19 cells protected mitochondrial network under oxidative stress conditions.

3.4. Mitochondrial Superoxide Production Is Reduced by CERKLb and CERKLc Overexpression in ARPE-19 Cells

Mitochondrial network disorganization is a typical sign of cellular damage and loss of mitochondrial homeostasis [22]. Under oxidative stress or pathogenic conditions, damaged mitochondria generate free radicals, such as mitochondrial superoxide, due to impaired antioxidant response [23]. Therefore, we measured mitochondrial oxidation using MitoSOX quantification in cells either overexpressing CERKLb and CERKLc or depleted in *CERKL* expression under both control and oxidative stress conditions (Figure 4A,B). A significant decrease in MitoSOX intensity was observed when overexpressing CERKLb and CERKLc in basal conditions, and this mitochondrial protection was maintained under oxidative stress (Figure 4C). On the other hand, neither control cells nor cells depleted in *CERKL* showed an increase in MitoSOX in any condition, thus pointing to other factors being necessary for mitochondrial superoxide production besides stress by sodium arsenite (Figure 4D).

In summary, these findings pointed to a protection of mitochondria as measured by mitochondrial superoxide production when CERKLb and CERKLc were overexpressed.

3.5. CERKL Knock-Down Alters Mitochondrial Respiration

Considering that (i) *CERKL* deficiency affects mitochondrial network organization in ARPE-19 cells, and (ii) oxygen consumption and other mitochondrial energy-related measurements in neural retinas of *KD/KO* mice are compromised, we performed Seahorse analysis to evaluate mitochondrial function and oxygen consumption rate (OCR) in *CERKL*-depleted ARPE-19 cells. We compared mitochondrial performance in control and stress conditions as well as under antioxidant pre-treatment (4 µM N-acetyl-L-cysteine (NAC) for 24 h).

Differentiated ARPE-19 cells displayed low oxygen consumption rates, which made changes between conditions very subtle. Under control conditions, OCR was reduced (black straight versus dotted lines) upon knock-down of *CERKL* expression (Figure 5A). In fact, all respiration-related parameters, including maximal respiration and non-mitochondrial oxygen consumption, showed a clear trend of diminishing in *CERKL*-deficient cells (Figure 5B–G). As expected, we found a decrease in the respiration parameters (basal and maximal respiration) after $NaAsO_2$ treatment in both scr1 and si*CERKL*1-transfected cells, conserving the tendency.

NAC pre-treatment results in an increase (two-fold) in mitochondrial and non-mitochondrial respiration in control cells, which allows them to resist oxidative stress conditions. However, *CERKL*-depleted cells are not able to respond to the antioxidant pre-treatment to these high levels and are thus not resilient to oxidative injury. Remarkably, mitochondrial respiration is decreased in *CERKL*-depleted cells, while non-mitochondrial oxygen consumption increases slightly in all conditions, probably as a cell compensatory mechanism.

Overall, these results denoted that *CERKL*-deficient ARPE-19 cells do not respond to antioxidant (NAC) protective pre-treatment and are thus not as resilient to oxidative stress as control cells.
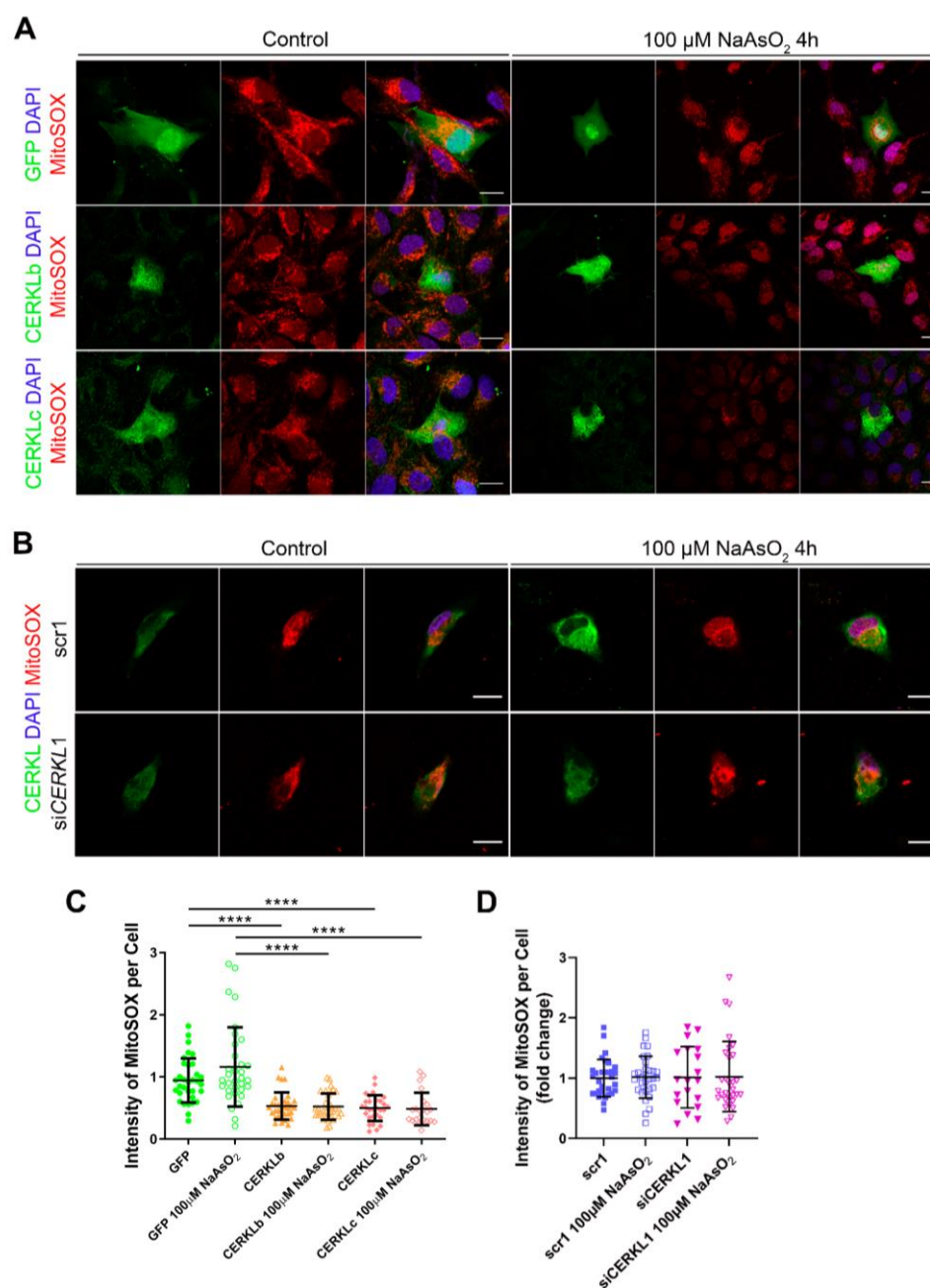
Figure 4. Quantification of MitoSOX in ARPE-19 cells overexpressing CERKLb and CERKLc or knocking down *CERKL*. (**A**) Overexpression of CERKLb and CERKLc reduces the production of mitochondrial superoxide. Immunofluorescence images from a single focal plane of differentiated ARPE-19 cells transfected with pEGFP-N2, CERKLb-GFP, and CERKLc-GFP under control and stress conditions were used to quantify MitoSOX fluorescence intensity (**C**). Mitochondrial superoxide was detected with MitoSOX (red), and nuclei were counterstained with DAPI (blue). Scale bar: 15 µm. (**B**) *CERKL* depletion is not sufficient to increase mitochondrial superoxide production under basal and stress conditions. Immunofluorescence images from a single focal plane of negative control (scr1) and *CERKL*-silenced (si*CERKL*1) differentiated ARPE-19 cells under basal and oxidative stress conditions were used to quantify MitoSOX fluorescence (**D**). Cells were stained with CERKL (green) and DAPI (blue), and mitochondrial superoxide was detected with MitoSOX (red). Scale bar: 15 µm. Data are represented as the mean ± SD, n = 28–33 cells per condition. Statistical analysis by Kruskal–Wallis test: *** p-value $\leq$ 0.001 and **** p-value $\leq$ 0.0001.
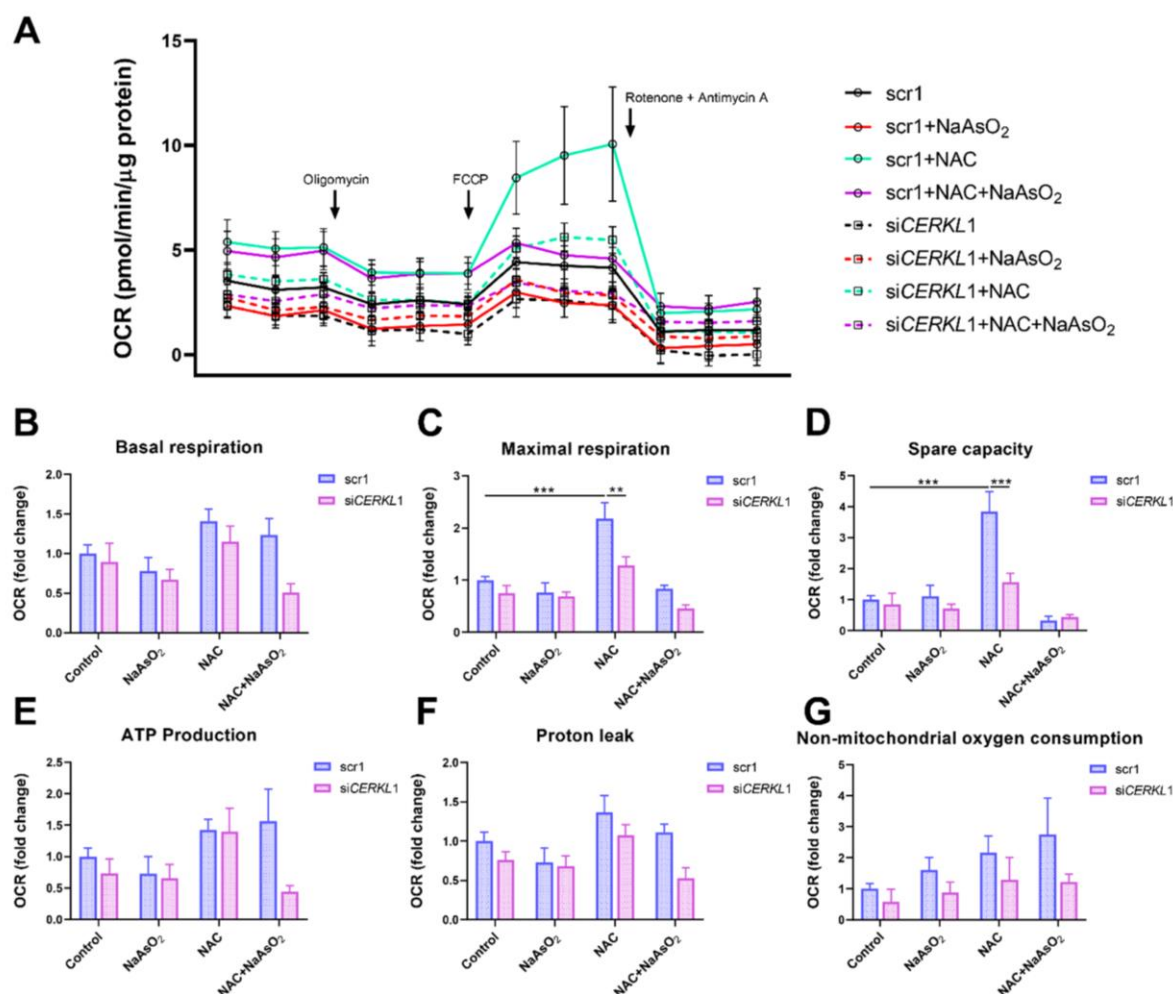
Figure 5. Oxygen consumption is impaired in *CERKL*-depleted ARPE-19 cells under different antioxidant (NAC pre-treatment) and oxidative stress (NaAsO$_2$ treatment) conditions. (**A**) Altered oxygen consumption rate (OCR) in *CERKL*-knocked-down cells in all conditions; straight lines indicate values from scrambled control cells, whereas dotted lines indicate si*CERKL* treated cells. (**B**) Basal respiration are the initial OCR levels without treatment. (**C**) Maximal respiration is obtained after the addition of FCCP (carbonyl cyanide-4-trifluoromethoxy phenyl-hydrazone). (**D**) Spare capacity is calculated by subtracting basal respiration from maximal respiration. Note that *CERKL*-depleted cells neither increase the respiratory capacity after antioxidant treatment nor maintain maximal respiration and spare capacity after oxidative injury. Oligomycin addition reveals (**E**) ATP production and (**F**) proton leak levels. (**G**) Non-mitochondrial oxygen consumption values are obtained after rotenone and antimycin A addition. Statistical test by two-way ANOVA: ** p-value ≤ 0.01, *** p-value ≤ 0.001.

4. Discussion

Mutations in many different genes cause retinal degeneration. Most of them affect specific photoreceptor functions (e.g., phototransduction), but mutations in genes expressed ubiquitously (e.g., splicing genes) or in the RPE (such as *RPE65*) can also alter photoreceptor homeostasis and lead to retinal cell death (reviewed in [24]). The correct function of RPE is crucial for photoreceptor survival, but how mutations in photoreceptor genes alter RPE is not well documented. However, dysfunctional proteins can have both an impact in photoreceptors and RPE, thus contributing to the retinal degeneration phenotype. In fact, patients carrying mutations in *CERKL* present early onset rod-cone dystrophy despite relatively preserved visual acuity and a very distinctive RPE phenotype, e.g., RPE

granularity and frank macular RPE atrophy [25]. A *cerkl* knock-out zebrafish model also shows defects in photoreceptor phagocytosis due to the dysfunction of RPE [26]. Although the precise function of CERKL is not yet fully determined, several reports associate CERKL with basic cell functions related to stress resilience, such as autophagy [9], stress granule production [11], and mitochondrial physiology and dynamics [10]. Within this context, we aimed to explore the alteration of RPE due to *CERKL* mutations both in vivo in a *Cerkl* mouse model and in vitro, using cultured cells to study the effect of *CERKL* overexpression and knock-down on the mitochondrial network organization.

This work showed that mitochondria in the RPE of the *Cerkl*$^{KD/KO}$ mouse (which expresses very low *CERKL* levels) show a significant decrease in length and area, in full agreement with previous results observed in photoreceptors and retinal ganglion cells [10], which reported an increase in mitochondrial fragmentation. To further dissect the contribution of CERKL to mitochondrial dynamics, particularly under oxidative stress conditions, we performed in vitro assays. The addition of sodium arsenite and other reagents to culture media is commonly used as a proxy for physiological oxidative stress conditions, as the cell effects can be easily quantified and compared with basal conditions [27], even though it might not elicit the full retinal cell response to injury.

Our results showed that the knock-down of endogenous *CERKL* levels in ARPE-19 cells reproduced the same results as observed in vivo, with cells displaying mitochondria with an altered shape and decreased length. This fragmentation effect was more apparent in cells under oxidative stress conditions, which presented around 20% less of mitochondrial area per cell in *CERKL*-depleted cells (Figure 2G). Although the mitochondrial network is altered, the production of superoxide radicals in mitochondria is not affected in any condition, thus indicating that at least in ARPE-19 cells, sodium arsenite does not induce superoxide production as an early response, irrespective of CERKL levels. Other reports claim that sodium arsenite is required but is not sufficient to induce the full cellular response to oxidative stress [28]. Notably, control cells under oxidative stress showed a 2.5-fold increase in endogenous CERKL protein expression but knocked-down cells were unable to induce this transcriptional response to injury. In this context, depletion of *CERKL* decreases the oxygen consumption rate, but this decrease is more prominent under oxidative stress conditions: in fact, *CERKL*-depleted cells are not responsive to antioxidants protective treatment, indicating that *CERKL* expression is associated with oxidative stress resilience and that this lack of *CERKL* hampers antioxidant-dependent response. These results are in agreement with the mitochondrial oxygen consumption impairment in the neural retinas of *Cerkl*$^{KD/KO}$ mice.

As mentioned, *CERKL* produces a high number of alternatively spliced transcripts that encode differential protein domains. To explore the potential protection against oxidative stress of the mitochondrial network due to *CERKL* expression, we analyzed the effects of overexpressing either the longest (558 aa) or the shortest protein isoform (419 aa) in ARPE-19 cells. When challenged by oxidative stress and in contrast with what happens in controls and in cells depleted in *CERKL*, cells overexpressing either isoform show healthy mitochondria in which the length and aspect are maintained, at least after 4 h of treatment. In fact, under stress, the total mitochondrial area per cell remains unaffected in cells transfected with CERKL constructs, whereas control cells show a reduction to half of the mitochondrial mass (Figure 3E).

These protective effects of CERKL overexpression upon mitochondrial physiology in the RPE were also supported by the analysis of damaging superoxide radicals in mitochondria, which was half that of controls in any condition. These results complement previous work on retinal neurons showing that the depletion of *CERKL* causes mitochondrial fragmentation and a substantial decrease in mitochondrial metabolism [10]. The resulting model based on our results is shown in Figure 6.
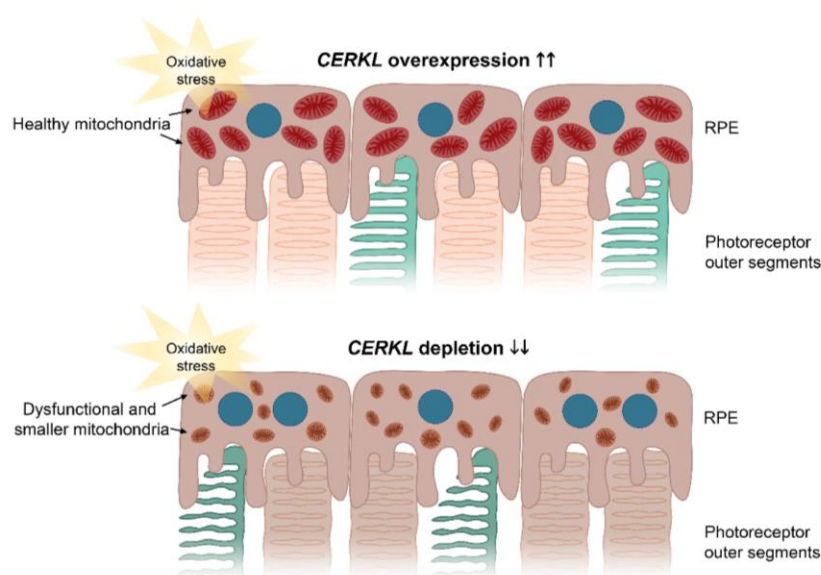
Figure 6. Image depicting the effects of *CERKL* overexpression and depletion in mitochondrial shape and size in RPE cells upon oxidative stress conditions. Under oxidative stress, *CERKL* overexpression (**upper panel**) protects RPE mitochondrial morphology, whereas depletion in *CERKL* (**lower panel**) causes mitochondrial fragmentation, respiratory alterations, and polynucleation in RPE. Dysfunction of RPE affects photoreceptor homeostasis and can lead to retinal degeneration. Blue—nuclei; brownish red—healthy mitochondria; brown—dysfunctional and smaller mitochondria.

Our results further reinforce the role of *CERKL* as a resilient gene, since oxidative stress treatment induces the expression of CERKL as a very early cell response: we observed a more than two-fold increase in endogenous CERKL 4 h after the addition of the arsenite reagent. On the other hand, the subcellular localization of the two CERKL isoforms is subtly different and changes depending on the perceived injury by oxidative stress. The shortest isoform (which does not display the DAGK domain) presents stronger mitochondrial localization than the longest isoform (25% versus 15% of the CERKL pool, respectively), with the latter localizing all over the cell, including the nucleus. Previous reports showed that the longer isoforms of CERKL increase the nuclear localization upon oxidative stress and formed part of stress granules [11]. We further complement these results by showing that the overexpression of CERKL protects mitochondria against oxidative injury.

5. Conclusions

Overall, our results suggest that one of the physiological roles of CERKL is to protect the mitochondrial network in retinal cells, both neurons and epithelium, against the injury of light/oxidative stress. In this context, some unusual and particular phenotypic traits of the RPE observed in the retinas of patients carrying *CERKL* mutations, may reflect the combination of photoreceptor and RPE alterations.

Finally, we propose that the high level of physiological interplay between photoreceptors and RPE cells warrants including RPE assessment in the clinical phenotype of RP and other retinal dystrophy patients. Mutations in many RP genes, such as *CERKL*, can potentially affect both tissues. By identifying RPE pathogenic events, particularly those related to oxidative stress, we could design specific drug- or cell-based therapies that target RPE to improve photoreceptor homeostasis and/or to halt photoreceptor neurodegeneration.

Institutional Review Board Statement: The study was approved by the Ethical Committee for Animal Experimentation (AEC) of the Generalitat of Catalonia (protocol C-449/18) in accordance with Spanish Royal Decree 53/2013 and the European Directive 2010/63/EU. It also received institutional approval from the Bioethics Committee and the Ethics Committee of Animal Research of the Universitat de Barcelona.

Informed Consent Statement: Not applicable.

Data Availability Statement: The data presented in this study are available in this article and supplementary material.

Conflicts of Interest: No competing interests are declared.

References

1. Ran, X.; Cai, W.; Huang, X.; Liu, Q.; Lu, F. Database tool 'RetinoGenetics': A comprehensive mutation database for genes related to inherited retinal degeneration. *Database* **2014**, *2014*, 1–6. [CrossRef]
2. Tuson, M.; Marfany, G.; Gonzàlez-Duarte, R. Mutation of CERKL, a Novel Human Ceramide Kinase Gene, Causes Autosomal Recessive Retinitis Pigmentosa (RP26). *Am. J. Hum. Genet.* **2004**, *74*, 128–138. [CrossRef]
3. Aleman, T.S.; Soumittra, N.; Cideciyan, A.V.; Sumaroka, A.M.; Ramprasad, V.L.; Herrera, W.; Windsor, E.A.M.; Schwartz, S.B.; Russell, R.C.; Roman, A.J.; et al. CERKL mutations cause an autosomal recessive cone-rod dystrophy with inner retinopathy. *Investig. Ophthalmol. Vis. Sci.* **2009**, *50*, 5944–5954. [CrossRef]
4. Garanto, A.; Riera, M.; Pomares, E.; Permanyer, J.; de Castro-Miró, M.; Sava, F.; Abril, J.F.; Marfany, G.; Gonzàlez-Duarte, R. High transcriptional complexity of the retinitis pigmentosa CERKL gene in human and mouse. *Investig. Ophthalmol. Vis. Sci.* **2011**, *52*, 5202–5214. [CrossRef]
5. Domènech, E.B.; Andres, R.; López-Iniesta, M.J.; Mirra, S.; García-Arroyo, R.; Milla, S.; Sava, F.; Andilla, J.; Alvarez, P.L.; De La Villa, P.; et al. A New Cerkl Mouse Model Generated by CRISPR-Cas9 Shows Progressive Retinal Degeneration and Altered Morphological and Electrophysiological Phenotype. *Investig. Ophthalmol. Vis. Sci.* **2020**, *61*, 14. [CrossRef]
6. Tuson, M.; Garanto, A.; Gonzàlez-Duarte, R.; Marfany, G. Overexpression of CERKL, a gene responsible for retinitis pigmentosa in humans, protects cells from apoptosis induced by oxidative stress. *Mol. Vis.* **2009**, *15*, 168–180.
7. Garanto, A.; Mandal, N.A.; Egido-Gabás, M.; Marfany, G.; Fabriàs, G.; Anderson, R.E.; Casas, J.; Gonzàlez-Duarte, R. Specific sphingolipid content decrease in Cerkl knockdown mouse retinas. *Exp. Eye Res.* **2013**, *110*, 96–106. [CrossRef]
8. Li, C.; Wang, L.; Zhang, J.; Huang, M.; Wong, F.; Liu, X.; Liu, F.; Cui, X.; Yang, G.; Chen, J.; et al. CERKL interacts with mitochondrial TRX2 and protects retinal cells from oxidative stress-induced apoptosis. *Biochim. Biophys. Acta Mol. Basis Dis.* **2014**, *1842*, 1121–1129. [CrossRef]
9. Hu, X.; Lu, Z.; Yu, S.; Reilly, J.; Liu, F.; Jia, D.; Qin, Y.; Han, S.; Liu, X.; Qu, Z.; et al. CERKL regulates autophagy via the NAD-dependent deacetylase SIRT1. *Autophagy* **2019**, *15*, 453–465. [CrossRef]
10. Mirra, S.; García-Arroyo, R.; Domènech, E.B.; Gavaldà-Navarro, A.; Herrera-Úbeda, C.; Oliva, C.; Garcia-Fernàndez, J.; Artuch, R.; Villarroya, F.; Marfany, G. CERKL, a retinal dystrophy gene, regulates mitochondrial function and dynamics in the mammalian retina. *Neurobiol. Dis.* **2021**, *156*, 105405. [CrossRef]
11. Fathinajafabadi, A.; Pérez-Jiménez, E.; Riera, M.; Knecht, E.; Gonzàlez-Duarte, R. CERKL, a retinal disease gene, encodes an mRNA-binding protein that localizes in compact and untranslated mRNPs associated with microtubules. *PLoS ONE* **2014**, *9*, e87898. [CrossRef]
12. Gallenga, C.E.; Lonardi, M.; Pacetti, S.; Violanti, S.S.; Tassinari, P.; Di Virgilio, F.; Tognon, M.; Perri, P. Molecular mechanisms related to oxidative stress in retinitis pigmentosa. *Antioxidants* **2021**, *10*, 848. [CrossRef] [PubMed]
13. Sparrow, J.R.; Hicks, D.; Hamel, C.P. The retinal pigment epithelium in health and disease. *Curr. Mol. Med.* **2010**, *10*, 802–823. [CrossRef]

14. Nissanka, N.; Moraes, C.T. Mitochondrial DNA damage and reactive oxygen species in neurodegenerative disease. *FEBS Lett.* **2018**, *592*, 728–742. [CrossRef]
15. Mirra, S.; Marfany, G. Mitochondrial Gymnastics in Retinal Cells: A Resilience Mechanism Against Oxidative Stress and Neurodegeneration. *Adv. Exp. Med. Biol.* **2019**, *1185*, 513–517. [PubMed]
16. Cid-Castro, C.; Hernández-Espinosa, D.R.; Morán, J. ROS as Regulators of Mitochondrial Dynamics in Neurons. *Cell. Mol. Neurobiol.* **2018**, *38*, 995–1007. [CrossRef]
17. Domènech, E.B.; Marfany, G. The relevance of oxidative stress in the pathogenesis and therapy of retinal dystrophies. *Antioxidants* **2020**, *9*, 347. [CrossRef]
18. Claybon, A.; Bishop, A.J.R. Dissection of a mouse eye for a whole mount of the retinal pigment epithelium. *J. Vis. Exp.* **2011**, *48*, 2563. [CrossRef]
19. Mullins, R.F.; Khanna, A.; Schoo, D.P.; Tucker, B.A.; Sohn, E.H.; Drack, A.V.; Stone, E.M. Is age-related macular degeneration a microvascular disease? *Adv. Exp. Med. Biol.* **2014**, *801*, 283–289. [CrossRef]
20. Ozaki, E.; Campbell, M.; Kiang, A.-S.; Humphries, M.; Doyle, S.L.; Humphries, P. Inflammation in age-related macular degeneration. *Adv. Exp. Med. Biol.* **2014**, *801*, 229–235. [CrossRef]
21. Chen, M.; Rajapakse, D.; Fraczek, M.; Luo, C.; Forrester, J.V.; Xu, H. Retinal pigment epithelial cell multinucleation in the aging eye—A mechanism to repair damage and maintain homoeostasis. *Aging Cell* **2016**, *15*, 436–445. [CrossRef] [PubMed]
22. Wai, T.; Langer, T. Mitochondrial Dynamics and Metabolic Regulation. *Trends Endocrinol. Metab.* **2016**, *27*, 105–117. [CrossRef]
23. Campochiaro, P.A.; Mir, T.A. Progress in Retinal and Eye Research The mechanism of cone cell death in Retinitis Pigmentosa. *Prog. Retin. Eye Res.* **2018**, *62*, 24–37. [CrossRef]
24. Dhurandhar, D.; Sahoo, N.K.; Mariappan, I.; Narayanan, R. Gene therapy in retinal diseases: A review. *Indian J. Ophthalmol.* **2021**, *69*, 2257–2265. [CrossRef]
25. Khan, A.O.; Abu-Safieh, L. Rod-Cone Dystrophy with Initially Preserved Visual Acuity Despite Early Macular Involvement Suggests Recessive CERKL Mutations. *Ophthalmic Genet.* **2015**, *36*, 369–372. [CrossRef]
26. Yu, S.; Li, C.; Biswas, L.; Hu, X.; Liu, F.; Reilly, J.; Liu, X.; Liu, Y.; Huang, Y.; Lu, Z.; et al. CERKL gene knockout disturbs photoreceptor outer segment phagocytosis and causes rod-cone dystrophy in zebrafish. *Hum. Mol. Genet.* **2017**, *26*, 2335–2345. [CrossRef]
27. Lyu, Q.; Ludwig, I.S.; Kooten, P.J.S.; Sijts, A.J.A.M.; Rutten, V.P.M.G.; van Eden, W.; Broere, F. Leucinostatin acts as a co-inducer for heat shock protein 70 in cultured canine retinal pigment epithelial cells. *Cell Stress Chaperones* **2020**, *25*, 235–243. [CrossRef]
28. Guidarelli, A.; Cerioni, L.; Fiorani, M.; Catalani, A.; Cantoni, O. Arsenite-Induced Mitochondrial Superoxide Formation: Time and Concentration Requirements for the Effects of the Metalloid on the Endoplasmic Reticulum and Mitochondrias. *J. Pharmacol. Exp. Ter.* **2020**, *373*, 62–71. [CrossRef]
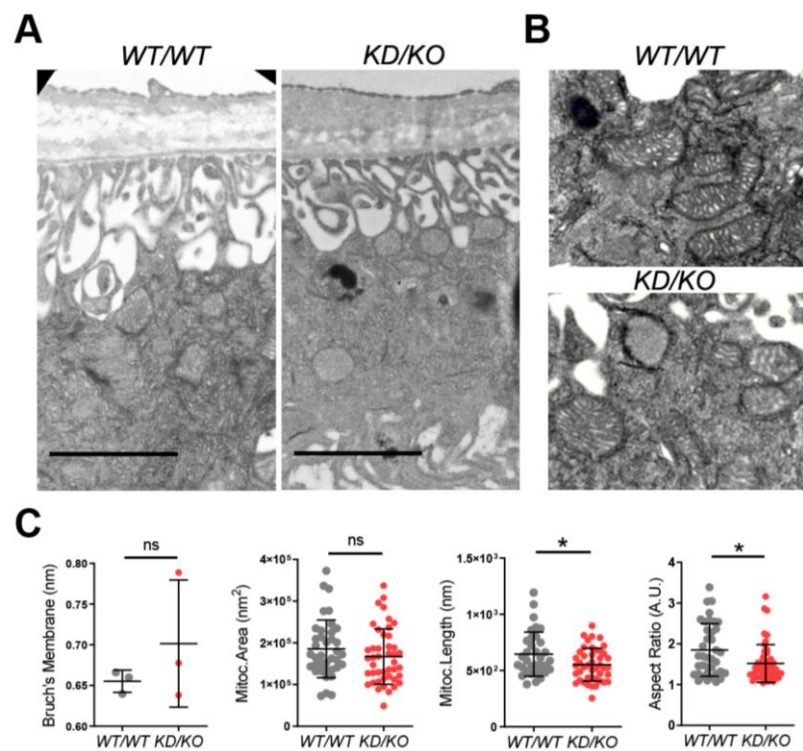
Figure S1. Mitochondrial fragmentation in RPE from 18-month-old *KD/KO* albino mice. (**A-B**) TEM microphotographies of retinal pigmented cells from *WT/WT* and *KD/KO* of old mice (18 months) were used to quantify different aspects of mitochondria. (**C**) Graphics of Bruch's membrane width, and mitochondrial area, length, and aspect ratio. Scale bar: 500 nm. The data are expressed as the mean ±SD, n=38-44 mitochondria from 3 animals per group. Statistical analysis by Mann-Whitney test: *p-value ≤ 0,05.

2.2. *Cerkl*^{KD/KO} retinas exhibit exacerbated response to light-induced stress

Publication 4

Title

Exacerbated response to oxidative stress in the Retinitis Pigmentosa *Cerkl*[KD/KO] mouse model triggers retinal degeneration pathways upon acute light stress

Authors

Rocío García-Arroyo, Elena B. Domènech, Carlos Herrera-Úbeda, Miguel A. Asensi, Cristina Núñez de Arenas, José M. Cuezva, Jordi Garcia-Fernàndez, Federico V. Pallardó, Serena Mirra and Gemma Marfany

Reference

Abstract

The retina is particularly vulnerable to genetic and environmental alterations that generate oxidative stress and cause cellular damage in photoreceptors and other retinal neurons, eventually leading to cell death. *CERKL* (*CERamide Kinase-Like*) mutations cause Retinitis Pigmentosa and Cone-Rod Dystrophy in humans, two disorders characterized by photoreceptor degeneration and progressive vision loss. *CERKL* is a resilience gene against oxidative stress, and its overexpression protects cells from oxidative stress-induced apoptosis. Besides, CERKL contributes to stress granule-formation and regulates mitochondrial dynamics in the retina. Using the

Cerkl[KD/KO] albino mouse model, which recapitulates the human disease, we aimed to study the impact of *Cerkl* knockdown on stress response and activation of photoreceptor death mechanisms upon light/oxidative stress. After acute light injury, we assessed immediate or late retinal stress response, by combining both omic and non-omic approaches. Our results show that *Cerkl* knockdown increases ROS levels and causes a basal exacerbated stress state in the retina, through alterations in glutathione metabolism and stress granule production, overall compromising an adequate response to additional oxidative damage. As a consequence, several cell death mechanisms are triggered in *Cerkl*[KD/KO] retinas after acute light stress. Our studies indicate that *Cerkl* gene is a pivotal player in regulating light-challenged retinal homeostasis and shed light on how mutations in *CERKL* lead to blindness by dysregulation of the basal oxidative stress response in the retina.

Personal contribution to this work

This article belongs to the main core of my Thesis. My personal contribution to this publication has been: a) animal handling, breeding and light-stress procedure development; b) analysis and clustering of genes from RNA-Seq results (Figures 1A, 2A, 6A, Supplementary Figure 1, Supplementary Tables 1 and 2); c) validation of RNA-Seq results at protein and metabolic level (Figures 1B, 1C, 2B, 2C, 3H, 3I, 4A, 4B and Supplementary Figure 2); d) preparation of samples for metabolomic analyses (Figures 2D, 2E, 3, Supplementary Figures 3 and 4); e) assessment of retinal stress, inflammation and cell death mechanisms (Figures 5, 6 and Supplementary Figure 6); f) design and creation of the figures; g) the discussion of the results (Figure 7); and h) draft writing and critical reading of the manuscript.

Exacerbated response to oxidative stress in the Retinitis Pigmentosa *Cerkl*$^{KD/KO}$ mouse model triggers retinal degeneration pathways upon acute light stress

Rocío García-Arroyo [a,b,c], Elena B. Domènech [a,b,c], Carlos Herrera-Úbeda [a,b], Miguel A. Asensi [c,d], Cristina Núñez de Arenas [c,e,f], José M. Cuezva [c,e,f], Jordi Garcia-Fernàndez [a,b], Federico V. Pallardó [c,d], Serena Mirra [a,b,c,**], Gemma Marfany [a,b,c,*]

[a] *Department of Genetics, Microbiology and Statistics, Universitat de Barcelona, Barcelona, Spain*
[b] *Institut de Biomedicina de la Universitat de Barcelona – Institut de Recerca Sant Joan de Déu (IBUB-IRSJD), Barcelona, Spain*
[c] *Centro de Investigación Biomédica En Red (CIBER) de Enfermedades Raras (CIBERER), ISCIII, Madrid, Spain*
[d] *Department of Physiology, University of Valencia-INCLIVA, Valencia, Spain*
[e] *Departament of Molecular Biology, Centro de Biología Molecular Severo Ochoa, Consejo Superior de Investigaciones Científicas-Universidad Autónoma de Madrid (CSIC-UAM), Madrid, Spain*
[f] *Instituto de Investigación Hospital 12 de Octubre, Madrid, Spain*

A B S T R A C T

The retina is particularly vulnerable to genetic and environmental alterations that generate oxidative stress and cause cellular damage in photoreceptors and other retinal neurons, eventually leading to cell death. *CERKL* (*CERamide Kinase-Like*) mutations cause Retinitis Pigmentosa and Cone-Rod Dystrophy in humans, two disorders characterized by photoreceptor degeneration and progressive vision loss. *CERKL* is a resilience gene against oxidative stress, and its overexpression protects cells from oxidative stress-induced apoptosis. Besides, CERKL contributes to stress granule-formation and regulates mitochondrial dynamics in the retina. Using the *Cerkl*$^{KD/KO}$ albino mouse model, which recapitulates the human disease, we aimed to study the impact of *Cerkl* knockdown on stress response and activation of photoreceptor death mechanisms upon light/oxidative stress. After acute light injury, we assessed immediate or late retinal stress response, by combining both omic and non-omic approaches. Our results show that *Cerkl* knockdown increases ROS levels and causes a basal exacerbated stress state in the retina, through alterations in glutathione metabolism and stress granule production, overall compromising an adequate response to additional oxidative damage. As a consequence, several cell death mechanisms are triggered in *Cerkl*$^{KD/KO}$ retinas after acute light stress. Our studies indicate that *Cerkl* gene is a pivotal player in regulating light-challenged retinal homeostasis and shed light on how mutations in *CERKL* lead to blindness by dysregulation of the basal oxidative stress response in the retina.

1. Introduction

The retina is daily exposed to bright light, which coupled with its own highly active and energy-demanding metabolism, ultimately generating oxidative damage, and facilitate the formation of reactive oxygen species (ROS). The accumulation of ROS alters the composition and structure of retinal nucleic acids, proteins, and lipids, eventually compromising the homeostasis and health of photoreceptors and other retinal neurons [1]. Thus, the retina requires accurate stress resilience

mechanisms and compensating antioxidant responses to ensure cell survival and physiological homeostasis [2].

In the retina, the resident microglia as well as the macroglia, play a pivotal role in counteracting stress stimuli by orchestrating defensive actions, tissue repair and immunoregulation. Their activation is characterized by proliferation and morphological changes, in a process called gliosis [3,4]. At the intracellular level, the endoplasmic reticulum and mitochondria are key hubs involved in sensing oxidative stress [5]. In addition, there are different specific protective mechanisms against

---

stress, such as the regulation of glutathione metabolism balance [6] and the formation of mRNA stress-granules and P-bodies, two structures that protect non-translated mRNAs after damaging stimuli [7,8]. Dysregulation, impairment or chronic activation of the antioxidant mechanisms in the retina is at the basis of many retinal neurodegenerative disorders.

Mutations in *CERKL* cause two related but distinct inherited retinal dystrophies: Retinitis Pigmentosa and Cone-Rod Dystrophy, both of them causing irreversible attrition of photoreceptor cells, which eventually results in total blindness [9–12]. Previous studies have postulated *CERKL* as a resilience gene against oxidative stress in the retina by participating in autophagy [13–15], apoptosis inhibition [16,17], mitochondrial dynamics and function regulation [15,18,19], and stress granules formation [20]. On the latter, CERKL has been shown to interact with different proteins that compose mRNA stress-granules and P-bodies [20]. Importantly, *CERKL* downregulation affects mitochondrial homeostasis and impairs mitochondrial response against oxidative stress, while *CERKL* overexpression protects cells from acute oxidative stress [18]. Nevertheless, the specific pathogenesis mechanisms of *CERKL* mutations have not been fully determined yet.

To thoroughly understand the molecular role and mechanisms in which CERKL is involved, and since the human retina of patients cannot be biochemically studied nor challenged, we studied a knockdown/knockout *Cerkl* mouse model (*Cerkl^{KD/KO}* or *KD/KO*). This model exhibits a remaining expression of 18% of some *Cerkl* isoforms, as those expressed from the proximal promoter are completely ablated [21]. Patients carry many different combinations of *CERKL* mutations, many as compound heterozygotes, with one allele producing a truncated or no protein at all (mRNA containing premature STOP codons are degraded by nonsense mediated decay) and other alleles that alter some but not all CERKL protein isoforms. In this context, our compound heterozygote mouse *KD/KO* model is genetically very similar to the mutations identified in human patients, and more relevant to our work, the slow progression of the retinal degeneration in our *KD/KO* retinas mimics that shown in human patients carrying *CERKL* mutations, being the final outcome retinal neurodegeneration and vision loss [21].

Light stress treatment has been largely employed to induce oxidative stress and thus promote retinal neurodegeneration to study the molecular mechanisms evoking this process in retinal dystrophies [22,23]. Taking advantage of the *KD/KO* mouse model, the main goal of this work has been the characterization of the response to acute light-induced stress upon *Cerkl* downregulation by exposing *KD/KO* albino mice to light stress and evaluating different parameters through RNA sequencing (RNA-Seq), protein and metabolites analyses as an early response to stress injury, as well as retinal morphology and remodelling two weeks after light stress damage. Our data revealed that *KD/KO* retinas show exacerbated oxidative stress response in basal conditions and thus, could not respond properly to light stress due to the impairment of different antioxidant mechanisms, such as glutathione balance and PABP mRNA-stress granules formation. Subsequently, several cell death pathways were triggered in *KD/KO* retinas resulting in neurodegeneration and retinal remodelling. Our results offer a highly detailed characterization of the basal REDOX status and oxidative/light stress response in the *Cerkl^{KD/KO}* mouse model, with the final aim to identify altered actionable antioxidant pathways as key targets for potential therapeutic intervention.

2. Materials and methods

2.1. Animal handling

WT/WT and *KD/KO* albino mice (B6(Cg)-Tyrc-2J/J) were bred and housed in the animal research facilities at the University of Barcelona. Animals were provided with food and water ad libitum and maintained in a temperature-controlled environment in a 12/12 h light–dark cycle. All animal handling and assays were performed according to the ARVO statement for the use of animals in ophthalmic and vision research, as well as the regulations of the Ethical Committee for Animal Experimentation (AEC) of the Generalitat de Catalunya (protocol C-449/18 (animal handling) and protocol C-220/18 (light stress assays)), according to the European Directive 2010/63/EU and other relevant national guidelines. Each cohort (genotype and condition) had equivalent proportion of male and female mice, as autosomal recessive retinitis pigmentosa affects similarly both biological sexes.

2.2. Genomic DNA and genotyping by PCR

DNA for genotyping was extracted from ear punches. Primers for genotyping and PCR conditions were described in Ref. [21].

2.3. Light-stress treatment

Light stress experiments were performed on albino adult mice (4–6-months-old), where retinas are more sensitive to light injury due to the absence of pigmenti in the retinal pigment epithelium (RPE). Animals were anesthetized using a mixture of Ketamine (100 ng/kg)/Xylacine (10 ng/kg). One eye was covered to avoid the light insult (control) and the other was treated with a drop of 10 mg/mL cyclopentolate to dilate the pupil prior 3000-lux white light exposition for 1 h. At the end of the treatment, mice were immediately sacrificed to obtain the retinal tissue for the stress-early response study. On the other hand, for the stress-late response study, both eyes of the same mouse were subjected to light stress (3000 lux for 1 h). Two weeks after treatment, mice were sacrificed to obtain the retinal tissue.

2.4. Primary ganglion cell culture

Coverslips were freshly coated with 60 μL of poly-ornithine (Sigma Aldrich, Saint Louis, Missouri, USA), air dried and subsequently washed with MilliQ water. A drop of 10 μg/mL Laminin (Roche, Saint Louis, Missouri, USA) in complete neurobasal medium (Neurobasal™-A medium, Thermo Fisher Scientific, Waltham, MA, USA) supplemented with 0.06% D-Glucose, 0.0045% NaHCO_3, 1 mM L-Glutamine and 1% Penicillin/Streptomycin was added on pre-treated coverslips and incubated overnight at 37 °C. After three washes with complete neurobasal medium, coverslips were used for primary RGCs culture. E16 mouse retinas (3 animals per genotype) were dissociated using the Neural Tissue Dissociation Kit (Miltenyi Biotec, Bergisch, Gladbach, Germany) following the manufacturer's instructions with minor modifications. In brief, after Enzyme mix 2 incubation, 2 vol of complete neurobasal medium were added for gentle dissociation with the pipette. Cells were pelleted by 5 min centrifugation at 0.3 rcf and resuspended in complete neurobasal medium. Approximately 100000 cells/well were seeded onto coated coverslips in a 24 well/plate. Neuronal supplements and factors were added: 1 × B27 (Invitrogen, Carlsbad, California, USA), 5 μM Forskolin (Sigma Aldrich, Saint Louis, Missouri, USA), 50 ng/mL Human BDNF (Peprotech, Rock Hill, NJ, USA), 20 ng/mL Rat CNTF (Peprotech, Rock Hill, NJ, USA). RGCs at 7 DIV were subjected to oxidative stress by treatment with 0.5 mM sodium arsenite for 45 min. Afterwards, cells were fixed with 4% PFA for 20 min, washed 3 times with 1 × PBS and cryoprotected (30% Glycerol, 25% Ethyleneglycol and 0.1 M PBS) for further experiments.

2.5. Immunofluorescence, confocal microscopy, and colocalization analysis

In immunocytochemistry experiments, cells were blocked using 2% sheep serum and 0,3% Triton-X-100 (St. Louis, MO, USA) in 1 × PBS during 1 h at RT. Subsequently, cells were incubated with primary antibodies overnight at 4 °C in blocking solution. Primary antibodies used were the following: CERKL2 (1:200, in house, [21]), CERKL5 (1:100, in house, [21]), PABP-488 (1:50, sc-166381 AF488, Santa Cruz Biotechnology, Dallas, TX, USA). After three washes with 1 × PBS, cells were

incubated with the secondary antibody Alexa Fluor 568 anti-Rabbit IgG (1:400, A-11011, Thermo Fisher Scientific) in blocking solution during 1 h at RT. Nuclei were stained using DAPI (1:1000, 10236276001, Roche Diagnostics, Indianapolis, IN, USA) and after rinsing with $1 \times$ PBS (3×5 min), samples were mounted using Mowiol 4–88 (Merck, Darmstadt, Germany).

For immunohistochemistry (IHC) of retinas, adult albino mice eyes were fixed overnight at 4 °C with 4% PFA, incubated with 30% sucrose overnight and embedded in OCT (ANAME, Quijorna, Madrid, Spain). Cryosections (12 μm) were collected and kept frozen at −80 °C until used. For IHC, cryosections were air-dried for 10 min, rehydrated with $1 \times$ PBS, permeabilized using 0.5% Triton X-100 for 15 min and blocked in blocking solution ($1 \times$ PBS containing 10% Normal Goat Serum and 0,3% Triton X-100) for 1 h at RT. Primary antibody incubation was performed overnight at 4 °C in blocking solution. After three rinses with $1 \times$ PBS (10 min each) cryosections were incubated for 1 h at RT with the corresponding secondary antibodies conjugated to a fluorophore. Finally, the slides were washed with $1 \times$ PBS (3×10 min) and cover-slipped with Mowiol 4–88 (Merck, Darmstadt, Germany). Primary antibodies and dilutions used were: RPE65 (1:500, sc-390787, SantaCruz Biotechnology), PABP (1:200, ab21060, Abcam), mouse anti-GFAP (1:300, MAB360, Millipore), Cone Arrestin (AB15282, Millipore), Phospho S358 MLKL (1:100, ab187091, Abcam), Bassoon (1:300, GTX13249, GeneTex), Cryaa (1:200, ab5595, Abcam), Crybb2 (1:200, sc-376006, SantaCruz Biotechnology). Secondary antibodies and dilutions used were the following: Alexa Fluor 488 anti-Rabbit IgG (1:400, A-11070, Thermo Fisher Scientific), Alexa Fluor 568 anti-Mouse IgG (1:400, A-11004, Thermo Fisher Scientific), DAPI (1:1000, Roche Diagnostics, Indianapolis, IN, USA).

Images were obtained in high-resolution microscopy (THUNDER Imager Live Cell & 3D Cell Culture & 3D Assay, Leica Microsystems, Wetzlar, Germany) and confocal microscopy (Zeiss LSM 880, Thornwood, NY, USA). Image analyses were performed using ImageJ (FIJI) software (National Institutes of Health, Bethesda, MD, USA). In this study, image intensity is considered proportional to the concentration of protein so, in order to provide a relative quantitative comparison, all the images were normalized to the same dynamic range. For analysis of total concentration of protein, the threshold value was adjusted to select the whole area of interest (e.g., the RPE) with signal, then the integrated density values were corrected using the CTCF formula (CTCF =Integrated Density – (Area of selected cell X Mean fluorescence of background readings)). Regarding the granules analysis, the threshold value was set to show only the brighter spots coming from the stress granules to further analyze the individual particles.

2.6. RNA isolation from mouse retinas and RNA-Seq

Three retinas per genotype and condition were homogenized using a Polytron PT1200E homogenizer (Kinematica, AG, Lucerne, Switzerland). Total RNA was isolated using the RNeasy mini kit (Qiagen, Germantown, MD), following the manufacturer's instructions with minor modifications (treatment with DNAse I during 1 h). Total RNA was quantified by Qubit® RNA BR Assay kit (Thermo Fisher Scientific) and the RNA integrity was estimated by using RNA 6000 Nano Bioanalyzer 2100 Assay (Agilent).

RNA-Seq libraries were prepared with KAPA Stranded mRNA-Seq Illumina® Platforms Kit (Roche) following the manufacturer's recommendations. Briefly, 100–300 ng of total RNA were used for poly-A fraction enrichment with oligo-dT magnetic beads, following mRNA fragmentation by divalent metal cations at high temperature. Strand specificity was achieved during the second strand synthesis performed in the presence of dUTP instead of dTTP. Blunt-ended double stranded cDNA was 3′adenylated and Illumina platform compatible adaptors with unique dual indexes and unique molecular identifiers (Integrated DNA Technologies) were ligated. The ligation product was enriched with 15 PCR cycles and the final library was validated on an Agilent 2100

Bioanalyzer with the DNA 7500 assay. The libraries were sequenced on HiSeq 4000 (Illumina) with a read length of 2x76bp+8bp+8bp using HiSeq 4000 SBS kit (Illumina) and HiSeq 4000 PE Cluster kit (Illumina), following the manufacturer's protocol for dual indexing. Image analysis, base calling and quality scoring of the run were processed using the manufacturer's software Real Time Analysis (RTA 2.7.7). RNA-Seq libraries and sequencing initial analysis were performed in the CNAG (Centro Nacional de Análisis Genómico, Barcelona). Differential expression analysis and heatmaps from RNA-Seq data were performed as in Ref. [15]. Gene Ontology (GO) Biological Process enrichment analysis was performed using Enrichr web server (https://maayanlab.cloud/Enrichr/) [24–26]. Gene pathway and functional clustering analyses were performed using GeneAnalytics™ (geneanalytics.genecards.org) and iDEP1.1 software [27]. The complete list of the RNA-Seq analysed genes is in the RNA-Seq Supplementary Data.

2.7. Western blotting

Adult retinas were lysed in RIPA buffer [50 mM Tris, pH 7.4, 150 mM NaCl, 1 mM EDTA, 1% NP-40, 0.25% Na-deoxycholate, protease inhibitors (Complete; Mini Protease Inhibitor Cocktail Tablets; Roche)] containing phosphatase inhibitors. Proteins were analysed by SDS-PAGE and transferred onto nitrocellulose membranes, which were blocked with 5% non-fat dry milk in $1 \times$ PBS containing 0.1%Tween 20 and incubated overnight at 4 °C with primary antibodies. After incubation with horseradish peroxidase-labeled secondary antibodies for 1 h at room temperature, immunodetection was developed using the ECL system (Lumi-Light Western Blotting Substrate, Roche). Images were acquired by ImageQuant™ LAS 4000 mini Image Analyzer (Fuji-film) and quantified using ImageJ software. α-TUBULIN or GAPDH loading controls were used to normalize protein values. The primary antibodies were the following: GSR (1:1000, 18257-1-AP, Proteintech), GPX4 (1:1000, 52455, Cell Signaling Technology), Caspase-7 p11 (1:1000, PA5-90312, Thermo Fisher Scientific), FTH1 (1:1000, 4393, Cell Signaling Technology), KEAP1 (1:1000, 8047, Cell Signaling Technology), TUBULIN (1:1000, T5168, Sigma), GAPDH (1:1000, ab8245, Abcam). The secondary antibodies were: HRP-labeled anti-mouse (1:2000, A5906, Sigma) and anti-rabbit (1:2000, NA934-100UL, GE Healthcare).

2.8. Retinal explants and ROS-Glo H_2O_2 assay

Eyes were enucleated from adult mice and dissected in $1 \times$ PBS containing 1% penicillin/streptomycin. Retinas were obtained after an incision in the pupil, cutting through the ora serrata and pulling from the posterior part of the eye. Then, 3 patches per retina were collected and cultured for 24 h in cell culture inserts (PICM03050, Millipore, Darmstadt, Germany) floating inside 6-multiwell plates containing retinal explant complete medium (Neurobasal™-A medium (Thermo Fisher Scientific, Waltham, Massachusetts, USA) supplemented with 0.06% D-Glucose, 0.0045% NaHCO₃, 1 mM L-Glutamine, 1% Penicillin/Streptomycin and $1 \times$ B27 (Invitrogen, Carlsbad, CA, USA)). A total of 8 patches from 4 retinas per genotype were treated with 0.5 mM sodium arsenite for 24 h to perform oxidative stress treatment. Afterwards, all patches were distributed onto a 96-multiwell white plate (Greiner, Vienna, Austria) and ROS-Glo H_2O_2 Assay (Promega, Madison, WI, USA) was performed following the manufacturer's instructions.

2.9. Glutathione metabolism determination

Five retinas per genotype and condition were analysed. Reduced glutathione (GSH), oxidized glutathione (GSSG), homocysteine and γ-glutamyl cysteine levels were determined as follows: each retina was homogenized in 100 μL of PBS-N-Ethylmaleimide (NEM) buffer (5 mM). To induce protein precipitation, perchloric acid was added at 4% final concentration, and samples were centrifuged at 10,000 rpm, 15 min at
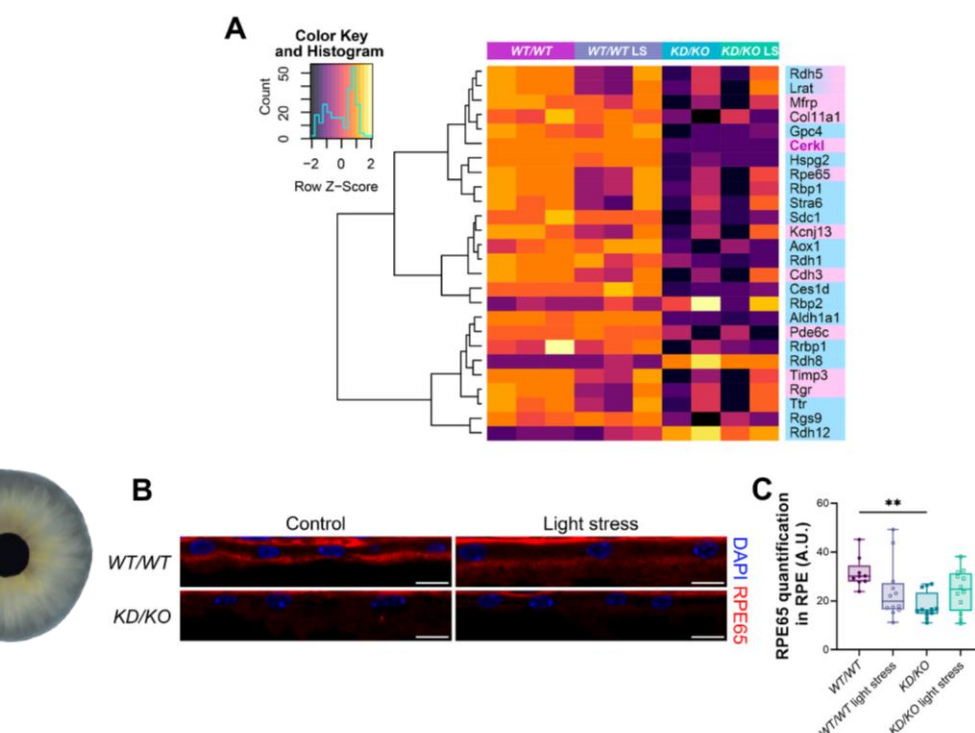
Fig. 1. Genes associated to inherited retinal dystrophies (IRDs) and phototransduction/visual cycle showed differential expression in *KD/KO* compared to *WT/WT* retinas (A) Heatmap with hierarchical clustering of differentially expressed genes associated with IRD genes (in pink) and phototransduction/visual cycle genes (in blue) in both control and light-stress (LS) conditions. (B) *RPE65* transcript and protein levels are significantly decreased in *KD/KO* retinal pigment epithelium (RPE) cells. Representative confocal images of RPE65 immunodetection (red) and nuclei staining (DAPI, in blue) from *WT/WT* and *KD/KO* RPE in control and under light-stress conditions (scale bar: 10 μm). Quantification of RPE65 signal intensity shown in (C), solely in the area of interest, reveals a significant decrease in *KD/KO* compared to *WT/WT* RPE. n = 12 ROIs from 4 animals per genotype and condition ** *p-value* ≤ 0.01. (For interpretation of the references to colour in this figure legend, the reader is referred to the Web version of this article.)

4 °C. Supernatants were transferred to a new tube for analysis and pellets were resuspended in 100 μL of NaOH (1 M) to obtain the total protein content using the BCA Protein Assay Kit (ThermoScientific, MA, USA). Then, metabolites of the transulfuration pathway were analysed by UPLC-MS/MS as described in Ref. [28]. Data were normalized by grams of total protein content.

2.10. Reverse phase protein in-house microarrays (RPPM)

Five retinas per genotype and condition were collected from adult albino *WT/WT* and *KD/KO* mice into liquid nitrogen right after light-induced stress treatment and subsequently lysed in 90 μL of Tissue Protein Extraction Reagent (T-PER, 78501, ThermoFisher Scientific) containing a cocktail of protease (Roche) and phosphatase (Sigma) inhibitors. Following protein extraction, samples were centrifuged at 15,000 g for 30 min at 4 °C. The RPPM technique was used for quantification of steady-state protein levels in the biopsies as recently described in detail [29–31]. Only monospecific antibodies recognizing the expected protein in cellular lysates were included in RPPM studies. Protein extracts from mouse retinas were diluted in PBS to a final protein concentration of 0.5 μg/μL before printing. Serially diluted protein extracts (0–1.5 μg/μL) derived from C2C12 mouse myoblast cells were prepared to assess printing quality and the linear response of protein recognition by the antibodies used [29]. Standard curves of BSA (0–2 μg/μl) and mouse IgGs (1–30 ng/μl) were also prepared as internal negative and positive controls, respectively. Approximately, 1.5 nL of each sample was spotted in triplicate onto nitrocellulose-coated glass slides (ONCYTE® SuperNOVA 8 pad—Grace Bio-Labs, 705118, Oregon, USA) using a iTWO-300P pico system printer (M2-Automation, Inc., Idaho, USA) equipped with a Piezo Driven Micro-Dispenser (PDMD) 30–150 pL at constant chamber humidity (RH 52%) and temperature (16 °C), and plate temperature (10 °C). After printing, arrays were allowed to dry and further blocked in Super G Blocking Buffer (10501, Grace Biolabs, Madrid, Spain). After, the arrays were incubated overnight at 4 °C with the indicated dilutions of the primary antibodies. After incubation, the arrays were washed with PBS-T and further incubated

with goat anti-mouse or goat anti-rabbit highly cross-adsorbed antibodies conjugated with CF™ 647 (1:500, SAB4600183–SAB4600185, Sigma Aldrich, Madrid, Spain). Pads incubated directly with secondary antibodies and with 0.0001% Fast Green FCF (F7252, Sigma Aldrich, Madrid, Spain) were used to evaluate potential unspecific binding to non-masked mouse IgGs and the total protein amount present in the spotted samples, respectively. Microarrays were scanned using Typhoon 9410 scanner (GE Healthcare, Inc. Madrid, Spain). The mean fluorescent intensity of the spots was measured using GenePix® Pro 7 (USA) and normalized relative to the protein amount contained in the sample obtained from the FCF stained pad. After quantification, the relative fluorescent intensity was converted into arbitrary units of expressed protein/ng of protein in the extract using as standard the linear plot of the C2C12 cell line [29,30].

2.11. Statistical analyses

Statistical analyses were performed using 1-way and 2-way ANOVA tests performing multiple comparison analysis. When data did not follow a normal distribution, Kruskal-Wallis test was used to determine statistical significance. ROUT test was used to determine statistical outliers (Q = 0.5%). Calculations were performed with GraphPad Prism statistical software, version 9. N is shown at each Figure legend. Statistical significance was set with a value of $p \leq 0.05$, (*$p \leq 0.05$, **$p \leq 0.01$, ***$p \leq 0.005$, ****$p \leq 0.001$). Data were expressed as min to max boxplots showing all points.

3. Results

3.1. RNA-Seq analysis revealed differentially expressed genes associated with retinal dystrophies and phototransduction/visual cycle in KD/KO retinas

Preceding research has associated CERKL protein to stress resilience and mitochondrial dynamics regulation, but its contribution to specific oxidative stress pathways still needs further investigation. In this study,
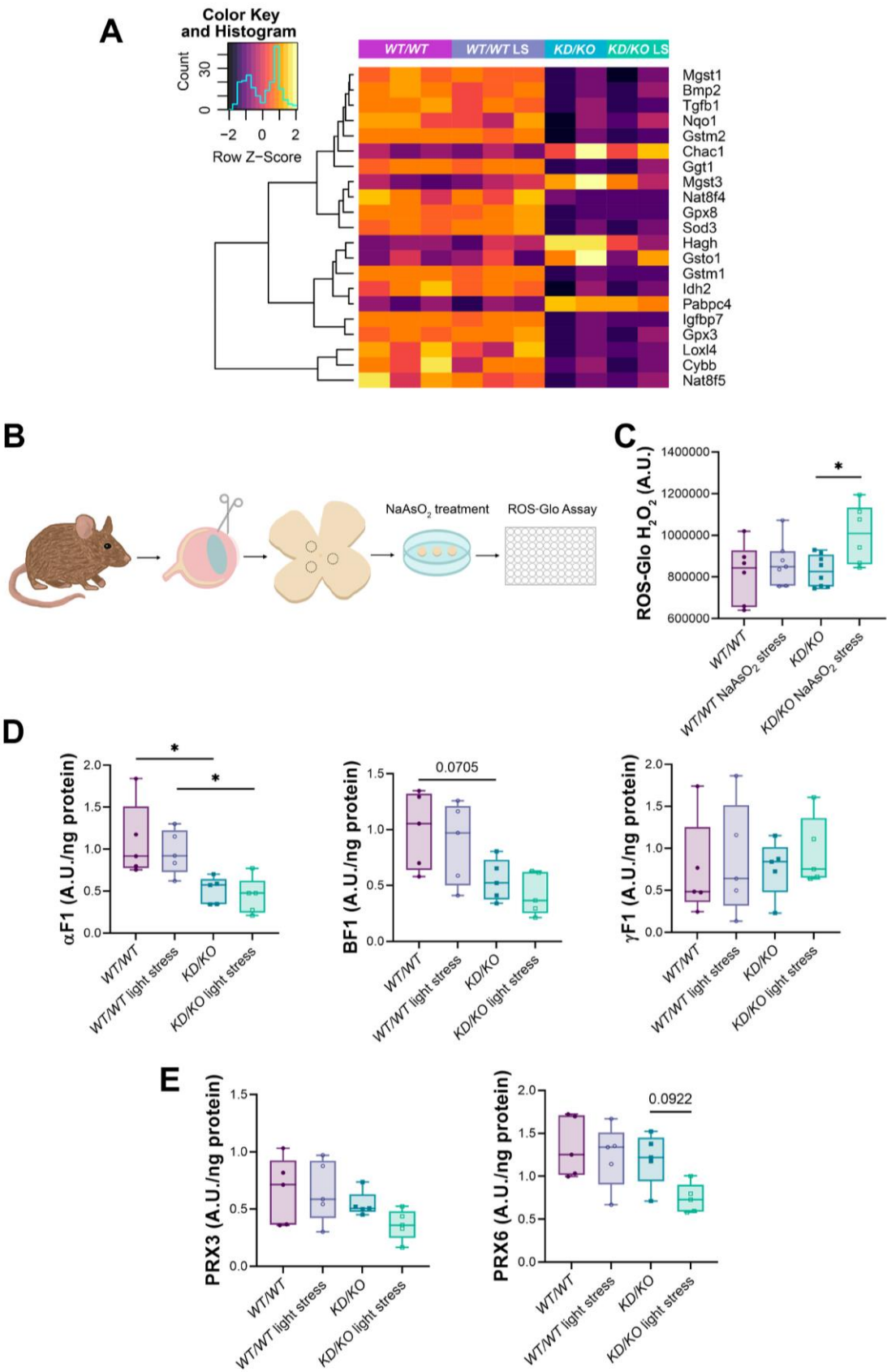
(caption on next page)

Fig. 2. Mitochondrial metabolism and antioxidant mechanisms are diminished in *KD/KO* retinas. (A) Heatmap with hierarchical clustering of differentially expressed genes associated with antioxidant responses. (B) Schematic representation of the assay including retinal patches obtention, sodium arsenite treatment and ROS-Glo H_2O_2 Assay. (C) Measurement of H_2O_2 levels by ROS-Glo H_2O_2 Assay reveals a significant increase in *KD/KO* retinal explants upon oxidative stress treatment. n = 6–8 retinal patches from 4 retinas per genotype and condition. (D) Alterations in the levels of different ATP synthase subunits in *KD/KO* retinas. Quantification of αF1, βF1 and γF1 proteins using reverse phase protein microarrays (RPPM). n = 5 animals per genotype and condition. (E) *KD/KO* retinas display a tendency to lower protein levels of PRX3 and PRX6 by means of microarray quantification. n = 5 animals per genotype and condition. * *p-value* ≤ 0.05. (Complementary data in Supplementary Fig. 3).

we aimed to determine CERKL role in the retina in response to acute light-stress insult. Retinas from *WT/WT* and *KD/KO* albino mice were exposed to 3000-lux white light for 1 h and assessed immediately after by RNA sequencing (RNA-Seq) analysis to explore their transcriptomic landscape in response to the light-stress treatment, as a first undirected

wide approach. We identified a large set of differentially expressed (DE) genes between the assessed samples. A threshold of $\log_2$ Fold Change ±0.5 was set to distinguish between up- and downregulated genes between genotypes and conditions (Supplementary Figure 1). Notably, the more outstanding differences were found between genotypes rather than
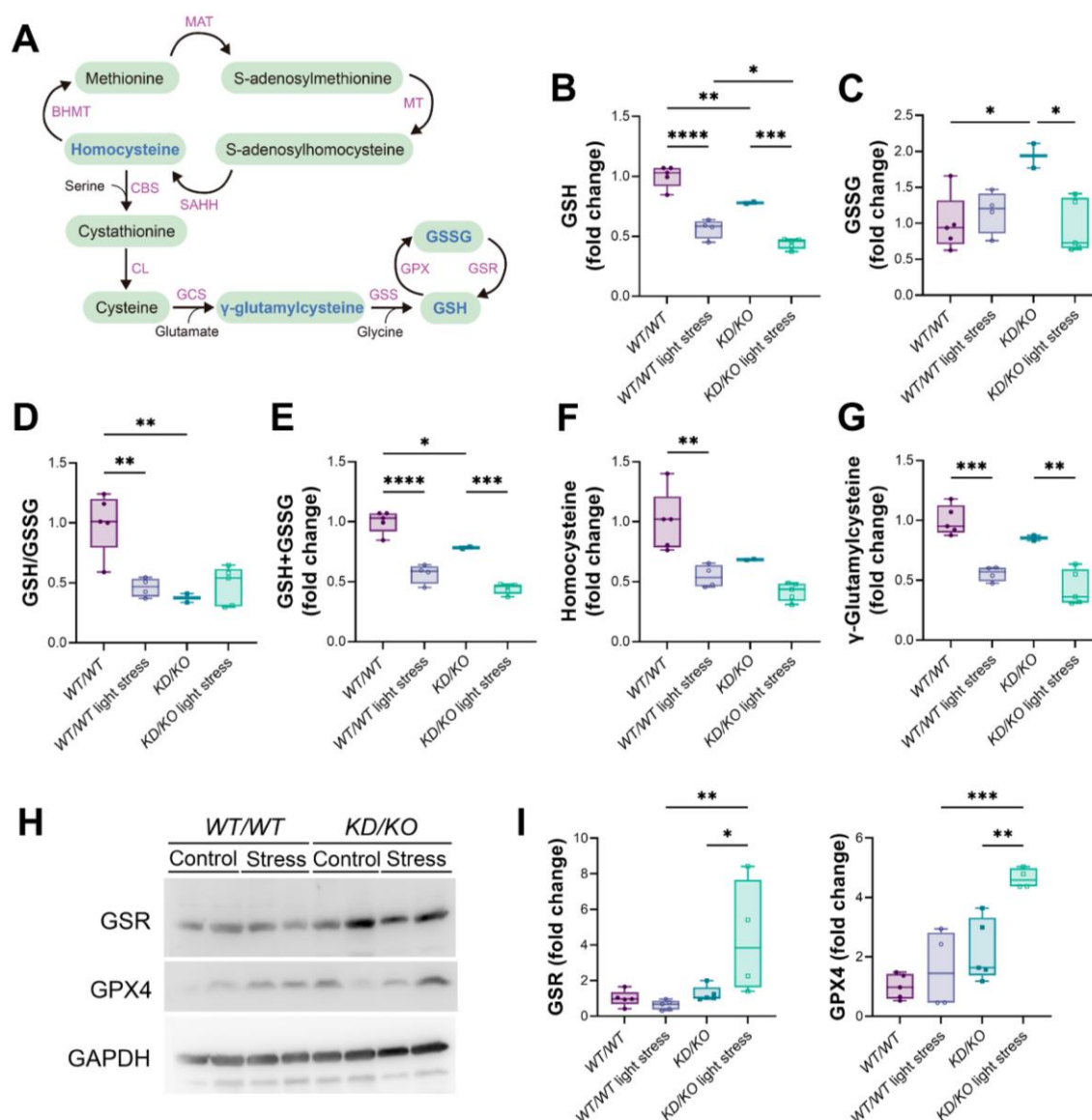
Fig. 3. Glutathione metabolism alteration in *KD/KO* retinas. (A) Schematic representation of glutathione metabolism and synthesis pathway (enzymes in purple). Metabolites altered in *KD/KO* retinas are highlighted in blue. (B–I) Glutathione metabolism and synthesis pathways are impaired in *KD/KO* retinas. (B-E) Quantification of the reduced (GSH) and oxidized (GSSG) forms of glutathione, as well as the GSH/GSSG ratio and total quantity of glutathione (GSH + GSSG) in *WT/WT* and *KD/KO* retinas in both control and light-stress conditions. (F, G) Measurement of homocysteine and γ-glutamylcysteine, precursors for the synthesis of glutathione, in *WT/WT* and *KD/KO* retinas in both control and light-stress treatment. n = 2–5 animals per genotype and condition. (H, I) GSR and GPX4 protein levels are significantly augmented in *KD/KO* retinas upon light-stress insult. (H) Representative Western-blot of GSR, GPX4 and GAPDH (as loading control) on retinal homogenates from *WT/WT* and *KD/KO* retinas in both control and light-stress conditions. (I) Quantification of GSR and GPX4 protein levels normalized with GAPDH levels. n = 4–5 animals per genotype and condition. * *p-value* ≤ 0.05, ** *p-value* ≤ 0.01, *** *p-value* ≤ 0.005, **** *p-value* ≤ 0.001. (Complementary data in Supplementary Fig. 4). (For interpretation of the references to colour in this figure legend, the reader is referred to the Web version of this article.)

between control/light-stress conditions. Besides, when analysing per genotypes, the number of downregulated genes in *KD/KO* retinas was approximately 5-fold higher than that of upregulated genes. Focusing on the upregulated genes in *KD/KO* in basal conditions, we observed a slight decrease in the levels of some genes when these retinas were subjected to light-stress insult (Supplementary Figure 1, upper panel).

Taking advantage of the "omic" data obtained by RNA-Seq, we identified many dysregulated cellular pathways. Notably, approximately 50% of all the upregulated Gene Ontology (GO) Biological Processes (32/75) in the *KD/KO* versus *WT/WT* retinas are directly related to stress response and pro-inflammatory pathways (Supplementary Table 1). In contrast, more than 60% of the downregulated GO Biological Processes (51/75) relate to organ development and differentiation pathways, including ocular development, visual cycle and sensory perception (Supplementary Table 2). Taken together, these data confirm that *KD/KO* retinas show both alteration of stress responses and dysregulation of homeostasis mechanisms.

We then concentrated on the different clusters of genes specifically involved in maintaining retinal function. One of these DE gene clusters was particularly interesting because the genes were related to inherited retinal dystrophies, IRDs (e.g., *Rpe65*, *Timp3*, *Mfrp*) (Fig. 1A, in pink) and/or implicated in the phototransduction/visual cycle process (e.g., *Lrat*, *Rdh12*, *Hspg2*, *Rdh1*, *Rgs9*) (Fig. 1A, in blue). As expected, in the retinal disorder-related gene cluster, *Cerkl* stands out by its highly decreased expression in *KD/KO* retinas (Fig. 1A, highlighted in purple). Of note, light stress did not increase the expression of *Cerkl* in the wild-type retinas, indicating that it is very stable transcriptionally and its involvement in stress might be post-translationally regulated, as suggested in Ref. [18].

Interestingly, most of these ocular-associated genes were downregulated in *KD/KO* retinas in both control and light stress conditions. We further validated our RNA results at the protein level by analysing the levels of RPE65 (a wellknown IRD gene) in the retinal pigment epithelium (RPE) of *WT/WT* and *KD/KO* retinal slices (Fig. 1B), and other proteins encoded by DE genes, such as CRYAA and CRYBB2, which encode crystallin proteins (Supplementary Figure 2). In agreement with the RNA-Seq data, the quantification of the fluorescent signal of RPE65 –as well as those of the tested CRY– were diminished in *KD/KO* RPE (Fig. 1C). In summary, our results unveil a clear pattern of DE genes between *WT/WT* and *KD/KO* retinas, most of them being downexpressed in *KD/KO* mice. The low expression level of relevant photoreceptor and RPE genes confirms the retinal dysfunction in the *KD/KO* retinas.

3.2. Antioxidant responses, mitochondrial function and glutathione metabolism are impaired in KD/KO retinas

As CERKL is involved in the oxidative stress response, we evaluated whether different antioxidant response pathways were altered in the *KD/KO* retinas. The RNA-Seq cluster analysis identified a group of DE genes related to different oxidative defence mechanisms (Fig. 2A). Antioxidant genes, such as *Sod3*, showed a decreased expression in *KD/KO* retinas, which could generate an increase in ROS, particularly after oxidative challenge. We thus assessed the antioxidant state of *KD/KO* retinas by performing retinal explants and exposing them to 500 μM sodium arsenite (NaAsO$_2$) to induce oxidative stress. H$_2$O$_2$ levels were subsequently evaluated through the ROS-Glo H$_2$O$_2$ Assay (procedure represented in Fig. 2B), yielding significantly increased levels of H$_2$O$_2$ in *KD/KO* retinas as a consequence of oxidative stress treatment (Fig. 2C).

Maintaining retinal ROS balance requires a refined equilibrium between the endogenous –due to the high metabolic rate of the retina– and exogenous –mainly light and pollution– stress factors and the enzymatic/non-enzymatic mechanisms involved in the antioxidant defence. Photoreceptor energy-demanding metabolism is principally sustained by oxidative phosphorylation (OXPHOS). In fact, mitochondria are one of the principal hubs in sensing stress and initiating

antioxidant response inside cells [32]. Previous work determined that many genes encoding proteins involved in mitochondrial dynamics and metabolism were altered in *KD/KO* retinas [15], but a complete metabolic analysis was not performed. Using reverse phase protein microarrays (RPPM), we assessed the levels of more than 40 proteins involved in different metabolic pathways in *KD/KO* versus *WT/WT* retinas after light-stress insult (Supplementary Figure 3). Focusing on OXPHOS proteins, we detected a decrease in the levels of the ATP synthase subunits alpha (αF1) and beta (BF1) levels in *KD/KO* retinas, particularly after light-stress insult, whereas no differences in the levels of subunit gamma (γF1) were detected (Fig. 2D). All these alterations confirmed mitochondrial dysfunction in *KD/KO* retinas. Peroxiredoxins (PRXs) are a family of antioxidant enzymes composed of six isoforms (PRX1-6) that are expressed in the retina distributed among the different layers, cell types and organelles. For instance, PRX3 localizes to mitochondria and PRX6 is expressed in astrocytes and Müller cells [33]. Quantification of PRX3 and PRX6 protein levels through RPPM showed a trend to decrease in *KD/KO* retinas upon light-induced stress (Fig. 2E).

Remarkably, most of the DE genes included in this RNA-Seq cluster of antioxidant defence (Fig. 2A) were related to glutathione (GSH) metabolism, such as *Chac1* and *Gsto1* (upregulated in *KD/KO* versus *WT/WT*), and *Gpx3*, *Gpx8*, and *Ggt1* (downregulated in *KD/KO* versus *WT/WT*). The GSH-centered antioxidant system is one of the principal oxidative defence mechanisms of the retina by contributing to the maintenance and regulation of redox homeostasis (GSH synthesis is indicated in Fig. 3A). A decrease in GSH levels, as well as an imbalance in the ratio between the reduced (GSH) and oxidized (GSSG) forms, is associated to several retinal disorders, such as Retinitis Pigmentosa and age-related macular degeneration [6]. Taking this into consideration, we determined the levels of GSH and GSSG along with glutathione precursors levels. Our results showed a significant decrease of GSH levels as well as a significant increase in the levels of GSSG in *KD/KO* retinas compared to *WT/WT*, resulting in decreased GSH/GSSG ratio and a diminished amount of glutathione (GSH + GSSG) (Fig. 3B–E). Regarding the response to light-induced stress, GSH levels were significantly decreased in both *WT/WT* and *KD/KO* retinas, while levels of GSSG remained similar in *WT/WT* after stress (Fig. 3B–C). Therefore, GSH/GSSG ratio was significantly decreased in light-stressed *WT/WT* retinas, whereas it was not different in *KD/KO* after light stress, probably because it was already reduced in control conditions (Fig. 3D). In contrast, the total amount of glutathione (GSH + GSSG) was significantly decreased in both *WT/WT* and *KD/KO* retinas as a consequence of light-induced stress (Fig. 3E). Besides, in response to stress the levels of some GSH precursors: homocysteine and γ-glutamylcysteine levels decrease in both *WT/WT* and *KD/KO*, retinas (Fig. 3F–G). No significant differences between experimental conditions were found in the rest of the precursors (Supplementary Figure 3).

GSH/GSSG redox cycle was further studied by quantifying the levels of GSR and GPX4, enzymes directly involved in the reduction and oxidation of glutathione, through Western-blot analysis of *WT/WT* and *KD/KO* retinal lysates after light-induced stress. These results revealed *KD/KO* retinas displayed significantly higher levels of both GSR and GPX4 in response to light stress (Fig. 3H–J).

To summarize, our findings unveil the impairment of different antioxidant responses in *KD/KO* retinas. In particular, ROS detoxification, glutathione synthesis and redox cycle are already altered in *KD/KO* in basal conditions, and further oxidative challenge increases this imbalance.

3.3. KD/KO retinas and RGCs display an exacerbated PABP-mediated response

One of the few stress-related genes that showed increased expression in *KD/KO* retinas is *Pabpc4* (Fig. 2A). PABP is a main component of stress granules, membraneless organelles that are rapidly formed upon cellular stress to recruit untranslated mRNAs together with other proteins and

7
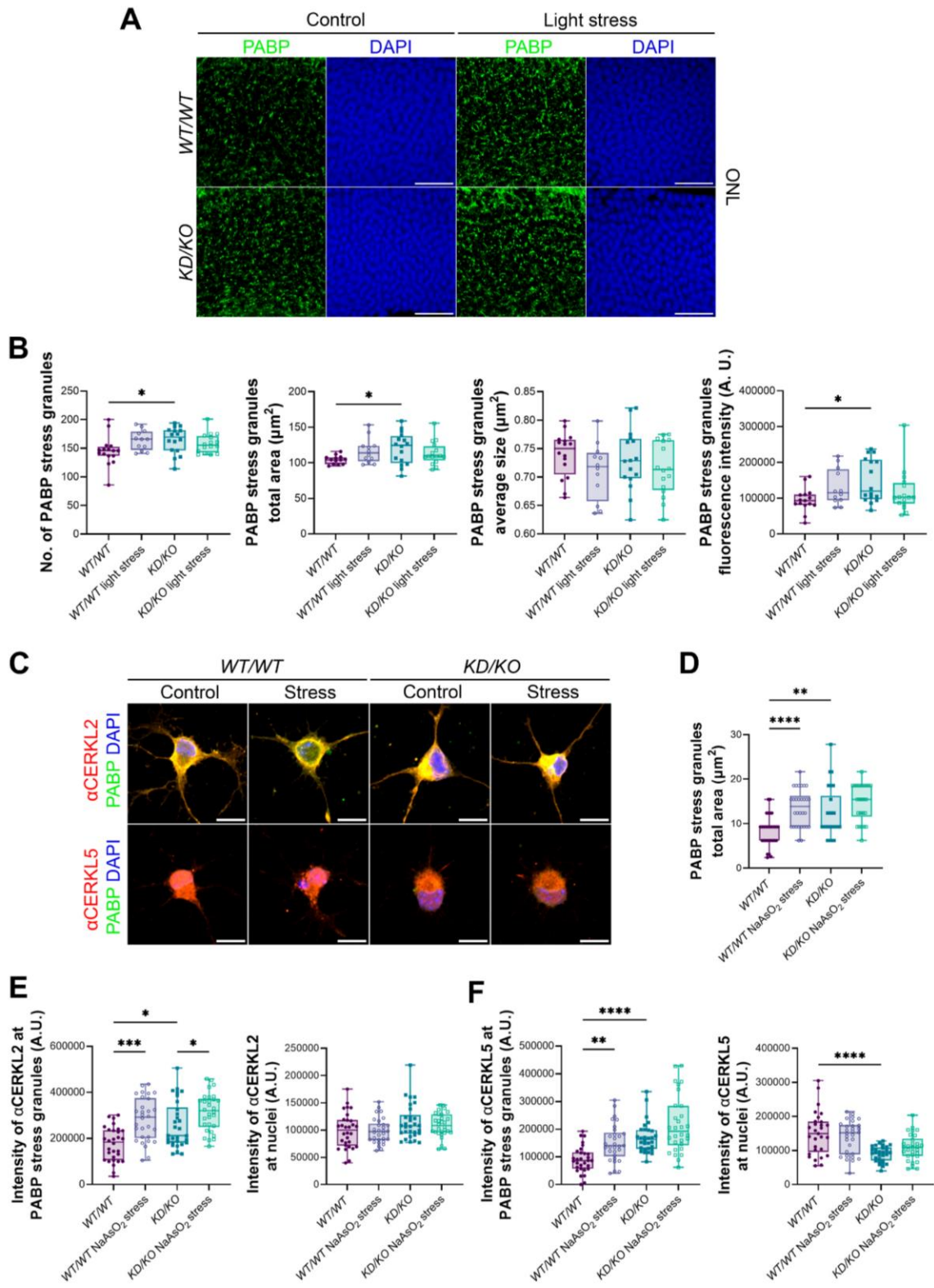
(caption on next page)

Fig. 4. PABP-mediated antioxidant response is exacerbated in *KD/KO* retinas and retinal ganglion cells (RGCs). (**A**) Representative confocal image of PABP mRNA-stress granules in the outer nuclear layer (ONL) of *WT/WT* and *KD/KO* retinas in control and light-stress conditions. Scale bar: 20 μm. (**B**) *KD/KO* retinas present higher number of PABP granules with increased levels of PABP. Quantification of the number of granules, total area, average size and PABP intensity in mRNA-stress granules. n = 12 ROIs from 4 animals per genotype and condition. (**C**) Representative confocal images of RGC somas for each studied condition. Scale bar: 10 μm. (**D**) PABP stress granules area is significantly increased in *WT/WT* RGCs upon sodium arsenite (NaAsO₂) induced stress as well as in *KD/KO* RGCs at basal conditions. Quantification of PABP stress granules total area in RGCs somas. n = 30 neurons from 3 animals per genotype and condition. (**E**) CERKL isoforms containing exon 2 (αCERKL2) display higher colocalization at stress granules under stress conditions, as well as in *KD/KO* RGCs in basal conditions. Quantification of CERKL isoforms displaying exon 2 colocalization at stress granules and nuclei in *WT/WT* and *KD/KO* RGCs in control and stress conditions. n = 30 neurons from 3 animals per genotype and condition. (**F**) CERKL isoforms that present exon 5 (αCERKL5) show higher colocalization at stress granules in *KD/KO* RGCs, and in *WT/WT* RGCs upon oxidative stress, as well as a significant decrease in the nuclear shift in *KD/KO* RGCs. Quantification of the intensity of CERKL isoforms expressing exon 5 at stress granules and nuclei of *WT/WT* and *KD/KO* RGCs in both control situation and under oxidative stress treatment. n = 30 neurons from 3 animals per genotype and condition. * *p-value* ≤ 0.05, ** *p-value* ≤ 0.01, *** *p-value* ≤ 0.005, **** *p-value* ≤ 0.001 (Complete images in Supplementary Fig. 5).
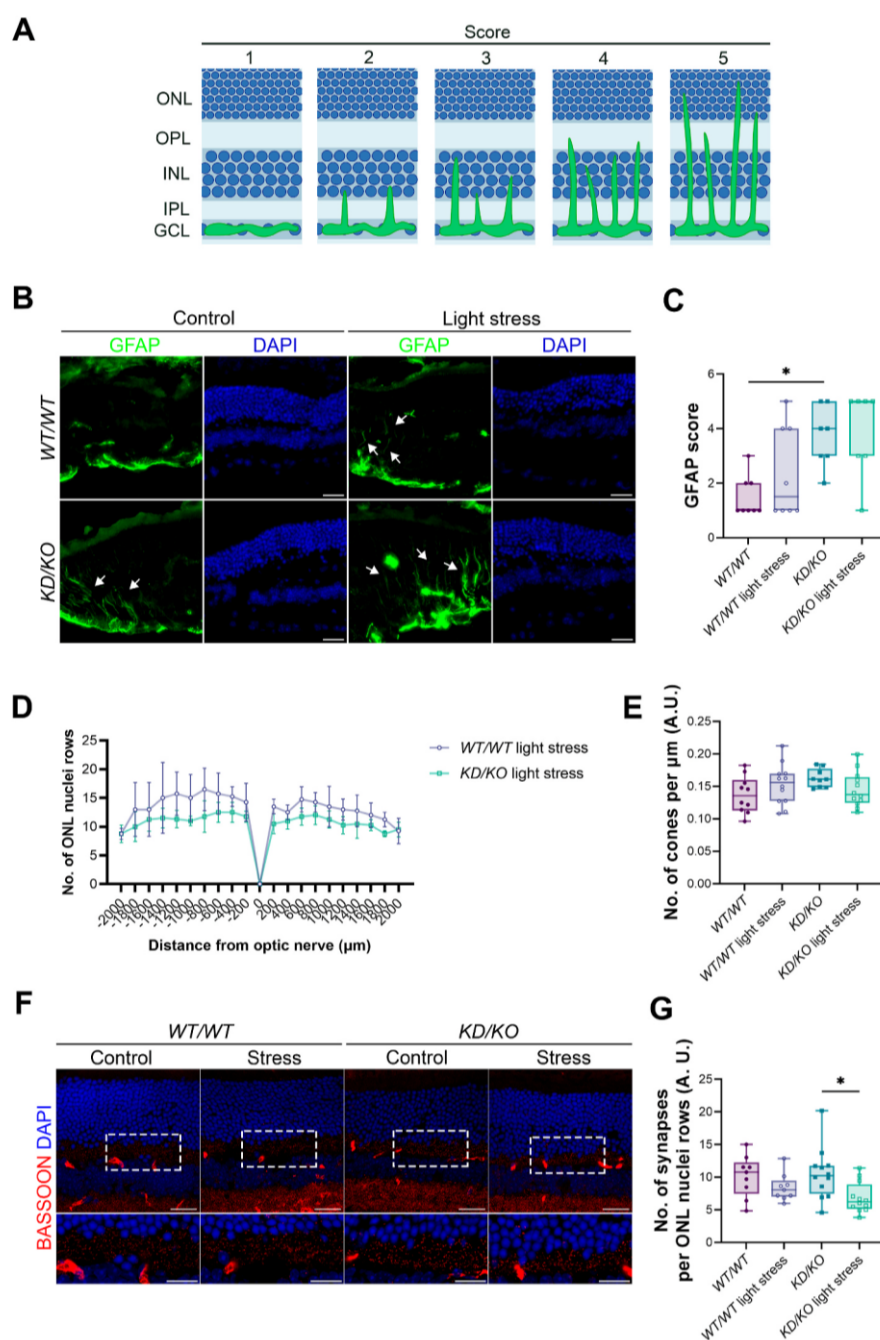
Fig. 5. Retinal remodelling two weeks after light-stress injury in *KD/KO* retinas. (**A**) Schematic representation of GFAP scores based on [34]. Reactive astrocytes and Müller glial cells are represented in green. ONL: outer nuclear layer, OPL: outer plexiform layer, INL: inner nuclear layer, IPL: inner plexiform layer, GCL: ganglion cell layer. (**B**) Glial branching reaches higher retinal layers in *KD/KO*. Representative fluorescence microscopy images of GFAP-positive astrocytes (green) and nuclei staining (DAPI in blue) in *WT/WT* and *KD/KO* retinas 2 weeks after light-stress treatment. White arrows indicate GFAP-positive ramifications. Scale bar: 20 μm. (**C**) GFAP score quantification shows higher levels of GFAP branching in *KD/KO* retinas. n = 7–8 ROIs from 4 animals per genotype and condition. (**D**) *KD/KO* retinas show a tendency to decreased number of photoreceptor nuclei rows two weeks after light insult. Quantification of photoreceptor nuclear rows (ONL) showing *WT/WT* and *KD/KO* values after light stress treatment. (**E**) No differences in the number of cones along the retina between all conditions and genotypes were observed. (**F**) Diminished number of synapses in *KD/KO* retinas as a late consequence of light stress. Representative confocal images of *WT/WT* and *KD/KO* retinal slices after stress damage immunodetecting BASSOON (red) and staining nuclei (DAPI in blue). Scale bar: 25 μm. High magnification images exhibit photoreceptor synapse buttons minutely. Scale bar: 15 μm. (**G**) Quantification of the number of synaptic buttons labeled with BASSOON normalized by the rows of photoreceptor nuclei. n = 8 ROIs from 4 retinas per genotype and condition. * *p-value* ≤ 0.05. (Complementary data in Supplementary Fig. 6). (For interpretation of the references to colour in this figure legend, the reader is referred to the Web version of this article.)

9
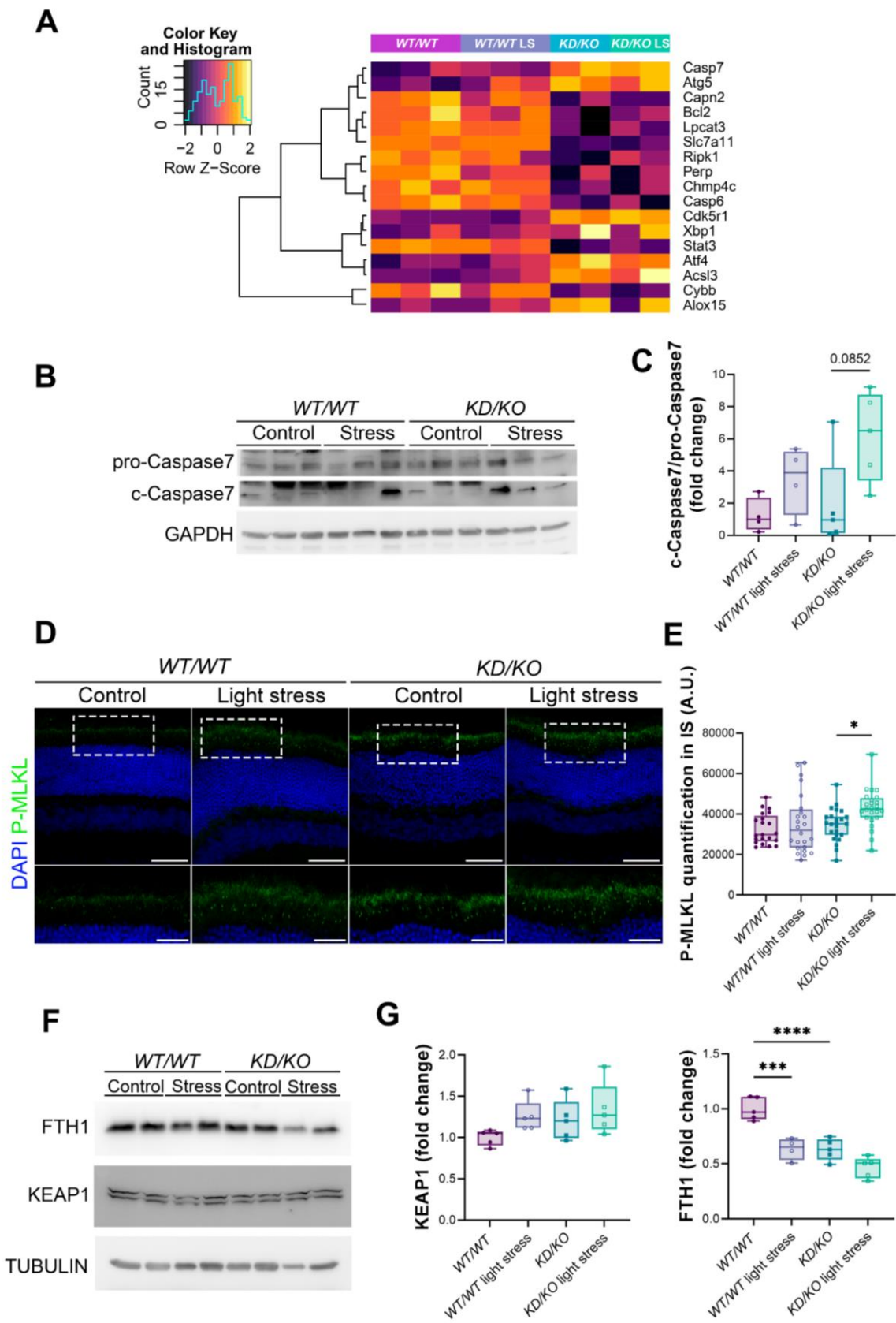
(caption on next page)

Fig. 6. Activation of different cell death mechanisms in *KD/KO* retinas upon light-stress damage. (**A**) Heatmap showing hierarchical clustering of differentially expressed genes involved in cell death pathways. (**B, C**) Activation of apoptosis in *KD/KO* retinas as a response to light stress through cleavage of CASPASE-7. (**B**) Western-blot of *WT/WT* and *KD/KO* retinal lysates immunodetecting CASPASE-7 and its cleaved isoform. GAPDH is used as loading control. (**C**) Quantification of cleaved-CASPASE-7:pro-CASPASE7 ratio (c-Caspase7/pro-Caspase7) shows a moderate increment in *KD/KO* retinas after stress treatment. (**D, E**) Necroptosis is triggered after MLKL phosphorylation in photoreceptor inner segments of *KD/KO* retinas under light-stress injury. (**D**) Representative fluorescent image of P-MLKL (green) in *WT/WT* and *KD/KO* retinas under light stress. DAPI is used to stain nuclei (blue). Scale bar: 50 μm. High magnification images show photoreceptor inner segment in more detail. Scale bar: 25 μm. (**E**) Quantification of P-MLKL fluorescence in the inner segment (IS) of WT and *KD/KO* photoreceptors after light-induced stress treatment. n = 24 ROIs from 4 animals per genotype and condition. (**F, G**) *KD/KO* retinas display decreased levels of FTH1 in both basal and light-induced stress conditions, reaching ferroptosis. (**F**) Western blot of *WT/WT* and *KD/KO* retinal homogenates after light-stress treatment immunodetecting FTH1, KEAP1 and TUBULIN (loading control). (**G**) Measurement of FTH1 and KEAP1 protein levels normalized using TUBULIN in WT and *KD/KO* retinal lysates upon light damage. n = 5 retinas per genotype and condition. * *p-value* ≤ 0.05, ** *p-value* ≤ 0.01, *** *p-value* ≤ 0.005, **** *p-value* ≤ 0.001. (For interpretation of the references to colour in this figure legend, the reader is referred to the Web version of this article.)

protect them from degradation [7]. These stress assemblies play key roles in cell thriving and survival upon stress [8]. In previous studies, CERKL has been described to interact with different proteins involved in the formation of stress granules, such as eIF3B and PABP [20]. Taking advantage of the *KD/KO* mouse model, we aimed to examine the stress granule-mediated response to light-induced stress in *KD/KO* retinas. Analysis and quantification of PABP stress granules in *WT/WT* and *KD/KO* outer nuclear layer (ONL) after light insult revealed a significant increase in the number and total area occupied by stress granules in *KD/KO* ONL in control conditions, while the average size of stress granules is the same between genotypes and conditions (Fig. 4A–B). Moreover, we found a significantly higher intensity of PABP in stress granules in *KD/KO* retinas in basal conditions (Fig. 4B).

Additionally, similar experiments were performed in *WT/WT* and *KD/KO* retinal ganglion cell (RGCs) primary cultures where oxidative stress has been induced with sodium arsenite (NaAsO₂). PABP and CERKL were immunodetected to study stress granules formation and colocalization with CERKL in the somas of *WT/WT* and *KD/KO* RGCs (Fig. 4C, complete images of RGCs in Supplementary Figure 4), with two in house antibodies that recognize different CERKL isoforms [21]: αCERKL2 recognizes an epitope encoded in exon 2 (Fig. 4C upper panel, Supplementary Figure 5A) whereas αCERKL5 recognizes an epitope encoded in exon 5 (Fig. 4C lower panel, Supplementary Figure 5B). A significant increase in the total area occupied by stress granules in the cytoplasm of *WT/WT* RGCs was clearly detected as a response to oxidative stress. Interestingly, we observed a similar increase in *KD/KO* RGCs at basal conditions (Fig. 4D), in agreement with the results obtained in vivo in *KD/KO* photoreceptors (Fig. 4A–B). Colocalization analysis showed higher colocalization of isoforms detected by αCERKL2 with stress granules in *KD/KO* RGCs compared with *WT/WT* in basal conditions, and a significant higher colocalization with stress granules in both *WT/WT* and *KD/KO* RGCs upon oxidative stress treatment (Fig. 4E). No changes in the localization of αCERKL2 at the nuclei were observed (Fig. 4E). On the other hand, CERKL isoforms that contain exon 5-peptide displayed a similar pattern of colocalization with stress granules compared to CERKL2 in all conditions, but for a significant decrease of nuclear αCERKL5 localization in *KD/KO* RGCs (Fig. 4F).

Therefore, PABP stress granules-mediated response is already highly activated in *KD/KO* whole retinas and in primary RGCs in basal conditions at similar levels to *WT/WT* retinas upon stress damage. Nonetheless, *KD/KO* retinas cannot further respond to additional external oxidative stress stimuli.

3.4. Retinal remodelling in KD/KO two weeks after light-induced injury

In order to study late-onset effects of light stress damage in *KD/KO* retinas, we performed light stress treatment in *WT/WT* and *KD/KO* mice and assessed their retinas two weeks after injury. Glial cells participate actively in retinal homeostasis through morphological and biochemical changes. In reactive gliosis, GFAP-positive astrocytes specifically undergo hypertrophy by projecting ramifications from the inner up to the outer layers of the retina, and Müller glial cells also start expressing GFAP [4]. To analyze the level of gliosis, we have followed a pre-set

scale with different scores of glia activation depending on the retinal layers reached by glial ramifications [34], in which higher scores mean more advanced gliosis (Fig. 5A). We detected GFAP-positive reactive cells in retinal cryosections of *WT/WT* and *KD/KO* mice two weeks after light-stress treatment (Fig. 5B, white arrows). Score analysis revealed an increased gliosis in light stress conditions that does not reach significance within each genotype. However, we did find significant higher levels of gliosis in *KD/KO* versus *WT/WT* retinas at basal conditions, meaning that *Cerkl* downregulation produces a strong glial activation without further stressing factors (Fig. 5C).

Furthermore, we tested the effects of long-term light-induced damage in *KD/KO* retinas by performing comparative morphometric analyses and layer structure assessment. Outer nuclear layer (ONL), inner nuclear layer (INL) and total retinal thickness as well as the number of photoreceptor nuclei rows were measured in *WT/WT* and *KD/KO* retinas. For most measurements, no significant differences between genotype or condition were observed (Supplementary Figure 6). However, focusing on the number of photoreceptor nuclei rows after light stress, we detected a moderate decrease in the number of photoreceptor nuclear rows in *KD/KO* compared to *WT/WT* retinas (Fig. 5D). This photoreceptor slight decrease most probably corresponds to rod's death, as the number of cones per area is preserved in all genotypes and conditions (Fig. 5E). Nonetheless, when considering this discrete ONL thinning in the retinas of 6-months-old animals, we should take into account that the retinal degeneration in our *KD/KO* model progresses slowly and is detected at older ages (more than 12-months-old animals), and what we observe here in response to light stress are the initial steps leading to retinal degeneration.

We also checked whether synaptic retinal remodelling might be occurring as a late response to light stress by quantifying the number of photoreceptor synapses in post-synaptic inner neurons through immunodetection of the synapse marker BASSOON in *WT/WT* and *KD/KO* retinas (Fig. 5F). Quantification of synapses in the outer plexiform layer suggested *KD/KO* retinas presented a significant decrease in the number of synapses per photoreceptor as a late consequence of light-induced stress (Fig. 5G).

In summary, retinal remodelling is observed in *KD/KO* mice two weeks after light-stress treatment via both moderate photoreceptor loss and a decrease in the number of synapses per photoreceptor.

3.5. Cell death mechanisms activation after light stress treatment in KD/KO retinas

As an ultimate outcome of defective antioxidant responses to oxidative damage, apoptotic and non-apoptotic programmed cell death pathways are eventually triggered, being the main cause of retinal neurodegeneration and vision loss in patients of retinal dystrophies [35, 36]. Therefore, we checked the regulation of different degenerative mechanisms performing a cluster analysis of RNA-Seq results, which resulted in a group of DE genes associated with various cell death pathways (Fig. 6A). Among them, we found DE genes related to apoptosis (e.g., *Casp7*, *Bcl2* and *Casp6*), necroptosis (e.g., *Ripk1*) and ferroptosis (e.g., *Slc7a11* and *Alox15*).

Among the different programmed cell death mechanisms, apoptosis has been considered the main cell death pathway occurring in the retina [35]. In the apoptotic process, both intrinsic and extrinsic apoptotic signalling cascades ultimately activate caspase-3 and caspase-7 as final effectors. We checked out the activation of apoptosis by quantifying the levels of cleaved CASPASE-7 (c-Caspase7) in comparison to uncleaved CASPASE-7 levels (pro-Caspase7) through Western-blot analysis of *WT/WT* and *KD/KO* retinal lysates upon light-induced injury (Fig. 6B). These results revealed a moderate but non-significant increase in the cleavage of pro-apoptotic CASPASE-7 in *KD/KO* retinas after stress treatment (Fig. 6C).

Moreover, other regulated degenerative mechanisms can be triggered in the retina, such as necroptosis and ferroptosis. In the necroptotic pathway, different kinases (RIPK1 and RIPK3) are activated in cascade to finally phosphorylate MLKL. Phosphorylated MLKL (P-MLKL) is then transported to the cell membrane, where it causes cell death by disruption of membrane integrity [37,38]. Thus, we assessed the location and quantity of P-MLKL in the photoreceptor membrane of *WT/WT* and *KD/KO* retinas after light-stress insult (Fig. 6D). In light-stressed *KD/KO* retinas the levels of P-MLKL localizing to the photoreceptor membrane were significantly increased in comparison to control *KD/KO*, indicating that necroptosis is triggered in *KD/KO* photoreceptors as a consequence of light-stress injury (Fig. 6E).

Ferroptosis is a programmed cell death pathway characterized by iron accumulation, oxidative stress, loss of mitochondrial integrity and low glutathione levels, which results in oxidation of nucleic acids, proteins, and lipids. All these ROS-derived alterations finally rise lethal calcium influx [39]. The iron responsive genes, such as FTH1 and other proteins involved in the ferroptotic cascade are induced by binding of NRF2 to the antioxidant responsive elements (AREs) in their promoters [40]. NRF2 is a master antioxidant transcription factor regulator whose levels are tightly controlled by the ubiquitin ligase KEAP1, which ubiquitylates NRF2, tagging it for proteasome degradation [41]. Notably, the NRF2/KEAP1 axis is slightly impaired in *KD/KO* retinas in basal conditions, as the transcriptional levels of *Nfe2l2* (the gene encoding NRF2) are slightly but significantly reduced down to 80% in *KD/KO* retinas compared to *WT/WT,* whereas those of KEAP1 are increased around 1.3-fold (RNA-Seq Supplementary Data). Therefore, we assessed the levels of KEAP1 and FTH1 (a ferroptosis suppressor gene induced by NRF2) by Western-blot analysis of *WT/WT* and *KD/KO* retinal lysates after light stress (Fig. 6F). In agreement with the RNA-Seq data, quantification of the ubiquitin ligase KEAP1 levels revealed a slight increase in *WT/WT* retinas in response to stress, as well as in *KD/KO* retinas in control and stress conditions. As a consequence, the levels of FTH1 were significantly reduced in light-stressed *WT/WT* and control *KD/KO* retinas, compared to control *WT/WT*. In addition, *KD/KO* retinas showed further decrease in the levels of FTH1 upon light-induced stress (Fig. 6G). The final consequence of the observed alterations is the activation of ferroptosis.

To conclude, multiple mediated cell death mechanisms are activated at different levels in *KD/KO* retinas in response to light-induced stress.

4. Discussion

Inherited retinal dystrophies (IRDs) are a heterogeneous group of disorders caused by mutations in more than 300 genes/loci (RetNet, the Retinal Information Network, 1996–2023, https://web.sph.uth.edu/Ret Net/). IRD-causative genes display many different functions in photoreceptor and other retinal cells, from specific structural roles (e.g., *CEP290, PROM1*), photoreception and phototransduction (e.g., *Rhodopsin, PDE6B*) or photoreceptor differentiation (e.g., *NRL, NR2E3*). Although the specific biochemical function is not always precisely determined (as is the case for *EYS, FAM161A or RPGR,* among others), the mutations in IRD genes cause the same phenotypic outcome: degeneration of photoreceptor cells and progressive visual decline, which eventually leads to blindness. Some IRDs are caused by failure in

specific enzymatic and non-enzymatic protective antioxidant systems, thus inducing a higher susceptibility to oxidative stress caused by endogenous and/or exogenous damaging factors, such as the continuous impact of light [42,43]. In this context, *CERKL* has been described as a resilience gene against oxidative stress in the retina and other tissues, although its particular and specific function has not yet been fully elucidated. With this work, we aimed to deepen in the CERKL protective role in the retina, particularly in response to acute light stress treatment, first by identifying differentially expressed genes upon light stress robustly associated to *Cerkl* knockdown; and second, by assessing antioxidant mechanisms in the retinas in the *Cerkl^{KD/KO}* (KDKO) model in order to identify potential actionable pathways for specific antioxidant therapeutic treatments.

Notably, results from RNA-Seq showed consistent transcriptional differences between genotypes, but very slight variations in response to light stress. Although surprising at first sight, we should note that transcriptomic analysis was performed after 1 h of light stress, and most probably, early oxidative defence pathways or even cell death mechanisms (see below) activation after acute injury rely on post-transcriptional but not transcriptional events. Longer exposure to light might reveal further altered cell pathways, although chronic light stress most probably induces strong retinal remodelling and inflammation as reported in Ref. [22]. Overall, our results though reinforce that knockdown of *Cerkl* alters directly or indirectly the expression of multiple genes, being most of them downregulated, including many IRD and phototransduction/visual cycle genes, thus reflecting photoreceptor and RPE dysfunction.

Previous studies reported that wild type CERKL was shown to be involved in the formation of RNA stress granules and P-bodies [20]. Here we report for the first time that mRNA stress granule response is exacerbated in *KD/KO* retinas in basal conditions, reaching levels similar to those of stressed *WT/WT* retinas. Surprisingly, acute light-/oxidative treatment did not cause an increase of stress granule response in *KD/KO* retinal cells, compared to the already overactivated response in basal conditions. On the other hand, a similar response was detected when assessing the GSH/GSGG ratio and the total quantity of glutathione in *WT/WT* vs *KD/KO* retinas. Again, in the absence of further environmental stressors, glutathione metabolism was already impaired in *KD/KO* retinas, showing similar levels of GSH/GSSG balance and glutathione total amount as *WT/WT* light-exposed retinas.

Among all the enzymatic oxidative defence mechanisms, CERKL has been shown to interact with the antioxidant enzyme TRX2 to ensure its redox function [17]. In this work we have also found alterations in the levels of other antioxidant enzymes in *KD/KO* retinas, such as PRX3 and PRX5, particularly after light-induced stress. Concerning the enzymatic machinery involved in glutathione metabolism, our findings showed increased levels of different enzymes, such as GSR, GPX4 and CHAC1, in *KD/KO* light-exposed retinas. Overregulation of these proteins, particularly GPX4 and CHAC1, is indicative of oxidative stress protection [44–46], whereas GPX downregulation is related to increased oxidative damage, as shown in *rd1* mouse model retinas [47]. Thus, in *KD/KO* retinas, downregulation of PRXs and overregulation of glutathione related enzymes might also occur as a compensatory reaction to the lowered levels of GSH to assure the glutathione-based response to light stress.

All these findings, together with those related to stress granule formation and the alterations detected in NRF2/KEAP1 axis, indicate that *KD/KO* retinas already suffer from endogenous oxidative stress in normal conditions and fail to further activate antioxidant mechanisms against external stress stimuli.

The contribution of CERKL to mitochondrial dynamics and metabolism has already been assessed in previous work, in which *CERKL/ Cerkl* downregulation resulted in smaller and dysfunctional mitochondria, whereas *CERKL* overexpression protected mitochondrial morphology and function from oxidative stress [15,18,19]. Here, we also describe alterations in the levels of different subunits of the ATP
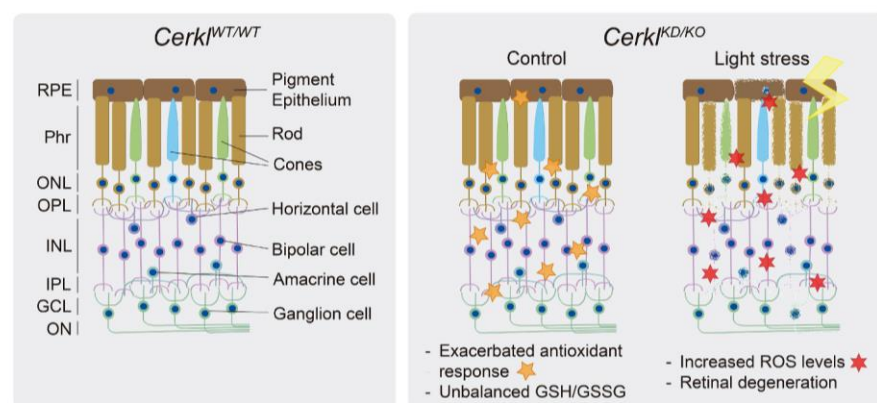
Fig. 7. Model of retinal degeneration in *Cerkl*^{KD/KO} due to oxidative stress response dysregulation. The *WT/WT* retina shows the laminar distribution of retinal neuronal cells (right panel). In contrast, *KD/KO* retinas show: i) an upregulation of oxidative stress response (e.g., stress granule formation and gliosis) and ii) unbalanced glutathione metabolites, even in basal conditions. This dysregulated response is further exacerbated upon light-stress, with increased $H_2O_2 \rightarrow$ ROS production, which eventually leads to retinal degeneration. RPE: retinal pigment epithelium, Phr: photoreceptor layer, ONL: outer nuclear layer, OPL: outer plexiform layer, INL: inner nuclear layer, IPL: inner plexiform layer, GCL: ganglion cell layer, ON: optic nerve.

synthase upon *Cerkl* knockdown. As a vicious circle, energy-supply mechanisms produce ROS, but ROS can also damage energy-supply systems. On the other hand, if there is not sufficient energy production the repair systems cannot act properly, and the resulting imbalance eventually may lead to cell death [48]. Given that, apart from alterations in mitochondrial metabolism, we also describe increased levels of H_2O_2 and ROS and dysregulated antioxidant responses in *KD/KO* light-exposed retinas, it is difficult to elucidate which is the first link in the chain initiating this vicious circle.

CERKL is a gene with highly complex regulation, including different transcription start sites and alternative splicing events. As a result, at least four main protein isoforms can be found in the human, and three in the mouse retinas [49]. These isoforms display different protein domains and might thus play different roles. Interestingly, although *Cerkl* expression is not increased after light stress in the wild-type retinas, the subcellular localization of different CERKL protein isoforms shifts, thus reflecting post-translational regulation in response to stress. Thus, while CERKL isoforms containing either exon 2 and/or exon 5 are localized ubiquitously through the soma and dendrites of *WT/WT* RGCs, in *KD/KO* RGCs, a limited pool of exon 2-containing isoforms is detected in the nuclei, but most of the residual CERKL mainly localizes to stress granules, as a crucial CERKL-mediated stress response mechanism.

As a common point in different neurodegenerative retinal disorders, glial cells are activated in response to damage and degeneration of retinal cells, eventually inducing an inflammation state in the retina [50]. Accordingly, our results showed an increment of gliosis in *KD/KO* retinas, regardless of light-stress treatment, that is indicative of chronic damage in *KD/KO* retinas, and results in deleterious effects that may contribute to retinal neurodegeneration [4]. Moreover, we observed a late light-responsive loss of synaptic contacts between photoreceptor cells and post-synaptic neurons in the *KD/KO* retinas (at two weeks post-injury), suggesting retinal connection remodelling as part of the neurodegenerative process as reviewed in Refs. [51,52].

As a final outcome of light-induced stress, impaired antioxidant responses and gliosis, we observed activation of several cell death mechanisms at different levels, including necroptosis, ferroptosis and apoptosis. Activation of necroptosis in *KD/KO* photoreceptors promotes cell death, as an expected response to light-stress damage [53]. Moreover, the detected increase in ferroptosis in *KD/KO* retinas may be due to several alterations: i) significantly lower RNA levels of the antioxidant response master regulator NRF2 ($\log_2$ Fold Change of -0.3383), ii) the slight increase in KEAP1 protein levels, the ubiquitin ligase that promotes NRF2 degradation [41]), and iii) the subsequent significant decrease of FTH1, an anti-ferroptotic protein involved in ferrous iron scavenging [54,55], as a consequence of the alteration of the glutathione system [44,46], leading to iron release. Finally, and in agreement with other IRD mouse models, apoptosis –although detectable– was not the principal cell death mechanism activated in *KD/KO* retinas [56].

Coherently, the inflammatory response mediated by glia is strongly associated with non-apoptotic cell death pathways, such as ferroptosis and necroptosis. Overall, *KD/KO* light-exposed retinas display several cell death mechanisms, which might be cell-specific. Further work is required to assess the relevance of each pathway in retinal degeneration.

5. Conclusions

Altogether, these studies provide further evidence of the importance of CERKL for the proper regulation, control, and balance of antioxidant systems in response to acute light stress in the retina. In addition, *Cerkl* downregulation causes retinal oxidative stress in basal conditions, and this chronic overactivation of different oxidative defence mechanisms does not allow to respond further upon stress injury. Eventually, the balance between antioxidant mechanisms and ROS levels is altered and triggers different cell death mechanisms in *KD/KO* retinas. Our findings (model in Fig. 7) shed light on the pathogenesis mechanisms of *CERKL* mutations, which eventually cause retinal degeneration and blindness by impairing the oxidative stress response in the retina. In this context, specific therapeutical approaches by gene therapy adding *CERKL* or by antioxidant treatments targeting key actionable pathways [57] seem promising strategies to halt IRD disease progression.

Author contributions

Conceptualization and supervision, G.M. and S.M.; methodology, R. G.-A., E.B.D., M.A.A. and C.N.A.; bioinformatical analysis, C.H.-U.; formal analysis, R.G.-A., E.B.D., C.H.-U., M.A.A., C.N.A., J.M.C., J.G.-F., F.V.P., G.M. and S.M.; resources, J.M.C., F.V.P., G.M. and S.M.; writing-original draft preparation, R.G.-A., G.M. and S.M.; writing-review and editing, R.G.-A., G.M. and S.M. All authors have revised and agreed to the final draft of the manuscript.

Funding

Declaration of competing interest

None of the authors of the manuscript by García-Arroyo et al.

"**Exacerbated response to oxidative stress in the Retinitis Pigmentosa** *Cerkl*$^{KD/KO}$ **mouse model induces retinal degeneration upon acute light injury**" has any conflict of interest to declare.

Data availability

Data will be made available on request.

Acknowledgments

Appendix A. Supplementary data

Supplementary data to this article can be found online at https://doi.org/10.1016/j.redox.2023.102862.

References

[1] V.E. Baksheeva, V.V. Tiulina, N.K. Tikhomirova, O.S. Gancharova, S.V. Komarov, P.P. Philippov, A.A. Zamyatnin, I.I. Senin, E.Y. Zernii, Suppression of light-induced oxidative stress in the retina by mitochondria-targeted antioxidant, Antioxidants 8 (2019), https://doi.org/10.3390/antiox8010003.

[2] E.B. Domènech, G. Marfany, The relevance of oxidative stress in the pathogenesis and therapy of retinal dystrophies, Antioxidants 9 (2020) 1–22, https://doi.org/10.3390/antiox9040347.

[3] K. Rashid, I. Akhtar-Schaefer, T. Langmann, Microglia in retinal degeneration, Front. Immunol. 10 (2019) 1–19, https://doi.org/10.3389/fimmu.2019.01975.

[4] P.V. Subirada, M.C. Paz, M.E. Ridano, V.E. Lorenc, M.V. Vaglienti, P.F. Barcelona, J.D. Luna, M.C. Sánchez, A journey into the retina: Müller glia commanding survival and death, Eur. J. Neurosci. 47 (2018) 1429–1443, https://doi.org/10.1111/ejn.13965.

[5] S. Mirra, G. Marfany, Mitochondrial gymnastics in retinal cells: a resilience mechanism against oxidative stress and neurodegeneration, in: Adv Exp Med Biol, 2019, pp. 513–517, https://doi.org/10.1007/978-3-030-27378-1_84.

[6] P.G. Sreekumar, D.A. Ferrington, R. Kannan, Glutathione metabolism and the novel role of mitochondrial gsh in retinal degeneration, Antioxidants 10 (2021) 1–18, https://doi.org/10.3390/antiox10050661.

[7] P. Anderson, N. Kedersha, Stress granules, Curr. Biol. 19 (2009) 397–398, https://doi.org/10.1016/j.cub.2009.03.013.

[8] W. van Leeuwen, C. Rabouille, Cellular stress leads to the formation of membraneless stress assemblies in eukaryotic cells, Traffic 20 (2019) 623–638, https://doi.org/10.1111/tra.12669.

[9] T.S. Aleman, N. Soumittra, A.V. Cideciyan, A.M. Sumaroka, V.L. Ramprasad, W. Herrera, E.A.M. Windsor, S.B. Schwartz, R.C. Russell, A.J. Roman, C. F. Inglehearn, G. Kumaramanickavel, E.M. Stone, G.A. Fishman, S.G. Jacobson, CERKL mutations cause an autosomal recessive cone-rod dystrophy with inner retinopathy, Invest. Ophthalmol. Vis. Sci. 50 (2009) 5944–5954, https://doi.org/10.1167/iovs.09-3982.

[10] M. Tuson, G. Marfany, R. Gonzàlez-Duarte, Mutation of CERKL, a novel human ceramide kinase gene, causes autosomal recessive retinitis pigmentosa (RP26), Am. J. Hum. Genet. 74 (2004) 128–138.

[11] A.O. Khan, L. Abu-Safieh, Rod-Cone dystrophy with initially preserved visual acuity despite early macular involvement suggests recessive CERKL mutations, Ophthalmic Genet. 36 (2015) 369–372, https://doi.org/10.3109/13816810.2014.889168.

[12] M. Ali, V.L. Ramprasad, N. Soumittra, M.D. Mohamed, H. Jafri, M. Danciger, M. Mckibbin, G. Kumaramanickavel, C.F. Inglehearn, A missense mutation in the nuclear localization signal sequence of CERKL (p .R106S) causes autosomal recessive retinal degeneration, Mol. Vis. 14 (2008) 1960–1964.

[13] X. Hu, Z. Lu, S. Yu, J. Reilly, F. Liu, D. Jia, Y. Qin, S. Han, X. Liu, Z. Qu, Y. Lv, J. Li, Y. Huang, T. Jiang, H. Jia, Q. Wang, J. Liu, X. Shu, Z. Tang, M. Liu, CERKL regulates autophagy via the NAD-dependent deacetylase SIRT1, Autophagy 15 (2019) 453–465, https://doi.org/10.1080/15548627.2018.1520548.

[14] S. Huang, Z. Hong, L. Zhang, J. Guo, Y. Li, K. Li, CERKL alleviates ischemia reperfusion-induced nervous system injury through modulating the SIRT1/PINK1/Parkin pathway and mitophagy induction, Biol. Chem. 403 (2022) 1–11.

[15] S. Mirra, R. García-Arroyo, E.B. Domènech, A. Gavaldà-Navarro, C. Herrera-Úbeda, C. Oliva, J. García-Fernàndez, R. Artuch, F. Villarroya, G. Marfany, CERKL, a retinal dystrophy gene, regulates mitochondrial function and dynamics in the mammalian retina, Neurobiol. Dis. 156 (2021), 105405, https://doi.org/10.1016/j.nbd.2021.105405.

[16] M. Tuson, A. Garanto, R. Gonzàlez-Duarte, G. Marfany, Overexpression of CERKL, a gene responsible for retinitis pigmentosa in humans, protects cells from apoptosis induced by oxidative stress, Mol. Vis. 15 (2009) 168–180.

[17] C. Li, L. Wang, J. Zhang, M. Huang, F. Wong, X. Liu, F. Liu, X. Cui, G. Yang, J. Chen, Y. Liu, J. Wang, S. Liao, M. Gao, X. Hu, X. Shu, Q. Wang, Z. Yin, Z. Tang, M. Liu, CERKL interacts with mitochondrial TRX2 and protects retinal cells from oxidative stress-induced apoptosis, Biochim. Biophys. Acta, Mol. Basis Dis. 1842 (2014) 1121–1129, https://doi.org/10.1016/j.bbadis.2014.04.009.

[18] R. García-Arroyo, A. Gavaldà, F. Villarroya, G. Marfany, S. Mirra, Overexpression of CERKL protects retinal pigment epithelium mitochondria from oxidative stress effects, Antioxidants 10 (2021) 1–16.

[19] R. García-Arroyo, G. Marfany, S. Mirra, CERKL, a retinal dystrophy gene, regulates mitochondrial transport and dynamics in hippocampal neurons, Int. J. Mol. Sci. 23 (2022), https://doi.org/10.3390/ijms231911593.

[20] A. Fathinajafabadi, E. Pérez-Jiménez, M. Riera, E. Knecht, R. Gonzàlez-Duarte, CERKL, a retinal disease gene, encodes an mRNA-binding protein that localizes in compact and untranslated mRNPs associated with microtubules, PLoS One 9 (2014), https://doi.org/10.1371/journal.pone.0087898.

[21] E.B. Domènech, R. Andres, M.J. López-Iniesta, S. Mirra, R. García-Arroyo, S. Milla, F. Sava, J. Andilla, P.L. Alvarez, P. De La Villa, R. Gonzàlez-Duarte, G. Marfany, A new Cerkl mouse model generated by CRISPR-cas9 shows progressive retinal degeneration and altered morphological and electrophysiological phenotype, Invest. Ophthalmol. Vis. Sci. 61 (2020), https://doi.org/10.1167/IOVS.61.8.14.

[22] O. Kutsyr, X. Sánchez-Sáez, N. Martínez-Gil, E. de Juan, P. Lax, V. Maneu, N. Cuenca, Gradual increase in environmental light intensity induces oxidative stress and inflammation and accelerates retinal neurodegeneration, Invest. Ophthalmol. Vis. Sci. 61 (2020), https://doi.org/10.1167/IOVS.61.10.1.

[23] M. Samardzija, V. Todorova, L. Gougoulakis, M. Barben, S. Nötzli, K. Klee, F. Storti, A. Gubler, C. Imsand, C. Grimm, Light stress affects cones and horizontal cells via rhodopsin-mediated mechanisms, Exp. Eye Res. 186 (2019), 107719, https://doi.org/10.1016/j.exer.2019.107719.

[24] M.V. Kuleshov, M.R. Jones, A.D. Rouillard, N.F. Fernandez, Q. Duan, Z. Wang, S. Koplev, S.L. Jenkins, K.M. Jagodnik, A. Lachmann, M.G. McDermott, C. D. Monteiro, G.W. Gundersen, A. Maayan, Enrichr: a comprehensive gene set enrichment analysis web server 2016 update, Nucleic Acids Res. 44 (2016), W90–W97, https://doi.org/10.1093/nar/gkw377.

[25] Z. Xie, A. Bailey, M.V. Kuleshov, D.J.B. Clarke, J.E. Evangelista, S.L. Jenkins, A. Lachmann, M.L. Wojciechowicz, E. Kropiwnicki, K.M. Jagodnik, M. Jeon, A. Ma'ayan, Gene set knowledge discovery with Enrichr, Curr Protoc 1 (2021), https://doi.org/10.1002/cpz1.90.

[26] E.Y. Chen, C.M. Tan, Y. Kou, Q. Duan, Z. Wnag, G.V. Meirelles, N.R. Clark, A. Ma'ayan, Enrichr: interactive and collaborative HTML5 gene list enrichment analysis tool Edward, BCM Bioinf. 14 (2013) 1–15, https://doi.org/10.1007/s00701-014-2321-4.

[27] S.X. Ge, E.W. Son, R. Yao, iDEP: an integrated web application for differential expression and pathway analysis of RNA-Seq data, BMC Bioinf. 19 (2018) 1–24, https://doi.org/10.1186/s12859-018-2486-6.

[28] J. Escobar, Á. Sánchez-Illana, J. Kuligowski, I. Torres-Cuevas, R. Solberg, H. T. Garberg, M.U. Huun, O.D. Saugstad, M. Vento, C. Cháfer-Pericás, Development of a reliable method based on ultra-performance liquid chromatography coupled to tandem mass spectrometry to measure thiol-associated oxidative stress in whole blood samples, J. Pharm. Biomed. Anal. 123 (2016) 104–112, https://doi.org/10.1016/j.jpba.2016.02.007.

[29] L. Torresano, F. Santacatterina, S. Domínguez-Zorita, C. Nuevo-Tapioles, A. Núñez-Salgado, P.B. Esparza-Moltó, L. González-Llorente, I. Romero-Carramiñana, C. Núñez de Arenas, B. Sánchez-Garrido, L. Nájera, C. Salas, M. Provencio, J. M. Cuezva, Analysis of the metabolic proteome of lung adenocarcinomas by reverse-phase protein arrays (RPPA) emphasizes mitochondria as targets for therapy, Oncogenesis 11 (2022), https://doi.org/10.1038/s41389-022-00400-y.

[30] F. Santacatterina, L. Torresano, A. Núñez-Salgado, P.B. Esparza-Molto, M. Olive, E. Gallardo, E. García-Arumi, A. Blazquez, A. González-Quintana, M.A. Martín, J. M. Cuezva, Different mitochondrial genetic defects exhibit the same protein signature of metabolism in skeletal muscle of PEO and MELAS patients: a role for oxidative stress, Free Radic. Biol. Med. 126 (2018) 235–248, https://doi.org/10.1016/j.freeradbiomed.2018.08.020.

[31] C. Martínez-Fernández De La Cámara, A.M. Hernández-Pinto, L. Olivares-González, C. Cuevas-Martín, M. Sánchez-Aragó, D. Hervás, D. Salom, J.M. Cuezva, E.J. De La Rosa, J.M. Millán, R. Rodrigo, Adalimumab reduces photoreceptor cell death in a mouse model of retinal degeneration, Sci. Rep. 5 (2015) 1–13, https://doi.org/10.1038/srep11764.

[32] X. Guo, G. Aviles, Y. Liu, R. Tian, B.A. Unger, Y.H.T. Lin, A.P. Wiita, K. Xu, M. A. Correia, M. Kampmann, Mitochondrial stress is relayed to the cytosol by an OMA1–DELE1–HRI pathway, Nature 579 (2020) 427–432, https://doi.org/10.1038/s41586-020-2078-2.

[33] G. Chidlow, J.P.M. Wood, B. Knoops, R.J. Casson, Expression and distribution of peroxiredoxins in the retina and optic nerve, Brain Struct. Funct. 221 (2016) 3903–3925, https://doi.org/10.1007/s00429-015-1135-3.

[34] P.J. Anderson, H. Watts, C. Hille, K. Philpott, P. Clark, M. Crocher, S. Gentleman, L.-S. Jen, Glial and endothelial blood-retinal barrier responses to amyloid-β in the neural retina of the rat, Clin. Ophthalmol. 2 (2008) 801, https://doi.org/10.2147/opth.s3967.

[35] N.D. Chinskey, C.G. Besirli, D.N. Zacks, Retinal cell death and current strategies in retinal neuroprotection, Curr. Opin. Ophthalmol. 25 (2014) 228–233, https://doi.org/10.1097/ICU.0000000000000043.

[36] G. Dvoriantchikova, K.R. Lypka, E.V. Adis, D. Ivanov, Multiple types of programmed necrosis such as necroptosis, pyroptosis, oxytosis/ferroptosis, and parthanatos contribute simultaneously to retinal damage after ischemia–reperfusion, Sci. Rep. 12 (2022) 1–15, https://doi.org/10.1038/s41598-022-22140-0.

[37] L. Sun, H. Wang, Z. Wang, S. He, S. Chen, D. Liao, L. Wang, J. Yan, W. Liu, X. Lei, X. Wang, Mixed lineage kinase domain-like protein mediates necrosis signaling downstream of RIP3 kinase, Cell 148 (2012) 213–227, https://doi.org/10.1016/j.cell.2011.11.031.

[38] A.L. Samson, Y. Zhang, N.D. Geoghegan, X.J. Gavin, K.A. Davies, M.J. Mlodzianoski, L.W. Whitehead, D. Frank, S.E. Garnish, C. Fitzgibbon, A. Hempel, S.N. Young, A.V. Jacobsen, W. Cawthorne, E.J. Petrie, M.C. Faux, K. Shield-Artin, N. Lalaoui, J.M. Hildebrand, J. Silke, K.L. Rogers, G. Lessene, E.D. Hawkins, J.M. Murphy, MLKL trafficking and accumulation at the plasma membrane control the kinetics and threshold for necroptosis, Nat. Commun. 11 (2020) 1–17, https://doi.org/10.1038/s41467-020-16887-1.

[39] J. Lewerenz, G. Ates, A. Methner, M. Conrad, P. Maher, Oxytosis/ferroptosis-(Re-)emerging roles for oxidative stress-dependent non-apoptotic cell death in diseases of the central nervous system, Front. Neurosci. 12 (2018), https://doi.org/10.3389/fnins.2018.00214.

[40] A. Anandhan, M. Dodson, C.J. Schmidlin, P. Liu, D.D. Zhang, Breakdown of an ironclad defense system: the critical role of NRF2 in mediating ferroptosis, Cell Chem. Biol. 27 (2020) 436–447, https://doi.org/10.1016/j.chembiol.2020.03.011.

[41] L. Baird, M. Yamamoto, The molecular mechanisms regulating the KEAP1-NRF2 pathway, Mol. Cell Biol. 40 (2020) 1–23, https://doi.org/10.1128/mcb.00099-20.

[42] P.A. Campochiaro, R.W. Strauss, L. Lu, G. Hafiz, Y. Wolfson, S.M. Shah, R. Sophie, T.A. Mir, H.P. Scholl, Is there excess oxidative stress and damage in eyes of patients with retinitis pigmentosa? Antioxidants Redox Signal. 23 (2015) 643–648, https://doi.org/10.1089/ars.2015.6327.

[43] S. Usui, B.C. Oveson, S.Y. Lee, Y. Jo, T. Yoshida, K. Miki, T. Iwase, L. Lu, P.A. Campochiaro, NADPH oxidase plays a central role in cone cell death in retinitis pigmentosa, J. Neurochem. 110 (2010) 1028–1037, https://doi.org/10.1111/j.1471-4159.2009.06195.x.NADPH.

[44] B.R. Cardoso, D.J. Hare, A.I. Bush, B.R. Roberts, Glutathione peroxidase 4: a new player in neurodegeneration? Mol. Psychiatr. 22 (2017) 328–335, https://doi.org/10.1038/mp.2016.196.

[45] L. Lu, B.C. Oveson, Y.J. Jo, T.W. Lauer, S. Usui, K. Komeima, B. Xie, P.A. Campochiaro, Increased expression of glutathione peroxidase 4 strongly protects retina from oxidative damage, Antioxidants Redox Signal. 11 (2009) 715–724, https://doi.org/10.1089/ars.2008.2171.

[46] Y. Liu, D. Wu, Q. Fu, S. Hao, Y. Gu, W. Zhao, S. Chen, F. Sheng, Y. Xu, Z. Chen, K. Yao, CHAC1 as a novel contributor of ferroptosis in retinal pigment epithelial cells with oxidative damage, Int. J. Mol. Sci. 24 (2023), https://doi.org/10.3390/ijms24021582.

[47] P. Ahuja-Jensen, S. Johnsen-Soriano, S. Ahuja, F. Bosch-Morell, M. Sancho-Tello, F.J. Romero, M. Abrahamson, T. Van Veen, Low glutathione peroxidase in rd1 mouse retina increases oxidative stress and proteases, Neuroreport 18 (2007) 797–801, https://doi.org/10.1097/WNR.0b013e3280c1e344.

[48] Y. Ozawa, Oxidative stress in the light-exposed retina and its implication in age-related macular degeneration, Redox Biol. 37 (2020), 101779, https://doi.org/10.1016/j.redox.2020.101779.

[49] A. Garanto, M. Riera, E. Pomares, J. Permanyer, M. de Castro-Miró, F. Sava, J.F. Abril, G. Marfany, R. Gonzàlez-Duarte, High transcriptional complexity of the retinitis pigmentosa CERKL gene in human and mouse, Invest. Ophthalmol. Vis. Sci. 52 (2011) 5202–5214, https://doi.org/10.1167/iovs.10-7101.

[50] A. Noailles, V. Maneu, L. Campello, P. Lax, N. Cuenca, Systemic inflammation induced by lipopolysaccharide aggravates inherited retinal dystrophy, Cell Death Dis. 9 (2018), https://doi.org/10.1038/s41419-018-0355-x.

[51] B.W. Jones, R.E. Marc, Retinal remodeling during retinal degeneration, Exp. Eye Res. 81 (2005) 123–137, https://doi.org/10.1016/j.exer.2005.03.006.

[52] N. Martínez-Gil, V. Maneu, O. Kutsyr, L. Fernández-Sánchez, X. Sánchez-Sáez, C. Sánchez-Castillo, L. Campello, P. Lax, I. Pinilla, N. Cuenca, Cellular and molecular alterations in neurons and glial cells in inherited retinal degeneration, Front. Neuroanat. 16 (2022) 1–18, https://doi.org/10.3389/fnana.2022.984052.

[53] Z. Yu, V.S.M.C. Correa, N.E. Efstathiou, H. Albertos-Arranz, X. Chen, K. Ishihara, Y. Iesato, T. Narimatsu, D. Ntentakis, D.G. Vavvas, UVA induces retinal photoreceptor cell death via receptor interacting protein 3 kinase mediated necroptosis, Cell Death Dis. 8 (2022) 1–11, https://doi.org/10.1038/s41420-022-01273-1.

[54] Y. Tian, J. Lu, X. Hao, H. Li, G. Zhang, X. Liu, X. Li, C. Zhao, W. Kuang, D. Chen, M. Zhu, FTH1 inhibits ferroptosis through ferritinophagy in the 6-OHDA model of Parkinson's disease, Neurotherapeutics 17 (2020) 1796–1812, https://doi.org/10.1007/s13311-020-00929-z.

[55] W. Shu, B.H. Baumann, Y. Song, Y. Liu, X. Wu, J.L. Dunaief, Ferrous but not ferric iron sulfate kills photoreceptors and induces photoreceptor-dependent RPE autofluorescence, Redox Biol. 34 (2020) 101469, https://doi.org/10.1016/j.redox.2020.101469.

[56] J. Sancho-Pelluz, B. Arango-Gonzalez, S. Kustermann, F.J. Romero, T. Van Veen, E. Zrenner, P. Ekström, F. Paquet-Durand, Photoreceptor cell death mechanisms in inherited retinal degeneration, Mol. Neurobiol. 38 (2008) 253–269, https://doi.org/10.1007/s12035-008-8045-9.

[57] W. Xiong, A.E.M.C. Garfinkel, Y. Li, L.I. Benowitz, C.L. Cepko, NRF2 promotes neuronal survival in neurodegeneration and acute nerve damage, J. Clin. Invest. 125 (2015) 1433–1445, https://doi.org/10.1172/JCI79735.
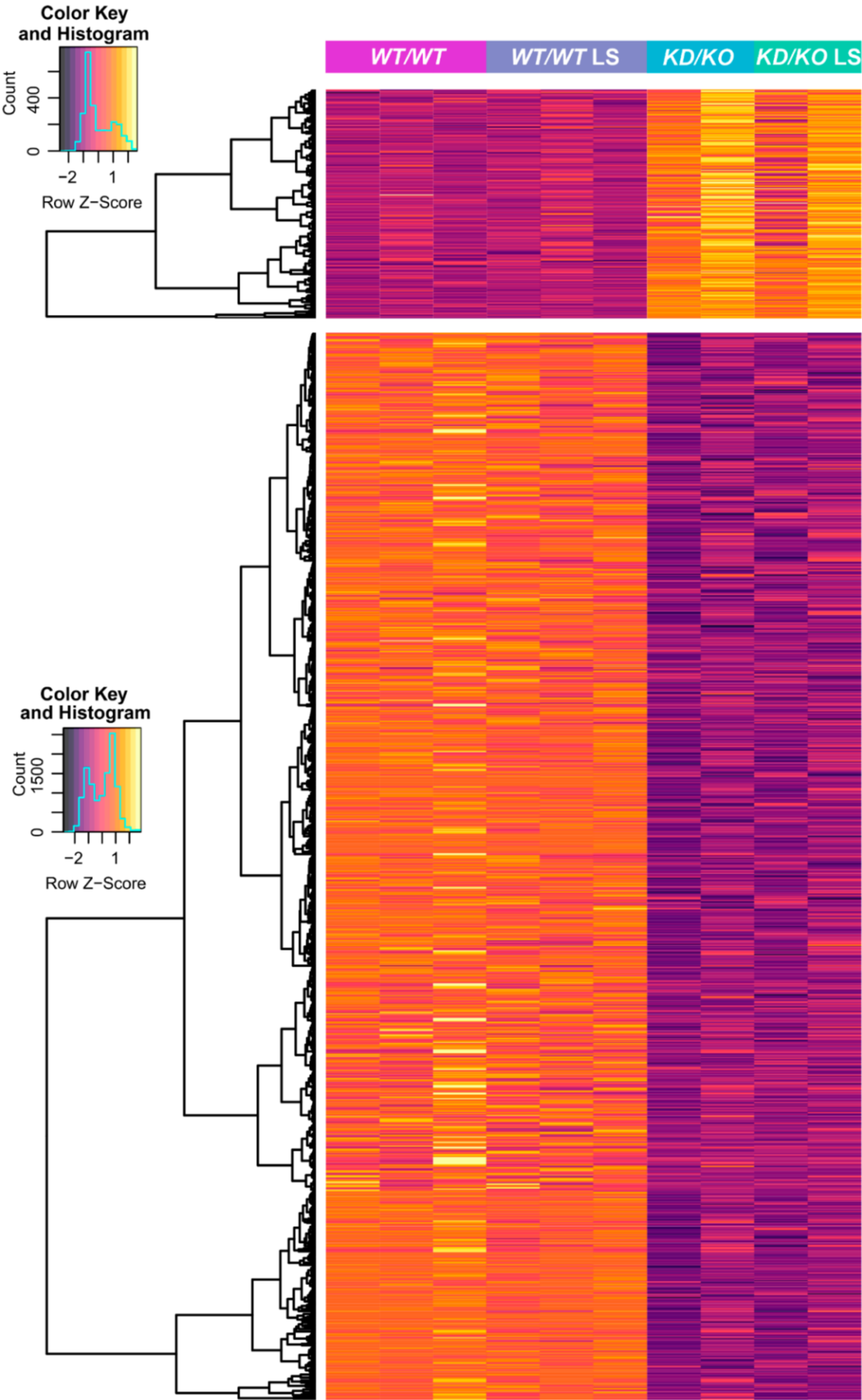
Supplementary Figure 1. Differentially expressed genes from RNA-Seq analysis of *KD/KO* versus *WT/WT* retinas in control and light-stress conditions. Heatmap with hierarchical clustering of all up- ($\log_2$ Fold Change ≥ 0.5, upper panel) and downregulated ($\log_2$ Fold Change ≤ -0.5, lower panel) genes (*p-value* ≤ 0.05) resulting from RNA-Seq analysis of *KD/KO* versus *WT/WT* retinas, in control and light-stress (LS) conditions.

2
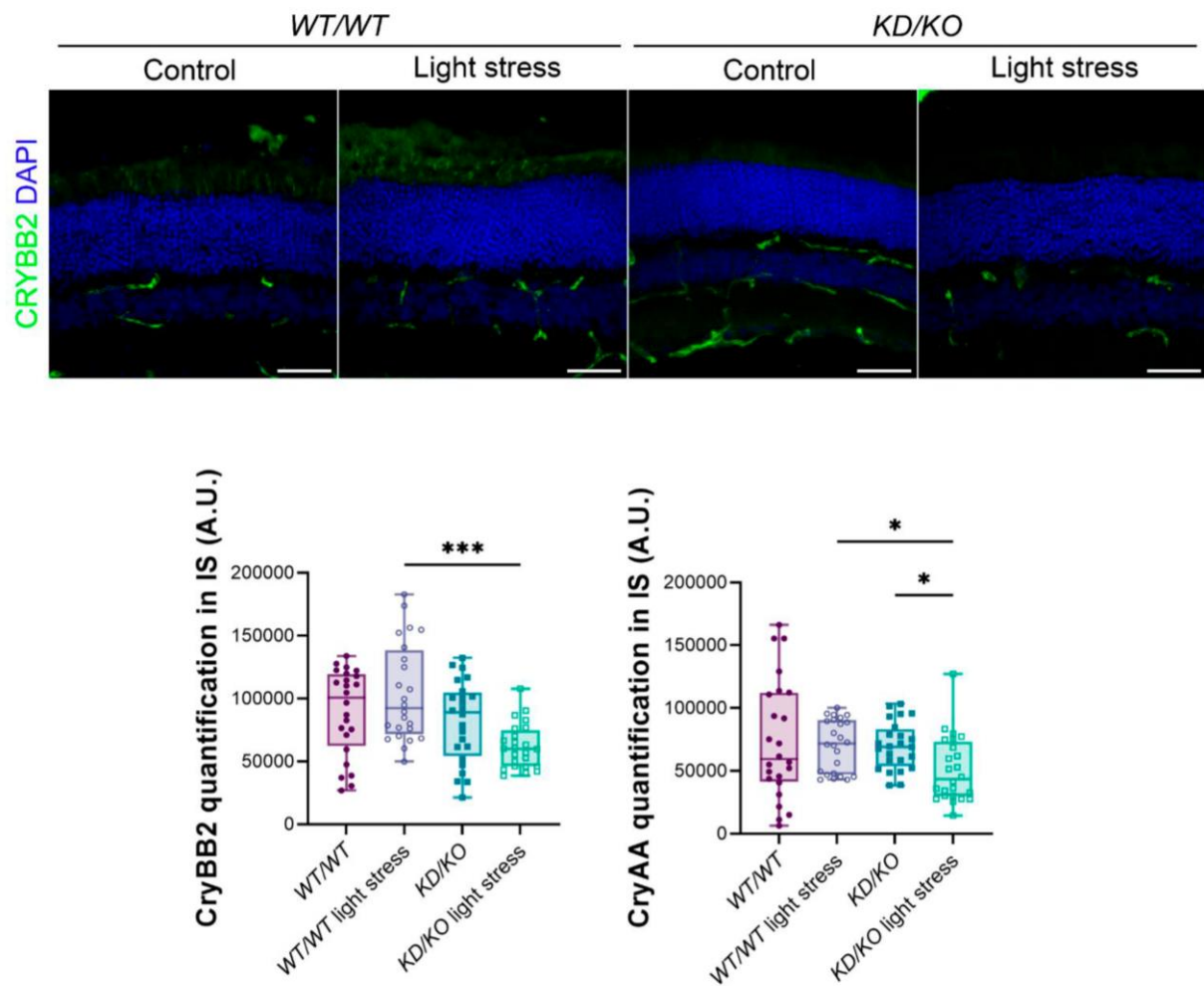
Supplementary Figure 2. CRYBB2 and CRYAA protein levels are significantly decreased in *KD/KO* retinas. Representative fluorescence image of *WT/WT* and *KD/KO* retinal slices in control and light-stress conditions immunodetecting CRYBB2 (green) and staining nuclei (DAPI in blue). Scale bar: 40 μm. Quantification of the levels of CryBB2 and CryAA proteins in the inner segment (IS) of photoreceptors of *WT/WT* and *KD/KO* retinas after light stress insult. n = 24 ROIs from 4 animals per genotype and condition. * *p-value* ≤ 0.05, *** *p-value* ≤ 0.005

3
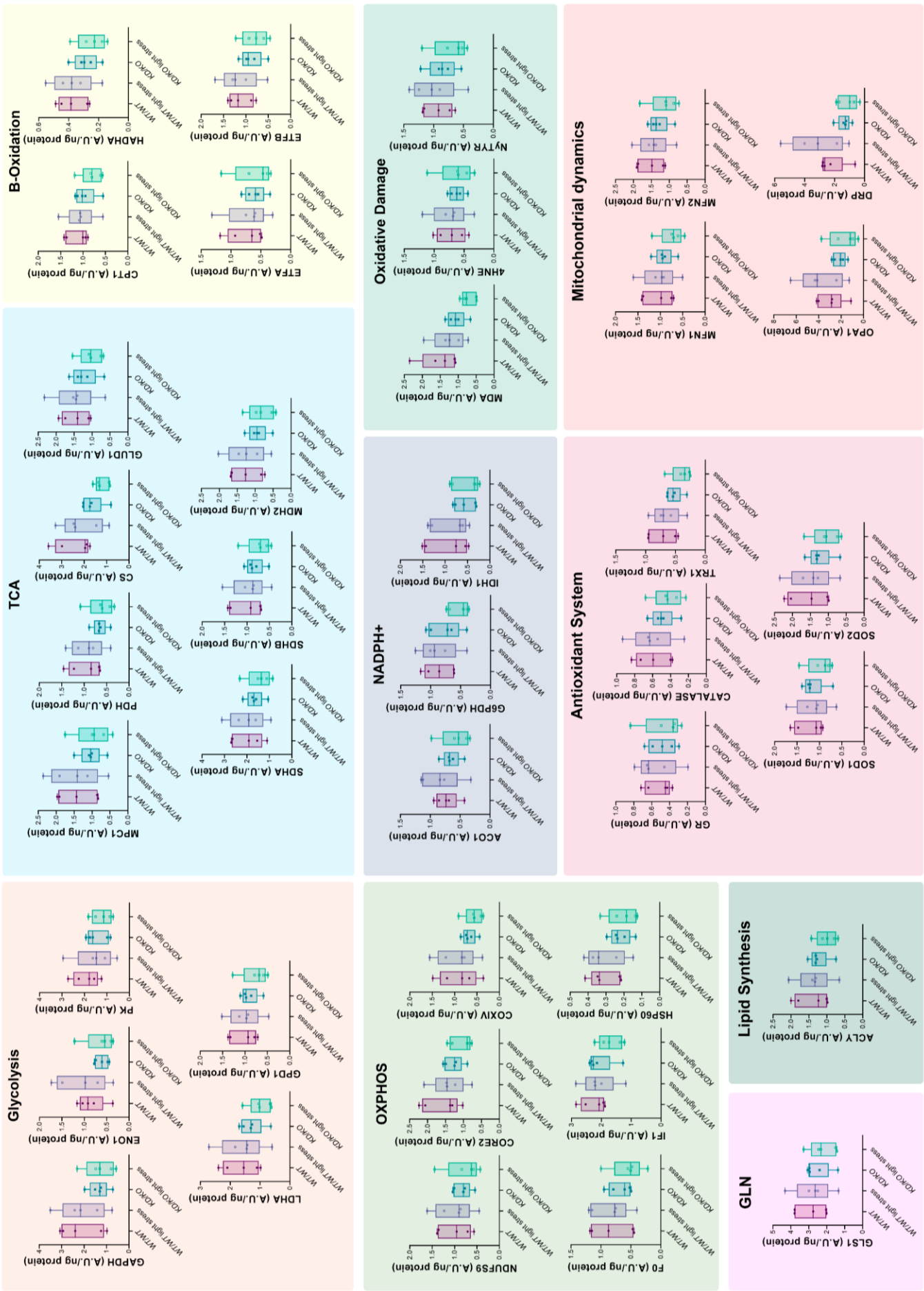
Supplementary Figure 3. Analysis of different proteins related to metabolic pathways in *WT/WT* and *KD/KO* retinas after light stress. All the proteins analysed by reverse phase protein in-house microarrays are clustered in different squares representing the pathways in which they are involved. The following pathways have been analysed: glycolysis, tricarboxylic acid cycle (TCA), B-oxidation, oxidative phosphorylation (OXPHOS), NADPH+, oxidative damage, glutamine (GLN), lipid synthesis, antioxidant system and mitochondrial dynamics.

5
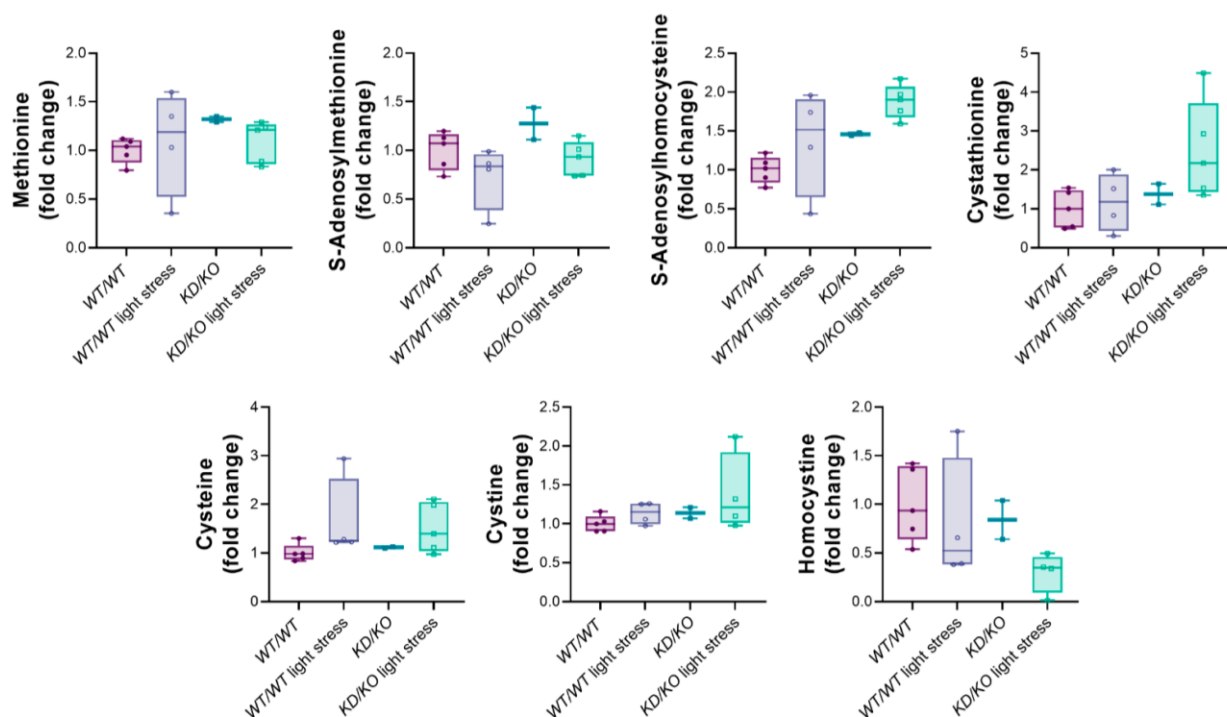
Supplementary Figure 4. Several metabolites of the glutathione metabolic pathway show no differences in retinal protein lysates neither by genotype nor by light stress conditions. In contrast to many glutathione pathway metabolites analysed in main Figure 3, some specific metabolites, i.e. methionine, S-adenosylmethionine, S-adenosylhomocysteine, cystathionine, cysteine, cystine and homocystine, do not show differences between *KD/KO* vs *WT/WT* retinas, either untreated or after light-stress injury.

6
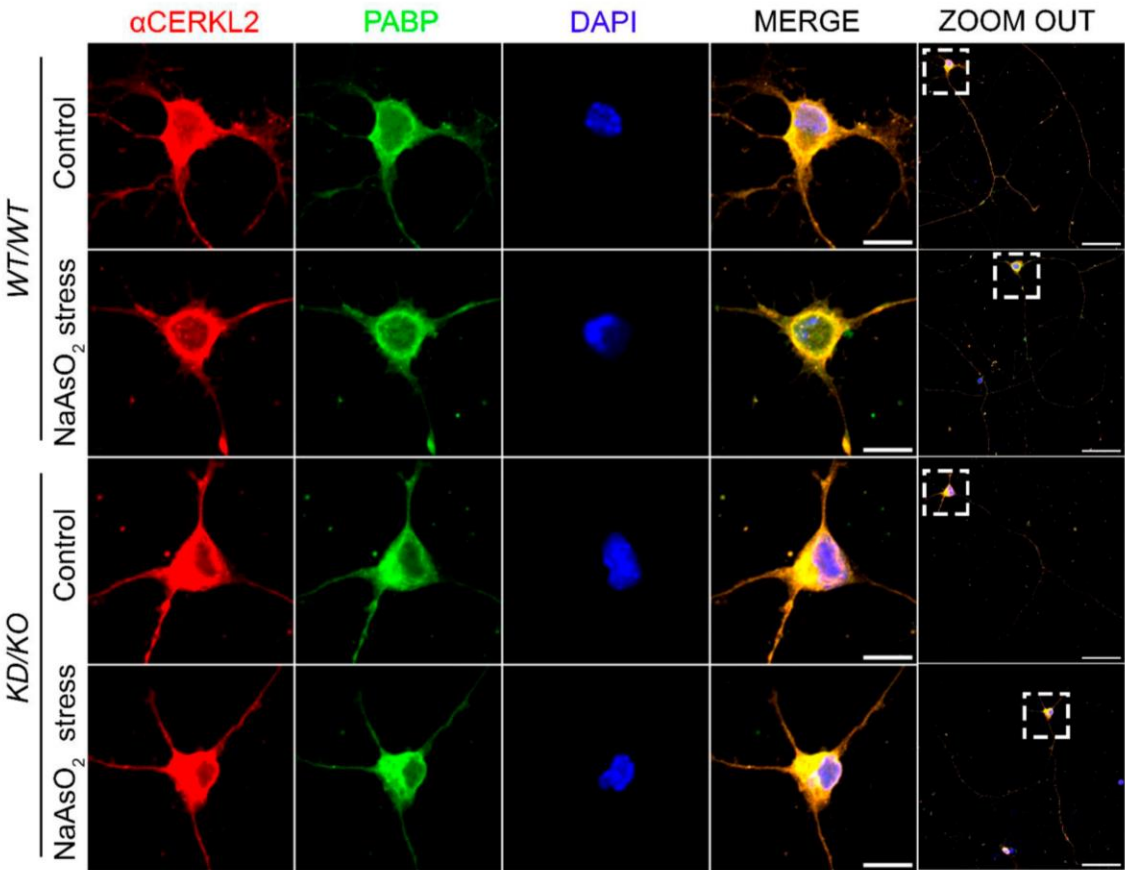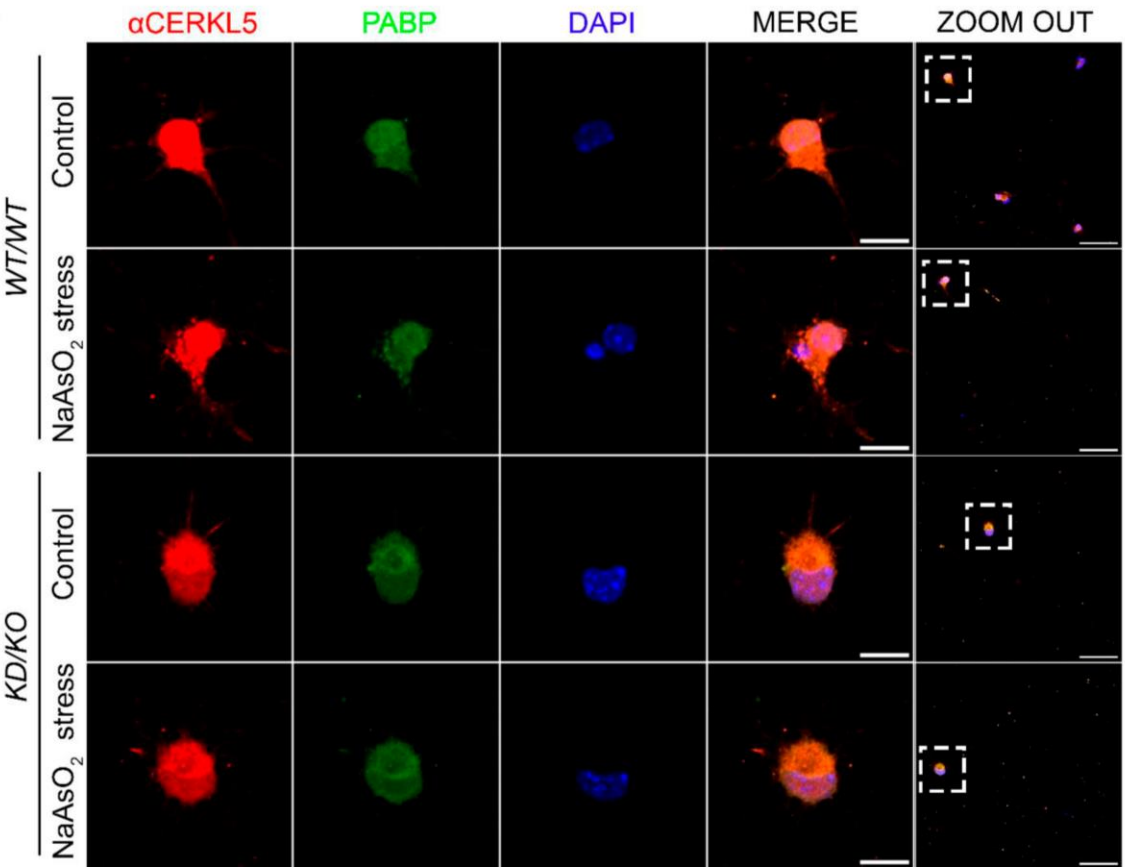
Supplementary Figure 5. CERKL and PABP localize in stress granules in *WT/WT* and *KD/KO* RGCs after sodium arsenite (NaAsO₂) treatment. Immunocytochemistry of RGCs detecting CERKL isoforms containing either an epitope peptide encoded in exon 2 with αCERKL2 (**A**) or in exon 5 with αCERKL5 (**B**) (red), PABP (green) and nuclei (DAPI in blue). Scale bar: 10 μm. Zoomed-out images show whole RGCs. Scale bar: 40 μm.

8
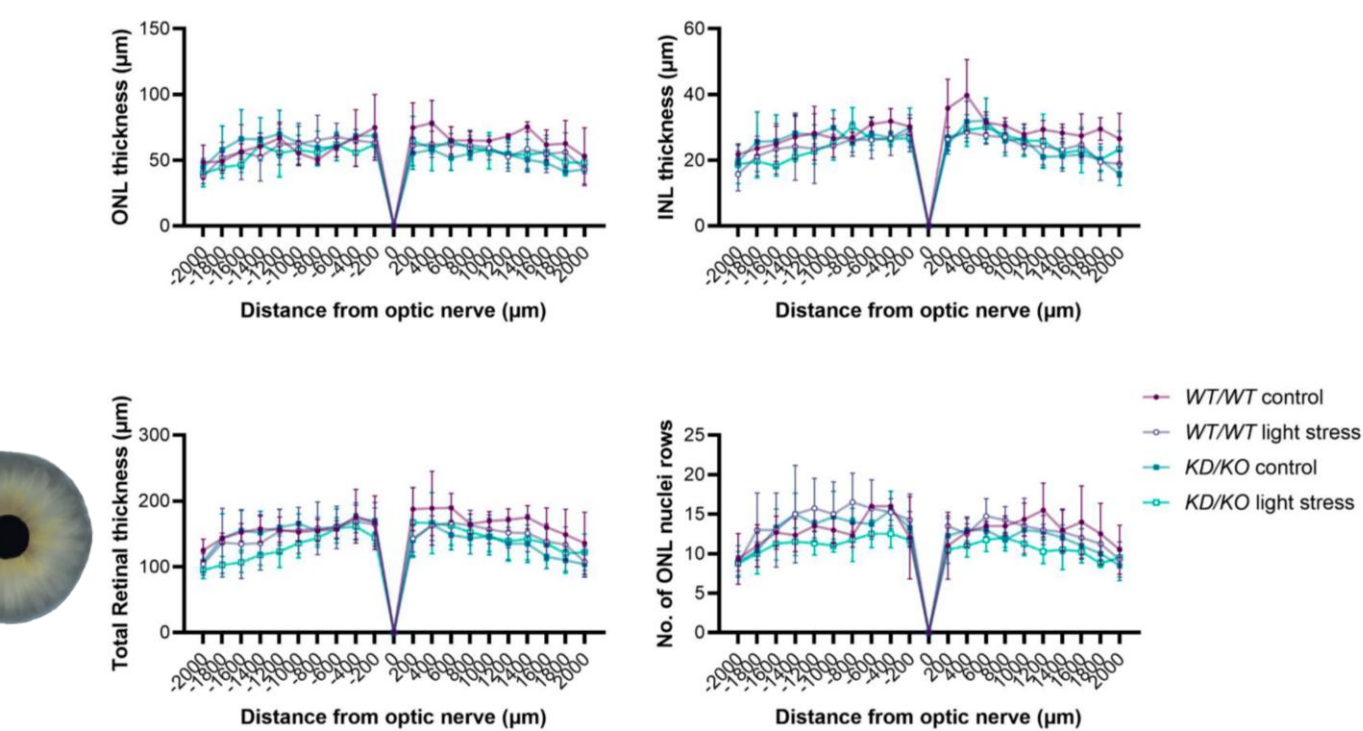
Supplementary Figure 6. Morphometrical measurements of *WT/WT* and *KD/KO* retinas two weeks after light-stress injury. Morphological measurements of outer nuclear layer (ONL), inner nuclear layer (INL) and total retina thickness as well as number of photoreceptor nuclear rows.

9

Supplementary Table 1. Top 75 most enriched of GO Biological Processes in the upregulated DE genes between *WT/WT* and *KD/KO* retinas. Pathways related to stress and inflammatory response are highlighted in bold.

Index	Term	Overlap	P-value	Adjusted P-value	Odds Ratio	Combined score
1	**Positive Regulation Of Endoplasmic Reticulum Stress-Induced Intrinsic Apoptotic Signaling Pathway (GO:1902237)**	3/6	1.87E-05	0.00963911	101.533333	1105.39984
2	**Regulation Of Transcription From RNA Polymerase II Promoter In Response To Stress (GO:0043618)**	3/12	1.97E-04	0.05379995	33.834188	288.709815
3	**Regulation Of DNA-templated Transcription In Response To Stress (GO:0043620)**	2/7	0.00198195	0.18576232	40.4020408	251.44923
4	Negative Regulation Of Bone Resorption (GO:0045779)	2/9	0.00335357	0.2668989	28.8556851	164.411931
5	**Positive Regulation Of Transcription From RNA Polymerase II Promoter In Response To Stress (GO:0036003)**	3/17	5.87E-04	0.10080183	21.7450549	161.807646
6	**Positive Regulation Of Response To Endoplasmic Reticulum Stress (GO:1905898)**	3/18	6.99E-04	0.10292857	20.294359	147.460728
7	**Positive Regulation Of Interleukin-13 Production (GO:0032736)**	2/10	0.00416472	0.27000428	25.247449	138.38393
8	**Positive Regulation Of Transcription From RNA Polymerase II Promoter In Response To Endoplasmic Reticulum Stress (GO:1990440)**	2/10	0.00416472	0.27000428	25.247449	138.38393
9	**Intrinsic Apoptotic Signaling Pathway In Response To Endoplasmic Reticulum Stress (GO:0070059)**	4/30	2.09E-04	0.05379995	15.6827914	132.903391
10	Negative Regulation Of Bone Remodeling (GO:0046851)	2/11	0.00505717	0.29116282	22.4410431	118.644622
11	Cellular Response To Leucine Starvation (GO:1990253)	2/12	0.00602924	0.31080741	20.1959184	103.224046
12	**Intrinsic Apoptotic Signaling Pathway (GO:0097193)**	8/105	9.83E-06	0.00963911	8.55344547	98.6220743
13	**Regulation Of Endoplasmic Reticulum Stress-Induced Intrinsic Apoptotic Signaling Pathway (GO:1902235)**	3/24	0.0016593	0.17107369	14.4915751	92.7657928
14	Lipid Oxidation (GO:0034440)	2/13	0.00707928	0.33176093	18.3589981	90.877382
15	Regulation Of Epinephrine Secretion (GO:0014060)	1/5	0.04853408	0.43311385	25.1243655	76.0134927
16	Negative Regulation Of Lipoprotein Lipase Activity (GO:0051005)	1/5	0.04853408	0.43311385	25.1243655	76.0134927
17	**PERK-mediated Unfolded Protein Response (GO:0036499)**	1/5	0.04853408	0.43311385	25.1243655	76.0134927
18	Regulation Of Guanylate Cyclase Activity (GO:0031282)	1/5	0.04853408	0.43311385	25.1243655	76.0134927
19	Activation Of Cysteine-Type Endopeptidase Activity Involved In Apoptotic Process By Cytochrome C (GO:0008635)	1/5	0.04853408	0.43311385	25.1243655	76.0134927
20	**Regulation Of Translation In Response To Endoplasmic Reticulum Stress (GO:0036490)**	1/5	0.04853408	0.43311385	25.1243655	76.0134927
21	**Positive Regulation Of NK T Cell Proliferation (GO:0051142)**	1/5	0.04853408	0.43311385	25.1243655	76.0134927
22	**Positive Regulation Of T-helper 2 Cell Differentiation (GO:0045630)**	1/5	0.04853408	0.43311385	25.1243655	76.0134927
23	Positive Regulation Of Cholesterol Biosynthetic Process (GO:0045542)	1/5	0.04853408	0.43311385	25.1243655	76.0134927
24	**Positive Regulation Of Extrinsic Apoptotic Signaling Pathway Via Death Domain Receptors (GO:1902043)**	1/5	0.04853408	0.43311385	25.1243655	76.0134927
25	Positive Regulation Of Osteoblast Proliferation (GO:0033690)	1/5	0.04853408	0.43311385	25.1243655	76.0134927

	Term	Overlap	P-value	Adjusted P-value		
26	Positive Regulation Of Sterol Biosynthetic Process (GO:0106120)	1/5	0.04853408	0.43311385	25.1243655	76.0134927
27	**Regulation Of Interleukin-13 Production (GO:0032656)**	2/15	0.00940681	0.35920088	15.532967	72.481812
28	Negative Regulation Of Protein Processing (GO:0010955)	2/15	0.00940681	0.35920088	15.532967	72.481812
29	Intermediate Filament Organization (GO:0045109)	5/68	5.68E-04	0.10080183	8.11703265	60.655017
30	**ATF6-mediated Unfolded Protein Response (GO:0036500)**	1/6	0.05795593	0.43311385	20.0984772	57.2419192
31	G Protein-Coupled Receptor Internalization (GO:0002031)	1/6	0.05795593	0.43311385	20.0984772	57.2419192
32	Negative Regulation Of Plasminogen Activation (GO:0010757)	1/6	0.05795593	0.43311385	20.0984772	57.2419192
33	Adult Feeding Behavior (GO:0008343)	1/6	0.05795593	0.43311385	20.0984772	57.2419192
34	Auditory Receptor Cell Morphogenesis (GO:0002093)	1/6	0.05795593	0.43311385	20.0984772	57.2419192
35	Auditory Receptor Cell Stereocilium Organization (GO:0060088)	1/6	0.05795593	0.43311385	20.0984772	57.2419192
36	Regulation Of Osteoclast Development (GO:2001204)	1/6	0.05795593	0.43311385	20.0984772	57.2419192
37	**Bleb Assembly (GO:0032060)**	1/6	0.05795593	0.43311385	20.0984772	57.2419192
38	Regulation Of Striated Muscle Cell Differentiation (GO:0051153)	1/6	0.05795593	0.43311385	20.0984772	57.2419192
39	Positive Regulation Of Aspartic-Type Endopeptidase Activity Involved In Amyloid Precursor Protein Catabolic Process (GO:1902961)	1/6	0.05795593	0.43311385	20.0984772	57.2419192
40	Serine Transport (GO:0032329)	1/6	0.05795593	0.43311385	20.0984772	57.2419192
41	Smooth Muscle Cell Migration (GO:0014909)	1/6	0.05795593	0.43311385	20.0984772	57.2419192
42	Hepatocyte Growth Factor Receptor Signaling Pathway (GO:0048012)	1/6	0.05795593	0.43311385	20.0984772	57.2419192
43	Host-Mediated Regulation Of Intestinal Microbiota Composition (GO:0048874)	1/6	0.05795593	0.43311385	20.0984772	57.2419192
44	Positive Regulation Of Striated Muscle Contraction (GO:0045989)	1/6	0.05795593	0.43311385	20.0984772	57.2419192
45	**Regulation Of NK T Cell Proliferation (GO:0051140)**	1/6	0.05795593	0.43311385	20.0984772	57.2419192
46	**Regulation Of T-helper Cell Differentiation (GO:0045622)**	1/6	0.05795593	0.43311385	20.0984772	57.2419192
47	Negative Regulation Of Blood Vessel Endothelial Cell Proliferation Involved In Sprouting Angiogenesis (GO:1903588)	1/6	0.05795593	0.43311385	20.0984772	57.2419192
48	**Signal Transduction By P53 Class Mediator (GO:0072331)**	3/33	0.00419017	0.27000428	10.1394872	55.5138264
49	Positive Regulation Of Epidermal Cell Differentiation (GO:0045606)	2/18	0.0134431	0.38237934	12.6186224	54.3772966
50	Regulation Of Megakaryocyte Differentiation (GO:0045652)	2/19	0.01492772	0.38237934	11.8757503	49.9320115
51	**Release Of Cytochrome C From Mitochondria (GO:0001836)**	2/19	0.01492772	0.38237934	11.8757503	49.9320115
52	Establishment Of Skin Barrier (GO:0061436)	2/19	0.01492772	0.38237934	11.8757503	49.9320115
53	Negative Regulation Of Cyclin-Dependent Protein Serine/Threonine Kinase Activity (GO:0045736)	2/19	0.01492772	0.38237934	11.8757503	49.9320115
54	Negative Regulation Of Cyclin-Dependent Protein Kinase Activity (GO:1904030)	2/20	0.01647945	0.39512359	11.2154195	46.0464867

11

55	Regulation Of Cilium Beat Frequency (GO:0003356)	1/7	0.06728494	0.43311385	16.7478849	45.1995071
56	ER Overload Response (GO:0006983)	1/7	0.06728494	0.43311385	16.7478849	45.1995071
57	Negative Regulation Of Mitochondrial Membrane Potential (GO:0010917)	1/7	0.06728494	0.43311385	16.7478849	45.1995071
58	SREBP Signaling Pathway (GO:0032933)	1/7	0.06728494	0.43311385	16.7478849	45.1995071
59	T-helper 17 Cell Lineage Commitment (GO:0072540)	1/7	0.06728494	0.43311385	16.7478849	45.1995071
60	Nonribosomal Peptide Biosynthetic Process (GO:0019184)	1/7	0.06728494	0.43311385	16.7478849	45.1995071
61	Peptidyl-Lysine Deacetylation (GO:0034983)	1/7	0.06728494	0.43311385	16.7478849	45.1995071
62	Peptidyl-Tyrosine Dephosphorylation Involved In Inactivation Of Protein Kinase Activity (GO:1990264)	1/7	0.06728494	0.43311385	16.7478849	45.1995071
63	Regulation Of Skeletal Muscle Fiber Development (GO:0048742)	1/7	0.06728494	0.43311385	16.7478849	45.1995071
64	Positive Regulation Of Aspartic-Type Peptidase Activity (GO:1905247)	1/7	0.06728494	0.43311385	16.7478849	45.1995071
65	Cytochrome Complex Assembly (GO:0017004)	1/7	0.06728494	0.43311385	16.7478849	45.1995071
66	Positive Regulation Of Epithelial Tube Formation (GO:1905278)	1/7	0.06728494	0.43311385	16.7478849	45.1995071
67	Stress-Induced Premature Senescence (GO:0090400)	1/7	0.06728494	0.43311385	16.7478849	45.1995071
68	Fatty Acid Alpha-Oxidation (GO:0001561)	1/7	0.06728494	0.43311385	16.7478849	45.1995071
69	Glycine Metabolic Process (GO:0006544)	1/7	0.06728494	0.43311385	16.7478849	45.1995071
70	Positive Regulation Of Natural Killer Cell Proliferation (GO:0032819)	1/7	0.06728494	0.43311385	16.7478849	45.1995071
71	Ventricular Cardiac Muscle Cell Membrane Repolarization (GO:0099625)	1/7	0.06728494	0.43311385	16.7478849	45.1995071
72	Hepoxilin Biosynthetic Process (GO:0051122)	1/7	0.06728494	0.43311385	16.7478849	45.1995071
73	Hepoxilin Metabolic Process (GO:0051121)	1/7	0.06728494	0.43311385	16.7478849	45.1995071
74	Histone Lysine Demethylation (GO:0070076)	1/7	0.06728494	0.43311385	16.7478849	45.1995071
75	Positive Regulation Of Ryanodine-Sensitive Calcium-Release Channel Activity (GO:0060316)	1/7	0.06728494	0.43311385	16.7478849	45.1995071

——217——

Supplementary Table 2. Top 75 most enriched of GO Biological Processes in the downregulated DE genes between *WT/WT* and *KD/KO* retinas. Genes involved in organ development and differentiation are highlighted in bold. Genes relevant for ocular and retinal function and physiology (visual cycle and sensory perception) are indicated in green. In orange, pathways related to regulation of apoptosis.

Index	Term	Overlap	P-value	Adjusted P-value	Odds Ratio	Combined Score
1	**Regulation Of Basement Membrane Organization (GO:0110011)**	5/5	3.42E-07	8.51E-05	94900	1412972.96
2	**Regulation Of Type B Pancreatic Cell Proliferation (GO:0061469)**	4/5	3.23E-05	0.00248698	74.7204724	772.715697
3	**Positive Regulation Of Integrin-Mediated Signaling Pathway (GO:2001046)**	7/12	5.56E-07	1.20E-04	26.2240869	377.706593
4	**Basement Membrane Organization (GO:0071711)**	6/10	3.05E-06	3.80E-04	28.0710059	356.503373
5	**Elastic Fiber Assembly (GO:0048251)**	4/6	9.29E-05	0.00546631	37.3582677	346.842425
6	Gamma-Aminobutyric Acid Transport (GO:0015812)	4/6	9.29E-05	0.00546631	37.3582677	346.842425
7	**Extracellular Matrix Organization (GO:0030198)**	42/176	2.27E-17	7.35E-14	6.03983152	231.471306
8	Aromatic Compound Catabolic Process (GO:0019439)	4/7	2.08E-04	0.00922051	24.9041995	211.144464
9	Lens Fiber Cell Development (GO:0070307)	4/7	2.08E-04	0.00922051	24.9041995	211.144464
10	**Blood Vessel Endothelial Cell Proliferation Involved In Sprouting Angiogenesis (GO:0002043)**	3/5	0.00122392	0.02916467	27.9911504	187.700145
11	**Notochord Development (GO:0030903)**	3/5	0.00122392	0.02916467	27.9911504	187.700145
12	**Positive Regulation Of Extrinsic Apoptotic Signaling Pathway Via Death Domain Receptors (GO:1902043)**	3/5	0.00122392	0.02916467	27.9911504	187.700145
13	Collagen Fibril Organization (GO:0030199)	14/42	1.02E-08	7.90E-06	9.4194831	173.329966
14	**Positive Regulation Of Extracellular Matrix Assembly (GO:1901203)**	4/8	3.99E-04	0.01360093	18.6771654	146.17481
15	**Regulation Of Actin Cytoskeleton Reorganization (GO:2000249)**	9/25	2.19E-06	3.01E-04	10.5511869	137.480649
16	**Cartilage Development (GO:0051216)**	15/52	2.81E-08	1.14E-05	7.64138766	132.867437
17	**Positive Regulation Of Muscle Cell Differentiation (GO:0051149)**	6/15	5.83E-05	0.00370038	12.4727153	121.607681
18	**Canonical Wnt Signaling Pathway (GO:0060070)**	17/65	1.72E-08	9.27E-06	6.68502825	119.521856
19	**Embryonic Digestive Tract Development (GO:0048566)**	7/19	2.58E-05	0.00208685	10.9226719	115.404816
20	**Regulation Of Integrin-Mediated Signaling Pathway (GO:2001044)**	7/19	2.58E-05	0.00208685	10.9226719	115.404816
21	**Regulation Of Extracellular Matrix Organization (GO:1903053)**	8/23	1.10E-05	0.00114746	9.99472991	114.126039
22	**Bleb Assembly (GO:0032060)**	3/6	0.00235497	0.0428196	18.6597837	112.914593
23	**Gland Morphogenesis (GO:0022612)**	3/6	0.00235497	0.0428196	18.6597837	112.914593
24	**Glandular Epithelial Cell Development (GO:0002068)**	3/6	0.00235497	0.0428196	18.6597837	112.914593

13

#	Term	Overlap	P-value	Adjusted P-value	Odds Ratio	Combined Score
25	**Maintenance Of Protein Location In Extracellular Region (GO:0071694)**	3/6	0.00235497	0.0428196	18.6597837	112.914593
26	Sulfur Amino Acid Catabolic Process (GO:0000098)	3/6	0.00235497	0.0428196	18.6597837	112.914593
27	**Type B Pancreatic Cell Development (GO:0003323)**	3/6	0.00235497	0.0428196	18.6597837	112.914593
28	**Embryonic Eye Morphogenesis (GO:0048048)**	4/9	6.89E-04	0.02010212	14.9409449	108.767124
29	Mesenchymal To Epithelial Transition (GO:0060231)	4/9	6.89E-04	0.02010212	14.9409449	108.767124
30	**Negative Regulation Of Extracellular Matrix Organization (GO:1903054)**	4/9	6.89E-04	0.02010212	14.9409449	108.767124
31	**Wnt Signaling Pathway (GO:0016055)**	18/76	3.55E-08	1.28E-05	5.86062358	100.539151
32	**Extracellular Structure Organization (GO:0043062)**	23/109	5.10E-09	6.62E-06	5.06825127	96.7768978
33	External Encapsulating Structure Organization (GO:0045229)	23/110	6.14E-09	6.62E-06	5.00973034	94.7285992
34	Negative Regulation Of Fibroblast Growth Factor Receptor Signaling Pathway (GO:0040037)	5/13	3.12E-04	0.01209621	11.682266	94.3130231
35	**Extracellular Matrix Assembly (GO:0085029)**	6/17	1.32E-04	0.00689212	10.2038731	91.1475642
36	Acidic Amino Acid Transport (GO:0015800)	4/10	0.00110258	0.02788331	12.4501312	84.7866245
37	**Lens Fiber Cell Differentiation (GO:0070306)**	4/10	0.00110258	0.02788331	12.4501312	84.7866245
38	Endodermal Cell Differentiation (GO:0035987)	9/31	1.64E-05	0.00151775	7.67116267	84.5176288
39	Sprouting Angiogenesis (GO:0002040)	13/52	1.45E-06	2.35E-04	6.26977822	84.2284744
40	Positive Regulation Of Epithelial Cell Proliferation (GO:0050679)	24/123	1.22E-08	7.90E-06	4.5955945	83.736715
41	Regulation Of Wnt Signaling Pathway (GO:0030111)	22/109	2.58E-08	1.14E-05	4.78711446	83.6377245
42	Carboxylic Acid Transport (GO:0046942)	13/53	1.83E-06	2.83E-04	6.11271102	80.7468338
43	Regulation Of Collagen Biosynthetic Process (GO:0032965)	6/18	1.89E-04	0.0087628	9.3530572	80.1664273
44	Regulation Of Oligodendrocyte Differentiation (GO:0048713)	6/18	1.89E-04	0.0087628	9.3530572	80.1664273
45	Ureteric Bud Development (GO:0001657)	6/18	1.89E-04	0.0087628	9.3530572	80.1664273
46	Ureteric Bud Morphogenesis (GO:0060675)	6/18	1.89E-04	0.0087628	9.3530572	80.1664273
47	Cell Surface Receptor Signaling Pathway Involved In Cell-Cell Signaling (GO:1905114)	8/27	4.15E-05	0.00298257	7.888912	79.6047229
48	Respiratory Tube Development (GO:0030323)	8/27	4.15E-05	0.00298257	7.888912	79.6047229
49	Regulation Of Osteoblast Differentiation (GO:0045667)	18/85	2.21E-07	5.96E-05	5.07096255	77.7127482
50	**Negative Regulation Of Striated Muscle Cell Apoptotic Process (GO:0010664)**	3/7	0.00396525	0.05970009	13.9941003	77.3899779
51	Positive Regulation Of Fibroblast Migration (GO:0010763)	3/7	0.00396525	0.05970009	13.9941003	77.3899779
52	**Postsynapse Organization (GO:0099173)**	3/7	0.00396525	0.05970009	13.9941003	77.3899779
53	Regulation Of Extracellular Matrix Constituent Secretion (GO:0003330)	3/7	0.00396525	0.05970009	13.9941003	77.3899779

14

54	Regulation Of Mesenchymal Stem Cell Differentiation (GO:2000739)	3/7	0.00396525	0.05970009	13.9941003	77.3899779
55	Regulation Of Transforming Growth Factor Beta Activation (GO:1901388)	3/7	0.00396525	0.05970009	13.9941003	77.3899779
56	Cell-Cell Signaling By Wnt (GO:0198738)	7/23	1.05E-04	0.00585148	8.19027641	75.0476652
57	Glial Cell Development (GO:0021782)	7/23	1.05E-04	0.00585148	8.19027641	75.0476652
58	Sensory Perception Of Light Stimulus (GO:0050953)	20/102	1.82E-07	5.36E-05	4.60926829	71.5291949
59	Odontogenesis (GO:0042476)	10/39	1.87E-05	0.00168111	6.47012632	70.4414637
60	Positive Regulation Of Collagen Biosynthetic Process (GO:0032967)	5/15	6.68E-04	0.02001841	9.34482759	68.323527
61	Regulation Of Muscle Cell Differentiation (GO:0051147)	7/24	1.42E-04	0.00727212	7.70808896	68.3166046
62	Positive Regulation Of Vascular Permeability (GO:0043117)	4/11	0.00166295	0.03414105	10.6709786	68.2853002
63	Regulation Of Epithelial Cell Apoptotic Process (GO:1904035)	4/11	0.00166295	0.03414105	10.6709786	68.2853002
64	Regulation Of Phospholipase C Activity (GO:1900274)	4/11	0.00166295	0.03414105	10.6709786	67.9602007
65	Chondrocyte Differentiation (GO:0002062)	8/29	7.32E-05	0.00455605	7.1363418	66.7984503
66	Embryonic Organ Development (GO:0048568)	16/77	1.35E-06	2.30E-04	4.94259029	64.5857735
67	Regulation Of Kinase Activity (GO:0043549)	17/85	1.12E-06	2.02E-04	4.71385842	63.5095137
68	Positive Regulation Of Phospholipase Activity (GO:0010518)	6/20	3.62E-04	0.01265522	8.01606086	63.5095137
69	Pulmonary Valve Development (GO:0003177)	6/20	3.62E-04	0.01265522	8.01606086	63.0190375
70	Non-Canonical Wnt Signaling Pathway (GO:0035567)	10/41	3.00E-05	0.00237207	6.05206004	61.8778651
71	Visual Perception (GO:0007601)	19/101	7.19E-07	1.45E-04	4.37443045	60.3276516
72	Skeletal System Development (GO:0001501)	25/149	1.39E-07	4.50E-05	3.82071649	59.288444
73	Mesonephric Tubule Development (GO:0072164)	5/16	9.31E-04	0.02532252	8.49484998	59.288444
74	Positive Regulation Of Collagen Metabolic Process (GO:0010714)	5/16	9.31E-04	0.02532252	8.49484998	57.3076693
75	Positive Regulation Of Phosphatidylinositol 3-Kinase Activity (GO:0043552)	7/26	2.46E-04	0.01036301	6.89598379	57.3076693

15
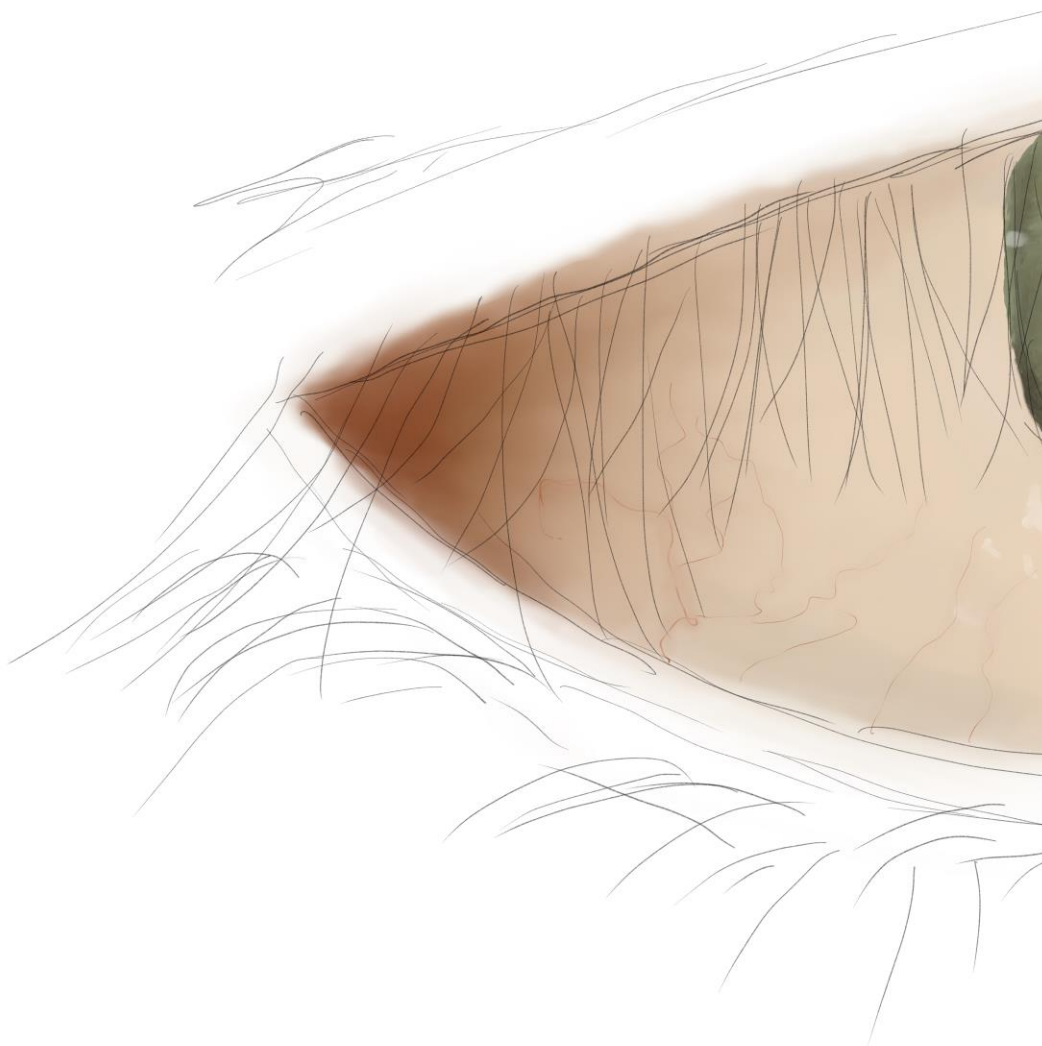
CHAPTER 3

Generation of *CERKL*[R257X] hiPSC-derived 3D retinal organoids
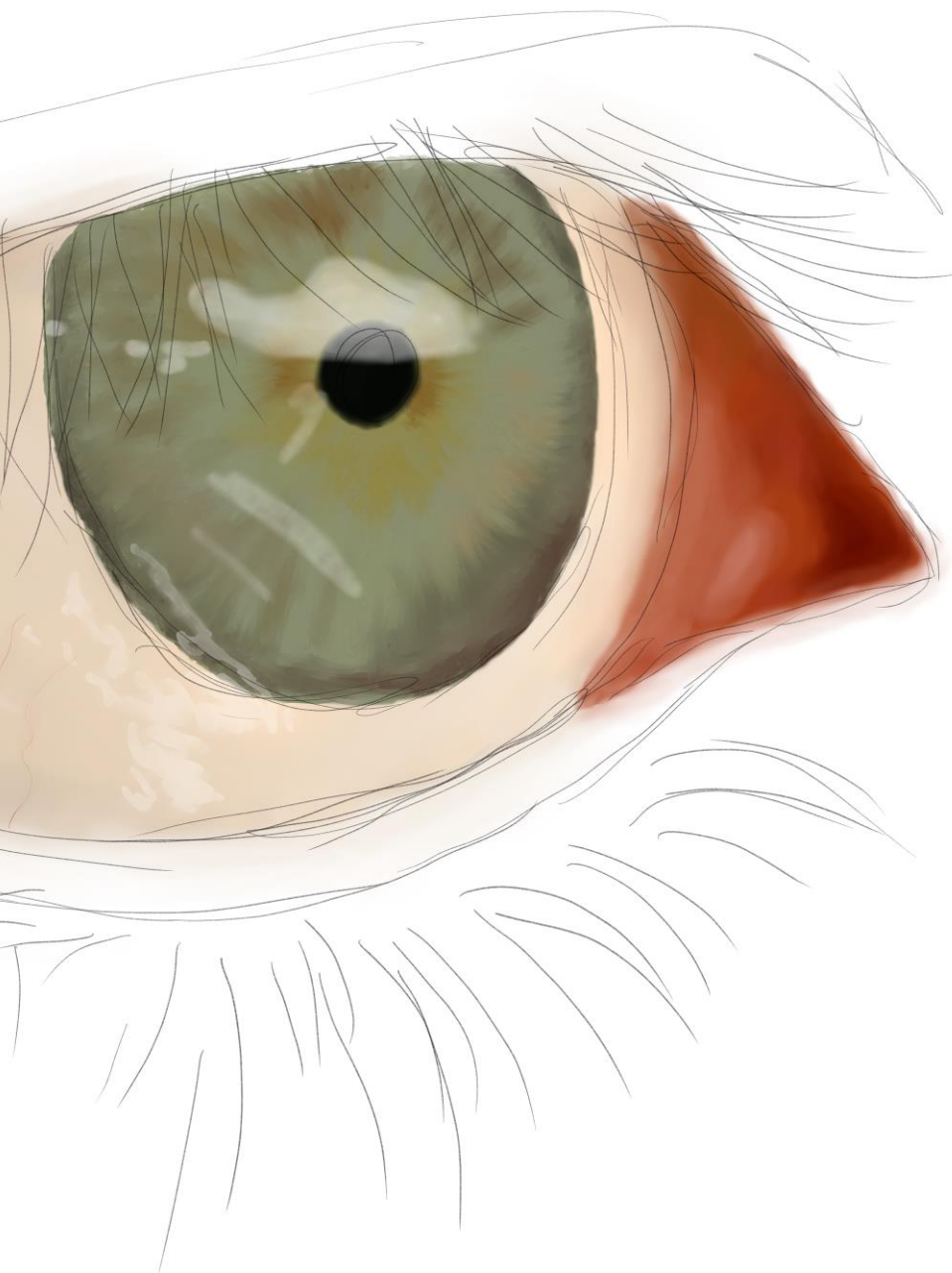
Background

In collaboration with the group led by Drs Dunja Lukovic and Slaven Erceg in CIPF (Centro de Investigación Príncipe Felipe), in Valencia, our research group contributed to the generation of a stable line of human induced pluripotent stem cells (hiPSCs) from a patient carrying the mutation $CERKL^{R257X}$ in homozygosis and their healthy sibling (222). To deeply dissect the phenotypic alterations derived from the mutation $CERKL^{R257X}$, patient's and sibling's hiPSC were differentiated into 3D retinal organoids. Analysis of initial timepoints showed correct differentiation and lamination of the retinal layers in both patient's and sibling's retinal organoids. In addition, $CERKL^{R257X}$ patient-derived retinal organoids presented aberrant PABP-mediated response to stress and increased cell apoptosis, especially in response to induced oxidative stress (223). These phenotypic features highly resemble the characteristic and already observed exacerbated stress response of the *KD/KO* mouse model, providing additional evidence to alterations in antioxidant defence mechanisms due to mutations in *CERKL*.

Furthermore, preliminary RNA-Seq studies from this first differentiation batch of retinal organoids indicated that several genes were differentially expressed between genotypes, but also conditions (control versus oxidative stress) (Figure 18). Despite sharing many of the most enriched Gene Ontology (GO) biological processes (including impaired visual cycle and altered response to oxidative stress), most of the differentially expressed genes in retinal organoids were different from those observed in the RNA-Seq analysis of the *KD/KO* mouse model (Results Chapter 2.2, Publication 4), suggesting that distinct pathways are activated depending on the specific *CERKL* mutation and/or the organism species. However, these analyses were performed using a very limited sample size and should be replicated to achieve statistical significance. Additionally, the sanitary crisis derived from COVID-19 pandemics caused the immediate halt of the retinal organoids' differentiation, without the possibility to achieve late stages where neurodegenerative –rather than developmental– traits could be assessed.
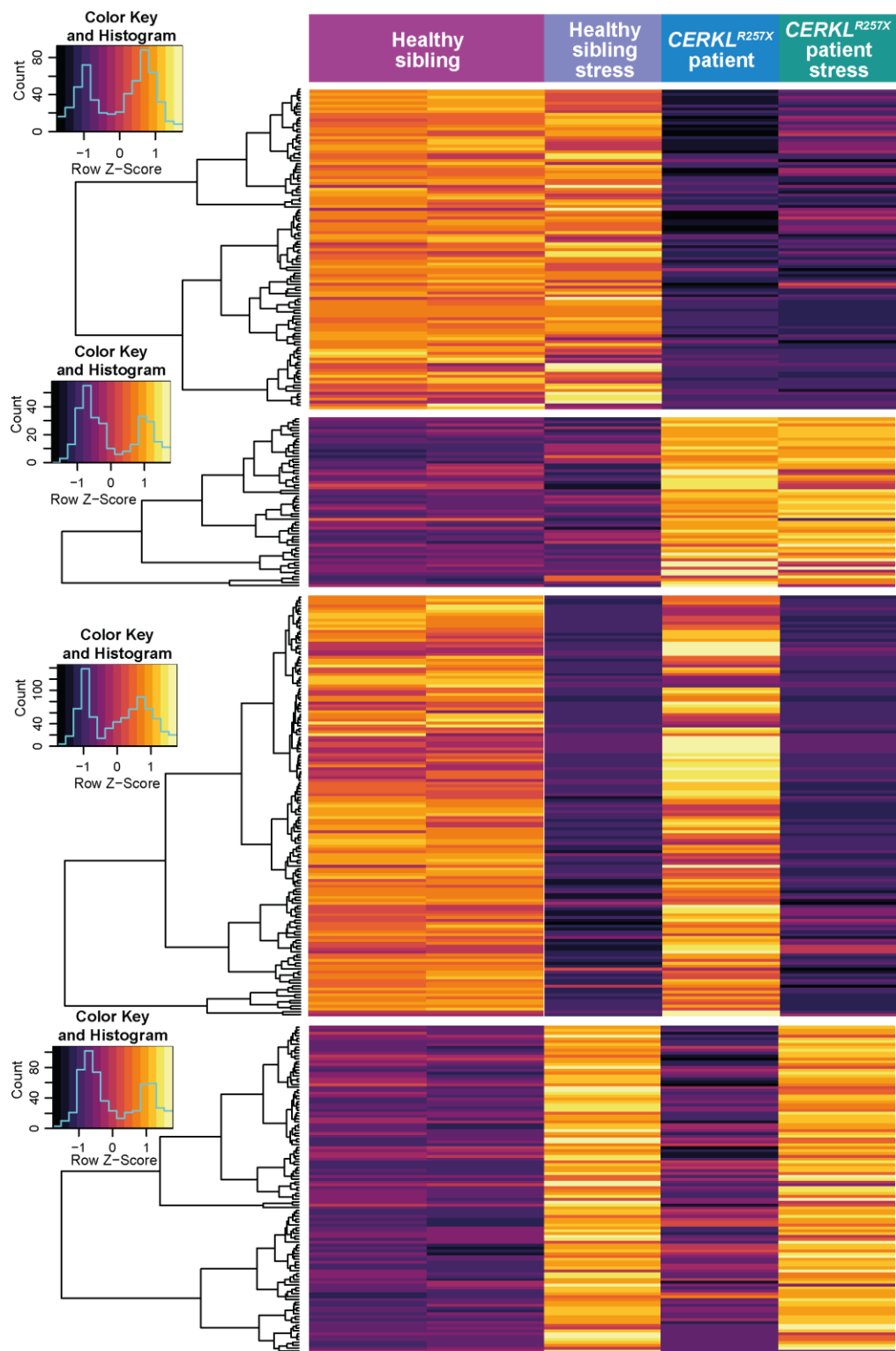
Figure 18. Heatmap showing hierarchical clustering of differentially expressed genes in *CERKL^R257X* patient's and sibling's retinal organoids. Each heatmap shows the differentially expressed genes that are up- or downregulated between genotypes or conditions (control versus oxidative stress).

Therefore, we will complement these preliminary results by differentiating *CERKL^R257X* patient's and sibling's hiPSC into 3D retinal organoids. Moreover, to overcome the limitation of the reduced sample size, we will also generate a *CERKL^R257X* hiPSC isogenic line using CRISPR/Cas9 system, to compare the phenotypic alterations derived from *CERKL^R257X* mutation using two different genetic backgrounds after differentiation into retinal organoids.

Strategy of CRISPR-Cas9 edition to generate of a *CERKL^R257X* isogenic hiPSC line

The obtention of a *CERKL^R257X* isogenic iPSC line would allow to increase the biological replicates in posterior experiments and verify if the phenotypic alterations observed are caused by this specific mutation in *CERKL*, regardless of the genetic background.
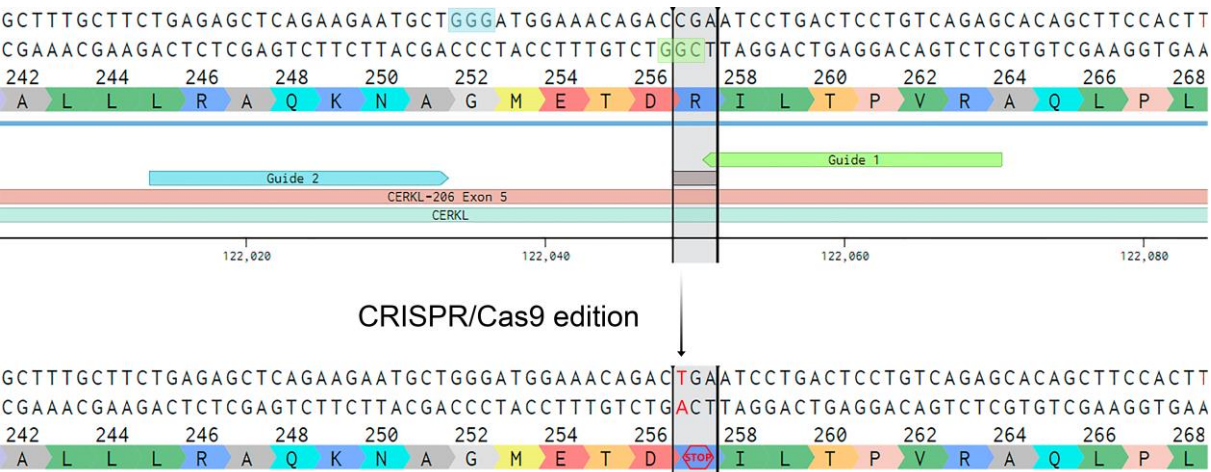
Figure 19. CRISPR/Cas9 edition strategy to introduce *CERKL^R257X* mutation. In the upper panel, the selected gRNAs (guide 1 in green and guide 2 in blue) and their recognized PAM sequences (PAM-guide 1 in green and PAM-guide 2 in blue), which are near the target region (in grey) in the exon 5 of *CERKL* gene. After CRISPR/Cas9 edition, we expect the introduction of the *CERKL^R257X* mutation (in red).

Therefore, we designed a gene-edition strategy based on CRISPR/Cas9 system to recreate the *CERKL^R257X* mutation in an isogenic hiPSC WT control line. Specifically, protospacer-adjacent motif (PAM) sequences (nucleotides: NGG) near the specific site of the mutation were identified and two guide RNAs (gRNAs) with high on-target and low off-target scores were selected (Figure 19). To induce the generation of this precise mutation, a single-stranded oligodeoxynucleotide (ssODN) template

including the *CERKL^R257X* mutation was used to favour homology-directed repair (HDR) of the DNA double-strand break and, therefore, generate the desired knock-in.

Genotyping approach to test efficiency of CRISPR/Cas9 gene-editing system

To distinguish between the wild-type and the correctly edited allele of *CERKL*, we have followed a genotyping outline described by Tuson *et al*. in 2004 (105). Briefly, it consists of a PCR using a primer that generates an enzymatic restriction site recognized by EcoRII enzyme in the wild-type allele, but not in the *CERKL^R257X* allele. Consequently, upon enzymatic digestion with EcoRII, wild-type alleles will be cut producing two bands, whereas *CERKL^R257X* alleles will remain undigested (Figure 20). Thus, solely performing a PCR followed by an enzymatic digestion, we were able to correctly genotype the colonies derived from CRISPR/Cas9 edition and, subsequently, select those that included the precise gene edition.
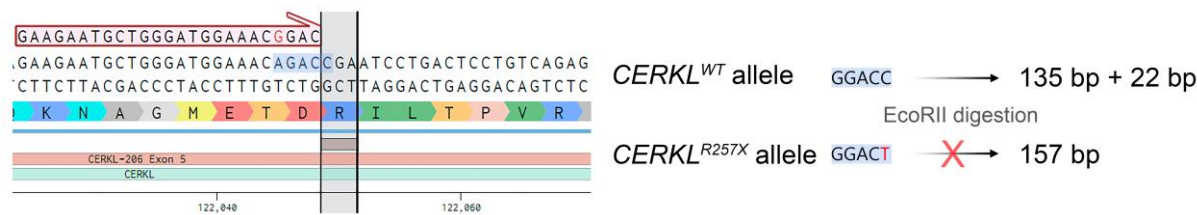
Figure 20. Genotyping strategy to assess the introduction of the *CERKL^R257X* mutation. In the left panel, sequence of *CERKL* showing the edition-target region (grey) and the primer used to introduce the point mutation (red) which generates a restriction site (blue). In the right panel, restriction site generated in the *CERKL^WT* and *CERKL^R257X* alleles (blue). EcoRII restriction enzyme only recognizes *CERKL^WT* allele, generating a 135-bp + 22-bp bands.

Our strategy for the gene edition was to produce ribonucleoproteins (RNPs) with the selected gRNAs and the protein Cas9 and deliver them into hiPSC by nucleofection. However, after carrying out the gene-edition experiment several times, we were not able to obtain any percentage of gene-edited cells in the mixed population of hiPSC neither by PCR followed by enzymatic digestion (Figure 21A) nor by Sanger sequencing (Figure 21B), even when we used both gRNAs.
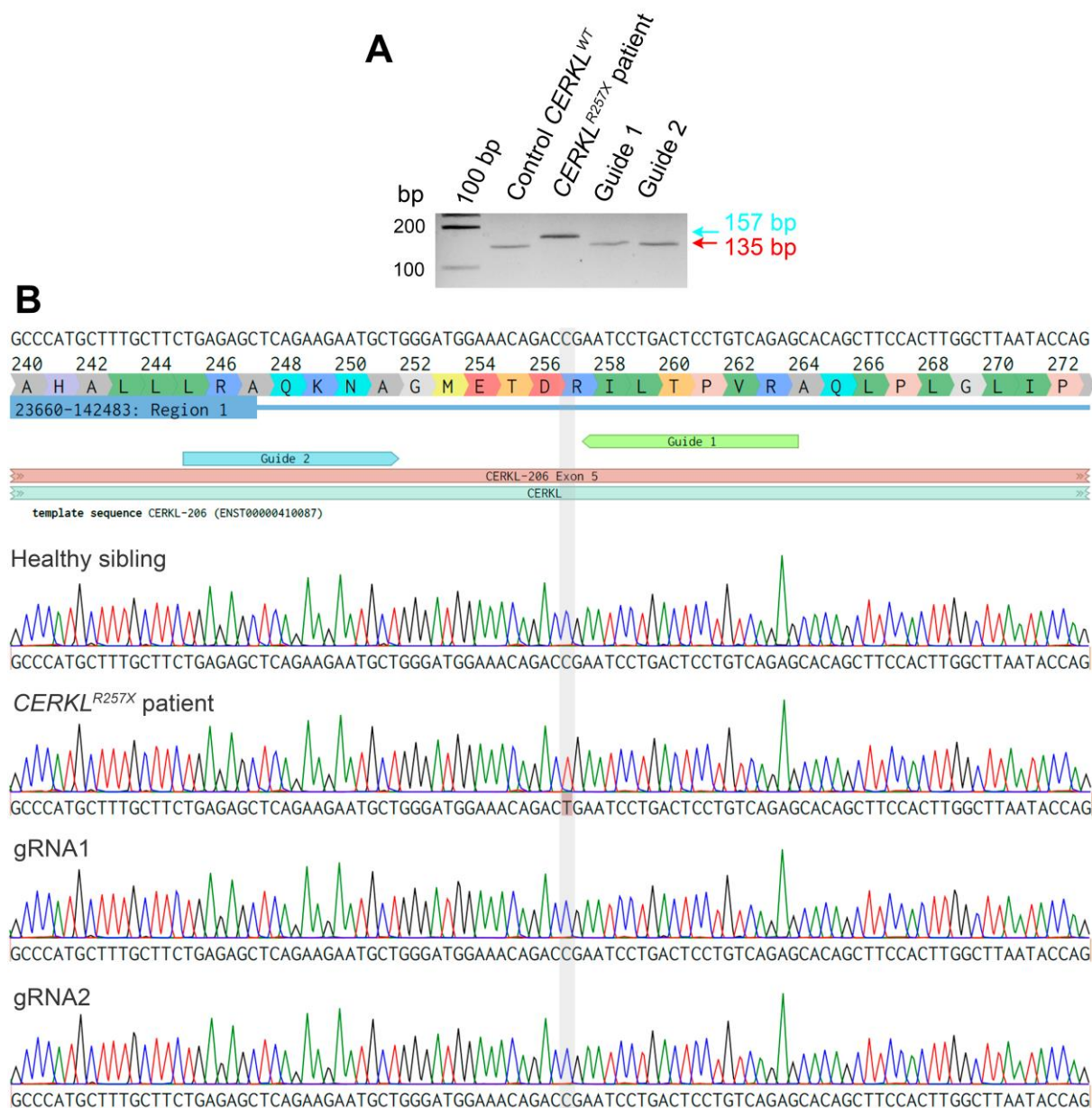
Figure 21. Genotyping analysis of hiPSC after the CRISPR/Cas9 edition to generate the *CERKL^{R257X}* mutation. (A) Agarose (4%) gel of PCR followed by EcoRII enzymatic digestion to genotype mixed populations after CRISPR/Cas9 edition. Line 1: control *CERKL^{WT/WT}* hiPSC; line 2: patient's *CERKL^{R257X}* hiPSC; line 3: hiPSC resulting from CRISPR/Cas9 edition using guide 1; line 4: hiPSC after CRISPR/Cas9 edition with guide 2. The expected 157-bp band after the digestion in *CERKL^{R257X}* allele is indicated with a blue arrow, whereas the 135-bp band resulting from *CERKL^{WT}* allele is indicated with a red arrow. (B) In the upper panel, the sequence of *CERKL* showing the edition-target nucleotide (grey). Electropherograms showing sequences from sibling's and *CERKL^{R257X}* patient's hiPSC were used as controls. None of the analysed samples from mixed hiPSC populations after CRISPR/Cas9 edition using gRNA1 or gRNA2 carried the mutation.

Notably, instead of the Nucleofector 4D, which was already used by other members of the group yielding high gene-edition efficiency, we had to use the Nucleofector II/2b device to deliver the RNPs to hiPSCs. The Nucleofector II/2b device is an older version of this technology and does not seem to be as efficient in delivering the CRISPR/Cas9 RNPs into cells as the Nucleofector 4D. Therefore, after purchasing the Nucleofector 4D, we are planning to repeat our gene-editing experiments using this new device.

Differentiation of *CERKL^{R257X}* patient's hiPSC into 3D retinal organoids

Although the patient's hiPSCs had been already differentiated into 3D retinal organoids in collaboration with Dr Lukovic in Valencia, the differentiation period needed to be terminated due to COVID-19 sanitary crisis and thus, the phenotypic analyses were very preliminary. As a consequence, we aimed to repeat the differentiation of *CERKL^{R257X}* hiPSCs into retinal organoids to perform detailed a molecular and functional characterization of early pathological biomarkers and disease progression.

The protocol to obtain fully differentiated retinal organoids is very long (up to 300 days) because retinal differentiation *in vitro* perfectly emulates the embryonic differentiation times, thus needing up to 8 months to obtain well differentiated retinal organoids. Retinal organoids' differentiation begins with a bidimensional confluent culture of hiPSC that are incubated with media including neural- and retinal-fate factors (E6 and NIM media) to induce the formation of neuroretinal vesicles (NRVs). Then, between day 30 and 40 of differentiation, NRVs are dissected from the plate to constitute the tridimensional potential retinal organoids. Excised NRVs are next cultured using different media –rich in appropriate retinal induction and retinal maturation trophic factors (RDM, RMM1, RMM2 and RMM3 media)– during the next months to finally obtain differentiated retinal organoids with laminated structure and photoreceptor OSs (Figure 22). During the differentiation of patient's and sibling's retinal organoids, we observed that both lines were able to form NRVs that are now being differentiated into retinal organoids (Figure 22).

Unfortunately, we received the patient's hiPSCs in July 2023 and started the differentiation in September 2023. As a result, at the time of depositing this PhD

Thesis, retinal organoids have undergone only around 150 days of differentiation. This period, in which photoreceptors OSs are already formed, represents the first selected timepoint for our studies of retinal architecture and early pathogenic biomarkers in *CERKL^{R257X}* retinal organoids. Therefore, no phenotypic characterization could be included in the written memory as a consequence of the limited time available.
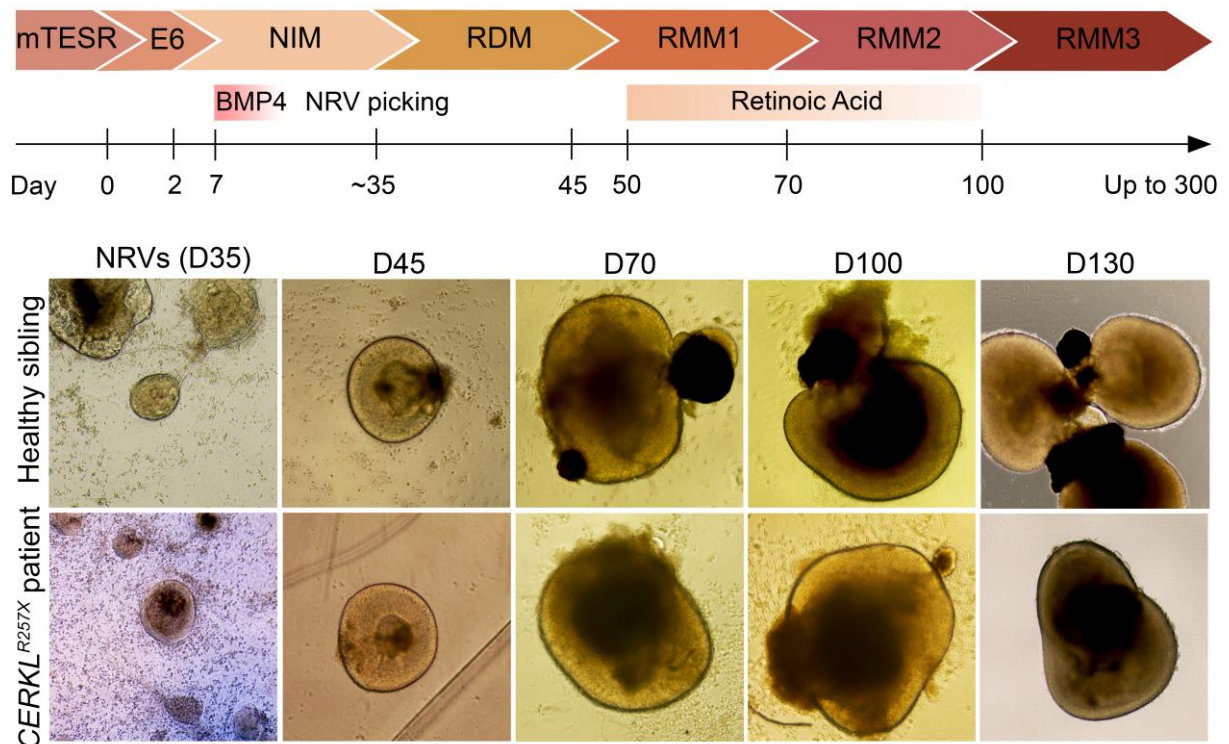
Figure 22. **Timeline of 3D retinal organoids' differentiation.** Retinal organoids require 6 different retinal-inducing media (E6, NIM, RDM, RMM1, RMM2 and RMM3) and the addition of specific trophic factors, such as BMP4 and retinoic acid, to get a fully differentiated structure. So far, both sibling's and patient's retinal organoids exhibit normal differentiation parameters at each timepoint. D: day of differentiation.

MATERIAL AND METHODS

RNA-Seq analysis

Gene Ontology (GO) Biological Process enrichment and gene pathway analyses were performed using Enrichr web server (https://maayanlab.cloud/Enrichr/) (224–226) and GeneAnalytics™ (https://geneanalytics.genecards.org).

Human iPSC culture

Healthy sibling's and *CERKL^R257X* patient's human induced pluripotent stem cells (hiPSCs) (both derived from human fibroblasts reprogrammed by Dr Dunja Lukovic's group (222)), as well as BJ hiPSCs (derived from human fibroblasts reprogrammed in Prof. Hardcastle's and Prof. Cheetham's groups) were cultured in mTeSR Plus Basal medium supplemented with 5× mTeSR™ Plus Supplement (Stemcell Technologies, Vancouver, Canada; 100-0276) on wells previously coated with Geltrex™ (Thermo Fisher Scientific, Rockford, IL, USA; A1413301) for 1 hour in a 5 % CO_2 cell culture humidified incubator at 37 °C. The medium was replaced by fresh medium three times per week after a wash with 1× PBS.

Design of sgRNAs for CRISPR/Cas9 gene edition

To generate *CERKL^R257X* CRISPR-edited BJ hiPSCs, we designed two guide RNAs (gRNAs, also known as CRISPR RNA (crRNA)) using the CRISPR design software available in Benchling (https://benchling.com) maximising on-target efficiency and minimising off-target effects (227,228). Both gRNAs (gRNA_1: 5'CTCTGACAGGAGTCAGGATT 3'; and gRNA_2: 5'TGAGAGCTCAGAAGAATGCT 3') recognized a sequence near the target nucleotide to generate the desired point mutation (see Figure 19 in the Results section). To favour homology-directed repair (HDR) in the target site and introduce the desired mutation, generating a knock-in, we also designed two 127-bp single-stranded oligodeoxynucleotide (ssODN) repair templates that had the sequence of the desired mutation for each gRNA (ssODN_1: 5' AGCTCAGAAGAATGCTGGGATGGAAACAGACTGAATCCTGACTCCTGTCAGA GCACAGCTTCCACTTGGCTTAATACCAGCAGGCAAGGGAGTGGCTACAGATTCAT TAAACTGACCCTTCTCCCTC 3'; and ssODN_2: 5' AATCTGTAGCCACTCCCTTGCC TGCTGGTATTAAGCCAAGTGGAAGCTGTGCTCTGACAGGAGTCAGGATTCAGTCTG

TTTCCATTCCAGCATTCTTCTGAGCTCTCAGAAGCAAAGCATGGGCTAC 3'). The 127-bp ssODN templates were designed following previously optimised specifications, with 36-nucleotide-left and 91-nucleotide-right homology arms, as well as additional synonymous changes to eliminate the protospacer-adjacent motive (PAM) of gRNAs 1 and 2 and thus prevent reannealing and re-editing of the locus (229,230). gRNAs were ordered as two-component crRNA, the custom-designed 17-20 nucleotides sequence complementary to the target DNA, and trans-activating CRISPR RNA (tracrRNA), which is the invariable sequence used as binding scaffold for the Cas9 nuclease. The ssODN templates were ordered as an Alt-R modified Alt-RTM HDR donor oligo in IDT Technologies (Coralville, IA, USA).

hiPSCs nucleofection and analysis of individual colonies

Nucleofection of BJ hiPSCs with *CERKL*-targeting ribonucleoprotein (RNP) and the ssODN template was performed according to IDT Alt-R CRISPR system. First, to improve cell viability and survival, hiPSCs were cultured in StemFlex™ medium (Thermo Fisher Scientific, Rockford, IL, USA; A3349401) supplemented with 10 µM ROCK inhibitor Y27632 (StemCell Technologies; 72308) for 2 hours prior to harvest. crRNA and tracrRNA were assembled in 1:1 equimolar concentrations to a final duplex concentration of 50 µM, equivalent to 130 pmol of crRNA:tracrRNA duplex per reaction. crRNA:tracrRNA mix was incubated at 95 °C for 5 minutes and then cooled down to room temperature for 10-15 minutes. Next, Cas9 RNP complex assembly was performed by adding 125 pmol of *Streptococcus pyogenes* Cas9 nuclease (IDT Technologies, Coralville, IA, USA; 1081058) per reaction, and incubated for 10-20 minutes at room temperature. Subsequently, 120 pmol of Alt-R® Cas9 Electroporation Enhancer (IDT Technologies, Coralville, IA, USA; 1075916) and 200 pmol of the ssODN template (ssODN_1 for gRNA_1 and ssODN_2 with gRNA2) were added to Cas9:gRNA_1 and Cas9:gRNA_2 assemblies. Then, this mix was incorporated to 2×10^5 BJ hiPSCs resuspended in 100 µL of Human Stem Cell Nucleofector™ supplemented Solution (Lonza, Morrisville, NC, USA; VPH-5002) and transferred to a Nucleofector cuvette. Samples were subsequently nucleofected using a Lonza Nucleofector II/2b device (Lonza, Morrisville, NC, USA; AAB-1001), using the A-023 or B-016 nucleofection programs. After 10 minutes, hiPSCs were

seeded onto 24-well plates, previously coated for 2 hours at 37 °C with 0.5 µg/cm² rhLaminin 521 (Thermo Fisher Scientific, Rockford, IL, USA; A29249), in StemFlex™ medium supplemented with ROCK inhibitor and 100 µg/mL primocin antibiotic (Invivogen, San Diego, CA, USA; ant-pm-2). Alt-RTM HDR Enhancer (1:100) (IDT Technologies, Coralville, IA, USA; 10007921), which maximises the CRISPR gene-edition efficiency, was added in one extra well per gRNA. The following day, the medium was changed with fresh StemFlex™ medium with primocin.

Once 70-90 % confluency was reached, half of the cells were passaged onto a rhLaminin 521-coated 6-well plate with StemFlex™ medium for 6 days and the other half was used for genomic DNA extraction to genotype the mixed cell population and check CRISPR/Cas9 editing efficiency. Six days later, cells were split again onto a rhLaminin 521-coated 6-well plate at different densities (4000, 2000, 1000, 500, 250 and 125 cells/well) to obtain single-cell-derived hiPSC colonies using StemFlex™ medium and primocin antibiotic. Approximately 5-6 days later, individual hiPSC colonies were isolated with the P200 pipette and seeded on Geltrex™-coated 24-well plates in mTeSR medium. hiPSC colonies were further cultured before extracting genomic DNA for genotyping.

Genotyping PCR and enzymatic digestion

Genomic DNA extraction from mixed population and single-cell-derived colonies of hiPSCs was conducted using the Monarch® Genomic DNA purification kit (New England Biolabs, Ipswich, MA, USA; T3010L) following the manufacturer's instructions. Genotyping was performed by mutation restriction analysis according to Tuson *et al*. (105). Briefly, we used a forward primer (5' GAAGAATGCTGGGATGGAAACGGAC 3') that contained a mismatch nucleotide (underlined), creating a EcoRII (also known as AvaI) restriction site in the *CERKL* wild-type sequence. Together with the reverse primer (5' GTTGTGCTGTCTAGATTAGC 3'), a PCR was performed. The PCR program was as follows: 94 °C for 5 minutes and 40 cycles of 94 °C for 30 seconds, 50 °C for 30 seconds and 72 °C for 10 seconds. The 157-bp PCR products were digested using EcoRII enzyme (Fisher Scientific; ER0312) and analysed through 4 % low-melting agarose gel electrophoresis.

Sanger Sequencing

Sanger sequencing was performed to verify the introduction of the desired point mutation after CRISPR/Cas9 edition. The sequencing reaction was performed using the BigDye™ Terminator v3.1 Cycle Sequencing Kit (Thermo Fisher Scientific, Rockford, IL, USA; 4337455). The sequencing mix included 0.5 µM of each primer (CRISPR_forward 5′ TTGTGTTTGTGTTGTCTTACCCA 3′; CRISPR_reverse 5′ gctgtCTAGATTAGCAAGTAAGAAAGGA 3′), 1× BigDye Buffer (Applied Biosystems), 1 µL of BigDye™ Terminator v3.1 Ready, the appropriate amount of DNA and PCR-grade H$_2$O up to 10 µL. The sequencing PCR program was as follows: 94 °C for 2 minutes and 28 cycles of 96 °C for 10 seconds, 50 °C for 5 seconds and 60 °C for 4 minutes. Sequencing results were analysed using the alignment software available in Benchling (https://benchling.com), which aligns the obtained reads to a reference sequence.

Differentiation of hiPSC into 3D retinal organoids

hiPSCs were differentiated into retinal organoids as previously described (231). Briefly, cells were cultured on Geltrex™-coated 6-well plates with mTeSR medium until they reached 90-95 % confluency. Then, at day 0 of differentiation, essential 6 medium (E6; Life Technologies, Carlsbad, CA, USA; A1516401) was added to the cells (4 mL/well) and replaced with fresh E6 medium after 24 hours. From day 2, cells were cultured with 4 mL/well of neural induction medium (NIM) (1 % N-2 supplement (Life Technologies, Carlsbad, CA, USA; 17502048) and 1 % Pen/Strep, 1 % GlutaMAX™ (Life Technologies, Carlsbad, CA, USA; 35050038) in Advanced DMEM:F-12 (Life Technologies, Carlsbad, CA, USA; 12634010)). Medium was changed three times a week (4 ml on Mondays and Wednesdays, and 6ml on Fridays to double feed the cells). On day 7 of differentiation, 1.5 nM human bone morphogenetic protein-4 (BMP-4; Prepotech, Cranbury, NJ, USA; 120- 05) was added to cells in NIM and, the following day, half of the medium was replaced with fresh NIM. Then, until day 17, half-medium changes were done every other day to dilute BMP-4 concentration. Two weeks after, the appearance of neuroretinal vesicles (NRVs) can be checked. Between day 35 and 40, individual NRVs were dissected from the hiPSC-derived bidimensional cultures with the help of an inverted microscope (EVOS

XL Core; Thermo Fisher Scientific, Rockford, IL, USA; #AMEX1000) inside the cell culture hood. Individually excised NRVs were cultured in 150-200 µL of NIM on ultra-low attachment 96-well plates (Merck, Darmstadt, Germany; CLS7007) and half of the medium was replaced three times a week. To maximise NRV obtention, the checkerboard technique was used to scrap the remaining cells in the wells. This procedure consisted in breaking the hiPSC-derived bidimensional culture into smaller pieces and transferring them into a Petri dish, where they were grown in suspension with 10 mL of NIM (372). Approximately on day 37, NRVs were incubated in retinal differentiation medium (RDM) (2 % B27 supplement (Life Technologies, Carlsbad, CA, USA; 17504044), 1 % non-essential amino acids (NEEA; Life Technologies, Carlsbad, CA, USA; 11140050), and 1 % Pen/Strep in DMEM:F-12 (ratio 3:1)), and half of the medium was changed every other day. On day 44, the medium was changed to retinal maturation medium (RMM) 1 (10 % FBS, 2 % B27 supplement, 1 % GlutaMAX™, 1 % Pen/Strep and 100 µM Taurine (Merck, Darmstadt, Germany; T8691) in DMEM:F-12 (ratio 3:1)), with half-medium change every other day. From day 50, RMM1 medium was supplemented with 1 µM fresh retinoic acid (RA; Merck, Darmstadt, Germany; R2625). From day 70, cells were cultured in RMM2, which has the same composition as RMM1 but introducing 1 % N2 supplement and reducing the concentration of RA to 0.5 µM. To promote photoreceptor differentiation, cells were grown in RMM3 from day 100, without RA and B27 supplement. After day 100, well laminated organoids were transferred from the 96-well plate and Petri dish to low-attachment 25-well square dishes (Thermo Fisher Scientific, Rockford, IL, USA; 11339273) and incubated in 2 mL of RMM3 with half-medium changes twice a week. Unfortunately, at the time of the submission of this Thesis, we reached day 142 of differentiation. Therefore, the protocol had not been entirely completed, and the differentiation process was still ongoing.
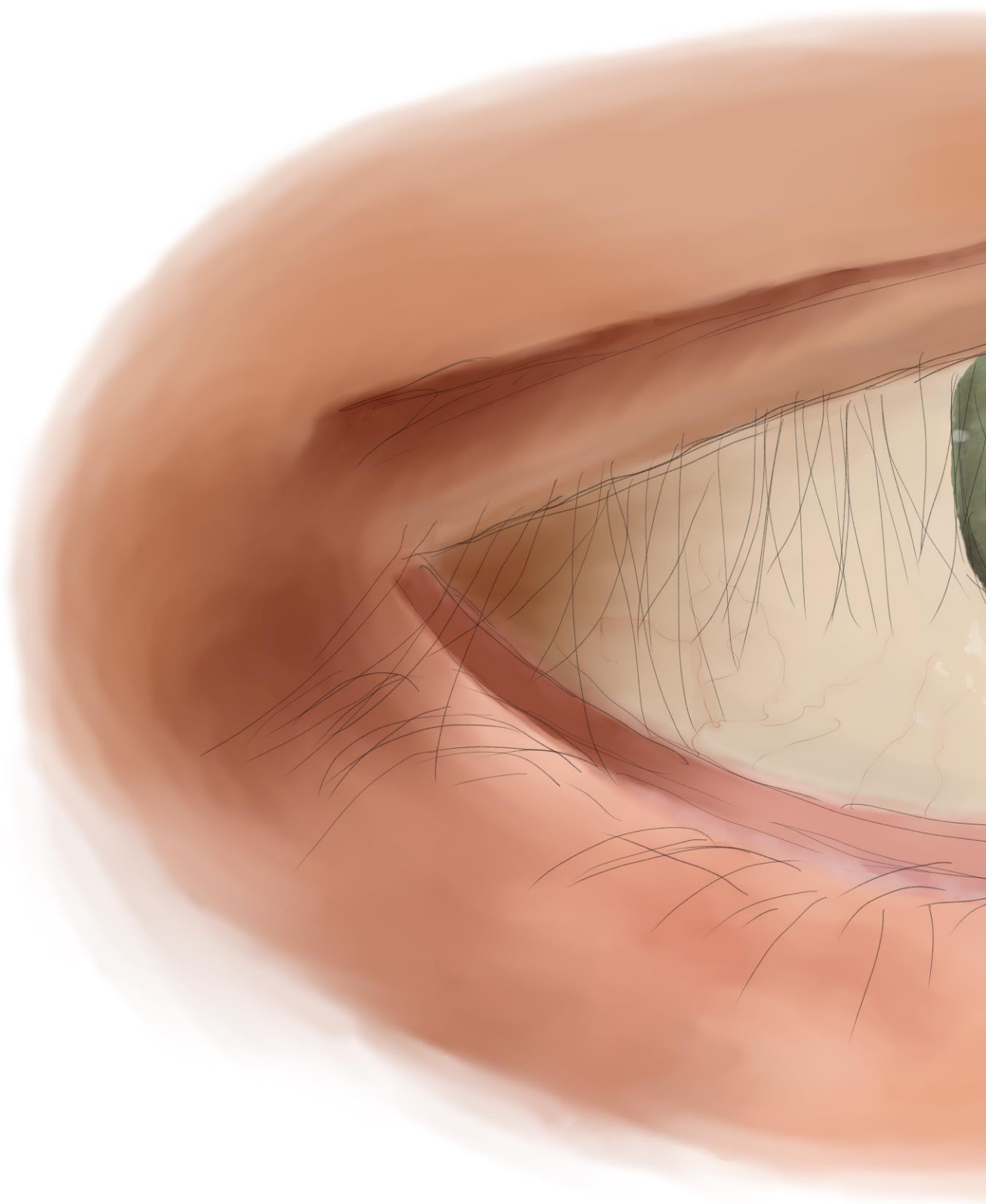
CHAPTER 4

Approaches to gene augmentation therapy : AAVs and nanoparticles
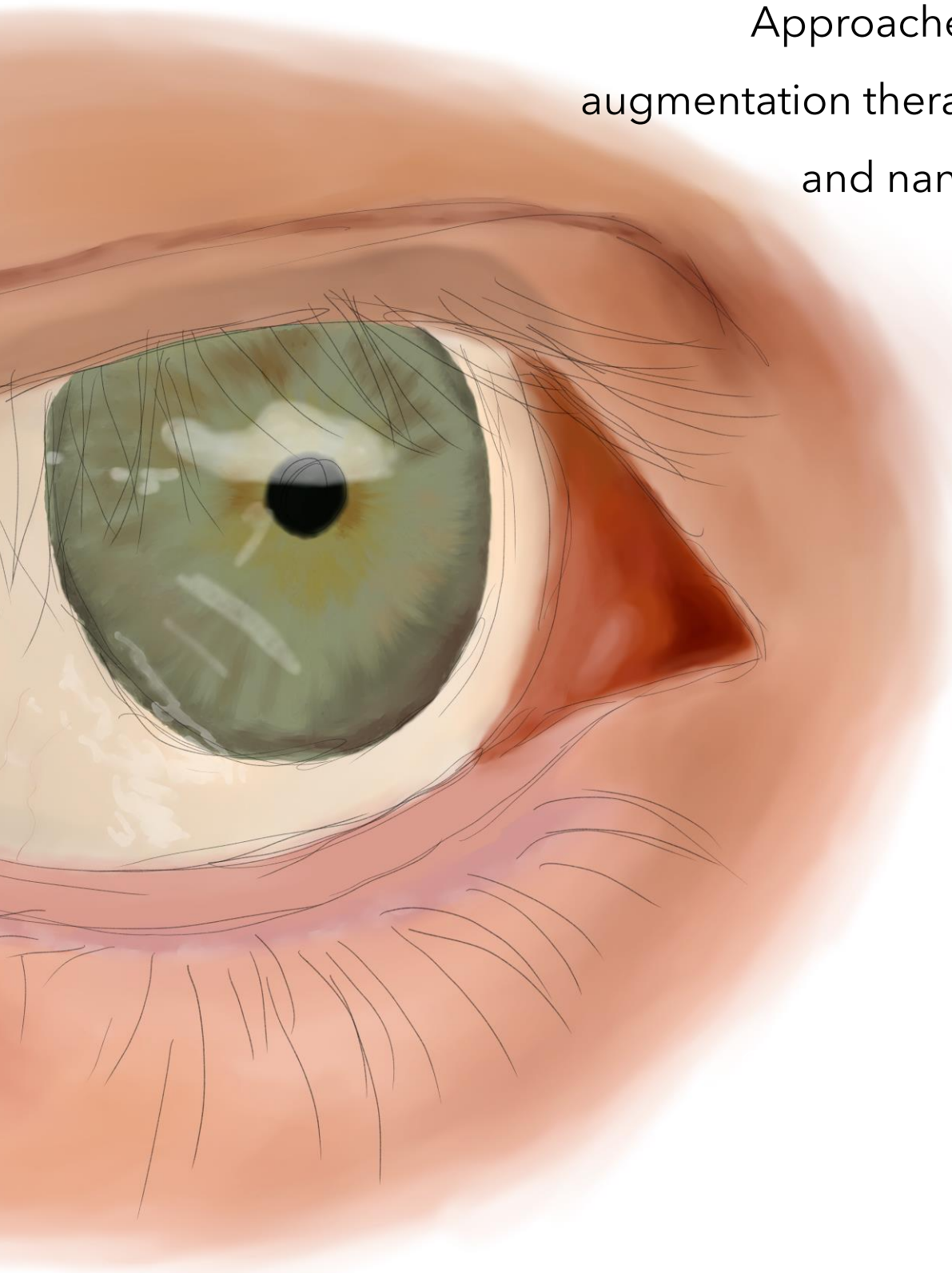
Design of CERKLa AAV-based therapeutic strategy for *CERKL*-related IRDs

In light of the absence of a treatment for *CERKL*-associated IRDs, we have explored the development of a *CERKL* AAV-based gene-augmentation therapeutic approach in collaboration with the research group led by Dr Ivana Trapani, at the Telethon Institute of Genetics and Medicine (TIGEM), in Naples, Italy.

Adeno-associated viruses (AAVs) are thus far considered the leading platform for gene therapy of IRDs, due to their excellent safety and efficacy profile shown in dozens of clinical trials. Subretinal injection is the most effective route for transducing photoreceptor cells. Thanks to our recent molecular and cellular characterization of the *KD/KO* retina, which has been the main objective of this Thesis, the *Cerkl^{KD/KO}* mouse model represents an invaluable model to test the feasibility of AAV-mediated CERKL transfer in degenerating photoreceptors with therapeutical propose.

This gene-replacement treatment will serve as a feasible proof-of-concept aimed at preventing, halting, or potentially reverting the retinal alterations observed in *KD/KO* mice, but also in patient-derived retinal organoids offering a potential treatment for patients carrying mutations in *CERKL*.

Cloning *CERKLa* into AAV backbone and testing its proper expression *in vitro*

For the purpose of generating the vector for AAV-based therapy, we cloned the cDNA of *CERKLa* into the plasmid p8.GFP-3×FLAG, which contains the Green Fluorescent Protein (GFP) in frame with the epitope 3×FLAG (3×DYKDDDDK). A cassette exchange approach was designed to remove the GFP-encoding fragment and insert the *CERKLa* coding sequence, thus, finally obtaining a fusion protein between CERKLa and the 3×FLAG epitope cloned into the AAV2 backbone (Figure 23).

In brief, the original plasmid, p8.GFP-3×FLAG (Figure 24A, Lane 1), was digested using BsrGI and KpnI restriction enzymes to excise the GFP-coding fragment. This restriction produced two bands: the expected band size of the vector, with a lower size (4 kb, Figure 24A, Lane 3) compared to the linearized plasmid (4.6 kb, Figure 24A, Lane 2) and the released GFP-coding fragment (Figure 24A, Lane 3).
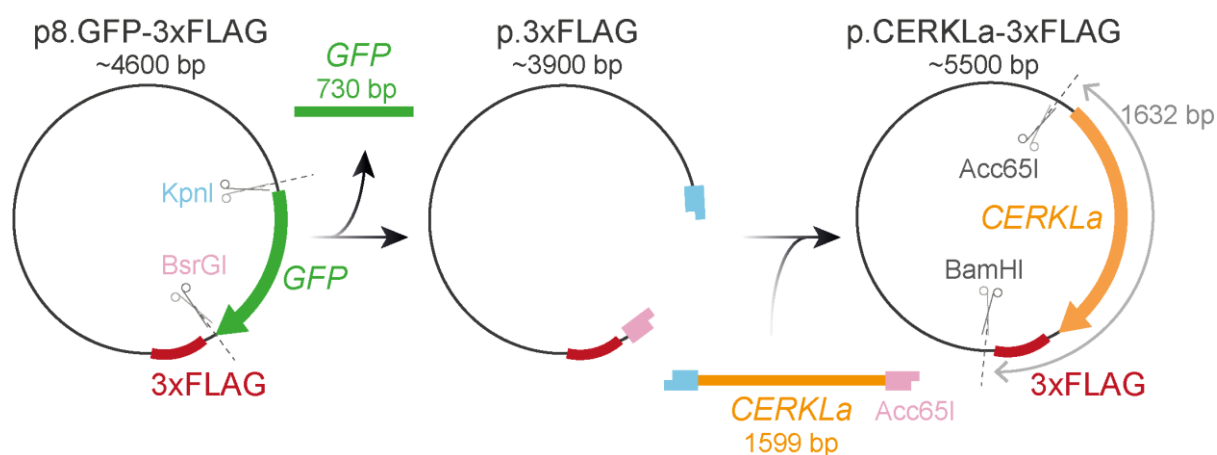
Figure 23. Cloning procedure to introduce *CERKLa* cDNA into the p8.GFP-3×FLAG vector backbone. The p8.GFP-3×FLAG plasmid was digested using KpnI and BsrGI to excise the GFP-encoding DNA sequence. The *CERKLa* cDNA was amplified by PCR adding the restriction sites of KpnI and Acc65I (compatible with BsrGI) at its ends to insert it into the digested p.3×FLAG plasmid backbone, resulting in the p.CERKLa-3×FLAG construct. To evaluate the insertion and integrity of *CERKLa* coding sequence into the AAV vector backbone, the final recombinant plasmids were digested using Acc65I and BamHI.

The *CERKLa* cDNA was amplified by PCR using specific primers to insert the the target sites of Acc65I and KpnI at the ends of *CERKLa* coding sequence (Figure 24A, Lane 4). Subsequently, we ligated the vector and insert DNAs to obtain the in-frame p.CERKLa-3×FLAG construct.

Plasmid DNA from 12 colonies was isolated and analysed. We identified 5 clones that exhibited the expected restriction pattern corresponding to the p.CERKLa-3×FLAG construct (Figure 24B), which after restriction digestion produced the expected 1.6-kb band of the *CERKLa*-3×FLAG-coding fragment. Subsequently, plasmids from positive clones were sequenced (Figure 24C) to confirm the in-frame insertion of the *CERKLa* fragment with the 3×FLAG epitope in three out of 5 clones.
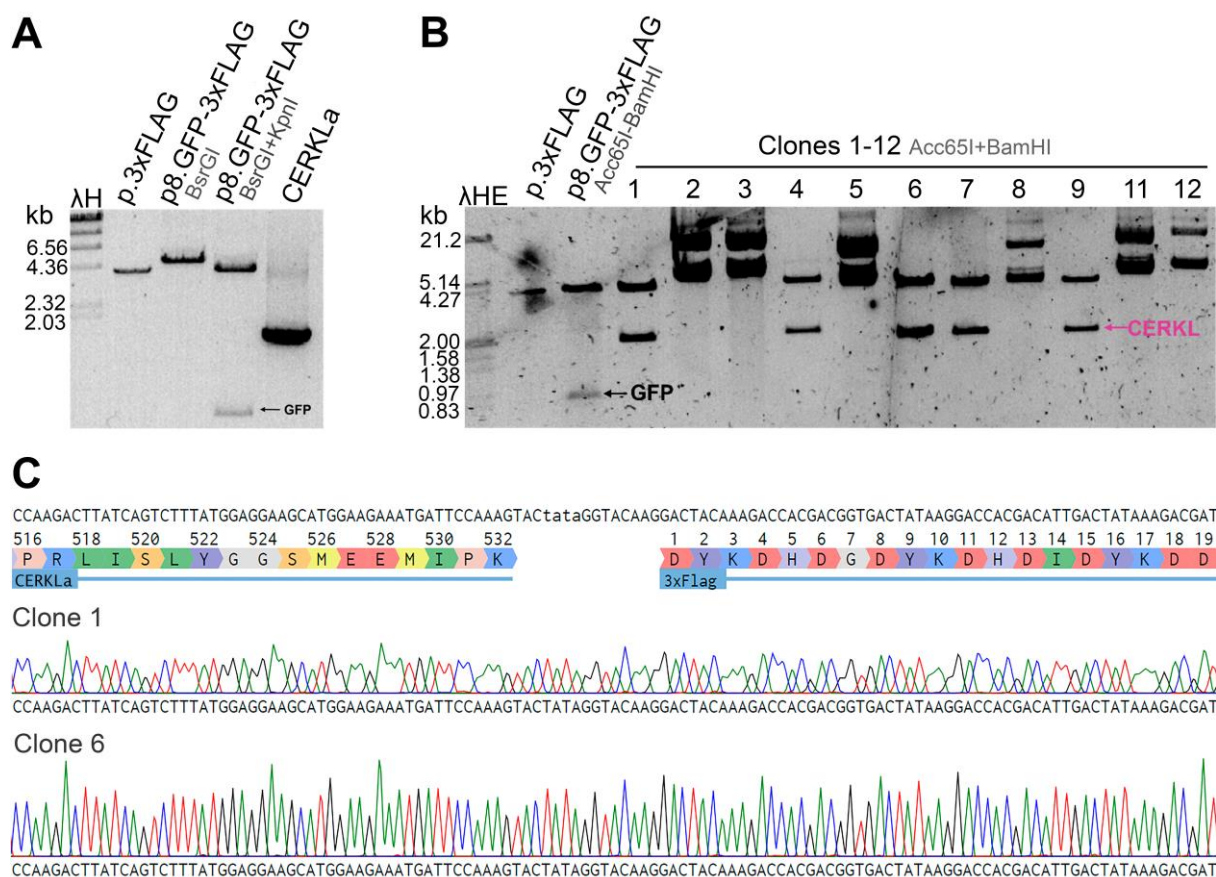
Figure 24. Generation of the recombinant AAV-derived construct to express CERKLa. (A) Agarose (1 %) gel electrophoresis of digested vector and insert (*CERKLa*) DNAs. Molecular weight marker: Lambda DNA/HindIII (λH); Lane 1: p.3×FLAG obtained after digestion (BsrGI+KpnI) of p8.GFP-3×FLAG and purification of the vector backbone; Lane2: linearized p8.GFP-3×FLAG with BsrGI digestion as a size control; Lane3: digested p8.GFP-3×FLAG (BsrGI+KpnI), yielding the vector backbone and GFP bands; Lane 4: *CERKLa* cDNA amplicon PCR product digested with Acc65I and KpnI. (B) Agarose (1 %) gel electrophoresis of plasmids isolated from *E. coli* colonies after ligation and transformation. Molecular weight marker: Lambda DNA/HindIII+EcoRI (λHE). Lane 1: purified p.3×FLAG (control vector); Lane 2: digested p8.GFP-3×FLAG (BsrGI+KpnI), yielding the vector backbone (4 kb) and GFP bands (730 bp); Lanes 3-13: Isolated plasmids from the 12 colonies (Clones 1-12) digested with Acc65I and BamHI to identify recombinant clones with the p.CERKLa-3×FLAG plasmid, note that some clone plasmids contain *CERKLa* (marked in pink). (C) Sanger sequencing electropherogram of the clones 1 and 6 showed the correct insertion of *CERKLa* into the AAV-derived backbone in-frame with the tag 3×FLAG.

Upon verification of the p.CERKLa-3×FLAG sequence, the three constructs were selected for *in vitro* expression assessment by immunocytochemistry (Figure 25A) and Western blotting (Figure 25B). Both techniques evidenced that 2 out of the 3 plasmids successfully expressed the fusion peptide CERKLa-3×FLAG (63 kDa),

confirming the correct expression of the construct. These validated constructs were subsequently employed to generate recombinant AAV2/8_CERKLa-3×FLAG by the group of Dr Ivana Trapani.
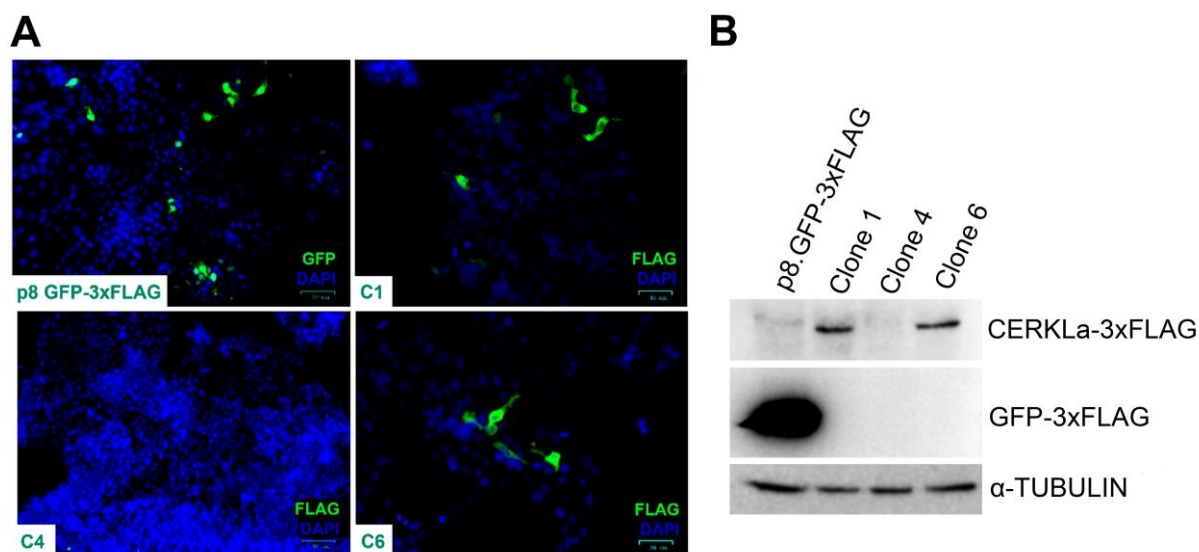
Figure 25. p.CERKLa-3×FLAG is properly expressed *in vitro*. (A) Immunocytochemistry of HEK293 cells transfected with p8.GFP-3×FLAG (control) and p8.CERKLa-3×FLAG construct isolated from clones 1, 4 and 6 (C1, C4 and C6) immunodetecting GFP or FLAG (green) and counterstaining nuclei with DAPI (blue). (B) Western blot analysis of transfected-HEK293 lysates immunodetecting FLAG, GFP and α-TUBULIN.

AAV2/8_CERKLa-3×FLAG production and evaluation of its expression by subretinal injection

Using the p.CERKLa-3×FLAG plasmid, which contains the *CERKLa* cDNA in-frame with the tag 3×FLAG inside the backbone of a AAV-derived vector, the research group led by Dr Ivana Trapani in TIGEM produced the recombinant AAV2/8_ CERKLa-3×FLAG virus. Then, they assessed the transduction efficiency of AAV2/8_ CERKLa-3×FLAG by subretinal injections in 1-month-old *WT/WT* mice. Four weeks after the injection, they evaluated the expression of the fusion protein CERKLa-3×FLAG by Western blot analysis in AAV-injected retinas and eyecups (RPE). As expected, CERKLa-3×FLAG expression was detected in some injected retinas, although it was particularly intense in the RPE (eyecup) (Figure 26), indicating that AAV2/8_CERKLa-3×FLAG efficiently transduces mouse retinas and RPE.
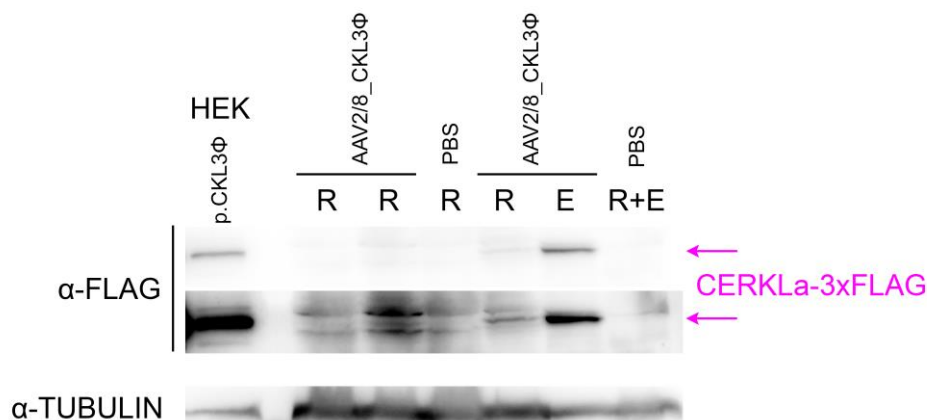
Figure 26. AAV2/8_CERKLa-3×FLAG is transduced and expressed *in vivo* after subretinal injection. Western blot analysis of protein lysates from retinas (R) and eyecups (E) injected with either AAV2/8_CERKLa-3×FLAG (AAV2/8_CKL3Φ) or PBS (negative control), as well as HEK293 cells transfected with p.CERKLa-3×FLAG (p.CKL3Φ) as positive control. Immunodetection using α-FLAG antibody revealed expression of CERKLa-3×FLAG protein (pink arrows) in some injected retinas and eyecups (RPE).

AAV2/8_CERKLa-3×FLAG vector was provided by Dr Ivana Trapani to explore its potential therapeutic effects in the *KD/KO* mouse model. In our group, we performed subretinal injections of AAV2/8_CERKLa-3×FLAG, together with AAV2/7m8_GFP (expressing GFP in an AAV with a different serotype to avoid cell entry competition), as a positive control of injection. First, we assessed the efficiency of the injection (AAV2/8_CERKLa-3×FLAG : AAV2/7m8_GFP were coinjected at ratio 5:1), in 1-month-old *WT/WT* and *KD/KO* mice. However, we were not able to detect CERKLa-3×FLAG protein expression in nearly any retina or RPE (eyecup) extract. Nevertheless, transduction efficiency through subretinal injection seemed reasonably competent, as almost all the injected retinas and RPE homogenates presented strong GFP expression (Figure 27). Therefore, we surmised that there might be some problem specifically affecting AAV2/8_CERKLa-3×FLAG vectors proper transduction.
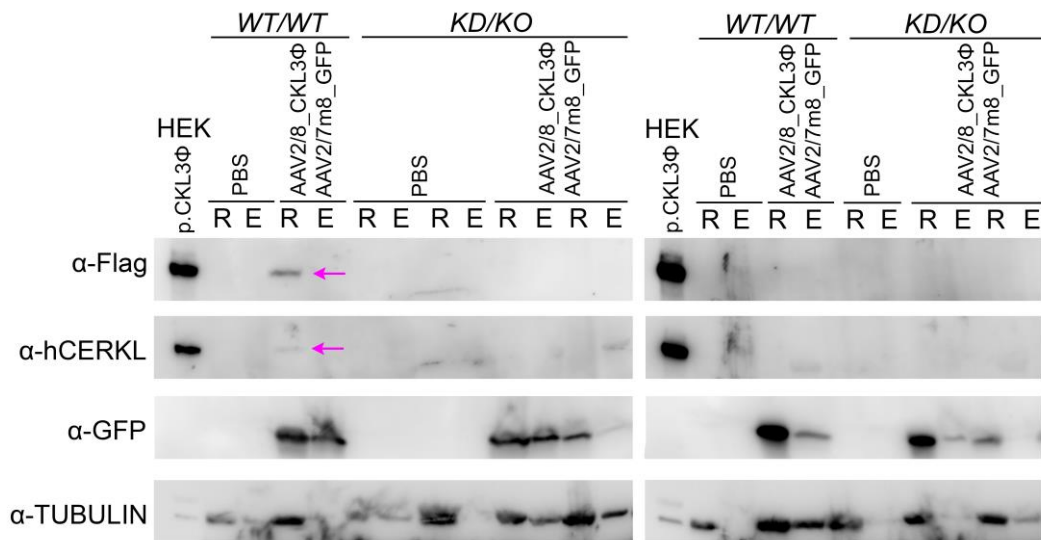
Figure 27. AAV2/8_CERKLa-3×FLAG is not efficiently expressed *in vivo* after subretinal injection in our hands. Western blot analysis of protein lysates from retinas (R) and eyecups (E) from *WT/WT* and *KD/KO* mice co-injected with AAV2/8_CERKLa-3×FLAG (AAV2/8_CKL3Φ) and AAV2/7m8_GFP, or with PBS (negative control). Protein lysate from HEK293 cells transfected with p.CERKLa-3×FLAG (p.CKL3Φ) was included as positive control. Immunodetection using α-FLAG and α-human CERKL (hCERKL) antibodies revealed expression of CERKLa-3×FLAG fusion protein (pink arrows) in only one injected retina. Although most of them were correctly injected and expressed GFP.

What factors are hindering the functionality of AAVs?

After the unexpected results using AAV2/8_CERKLa-3×FLAG *in vivo*, we analysed which was the factor contributing to their non-functionality, considering the following aspects: 1) the presence of DNA inside AAV capsids; 2) the correct transduction, transcription, and translation of AAV2/8_CERKLa-3×FLAG; 3) whether human CERKL (p.CERKLa-3×FLAG plasmid) could be properly expressed by mouse cells; 4) if the tag included in the CERKL-derived fusion peptide had an impact on the expression of the CERKL-3×FLAG fusion protein (Figure 28).

The p.CERKLa-3×FLAG construct was previously tested *in vitro* using HEK293 cells (a human cell line of embryonic kidney cells) and successfully expressed CERKLa-3×FLAG protein that could be easily detected by immunocytochemistry and Western blot analyses (Figure 25). Nevertheless, we wondered if the differences between human and mouse CERKL coding sequence might affect the correct expression of human CERKL in mouse cells because of differential codon usage between species.

We concluded that this was not the case because, in previous work, we had successfully overexpressed human CERKLa-GFP in mouse cells (Results Chapter 1, Publication 2). Based on our previous results overexpressing CERKLa-GFP, we hypothesized whether the tag, 3×FLAG or GFP, could influence human CERKL expression in mouse cells. To test this hypothesis, we overexpressed hCERKLa-3×FLAG and hCERKLa-GFP constructs in mouse primary RPE cells and observed expression of both CERKL-derived fusion proteins (Figure 29), indicating that human CERKL can be properly expressed by mouse cells, irrespective of the tag. Consequently, we concluded that the problem might reside in the AAV2/8_CERKLa-3×FLAG virus rather than in the p.CERKLa-3×FLAG construct.
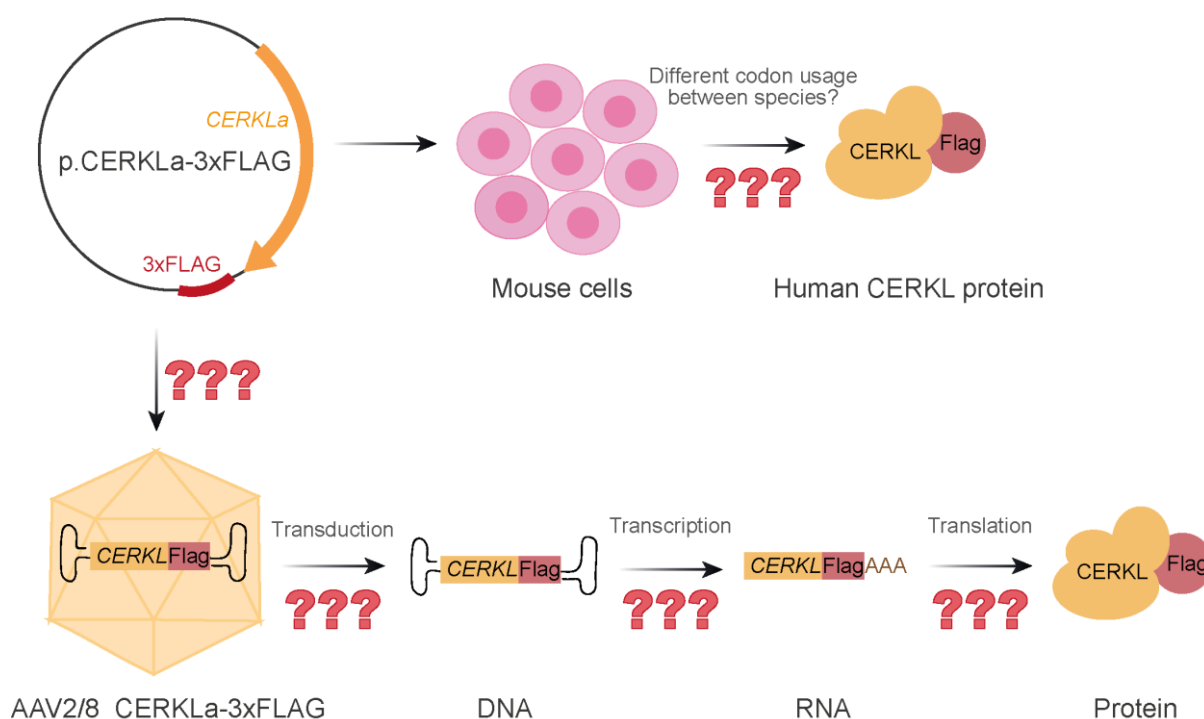
Figure 28. Graphical summary of the potential steps involved in the production and correct expression of AAV2/8_CERKLa-3×FLAG. A list of potential checkpoints was considered: 1) Could mouse cells properly express human CERKL protein? 2) Did AAV2/8_CERKLa-3×FLAG vectors contain DNA? 3) Did AAV2/8_CERKLa-3×FLAG efficiently transduce cells and introduce their DNA? 4) Could viral DNA be transcribed to RNA? 5) Was viral-derived RNA finally translated into CERKLa-3×FLAG protein?
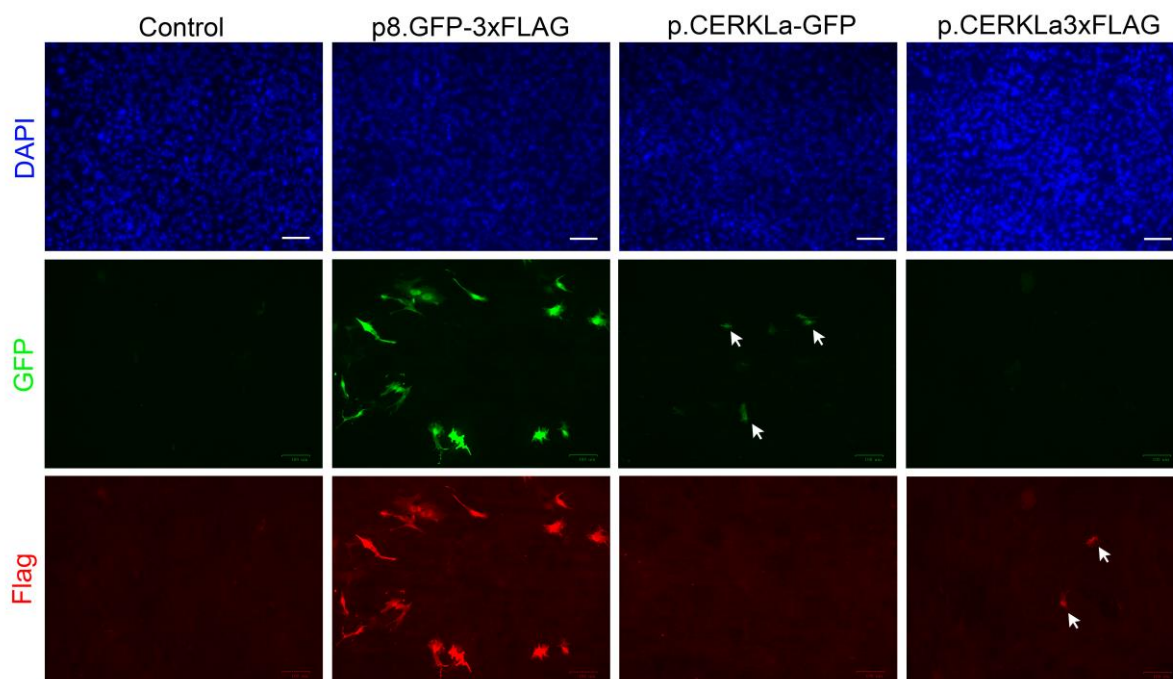
Figure 29. Human CERKL can be expressed by mouse cells. Immunocytochemistry images of primary mouse RPE cells transfected with p8.GFP-3×FLAG (positive control), p.CERKLa-GFP and p.CERKLa-3×FLAG constructs to induce the production of human CERKL protein with different tags (GFP or 3×FLAG). We detected positive cells in all conditions (white arrows indicate hCERKLa-positive cells). Scale bar: 100 μm.

To explore the hypothesis of some alterations in the AAV2/8_CERKLa-3×FLAG virus, we first confirmed the presence of CERKLa-3×FLAG-coding DNA inside AAV capsids by PCR (Figure 30). The amount of DNA included in the PCR was normalized considering the viral titer for AAVs and the DNA concentration and plasmid size for the constructs. Our results indicated that the annotated viral titer was correct.

Next, to test the transduction, transcription, and translation competence of AAV2/8_CERKLa-3×FLAG virus *in vitro*, we infected ARPE-19 cells with AAV2/8_CERKLa-3×FLAG, as well as with AAV8_GFP as positive control. Moreover, AAV2/7m8_GFP vectors were used as an alternative AAV capsid compared to AAV8_GFP. To assess AAV transduction, genomic DNA extraction from AAV-infected ARPE-19 cells was followed by PCR analysis. PCR results showed the presence of CERKLa-3×FLAG DNA in transduced ARPE-19 cells (Figure 31). Additionally, we observed the correct DNA incorporation of AAV8_GFP and AAV2/7m8_GFP vectors in ARPE-19 cells (Figure 31). Therefore, all tested AAV vectors proficiently introduced their DNA into ARPE-19 cells.
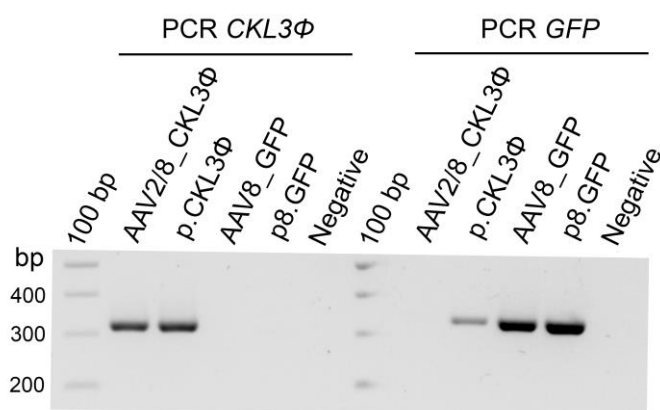
Figure 30. AAV2/8_CERKLa-3×FLAG vectors contain *CERKLa-3×FLAG*-coding DNA. Agarose (1 %) gel electrophoresis showing PCR products after amplifying *CERKLa-3×FLAG* (*CKL3Φ*) or *GFP*-coding DNAs in AAV2/8_CERKLa-3×FLAG (AAV2/8_CKL3Φ) or AAV8_GFP viral vectors, as well as in p.CERKLa-3×FLAG or p8.GFP plasmids. Water was added as negative control of the PCR.
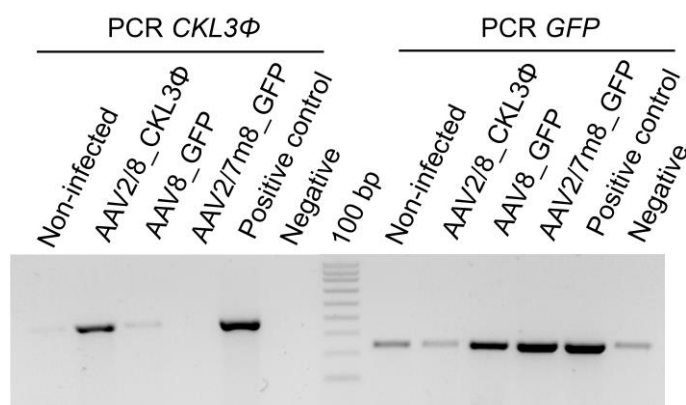
Figure 31. AAV2/8_CERKLa-3×FLAG vectors are able to transduce ARPE-19 cells. Agarose (1 %) gel electrophoresis showing PCR products after amplifying *CERKLa-3×FLAG* (*CKL3Φ*) or *GFP* sequences in DNA extracts from ARPE-19 cells infected with AAV2/8_CERKLa-3×FLAG (AAV2/8_CKL3Φ), AAV8_GFP and AAV2/7m8_GFP (positive control) vectors. DNA extracted from AAV2/8_CERKLa-3×FLAG virus was used as positive control to amplify *CERKLa-3×FLAG*; and DNA extracted from AAV2/7m8_GFP virus was used as positive control to amplify *GFP*. Water was used as negative control of the PCRs. Note that there is a slight contamination in the negative control of the *GFP* amplification.

Next, we evaluated the transcription of viral DNA into RNA through RNA extraction, cDNA production and PCR. Unfortunately, our results revealed the absence of *CERKLa-3×FLAG* cDNA in ARPE-19 cells transduced with AAV2/8_CERKLa-3×FLAG (Figure 32), indicating that AAV2/8_CERKLa-3×FLAG DNA is not efficiently

transcribed into RNA. On the other hand, the DNA from AAV8_GFP and AAV2/7m8_GFP viruses was properly transcribed into RNA (Figure 32).
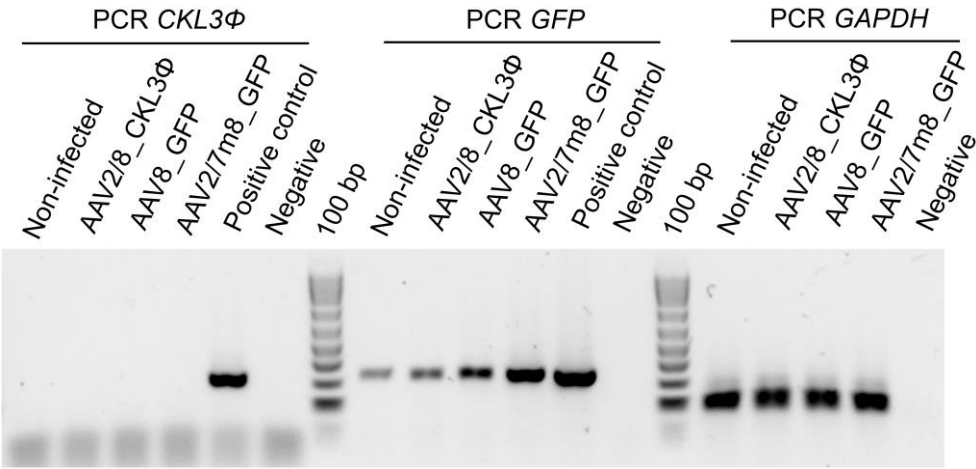
Figure 32. AAV2/8_CERKLa-3×FLAG-DNA is not transcribed in ARPE-19 cells. Agarose (1 %) gel electrophoresis showing PCR products after RNA extraction and cDNA amplification from ARPE-19 cells infected with AAV2/8_CERKLa-3×FLAG (AAV2/8_CKL3Φ), AAV8_GFP and AAV2/7m8_GFP (positive control) vectors. *GAPDH* amplification was performed to verify the presence of cDNA in the analysed samples. DNA extracted from AAV2/8_CERKLa-3×FLAG virus was used as positive control to amplify *CERKLa-3×FLAG* (*CKL3Φ*); and DNA extracted from AAV2/7m8_GFP virus was used as positive control to amplify *GFP*. Water was used as negative control of the PCRs.

Finally, we studied AAV2/8_CERKLa-3×FLAG expression at the protein level by immunocytochemistry (Figure 33A) and Western blot analyses (Figure 33B). As expected after not being able to detect viral transcription, these assays yielded negative results. While ARPE-19 cells transduced with AAV8_GFP and AAV2/7m8_GFP vectors were GFP-positive, AAV2/8_CERKLa-3×FLAG-infected cells did not show any expression of CERKLa-3×FLAG protein (Figure 33). Notably, in line with previous reports (193,232), we observed higher transduction and protein expression efficiency when using AAV2/7m8_GFP, compared to AAV8_GFP (Figure 33) .
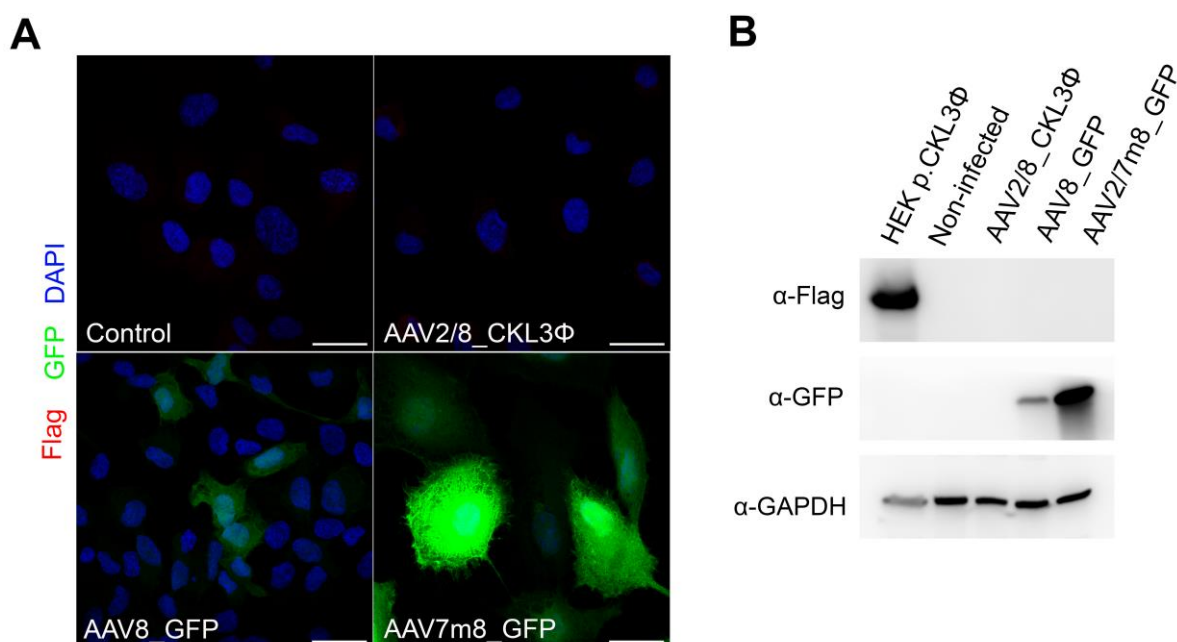
Figure 33. AAV2/8_CERKLa-3×FLAG-transduced cells do not express CERKLa-3×FLAG fusion protein. (A) Immunocytochemistry of ARPE-19 cells infected with AAV2/8_CERKLa-3×FLAG (AAV2/8_CKL3Φ), AAV8_GFP or AAV2/7m8_GFP vectors immunodetecting GFP (green) and FLAG (red), as well as counterstaining nuclei with DAPI (blue). Scale bar: 25 μm. (B) Western blot analysis of protein lysates from ARPE-19 cells infected with AAV2/8_CERKLa-3×FLAG (AAV2/8_CKL3Φ), AAV8_GFP or AAV2/7m8_GFP vectors immunodetecting FLAG, GFP and GAPDH.

Overall, our data implies AAV2/8_CERKLa-3×FLAG vectors do contain DNA but it is not transcribed into RNA, thus preventing the production of the protein. Therefore, we inferred that AAV2/8_CERKLa-3×FLAG vectors were "dead", possibly as a result of the transport of the packaged virus from Naples to Barcelona.

Viral production and expression assessment of AAV2/7m8_CERKLa-3×FLAG

Given the unsuccessful results using AAV2/8_CERKLa-3×FLAG produced in Naples, we decided to produce these viral vectors in the viral production unit of Universitat Autònoma de Barcelona (UAB). Additionally, taking into consideration the observed higher efficiency of AAV7m8 capsid (Figure 33) and its ability to transduce retinal organoids (193), we decided to use the AAV7m8 capsid to generate AAV2/7m8_CERKLa-3×FLAG vectors.

Before testing AAV2/7m8_CERKLa-3×FLAG *in vivo* by subretinal injection in mice, we first evaluated AAV2/7m8_CERKLa-3×FLAG transduction efficiency *in vitro* in

ARPE-19 cells. Immunocytochemistry (Figure 34A) and Western blotting (Figure 34B) analyses demonstrated that AAV2/7m8_CERKLa-3×FLAG was capable of transducing ARPE-19 cells, thus successfully producing CERKLa-3×FLAG protein (Figure 34). These results further supported the inference that AAV2/8_CERKLa-3×FLAG viruses produced in Naples were damaged during transport, probably due to cold chain breech.
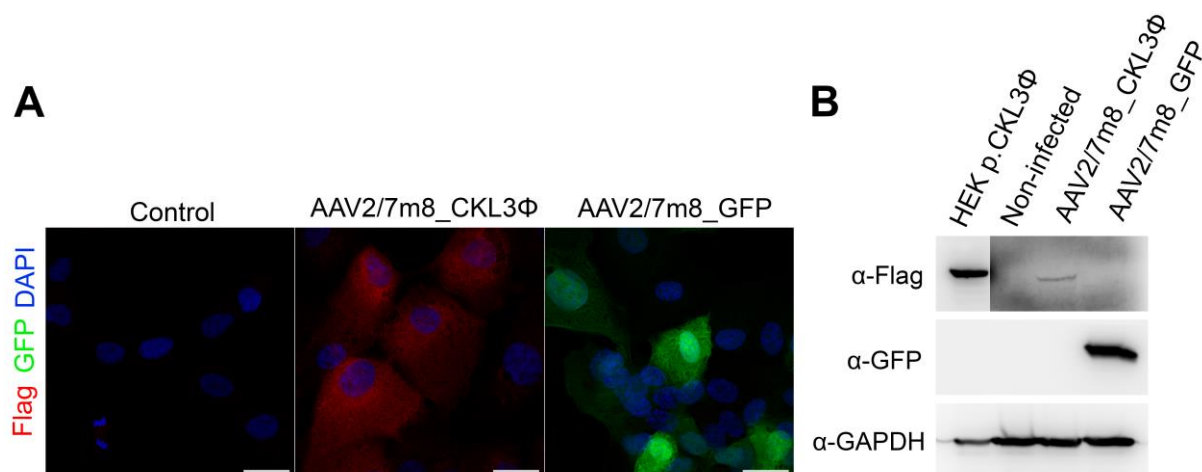
Figure 34. The new AAV2/7m8_CERKLa-3×FLAG viruses efficiently transduce ARPE-19, which express CERKLa-3×FLAG protein. (A) Immunocytochemistry of ARPE-19 cells infected with AAV2/7m8_CERKLa-3×FLAG (AAV2/7m8_CKL3Φ) or AAV2/7m8_GFP vectors showed positive GFP (green) and FLAG (red) staining, nuclei were counterstained with DAPI (blue). Scale bar: 25 μm. (B) Western blot of protein lysates from ARPE-19 cells infected with AAV2/7m8_CERKLa-3×FLAG (AAV2/8_CKL3Φ) or AAV2/7m8_GFP vectors immunodetected with antibodies against FLAG, GFP and GAPDH.

Consequently, now we can undertake one of the main goals of this project: the assessment of potential therapeutic outcomes of AAV2/7m8_CERKLa-3×FLAG using subretinal injections in *KD/KO* mice. To do so, we are currently proceeding with the breedings to obtain an appropriate number of *WT/WT* and *KD/KO* mice to perform the corresponding subretinal injections and analyse the phenotypic rescue at the adequate timepoints.

DNA-wrapped gold nanoparticles as gene-delivery system: Background

The development of gene-therapies for IRDs has been increasingly growing during the last years and the design and use of nanomaterials as vectors to deliver therapeutic genes are showing its huge potential in improving the efficacy and safety of current therapies and surgical procedures. Nanomaterial-based drug delivery methods allow to increase the bioavailability of bioactive molecules, prolong its release, and decrease either dose or injection frequency *in vitro* and *in vivo* compared to other delivery systems. In addition, delivery systems using nanomaterials may overcome the limited packaging capacity of AAVs, as well as associated immunogenic responses (233).

Our research group, in collaboration with Dr Sonia Trigueros, an expert in the field of nanoparticles, gathered preliminary evidence of promising nano-based gene-delivery approach for therapy. We showed that DNA-wrapped gold nanoparticles (AuNPs) efficiently achieved gene-delivery *in vitro* in ARPE-19 cells (234). These results shed light on the opportunity to use this technology as an alternative approach to viral vectors in gene-augmentation treatments for IRDs.

As a continuation of these first gene-delivery attempts using AuNPs in ARPE-19 cells, I have continued this research line using a more physiological tissue, mouse retinal explants, again in collaboration with Dr Sonia Trigueros.

Transfection of retinal explants using DNA-wrapped gold nanoparticles

Retinal explants represent a useful tool to study retinal architecture and physiology without disturbing the structure of the tissue and preserving cell-cell interactions. Maintaining retinal explants in culture is a delicate procedure. It requires sterile conditions for the dissection and incubation of the tissue, as well as experimented skills for the proper surgical isolation of the retina. In our experience, the maximum incubation time without bacterial contamination has been 24 hours.

I first aimed to optimize the protocol for obtaining retinal explants and performing immunohistochemistry while maintaining the retinal structure. Once we achieved to preserve the retinal morphology, we transfected mouse retinal explants with DNA-wrapped AuNPs. We considered GFP as a useful reporter gene to detect transfected

cells and thus transfected retinal explants with AuNPs-pEGFP-N2. GFP-positive cells were observed in retinal flat-mounts after 24 hours (Figure 35).
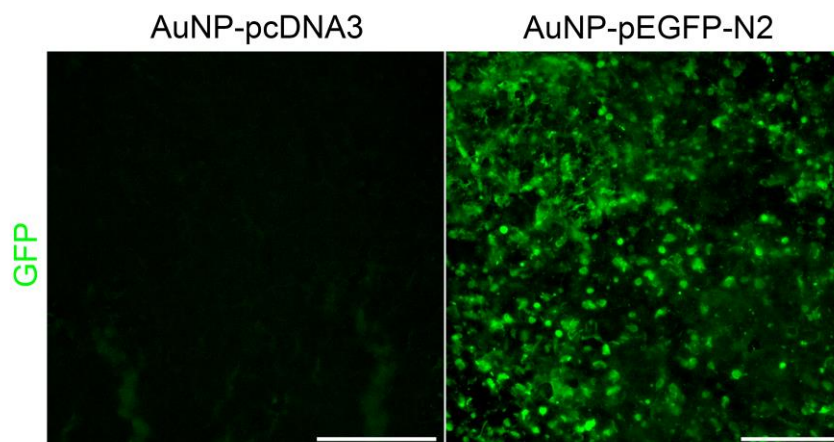
Figure 35. **Transfection of retinas** *ex vivo* **using DNA-wrapped AuNPs results in GFP-positive cells.** Transfection using AuNP-pcDNA3 (negative control) and AuNP-pEGFP-N2 in 24-hours cultured retinal explants. Scale bar: 50 µm.

Transfection with DNA-wrapped gold nanoparticles targets rod photoreceptors

We were interested in assessing whether AuNPs showed some target specificity in delivering DNA to specific retinal cell types. To this end, we immunodetected the transfected reporter gene (GFP) together with cell-specific biomarkers. Although the levels of transfection are not high, we could observe that the GFP signal colocalized with the rod-specific biomarker IMPDH-1, indicating that DNA-AuNPs are able to transfect rods (Figure 36A). However, we were not able to detect colocalization between GFP and the cone-specific biomarker cone arrestin (Figure 36B). As the number of cones in the mouse retina is very low, and the transfection efficiency was also limited, we cannot conclude whether DNA-AuNPs targeted specifically rods but not cones, or was just a unique observation due to the low number of transfected cells that needs replication.
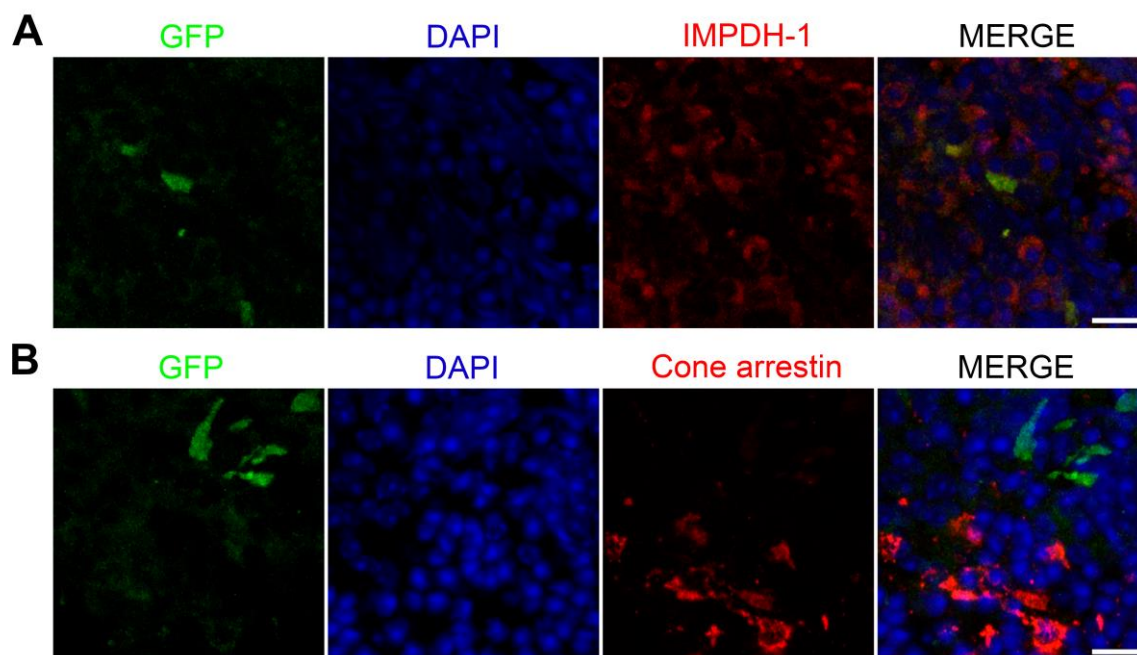
Figure 36. AuNP-pEGFP-N2 can transfect rod photoreceptor cells. (A) Representative confocal image showing GFP-positive cells colocalizing with rod-specific biomarker IMPDH-1 (red). Scale bar: 10 µm. (B) Representative confocal image indicating no colocalization between GFP-positive cells and the cone-biomarker cone arrestin (red). Scale bar: 10 µm.

In summary, our results provide solid evidence of photoreceptor cells transfection in retinal explants using DNA-wrapped gold nanoparticles, even though the efficiency is still low, suggesting that the usage of DNA-wrapped AuNPs might be a feasible delivery system for gene therapies in the retina. Nonetheless, further work is required both to improve the efficiency of this technique, as well as to accurately define the transfected retinal cell types by immunodetection using cryosections.

MATERIAL AND METHODS

Animal handling

C57BL/6J *Cerkl*^{WT/WT} and *Cerkl*^{KD/KO} mice were bred and housed in the animal research facility of the Faculty of Pharmacy at the University of Barcelona. Animals were provided with food and water *ad libitum* and maintained in a temperature-controlled environment in a 12/12 hours light–dark cycle. All animal handling and assays were performed according to the ARVO statement for the use of animals in ophthalmic and vision research, as well as the regulations of the Ethical Committee for Animal Experimentation (AEC) of the Generalitat de Catalunya (protocol C-449/18 for maintenance and C-15/22 for gene therapy), according to the European Directive 2010/63/EU and other relevant national guidelines. Each cohort had equivalent proportion of male and female mice, as autosomal recessive retinitis pigmentosa affects similarly both biological sexes.

Genomic DNA and genotyping by PCR

DNA for genotyping was extracted from ear punches. Primers for genotyping and PCR conditions were previously described in (159).

Cloning *CERKLa* into the p8 GFP-3×FLAG plasmid

The p8.GFP-3×FLAG plasmid was digested with the restriction enzymes KpnI (Thermo Fisher Scientific, Waltham, MA, USA; FD0524) and BsrGI (New England BioLabs, Ipswich, MA, USA; R0575S) using Buffer C (PROMEGA, Madison, WI, USA; R003A) during two hours at 37 °C to free the GFP-encoding fragment. The resultant backbone (p.3×FLAG), required for AAVs construction, was purified using the kit NZYGelpure (NZYTech, Lisbon, Portugal; MB01101), according to manufacturer's instructions, after 1 % agarose gel electrophoresis.

PCR was conducted to amplify the *CERKLa* cDNA insert using the polymerase AccuPrime™ Taq DNA High Fidelity (Invitrogen, Waltham, MA, USA; 12346-086) and appropriate primers (forward 5′ GG<u>GGTACC</u>CCAATACGACTCACTATAGGGAGACC 3′, reverse 5′ TATA<u>GGTACC</u>TATAGTACTTTGGAATCATTTCTTCCAT 3′) containing restriction targets (underlined) for KpnI (5′ end) and Acc65I (3′ end). The PCR product

was purified with the NZYGelpure kit (NZYTech, Lisbon, Portugal; MB01101) according to the manufacturer's indications and subsequently digested with KpnI and Acc65I (Thermo Fisher Scientific, Waltham, MA, USA; FD0904) using the FastDigest Green buffer (Thermo Fisher Scientific, Waltham, MA, USA; B72).

Purified *CERKLa* cDNA insert and AAV-vector backbone were ligated in a 3:1 ratio with T4 DNA ligase (Invitrogen Waltham, MA, USA; IVGN2104) overnight at 17 °C. After bacterial transformation, the recombinant constructs were identified by differential restriction pattern using BamHI (Thermo Fisher Scientific, Waltham, MA, USA; FD0054) and Acc65I restriction digestion.

Bacterial transformation and culture

For bacterial transformation, DNA was introduced in competent DH5α *Escherichia coli* cells by heat shock (42 °C for 90 seconds). Cells were then kept in ice for 2 minutes, recovered at 37 °C for 1 hour in Lysogeny broth (LB) and plated in LB-agar plates supplemented with kanamycin for incubation overnight at 37 °C. Then, individual recombinant colonies were picked and transferred into 3-5 mL LB tubes with 25 µg/ml kanamycin and incubated overnight at 37 °C in a shaker. The following day, plasmid purification was performed with QIAprep Spin Miniprep Kit (Qiagen, Germantown, MD, USA; 27104) following manufacturer's indications.

DNA sequencing

Sanger sequencing was performed to verify the sequence integrity, orientation of the inserts and reading frame using the BigDyeTM Terminator v3.1 Cycle Sequencing Kit (Thermo Fisher Scientific, Rockford, IL, USA; 4337455). For each reaction, we used 0.5 µM of each primer (forward and reverse) (Table 3), 1× BigDye Buffer (Applied Biosystems), 1 µL of BigDyeTM Terminator v3.1 Ready, the appropriate amount of DNA and PCR-grade H_2O up to 10 µL. The PCR program was as follows: 94 °C for 2 minutes and 28 cycles of 96 °C for 10 seconds, 50 °C for 5 seconds and 60 °C for 4 minutes. Electropherograms were analysed using the alignment software available in Benchling (https://benchling.com), which aligns the obtained reads to a reference sequence.

. Primers used for p.CERKLa-3×FLAG construct sequencing.

Name	Sequence (5' → 3')
CERKL Exon 3 Reverse	TGCAAGCTTCAACAGAGGTTCAAC
CERKL Exon 6 Forward	GTTCCTCATGTGATAACTGCAACTGC
CERKL Exon 7 Reverse	AAGCTTGCCAGCGGTGC
CERKL Exon 11 Forward	CGAAACACTTCTCGGCCAGAAT
CERKL Exon 12 Reverse	CCTCAACAGTGTAAGTCTCAACAAATGG

Subretinal injection of AAV vectors

One-month-old C57BL/6J *Cerkl*$^{WT/WT}$ and *Cerkl*$^{KD/KO}$ mice were anesthetized using a mixture of Ketamine (100 ng/kg)/Xylacine (10 ng/kg) by intraperitoneal injection. Then, with the help of a dissecting microscope, the eye was slightly pulled out to perform a conjunctivectomy at the level of the limbus, followed by a sclerotomy using a 30-gauge needle. Next, the 33-gauge needle (Hamilton, Reno, NV, USA; HAM 7762-06) of a Hamilton syringe (Hamilton, Reno, NV, USA; HAMI7635-01) was introduced in the subretinal space created by the sclerotomy to deliver 1 µL of AAV solution (or 1× PBS in control injected eyes), containing a maximum concentration of 1×10^9 viral particles per µL and a 1:5 ratio between AAV2/7m8_GFP and AAV2/8_CERKLa-3×FLAG, respectively. After removal of the syringe, 0.3 % gentamicin antibiotic cream was applied to the injected eyes. Injected retinas were harvested after careful dissection and isolation from RPE and assessed 1-2 months after subretinal injection.

Cell culture, transfection and AAV transduction

To confirm the correct expression of p.CERKLa-3×FLAG in human and mouse cells, we transfected HEK293 (human embryonic kidney cell line) and *WT/WT* mouse pRPE (stablished line, see Material and Methods from Results Chapter 1.3) cells using lipofectamine 3000 (Thermo Fisher Scientific, Waltham, MA, USA; L3000015). ARPE-19 cells were used to verify the transduction efficiency of AAV2/8_CERKLa-3×FLAG and AAV2/7m8_CERKLa-3×FLAG vectors.

Prior to transfection and transduction assays, HEK293 and ARPE-19 cells were cultured and grown in complete medium (HEK293 complete medium: 1 %

penicillin/streptomycin and 10 % FBS in DMEM; ARPE-19 complete medium: 1 % penicillin/streptomycin and 10 % FBS in DMEM:F12 (ratio 1:1)) until needed.

For transfection, a mix containing 25 µL of Opti-MEM Reduced Serum Medium (Thermo Fisher Scientific, Waltham, MA, USA; 31985070), 500 µg of DNA and 1 µL of P3000 reagent was added to a mix containing 25 µL of Opti-MEM Reduced Serum Medium and 1 µL of lipofectamine 3000 and incubated at room temperature for 10-15 minutes. Finally, the DNA:lipofectamine 3000 mix was added to 1.5×10^5 cells (HEK293 or mouse pRPE) seeded onto a 24-well plate wells in complete medium and incubated for 72 hours at 37 °C and 5 % CO_2 in a humified cell culture incubator. For immunocytochemistry experiments, cells were seeded onto poly-L-lysin-coated coverslips.

For AAV transduction, 1.16×10^5 ARPE-19 cells were seeded onto 24-well plate wells in 200 µL of DMEM:F12 (ratio 1:1). Cells were infected with the selected AAV using a 10^5 multiplicity of infection (MOI), equivalent to a total amount of 1.16×10^{10} viral particles per well. After 2 hours of incubation at 37 °C and 5 % CO_2 in a humified cell culture incubator, 400 µL of ARPE-19 complete medium was added to the cells, which were further incubated for 72 hours to obtain genomic DNA and RNA or conduct protein analyses by immunocytochemistry and Western blot.

Retinal explants culture

Eyes were enucleated from adult *WT/WT* mice and dissected in 1× PBS supplemented with 1 % penicillin/streptomycin. Next, retinas were obtained after cutting through the ora serrata and pulling from the posterior part of the eye. Then, retinas were flattened after 3-4 radial cuts from the extremes to the centre and cultured with photoreceptors face up for 2 hours in cell culture inserts (Millipore, Darmstadt, Germany; PICM03050) floating inside 6-multiwell plates containing retinal explant complete medium (Neurobasal™-A medium (Thermo Fisher Scientific, Waltham, MA, USA; 10888022) supplemented with 0.06 % D- Glucose, 0.0045 % $NaHCO_3$, 1 mM L-Glutamine, 1 % Penicillin/Streptomycin and 1× B27 (Invitrogen, Carlsbad, CA, USA; A3582801)) prior to transfection with DNA-wrapped gold nanoparticles. After transfection, retinal explants were further incubated for 24 hours in a humidified cell culture incubator at 37 °C and 5 % CO_2.

RESULTS

Transfection with DNA-wrapped gold nanoparticles

As previously described by Trigueros *et al.* (234), 100 µL of 40 nm gold nanoparticles (Sigma-Aldrich, St. Louis, MO, USA; S-741981) were mixed with 1 µg of plasmid DNA (pEGFP-N2 or pcDNA3) to produce plasmid DNA-gold nanoparticles hybrid structures. A 20 µL drop of DNA-wrapped gold nanoparticles (pEGFP-N2 or pcDNA3 as negative control) was added onto retinal explants. Photothermal plasmon resonance of the gold nanoparticles was activated by white light irradiation (235). Subsequently, retinal explants were relocated to the incubator for 24 hours prior to analysis of the transfection efficiency. The specific details of the DNA-nanoparticle wrapping reaction and transfection are currently subject to a patent and published under standard free patent procedures (236).

RNA extraction and cDNA synthesis

RNA extraction and purification from cells was performed using the RNeasy Plus Mini Kit (Qiagen, Hilden, Germany; 74134) according to manufacturer's indications. After elution in 30 µL, 1.5 µL of Ambion™ DNase I (Thermo Fisher Scientific, Rockford, IL, USA; AM2222) was added to the samples and incubated for 1.5 hours at 37 °C. Next, genomic DNA clean-up was performed using High Pure RNA Isolation Kit (Roche Diagnostics, Indianapolis, IN; 11828665001) following manufacturer's instructions. To evaluate RNA purification, PCR was performed using 2 µL of RNA sample and primers against the housekeeping gene *GAPDH* (hGAPDH forward: 5' CGACCA CTTTGTCAAGCTCA 3' and hGAPDH reverse: 5' TGTGAGGAGGGGAGATTCAG 3'). The PCR program was as follows: 94 °C for 5 minutes and 35 cycles of 94 °C for 30 seconds, 64 °C for 30 seconds and 72 °C for 10 seconds. Once the RNA sample was pure and free of genomic DNA contamination, copy DNA (cDNA) was generated by reverse transcription PCR (RT-PCR) using 15 µL of RNA with the qScript cDNA Synthesis Kit (QuantaBio, Beverly, MA, USA; 95047-100) according to manufacturer's specifications. Finally, cDNA synthesis was verified with *GAPDH* PCR as previously explained.

AAV-coding regions amplification by PCR

To verify the presence of DNA inside AAV capsids in addition to AAV transduction and transcription, we performed PCRs to amplify specific *CERKLa-3×FLAG* or *GFP-*coding sequences.

Viral DNA was extracted from AAV capsids first by adding 1 μL of Ambion™ DNase I to $1.16×10^{10}$ viral particles, followed by incubation during 1 hour at 37 °C to eliminate external DNA. Then, Ambion™ DNase I was inactivated and AAV capsids were denatured by incubation at 95 °C for 10 minutes. To normalize the quantity of DNA in the following PCR, we added the same approximate amount of p.CERKLa-3×FLAG and p8.GFP-3×FLAG plasmid DNAs (positive controls) compared to the number of viral particles, after considering the molecular size and concentration of each vector.

Viral DNA, total DNA and cDNA from transduced cells were used to amplify *CERKLa-3×FLAG* or *GFP*-encoding sequences by PCR using appropriate pairs of primers (Table 4). The PCR program was as follows: 94 °C for minutes and 35 cycles of 94 °C for 30 seconds, 62 °C for 30 seconds and 72 °C for 35 seconds. PCR products were analysed by 1 % agarose gel electrophoresis.

Table 4. Primers used to amplify CERKLa-3×FLAG or GFP-coding sequences.

Name	Sequence (5' → 3')
p. CERKLa-3×FLAG 5'UTR Forward 1	GGTTTAGTGAACCGTCAGATCACTAGT
CERKLa Reverse 1	CTTAGAATCACCCGCCGG
CERKLa Forward 2	CAGTCTTTATGGAGGAAGCATGG
p. CERKLa-3×FLAG 3'UTR Reverse 2	GGGCCACAACTCCTCATAAAGA
GFP Forward	AAGGACGACGGCAACTACAAG
GFP Reverse	CTTCTCGTTGGGGTCTTTGC

Immunocytochemistry and immunohistochemistry

After fixation with 4 % PFA for 15 minutes at room temperature, cells were permeabilized during 20 minutes with 0.2 % Triton X-100 (Scharlab, Hamburg, Germany; TR04441000) in 1× PBS and blocked with 1× PBS containing 5 % normal goat serum (Life technologies, Carlsbad, CA, USA; 16210064) for 1 hour at room temperature.

RESULTS

Retinal explants were fixed within the culture insert with 4 % PFA at room temperature for 1 hour. Retinal explant flat-mounts were permeabilized three times with 2 % triton X-100 (Scharlab, Hamburg, Germany; TR04441000) in 1× PBS for 10 minutes and blocked using 10 % normal goat serum (Life technologies, Carlsbad, CA, USA; 16210064) in 1× PBS for 1 hour at room temperature.

Then, cells or retinal explants were incubated with primary antibodies (anti-FLAG M2 (Sigma-Aldrich; F1804; 1:250), anti-GFP 488 (Thermo Fisher Scientific; A-21311; 1:250), anti-IMPDH1 (inhouse antibody kindly gifted by Dr Ana Méndez; 1:250), and anti-cone arrestin (Millipore; AB15282; 1:250)) in blocking solution overnight at 4 °C and secondary antibodies (AlexaFluor 488 anti-Mouse (Thermo Fisher Scientific, Rockford, IL, USA; A11017; 1:500), AlexaFluor 568 anti-Mouse (Thermo Fisher Scientific; A11004; 1:500), (PNA 647 (Invitrogen; L32460; 1:50), and AlexaFluor 568 anti-Rabbit (Thermo Fisher Scientific; A11001; 1:500)) with DAPI (Sigma-Aldrich, St. Louis, MO, USA; 10236276001; 1:1000) for 1 hour at room temperature. Finally, samples were mounted using Mowiol 4-88 (Merck, Kenilworth, NJ, USA) and visualized by fluorescence microscopy (ZOE Fluorescent Cell Imager, BioRad, Madrid, Spain), high-resolution microscopy (THUNDER Imager Live Cell & 3D Cell Culture & 3D Assay, Leica Microsystems, Wetzlar, Germany) or confocal microscopy (Zeiss LSM 880, Thornwood, NY, USA). Fluorescence images were analysed using ImageJ software.

Western blotting

Adult mouse retinas were lysed in RIPA buffer (50 mM Tris, pH 7.4, 150 mM NaCl, 1 mM EDTA, 1 % NP-40, 0.25 % Na-deoxycholate, protease inhibitors (Complete; Mini Protease Inhibitor Cocktail Tablets; Roche)) containing phosphatase inhibitors. Cell protein homogenates were directly collected by adding 30 μL of 1× Loading Buffer (60 mM TrisHCl pH 6.8, 10 % glycerol, 2 % Sodium Dodecyl Sulphate, 0.1 % Bromophenol blue in Milli®-Q water) and 5 % β-mercaptoethanol, and boiled for 5 minutes at 95 °C. Proteins were analysed by SDS-PAGE and transferred onto nitrocellulose membranes, which were blocked with 5 % non-fat dry milk in 1× PBS containing 0.1 % Tween 20 and incubated overnight at 4 °C with primary antibodies. After incubation with horseradish peroxidase-labelled secondary antibodies for 1

hour at room temperature, immunodetection was developed using the ECL system (Lumi-Light Western Blotting Substrate, Roche). Images were acquired by ImageQuant™ LAS 4000 mini Image Analyzer (Fuji-film) and quantified using ImageJ software. GAPDH loading control was used to normalize protein values. The primary antibodies were the following: anti-GAPDH (Sigma; G9545; 1:1000), anti-FLAG (Thermo Fisher Scientific; PA1-984B; 1:500), and anti-GFP (Abcam; ab290; 1:1000). The secondary antibodies were: HRP-labelled anti-mouse (Sigma; A5906; 1:2000) and anti-rabbit (GE Healthcare; NA934-100UL; 1:2000).
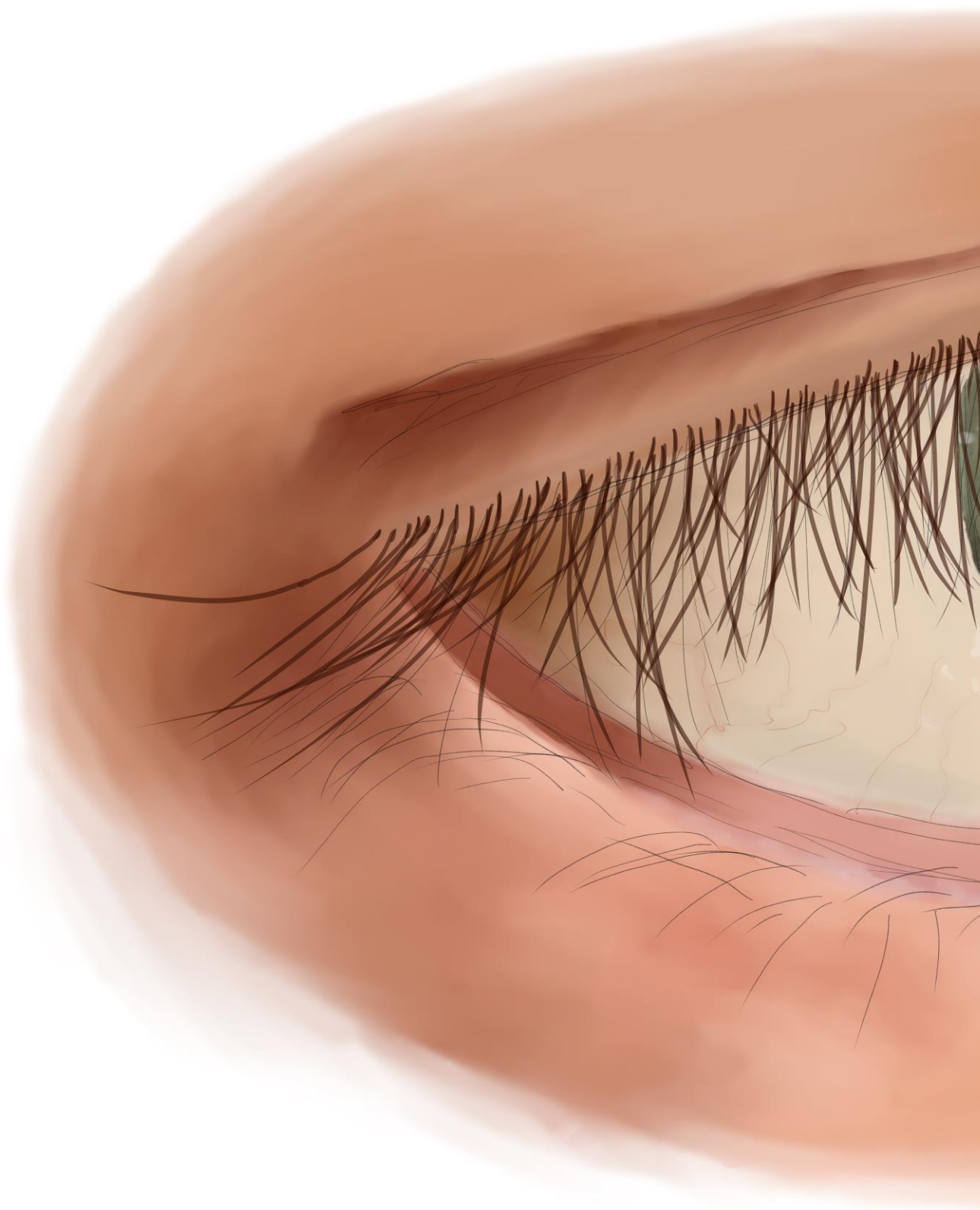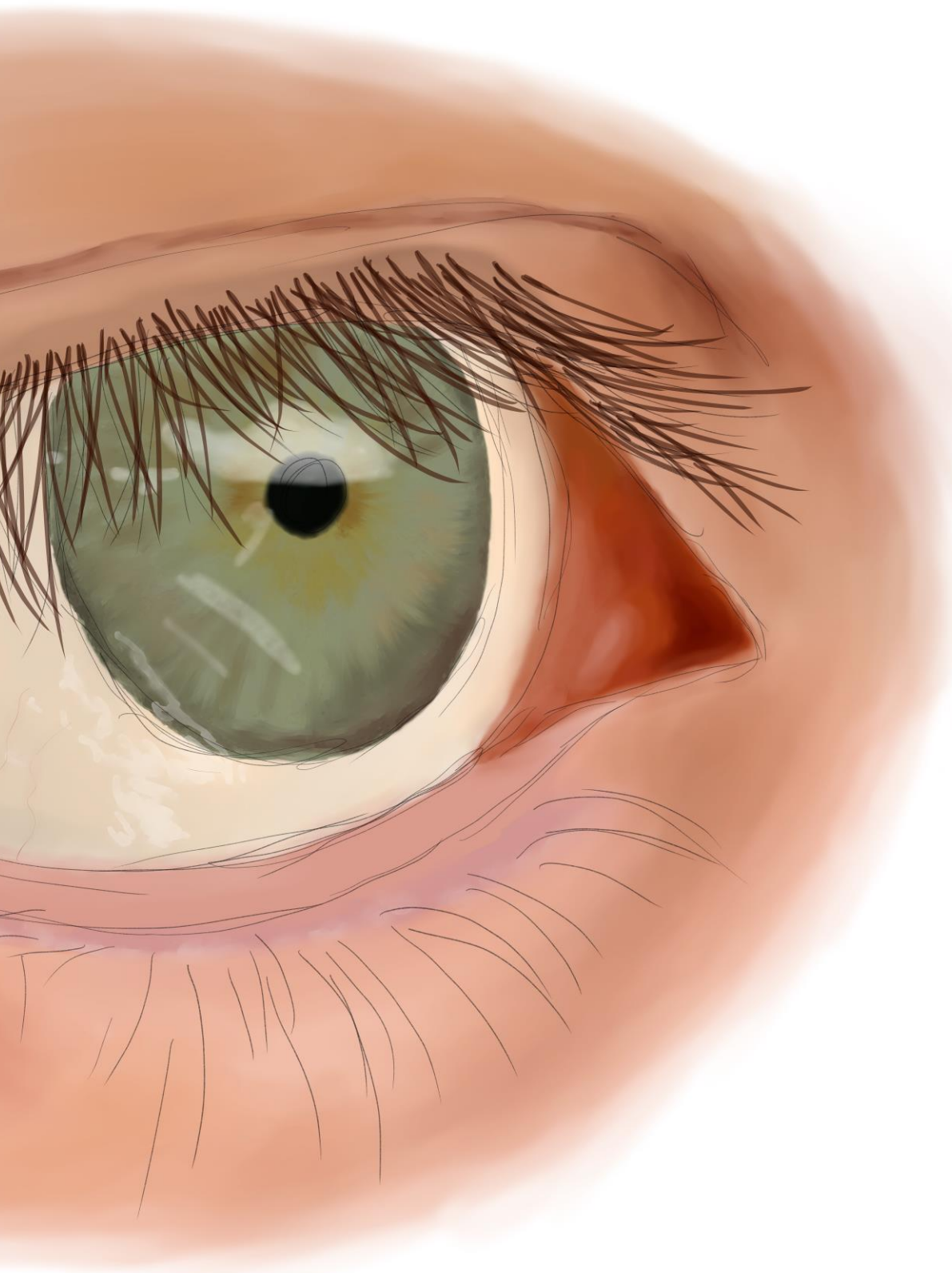
DISCUSSION

1. What is the physiological function of CERKL?

Since the discovery of the *CERKL* gene twenty years ago, multiple studies driven by various research groups have attempted to elucidate the function of CERKL using both animal and *in vitro* approaches without obtaining a clear and definite response. Nonetheless, all these investigations have largely contributed to the understanding of the nature of CERKL physiological role, clarifying the indubitable impact of CERKL in the accurate functioning of the retina. At the beginning of this Thesis, previous work had already associated CERKL with several mechanisms important to maintain retinal homeostasis, including protection against apoptosis, formation of stress granules, regulation of autophagy and modulation of mitochondrial antioxidant systems (143,149,151,152).

Here, we have further characterized the retinitis pigmentosa mouse model *Cerkl*[KD/KO], or *KD/KO* in short (which retains less than 10 % of *Cerkl* expression and undergoes progressive retinal degeneration and vision impairment (159)), in order to unravel the function of CERKL in a physiological environment devoid of this gene by carefully identifying and dissecting the altered pathways involved in *CERKL*-associated retinal degeneration.

1.1. CERKL modulates mitochondrial network dynamics and energetic metabolism

Considering the previously described interaction of endogenous CERKL with the mitochondrial antioxidant protein TRX2 in NIH3T3 cells (mouse fibroblast cell line) (149), our initial aim consisted in dissecting CERKL-mitochondria interplay in the retina and analysing the impact of *Cerkl* depletion in mitochondrial homeostasis and function.

We here describe the role of CERKL in modulating mitochondrial network dynamics. As previously commented in the introduction (Section 2.3), the mitochondrial network is an extremely dynamic entity that, in response to physiological cues, is continuously remodelling its morphology and subcellular distribution by means of several mechanisms, including fusion, fission, mitophagy and transport. The careful analysis of mitochondrial network morphology in different

retinal cell types –photoreceptor cells, retinal pigment epithelium (RPE) and retinal ganglion cells (RGCs)– has consistently revealed mitochondrial fragmentation associated with *Cerkl* depletion. In line with this observation, the assessment of the principal proteins associated to mitochondrial dynamics, along with the quantitative analysis of fusion/fission events using live-imaging techniques, indicated decreased mitochondrial fusion and overactivated fission due to *Cerkl* downregulation. A regulated balance between mitochondrial fusion and fission events is essential to maintain homeostasis and mitochondrial health, particularly in environmental or genetic stress conditions (237). Indeed, damaged mitochondria can be rescued by fusion with healthy mitochondria allowing functional complementation to restore their molecular content, membrane potential and homeostasis (238). In contrast, fission is usually associated with the segregation of unhealthy and dysfunctional mitochondria that are targeted to degradation through mitophagy (239). Notably, besides mitochondrial size reduction, we have also described accumulation of mitochondria in *Cerkl*-depleted photoreceptor cells, a result that points to an increased mitochondrial biogenesis or defective mitophagy. Conversely, and also in line with these results, overexpression of CERKL in 661W photoreceptor-derived cells caused a significant increase in mitophagy.

Furthermore, the analysis of mitochondrial morphology in *KD/KO* RGC axons evidenced a heterogeneous distribution of mitochondria throughout the axonal length, with the more distal regions being enriched in smaller mitochondria. In agreement with that observation, mitochondrial trafficking was reduced in the axons of *KD/KO* hippocampal neurons, with decreased average velocity and accumulated distance. Particularly in neurons, mitochondrial trafficking is a pivotal mechanism underlying the correct subcellular distribution of mitochondria from the soma –where mitochondrial biogenesis occurs– to neurites and axons, in order to fulfil the subcellular needs and maintain neuronal survival and function (240,241). Hence, these findings reflect mitochondrial trafficking alterations due to *Cerkl* depletion, which probably culminate in the RGC cytoarchitectural changes observed in previous work, encompassing a more complex dendritic arbour and shortened axons (159), as well as functional impairment of the ganglion cell layer described in the *Cerkl*[KD/KD] model (158).

All the described alterations affecting mitochondrial dynamics are indicative of metabolic stress and homeostatic imbalance. The retina is a high metabolic rate tissue that relies in glycolysis and oxidative phosphorylation (OXPHOS) to provide for its high energy demands, although the latter has been demonstrated to be more advantageous in terms of energetic yield. In particular, photoreceptor mitochondria have been shown to perform close to their maximal respiratory capacity, with a limited reserve capacity of 25 % (242). Consequently, alterations in aerobic energetic metabolism can compromise photoreceptors survival. Our data from functional assays in the retina points to CERKL exerting an influence on mitochondrial respiration, but not in glycolysis or glucose oxidation. Here we demonstrate that *Cerkl* downregulation impairs mitochondrial bioenergetics in the neuroretina and RPE, coupled with differential alterations in various OXPHOS proteins. In this context, energy depletion may represent a metabolic trigger for the described wide spectrum of mitochondrial alterations that eventually cause oxidative stress in retinal cells.

Moreover, and in agreement with the report that described CERKL-TRX2 interaction (149), our immunostaining results verified the colocalization of a pool of endogenous and overexpressed CERKL isoforms with mitochondria in mouse retinal neurons and RPE cells. Using two inhouse antibodies, anti-CERKL2 and anti-CERKL5, which detect epitopes encoded by exon 2 or 5, respectively, we observed that the pool of endogenous CERKL isoforms containing exon 5 –thus recognized by anti-CERKL5 antibody– strongly colocalized with mitochondria, while CERKL isoforms displaying exon 2 diffusely localized through the cytoplasm and colocalized with mitochondria to a lesser extent. Based on these findings, we speculated that the ATP-binding site –encoded by exon 5– would be responsible for the interaction with mitochondria. In fact, the most prevalent mutation in *CERKL*, *CERKL^{R257X}* (also called *CERKL^{R283X}*), resides in exon 5, thus highlighting the relevance of this CERKL region.

Unexpectedly, data collected from overexpression experiments in ARPE-19 cells using multiple alternatively spliced CERKL isoforms, revealed that overexpression of the CERKLc-GFP isoform (devoid of exons 3, 4, 4b and 5, thus lacking the DAGK domain and ATP-binding site), consistently localized at mitochondria, even at a higher concentration than CERKLb-GFP (the longest human isoform, which includes

exon 4b), which localized all over the cell. Hence, we hypothesized that the structural domain participating in CERKL-mitochondria interaction should be common between CERKLb and CERKLc isoforms. As both isoforms share the N- and C-terminus, the common protein domains include the pleckstrin-homology (PH) domain, the two nuclear localization signals (NLS), the two nuclear export signals (NES) and the CERKL C-terminus. Given that several studies have widely discussed the binding properties of the PH domain to several membranes and lipids, including phosphoinositides and cardiolipin –two lipids present in mitochondria (243–245)–, we surmised that the PH domain might function as an anchor between CERKL and the mitochondrial membranes. Importantly, phosphoinositides are regulatory lipids that participate in the regulation of mitophagy, mitochondrial fission and energy production (245), whereas cardiolipin is a crucial mitochondrial lipid that contributes to properly structure the inner mitochondrial membrane. Of note, in response to mild stress, cardiolipin shifts its location from the inner to the outer mitochondrial membrane of damaged mitochondria, thus labelling them for mitophagy. Additionally, upon intense stress conditions, the outer mitochondrial membrane-associated cardiolipin is oxidized favouring the release of cytochrome c and other apoptotic factors, triggering apoptosis (246). In light of these data, we contemplated that CERKL interaction with mitochondria might be mediated by these lipids, especially considering the role of cardiolipin as a stress sensor, to potentially recruit CERKL to mitochondrial membranes in response to damage. Nonetheless, further research is needed to identify the CERKL domain required for mitochondrial targeting and the specific mitochondrial lipid or protein implicated in CERKL-mitochondrial association.

To sum up, the accumulation of fragmented mitochondria, coupled with the alteration in mitochondrial dynamics (reduced fusion, increased fission, altered mitochondrial distribution and trafficking) and the impairment of OXPHOS due to CERKL downregulation, altogether highlight the importance of CERKL in the proper regulation of mitochondrial network and bioenergetics, as well as the possible contribution of CERKL-mitochondria interaction to the retinal disease genesis and progression. Ergo, these exhaustive analyses provide new insights into the altered

metabolic pathways in *CERKL*-associated IRDs and open new opportunities to test pharmaceutical therapeutic approaches (further discussed in Discussion Section 3.1).

1.2. Autophagy activation is mediated by CERKL levels

In a global scenario of metabolic stress due to the accumulation of damaged and dysfunctional mitochondria, activation of autophagy can contribute to restore cellular homeostasis by i) compensating metabolic imbalance by supplying nutrients and energy; ii) eliminating oxidative stress-damaged cellular components and organelles; and iii) inducing the p62-KEAP1-NRF2 axis to activate the antioxidant response. Our collected data from RNA-Seq, Western blotting and immunodetection analyses indicates an enhanced activation of autophagy —but not mitophagy— in retinas with severe depletion of *Cerkl*, although this effect was not maintained during ageing, suggesting that these changes might act as acute protective mechanisms to restore cellular homeostasis and/or initial manifestations of cell death commitment. Nonetheless, colocalization analyses demonstrated that CERKL was not directly interacting with autophagic structures (detected by LAMP1 and p62). Interestingly and unexpectedly, our reported data are completely opposite to other reports that describe autophagy impairment, rather than activation, upon CERKL downregulation in RPE human cells and zebrafish retinas. In this study, Hu *et al* described the interaction between CERKL and SIRT1, an important deacetylase that regulates the autophagic flux. Indeed, CERKL contributes to the stabilization of SIRT1 and as expected, CERKL downregulation causes a decrease in SIRT1 levels (152). This phenomenon was also observed in the *KD/KO* model, despite of the contradictory and paradoxical results regarding autophagy ultimate outcome. These conflicting findings suggest the contribution of additional molecular players in autophagy regulation in the mammalian retina and highlight the necessity of complementary studies to outline the function of CERKL-SIRT1 interaction on autophagy induction in the mammalian retina. We propose that CERKL might operate as a regulatory component of the autophagic pathway, as an initial sensor or mediator, without playing a physical direct role in the process itself.

DISCUSSION

1.3. CERKL as a stress-sensor and antioxidant-regulator protein

CERKL has been proposed as an orchestrator of the oxidative stress retinal response, even though its precise molecular function remains enigmatic. Several studies have reported that the *in vitro* overexpression of CERKL —usually the full-length isoform, namely CERKLa— protects cells against oxidative stress-induced apoptosis, while the downregulation of CERKL compromises cell viability (143,148,149). In our *in vitro* studies, we decided to overexpress CERKLb isoform —a primate-exclusive isoform— instead of CERKLa, to test if the addition of exon 4b, which displays an extra helix outside the main core of the protein predicted structure, within the DAGK domain (Figure 37) could confer complementary protective roles. Moreover, overexpression of the shorter alternatively spliced isoform, CERKLc, was also performed to check the rescue ability of this isoform from oxidative stress even though it lacks the DAGK domain and ATP-binding site (Figure 37). Our data revealed that the overexpression of both CERKLb and CERKLc isoforms in ARPE-19 cells provides protection against oxidative stress and preserves mitochondrial network morphology. These findings align with the formerly commented colocalization of CERKLc with mitochondria, reinforcing the idea that exon 5-encoding region is not required for the interaction with these organelles. Additionally, CERKLb and CERKLc overexpression decreases the basal levels of mitochondrial superoxide in both control and oxidative stress conditions, thus reducing mitochondrial damage. Therefore, we here describe an additional stress-protective mechanism of CERKL that contributes to the maintenance of mitochondrial network morphology and redox status.

Previous investigations have unveiled the intricate transcriptional complexity of h*CERKL*/m*Cerkl* gene in both human and mouse retinas, yielding more than 20 different transcriptional isoforms (142). Our results from *in vitro* overexpression of both CERKLb and CERKLc isoforms showed no differences in their capacity to protect the mitochondrial network against oxidative stress, although their subcellular distribution and mitochondrial colocalization was slightly different, indicating that both alternatively spliced isoforms equally contribute to the protection against oxidative stress.
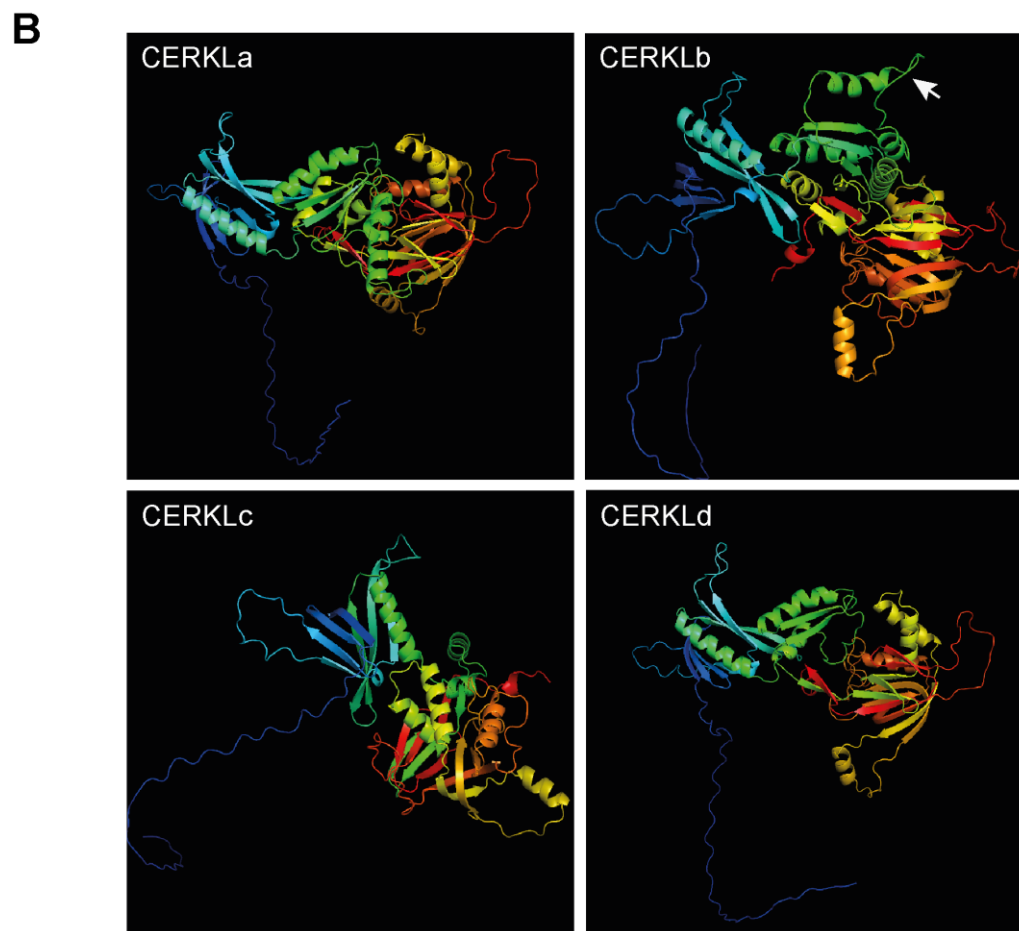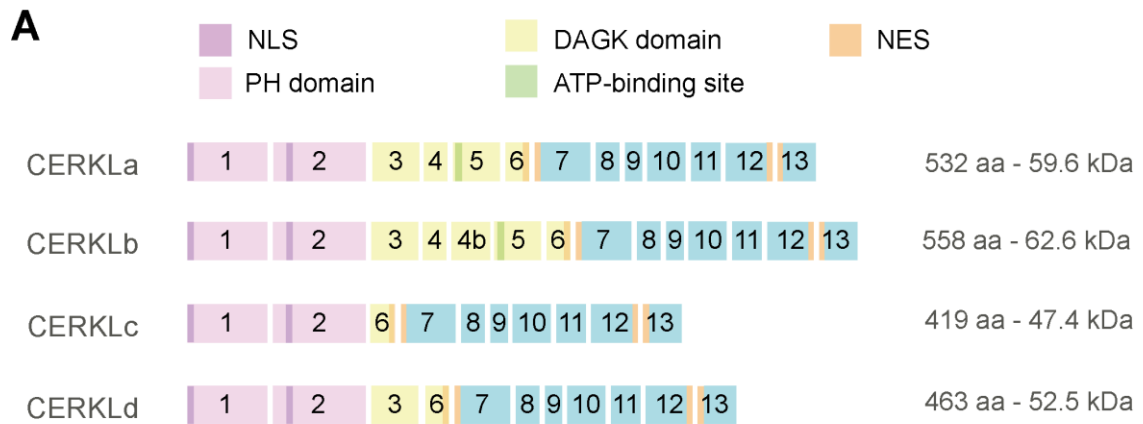
Figure 37. Similarities and differences in protein domains and 3D structure of alternatively spliced human CERKL isoforms. (A) Graphical representation of the protein domains (in colours) included in each alternatively spliced CERKL isoform. Each number indicates the exons present in each isoform. NLS: nuclear localization signal; PH domain: pleckstrin homology domain; DAGK domain: diacylglycerol kinase domain; NES: nuclear export signal. (B) Inferred 3D structure of each alternatively spliced CERKL isoform. The additional helix generated by exon 4b in CERKLb isoform is indicated by a white arrow. Structural analysis performed with Pymol software using rainbow illustration: blue corresponds to the N-terminus and red to the C-terminus. Structural data retrieved from AlphaFold Protein Structure Database (https://alphafold.ebi.ac.uk).

DISCUSSION

However, affectations in the full-length protein –as it happens for instance in patients carrying *CERKL*[R257X] mutation, located in exon 5, skipped in some CERKL isoforms– cause retinal neurodegeneration and vision impairment, thus suggesting that the presence or absence of protein domains in the numerous CERKL isoforms might result in differential intracellular physiological roles. Thus, this evidence highlights the importance of the proper function of the full-length isoform of CERKL to preserve retinal homeostasis.

In contrast with the results obtained from CERKL overexpression experiments, we observed that CERKL depletion aggravates the damage produced by light/oxidative stress. *CERKL* downregulation *in vitro* failed to maintain mitochondrial network morphology and bioenergetics, especially in response to oxidative stress. In agreement with other reports (148,149,151), we described the participation of different pools of CERKL isoforms in the production of stress assemblies in response to oxidative stress in *WT/WT* primary cultures of retinal ganglion cells (RGCs). Remarkably, *Cerkl*-depleted retinal neurons exhibited an exacerbated stress granule-mediated response in basal conditions, reaching similar levels to those observed in *WT/WT* upon stress, both *in vitro* and *in vivo*. In fact, oxidative/light stress did not enhance this response in *KD/KO*, compared with the already overactivated basal response. A similar behaviour was also detected when analysing glutathione metabolism, which was already impaired in *KD/KO* retinas in basal conditions, exhibiting equivalent levels of GSH/GSSG balance and total quantity of glutathione as *WT/WT* light-stressed retinas. In addition, CERKL participates in the regulation of some enzymatic antioxidant systems, particularly, CERKL interacts with the thioredoxin enzyme TRX2 and maintains its antioxidant function (149). Our findings indicate alterations in the levels of other peroxiredoxin enzymes in *KD/KO* retinas, such as PRX3 and PRX5, especially in response to light-stress, suggesting that CERKL may be also involved in the proper modulation of thioredoxin/peroxiredoxin enzymes. Thus, our data revealed an exacerbated but impaired antioxidant response in *KD/KO* retinas in basal conditions, possibly in response to a stress microenvironment due to *Cerkl* deficiency. In any case, these alterations make *KD/KO* retinas unable to further activate antioxidant mechanisms against additional stress

factors, which could definitely tip the scales towards activation of programmed cell death mechanisms instead of cell survival.

Furthermore, ROS levels were increased in *KD/KO* retinas upon stress conditions. An increase in ROS can damage mitochondria, which, at the same time, are the main source of ROS in cells, thus contributing to the generation of a vicious circle that ends up with ROS overproduction. In addition, the failure of the mitochondrial energy-supply system affects the proper functionality of repair systems, finally resulting in a redox imbalance that may lead to cell death (247). Given that we have described alterations in mitochondrial bioenergetics but also in the antioxidant response and maintenance of ROS levels, it is difficult to elucidate which is the first step initiating this vicious circle. On the one hand, CERKL might play a direct role in mitochondria, thus causing mitochondrial dysfunction when downregulated (149). On the other hand, several studies have postulated CERKL as a molecular hub in sensing stress, contributing to the antioxidant response through participation in different mechanisms (143,151). Nevertheless, all these different pathways are interconnected and are affected in the same direction upon *Cerkl* deficiency, pointing out that CERKL may exert an upstream regulatory function controlling all these mechanisms in health and disease. In fact, we detected a boost in CERKL levels in response to stress injury, further supporting the antioxidant role of CERKL. Nevertheless, the overregulation of CERKL levels was detected at the protein rather than transcriptional levels, pointing to a post-translational negative regulation of CERKL degradation in response to stress, as previously described upon hypoxia (248), or other mechanisms to increase protein stability in oxidative stress conditions.

In various neurodegenerative retinal disorders, a common feature is the activation of glial cells in response to the damage and degeneration of retinal cells, which elicits an inflammatory state within the retina (249). Our findings indicate an increase in gliosis in *KD/KO* retinas, irrespective of exposure to light-induced stress, probably as a consequence of the altered redox status and overactivation of antioxidant mechanisms that occurs due to *Cerkl* depletion, even in basal conditions. Indeed, gliosis implies chronic damage in *KD/KO* retinas, contributing to detrimental effects and potentially contributing to retinal neurodegeneration (6). Additionally, we

observed a late light-responsive loss of synaptic connections between photoreceptor cells and post-synaptic neurons in the *KD/KO* retinas (two weeks after injury), suggesting a remodelling of retinal connections as part of the neurodegenerative process, as discussed in other studies (7,250).

After describing alterations in many relevant mechanisms included in the oxidative defence system, we evaluated the antioxidant response p62-KEAP1-NRF2 master regulator axis, which was already altered in the analysis of autophagy (view Discussion Section 1.2). In a normal response to stress, p62 binds KEAP1 —the NRF2-ubiquitin ligase that targets NRF2 for proteasomal degradation (251)— to free NRF2. Consequently, NRF2 levels increase and NRF2 enter the nucleus to activate the transcription of many antioxidant genes, to restore the redox imbalance and suppress apoptosis activation (252). Nonetheless, in *KD/KO* retinas the p62-KEAP1-NRF2 axis is impaired at several levels: i) p62 levels are reduced; ii) levels of KEAP1 are slightly augmented; and iii) RNA levels of NRF2 are significantly lowered in *KD/KO* retinas. Consequently, several cell death mechanisms, including necroptosis, ferroptosis and apoptosis, are activated as a final outcome of light-induced injury, altered antioxidant mechanisms and gliosis. Therefore, the impairment of antioxidant responses eventually triggers retinal degeneration in *CERKL*-mutant retinas.

In summary, owing to our findings, we can conclude that *Cerkl*-depleted retinal cells are subjected to a basal overregulated stress status due to *Cerkl* deficiency and, consequently, are unable to cope with additional oxidative/light-stress damage, thus compromising retinal homeostasis. Furthermore, our data reflect the complexity of CERKL function within the retina, playing important roles in different cell types, from photoreceptor cells to RPE and RGCs. Therefore, in the exhaustive analysis of light-induced stress response in the *KD/KO* model, we have contributed to the assembly of several puzzle pieces into the intriguing challenge of understanding CERKL function in health and disease.

Figure 38. Graphical summary of the phenotypic features described in the *Cerkl*^{KD/KO} mouse model in basal and stress conditions. In *Cerkl*^{WT/WT} retinas, mitochondria are healthy and transported normally through axons (green arrows). *Cerkl*^{KD/KO} retinas display a set of alterations, mostly related to mitochondrial dysfunction and exacerbated stress responses. Upon light stress, *Cerkl*^{KD/KO} retinas suffer from increased ROS levels and neurodegeneration.

Cerkl^{WT/WT}

RPE
Rod
Cones
Horizontal cell
Müller glial cell
Bipolar cell
Microglia
Amacrine cell
RGC

RPE cell
Healthy mitochondria
Rod   Cone   RGC

Cerkl^{KD/KO}

- Accumulation of dysfunctional and fragmented mitochondria
- Activation of autophagy
- Exacerbated antioxidant response
- Multinucleation in RPE
- Gliosis
- Cytoarchitectural alterations in RGC
- Reduced mitochondrial trafficking ⟶

RPE cell
Rod   Cone   RGC

Cerkl^{KD/KO} under stress

- Ineffective stress response
- Increased ROS
- Fragmented and dysfunctional mitochondria
- Activation of cell death mechanisms
- Retinal neurodegeneration
- Loss of synaptic contacts

RPE cell
Degenerating rod and cone   RGC

Overall, we have described several early phenotypic biomarkers contributing to the pathogenesis of *CERKL*-associated IRDs, including alterations in mitochondrial network dynamics and metabolism, autophagy overregulation, exacerbated antioxidant responses and activation of cell death mechanisms. Our proposed model is illustrated in Figure 38, which highlights the complex nature of CERKL in regulating different processes, but particularly in the modulation of stress resilience, mitochondrial network, and metabolic homeostasis.

1.4. Is CERKL complete deletion lethal due to its physiological function in tissues other than the retina?

In the last five years, a growing number of studies have focused on the involvement of CERKL in stress resilience and apoptosis in tissues other than the retina, such as brain and epidermis. Peculiarly, CERKL expression is upregulated in zebrafish against viral infection as well as in human carcinoma cells, in order to provide a protection mechanism against damage in both cases (153,155). An additional report showed that CERKL overexpression alleviated brain injury produced by ischemia-reperfusion damage (154). In line with these results, our data from experiments in *KD/KO* hippocampal neurons revealed reduced mitochondrial trafficking, alterations in mitochondrial network organization and impaired oxidative phosphorylation. Therefore, the role of CERKL in preserving cellular homeostasis may be relevant also in non-retinal tissues. Consequently, it might be speculated that the complete deletion of *CERKL* could result in lethality or unviability of the individual. It is worth noting that the complete deletion of *CERKL* locus in homozygosis has not been identified in any patient yet, neither *CERKL* mutations have been associated to diseases other than IRDs. Therefore, we cannot discard the potential lethality of the complete loss of CERKL function.

On the other hand, previous analyses described the presence of evolutionarily conserved super-enhancer regulatory regions within *CERKL* locus that regulate the expression of *CERKL*, but also the upstream gene *NEUROD1* (223). NEUROD1 is a neural and pancreatic transcription factor involved in cell cycle regulation, neurogenesis in the retina and neuronal development (253,254). *NeuroD1* null mice are postnatally unviable due to severe diabetes, but the analysis of their neuronal

cells indicated that the cell viability is compromised (255,256). Indeed, in the *Cerkl^{KD/KO}* model the decreased expression of *Cerkl* highly correlates with a reduction in the expression of *NeuroD1*, pointing out that the phenotypical alterations observed in the *KD/KO* mouse model may be consequence of the hemizygous deletion in these regulatory sequences as well as of the synergic decreased expression levels of both *Cerkl* and *NeuroD1*. It is worth noting that targeted retinal deletion of *NeuroD1* in homozygosis causes severe photoreceptor alterations, with retinas being completely devoid of photoreceptors at 4 months of age (253), a much more severe phenotype than that observed in our *KD/KO* model, which still retains reduced *NeuroD1* levels. In conclusion, further research is required to fully understand the mechanism behind lethality in *Cerkl* knockout mice.

2. *CERKL^{R257X}* retinal organoids versus *Cerkl^{KD/KO}* mouse model: two complementary approaches

2.1. Similarities and differences

The usage of both hiPSC-derived 3D retinal organoids and gene-edited mice are both well-established models at the service of basic and translational research and are ideally used as complementary approaches to answer important biological questions. The total deletion or strong deficiency of genes in mouse models is a gold-standard technique to decipher the function of a particular gene in a whole physiological context. Animal models allow to analyse a large spectrum of physiological responses. Advances in retinal organoid technology provide the opportunity of modelling human retinal diseases *in vitro*, pinpointing the pathological mechanisms, and developing therapies for retinal degeneration (257). Thus, studies in animal models are excellently complemented with retinal organoids, a useful tool to model complex neurodegenerative diseases (such as IRDs) and confirm the functional data obtained in mouse.

In most of the patients carrying *CERKL* mutations, the full-length isoform of CERKL is generally affected, resulting in a truncated or dysfunctional protein due to nonsense and missense mutations, splicing alterations or indels (the detailed list of

DISCUSSION

CERKL mutations is in the Introduction, Table 1). Particularly in the *CERKL^R257X* mutation, the truncated protein isoforms may not even be produced due to nonsense-mediated mRNA decay.
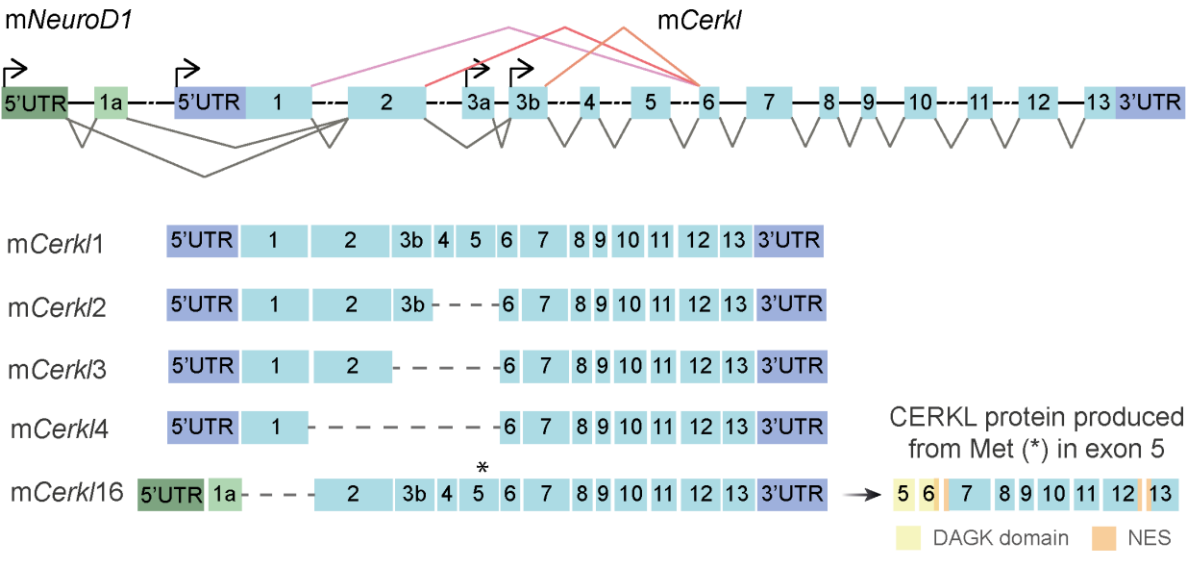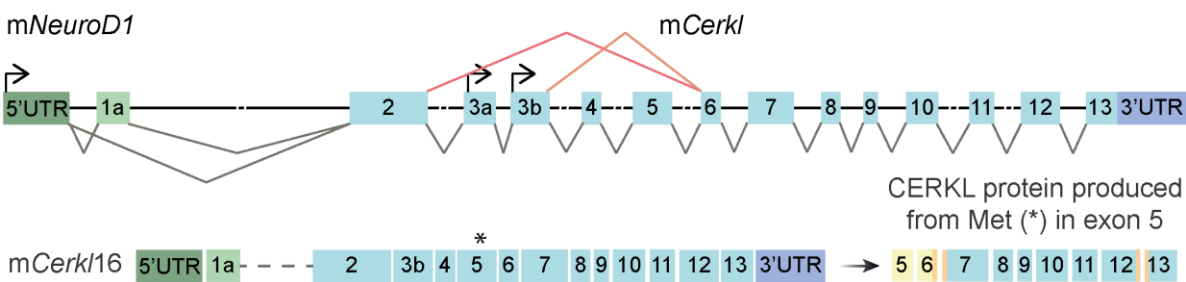
Figure 39. RNA isoforms and proteins derived from m*Cerkl^WT* and m*Cerkl^KD* alleles. In the upper panel, m*Cerkl^WT* allele presents 4 transcription start sites (black arrows), although the internal ones (3a and 3b) are not used in the retina. The RNA isoform m*Cerkl*1 is the full-length isoform and contains all the exons. Alternative splicing events, represented in colour (pink, red and orange), give rise to m*Cerkl*2, m*Cerkl*3 and m*Cerkl*4 isoforms. Non-canonical transcription start sites in *NeuroD1* produce m*Cerkl*16 isoform. The first in-frame methionine (Met, *) for m*Cerkl*16 isoform is located in exon 5, generating a protein isoform displaying the C-terminus of the DAGK domain (in yellow) and the two NES (in orange). DAGK: diacylglycerol kinase; NES: nuclear export signal. In the lower panel, representation of m*Cerkl^KD* allele and the derived RNA and protein isoforms produced from *NeuroD1* transcription start site. Information retrieved from (142).

Which are the transcripts and proteins produced in our *KD/KO* model? To answer this question, we have to bear in mind the high transcriptional complexity of m*Cerkl*.

In Figure 39 (upper panel), we have summarized the most abundant RNA isoforms in the wild-type retina generated from the alternative transcription start site from *NeuroD1* (m*Cerkl*16 isoform) and alternative splicing events (m*Cerkl*2, m*Cerkl*3 and m*Cerkl*4 isoforms) (Figure 39, upper panel) (142).

Instead, in the *KD/KO* mouse model, only *Cerkl* isoforms produced from the alternative *NeuroD1* transcription start site are generated (m*Cerkl*16 isoform) (Figure 39, lower panel). This occurs because the *KD/KO* mouse is a double heterozygote that possesses a knockdown (*KD*) allele that lacks the *Cerkl* promoter and first exon (Figure 39, lower panel), and also a complete knockout (*KO*) allele with no *Cerkl* expression in *trans*. As a consequence, all the isoforms generated from the proximal *Cerkl* promoter are not produced (Figure 39, lower panel). However, *KD/KO* mice maintain approximately 10 % of *Cerkl* expression produced from the upstream non-canonical transcription start site in *NeuroD1* gene, yielding the m*Cerkl*16 isoform (Figure 39, lower panel). Consequently, given that the first in-frame methionine –besides the initiating one in exon 1– is situated in exon 5, the m*Cerkl*16 isoform should produce a protein isoform devoid of the first 4 exons completely, where most of the described protein domains are located (Figure 39, lower panel), thus opening new questions about its subcellular location and physiological functions. Interestingly, CERKL isoforms produced from 3a and 3b internal transcription start sites –highly used in kidney– should also start in the methionine located in exon 5, resulting in the same C-terminal protein isoform. Nonetheless, a current research line in our group is studying the use of non-canonical translational initiation sites situated upstream the methionine in exon 5 in *CERKL* gene, which could also contribute to understand *CERKL* complex transcriptional and translational regulation and unveil feasible and novel CERKL isoforms.

It is worth noting here that none of the models, either the *CERKL*[R257X] patient's retinal organoids or the *KD/KO* mouse model, can produce the full-length isoform of CERKL, despite of the differential expression of alternatively spliced isoforms. On account of this fact, we consider that the detailed and exhaustive characterization of the *KD/KO* model will be helpful to focus our future studies and analyses of *CERKL*[R257X] patient's retinal organoids into specific pathways and metabolites, including the

organization and function of the mitochondrial network and the assessed antioxidant systems. However, considering the commented differences in the expression pattern of CERKL isoforms, as well as the secondary features derived from the whole deletion of *Cerkl* locus in the *KD/KO* model, in addition to the genetic background differences between species and physiological environments, we do not expect the same precise alterations in the *CERKL^{R257X}* retinal organoids as those described in the mouse model.

2.2. Future perspectives using *CERKL^{R257X}* retinal organoids

As the IRDs associated to mutations in *CERKL*, particularly retinitis pigmentosa in *CERKL^{R257X}* mutation, are late-onset diseases, the selected timepoints for the assessment of proper differentiation and analysis of molecular, cellular, and functional phenotypic biomarkers were 150 and 200 days of differentiation. At the first timepoint, we aim to study the structural lamination of the retinal organoids, as well as the formation of photoreceptor OSs. In addition, at this timepoint, we can also assess *CERKL* expression in the human tissue and early phenotypic disease biomarkers. On the other hand, retinal organoids will already be fully differentiated when they reach the second selected timepoint (day 200 of differentiation), thus allowing us the study of physiological alterations in the retinal function by electroretinograms, on top of the analysis of phenotypic disease biomarkers and cell death activation.

Besides the directed phenotypic evaluation of *CERKL^{R257X}* retinal organoids exploiting the detailed characterization of the *KD/KO* model, this new methodological tool opens the possibility to assess additional features of CERKL in health and disease. Given the complex transcriptional complexity underlying *CERKL* gene, we also plan to perform long-read RNA-Seq to unravel the RNA isoforms of CERKL that are produced in healthy human-derived retinal organoids, but also in retinal organoids carrying *CERKL^{R257X}* mutation. Moreover, although CERKL has not been proved as a lipid kinase, it is capable of binding lipids, such as glucosyl ceramide, galactosyl ceramide and sphingomyelin. Indeed, *Cerkl* deficiency leads to diminished levels of these sphingolipids in the *Cerkl^{KD/KD}* mouse model (258).

Accordingly, another interesting experiment would consist of a lipidomic analysis of healthy and *CERKL^R257X* retinal organoids.

Furthermore, an additional compelling perspective would include the evaluation of stress response in retinal organoids by performing oxidative or light-stress injury. In the previous study of *CERKL^R257X* patient's retinal organoids, sodium arsenite treatment was performed to induce oxidative stress. However, this might not be the most physiological treatment to produce stress in retinal organoids, and possibly derives in activation of non-canonical antioxidant responses. Therefore, we contemplate the potential use of light at different wavelengths and intensities to induce light stress responses, as retinal organoids have been described to respond to light through miRNA expression (259). However, this methodological strategy requires optimization to induce oxidative stress responses without damaging retinal organoids architecture.

Apart from all the possibilities emerging from the use of retinal organoids, differentiation of *CERKL^R257X* hiPSC into RPE might represent a complementary approach to the analyses obtained from the neuroretina in retinal organoids, especially considering that CERKL exerts a relevant role in RPE cells. Our findings revealed alterations in the mitochondrial network, coupled with mitochondrial dysfunction and increased multinucleation, which is a clear sign of stress damage *in vivo* (260), due to CERKL strong downregulation in RPE. In addition, other authors have reported impairment of autophagy and phagocytosis in *CERKL*-depleted RPE cells (152,163). All these evidences point to the relevant physiological role of CERKL in RPE, especially in protecting the mitochondrial network and homeostasis against the injury of oxidative stress, thus highlighting the importance to assess the effects of *CERKL^R257X* mutation in this cell type.

Finally, once we have conducted a phenotypic characterization of *CERKL^R257X* retinal organoids and RPE, different therapeutical strategies could be tested to revert the impaired pathways, such as the currently developing AAV2/7m8_CERKLa-3×FLAG therapeutic approach to complement the results obtained from *KD/KO* mice and provide solid evidence of the effectiveness of this treatment to be tested in patients carrying mutations in *CERKL*. A complementary strategy would include the

use of CRISPR/Cas9 technology to correct *CERKL*[R257X] mutation in the patient's hiPSCs and differentiate them into retinal organoids to assess the phenotypic rescue effect derived from the elimination of the causative mutation. However, the presence of off-target effects should be evaluated by next generation sequencing prior to differentiation, as we also plan to do in the current generation of *CERKL*[R257X] isogenic hiPSC line using CRISPR/Cas9 system.

Altogether, the use of hiPSC-derived retinal organoids and RPE presents new possibilities for understanding and deciphering the intricate function of CERKL in health and disease, by providing a physiological context closer to humans and patients.

3. Exploring therapeutic approaches for IRDs

3.1. Antioxidant treatment to enhance mitochondrial function and reduce redox imbalance

Alterations in the proper regulation of redox balance and mitochondrial energy production underlie the pathophysiology of many IRDs, including *CERKL*-associated retinal disorders, as described in this PhD Thesis. Accordingly, neuroprotective strategies that aim to diminish oxidative damage and preserve photoreceptors survival offer a great opportunity to treat IRDs without developing gene therapy (53). At present, several neuroprotective compounds have been tested in research and (pre)clinical studies that yielded positive results (261). To assess the effects of neuroprotective therapy in *CERKL* downregulation, we supplemented *CERKL*-depleted ARPE-19 with N-acetylcysteine, an antioxidant that enhances glutathione metabolism and neutralize ROS (262). However, N-acetylcysteine antioxidant treatment was not sufficient to restore mitochondrial function upon *CERKL* depletion, indicating that this compound was not directly acting in the specifically altered pathways by CERKL downregulation.

Nonetheless, there are additional neuroprotective compounds to be tested upon CERKL deficiency. Considering the interaction and regulation of CERKL with TRX2, the addition of thioredoxin would be an approach of particular interest. Indeed,

thioredoxin therapy has been described as beneficial in the *rd* mouse IRD model by reducing gliosis, activating glutathione metabolism, and protecting against photoreceptor cell death (263). Moreover, the supplement of mitochondrial nutrients and metabolic intermediates would represent another remarkable strategy, as several studies have demonstrated its improvement in photoreceptor survival and function (264,265). Finally, the addition of NRF2 using AAV vectors promotes photoreceptors and RPE survival in various mouse models of IRDs (266). Therefore, given that several antioxidant agents would result beneficial for *CERKL*-associated IRDs, a screening analysis testing the positive effects of different neuroprotective agents could be performed using patient's retinal organoids in order to evaluate the rescue effect in the phenotypic alterations. However, to date, no tested pharmacological agent has been shown to be effective enough in preventing or halting vision loss as to receive the approval by the FDA or the EMA. Much more basic work on the metabolic alterations of the retina has to be undertaken to identify safe and effective reagents to treat IRDs, either caused or not caused by *CERKL* mutations.

3.2. Challenges and opportunities derived from CERKLa-based gene therapy using AAV vectors: from selecting the correct CERKL isoform to targeting the adequate host cells

As previously commented, the production of the full-length isoform of CERKL, namely CERKLa, is generally affected in most patients carrying mutations in *CERKL*. This feature is replicated in the *KD/KO* mouse model, which is not able to generate the murine full-length isoform, known as m*Cerkl*1. Moreover, both human (CERKLa) and murine (mCerkl1) full-length isoforms are very similar in length (532 amino acids in human, and 525 amino acids in mouse), amino acid primary sequence, protein functional domains and 3D predicted structure (Figure 40). Given these similarities and considering that the final goal of this gene-therapeutic strategy are the human patients, we decided to elaborate our gene-addition therapeutic approach using the cDNA of human CERKLa isoform.
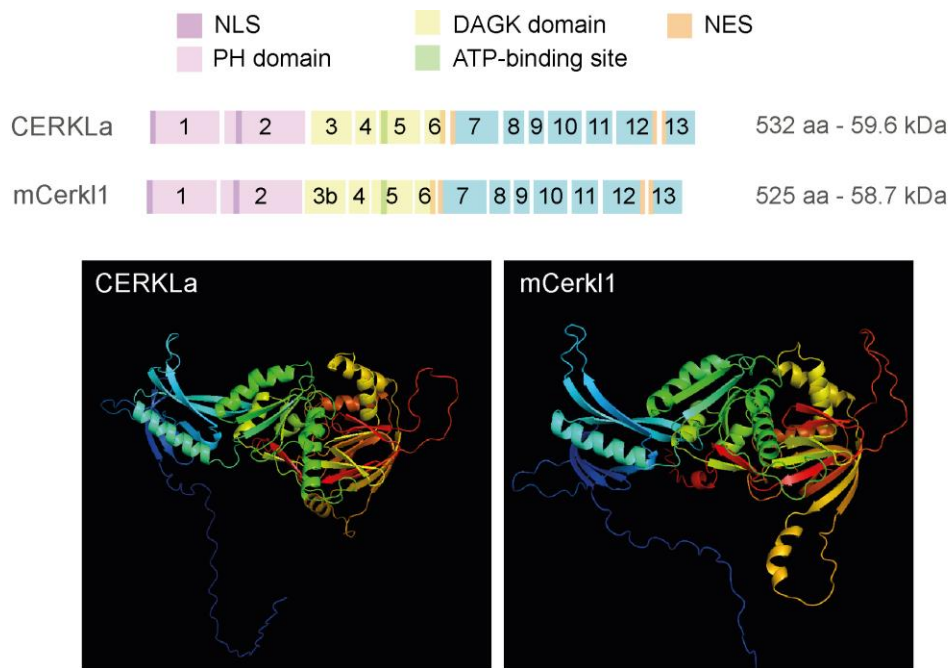
Figure 40. Comparison between hCERKLa and mCerkl1 protein isoforms. Both isoforms display the same protein domains (in colours), and their inferred 3D structure is very similar. Each number indicates the exons included in each isoform. NLS: nuclear localization signal; PH domain: pleckstrin homology domain; DAGK domain: diacylglycerol kinase domain; NES: nuclear export signal. Structural analysis performed with Pymol software using rainbow illustration: blue corresponds to the N-terminus and red to the C-terminus. Structural data retrieved from AlphaFold Protein Structure Database (https://alphafold.ebi.ac.uk).

In our first attempt to generate CERKLa-based gene replacement therapy using AAVs as vectors, we used the AAV8 capsid considering the previous experience and knowledge from our collaborators in TIGEM. The AAV8 capsid is able to efficiently transduce photoreceptor and RPE cells, where we had already described CERKL expression and function in maintaining cell homeostasis. Nonetheless, given the impaired transduction of AAV2/8_CERKL-3×FLAG vectors, the production of new AAV vectors carrying CERKL-3×FLAG was imperative to continue our experiments. This decision coincided in time with the initiation of the research line involving the differentiation of $CERKL^{R257X}$ patient's hiPSC into retinal organoids, so we opted for the utilization of the AAV7m8 capsid due to its superior transduction efficiency in retinal organoids in comparison with the AAV8 capsid. Additionally, the AAV7m8 capsid can efficiently transduce inner retinal cells, where CERKL is also expressed, including amacrine, bipolar, and retinal ganglion cells (RGCs). In fact, our experiments analysing CERKL downregulation in murine RGCs have revealed

alterations in the mitochondrial network organization and distribution, along with exacerbated stress granule-response to stress. These findings align with previous studies describing functional alterations in the ganglion cell layer in the *Cerkl^{KD/KD}* mouse model.

Overall, taking this evidence into consideration, substituting the capsid from the AAV8 to the AAV7m8 might result advantageous in terms of restoring CERKL expression and correct function in different retinal cell types, but also in patient's retinal organoids, which could contribute to the global amelioration of the phenotypic traits associated to the disease.

3.3. Upcoming prospects for CERKLa-based gene therapy

Taking advantage of the previous detailed phenotypic characterization of the *KD/KO* model, we will focus on the most physiologically relevant biomarkers in order to determine if this therapeutic strategy is effective in either preventing or halting retinal neurodegeneration and restoring vision. In this regard, we have planned the future experiments that need to be performed to analyse the rescue effects of AAV2/7m8_CERKLa-3×FLAG in mice. To better test the beneficial outcomes of this therapeutic approach, as well as to mimic the potential administration in humans, this therapy will be applied in 1-month-old mice, once the retina is fully developed and considered as adult retina.

Following the evaluation of the correct expression of the transgene *in vitro*, the first step will be to assess the correct expression of CERKLa-3×FLAG fusion protein derived from AAV2/7m8_CERKLa-3×FLAG transduction *in vivo* by subretinal injection. As gene overexpression using AAV vectors by subretinal injection requires at least 1 month for the proper expression of the transgene-encoded protein, this step will be validated in 2-month-old animals.

Subsequently, the phenotypic rescue in the *KD/KO* model will be conducted in adult mice of the same age of those used for the phenotypic characterization analyses (3-4 months old). Analyses using the phenotypic biomarkers identified in this work (such as alterations in mitochondrial trafficking and metabolism and oxidative stress response assayed by immunostaining and immunoblot approaches, as well as

SeaHorse functional studies) will be conducted in mouse adult retinas to test the phenotypic rescue capacity of the subretinal injections of AAV2/7m8_CERKLa-3×FLAG vectors *in vivo*. Finally, to assess the extent of the recovery of vision, which was impaired in old *KD/KO* mice (>12 months old), electroretinograms will be also performed. Due to the advanced age of these mice, this will be the last experiment to be conducted, albeit it is the most crucial for evaluating the rescue of retinal function and vision. Unfortunately, considering the extended waiting time required for these experiments, it has been impractical to include them in this Thesis. Nevertheless, the pursuit of this research line will continue in our research group.

In any case, considering CERKL as a stress-sensor hub that modulates several antioxidant responses and important mechanisms to preserve homeostasis and cell survival in the retina, we propose that the addition of CERKL would be beneficial for other IRD-patients affected by mutations in other genes as well, as long as they share the same misregulated pathways. Thus, we might consider the CERKL-based addition therapy as a broad-spectrum therapy for IRDs, as proposed for other genes, e.g. by modulation of NRL-NR2E3 pathway (267,268).

3.4. Gold nanoparticles as an alternative vehicle for gene-therapy products in IRDs

The use of AAVs as a delivery system has meant significant progress in the field of gene therapy bringing light into the lives of multiple patients suffering IRDs. Nonetheless, the use of AAVs implies an associated risk of immunogenic responses, which substantially increases if a second dose of the AAV-associated therapy is required or when the delivery of another gene product is needed. These associated disadvantages have led the search of alternative and safer vectors for gene delivery. In this context, nanoparticles represent a feasible vehicle for gene therapeutic approaches due to their high safety profile and modifiability, offering a broad range of possibilities. Several studies have demonstrated that the use of gold nanoparticles (AuNPs), the type of nanoparticles employed in our experiments, in retinal cells does not evoke cytotoxic effects both *in vitro* and *in vivo* (234,269).

Data collected from our experiments using DNA-wrapped AuNPs in retinal explants *ex vivo* as a proxy of gene therapy revealed detectable transfection in

photoreceptors, observing expression of the vector exclusively in rod photoreceptor cells. Nonetheless, the percentage of rod photoreceptor cells in the mouse retina is vastly superior compared to that of cones (only 3 % of cones). Therefore, although we were not able to detect GFP-positive cone photoreceptors, we cannot conclude that AuNPs cannot transfect cones due to their limited number in the retina. Another feasible explanation of AuNP rod-specific targeting may reside in the differences in the OS structural organization and varied packing density of membranous disks between rod and cone photoreceptors, as rods' OSs are more densely packed than cones OSs. In any case, in order to verify whether AuNPs specifically target rods, but not cones, a retinal context with a more balanced proportion of both photoreceptor cell types would be required, or also, larger numbers of AuNP-transfected retinas.

Overall, we have demonstrated the potential therapeutic use of AuNPs as a vector for gene delivery in IRDs. However, there are still considerable gaps in the understanding of AuNPs cell-specificity and increasing transfection efficiency. Thus, additional research is imperative to address these questions.

4. Final remarks

After many years of intensive effort, we have been able to thoroughly characterize the pathophysiological cellular mechanisms involved in *CERKL*-associated IRDs. Using the previously generated *KD/KO* mouse model, we have described increased autophagy, accumulation of fragmented mitochondria, impaired mitochondrial bioenergetics and trafficking, exacerbated stress response and activation of cell death mechanisms due to *Cerkl* depletion in different retinal cell types and hippocampal neurons. Hence, our findings highlight the relevance of CERKL in the regulation of a broad range of stress resilience mechanisms in the retina. The novel identification of early altered phenotypic biomarkers described in our studies will facilitate further analyses in *CERKL*-associated patient's retinal organoids, which represent an essential tool to reach a more complete understanding of the pathophysiology in *CERKL*-associated IRDs. Furthermore, the accurate knowledge of the different phenotypic alterations caused by *CERKL* deficiency provides the ideal

scenario to test different therapeutic approaches, such as antioxidant and/or gene augmentation strategies, to rescue and revert the pathological phenotype.
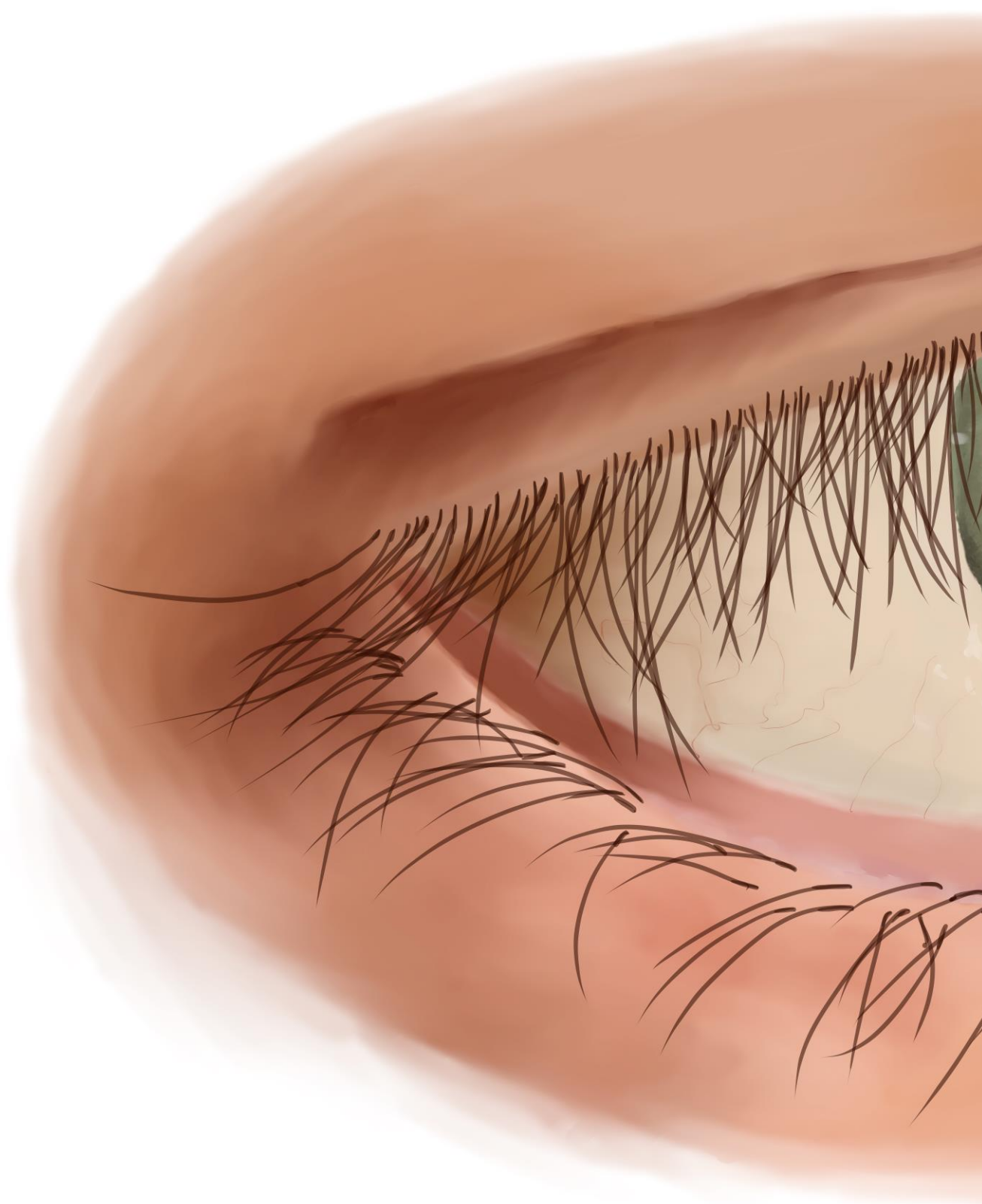
CONCLUSIONS
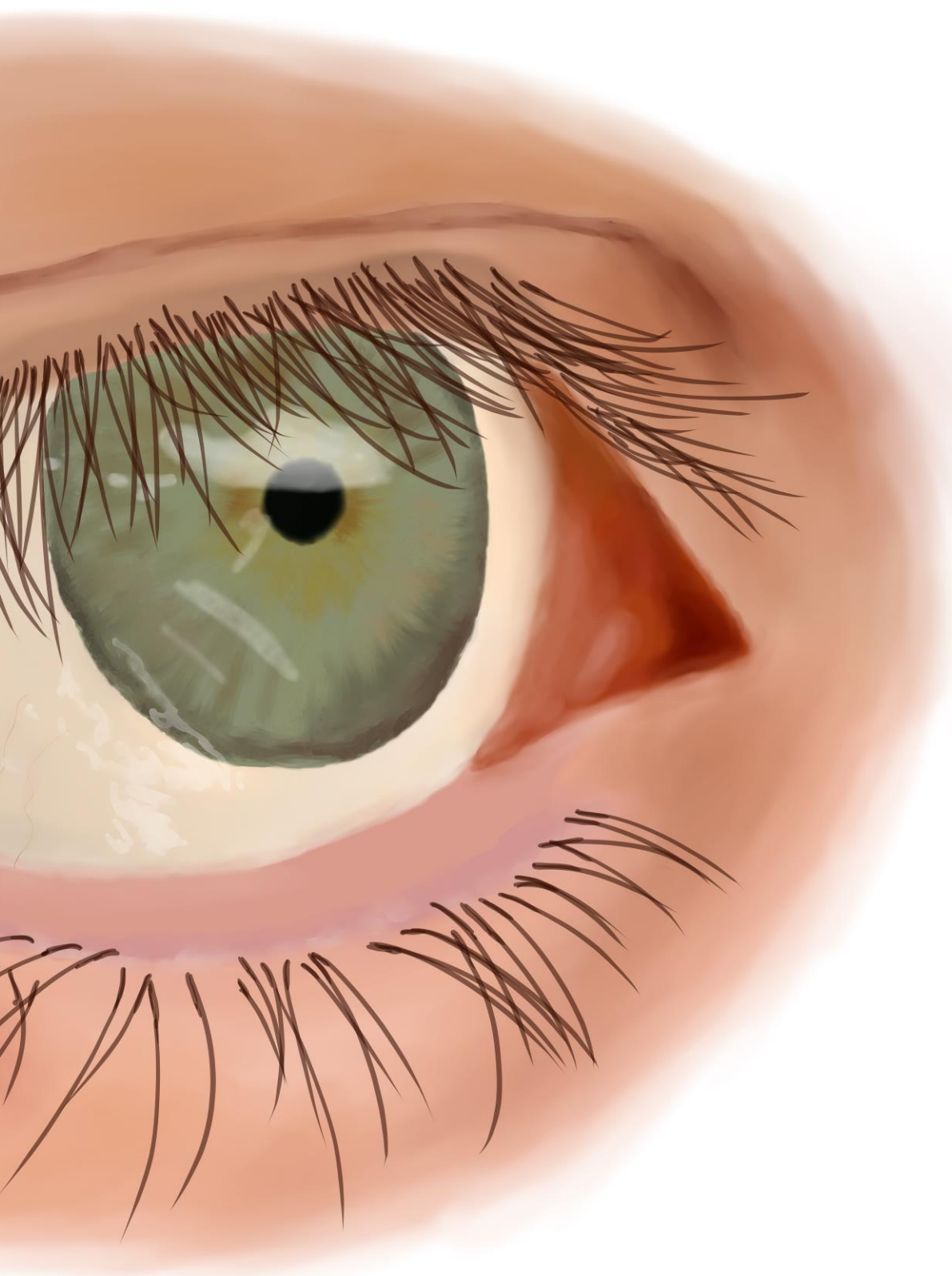
CONCLUSIONS

Unravelling the function of CERKL in autophagy and mitochondrial homeostasis.

- CERKL deficiency alters autophagy, mitochondrial dynamics and metabolism in the mammalian retina.

  > Retinas from *Cerkl*$^{KD/KO}$ mice exhibit increased autophagy in *in vitro* (retinal ganglion cell primary culture), *ex vivo* (retinal explants) and *in vivo* (mouse retinas) analyses.

  > Specific pools of endogenous CERKL isoforms colocalize with mitochondria in retinal ganglion cells and hippocampal neurons in primary culture, especially those detected by anti-CERKL5 antibody.

  > Mitochondrial mass is increased in *Cerkl*$^{KD/KO}$ retinas, although no alterations in mitochondrial biogenesis or mitophagy were observed. On the contrary, overexpression of hCERKLa-GFP promotes mitophagy in 661W cells.

  > *Cerkl* depletion in photoreceptor cells and retinal ganglion cells results in increased fragmented mitochondria, together with alterations in mitochondrial distribution through retinal ganglion cell axons.

  > Oxygen consumption and mitochondrial oxidative phosphorylation are impaired in *Cerkl*$^{KD/KO}$ retinas.

  > *Cerkl*$^{KD/KO}$ retinas present altered organic acids metabolism, in particular increased levels of succinate and pyroglutamic acid.

  > *Cerkl*$^{KD/KO}$ retinal pigment epithelium (RPE) cells possess fragmented mitochondria and multinucleation, whereas mitochondrial network is slightly altered in *Cerkl*$^{KD/KO}$ RPE cells in primary culture.

  > Endosome maturation is delayed in *Cerkl*$^{KD/KO}$ primary RPE (pRPE) cells. Additionally, *Cerkl*$^{KD/KO}$ pRPE cells can form a primary cilium, although the process of ciliary growth is also delayed.

CONCLUSIONS

- CERKL regulates mitochondrial morphology and trafficking in hippocampal neurons.

  > Overexpressed hCERKLa-GFP protein is associated with mitochondria trafficking in live axons of mouse hippocampal neurons, although it does not affect mitochondrial size, dynamics or transport.

  > *Cerkl* depletion increases mitochondrial fission by upregulating DRP1 phosphorylation (P-DRP1) in addition reducing long:short OPA1 ratio and MFN2 levels. Consequently, *Cerkl*$^{KD/KO}$ hippocampal neurons display fragmented mitochondria whose axon trafficking is further reduced.

  > As observed in the retina, mitochondrial metabolism through oxidative phosphorylation is altered in *Cerkl*$^{KD/KO}$ hippocampi as well.

Unveiling the role of CERKL in response to oxidative and light stress.

- CERKL overexpression protects mitochondria from oxidative stress in ARPE-19 cells.

  > Upon oxidative stress, *CERKL* silencing in ARPE-19 cells affects mitochondrial network and metabolism, while overexpression of hCERKLb-GFP and hCERKLc-GFP restores mitochondrial morphology, branching and redox status.

  > N-acetylcysteine antioxidant treatment is incapable to rescue mitochondrial damage in *CERKL*-silenced ARPE-19 cells.

- The response to light-induced stress in *Cerkl*$^{KD/KO}$ retinas is exacerbated.

  > Several phototransduction/visual cycle-associated and IRD-causative genes are downregulated in *Cerkl*-depleted retinas, such as *RPE65*, *LRAT* and *RDH5*.

  > In absence of stress factors, *Cerkl*$^{KD/KO}$ retinas experience an exacerbated response to stress, encompassing increased levels of ROS, unbalanced glutathione metabolism, upregulated PABP-mediated response, and gliosis.

> *Cerkl*-depleted retinas are not able to cope with light-induced stress, thus triggering retinal remodelling and activation of cell death pathways, including apoptosis, ferroptosis and necroptosis.

Generation of *CERKL^R257X* stable hiPSC line and differentiation to 3D retinal organoids.

- Several genes are differentially expressed (up- and downregulated) in RNA-Seq results from previously differentiated *CERKL^R257X* patient-derived retinal organoids.

- *CERKL^R257X* patient's hiPSCs can be properly differentiated into 3D retinal organoids, and at day 150 show correct laminar structure and formation of photoreceptor outer segments.

Development and validation of gene-augmentation therapeutic strategies.

- Design and test of CERKLa AAV-based gene therapy.

  > The cDNA of CERKLa was cloned into a plasmid containing AAV backbone and the construct correctly produced the recombinant CERKLa-3×FLAG fusion protein *in vitro*.

  > AAV2/8_CERKLa-3×FLAG vectors efficiently transduced mouse retinas after subretinal injections. Nevertheless, we were not able to reproduce these results due to alterations in the viability of the AAV2/8_CERKLa-3×FLAG vectors.

  > AAV2/7m8_CERKLa-3×FLAG virus competently transduces RPE cells *in vitro* and can produce the recombinant CERKLa-3×FLAG fusion protein.

- DNA-wrapped gold nanoparticles as an alternative delivery system for gene-augmentation therapies in IRDs.

  > DNA-wrapped gold nanoparticles are able to transfect retinas *ex vivo*.

  > DNA-wrapped gold nanoparticles can transfect differentiated photoreceptor cells, particularly rod photoreceptors.

REFERENCES

REFERENCES

1.   Chalupa LM, Werner JS. The visual neurosciences. London, England: The MIT Press; 2004.

2.   Hoon M, Okawa H, Della Santina L, Wong ROL. Functional architecture of the retina: Development and disease. Prog Retin Eye Res. 2014;42:44–84.

3.   Purves D, Augustine GJ, Fitzpatrick D, Hall WC, LaMantia AS, McNamara JO, et al. Neuroscience. In: Neuroscience. Third Edit. Sunderland, MA.: Sinaur Associates, Inc.; 2004. p. 229–58.

4.   Wu SM. Synaptic organization of the vertebrate retina: General principles and species-specific variations: The friedenwald lecture. Invest Ophthalmol Vis Sci. 2010;51(3):1264–74.

5.   Masland RH. Neuronal diversity in the retina. Curr Opin Neurobiol. 2001;11(4):431–6.

6.   Subirada P V., Paz MC, Ridano ME, Lorenc VE, Vaglienti M V., Barcelona PF, et al. A journey into the retina: Müller glia commanding survival and death. European Journal of Neuroscience. 2018;47(12):1429–43.

7.   Martínez-Gil N, Maneu V, Kutsyr O, Fernández-Sánchez L, Sánchez-Sáez X, Sánchez-Castillo C, et al. Cellular and molecular alterations in neurons and glial cells in inherited retinal degeneration. Front Neuroanat. 2022;16:1–18.

8.   Rashid K, Akhtar-Schaefer I, Langmann T. Microglia in retinal degeneration. Front Immunol. 2019;10(AUG):1–19.

9.   Swaroop A, Kim D, Forrest D. Transcriptional regulation of photoreceptor development and homeostasis in the mammalian retina. Nat Rev Neurosci. 2010;11(8):563–76.

10.   Khanna H. Photoreceptor Sensory Cilium: Traversing the Ciliary Gate. Cells. 2015;4(4):674–86.

11.   Imamoto Y, Shichida Y. Cone visual pigments. Vol. 1837, Biochimica et Biophysica Acta - Bioenergetics. Elsevier; 2014. p. 664–73.

12.   Ingram NT, Sampath AP, Fain GL. Why are rods more sensitive than cones? Vol. 594, Journal of Physiology. Blackwell Publishing Ltd; 2016. p. 5415–26.

REFERENCES

13. Tachibanaki S, Shimauchi-Matsukawa Y, Arinobu D, Kawamura S. Molecular Mechanisms Characterizing Cone Photoresponses. Photochem Photobiol. 2006;19–26.

14. Provis JM, Dubis AM, Maddess T, Carroll J. Adaptation of the central retina for high acuity vision: Cones, the fovea and the a vascular zone. Vol. 35, Progress in Retinal and Eye Research. 2013. p. 63–81.

15. Yu DY, Cringle SJ, Balaratnasingam C, Morgan WH, Yu PK, Su EN. Retinal ganglion cells: Energetics, compartmentation, axonal transport, cytoskeletons and vulnerability. Vol. 36, Progress in Retinal and Eye Research. 2013. p. 217–46.

16. Fudalej E, Justyniarska M, Kasarełło K, Dziedziak J, Szaflik JP, Cudnoch-Jędrzejewska A. Neuroprotective Factors of the Retina and Their Role in Promoting Survival of Retinal Ganglion Cells: A Review. Vol. 64, Ophthalmic Research. S. Karger AG; 2021. p. 345–55.

17. Osborne NN, Núñez-Álvarez C, Joglar B, del Olmo-Aguado S. Glaucoma: Focus on mitochondria in relation to pathogenesis and neuroprotection. Eur J Pharmacol. 2016;787:127–33.

18. Kolb H. Morphology and Circuitry of Ganglion Cells. 2007;(2):1–28.

19. Sanes JR, Masland RH. The Types of Retinal Ganglion Cells: Current Status and Implications for Neuronal Classification. Annu Rev Neurosci. 2015;38:221–46.

20. Nguyen-ba-charvet KT, Rebsam A. Neurogenesis and specification of retinal ganglion cells. Int J Mol Sci. 2020;21(2):1–24.

21. Rheaume BA, Jereen A, Bolisetty M, Sajid MS, Yang Y, Renna K, et al. Single cell transcriptome profiling of retinal ganglion cells identifies cellular subtypes. Nat Commun. 2018;9(1).

22. Strauss O. The retinal pigment epithelium in visual function. Physiol Rev. 2005;85(3):845–81.

23. Sparrow JR, Hicks D, Hamel CP. The Retinal Pigment Epithelium in Health and Disease. Curr Mol Med. 2010;10(9):802–23.

24. Lieffrig SA, Gyimesi G, Mao Y, Finnemann SC. Clearance phagocytosis by the retinal pigment epithelial during photoreceptor outer segment renewal: Molecular mechanisms and relation to retinal inflammation. Immunol Rev. 2023;319(July):81–99.

25. Hunter JJ, Morgan JIW, Merigan WH, Sliney DH, Sparrow JR, Williams DR. The susceptibility of the retina to photochemical damage from visible light. Prog Retin Eye Res. 2012;31(1):28–42.

26. Molday RS, Moritz OL. Photoreceptors at a glance. J Cell Sci. 2015;128(22):4039–45.

27. Grossniklaus HE, Geisert EE, Nickerson JM. Introduction to the Retina. In: Progress in Molecular Biology and Translational Science. Elsevier B.V.; 2015. p. 383–96.

28. Fu Y. Phototransduction in rods and cones. The Organization and the Retina and Visual System. 2010;

29. Lamb TD. Evolution of phototransduction, vertebrate photoreceptors and retina. Prog Retin Eye Res. 2013;36:52–119.

30. Saari JC. Biochemistry of Visual Pigment Regeneration. The Friedenwald Lecture. Invest Ophthalmol. 2000;41(2).

31. Kiser PD. Retinal pigment epithelium 65 kDa protein (RPE65): An update. Prog Retin Eye Res. 2022;88:101013.

32. Wang JS, Kefalov VJ. The Cone-specific visual cycle. Prog Retin Eye Res. 2011 Mar;30(2):115–28.

33. Cremers FPM, Boon CJF, Bujakowska K, Zeitz C. Special issue introduction: Inherited retinal disease: Novel candidate genes, genotype-phenotype correlations, and inheritance models. Genes (Basel). 2018;9(4):1–10.

34. Manley A, Meshkat BI, Jablonski MM, Hollingsworth TJ. Cellular and Molecular Mechanisms of Pathogenesis Underlying Inherited Retinal Dystrophies. Biomolecules. 2023;13(2):1–44.

REFERENCES

35. Schneider N, Sundaresan Y, Gopalakrishnan P, Beryozkin A, Hanany M, Levanon EY, et al. Inherited retinal diseases: Linking genes, disease-causing variants, and relevant therapeutic modalities. Prog Retin Eye Res. 2022;89:101029.

36. García Bohórquez B, Aller E, Rodríguez Muñoz A, Jaijo T, García García G, Millán JM. Updating the Genetic Landscape of Inherited Retinal Dystrophies. Front Cell Dev Biol. 2021;9:1–13.

37. Henderson RH. Inherited retinal dystrophies. Paediatrics and Child Health (United Kingdom). 2019;30(1):19–27.

38. John MC, Quinn J, Hu ML, Cehajic-Kapetanovic J, Xue K. Gene-agnostic therapeutic approaches for inherited retinal degenerations. Front Mol Neurosci. 2023;15:1–22.

39. Chew LA, Iannaccone A. Gene-agnostic approaches to treating inherited retinal degenerations. Front Cell Dev Biol. 2023;11:1–17.

40. London A, Benhar I, Schwartz M. The retina as a window to the brain - From eye research to CNS disorders. Nat Rev Neurol. 2013;9(1):44–53.

41. Serrat R, Mirra S, Figueiro-Silva J, Navas-Pérez E, Quevedo M, López-Doménech G, et al. The Armc10/SVH gene: Genome context, regulation of mitochondrial dynamics and protection against Aβ-induced mitochondrial fragmentation. Cell Death Dis. 2014;5(4).

42. Norkett R, Modi S, Birsa N, Atkin TA, Ivankovic D, Pathania M, et al. DISC1-dependent regulation of mitochondrial dynamics controls the morphogenesis of complex neuronal dendrites. Journal of Biological Chemistry. 2016;291(2):613–29.

43. Wang W, Li L, Lin WL, Dickson DW, Petrucelli L, Zhang T, et al. The ALS disease-associated mutant TDP-43 impairs mitochondrial dynamics and function in motor neurons. Hum Mol Genet. 2013;22(23):4706–19.

44. Jindal V. Interconnection Between Brain and Retinal Neurodegenerations. Mol Neurobiol. 2015 Jun 1;51(3):885–92.

45. Zhang J, Shi L, Shen Y. The retina: A window in which to view the pathogenesis of Alzheimer's disease. Ageing Res Rev. 2022 May 1;77.

46. Yap TE, Balendra SI, Almonte MT, Cordeiro MF. Retinal correlates of neurological disorders. Ther Adv Chronic Dis. 2019;10:1–32.

47. Domènech EB, Marfany G. The relevance of oxidative stress in the pathogenesis and therapy of retinal dystrophies. Antioxidants. 2020;9(4):1–22.

48. Lushchak VI. Free radicals, reactive oxygen species, oxidative stress and its classification. Chem Biol Interact. 2014;224:164–75.

49. Moldogazieva NT, Mokhosoev IM, Feldman NB, Lutsenko S V. ROS and RNS signalling: adaptive redox switches through oxidative/nitrosative protein modifications. Free Radic Res. 2018;52(5):507–43.

50. Singh A, Kukreti R, Saso L, Kukreti S. Oxidative Stress: A Key Modulator in Neurodegenerative Diseases. Molecules. Molecules. 2019;24(8):1583.

51. Kovács-Valasek A, Rák T, Pöstyéni E, Csutak A, Gábriel R. Three Major Causes of Metabolic Retinal Degenerations and Three Ways to Avoid Them. Int J Mol Sci. 2023;24(10).

52. Wang J, Li M, Geng Z, Khattak S, Ji X, Wu D, et al. Role of Oxidative Stress in Retinal Disease and the Early Intervention Strategies: A Review. Oxid Med Cell Longev. 2022;2022:1–13.

53. Pinilla I, Maneu V, Campello L, Fernández-Sánchez L, Martínez-Gil N, Kutsyr O, et al. Inherited Retinal Dystrophies: Role of Oxidative Stress and Inflammation in Their Physiopathology and Therapeutic Implications. Antioxidants. 2022;11(6).

54. Shu DY, Chaudhary S, Cho KS, Lennikov A, Miller WP, Thorn DC, et al. Role of Oxidative Stress in Ocular Diseases: A Balancing Act. Metabolites. 2023;13(2).

55. Sahu R, Kaushik S, Clement CC, Cannizzo ES, Scharf B, Follenzi A, et al. Microautophagy of Cytosolic Proteins by Late Endosomes. Dev Cell. 2011;20(3):405-6.

REFERENCES

56. Kaushik S, Cuervo AM. Chaperone-mediated autophagy: A unique way to enter the lysosome world. Trends Cell Biol. 2012;22(8):407–17.

57. Bento CF, Renna M, Ghislat G, Puri C, Ashkenazi A, Vicinanza M, et al. Mammalian Autophagy: How Does It Work? Annu Rev Biochem. 2016;85:685–713.

58. Boya P, Reggiori F, Codogno P. Emerging regulation and functions of autophagy. Nat Cell Biol. 2013;15(7):713–20.

59. Villarejo-Zori B, Jiménez-Loygorri JI, Zapata-Muñoz J, Bell K, Boya P. New insights into the role of autophagy in retinal and eye diseases. Mol Aspects Med. 2021;82.

60. Kaden TR, Li W. Autophagy, Mitochondrial Dynamics, and Retinal Diseases. Asia-Pacific Journal of Ophthalmology. 2013;2(5):341–8.

61. Warburg O. On the origin of cancer cells. Science (1979). 1956;123(3191):309–14.

62. Rajala RVS. Aerobic Glycolysis in the Retina: Functional Roles of Pyruvate Kinase Isoforms. Front Cell Dev Biol. 2020;8(April):1–11.

63. Trigo D, Avelar C, Fernandes M, Sá J, da Cruz e Silva O. Mitochondria, energy, and metabolism in neuronal health and disease. FEBS Lett. 2022;596(9):1095–110.

64. Yang D, Ying J, Wang X, Zhao T, Yoon S, Fang Y, et al. Mitochondrial Dynamics: A Key Role in Neurodegeneration and a Potential Target for Neurodegenerative Disease. Front Neurosci. 2021;15(April).

65. Lefevere E, Toft-Kehler AK, Vohra R, Kolko M, Moons L, Van Hove I. Mitochondrial dysfunction underlying outer retinal diseases. Mitochondrion. 2017;36(July 2016):66–76.

66. Mirra S, Marfany G. Mitochondrial Gymnastics in Retinal Cells: A Resilience Mechanism Against Oxidative Stress and Neurodegeneration. In: Advances in Experimental Medicine and Biology. 2019. p. 513-7.

67. Ito YA, Di Polo A. Mitochondrial dynamics, transport, and quality control: A bottleneck for retinal ganglion cell viability in optic neuropathies. Mitochondrion. 2017;36(July 2016):186–92.

68. Bagli E, Zikou AK, Agnantis N, Kitsos G. Mitochondrial Membrane Dynamics and Inherited Optic Neuropathies. In Vivo (Brooklyn). 2017;31(4):511–25.

69. Losón OC, Song Z, Chen H, Chan DC. Fis1, Mgg, MiD49, and MiD51 mediate Drp1 recruitment in mitochondrial fission. Mol Biol Cell. 2013;24:659–67.

70. López-Doménech G, Covill-Cooke C, Ivankovic D, Halff EF, Sheehan DF, Norkett R, et al. Miro proteins coordinate microtubule- and actin-dependent mitochondrial transport and distribution. EMBO J. 2018;37(3):321–36.

71. Boya P, Esteban-Martínez L, Serrano-Puebla A, Gómez-Sintes R, Villarejo-Zori B. Autophagy in the eye: Development, degeneration, and aging. Prog Retin Eye Res. 2016;55:206–45.

72. Wong-riley M. Energy metabolism of the visual system. Dove Press. 2010;2:99–116.

73. Kimball EC, Jefferys JL, Pease ME, Oglesby EN, Schaub J, Pitha I, et al. The effects of age on mitochondria, axonal transport, and axonal degeneration after chronic IOP elevation using a murine ocular explant model. Exp Eye Res. 2019;172:78–85.

74. Chan P, Stolz J, Kohl S, Chiang WC, Lin JH. Endoplasmic Reticulum Stress in Human Photoreceptor Diseases. Brain Res. 2016;1648(Pt B):538–41.

75. Gorbatyuk M, Starr CR, Gorbatyuk O. Endoplasmic Reticulum Stress: New Insights into the Pathogenesis and Treatment of Retinal Degenerative Diseases. Prog Mol Biol Transl Sci. 2020;79.

76. Zhang SX, Ma JH, Bhatta M, Fliesler SJ, Wang JJ. The Unfolded Protein Response in Retinal Vascular Diseases: Implications and Therapeutic Potential Beyond Protein Folding. Prog Retin Eye Res. 2015;0:111–31.

REFERENCES

77. Zhang S, Sanders E, Fliesler SJ, Wang JJ. Endoplasmic Reticulum Stress and the Unfolded Protein Responses in Retinal Degeneration. Exp Eye Res. 2014;0:30–40.

78. McLaughlin T, Medina A, Perkins J, Yera M, Wang JJ, Zhang SX. Cellular stress signaling and the unfolded protein response in retinal degeneration: mechanisms and therapeutic implications. Mol Neurodegener. 2022;17(1):1–19.

79. Lin JH, LaVail MM. Misfolded Proteins and Retinal Dystrophies. Adv Exp Med Biol. 2010;664:115–21.

80. Kaushal S, Ridge KD, Khorana HG. Structure and function in rhodopsin: the role of asparagine-linked glycosylation. Proc Natl Acad Sci U S A. 1994 Apr 26;91(9):4024–8.

81. Kaushal S, Khorana HG. Structure and function in rhodopsin. 7. Point mutations associated with autosomal dominant retinitis pigmentosa. Biochemistry. 1994 May 1;33(20):6121–8.

82. Liang CJ, Yamashita K, Muellenberg CG, Shichi H, Kobata A. Structure of the carbohydrate moieties of bovine rhodopsin. Journal of Biological Chemistry. 1979;254(14):6414–8.

83. Jing G, Wang JJ, Zhang SX. ER stress and apoptosis: A new mechanism for retinal cell death. Exp Diabetes Res. 2011;2012.

84. Ganea E, Harding JJ. Glutathione-related enzymes and the eye. Curr Eye Res. 2006;31(1):1–11.

85. Sreekumar PG, Ferrington DA, Kannan R. Glutathione metabolism and the novel role of mitochondrial gsh in retinal degeneration. Antioxidants. 2021;10(5):1–18.

86. Belalcázar AD, Ball JG, Frost LM, Valentovic MA, Wilkinson J. Transsulfuration Is a Significant Source of Sulfur for Glutathione Production in Human Mammary Epithelial Cells. ISRN Biochem. 2013;2013:1–7.

87. Lu SC. Regulation of hepatic glutathione synthesis: current concepts and controversies. The FASEB Journal. 1999;13(10):1169–83.

88. Campochiaro PA, Strauss RW, Lu L, Hafiz G, Wolfson Y, Shah SM, et al. Is There Excess Oxidative Stress and Damage in Eyes of Patients with Retinitis Pigmentosa? Antioxid Redox Signal. 2015;23(7):643–8.

89. Cardoso BR, Hare DJ, Bush AI, Roberts BR. Glutathione peroxidase 4: A new player in neurodegeneration? Mol Psychiatry. 2017;22(3):328–35.

90. Ahuja-Jensen P, Johnsen-Soriano S, Ahuja S, Bosch-Morell F, Sancho-Tello M, Romero FJ, et al. Low glutathione peroxidase in rd1 mouse retina increases oxidative stress and proteases. Neuroreport. 2007;18(8):797–801.

91. Lu L, Oveson BC, Jo YJ, Lauer TW, Usui S, Komeima K, et al. Increased expression of glutathione peroxidase 4 strongly protects retina from oxidative damage. Antioxid Redox Signal. 2009;11(4):715–24.

92. van Leeuwen W, Rabouille C. Cellular stress leads to the formation of membraneless stress assemblies in eukaryotic cells. Traffic. 2019;20(9):623–38.

93. Anderson P, Kedersha N. Stress granules. Current Biology. 2009;19(10):397–8.

94. Fang M, Liu Y, Huang C, Fan S. Targeting stress granules in neurodegenerative diseases: A focus on biological function and dynamics disorders. BioFactors. 2023;(October):1–17.

95. Plassmeyer SP, Holehouse AS. Stress granules offer first aid for leaky organelles. Nature. 2023 Nov 15;

96. Karlen SJ, Miller EB, Burns ME. Microglia Activation and Inflammation During the Death of Mammalian Photoreceptors. Annu Rev Vis Sci. 2020 Sep 15;6:149–69.

97. Langmann T. Microglia activation in retinal degeneration. J Leukoc Biol. 2007 Jun 1;81(6):1345–51.

98. Reichenbach A, Bringmann A. Glia of the human retina. Glia. 2020 Apr 1;68(4):768–96.

REFERENCES

99. Coorey NJ, Shen W, Chung SH, Zhu L, Gillies MC. The role of glia in retinal vascular disease. Clin Exp Optom. 2012 May;95(3):266–81.

100. Li J, Shui X, Sun R, Wan L, Zhang B, Xiao B, et al. Microglial Phenotypic Transition: Signaling Pathways and Influencing Modulators Involved in Regulation in Central Nervous System Diseases. Front Cell Neurosci. 2021 Sep 14;15.

101. Voigt AP, Binkley E, Flamme-Wiese MJ, Zeng S, DeLuca AP, Scheetz TE, et al. Single-Cell RNA Sequencing in Human Retinal Degeneration Reveals Distinct Glial Cell Populations. Cells. 2020 Feb 13;9(2).

102. Ekstrom P, Sanyal S, Narfstrom K, Chader GJ, Van Veen T. Accumulation of glial fibrillary acidic protein in Muller radial glia during retinal degeneration. Invest Ophthalmol Vis Sci. 1988;29(9):1363–71.

103. Luna G, Lewis GP, Banna CD, Skalli O, Fisher SK. Expression profiles of nestin and synemin in reactive astrocytes and Müller cells following retinal injury: A comparison with glial fibrillar acidic protein and vimentin. Mol Vis. 2010;16(November):2511–23.

104. Cuenca N, Fernández-Sánchez L, Campello L, Maneu V, De la Villa P, Lax P, et al. Cellular responses following retinal injuries and therapeutic approaches for neurodegenerative diseases. Prog Retin Eye Res. 2014 Nov 1;43:17–75.

105. Tuson M, Marfany G, Gonzàlez-Duarte R. Mutation of CERKL, a Novel Human Ceramide Kinase Gene, Causes Autosomal Recessive Retinitis Pigmentosa (RP26). Am J Hum Genet. 2004;74:128–38.

106. Bornancin F, Mechtcheriakova D, Stora S, Graf C, Wlachos A, Dévay P, et al. Characterization of a ceramide kinase-like protein. Biochim Biophys Acta Mol Cell Biol Lipids. 2005;1687(1–3):31–43.

107. Bayes M, Goldaracena B, Martinez-Mir A, Iragui-Madoz MI, Solans T, Chivelet P, et al. A new autosomal recessive retinitis pigmentosa locus maps on chromosome 2q31-q33. J Med Genet. 1998;35(2):141–5.

108. Ellingford JM, Barton S, Bhaskar S, O'Sullivan J, Williams SG, Lamb JA, et al. Molecular findings from 537 individuals with inherited retinal disease. J Med Genet. 2016 Nov 1;53(11):761–7.

109. Avela K, Sankila EM, Seitsonen S, Kuuluvainen L, Barton S, Gillies S, et al. A founder mutation in CERKL is a major cause of retinal dystrophy in Finland. Acta Ophthalmol. 2018;96(2):183–91.

110. Ali M, Ramprasad VL, Soumittra N, Mohamed MD, Jafri H, Danciger M, et al. A missense mutation in the nuclear localization signal sequence of CERKL (p .R106S) causes autosomal recessive retinal degeneration. Mol Vis. 2008;14:1960–4.

111. Weisschuh N, Mayer AK, Strom TM, Kohl S, Glöckle N, Schubach M, et al. Mutation Detection in Patients with Retinal Dystrophies Using Targeted Next Generation Sequencing. PLoS One. 2016 Jan 1;11(1).

112. Ezquerra-Inchausti M, Anasagasti A, Barandika O, Garai-Aramburu G, Galdós M, López de Munain A, et al. A new approach based on targeted pooled DNA sequencing identifies novel mutations in patients with Inherited Retinal Dystrophies. Sci Rep. 2018 Dec 1;8(1).

113. Roberts L, Ratnapriya R, du Plessis M, Chaitankar V, Ramesar RS, Swaroop A. Molecular Diagnosis of Inherited Retinal Diseases in Indigenous African Populations by Whole-Exome Sequencing. Invest Ophthalmol Vis Sci. 2016 Nov 1;57(14):6374–81.

114. Littink KW, Koenekoop RK, Born LI Van Den, Collin RWJ, Moruz L, Veltman JA, et al. Homozygosity Mapping in Patients with Cone – Rod Dystrophy : Novel Mutations and Clinical Characterizations. Invest Ophthalmol Vis Sci. 2010;51(11):5943–51.

115. Xu Y, Guan L, Shen T, Zhang J, Xiao X, Jiang H, et al. Mutations of 60 known causative genes in 157 families with retinitis pigmentosa based on exome sequencing. Hum Genet. 2014;133(10):1255–71.

116. Huang XF, Huang F, Wu KC, Wu J, Chen J, Pang CP, et al. Genotype-phenotype correlation and mutation spectrum in a large cohort of patients with inherited

retinal dystrophy revealed by next-generation sequencing. Genet Med. 2015 Apr 8;17(4):271–8.

117. Wang P, Li S, Sun W, Xiao X, Jia X, Liu M, et al. An Ophthalmic Targeted Exome Sequencing Panel as a Powerful Tool to Identify Causative Mutations in Patients Suspected of Hereditary Eye Diseases. Transl Vis Sci Technol. 2019 Mar 1;8(2).

118. Nishiguchi KM, Tearle RG, Liu YP, Oh EC, Miyake N, Benaglio P, et al. Whole genome sequencing in patients with retinitis pigmentosa reveals pathogenic DNA structural changes and NEK2 as a new disease gene. Proc Natl Acad Sci U S A. 2013 Oct 1;110(40):16139–44.

119. Perez-Carro R, Corton M, Sánchez-Navarro I, Zurita O, Sanchez-Bolivar N, Sánchez-Alcudia R, et al. Panel-based NGS Reveals Novel Pathogenic Mutations in Autosomal Recessive Retinitis Pigmentosa. Sci Rep. 2016 Jan 25;6.

120. Lee H, Deignan JL, Dorrani N, Strom SP, Kantarci S, Quintero-Rivera F, et al. Clinical exome sequencing for genetic identification of rare Mendelian disorders. JAMA. 2014 Nov 12;312(18):1880–7.

121. Jespersgaard C, Fang M, Bertelsen M, Dang X, Jensen H, Chen Y, et al. Molecular genetic analysis using targeted NGS analysis of 677 individuals with retinal dystrophy. Sci Rep. 2019 Dec 1;9(1).

122. Abu-Safieh L, Alrashed M, Anazi S, Alkuraya H, Khan AO, Al-Owain M, et al. Autozygome-guided exome sequencing in retinal dystrophy patients reveals pathogenetic mutations and novel candidate disease genes. Genome Res. 2013 Feb;23(2):236–47.

123. Patel N, Aldahmesh MA, Alkuraya H, Anazi S, Alsharif H, Khan AO, et al. Expanding the clinical, allelic, and locus heterogeneity of retinal dystrophies. Genet Med. 2016 Jun 1;18(6):554–62.

124. Khan AO, Abu-Safieh L. Rod-Cone Dystrophy with Initially Preserved Visual Acuity Despite Early Macular Involvement Suggests Recessive CERKL Mutations. Ophthalmic Genet. 2015;36(4):369–72.

125. Boulanger-Scemama E, El Shamieh S, Démontant V, Condroyer C, Antonio A, Michiels C, et al. Next-generation sequencing applied to a large French cone and cone-rod dystrophy cohort: mutation spectrum and new genotype-phenotype correlation. Orphanet J Rare Dis. 2015 Jun 24;10(1).

126. Matsui R, Cideciyan A V., Schwartz SB, Sumaroka A, Roman AJ, Swider M, et al. Molecular Heterogeneity Within the Clinical Diagnosis of Pericentral Retinal Degeneration. Invest Ophthalmol Vis Sci. 2015;56(10):6007–18.

127. Glöckle N, Kohl S, Mohr J, Scheurenbrand T, Sprecher A, Weisschuh N, et al. Panel-based next generation sequencing as a reliable and efficient technique to detect mutations in unselected patients with retinal dystrophies. Eur J Hum Genet. 2014;22(1):99–104.

128. Stone EM, Andorf JL, Whitmore SS, DeLuca AP, Giacalone JC, Streb LM, et al. Clinically Focused Molecular Investigation of 1000 Consecutive Families with Inherited Retinal Disease. Ophthalmology. 2017 Sep 1;124(9):1314–31.

129. Birtel J, Eisenberger T, Gliem M, Müller PL, Herrmann P, Betz C, et al. Clinical and genetic characteristics of 251 consecutive patients with macular and cone/cone-rod dystrophy. Sci Rep. 2018 Dec 1;8(1).

130. Auslender N, Sharon D, Abbasi AH, Garzozi HJ, Banin E, Ben-Yosef T. A common founder mutation of CERKL underlies autosomal recessive retinal degeneration with early macular involvement among Yemenite Jews. Invest Ophthalmol Vis Sci. 2007 Dec;48(12):5431–8.

131. Ellingford JM, Horn B, Campbell C, Arno G, Barton S, Tate C, et al. Assessment of the incorporation of CNV surveillance into gene panel next-generation sequencing testing for inherited retinal diseases. J Med Genet. 2018 Feb 1;55(2):114–21.

132. Birtel J, Gliem M, Mangold E, Müller PL, Holz FG, Neuhaus C, et al. Next-generation sequencing identifies unexpected genotype-phenotype correlations in patients with retinitis pigmentosa. PLoS One. 2018 Dec 1;13(12).

133. Carss K, Arno G, Erwood M, Stephens J, Sanchis-Juan A, Hull S, et al. Comprehensive Rare Variant Analysis via Whole-Genome Sequencing to

Determine the Molecular Pathology of Inherited Retinal Disease. Am J Hum Genet. 2017 Jan 5;100(1):75–90.

134. Azab B, Barham R, Ali D, Dardas Z, Rashdan L, Bijawi M, et al. Novel CERKL variant in consanguineous Jordanian pedigrees with inherited retinal dystrophies. Can J Ophthalmol. 2019 Feb 1;54(1):51–9.

135. De Castro-Miró M, Tonda R, Escudero-Ferruz P, Andrés R, Mayor-Lorenzo A, Castro J, et al. Novel Candidate Genes and a Wide Spectrum of Structural and Point Mutations Responsible for Inherited Retinal Dystrophies Revealed by Exome Sequencing. PLoS One. 2016 Dec 1;11(12).

136. Tang Z, Wang Z, Wang Z, Ke T, Wang QK, Liu M. Novel compound heterozygous mutations in CERKL cause autosomal recessive retinitis pigmentosa in a nonconsanguineous Chinese family. Arch Ophthalmol. 2009 Aug;127(8):1077–8.

137. Biswas P, Duncan JL, Maranhao B, Kozak I, Branham K, Gabriel L, et al. Genetic analysis of 10 pedigrees with inherited retinal degeneration by exome sequencing and phenotype-genotype association. Physiol Genomics. 2017 Apr 1;49(4):216–29.

138. Aleman TS, Soumittra N, Cideciyan A V., Sumaroka AM, Ramprasad VL, Herrera W, et al. CERKL mutations cause an autosomal recessive cone-rod dystrophy with inner retinopathy. Invest Ophthalmol Vis Sci. 2009;50(12):5944–54.

139. Fu Q, Wang F, Wang H, Xu F, Zaneveld JE, Ren H, et al. Next-generation sequencing-based molecular diagnosis of a Chinese patient cohort with autosomal recessive retinitis pigmentosa. Invest Ophthalmol Vis Sci. 2013;54(6):4158–66.

140. Wang L, Zhang J, Chen N, Wang L, Zhang F, Ma Z, et al. Application of Whole Exome and Targeted Panel Sequencing in the Clinical Molecular Diagnosis of 319 Chinese Families with Inherited Retinal Dystrophy and Comparison Study. Genes (Basel). 2018 Jul 19;9(7).

141. Ellingford JM, Campbell C, Barton S, Bhaskar S, Gupta S, Taylor RL, et al. Validation of copy number variation analysis for next-generation sequencing diagnostics. Eur J Hum Genet. 2017 Mar 22;25(6):719–24.

142. Garanto A, Riera M, Pomares E, Permanyer J, de Castro-Miró M, Sava F, et al. High transcriptional complexity of the retinitis pigmentosa CERKL gene in human and mouse. Invest Ophthalmol Vis Sci. 2011;52(8):5202–14.

143. Tuson M, Garanto A, Gonzàlez-Duarte R, Marfany G. Overexpression of CERKL, a gene responsible for retinitis pigmentosa in humans, protects cells from apoptosis induced by oxidative stress. Mol Vis. 2009;15:168–80.

144. Riera M, Burguera D, Garcia-Fernàndez J, Gonzàlez-Duarte R. CERKL Knockdown Causes Retinal Degeneration in Zebrafish. PLoS One. 2013;8(5):1–12.

145. Rovina P, Schanzer A, Graf C, Mechtcheriakova D, Jaritz M, Bornancin F. Subcellular localization of ceramide kinase and ceramide kinase-like protein requires interplay of their Pleckstrin Homology domain-containing N-terminal regions together with C-terminal domains. Biochim Biophys Acta Mol Cell Biol Lipids. 2009;1791(10):1023–30.

146. Inagaki Y, Mitsutake S, Igarashi Y. Identification of a nuclear localization signal in the retinitis pigmentosa-mutated RP26 protein, ceramide kinase-like protein. Biochem Biophys Res Commun. 2006;343(3):982–7.

147. Vekslin S, Ben-Yosef T. Spatiotemporal expression pattern of ceramide kinase-like in the mouse retina. Mol Vis. 2010;16(November):2539–49.

148. Mandal NA, Tran JTA, Saadi A, Rahman AK, Huynh TP, Klein WH, et al. Expression and localization of CERKL in the mammalian retina, its response to light-stress, and relationship with NeuroD1 gene. Exp Eye Res. 2013;106:24–33.

149. Li C, Wang L, Zhang J, Huang M, Wong F, Liu X, et al. CERKL interacts with mitochondrial TRX2 and protects retinal cells from oxidative stress-induced apoptosis. Biochim Biophys Acta Mol Basis Dis. 2014;1842:1121–9.

REFERENCES

150. Nevet MJ, Vekslin S, Dizhoor AM, Olshevskaya E V., Tidhar R, Futerman AH, et al. Ceramide kinase-like (CERKL) interacts with neuronal calcium sensor proteins in the retina in a cation-dependent manner. Invest Ophthalmol Vis Sci. 2012;53(8):4565–74.

151. Fathinajafabadi A, Pérez-Jiménez E, Riera M, Knecht E, Gonzàlez-Duarte R. CERKL, a retinal disease gene, encodes an mRNA-binding protein that localizes in compact and untranslated mRNPs associated with microtubules. PLoS One. 2014 Feb 3;9(2).

152. Hu X, Lu Z, Yu S, Reilly J, Liu F, Jia D, et al. CERKL regulates autophagy via the NAD- dependent deacetylase SIRT1. Autophagy. 2019;15(3):453–65.

153. Meyer JM, Lee E, Celli A, Park K, Cho R, Lambert W, et al. CERKL is upregulated in cutaneous squamous cell carcinoma and maintains cellular sphingolipids and resistance to oxidative stress. British Journal of Dermatology. 2020;7908.

154. Huang S, Hong Z, Zhang L, Guo J, Li Y, Li K. CERKL alleviates ischemia reperfusion-induced nervous system injury through modulating the SIRT1 / PINK1 / Parkin pathway and mitophagy induction. Biol Chem. 2022;403(7):1–11.

155. Chen DD, Lu LF, Xiong F, Wang XL, Jiang JY, Zhang C, et al. Zebrafish CERKL Enhances Host TBK1 Stability and Simultaneously Degrades Viral Protein via Ubiquitination Modulation. The Journal of Immunology. 2022;208:2196–206.

156. Graf C, Niwa S, Müller M, Kinzel B, Bornancin F. Wild-type levels of ceramide and ceramide-1-phosphate in the retina of ceramide kinase-like-deficient mice. Biochem Biophys Res Commun. 2008;373(1):159–63.

157. Kim H, Kim M, Im SK, Fang S. Mouse Cre-LoxP system: general principles to determine tissue-specific roles of target genes. Lab Anim Res. 2018;34(4):147–59.

158. Garanto A, Vicente-Tejedor J, Riera M, De la Villa P, Gonzàlez-Duarte R, Blanco R, et al. Targeted knockdown of Cerkl, a retinal dystrophy gene, causes mild affectation of the retinal ganglion cell layer. Biochim Biophys Acta Mol Basis Dis. 2012;1822(8):1258–69.

159. Domènech EB, Andres R, López-Iniesta MJ, Mirra S, García-Arroyo R, Milla S, et al. A New Cerkl Mouse Model Generated by CRISPR-Cas9 Shows Progressive Retinal Degeneration and Altered Morphological and Electrophysiological Phenotype. Invest Ophthalmol Vis Sci. 2020;61(8).

160. Hryhorowicz M, Lipiński D, Zeyland J. Evolution of CRISPR/Cas Systems for Precise Genome Editing. Int J Mol Sci. 2023;24(18).

161. Jiang H, Tang M, Xu Z, Wang Y, Li M, Zheng S, et al. CRISPR/Cas9 system and its applications in nervous system diseases. Genes Dis. 2024;11(2):675–86.

162. Kuil LE, Chauhan RK, Cheng WW, Hofstra RMW, Alves MM. Zebrafish: A Model Organism for Studying Enteric Nervous System Development and Disease. Front Cell Dev Biol. 2021;8(January):1–15.

163. Yu S, Li C, Biswas L, Hu X, Liu F, Reilly J, et al. CERKL gene knockout disturbs photoreceptor outer segment phagocytosis and causes rod-cone dystrophy in zebrafish. Hum Mol Genet. 2017;26(12):2335–45.

164. Huang P, Xiao A, Zhou M, Zhu Z, Lin S, Zhang B. Heritable gene targeting in zebrafish using customized TALENs. Nat Biotechnol. 2011;29(8):699–700.

165. Sharma K, Krohne TU, Busskamp V. The rise of retinal organoids for vision research. Int J Mol Sci. 2020;21(22):1–13.

166. Takahashi K, Tanabe K, Ohnuki M, Narita M, Ichisaka T, Tomoda K, et al. Induction of Pluripotent Stem Cells from Adult Human Fibroblasts by Defined Factors. Cell. 2007;131(5):861–72.

167. Krohne TU, Westenskow PD, Kurihara T, Friedlander DF, Lehmann M, Dorsey AL, et al. Generation of Retinal Pigment Epithelial Cells from Small Molecules and OCT4 Reprogrammed Human Induced Pluripotent Stem Cells . Stem Cells Transl Med. 2012;1(2):96–109.

168. Liang Y, Sun X, Duan C, Tang S, Chen J. Application of patient-derived induced pluripotent stem cells and organoids in inherited retinal diseases. Stem Cell Res Ther. 2023;14(1):1–17.

REFERENCES

169. Benati D, Leung A, Perdigao P, Toulis V, van der Spuy J, Recchia A. Induced Pluripotent Stem Cells and Genome-Editing Tools in Determining Gene Function and Therapy for Inherited Retinal Disorders. Int J Mol Sci. 2022;23(23).

170. Maeda T, Takahashi M. iPSC-RPE in Retinal Degeneration: Recent Advancements and Future Perspectives. Cold Spring Harb Perspect Med. 2023 Aug 1;13(8).

171. Zhou S, Flamier A, Abdouh M, Tétreault N, Barabino A, Wadhwa S, et al. Differentiation of human embryonic stem cells into cone photoreceptors through simultaneous inhibition of BMP, TGFβ and Wnt signaling. Development (Cambridge). 2015;142(19):3294–306.

172. Ji SL, Tang SB. Differentiation of retinal ganglion cells from induced pluripotent stem cells: A review. Int J Ophthalmol. 2019;12(1):152–60.

173. Afanasyeva TAV, Corral-Serrano JC, Garanto A, Roepman R, Cheetham ME, Collin RWJ. A look into retinal organoids: methods, analytical techniques, and applications. Cellular and Molecular Life Sciences. 2021;78(19–20):6505–32.

174. O'Hara-Wright M, Gonzalez-Cordero A. Retinal organoids: A window into human retinal development. Development (Cambridge). 2020;147(24).

175. Khan M, Arno G, Fakin A, Parfitt DA, Dhooge PPA, Albert S, et al. Detailed Phenotyping and Therapeutic Strategies for Intronic ABCA4 Variants in Stargardt Disease. Mol Ther Nucleic Acids. 2020 Sep 4;21:412–27.

176. Li G, Gao G, Wang P, Song X, Xu P, Xie B, et al. Generation and Characterization of Induced Pluripotent Stem Cells and Retinal Organoids From a Leber's Congenital Amaurosis Patient With Novel RPE65 Mutations. Front Mol Neurosci. 2019 Sep 11;12:458363.

177. Deng WL, Gao ML, Lei XL, Lv JN, Zhao H, He KW, et al. Gene Correction Reverses Ciliopathy and Photoreceptor Loss in iPSC-Derived Retinal Organoids from Retinitis Pigmentosa Patients. Stem Cell Reports. 2018 Apr 10;10(4):1267–81.

178. Gao ML, Lei XL, Han F, He KW, Jin SQ, Zhang YY, et al. Patient-Specific Retinal Organoids Recapitulate Disease Features of Late-Onset Retinitis Pigmentosa. Front Cell Dev Biol. 2020 Mar 6;8:514056.

179. Rachel RA, Yamamoto EA, Dewanjee MK, May-Simera HL, Sergeev Y V., Hackett AN, et al. CEP290 alleles in mice disrupt tissue-specific cilia biogenesis and recapitulate features of syndromic ciliopathies. Hum Mol Genet. 2015 Jul 1;24(13):3775–91.

180. Fenner BJ, Tan TE, Barathi AV, Tun SBB, Yeo SW, Tsai ASH, et al. Gene-Based Therapeutics for Inherited Retinal Diseases. Front Genet. 2022;12(January):1–17.

181. Ziccardi L, Cordeddu V, Gaddini L, Matteucci A, Parravano M, Malchiodi-Albedi F, et al. Gene Therapy in Retinal Dystrophies. Int J Mol Sci. 2019;20(5722):1–25.

182. Russell S, Bennett J, Wellman JA, Chung DC, Yu ZF, Tillman A, et al. Efficacy and safety of voretigene neparvovec (AAV2-hRPE65v2) in patients with RPE65-mediated inherited retinal dystrophy: a randomised, controlled, open-label, phase 3 trial. The Lancet. 2017 Aug 26;390(10097):849–60.

183. Drag S, Dotiwala F, Upadhyay AK. Gene Therapy for Retinal Degenerative Diseases: Progress, Challenges, and Future Directions. Invest Ophthalmol Vis Sci. 2023;64(7):39.

184. Tomkiewicz TZ, Nieuwenhuis SE, Cremers FPM, Garanto A, Collin RWJ. Correction of the Splicing Defect Caused by a Recurrent Variant in ABCA4 (c.769-784C>T) That Underlies Stargardt Disease. Cells. 2022 Dec 1;11(24):3947.

185. Amato A, Arrigo A, Aragona E, Manitto MP, Saladino A, Bandello F, et al. Gene Therapy in Inherited Retinal Diseases: An Update on Current State of the Art. Front Med (Lausanne). 2021;8(October):1–25.

186. Bennett J, Wilson^ J, Sun D, Forbes B, Maguire A. Adenovirus vector-mediated in vivo gene transfer into adult murine retina. Invest Ophthalmol Vis Sci. 1994 Apr 1;35(5):2535–42.

REFERENCES

187. Bulcha JT, Wang Y, Ma H, Tai PWL, Gao G. Viral vector platforms within the gene therapy landscape. Signal Transduct Target Ther. 2021 Dec 1;6(1).

188. Yáñez-Muñoz RJ, Balaggan KS, MacNeil A, Howe SJ, Schmidt M, Smith AJ, et al. Effective gene therapy with nonintegrating lentiviral vectors. Nat Med. 2006 Mar;12(3):348–53.

189. Cashman SM, Sadowski SL, Morris DJ, Frederick J, Kumar-Singh R. Intercellular trafficking of adenovirus-delivered HSV VP22 from the retinal pigment epithelium to the photoreceptors--implications for gene therapy. Mol Ther. 2002 Dec 1;6(6):813–23.

190. Ong T, Pennesi ME, Birch DG, Lam BL, Tsang SH. Adeno-Associated Viral Gene Therapy for Inherited Retinal Disease. Pharm Res. 2019 Feb 1;36(2).

191. Patel U, Boucher M, Léséleuc L de, Visintini S. Voretigene Neparvovec: An Emerging Gene Therapy for the Treatment of Inherited Blindness. CADTH Issues in Emerging Health Technologies. 2018 Mar 1;

192. Maguire AM, Russell S, Wellman JA, Chung DC, Yu ZF, Tillman A, et al. Efficacy, Safety, and Durability of Voretigene Neparvovec-rzyl in RPE65 Mutation–Associated Inherited Retinal Dystrophy: Results of Phase 1 and 3 Trials. Ophthalmology. 2019 Sep 1;126(9):1273–85.

193. Garita-Hernandez M, Routet F, Guibbal L, Khabou H, Toualbi L, Riancho L, et al. AAV-mediated gene delivery to 3D retinal organoids derived from human induced pluripotent stem cells. Int J Mol Sci. 2020;21(3):1–16.

194. Ferreira M V., Fernandes S, Almeida AI, Neto S, Mendes JP, Silva RJS, et al. Extending AAV Packaging Cargo through Dual Co-Transduction: Efficient Protein Trans-Splicing at Low Vector Doses. Int J Mol Sci. 2023 Jul 1;24(13).

195. McClements ME, Barnard AR, Singh MS, Charbel Issa P, Jiang Z, Radu RA, et al. An AAV Dual Vector Strategy Ameliorates the Stargardt Phenotype in Adult Abca4-/- Mice. Hum Gene Ther. 2019 May 1;30(5):590–600.

196. Trapani I, Colella P, Sommella A, Iodice C, Cesi G, de Simone S, et al. Effective delivery of large genes to the retina by dual AAV vectors. EMBO Mol Med. 2014 Feb;6(2):194–211.

197. Salman A, Kantor A, Mcclements ME, Marfany G, Trigueros S, Maclaren RE. Non-Viral Delivery of CRISPR / Cas Cargo to the Retina Using Nanoparticles : Current Possibilities , Challenges , and Limitations. Pharmaceutics. 2022;14(1842):1–23.

198. Collins FS, Varmus H. A New Initiative on Precision Medicine. New England Journal of Medicine. 2015 Feb 26;372(9):793–5.

199. Kou L, Bhutia YD, Yao Q, He Z, Sun J, Ganapathy V. Transporter-guided delivery of nanoparticles to improve drug permeation across cellular barriers and drug exposure to selective cell types. Front Pharmacol. 2018 Jan 26;9(JAN):337630.

200. Anselmo AC, Mitragotri S. Nanoparticles in the clinic: An update post COVID-19 vaccines. Bioeng Transl Med. 2021;6(3):1–20.

201. Mitchell MJ, Billingsley MM, Haley RM, Wechsler ME, Peppas NA, Langer R. Engineering precision nanoparticles for drug delivery. Nature Reviews Drug Discovery 2020 20:2. 2020 Dec 4;20(2):101–24.

202. Arnold J, Barbezetto I, Birngruber R, Bressler NM, Bressler SB, Donati G, et al. Verteporfin therapy of subfoveal choroidal neovascularization in age-related macular degeneration: Two-year results of a randomized clinical trial including lesions with occult with no classic choroidal neovascularization - Verteporfin in photodynamic the. Am J Ophthalmol. 2001;131(5):541–60.

203. Sarfraz M, Afzal A, Yang T, Gai Y, Raza SM, Khan MW, et al. Development of Dual Drug Loaded Nanosized Liposomal Formulation by A Reengineered Ethanolic Injection Method and Its Pre-Clinical Pharmacokinetic Studies. Pharmaceutics 2018, Vol 10, Page 151. 2018 Sep 6;10(3):151.

204. Leung AKK, Tam YYC, Chen S, Hafez IM, Cullis PR. Microfluidic Mixing: A General Method for Encapsulating Macromolecules in Lipid Nanoparticle Systems. Journal of Physical Chemistry B. 2015 Jul 16;119(28):8698–706.

REFERENCES

205. Zhang L, Beatty A, Lu L, Abdalrahman A, Makris TM, Wang G, et al. Microfluidic-assisted polymer-protein assembly to fabricate homogeneous functionalnanoparticles. Materials Science and Engineering: C. 2020 Jun 1;111:110768.

206. Yang W, Liang H, Ma S, Wang D, Huang J. Gold nanoparticle based photothermal therapy: Development and application for effective cancer treatment. Sustainable Materials and Technologies. 2019 Dec 1;22:e00109.

207. Wang J, Potocny AM, Rosenthal J, Day ES. Gold Nanoshell-Linear Tetrapyrrole Conjugates for near Infrared-Activated Dual Photodynamic and Photothermal Therapies. ACS Omega. 2020 Jan 14;5(1):926–40.

208. Li Z, Zhang Y, Feng N. Mesoporous silica nanoparticles: synthesis, classification, drug loading, pharmacokinetics, biocompatibility, and application in drug delivery. Expert Opin Drug Deliv. 2019 Mar 4;16(3):219–37.

209. Ferenchak K, Deitch I, Huckfeldt R. Antisense Oligonucleotide Therapy for Ophthalmic Conditions. Semin Ophthalmol. 2021;36(5–6):452–7.

210. Tomkiewicz TZ, Suárez-Herrera N, Cremers FPM, Collin RWJ, Garanto A. Antisense oligonucleotide-based rescue of aberrant splicing defects caused by 15 pathogenic variants in abca4. Int J Mol Sci. 2021 Apr 28;22(9):4621.

211. Cideciyan A V., Jacobson SG, Ho AC, Garafalo A V., Roman AJ, Sumaroka A, et al. Durable vision improvement after a single treatment with antisense oligonucleotide sepofarsen: a case report. Nature Medicine 2021 27:5. 2021 Apr 1;27(5):785–9.

212. Chirco KR, Martinez C, Lamba DA. Advancements in pre-clinical development of gene editing-based therapies to treat inherited retinal diseases. Vision Res. 2023 Aug 1;209:108257.

213. Carrella S, Indrieri A, Franco B, Banfi S. Mutation-Independent Therapies for Retinal Diseases: Focus on Gene-Based Approaches. Front Neurosci. 2020;14(September):1–8.

214. Osborne A, Khatib TZ, Songra L, Barber AC, Hall K, Kong GYX, et al. Neuroprotection of retinal ganglion cells by a novel gene therapy construct that achieves sustained enhancement of brain-derived neurotrophic factor/tropomyosin-related kinase receptor-B signaling. Cell Death Dis. 2018 Oct 1;9(10).

215. Xiong W, Garfinkel AEMC, Li Y, Benowitz LI, Cepko CL. NRF2 promotes neuronal survival in neurodegeneration and acute nerve damage. Journal of Clinical Investigation. 2015;125(4):1433–45.

216. Xue Y, Wang SK, Rana P, West ER, Hong CM, Feng H, et al. AAV-Txnip prolongs cone survival and vision in mouse models of retinitis pigmentosa. Elife. 2021;10:1–29.

217. Tomita H, Sugano E. Optogenetics. In: Advances in Experimental Medicine and Biology. 2021. p. 545–55.

218. McClements ME, Staurenghi F, MacLaren RE, Cehajic-Kapetanovic J. Optogenetic Gene Therapy for the Degenerate Retina: Recent Advances. Front Neurosci. 2020;14(November).

219. Sahel J alain, Boulanger-scemama E, Pagot C, Arleo A, Galluppi F, Martel JN, et al. Partial recovery of visual function in a blind patient after optogenetic therapy. Nat Med. 2021;27(7):1223–9.

220. Sánchez-Bellver L, Toulis V, Marfany G. On the Wrong Track: Alterations of Ciliary Transport in Inherited Retinal Dystrophies. Front Cell Dev Biol. 2021;9(March):1–25.

221. Mirra S, García-Arroyo R, Domènech EB, Gavaldà-Navarro A, Herrera-Úbeda C, Oliva C, et al. CERKL, a retinal dystrophy gene, regulates mitochondrial function and dynamics in the mammalian retina. Neurobiol Dis. 2021;156:105405.

222. Bolinches-Amorós A, León M, del Buey Furió V, Marfany G, Gonzàlez-Duarte R, Erceg S, et al. Generation of an iPSC line from a retinitis pigmentosa patient carrying a homozygous mutation in CERKL and a healthy sibling. Stem Cell Res. 2019;38(April):101455.

REFERENCES

223. Domènech EB. La funció de CERKL a la retina : generació d ' un model de ratolí i anàlisi de la seva implicació en la resposta a estrès oxidatiu. 2020;

224. Kuleshov M V., Jones MR, Rouillard AD, Fernandez NF, Duan Q, Wang Z, et al. Enrichr: a comprehensive gene set enrichment analysis web server 2016 update. Nucleic Acids Res. 2016;44(1):W90–7.

225. Chen EY, Tan CM, Kou Y, Duan Q, Wnag Z, Meirelles GV, et al. Enrichr: interactive and collaborative HTML5 gene list enrichment analysis tool Edward. BCM Bioinformatics. 2013;14(128):1–15.

226. Xie Z, Bailey A, Kuleshov M V., Clarke DJB, Evangelista JE, Jenkins SL, et al. Gene Set Knowledge Discovery with Enrichr. Curr Protoc. 2021;1(3).

227. Doench JG, Fusi N, Sullender M, Hegde M, Vaimberg EW, Donovan KF, et al. Optimized sgRNA design to maximize activity and minimize off-target effects of CRISPR-Cas9. Nat Biotechnol. 2016 Feb 1;34(2):184–91.

228. Hsu PD, Scott DA, Weinstein JA, Ran FA, Konermann S, Agarwala V, et al. DNA targeting specificity of RNA-guided Cas9 nucleases. Nat Biotechnol. 2013 Sep;31(9):827–32.

229. Paquet D, Kwart D, Chen A, Sproul A, Jacob S, Teo S, et al. Efficient introduction of specific homozygous and heterozygous mutations using CRISPR/Cas9. Nature. 2016 May 5;533(7601):125–9.

230. Richardson CD, Ray GJ, DeWitt MA, Curie GL, Corn JE. Enhancing homology-directed genome editing by catalytically active and inactive CRISPR-Cas9 using asymmetric donor DNA. Nat Biotechnol. 2016 Mar 1;34(3):339–44.

231. Corral-Serrano JC, Sladen PE, Ottaviani D, Rezek OF, Athanasiou D, Jovanovic K, et al. Eupatilin Improves Cilia Defects in Human CEP290 Ciliopathy Models. Cells. 2023 Jun 1;12(12).

232. Ramachandran PS, Lee V, Wei Z, Song JY, Casal G, Cronin T, et al. Evaluation of Dose and Safety of AAV7m8 and AAV8BP2 in the Non-Human Primate Retina. Hum Gene Ther [Internet]. 2017 Feb 1 [cited 2024 Feb 12];28(2):154–67. Available from: https://pubmed.ncbi.nlm.nih.gov/27750461/

233. Scheive M, Yazdani S, Hajrasouliha AR. The utility and risks of therapeutic nanotechnology in the retina. Ther Adv Ophthalmol. 2021;13:251584142110033.

234. Trigueros S, Domènech EB, Toulis V, Marfany G. In vitro gene delivery in retinal pigment epithelium cells by plasmid dna-wrapped gold nanoparticles. Genes (Basel). 2019;10(4).

235. Lajunen T, Viitala L, Kontturi LS, Laaksonen T, Liang H, Vuorimaa-Laukkanen E, et al. Light induced cytosolic drug delivery from liposomes with gold nanoparticles. Journal of Controlled Release. 2015 Apr 10;203:85–98.

236. Trigueros S. Nanostructure coated with a twist-strained double-stranded circular deoxyribonucleic|acid (dna), method for making and use. Method for Making and Use US Patent Application 20180318424, 11 August 2018.

237. Karbowski M, Youle RJ. Dynamics of mitochondrial morphology in healthy cells and during apoptosis. Cell Death Differ. 2003;10(8):870–80.

238. Liu YJ, McIntyre RL, Janssens GE, Houtkooper RH. Mitochondrial fission and fusion: A dynamic role in aging and potential target for age-related disease. Mech Ageing Dev. 2020;186(October 2019):111212.

239. Sun N, Youle RJ, Finkel T. The Mitochondrial Basis of Aging. Mol Cell. 2016;61(5):654–66.

240. Sheng ZH, Cai Q. Mitochondrial transport in neurons: Impact on synaptic homeostasis and neurodegeneration. Nat Rev Neurosci. 2012;13(2):77–93.

241. Schwarz TL. Mitochondrial trafficking in neurons. Cold Spring Harb Perspect Med. 2013;3(3):1–16.

242. Kooragayala K, Gotoh N, Cogliati T, Nellissery J, Kaden TR, French S, et al. Quantification of Oxygen Consumption in Retina Ex Vivo Demonstrates Limited Reserve Capacity of Photoreceptor Mitochondria. Invest Ophthalmol Vis Sci. 2015 Dec 1;56(13):8428–36.

243. Shimasaki K, Watanabe-Takahashi M, Umeda M, Funamoto S, Saito Y, Noguchi N, et al. Pleckstrin homology domain of p210 BCR-ABL interacts with cardiolipin

to regulate its mitochondrial translocation and subsequent mitophagy. Genes to Cells. 2018;23(1):22–34.

244. Schiaffarino O, Valdivieso González D, García-Pérez IM, Peñalva DA, Almendro-Vedia VG, Natale P, et al. Mitochondrial membrane models built from native lipid extracts: Interfacial and transport properties. Front Mol Biosci. 2022;9(September):1–15.

245. Lourdes SR, Gurung R, Giri S, Mitchell CA, McGrath MJ. A new role for phosphoinositides in regulating mitochondrial dynamics. Adv Biol Regul. 2023;(xxxx):101001.

246. Falabella M, Vernon HJ, Hanna MG, Claypool SM, Pitceathly RDS. Cardiolipin, Mitochondria, and Neurological Disease. Trends in Endocrinology and Metabolism. 2021;32(4):224–37.

247. Ozawa Y. Oxidative stress in the light-exposed retina and its implication in age-related macular degeneration. Redox Biol. 2020;37:101779.

248. Chen J, Liu F, Li H, Archacki S, Gao M, Liu Y, et al. PVHL interacts with Ceramide kinase like (CERKL) protein and ubiquitinates it for oxygen dependent proteasomal degradation. Cell Signal. 2015;27(11):2314–23.

249. Noailles A, Maneu V, Campello L, Lax P, Cuenca N. Systemic inflammation induced by lipopolysaccharide aggravates inherited retinal dystrophy. Cell Death Dis. 2018;9(3).

250. Jones BW, Marc RE. Retinal remodeling during retinal degeneration. Exp Eye Res. 2005;81(2):123–37.

251. Baird L, Yamamoto M. The Molecular Mechanisms Regulating the KEAP1-NRF2 Pathway. Mol Cell Biol. 2020;40(13):1–23.

252. Gao X, Hu W, Qian D, Bai X, He H, Li L, et al. The Mechanisms of Ferroptosis Under Hypoxia. Cell Mol Neurobiol. 2023 Oct 1;43(7):3329–41.

253. Ochocinska MJ, Muñoz EM, Veleri S, Weller JL, Coon SL, Pozdeyev N, et al. NeuroD1 is required for survival of photoreceptors but not pinealocytes: results from targeted gene deletion studies. J Neurochem. 2012 Oct;123(1):44–59.

254. Pan N, Jahan I, Lee JE, Fritzsch B. Defects in the cerebella of conditional Neurod1 null mice correlate with effective Tg(Atoh1-cre) recombination and granule cell requirements for Neurod1 for differentiation. Cell Tissue Res. 2009 Sep 17;337(3):407–28.

255. Jahan I, Kersigo J, Pan N, Fritzsch B. Neurod1 regulates survival and formation of connections in mouse ear and brain. Cell Tissue Res. 2010;341(1):95–110.

256. Naya FJ, Huang HP, Qiu Y, Mutoh H, DeMayo FJ, Leiter AB, et al. Diabetes, defective pancreatic morphogenesis, and abnormal enteroendocrine differentiation in BETA2/neuroD-deficient mice. Genes Dev. 1997 Sep 15;11(18):2323–34.

257. Hardcastle AJ, Sieving PA, Sahel JA, Jacobson SG, Cideciyan A V., Flannery JG, et al. Translational Retinal Research and Therapies. Transl Vis Sci Technol. 2018 Sep 1;7(5).

258. Garanto A, Mandal NA, Egido-Gabás M, Marfany G, Fabriàs G, Anderson RE, et al. Specific sphingolipid content decrease in Cerkl knockdown mouse retinas. Exp Eye Res. 2013;110:96–106.

259. Celiker C, Weissova K, Cerna KA, Oppelt J, Dorgau B, Gambin FM, et al. Light-responsive microRNA molecules in human retinal organoids are differentially regulated by distinct wavelengths of light. iScience. 2023;26(7):107237.

260. Chen M, Rajapakse D, Fraczek M, Luo C, Forrester J V., Xu H. Retinal pigment epithelial cell multinucleation in the aging eye - a mechanism to repair damage and maintain homoeostasis. Aging Cell. 2016 Jun;15(3):436–45.

261. Wubben TJ, Zacks DN, Besirli CG. Retinal neuroprotection: Current strategies and future directions. Curr Opin Ophthalmol. 2019 May 1;30(3):199–205.

262. Lee SY, Usui S, Zafar A bakr, Oveson BC, Jo YJ, Lu L, et al. N-acetylcysteine promotes long-term survival of cones in a model of retinitis pigmentosa. J Cell Physiol. 2011 Jul 1;226(7):1843–9.

263. Gimeno-Hernández R, Cantó A, Fernández-Carbonell A, Olivar T, Hernández-Rabaza V, Almansa I, et al. Thioredoxin Delays Photoreceptor Degeneration,

Oxidative and Inflammation Alterations in Retinitis Pigmentosa. Front Pharmacol. 2020 Dec 23;11:590572.

264. Xue Y, Wang SK, Rana P, West ER, Hong CM, Feng H, et al. Aav-txnip prolongs cone survival and vision in mouse models of retinitis pigmentosa. Elife. 2021;10.

265. Pagano G, Pallardó F V., Lyakhovich A, Tiano L, Trifuoggi M. Mitigating the pro-oxidant state and melanogenesis of Retinitis pigmentosa: by counteracting mitochondrial dysfunction. Cellular and Molecular Life Sciences 2021 78:23. 2021 Oct 31;78(23):7491–503.

266. Wu DM, Ji X, Ivanchenko M V., Chung M, Piper M, Rana P, et al. Nrf2 overexpression rescues the RPE in mouse models of retinitis pigmentosa. JCI Insight. 2021 Jan 25;6(2).

267. Moore SM, Skowronska-krawczyk D, Chao DL. Targeting of the NRL pathway as a therapeutic strategy to treat retinitis pigmentosa. J Clin Med. 2020;9(7):1–18.

268. Li S, Datta S, Brabbit E, Love Z, Woytowicz V, Flattery K, et al. Nr2e3 is a genetic modifier that rescues retinal degeneration and promotes homeostasis in multiple models of retinitis pigmentosa. Gene Ther. 2021;28(5):223–41.

269. Hayashi A, Naseri A, Pennesi ME, De Juan E. Subretinal delivery of immunoglobulin G with gold nanoparticles in the rabbit eye. Jpn J Ophthalmol. 2009 May 31;53(3):249–56.

ANNEX

ANNEX

Other articles related to this Thesis

1. Domènech EB, Andrés R, López-Iniesta MJ, Mirra S, García-Arroyo R, Milla S, Sava F, Andilla J, Loza-Álvarez P, de la Villa P, Gonzàlez-Duarte R, Marfany G. A New Cerkl Mouse Model Generated by CRISPR-Cas9 Shows Progressive Retinal Degeneration and Altered Morphological and Electrophysiological Phenotype. Invest Ophthalmol Vis Sci. 2020 Jul 1;61(8):14. doi: 10.1167/iovs.61.8.14. PMID: 32658961; PMCID: PMC7425692.

2. Aísa-Marín I, García-Arroyo R, Mirra S, Marfany G. The Alter Retina: Alternative Splicing of Retinal Genes in Health and Disease. Int J Mol Sci. 2021 Feb 12;22(4):1855. doi: 10.3390/ijms22041855. PMID: 33673358; PMCID: PMC7917623.

ANNEX

A New *Cerkl* Mouse Model Generated by CRISPR-Cas9 Shows Progressive Retinal Degeneration and Altered Morphological and Electrophysiological Phenotype

Elena B. Domènech,[1,2] Rosa Andrés,[1,2] M. José López-Iniesta,[1] Serena Mirra,[1,2] Rocío García-Arroyo,[1] Santiago Milla,[3] Florentina Sava,[1] Jordi Andilla,[4] Pablo Loza-Álvarez,[4] Pedro de la Villa,[3,5] Roser Gonzàlez-Duarte,[1,2,6] and Gemma Marfany[1,2,6,7]

[1]Department of Genetics, Microbiology and Statistics, University of Barcelona, Barcelona, Spain
[2]CIBERER/ISCIII, University of Barcelona, Barcelona, Spain
[3]Department of Systems Biology, University of Alcalá, Madrid, Spain
[4]ICFO–The Institute of Photonic Sciences, Barcelona Institute of Science and Technology, Barcelona, Spain
[5]Ramón y Cajal Institute for Health Research, Madrid, Spain
[6]DBGen Ocular Genomics, Barcelona, Spain
[7]Institute of Biomedicine, University of Barcelona, Barcelona, Spain

Purpose. Close to 100 genes cause retinitis pigmentosa, a Mendelian rare disease that affects 1 out of 4000 people worldwide. Mutations in the ceramide kinase-like gene (*CERKL*) are a prevalent cause of autosomal recessive cause retinitis pigmentosa and cone–rod dystrophy, but the functional role of this gene in the retina has yet to be fully determined. We aimed to generate a mouse model that resembles the phenotypic traits of patients carrying *CERKL* mutations to undertake functional studies and assay therapeutic approaches.

Methods. The *Cerkl* locus has been deleted (around 97 kb of genomic DNA) by gene editing using the CRISPR-Cas9 D10A nickase. Because the deletion of the *Cerkl* locus is lethal in mice in homozygosis, a double heterozygote mouse model with less than 10% residual *Cerkl* expression has been generated. The phenotypic alterations of the retina of this new model have been characterized at the morphological and electrophysiological levels.

Results. This *Cerkl*$^{KD/KO}$ model shows retinal degeneration, with a decreased number of cones and progressive photoreceptor loss, poorly stacked photoreceptor outer segment membranes, defective retinal pigment epithelium phagocytosis, and altered electrophysiological recordings in aged retinas.

Conclusions. To our knowledge, this is the first *Cerkl* mouse model to mimic many of the phenotypic traits, including the slow but progressive retinal degeneration, shown by human patients carrying *CERKL* mutations. This useful model will provide unprecedented insights into the retinal molecular pathways altered in these patients and will contribute to the design of effective treatments.

Keywords: *CERKL*, CRISPR, gene editing, retinitis pigmentosa, cone–rod dystrophy

Retinitis pigmentosa (RP) (OMIM #268000) belongs to a group of heterogeneous inherited retinal dystrophies that affect 1 in 3000 to 5000 people worldwide[1–3] RP, a highly clinically and genetically heterogeneous disease, is characterized by degeneration of photoreceptors, with alteration of rods in the early stages followed by cone death at later stages of the disease[1] Mutations in *CERKL* cause non-syndromic autosomal recessive RP (OMIM #608380), although it has also been associated with autosomal recessive cone–rod dystrophy (CRD) (first alterations detected in cones and later in rods).[4–8]

CERKL shares more than 50% homology to CERK, a kinase that phosphorylates ceramide to ceramide 1-phosphate, a sphingolipid metabolite involved in prolif-eration, apoptosis, phagocytosis, and inflammation[9–11]; however, no kinase activity has been confirmed for CERKL thus far.[12] CERKL shows a highly dynamic subcellular localization, as it can shift from nucleus to cytoplasm, and it has also been associated with Golgi vesicles and endoplasmic reticulum and mitochondria membranes[13,14] Previous results support its involvement in protecting cells against oxidative stress injury.[13,15] *CERKL* is expressed not only in the retina but also in several adult and fetal tissues in human and mouse. In humans, the highest expression of *CERKL* is detected in the retina, some brain regions, lung, and kidney,[4] whereas in the adult mouse, the highest levels of expression can be detected in the retina, liver, and testis.[16]

1

Attempts to generate a mouse model to both unveil the physiological function of CERKL and generate an RP model to study the progression of the retinal disorder have not been successful.[17] A knockout (KO) murine model generated by deleting the proximal promoter and the first exon of *CERKL* using cre/loxP turned into a knockdown, due to the use of alternative promoters. The levels of sphingolipids were altered in the model,[13] but no retinal morphological degeneration was detected except for electroretinographic alterations in the oscillatory potentials (OPs) of the retinal ganglion cell layer.[18] It is plausible that the high transcriptional complexity of *CERKL*, which produces more than 20 transcript isoforms in humans and mice due to the combination of extensive alternative splicing and the use of additional promoters hampers the generation of a mouse model that mimics the human phenotype.[16] Nonetheless, the morpholino knockdown of *Cerkl* in zebrafish embryos caused abnormal eye development, and the retina showed lamination defects, altered photoreceptor outer segments, and increased apoptosis, thus supporting the relevance of *Cerkl* for survival and protection of the retina.[19] On the other hand, the study of the retinal neurodegeneration phenotype in morpholino-treated zebrafish embryos cannot be easily extrapolated to adult humans; therefore, the generation of a genetically amenable model to unveil the physiological role of *CERKL* and study the effect of associated mutations still remains a challenge.

In this work, we have generated the deletion of the whole *Cerkl* locus (approximately 100 kb) by gene editing using a CRISPR/Cas9 D10A nickase. Unexpectedly, the complete ablation of *Cerkl* in homozygosis resulted in embryonic/perinatal lethality in mouse. We have thus generated a new double heterozygote model in which the expression of *Cerkl* is reduced to less than 10% in the retina.

MATERIALS AND METHODS

Animal Handling and Ethics Statement

Murine tissue samples were obtained from C57BL/6J and Albino B6(Cg)-Tyrc-2J/J (Jackson Laboratory, Bar Harbor, ME, USA) background mice at different ages. Animal handling was performed according to the ARVO Statement for the Use of Animals in Ophthalmic and Vision Research, as well as the regulations of the animal care facilities at the University of Barcelona. All procedures were evaluated and approved by the Animal Research Ethics Committee of the University of Barcelona.

Cerkl^{KOKO} Mouse Model Generation by CRISPR/Cas9 System

The CRISPR/Cas9 system was used to generate a *Cerkl^{KOKO}* mouse model by deleting the whole *Cerkl* locus, approximately 97 kb. To minimize potential off-targets, we used the D10A Cas9 nickase (Addgene, Watertown, MA, USA). For the deletion, two guides per site were designed (a total of four) (Fig. 1) and injected in murine zygotes together with the endonuclease Cas9 D10A mRNA. To facilitate the generation of a recombinant deletion allele, single-stranded donor oligonucleotides (ssODNs) with the flanking sequence of the expected deleted allele were also microinjected. In our conditions, ssODNs appeared integrated in the target site in some alleles but did not enhance deletion, as none of the recovered alleles in the mosaic pups contained the precise designed allele. All embryonic procedures up to the gener-

ation of the founder mice were performed at the Mouse Mutant Core Facility, Institute for Research in Biomedicine (Barcelona, Spain).

Mosaic pups were genotyped, and DNA samples from ear punches were screened by PCR using specific primers for detection of gene edited alleles (only at 5' or 3' sites, full deletion, inversion) (Table). PCR products were electrophoresed in high-resolution agarose gels, and gene edition was confirmed by Sanger sequencing. To confirm that the CRISPR/Cas9 technique did not introduce any off-target deletions or mutations, all of the potential off-target sequences determined by a prediction software (up to three mismatches with single guide RNA) were analyzed. PCR primers for potential off-target regions are listed in Supplementary Table S1. After discarding any off-target events or on-target chromosomal rearrangements (inversions/duplications), selected founder animals were crossed with wild-type black or albino animals in order to transmit the *Cerkl* allele bearing the 97 kb deletion to the offspring. Additional matings with a floxed *Cerkl^{KD}* model[18] were performed to obtain the heterozygote *Cerkl^{KD/KO}* lineage in both the C57BL/6J and Albino B6 murine backgrounds.

For arborization studies, selected matings between two strains, the transgenic Thy1-YFP-H mice (a kind gift from Ángel Carrión[20]) and *Cerkl^{KD/KO}* mice (generated in this work), were performed to generate a new mouse line, *Cerkl^{KD/KO}/Thy1-YFP*.

Genomic DNA and Genotyping by PCR

DNA for genotyping was extracted from ear punches from weaning mouse pups, following standard procedures. In brief, each sample was lysed in a mild lysis buffer and incubated overnight with proteinase K, and the nucleic acid was precipitated with ethanol. Primers for genotyping each strain are depicted in Figure 1 and listed in the Table. Three-step PCR conditions for amplification of genomic DNA were used for individual genotyping.

RNA Isolation and RT-qPCR

For each genotype, three to six independent animal samples were homogenized using a Polytron PT1200E homogenizer (Kinematica AG, Lucerne, Switzerland). Total RNA was isolated using the RNeasy Mini Kit (Qiagen, Hilden, Germany), following the manufacturer's instructions with minor modifications (treatment with DNAse I during first hour). Reverse transcription reactions were carried out using the qScript cDNA Synthesis Kit (Quanta BioSciences, Inc., Gaithersburg, MD, USA). Real-time PCR (qPCR) was performed using LightCycler 480 SYBR Green I Master and a LightCycler 480 Multiwell Plate 384 (Roche Diagnostics GmbH, Penzberg, Germany) in a final reaction volume of 10 µL (primers are listed in the Table). Raw data were analyzed with the Advanced Relative Quantification method (LightCycler 480). The Mann–Whitney test was performed to assess statistical significance.

Cell Culture and Constructs

The coding region of hCERKL532 cDNA (NM_201548.4) and mCerkl525 cDNA were cloned into pcDNA3.1. Site-directed mutagenesis by inverse PCR was performed when coding mCerkl525 cDNA (NM_001048176.1) to generate constructs carrying the deletion of exon 2, exon 5, and exon 12 in frame. The constructs were transfected in HEK293 using Lipotrans-
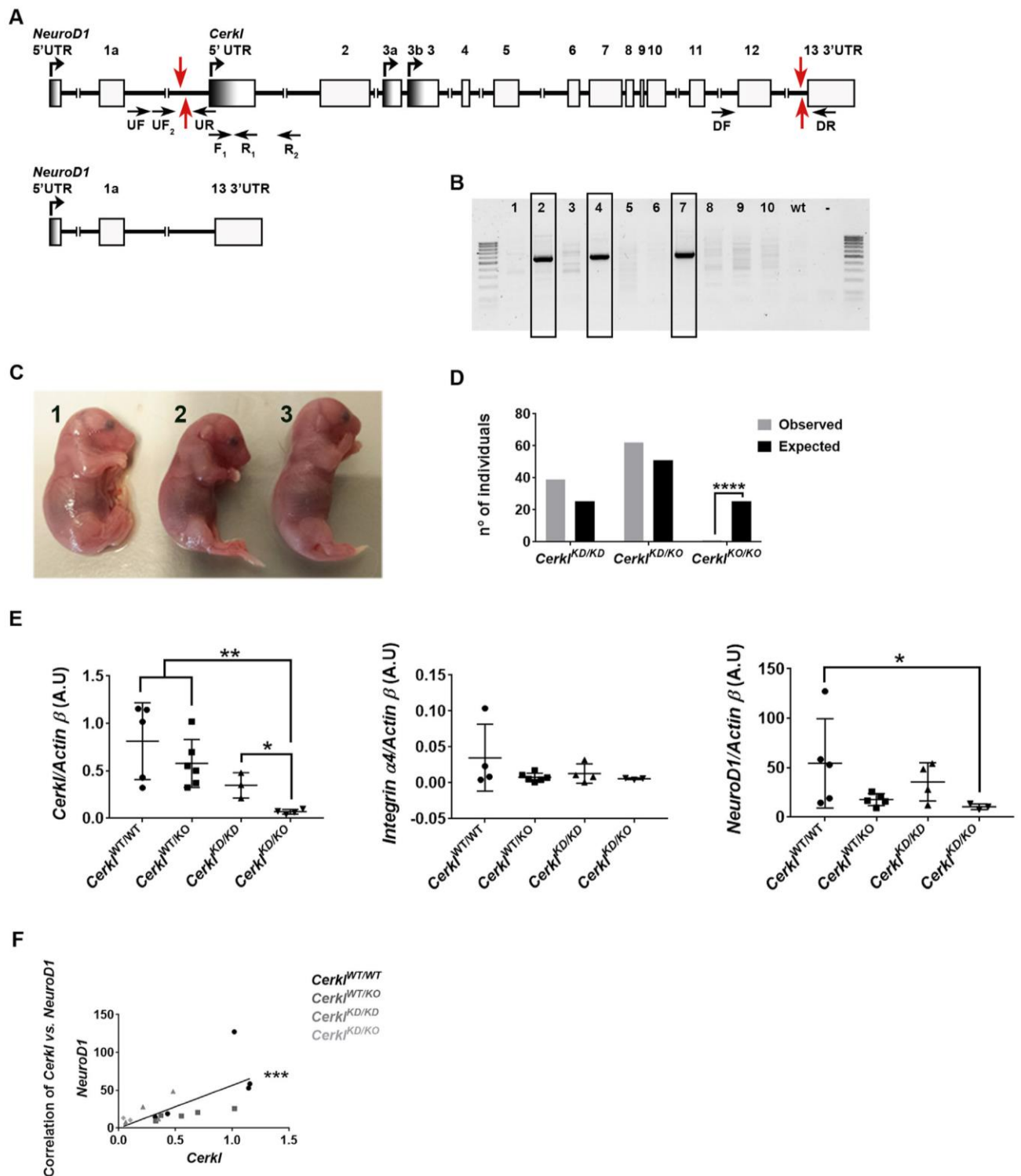
Figure 1. Generation of a *Cerkl*[KO/KO] mouse model by CRISPR/Cas9 gene editing. (**A**) Representation of the *Cerkl* locus with the position of exons and active promoters in the retina and of the targeting sequences for the four CRISPR gRNAs (*red arrows*). The resulting gene structure of the CRISPR-edited allele with full deletion from the proximal promoter to exon 13 is indicated below. *Black arrows* indicate the position of the primers used for genotyping. (**B**) PCR genotyping analysis (using forward primers [UF] and reverse primers [DR]) of the mosaic *Cerkl*[KO] pups obtained after CRISPR/Cas9 zygote microinjections. (**C**) Image of three E18 embryos showing the only homozygous *Cerkl*[KO/KO] mouse recovered (1) and the other two siblings, whose genotype was *Cerkl*[KD/KO] (2 and 3). No gross morphological alterations were observed. (**D**) Complete ablation of the *Cerkl* locus causes perinatal lethality in mice. Only one embryo (E18, shown in **C**) out of 102 mice (adding embryos and newborns) from matings between *Cerkl*[KD/KO] heterozygotes was a *Cerkl*[KO/KO] homozygote. $P < 0.0001$ (χ^2 test) represents statistically significant differences between the expected results (25%) and the observed results (0.98%) for the *Cerkl*[KO/KO]

genotype. The offspring of the matings were 1:2 instead of 1:2:1, thus supporting the lethality of the $Cerkl^{KO/KO}$ genotype. (E, F) Effect of the *Cerkl* knockout allele on the expression levels of genes in the same *locus*. Transcriptional levels of *Cerkl*, *Integrin α4*, and *NeuroD1* (E) in the retinas of *Cerkl* CRISPR-ed P60 mice ($n = 3$–6), C57BL/6J mice strain. Levels were normalized against *Actin B* expression. Statistical significance is indicated with asterisks (*$P < 0.05$, **$P < 0.01$; Mann–Whitney test). Correlation analyses between the *Cerkl* and the *NeuroD1* values (F) are also shown. Statistical significance, assessed by the Spearman correlation test, confirmed a strong correlation between the expression of *Cerkl* and *NeuroD1* genes (***$P < 0.001$).

TABLE. Sequences of Primers Used in PCR Assays

Name	Forward (5′→3′)	Assay	Name	Reverse (5′→3′)	Assay
Cerkl UF$_2$	GAAGCCCTGAAGGAGACAACTC	CRISPR/Cas9	*Cerkl* UR	CTCTACCTGGATGCGACAGC	CRISPR/Cas9
Cerkl DF	GAAAACCTGGGGCTATCTGGT	CRISPR/Cas9			
Cerkl UF	CAGGACAGTTCTGGAGTTGATG	CRISPR/Cas9 Genotyping	*Cerkl* DR	GGGAGCAGGGCTAGAGAGTAT	CRISPR/Cas9 Genotyping
Cerkl F$_1$	ACACATTAGAAGCCCTGAAGGA	Genotyping	*Cerkl* R$_1$	TCTTTGTGCTGTAGCAGTGACC	Genotyping
			Cerkl R$_2$	TTCTCCCGCTGTGATTGC	
Thy-1 F	TCTGAGTGGCAAAGGACCTTAGG	Genotyping	*Thy-1 R*	CGCTGAACTTGTGGCCGTTTACG	Genotyping
NeuroD1 Fw	AACAACAGGAAGTGGAAACATGACC	Real-time qPCR	*NeuroD1* Rv	ACACTCATCTGTCCAGCTTGGG	Real-time qPCR
Integrin α4 Fw	CAGTGGAGAGCCTTGTGGGAA	Real-time qPCR	*Integrin α4* Rv	GTGCCCACAAGTCACGATAGAGC	Real-time qPCR
Actin β Fw	GATGACCCAGATCATGTTTGAGACC	Real-time qPCR	*Actin β* Rv	CTCCGGAGTCCATCACAATGC	Real-time qPCR

fectine (Niborlab, Guillena, Spain). Four hours after transfection, the medium was changed, and the cells were then harvested after 48 hours of growth for subsequent assays.

In-House Antibody Generation

We generated in-house anti-CERKL antibodies against specific mouse CERKL antigenic peptides—CERKL2 (peptide encoded in exon 2): CLKEQRNKLKDSTLDL; CERKL5 (peptide encoded in exon 5): CSEAARALLLRAQK-NAGVE; and CERKL12 (peptide encoded in exon 12): CVDGDLMEAASEVHIR. Peptides were conjugated to the keyhole limpet hemocyanin carrier and subsequently injected into rabbits together with complete Freund's adjuvant or incomplete Freund's adjuvant adjuvants for antibody production. These antibodies were used for western blot, immunofluorescence, and immunoprecipitation assays. The specificity of the antibodies was tested using constructs with specific in-frame deletions spanning the immunogenic peptides.

Western Blot Immunodetection

Adult retinas and other tissue samples were lysed in radioimmunoprecipitation assay buffer consisting of 50-mM Tris (pH 7.4), 150-mM NaCl, 1-mM EDTA, 1% NP-40, 0.25% Na-deoxycholate, and protease inhibitors. Transiently transfected HEK293 cells were lysed using 1× Laemmli buffer. Samples were electrophoresed in a sodium dodecyl sulfate polyacrylamide gel electrophoresis gel and transferred onto a polyvinylidene difluoride (PVDF) western blotting membrane (Roche Diagnostics), which was blocked with 5% non-fat dry milk and 5% BSA (Sigma-Aldrich, St. Louis, MO, USA) in PBS containing 0.1% Tween 20 (Sigma-Aldrich). Primary antibodies were incubated overnight at 4°C followed by incubation with the corresponding secondary antibodies for 1 hour at room temperature using standard procedures: rabbit αCERKL2 (1:1000, in-house), rabbit αCERKL5 (1:1000, in-house), mouse αGFAP (1:500; MAB8360, MilliporeSigma, Burlington, MA, USA), mouse αGAPDH (1:1000; ab8245, Abcam, Cambridge, UK), horseradish peroxidase (HRP)-conjugated α-mouse (1:2000;

ab5706, Abcam), Rabbit IgG HRP Linked Whole Ab (1:2000, NA934VS; GE HealthCare, Chicago, IL, USA).

Immunohistochemistry on Mouse Retina Cryosections

Eyes from mice 2 to 18 months old were enucleated, fixed, and embedded as described elsewhere.[21] Cryosections (12-µm section) were collected and kept frozen at –80°C until used. For immunohistochemistry (IHC), cryosections were air dried for 10 minutes and rehydrated with 1× PBS (3 × 5 minutes) and blocked in blocking solution (1× PBS containing 2% sheep serum and 0.3% Triton X-100 [Sigma-Aldrich]) for 1 hour at room temperature. Primary antibody incubation was performed overnight at 4°C. After three rinses with 1× PBS (10 minutes each), cryosections were incubated for 1 hour at room temperature with the corresponding secondary antibodies conjugated to a fluorophore. Finally, the slides were washed with 1× PBS (3 × 10 minutes) and coverslipped with Fluoprep (BioMerieux, Marcy-l'Étoile, France). The primary antibodies and dilutions used included rabbit αCERKL2 (1:200, in-house), rabbit αCERKL5 (1:100, in-house), mouse αRhodopsin (1:300, ab5417; Abcam), rabbit αL-/M-opsin (1:300, ab5405; MilliporeSigma), rabbit αS-opsin (1:300, ab5407; MilliporeSigma), 4′,6-diamidino-2-phenylindole (DAPI, 1:1000, 10236276001; Sigma-Aldrich), mouse αGFAP (1:200, MAB8360; MilliporeSigma), PNA (1:50, L32460; Invitrogen, Carlsbad, CA, USA), and mouse αTUJ-1 (1:1000, 801201; BioLegend, San Diego, CA, USA). Image visualization was performed using confocal microscopy and optical transmission microscopy utilizing the LSM 880 confocal laser scanning microscope (Carl Zeiss Meditec, Jena, Germany) and Leica TCS-SP2 True Confocal Scanner (Leica Microsystems, Wetzlar, Germany), as well as high-resolution microscopy utilizing the Leica TCS SP5 STED CW.

Retinal Sections for Morphometrical Measurements and Transmission Electron Microscopy

Eyes from $Cerkl^{KD/KO}$ and $Cerkl^{WT/WT}$ mice (albino strain) were perforated using a needle, and the eyes were immersed

in fixative solution (2.5% glutaraldehyde, 2% paraformaldehyde in 0.1-M phosphate buffer) and incubated at 4°C overnight. They were then rinsed with buffer, post-fixed in 1% osmium tetroxide and 0.8% $K_4Fe(CN)_6$, and maintained in the dark for 2 hours at 4°C, followed by another rinse in double distilled water to remove the osmium. Eyes were dehydrated in increasing concentrations of acetone and then infiltrated and embedded in Epon (Electron Microscopy Sciences, Hatfield, PA, USA). Blocks were obtained after polymerization at 60°C for 48 hours. Semithin sections 1 µm thick were obtained using a Leica UC6 Ultramicrotome; they were dyed with 0.5% methylene blue and observed using a Leica DM200 microscope. Sections containing the optic nerve were photographed under a Leica MZFLIII fluorescence stereomicroscope and ZOE Fluorescent Cell Imager (Bio-Rad, Hercules, CA, USA). Fiji software (ImageJ; National Institutes of Health, Bethesda, MD, USA) was used to measure retinal layer thickness at 200-µm intervals.

For transmission electron microscope (TEM) imaging, ultrathin (60-nm) sections were obtained using a Leica UC6 Ultramicrotome. These sections were stained with 2% Urany-Less (Electron Microscopy Sciences) and lead citrate and observed in a Jeol EM J1010 (Jeol Ltd., Tokyo, Japan). Images were acquired at 80 kV with a 1000 × 1000 MegaView CCD camera (Olympus Soft Imaging Solutions, Münster, Germany). For retinal pigment epithelium (RPE) phagosome/lysosome distribution analysis, the RPE cell was longitudinally divided in two halves (basal and apical), and the number of each vesicle type was counted per eye.

Retinal Whole Mount

For whole-mount retina staining, retinas from *Cerkl*[WT/WT], *Cerkl*[WT/KO], and *Cerkl*[KD/KO] mice (2–18 months old) were placed on glass slides photoreceptors side up, flattened by cutting the edges, fixed in 4% paraformaldehyde for 1 hour at room temperature, and rinsed with 1× PBS (3 × 5 minutes). The retinas were then blocked in blocking solution (1× PBS containing 2% sheep serum and 0.3 % Triton X-100) for 1 hour at room temperature and incubated for 1 hour with Invitrogen Alexa Fluor 647 conjugate (Thermo Fisher Scientific, Waltham, MA) in blocking solution (1:50). Retinas were washed with 1× PBS (3 × 5 minutes), mounted with Fluoprep (BioMerieux), and photographed with a Leica TCS-SP2 confocal microscope. For arborization studies, retinas from 3-month-old *Cerkl*[WT/WT]/*Thy1-YFP* and *Cerkl*[KD/KO]/*Thy1-YFP* mice were placed on glass slides ganglion cells up, flattened by cutting the edges, fixed in 4% paraformaldehyde for 1 hour at room temperature, rinsed with 1× PBS (3 × 10 minutes), and permeabilized in 1× PBS with 0.1% Triton X-100 for 15 minutes. Blocking was performed for 1 hour in 1% FBS (Roche Diagnostics) in PBS. Rabbit Anti-GFP Antibody (1:50, ab290; Abcam) was used overnight at 4°C to amplify the yellow fluorescent protein (YFP) signal. Retinal whole mounts were rinsed for 10 minutes in 3× PBS and incubated at room temperature for 1 hour with secondary antibody conjugated to Invitrogen Alexa Fluor 488 (1:100; Thermo Fisher Scientific) and DAPI. After three washes in 1× PBS (10 minutes), retinas were mounted with Mowiol (Sigma-Aldrich).

Primary Retinal Ganglion Cell Culture

For primary retinal ganglion cell (RGC) culture, coverslips were coated with poly-L-ornithine (Sigma-Aldrich).

A drop of complete Invitrogen Neurobasal medium (Thermo Fisher Scientific), supplemented with 0.06% D-glucose, 0.0045% $NaHCO_3$, 1-mM L-glutamine, and 1% penicillin/streptomycin) plus 10 µg/mL laminin (Roche Diagnostics), was added on coated coverslips. The cultures were incubated overnight at 37°C and washed three times with complete Neurobasal medium before cell culture. P0 mouse retinas were dissociated using the Neural Tissue Dissociation Kit (Miltenyi Biotec, Bergisch Gladbach, Germany) following the manufacturer's instructions with minor modifications. Approximately 100,000 cells per well were seeded onto freshly prepared coverslips in 24-well plates. Neuronal supplements and factors were added: Invitrogen B-27 (1×; Thermo Fisher Scientific), 5-µM Forskolin (Sigma-Aldrich), 50-ng/mL human brain-derived neurotrophic factor (PeproTech, Rock Hill, NJ, USA), and 20-ng/mL rat ciliary neurotrophic factor (PeproTech). After 7 days of in vitro neuron differentiation, cells were fixed with 4% paraformaldehyde for 20 minutes, washed three times with 1× PBS, and cryoprotected (30% glycerol, 25% ethylene glycol, and 0.1-M PBS) for further experiments.

In Vivo and In Vitro Arborization Studies

Image visualization was performed using a Zeiss LSM 880 confocal microscope. The mouse retina has more than 30 distinct ganglion cell subtypes, which can be distinguished by their morphological and functional features.[22,23] In vitro cultured mouse RGCs were recognized by their morphology and long axons after immunostaining for anti-beta III tubulin antibody (TUJ-1). For analysis of in vivo RGC morphology, YFP-positive RGCs from *Cerkl*[WT/WT]/*Thy1-YFP* and *Cerkl*[KD/KO]/*Thy1-YFP* mice were identified by the presence of an axon and the morphology of large-field RGCs.[22] For arborization quantification, confocal images were analyzed using ImageJ software, and dendritic arbors of ganglion cells were traced on projected z-stacks using a Fiji NeuronJ plugin.

Electroretinograms

Eight *Cerkl*[wt/wt] mice and eight *Cerkl*[KD/KO] mice were used for electroretinogram recordings. Dark-adapted animals were anesthetized with an intraperitoneal injection of Ketalar (ketamine, 95 mg/kg; Parke-Davis, Wellington, New Zealand) and Rompun (xylazine, 5 mg/kg; Bayer, Leverkusen, Germany) in saline solution (NaCl 0.9%). Pupils were dilated with 1% tropicamide (Alcon Cusí S.A., El Masnou, Barcelona, Spain). A Burian–Allen corneal electrode (Hansen Ophthalmic Development, Coralville, IA, USA) was used to record ERGs from the right eye. An electrode was placed 1 to 2 mm from the cornea, and a drop of 2% METHOCEL (methylcellulose; DuPont, Bomlitz, Germany) was placed between the cornea and the electrode to ensure electrical conductivity. Animal handling was performed under dim red light (>640 nm), and mice were maintained for >5 minutes in absolute darkness before recording. Mouse temperature was maintained at 37°C with a water heating pad. Full-field flash ERG was performed with a Ganzfeld dome. The intensity of light stimuli was measured with a Mavo-Monitor USB photometer (Gossen, Nürenberg, Germany) at the level of the eye. At each light intensity, four to six consecutive recordings were averaged. The interflash interval in scotopic conditions ranged from 3 seconds for

dim flashes up to 30 seconds for the highest intensity stimuli. Under photopic conditions, the interval between light flashes was fixed at 1 second. ERG signals were amplified and bands filtered between 0.3 and 1000 Hz with a CP511 AC amplifier (Grass Instruments, Quincy, MA, USA). Electrical signals were digitized at 2 kHz with Labchart Pro software and a PowerLab data acquisition device (AD Instruments, Chalgrove, UK). Bipolar recording was performed between the corneal electrode and a reference electrode located in the mouth, with a ground electrode located on the tail. The stimulation protocols were designed according to the International Society for Clinical Electrophysiology of Vision.[24] Rod-mediated responses were recorded under dark adaptation using light flashes of 0.01 cd·s/m^2. Mixed rod- and cone-mediated responses were recorded in response to light flashes of 3 cd·s/m^2. Cone-mediated responses were obtained for light flashes of 3 cd·s/m^2 on a rod-saturating background of 30 cd/m^2. Oscillatory potentials were isolated using white flashes of 3 cd·s/m^2 and band-pass filtered between 100 and 10,000 Hz. The amplitudes of the a-wave, b-waves, and OPs were measured offline,[24] and results were averaged in both animal groups. The amplitudes of the ERG-recorded traces were measured by an observer blind to the animal genotype. ERG parameters recorded from *Cerkl*$^{wt/wt}$ and *Cerkl*$^{KD/KO}$ animals of different ages were statistically analyzed by Student's *t*-test.

RESULTS

CRISPR/Cas9 Deletion of the *Cerkl* Locus

To produce the deletion of the whole *Cerkl* locus (97 Kb) and minimize potential off-target effects, the gene-editing strategy selected relied on the use of the Cas9 D10A nickase, which requires four guides (gRNAs), two per site (see Fig. 1A and Supplementary Fig. S1 for guide RNA positions and details). This deletion extended from the proximal promoter to exon 12 but did not affect exon 13, which is also transcribed in the opposite direction as part of the *Integrin-α4* 3′ untranslated region. The mRNA encoding the Cas9 D10A nickase and the four gRNAs were injected into zygotes. Mosaic pups were genotyped by PCR to identify those carrying gene-edited alleles. Nearly 50% of the microinjected mice were genetically modified at the target gene, at either the 5′ or 3′ gRNA target sites. Six out of 46 mice (13%) carried the expected 97-kb deletion (Fig. 1B), which confirmed that large deletions could be generated with the same frequency as moderate deletions (less than 1 kb) with the Cas9 nickase. The microinjection of Cas9 mRNA instead of an expression plasmid restricted the action to the first zygote divisions, so that the number of alleles per mosaic was very low (mainly one modified allele, rarely two, plus the wild-type). Specific primer pairs were designed to check both the deletion of the full locus and the gene edition at any of the two cleavage sites (Table). When the specific band for the deletion or gene modification was identified, gene editing was confirmed by Sanger sequencing of the PCR bands (Supplementary Fig. S2). Our results showed that guides at 5′ were much more successful than guides at 3′, suggesting preferences in the endonuclease action probably by sequence context, secondary structure, or closeness between the protospacer adjacent motif (PAM) sequences of the two guides. Each of the six *Cerkl*-deleted alleles showed different gene-edited sequences around the PAM sites (Supplementary Fig. S2). All of the mosaic animals carrying the full

Cerkl^{KO} allele were checked for off-target modifications (see Materials and Methods section) and/or chromosomal rearrangements in the *Cerkl* locus, but none was identified (data not shown).

Cerkl Complete Ablation Causes Embryonic/Perinatal Lethality

To generate the *Cerkl*$^{KO/KO}$ model, heterozygous mice were mated (in black and albino backgrounds). Unfortunately, after repeated attempts none of the live offspring mice was homozygous for the *Cerkl* deletion in any background. These unexpected results suggested that either the complete ablation of *Cerkl* expression or the deletion of nearly 100 kb of the *Cerkl* genomic locus was lethal. To test whether this lethality occurred during embryonic or perinatal stages, embryos (age E13–E18) from selected matings were genotyped. Only one out of 35 embryos was homozygous for the deletion, but no gross abnormalities could be observed in the *Cerkl*$^{KO/KO}$ embryo (Fig. 1C).

Because the full *Cerkl* knockout model was lethal, we resorted to generating a new animal model in which the expression of *Cerkl* was extremely reduced, the double heterozygote *Cerkl*$^{KD/KO}$. *Cerkl*$^{KD/KO}$ mice carry the KO allele in trans with the knockdown allele *Cerkl*^{KD} (generated previously[18]). Of note, the matings between *Cerkl*$^{KD/KO}$ double heterozygotes never produced a homozygote *Cerkl*$^{KO/KO}$ animal. Altogether, considering all the live mice (67) and embryos (35) obtained by these multiple crossings, only one E18 embryo out of 102 animals was a full knockout, which confirms the lethality of this CRISPR gene-edited allele in homozygosis (χ^2 test, $P < 0.0001$) (Fig. 1D). The work presented here relies on the *Cerkl*$^{KD/KO}$ mice as a model to study the retinal phenotype caused by *Cerkl* mutations.

Cerkl Expression in the *Cerkl*$^{KD/KO}$ Murine Retinas

The murine *Cerkl* gene maps at chromosome 2 between *NeuroD1*, which is transcribed in the same direction as *Cerkl*, and *Itga4*, which is transcribed in the opposite direction. The *Cerkl* locus is relatively large and may contain regulatory regions of the adjacent genes; therefore, *Cerkl* deletion might alter their expression. The expression of *Cerkl* and flanking genes was quantified in adult murine retinas *Cerkl*$^{KD/KO}$ (P60) by RT-qPCR and compared to other genotypes. On average, the expression levels of *Cerkl* in the retina were reduced to 71% in *Cerkl*$^{WT/KO}$, 42% in *Cerkl*$^{KD/KD}$ (as reported previously[18]), and 8.5% in *Cerkl*$^{KD/KO}$. This drastic decrease in *Cerkl* expression in our model was statistically significant in comparison to *Cerkl*$^{WT/WT}$ and any of the other genotypes (Fig. 1E), indicating that the double heterozygote could be used as a knockdown that barely expressed *Cerkl*. On the other hand, *Itga4* was apparently expressed at very similar levels in the different *Cerkl* genotypes (Fig. 1E). In contrast, *NeuroD1* expression was significantly reduced in *Cerkl*$^{KD/KO}$ retinas in comparison with those of *Cerkl*$^{WT/WT}$ ($P < 0.05$). *NeuroD1* expression was lower in all the genotypes that carried one allele with the full deletion of *Cerkl* in heterozygosis (Fig. 1E) and was highly correlated with that of *Cerkl* in the different genotypes (Fig. 1F). These results may reflect the fact that *Cerkl* and *NeuroD1* share the same promoter (the *NeuroD1* promoter is an alternative promoter of *Cerkl*), but they may also indicate that the *Cerkl* locus contains regulatory sequences of *NeuroD1*.

CERKL Isoforms Are Differentially Expressed in the Murine Retina

Cerkl shows a high transcriptional complexity, having more than 20 transcripts and more than a dozen protein isoforms due to alternative splicing and the use of at least three different alternative promoters.[16] To detect different CERKL isoforms, several in-house antibodies were generated against the mouse protein, and domains were selected that were not highly conserved between human and mouse sequences; anti-CERKL5 recognizes a peptide encoded in exon 5, whereas anti-CERKL2 recognizes a peptide encoded in exon 2. The specificity of the antibodies was tested against proteins encoded by CERKL constructs bearing deletions of the target peptide region of each antibody, and they showed specificity for the mouse but not the human CERKL protein (Fig. 2A). The antibodies were also tested using different mouse tissues, but the number and size of protein isoforms recognized by each antibody were difficult to assess due to the high number of protein isoforms produced by *Cerkl* (Fig. 2A).

These antibodies were used for immunohistochemistry on retinal cryosections to observe the spatial pattern of CERKL in the retina. CERKL expression was detected in the ganglion cell, inner nuclear, and photoreceptor layers. Interestingly, when using anti-CERKL5, rods appeared more intensely labeled in contrast to the pattern detected with anti-CERKL2, which primarily labeled cones and their nuclei (Fig. 2B). These results indicate that different protein isoforms could be detected with antibodies against different domains. Using high-resolution confocal microscopy and focusing exclusively on the photoreceptor layer, we observed that the antibodies did not exclusively label rods or cones, but rather they recognized protein isoforms preferentially expressed in rods (anti-CERKL5) or cones (anti-CERKL2) (Fig. 2C, upper panel). These results indicate that distinct alternatively spliced isoforms carrying different protein domains are enriched in specific photoreceptor cell types. The specificity of these antibodies was validated on retinal cryosections of our *Cerkl*[KD/KO] model, in which we barely detected CERKL expression, thus confirming the results of transcript analysis (Fig. 2C, lower panel). CERKL was also highly expressed in the RPE, as detected by immunodetection with the two antibodies (Supplementary Fig. S3).

Cerkl[KD/KO] Retinas Show Photoreceptor Cell Layer Alterations with a Decreased Number of Cones

We hypothesized that the low expression of *Cerkl* in our mouse model might mimic the effect of *CERKL* mutations in human patients. In humans, mutations in *CERKL* cause both RP and CRD, and the phenotypic traits are usually reported in late teens or young adults. Therefore, we surmised that the age of around 1 year was an appropriate time frame to detect retinal alterations solely due to the depletion in *Cerkl* expression and before age-related neurodegeneration might blur the genetic effect.

As a first approach, a comparative morphometric analysis of retinal morphology and layer structure between retinas from *Cerkl*[KD/KO] and *Cerkl*[WT/WT] mice was performed (Fig. 3). Regional differences in retinal thickness were clearly observed in the *Cerkl*[KD/KO] retinas, which displayed a wavy outer nuclear layer, with zones with fewer nuclei and others with an increased number of nuclei compared to the wild-type counterparts (Fig. 3A, zoom magnification). Consis-

tent observations showed that, in the whole retina, half of them seemed thicker (with enlargement of the inner nuclear and plexiform layers) and the other half of them appeared thinner in the *Cerkl*[KD/KO] retinas (Fig. 3B, upper left panel). The most relevant observation was the consistent and significant decrease in the number of nuclei rows in the outer nuclear layer of the *Cerkl*[KD/KO] mice detected on both sides of the retina. Notably, the number of photoreceptor nuclei rows was statistically significantly decreased along the whole retina of the *Cerkl*[KD/KO], which is a hallmark of severe retinal degeneration (Fig. 3B, upper right panel). The *Cerkl*[KD/KO] mice retina in comparison with the *Cerkl*[WT/WT] exhibited irregular thickness along the retina, severe layer organization defects, and a decreased number of photoreceptor nuclei.

These results prompted us to determine whether rods or cones were most affected in the *Cerkl*[KD/KO] mouse model. To study whether the decrease in the number of nuclei was progressive, the retinas of young mice (2 months old) and older mice ($\geq$11 months old) were compared. The attrition of cone photoreceptors was evaluated by whole mounts of retinas stained with PNA to visualize and quantify the number of cones (see Fig. 4 and Supplementary Fig. S4). The number of cones in old *Cerkl*[KD/KO] mice (11–18 months of age, or $\geq$11 months old) was notably diminished in comparison to *Cerkl*[WT/WT] (Fig. 4). This decrease in the number of cones is statistically significant, and it was also detected in younger mice (2 months) when the values obtained within each genotype are more robust and compact. With age, the number of cones was more variable in both genotypes, but, as mentioned, the decrease was more apparent in the *Cerkl*[KD/KO] retinas. Therefore, the depletion of *Cerkl* expression caused an early-onset decrease in the number of cones, as detected in both young and old animals.

Of note, and as an external ocular phenotype, the lens of old but not of young animals presented non-uniform calcified cataracts, which were not present in the wild-type animals (Supplementary Fig. S5). Although it does not occur often, some human patients bearing *CERKL* mutations have been reported to develop posterior subcapsular cataracts, very similar to those observed in our model.[25,26]

Alteration of Rod and Cone Photoreceptor Outer Segments in *Cerkl*[KD/KO] Retinas

We next focused on the photoreceptor morphology and structure by performing immunohistochemistry on retinal cryosections from the *Cerkl*[KD/KO] model in young mice (2 months old) and older mice (11–18 months old). The dorsal and ventral regions in retinal cryosections can be distinguished because in the C57BL/6J strain the distribution of short-wavelength-sensitive opsin (S-opsin) and medium-/long-wavelength-sensitive opsin (M-/L-opsin) cones are distributed in opposing gradients, as S-opsin cones are more concentrated in the ventral region and M-/L-opsin cones are more concentrated in the dorsal retina[27,28] (blue and red gradient lines in the scheme at the top of Fig. 5 indicate the opposing gradient of M-/L- and S-opsin cones, respectively).

After immunodetection of rods (rhodopsin) and cones (S-opsin, M-opsin, and PNA, which stains all cone types), *Cerkl*[KD/KO] retinas showed statistically significant longer rod outer segments (OSs) and cone sheaths along the dorsal retina of the retina, doubling the length of those in
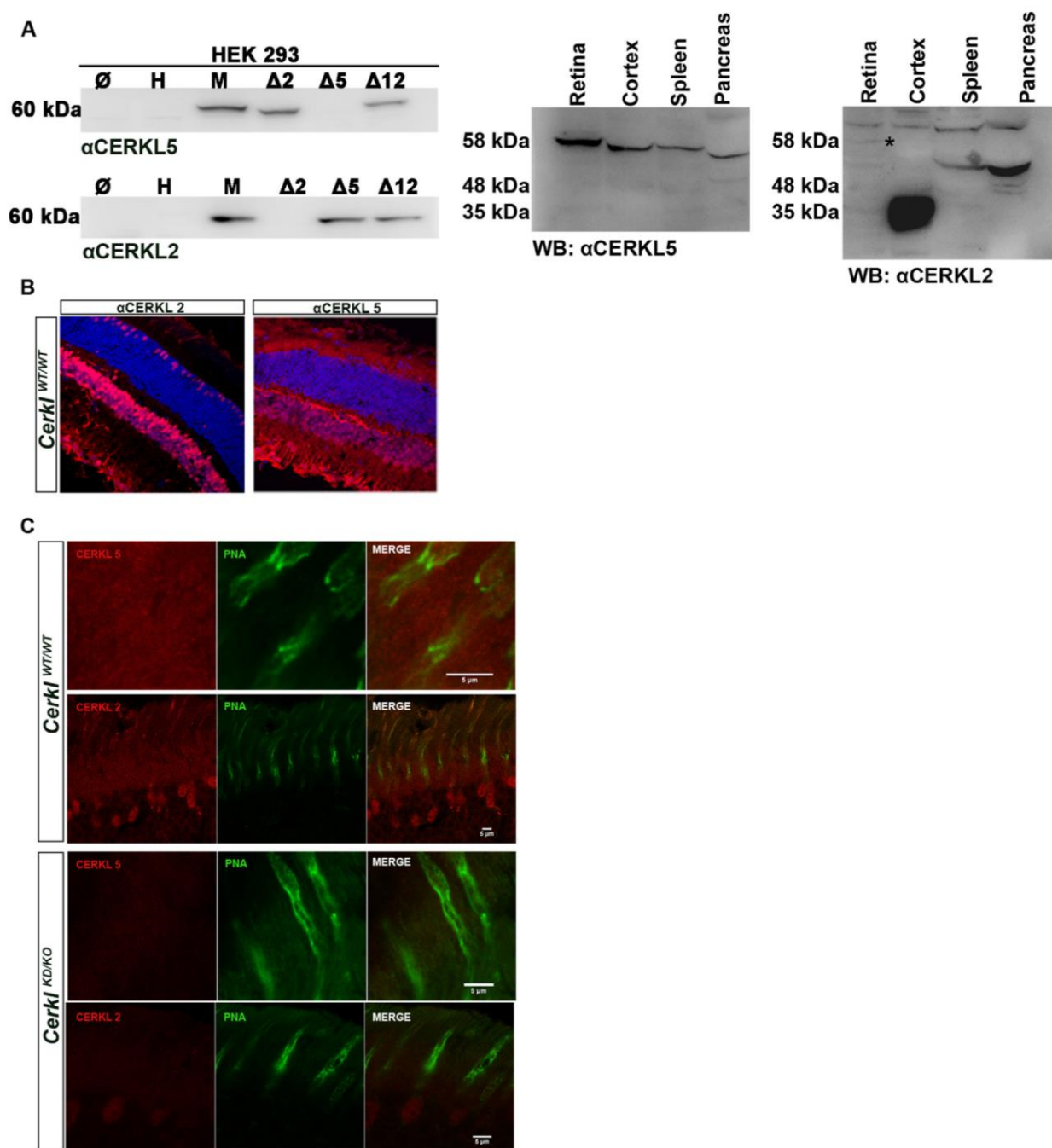
Figure 2. CERKL immunolocalization in murine retina sections. (**A**) Western blot of HEK293 cells transfected with different *Cerkl* constructs bearing specific peptide deletions generated to test the specificity of the rabbit polyclonal antibodies generated in-house against two different peptides, one encoded in exon 2 (αCERKL2) and another encoded in exon 5 (αCERKL5). These exons are differentially spliced or expressed in CERKL transcript isoforms.[16] The antibodies are specific for the murine CERKL protein (M) and do not recognize the human CERKL (H). The antibodies were also tested in different mouse tissues and detected bands of different sizes and intensities due to isoforms produced by multiple alternative splicing and alternative promoters. (**B**) CERKL isoforms are differentially expressed throughout retinal layers, as detected by αCERKL2 and/or αCERKL5. αCERKL2 detects isoforms that are mainly expressed in the nuclei of cones, inner nuclear layer (INL), and ganglion cell layer (GCL), whereas αCERKL5 detects isoforms highly expressed in rods, the outer plexiform layer (OPL), the INL, the plexiform layer (IPL), and the GCL. (**C**) High-resolution confocal microscopy confirmed the distribution of this preferential CERKL isoform in photoreceptors, as the isoforms detected by αCERKL2 were preferentially detected in cones (nuclei, inner and outer segments) and more weakly in rods, in contrast to the isoforms detected by αCERKL5, which are highly expressed in the inner and outer photoreceptor segments (both rods and cones) but undetectable in photoreceptor nuclei. Immunodetection of CERKL in the *Cerkl*[KD/KO] mice retinas was strongly decreased, as expected by the low remaining levels of CERKL expression (below 20% of the *Cerkl*[WT/WT] controls). CERKL is shown in *red*, peanut agglutinin (PNA) is shown in *green*; and nuclei counterstained with DAPI are shown in *blue*. All of the animals were C57BL/6J.
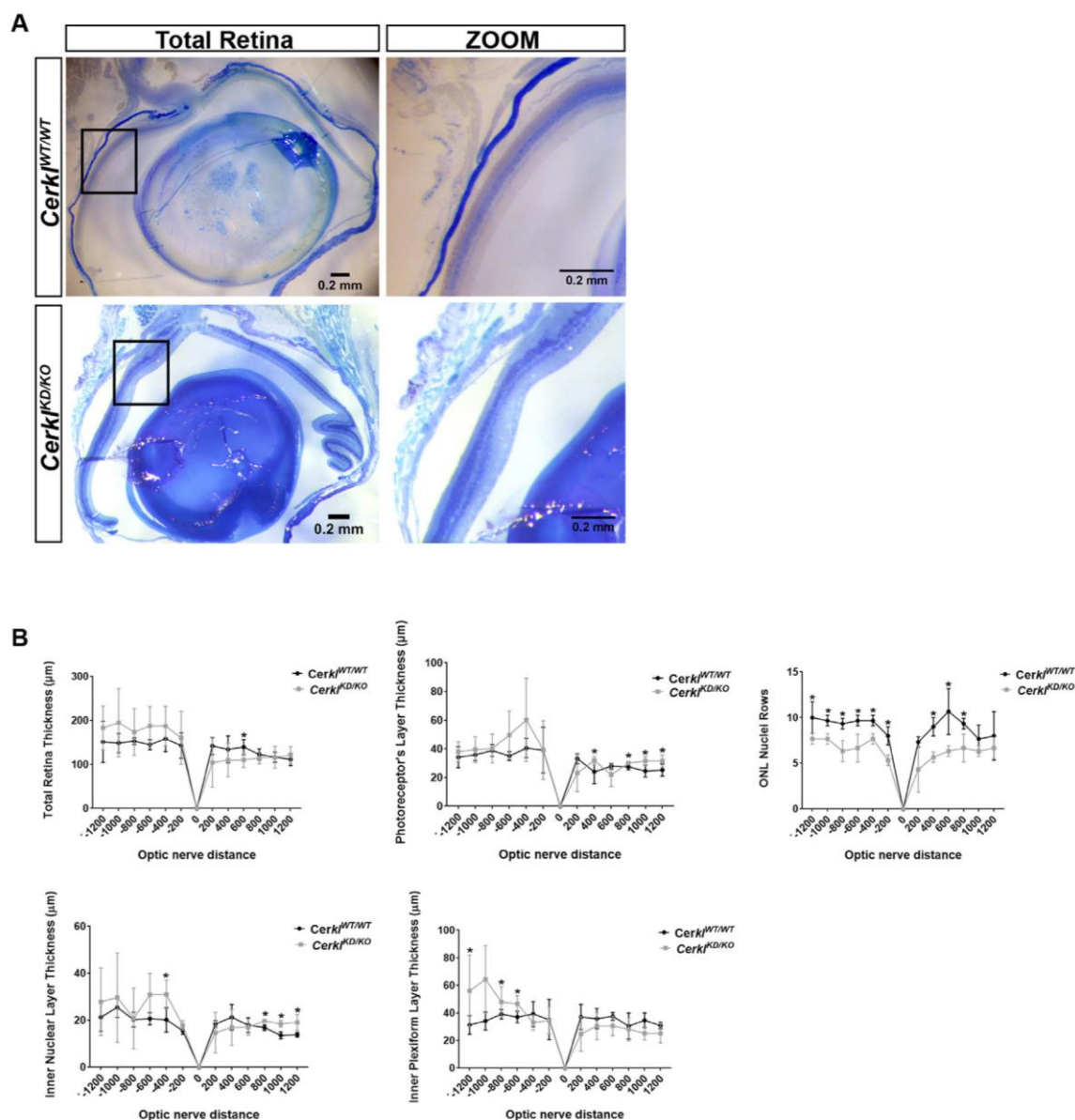
Figure 3. Retinal morphometric measures of *Cerkl*^{KD/KO} and *Cerkl*^{WT/WT} mice. (**A**) Stereo microscope representative images of *Cerkl*^{KD/KO} and *Cerkl*^{WT/WT} mouse retinas (semi-thin sections of epoxy-embedded eyes of 1-year-old mice) used for morphometry ($n = 3$ per group). (**B**) The thickness of each retinal layer along the retina was measured at every 200 μm from the optic nerve, which was set up as point 0. Differences in retinal layer thickness were detectable in *Cerkl*^{KD/KO} retinas compared to controls. Statistically significant differences are indicated with asterisks (*$P < 0.05$, Mann–Whitney test). *Scale bar*: 200 nm (*black*). Control and mutant animals were from an albino B6(Cg)-Tyrc-2J/J strain background.

Cerkl^{WT/WT} ([Figs. 5](#)A, [5](#)B; black bars at the side, 2-month-old mice). Also, in these regions, S-opsin and M-opsin proteins are detected up to the middle of the cone sheath compared to what is observed in the *Cerkl*^{WT/WT} retinas ([Fig. 5](#), quantification panels at the right). In contrast, the length of rod OSs and cone sheaths and the distribution of cone opsins gradually return to values similar to those of controls in the S cone-rich ventral retina ([Fig. 5](#)C). These results were also consistent in aged retinas (data not shown).

A trait of retinal neurodegeneration is retinal gliosis, which indicates a glial response to retinal dysfunction. Glial fibrillary acidic protein (GFAP) is considered a macroglia marker. The *Cerkl*^{KD/KO} retinas showed a marked and statis-

tical increase in GFAP expression, thus indicating reactive gliosis due to retinal stress ([Figs. 5](#)D, [5](#)E).

Stacking Defects of the Photoreceptor Membraneous Disks in the *Cerkl*^{KD/KO}

The ultrastructural alterations of the photoreceptor layer in this model were analyzed by transmission electron microscopy in old animals ([Fig. 6](#)). In wild-type retinas, photoreceptor OSs were ordered in parallel and packed with closely stacked membraneous disks (where photoreception and phototransduction occur). However, *Cerkl*^{KD/KO} photore-

A

B
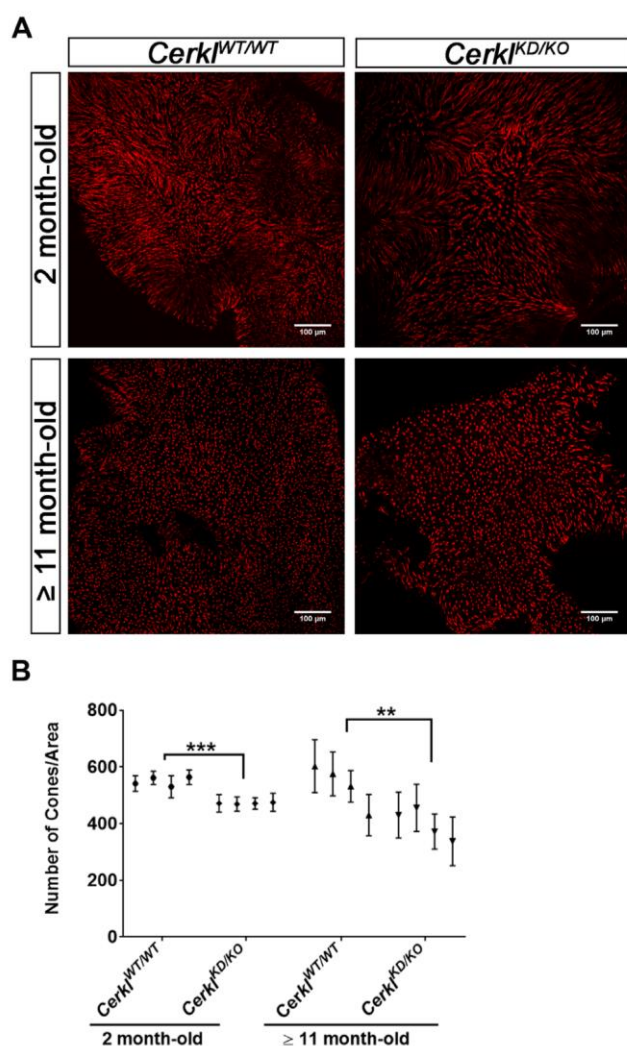
Figure 4. Cone count in whole mount retinas. (**A**) Murine retinas of *Cerkl*[WT/WT] and *Cerkl*[KD/KO] mice ($n = 4$) at 2 months and ≥ 11 months of age were flattened, fixed, and stained with PNA conjugated to Alexa Fluor 647 (*red*). The number of cones was counted by positioning three regions of interest (ROIs; area 164.79 μm^2) in different parts of the image and summing the cones of each ROI. For each retina we analyzed 10 to 12 images in order to cover the whole retina. (**B**) Statistical significance showed differences among genotypes by two-way ANOVA test ($^{**}P < 0.01$, $^{***}P < 0.001$). *Scale bar*: 100 μm (*white*). All of the animals were C57BL/6J.

ceptors displayed disordered and loosely stacked disks, and the OSs appear disarrayed (Figs. 6A, 6B; additional images in Supplementary Fig. S6). Quantification of photoreceptor OS length confirmed that the *Cerkl*[KD/KO] photoreceptors were significantly longer than those of the controls (Fig. 6A, right panel), in agreement with what we observed in the confocal IHC images (Fig. 5). Moreover, photoreceptor OSs in *Cerkl*[KD/KO] showed double membrane vesicles (indicated with a V in Fig. 6C) that disrupted the stacking of disks.

By increasing the magnification, were also able to study the RPE morphology. RPE performs the daily shedding of the photoreceptor OS tips by phagocytosis. A possible explanation for the extreme length of photoreceptor OSs observed in *Cerkl*[KD/KO] retinas could be alteration of RPE phagocyto-

sis. This hypothesis is in agreement with the highly disorganized microvilli observed in this model compared to control retinas (indicated with an M in Fig. 6B). In this context, it is worth remarking that *Cerkl* was highly expressed in the RPE (Supplementary Fig. S3). We observed that microvilli from control retinas surrounded the tip of photoreceptor OSs, whereas *Cerkl*[KD/KO] microvilli were disarrayed and did not wrap the OS tips, thus pointing to defective phagocytosis. Within the RPE cell, trafficking of the phagosome vesicles until fusion with lysosomes was observed. Early and late phagosome vesicles could be distinguished from lysosomes by the density and color of the captured material. We performed TEM imaging in albino strains, the RPE of which does not have pigment in the melanosomes, and studied the number and distribution of apical and basal phagosomes/endosomes, as well as lysosomes in old mouse RPEs (Fig. 6D). Although the number of total phagosomes did not differ significantly between *Cerkl*[KD/KO] and control retinas of the same age (Fig. 6E, left), their distribution was altered, and the number of basal endosomes was statistically significantly increased in the *Cerkl*[KD/KO] model Fig. 6E, right). The total number of lysosomes is also altered between the two groups of animals and increases close to twofold in the RPE *Cerkl*[KD/KO] (Fig. 6F).

In summary, *Cerkl*[KD/KO] mouse retinas showed (1) disarrayed photoreceptor segments, with disorganized and loosely stacked disks; (2) defects in retinal pigment epithelium microvilli; (3) round vesicles within photoreceptor OSs; and (4) increased numbers of basal phagosomes/endosomes and total lysosomes in the RPE compared to *Cerkl*[WT/WT], all of which are highly indicative of retinal dysfunction and vision impairment.

In Vitro and In Vivo Studies of Neurite Arborization in *Cerkl*[KD/KO] in RGCs

In the previous knockdown *Cerkl*[KDKD] mouse model, the retina showed no clear phenotype except for mild, although consistent and statistically significant, electrophysiological alterations in the OPs of RGCs. Because the double heterozygote *Cerkl*[KD/KO] shows a lower level of *Cerkl* expression (less than 10% compared to controls), RGCs might be even more affected at the morphological and functional levels. To analyze the RGC population phenotypic traits, we dissected retinas and cultured primary RGCs (P0, P1) for longer than 1 week *in vitro*. After 1 week, the ganglion cells spread neurites, dendrites, and axon, which could be distinguished and analyzed (Fig. 7A). Notably, the axons of the *Cerkl*[KD/KO] RGCs were shorter than those of control RGCs (Fig. 7B). Also, the total number of neurites was statistically significantly higher (Fig. 7C), but the average length appeared to be shorter (Fig. 7D). In fact, the number of primary neurites increased, although their length was not different (Fig. 7E). In summary, *in vitro* RGC primary cultures of *Cerkl*[KD/KO] showed differences in the arborization response and displayed shorter axons and increased numbers of neurites, although the length of the dendritic projections remained unaltered.

For the *in vivo* analysis of RGC arborization, we used a Thy1-YFP-H transgenic line in which the YFP transgene is controlled by the Thy-1 promoter and expressed in a small fraction of RGCs.[20] We analyzed the dendritic morphology of large field ganglion cells (see Materials and Methods section) in flat whole-mount retinas from *Cerkl*[KD/KO]/*Thy1-YFP* adult
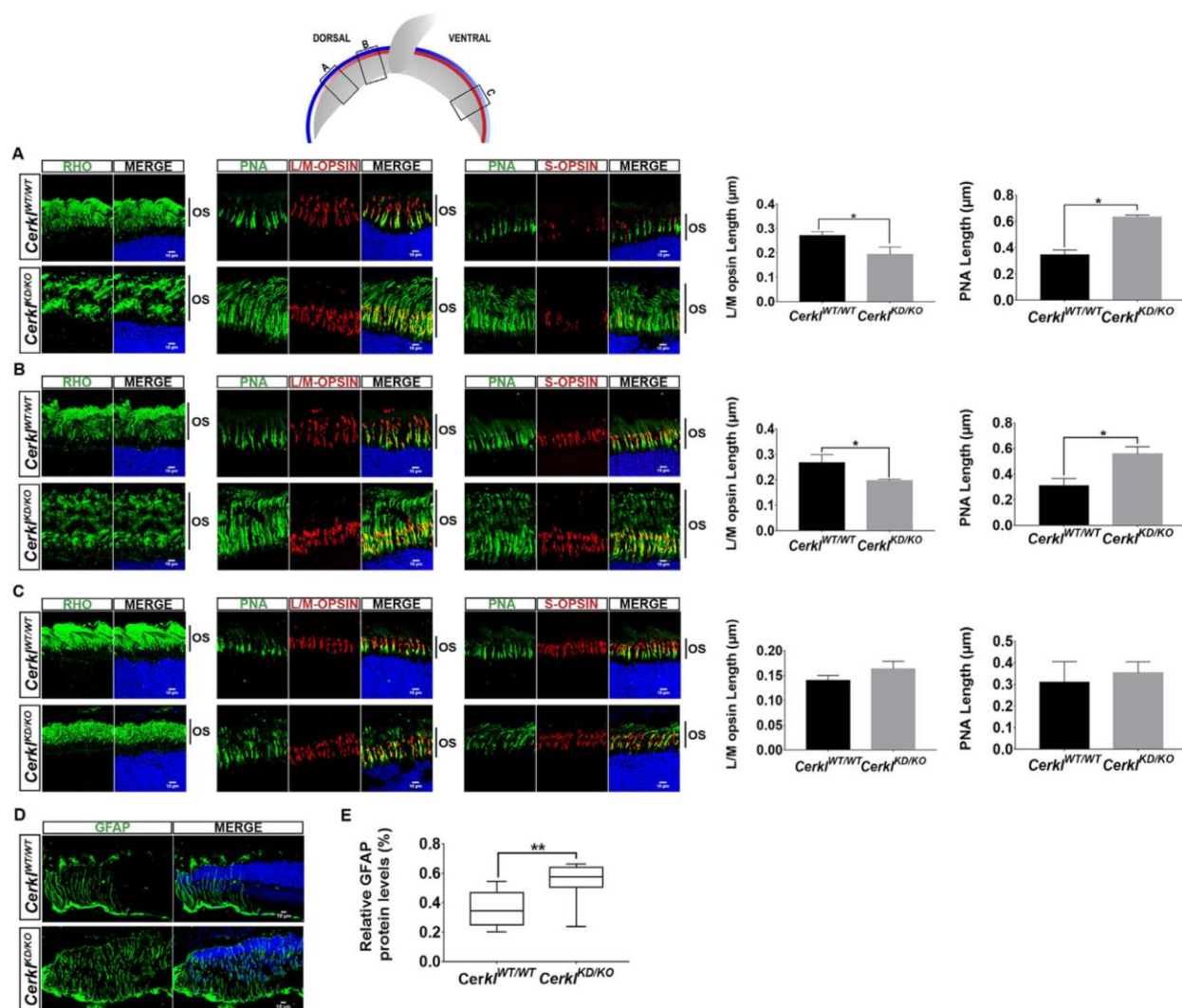
FIGURE 5. Alteration of photoreceptor OS length in *Cerkl*$^{KD/KO}$ mice. The scheme at the top shows the position of the images in the dorsal and ventral retina. The M-/L-opsin (*blue line*) and S-opsin (*red line*) cones were distributed in an opposing gradient. (**A–C**) Immunodetection of rhodopsin (*green*), M-/L-opsin, and S-opsin (each in *red*) in retinal cryosections at the optic nerve level of *Cerkl*$^{KD/KO}$ versus the *Cerkl*$^{WT/WT}$ mouse retinas showed a notable enlargement of the photoreceptor layer due to elongation of the rod OSs and cone sheaths (stained by PNA), as indicated by vertical bars. This OS elongation in *Cerkl*$^{KD/KO}$ mice showed a consistent gradient distribution along the retina, being much more prominent at different locations of the dorsal retina (low number of S-opsin cones and high number of M-opsin cones) as shown in **A** and **B**, slowly decreasing to normal OS length in the ventral retina (higher number of S-opsin cones and lower number of M-cones) in **C**. Images are representative of three different animals (2 months old). Quantification of cone sheath length (PNA) and M-/L-opsin localization in regions **A** and **B** show an elongation of the sheath and a shorter opsin-functional outer segment in *Cerkl*$^{KD/KO}$ compared to *Cerkl*$^{WT/WT}$, suggesting opsin mislocalization in dorsal but not in ventral retina (*$P < 0.05$, Mann–Whitney test). (**D**) Increased levels of GFAP (in *green*) were detected in retinal cryosections comparing *Cerkl*$^{WT/WT}$ and *Cerkl*$^{KD/KO}$ mice and are indicative of macrogliosis. (**E**) The GFAP increase in the *Cerkl*$^{KD/KO}$ mouse retinas compared to *Cerkl*$^{WT/WT}$ was quantified by western immunodetection and showed statistical significance ($n = 8$ per group; $P < 0.01$, Student's *t*-test). In all images, nuclei are counterstained with DAPI (in *blue*). *Scale bar*: 10 μm (*white*). All of the animals were C57BL/6J.

mice compared to *Cerkl*$^{WT/WT}$/*Thy1-YFP* controls (Fig. 7G). The area of the dendritic field was determined as the area of a polygon obtained by joining the distal dendritic extremities. RGC dendrites were traced to determine the total dendritic length and the number of primary dendrites. In contrast to the *in vitro* results, no clear mophological differences were apparent between RGCs from *Cerkl*$^{WT/WT}$/*Thy1-YFP* or *Cerkl*$^{KD/KO}$/*Thy1-YFP* retinas, not in total dendrite length, dendritic field area, or number of primary dendrites (Figs. 7H–7J), pointing to a differential response to the stress of dissection and culture more than to an intrinsic trait.

Retinal Electrophysiology of the *Cerkl*$^{KD/KO}$ Mice

In the previous knockdown *Cerkl*$^{KD/KD}$ mouse model, neither ERGs nor retinal morphology showed any clear retinal neurodegeneration phenotype, except for alterations in the OPs. This phenotype remained consistent and was not
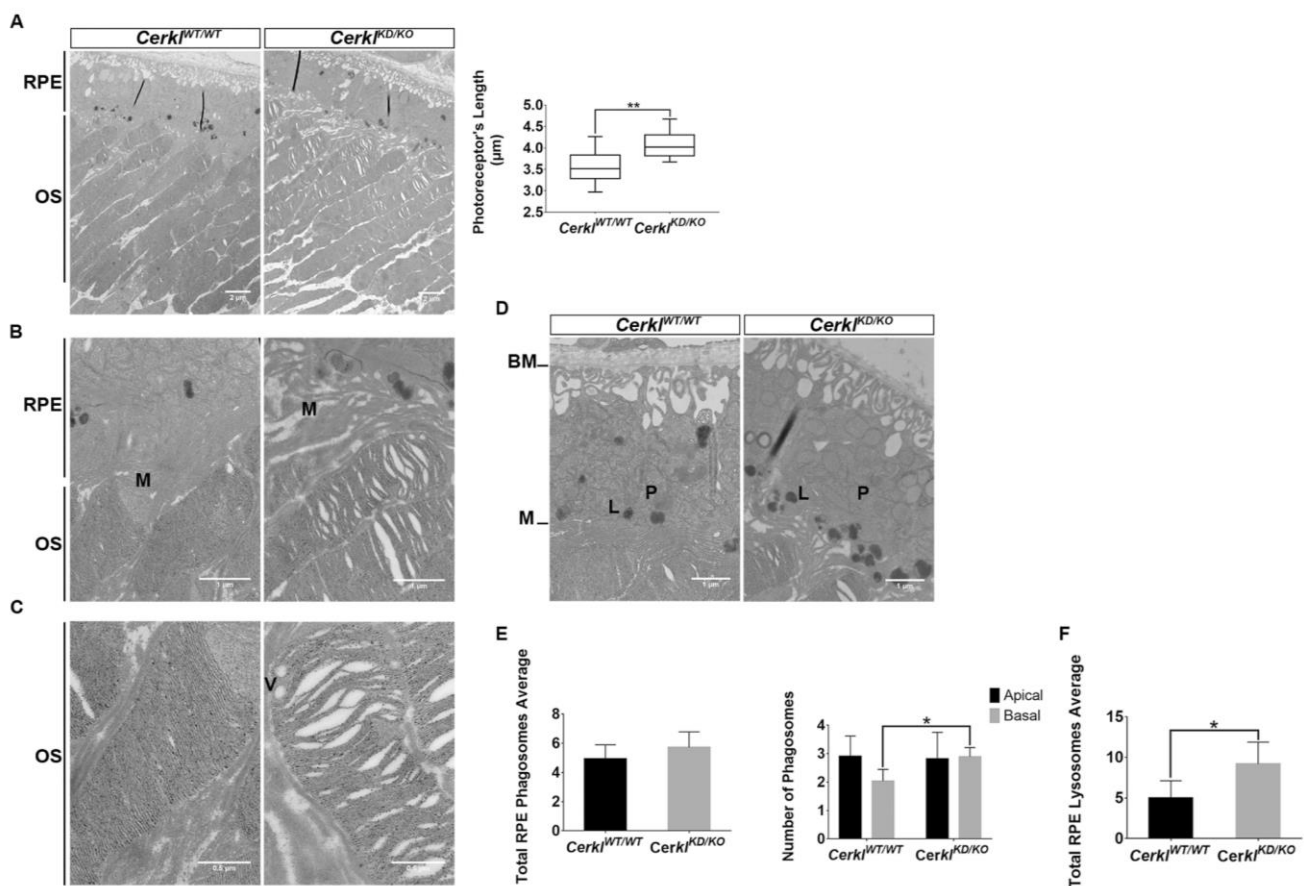
FIGURE 6. *Cerkl*[KD/KO] retinas showed defects in the photoreceptor outer segments and alterations in RPE-mediated phagocytosis. Retinas of *Cerkl*[KD/KO] compared to *Cerkl*[WT/WT] mice (all albino B6(Cg)-Tyrc-2J/J mice) showed clear defects on photoreceptor OSs as revealed by TEM at increasing magnifications (5000×, 20000×, and 40000×): (**A**) The membraneous disks of *Cerkl*[KD/KO] photoreceptor OSs were loosely stacked and showed vacuoles in between disks compared to the compact disk staking in control retinas. Quantification of the photoreceptor OS length showed significantly longer OSs in *Cerkl*[KD/KO] photoreceptors compared to those of *Cerkl*[WT/WT] mice ($^{**}P < 0.01$, Student's *t*-test), with three measures per animal ($n = 3$) per genotype. (**B**) Microvilli (indicated by M) from *Cerkl*[KD/KO] mice RPE appeared disorganized instead of closely wrapped around the photoreceptor tips as observed in *Cerkl*[WTWT] RPE. (**C**) High magnification of the photoreceptor OS tips focusing on the disk disorganization in *Cerkl*[KD/KO] compared to *Cerkl*[WTWT]. Double membrane vesicles (V) disrupt the membrane disk stacking in *Cerkl*[KD/KO] OSs. *Scale bars*: 2 µm, 1 µm, and 0.5 µm, respectively. TEM high magnification of *Cerkl*[KD/KO] and *Cerkl*[WTWT] retinas was performed to analyze the number and distribution of phagosomes and lysosomes within RPE cells: (**D**) Representative RPE images of *Cerkl*[KD/KO] and *Cerkl*[WTWT] for analyzing phagosomes (P) and lysosomes (L). Microvilli (M) formed at the apical region, whereas Bruch's membrane (BM) indicates the basal region. (**E**) The total number of phagosome/endosome vesicles did not differ significantly (*left*), but a higher number of vesicles was observed in the RPE basal versus apical region in *Cerkl*[KD/KO] compared to controls (*right*). (**F**) The total number of lysosomes also increased in the RPE cells of *Cerkl*[KD/KO] ($^*P < 0.05$, Mann–Whitney test). There were 15 representative images per retina and three animals per group. *Scale bar*: 1 µm. All animals were from an albino B6(Cg)-Tyrc-2J/J mice strain.

progressive with age. We surmised that this new model, with a lower expression of *Cerkl*, might show some retinal neurodegeneration detectable by ERGs. In young-adult mice (6–10 months old), we did not observe significant changes in any of the ERG measurements in comparison with wild-type animals (Fig. 8A). Because RP in humans is characterized by the progressive loss of photoreceptors, we deemed it reasonable to study the same cohort of animals (the two groups of animals) at older ages. Retinal degeneration is clearly observed in 18-month-old *Cerkl*[KD/KO] mice compared to *Cerkl*[WT/WT] mice (Fig. 8B). Rod (b-scot) and cone (b-phot) activity was statistically significant diminished, particularly in cones. These alterations were also reflected in postsynaptic photoreceptor activity (b-mix). In agreement with the previous mouse model, the OP responses, mostly contributed by the electrical activity of RGCs and amacrine cells, were the recordings affected most. Taking the morphometric and retinal morphology studies together with the ERGs, the *Cerkl*[KD/KO] retinas showed clear phenotypic structural alterations from a young age, but the electrophysiological response was not affected initially. However, with time, the abrogation of *Cerkl* expression caused progressive retinal dysfunction and vision impairment, similar to what occurs in humans carrying mutations in the *CERKL* gene.

DISCUSSION

Previous attempts to generate animal models to unveil *CERKL* physiological function have been hampered by the high transcriptional complexity of *CERKL*.[16–19] Our first mouse model retained the expression of several *Cerkl* isoforms (40% of *Cerkl* expression) and did not show any
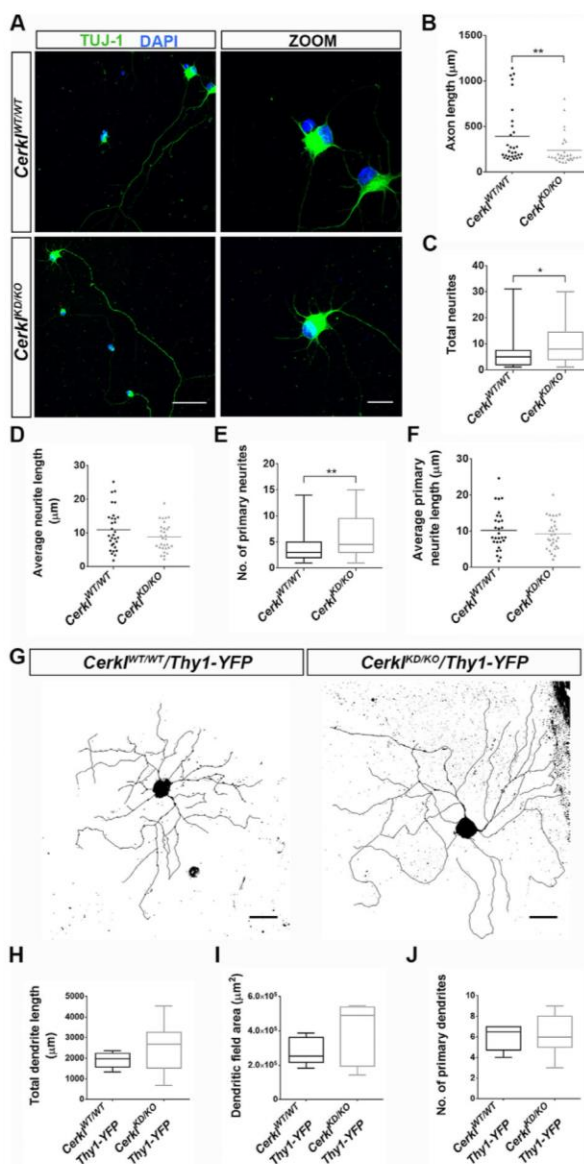
FIGURE 7. Differences in neurite arborization between *Cerkl*[KD/KO] and *Cerkl*[WT/WT] RGCs. In vitro RGC neurite arborization after 1 week of primary cell culture of P0 retinas. (**A**) Representative confocal images of primary RGCs from *Cerkl*[WTWT] and *Cerkl*[KD/KO] mice. TUJ-1-labeled neuronal cells (*green*) and nuclei were counterstained with DAPI (*blue*). *Scale bars*: 50 µm; 15 µm in high-magnification micrographs. (**B**) Axon length quantification showed that axons were significantly shorter in *Cerkl*[KD/KO] RGCs compared to those in *Cerkl*[WT/WT]. Analysis of total RGC neurites showed that, although the total number was slightly higher in *Cerkl*[KD/KO] compared to *Cerkl*[WT/WT] mice (**C**), their average length was very similar between the two genotypes (**D**). Analysis of primary RGC neurites pointed to slight significant differences in the number (**E**) but not in their average length (**F**) between genotypes. Results are presented as mean ± SEM (n = total of 30 neurons from 4–6 animals per group). In vivo RGC neurite arborization: (**G**) Dendritic arborization of retinal ganglion cells in vivo in *Cerkl*[WT/WT]/Thy1-YFP and *Cerkl*[KD/KO]/Thy1-YFP transgenic mice. Projected z-stacks of YFP-labeled large-field ganglion cells in *Cerkl*[WT/WT]/Thy1-YFP and *Cerkl*[KD/KO]/Thy1-YFP adult mice. *Scale bar*: 100 µm. No significant differences were found between genotypes when measuring in vivo total dendritic length (**H**), dendritic field area (**I**), or number of primary dendrites (**J**). Results are presented as mean ± SEM (n = 6–7 neurons from 3–5 animals). Statistical analyses were performed by either Student's *t*-test (**C–F**) or Mann–Whitney test (**B, H–J**), depending on whether or not they adjusted to normality ($^*P \leq 0.05$, $^{**}P \leq 0.01$).

severe retinal disorder except for a mild RGC alteration.[18] *CERKL* is one of the most prevalent genes in the Spanish cohort of patients affected with autosomal recessive RP or CRD (5% prevalence).[26] Because no other mouse model of retinal degeneration was available for this gene, we generated a novel *Cerkl* knockout mouse model by CRISPR/Cas9 gene editing. Unfortunately, the complete ablation of *Cerkl* is not viable in homozygosis; therefore, we generated the double heterozygote *Cerkl*[KD/KO], which retains less than 10% of *Cerkl* expression and thus provides a valuable model of slow retinal degeneration (physiological alterations are observed in mice at 18 months of age but not at 6–10 months), which mimics the relatively late-onset (second decade of life) but progressive degenerative disease observed in most patients bearing *CERKL* mutations.

The lethality of complete *Cerkl* ablation could be explained either by CERKL function being directly required for organism viability or by the presence of relevant regulatory elements for nearby genes embedded in the *Cerkl* locus. *Cerk* is rather ubiquitously expressed, including many vital organs,[4,16] so lethality due to full *Cerkl* abrogation cannot be discarded. On the other hand, several *cis*-regulatory elements (enhancer sequences) have been functionally described within the *CERKL* locus in human cell lines (descriptions available at https://www.genecards.org/ and https://genome.ucsc.edu/) and appear to be physically associated with both *CERKL* and the upstream *NEUROD1* gene promoters. The evolutionary conservation of these super-enhancers in vertebrate genomes supports their functional relevance. *NeuroD1* is a neural and pancreatic transcription factor implicated in cell-cycle regulation, retinal cell genesis, and neuronal development,[29,30] and *NeuroD1* null mice die within a few days after birth due to severe diabetes.[31] Because we have observed that the deletion of *Cerkl* significantly decreases the expression of *NeuroD1*, a plausible explanation for the lethality caused by the homozygous *Cerkl* deletion may be caused by both the direct loss of *Cerkl* expression in vital organs, such as liver or lungs, and the very low expression of *NeuroD1* caused by the deletion of its enhancers. Further evidence should be gathered to understand the causes of the lethality associated with *Cerkl* locus deletion. It is worth noting that the most common *CERKL* mutation in humans (found in homozygosis and most often in double heterozygosis with other rarer mutations), c.847C>T (p.R283*),[4] is not a complete null allele, as the mutation introduces a stop codon in exon 5, an exon that is included in some but not all isoforms due to alternative splicing.[16]

The high transcriptional complexity of *Cerkl* in the retina suggested preferential isoform expression in different neuron cell types. This is why we generated in-house antibodies, CERKL2 and CERKL5, against peptides encoded in different exons that recognize a different subset of CERKL isoforms. Immunohistochemistry of mouse retinal cryosections and high-resolution microscopy showed that isoforms containing exon 2 were preferentially expressed in cones, whereas those containing exon 5 were expressed more in rods, thus supporting the suggestion that different CERKL isoforms are preferentially expressed in rods versus cones and also lending credence to a differential func-
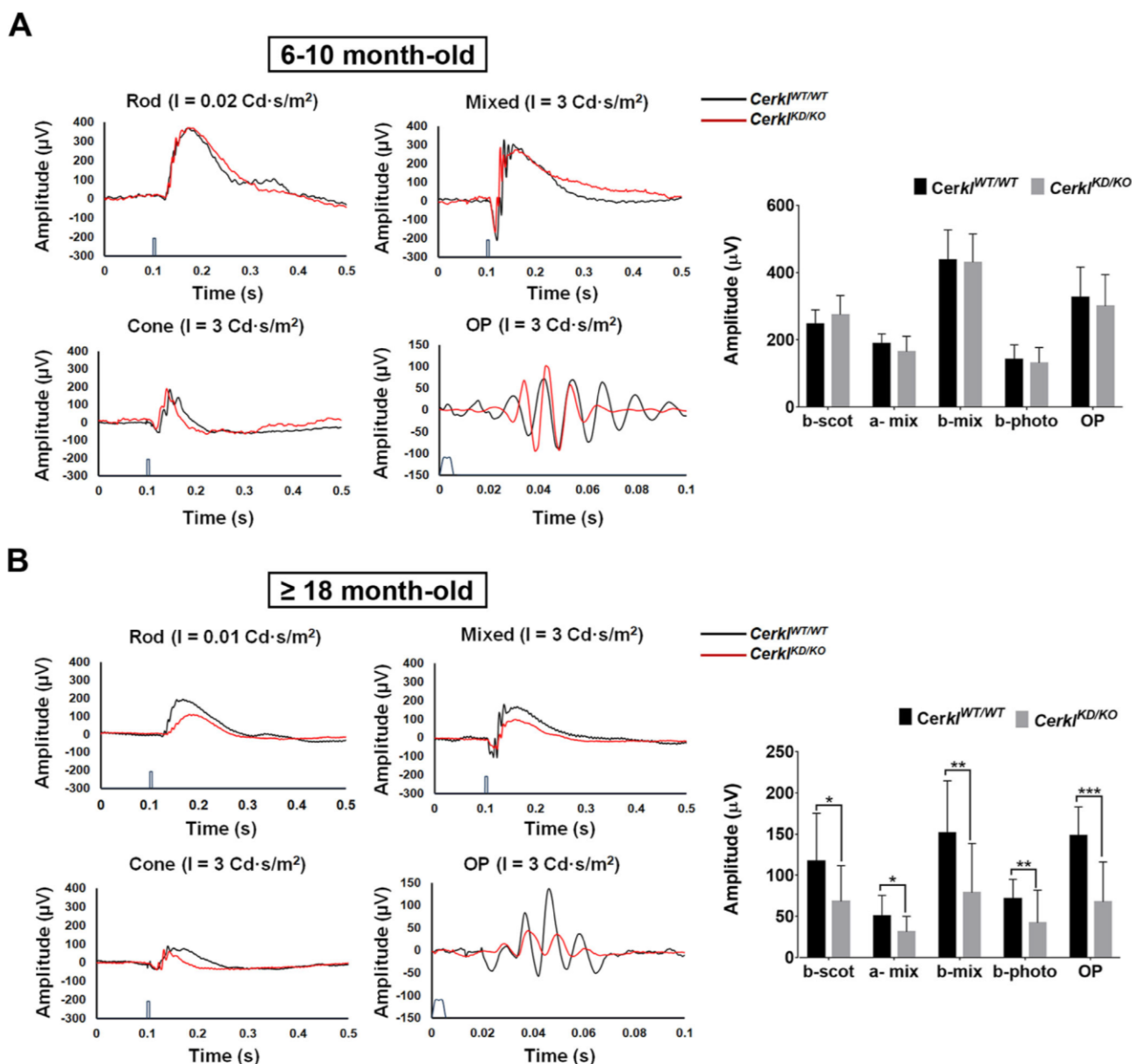
FIGURE 8. Electrophysiological recordings) of *Cerkl*[KD/KO] show progressive neurodegeneration and functional alteration of both rods and cones in aged mice. Figure shows representative ERG recordings obtained from one *Cerkl*[WTWT] animal (*black traces*) and one *Cerkl*[KD/KO] animal (*red traces*), and histogram representation of the averaged ERG wave amplitude for the two animal groups. (**A**) ERG measurements in young *Cerkl*[KD/KO] mice (6–10 months) show no clear alteration in either photoreceptor function in scotopic (rods) and photopic (cones) conditions or post-synaptic activity compared to age-matched controls ($n = 6$–8 animals per group). (**B**) In contrast, after aging ($\geq$18 months), the same cohort of animals shows scotopic (b-scot) and photopic (b-photo) alterations in *Cerkl*[KD/KO] retinas, with a clear decrease in photoreceptor activity (a-mix, considering both rod and cone activity). This decrease was also observed in postsynaptic activity (b-mix) and was particularly evident in OPs, reflecting the synaptic activity of RGC and amacrine cells, overall indicating a progressive functional impairment of the retina in *Cerkl*[KD/KO] mice. The timing of stimulus application is shown on the time scale (for light stimuli details, see the Materials and Methods section). Bars represent data (mean ± SD) for b-scot, a-mix, b-mix, b-phot, and OP from *Cerkl*[WTWT] and *Cerkl*[KD/KO] mice. Statistical significant differences (one-tailed Student's *t*-test) are indicated above the histogram bars ($^{*}P < 0.05$, $^{**}P < 0.01$, $^{***}P < 0.001$). All of the recordings were obtained from the C57BL/6J mice strain.

tion for the multiple isoforms. Further work on the effect of reported mutations on the function of different *CERKL* isoforms may explain why in some patients the phenotypic traits are clinically associated with RP or CRD, which differ in whether rods (peripheral retina) or cones (macula) are first affected, respectively (see Supplementary Table S2 for a complete list of CERKL mutations and reported reti-

nal phenotypes in human patients). However, genotype–phenotype correlation in human patients may be particularly difficult for *CERKL*, as the same pathogenic mutation in homozygosis can cause either autosomal recessive RP with high macular affectation[25] or autosomal recessive CRD,[7,32] not only in different families but also in sibling patients within the same family,[33] the main conclusion being that

CERKL function is relevant for both types of photoreceptors. Also, the severity of retinopathy and visual loss in humans differ even in homozygous patients of the same family. Overall, it is tempting to speculate that both the type of mutation and the CERKL isoform affected, as well as additional mutations of modifier genes in each patient, might eventually determine which type of photoreceptors is initially more vulnerable to *CERKL* dysfunction; yet, after photoreceptor apoptosis is initiated, the disease progresses until all photoreceptors and eventually, all the retina—including inner cells—is affected. In this context, mice do not have a macula, but our mouse model is more similar to the CRD phenotype, as we will discuss below.

Concerning the retinal phenotype in this *Cerkl*[KD/KO] mouse model, we observed an extreme elongation of rod OSs and cone sheaths, as well as opsin mislocalization in cone OSs, at an early age (retinas 2 months old) following a dorsal to ventral longitudinal gradient in the retina, thus indicating an as-yet unknown *Cerkl* role in photoreceptor patterning. Furthermore, these very low levels of *Cerkl* expression can lead to photoreceptor OS disorganization, severe disk stacking alteration, and vesicle accumulation. All of these features could be explained by RPE phagocytosis dysfunction. In this context, a very recent report also associated suppression of *Cerkl* expression to defects in autophagy/macrophagy.[34] It is worth noting that aged *Cerkl*[KD/KO] retinas (18 months old) display disarrayed RPE microvilli unable to engulf OS tips. In fact, the *Cerkl*[KD/KO] RPE shows high microvilli disorganization, phagosome accumulation in the basal membrane, and an increased number of total lysosomes, in full agreement with the results reported in a zebrafish *Cerkl* knockout model,[35] overall suggesting a novel retinal role for CERKL in the regulation of vesicle formation, autophagy, and OS phagocytosis.

Another morphological defect observed in the *Cerkl*[KD/KO] mouse retinas is the difference in retinal thickness, probably due to the contribution of several traits: differential decrease in the number of nuclei rows, different thickness of the inner plexiform layer, and regional differences in the length of the photoreceptor OSs in an inverted gradient to S-opsin cone distribution. This is related to a slow but progressive neurodegeneration in aged *Cerkl*[KD/KO] retinas, as demonstrated by the progressive loss of cones and a clear decrease in the number of photoreceptor nuclei over time. Remarkably, similar traits are observed in human patients bearing *CERKL* mutations in advanced disease stages, with thinning of the fovea (extremely rich in cones) with loss of the outer nuclear layer or abnormal lamination, as visualized by careful optic coherence tomography imaging.[7,25,30] The drastic reduction of *Cerkl* expression impinges on retinal homeostasis; consequently, GFAP expression by retinal astrocytes and Müller cells appear to be increased in *Cerkl*[KD/KO], which is similar to findings in mouse models for retinitis pigmentosa and other inherited retinal diseases.[28,36]

To sum up, we generated a new *Cerkl* mouse model retaining less than 10% of *Cerkl* expression that mimics human CRD traits due to early cone loss and subsequent progressive degeneration of all photoreceptors. With age, our mouse model shows decreased number of cones, loss of photoreceptor nuclei, elongated OSs with mislocalized opsins, alterations in the RPE microvilli and phagocytosis, and stress-associated alterations (such as increased GFAP expression). These morphological alterations cause retinal physiological dysfunction and trigger photoreceptor apoptosis. Remarkably, the initial ERGs of 6-month-old mice (young mice) did not show significant differences compared to age-matched controls, but electrophysiological altered responses became very apparent in 18-month-old mice. In this respect, although not all of the phenotypic traits are shared between human and mouse, the retinal phenotype of the *Cerkl*[KD/KO] mouse model is by far more similar to the slow and progressive retinal neurodegeneration shown by human patients bearing the most prevalent *CERKL* mutation (p.R283*) than to other reported mouse models. This valuable model will be instrumental in determining the role of CERKL in the retina and testing the efficacy of potential therapeutic approaches.

Disclosure: **E.B. Domènech**, None; **R. Andrés**, None; **M.J. López-Iniesta**, None; **S. Mirra**, None; **R. García-Arroyo**, None; **S. Milla**, None; **F. Sava**, None; **J. Andilla**, None; **P. Loza-Álvarez**, None; **P. de la Villa**, None; **R. Gonzàlez-Duarte**, None; **G. Marfany**, None

References

1. Ferrari S, Di Iorio E, Barbaro V, Ponzin D, Sorrentino FS, Parmeggiani F. Retinitis pigmentosa: genes and disease mechanisms. *Curr Genomics*. 2011;12:238–249.
2. Haim M. Epidemiology of retinitis pigmentosa in Denmark. *Acta Ophthalmol Scand*. 2002;80:1–34.
3. Verbakel SK, van Huet RAC, Boon CJF, et al. Non-syndromic retinitis pigmentosa. *Prog Retin Eye Res*. 2018;66:157–186.
4. Tuson M, Marfany G, Gonzàlez-Duarte R. Mutation of *CERKL*, a Novel Human Ceramide Kinase Gene, Causes Autosomal Recessive Retinitis Pigmentosa (RP26). *Am J Hum Genet*. 2004;74:128–138.
5. Littink KW, Koenekoop RK, van den Born LI, et al. Homozygosity mapping in patients with cone-rod dystrophy: novel mutations and clinical characterizations. *Invest Ophthalmol Vis Sci*. 2010;51:5943–5951.
6. Auslender N, Sharon D, Abbasi AH, Garzozi HJ, Banin E, Ben-Yosef T. A common founder mutation of *CERKL* underlies autosomal recessive retinal degeneration with early macular involvement among Yemenite Jews. *Invest Ophthalmol Vis Sci*. 2007;48:5431–5438.
7. Aleman TS, Soumittra N, Cideciyan AV, et al. CERKL mutations cause an autosomal recessive cone-rod dystrophy with inner retinopathy. *Invest Ophthalmol Vis Sci*. 2009;50:5944–5954.
8. Ali M, Ramprasad VL, Soumittra N, et al. A missense mutation in the nuclear localization signal sequence of *CERKL* (p.R106S) causes autosomal recessive retinal degeneration. *Mol Vis*. 2008;14:1960–1964.
9. Inagaki Y, Mitsutake S, Igarashi Y. Identification of a nuclear localization signal in the retinitis pigmentosa-mutated RP26

protein, ceramide kinase-like protein. *Biochem Biophys Res Commun*. 2006;343:982–987.

10. Gomez-Muñoz A, Gangoiti P, Arana L, et al. New insights on the role of ceramide 1-phosphate in inflammation. *Biochim Biophys Acta*. 2013;1831:1060–1066.

11. Gómez-Muñoz A, Gangoit P, Granado MH, Arana L, Ouro A. Ceramide-1-phosphate in cell survival and inflammatory signaling. In: Chalfant C, Del Poeta M , eds. *Sphingolipids as Signaling and Regulatory Molecules*. New York, NY: Springer; 2010;118–130.

12. Bornancin F, Metchcheriakova D, Stora S, et al. Characterization of a ceramide kinase-like protein. *Biochim Biophys Acta*. 2005;1687:31–43.

13. Tuson M, Garanto A, Gonzàlez-Duarte R, Marfany G. Overexpression of *CERKL*, a gene responsible for retinitis pigmentosa in humans, protects cells from apoptosis induced by oxidative stress. *Mol Vis*. 2009;15:168–180.

14. Li C, Wang L, Zhang J, et al. CERKL interacts with mitochondrial TRX2 and protects retinal cells from oxidative stress-induced apoptosis. *Biochim Biophys Acta*. 2014;1842:1121–1129.

15. Fathinajafabadi A, Pérez-Jiménez E, Riera M, Knecht E, Gonzàlez-Duarte R. *CERKL*, a retinal disease gene, encodes an mRNA-binding protein that localizes in compact and untranslated mRNPs associated with microtubules. *PLoS One*. 2014;9:e87898.

16. Garanto A, Riera M, Pomares E, et al. High transcriptional complexity of the retinitis pigmentosa *CERKL* gene in human and mouse. *Invest Ophthalmol Vis Sci*. 2011;52:5202–5214.

17. Graf C, Niwa S, Müller M, Kinzel B, Bornancin F. Wild-type levels of ceramide and ceramide-1-phosphate in the retina of ceramide kinase-like-deficient mice. *Biochem Biophys Res Commun*. 2008;373:159–163.

18. Garanto A, Vicente-Tejedor J, Riera M, et al. Targeted knockdown of *Cerkl*, a retinal dystrophy gene, causes mild affectation of the retinal ganglion cell layer. *Biochim Biophys Acta*. 2012;1822:1258–1269.

19. Riera M, Burguera D, Garcia-Fernàndez J, Gonzàlez-Duarte R. *CERKL* knockdown causes retinal degeneration in zebrafish. *PLoS One*. 2013;8:e64048.

20. Feng G, Mellor RH, Bernstein M, et al. Neurotechnique imaging neuronal subsets in transgenic mice expressing multiple spectral variants of GFP. *Neuron*. 2000;28:41–51.

21. Toulis V, Garanto A, Marfany G. Combining zebrafish and mouse models to test the function of deubiquitinating enzyme (DUBs) genes in development: role of USP45 in the retina. In: Matthiesen R , ed. *Proteostasis: Methods and Protocols*, New York, NY: Springer; 2016;85–101.

22. Sun W, Li N, He S. Large-scale morphological survey of mouse retinal ganglion cells. *J Comp Neurol*. 2002;451:115–126.

23. Kong JH, Fish DR, Rockhill RL, Masland RH. Diversity of ganglion cells in the mouse retina: Unsupervised morphological classification and its limits. *J Comp Neurol*. 2005;489:293–310.

24. McCulloch DL, Marmor MF, Brigell MG, et al. ISCEV standard for full-field clinical electroretinography (2015 update). *Doc Ophthalmol*. 2015;130:1–12.

25. Avila-Fernandez A, Riveiro-Alvarez R, Vallespin E, et al. *CERKL* mutations and associated phenotypes in seven Spanish families with autosomal recessive retinitis pigmentosa. *Invest Ophthalmol Vis Sci*. 2008;49:2709–2713.

26. Zahid S, Branham K, Schlegel D, et al. *Retinal Dystrophy Gene Atlas*. Cham, Switzerland: Springer International. 2018;51–53.

27. Roberts MR, Sirinivas M, Forrest D, Morreale de Escobar G, Reh TA. Making the gradient: thyroid hormone regulates cone opsin expression in the developing mouse retina. *Proc Natl Acad Sci U S A*. 2006;103:6218–6223.

28. Chen J, Nathans J. Genetic ablation of cone photoreceptors eliminates retinal folds in the *retinal degeneration 7 (rd7)* mouse. *Invest Ophthalmol Vis Sci*. 2007;48:2799–2805.

29. Ochocinska MJ, Muñoz EM, Veleri S, et al. NeuroD1 is required for survival of photoreceptors but not pinealocytes: results from targeted gene deletion studies. *J Neurochem*. 2012;123:44–59.

30. Pan N, Jahan I, Lee JE, Fritzsch B. Defects in the cerebella of conditional *Neurod1* null mice correlate with effective Tg(Atoh1-cre) recombination and granule cell requirements for *Neurod1* for differentiation. *Cell Tissue Res*. 2009;337:407–428.

31. Naya FJ, Huang HP, Qiu Y, et al. Diabetes, defective pancreatic morphogenesis, and abnormal enteroendocrine differentiation in BETA2/NeuroD-deficient mice. *Genes Dev*. 1997;11:2323–2334.

32. Sensiglio JD, Cho GY, Paavo M, et al. Hyperautofuorescent dots are characteristic in ceramide kinase like-associated retinal degeneration. *Sci Rep*. 2019;9:876.

33. Rodríguez-Muñoz A, Aller E, Jaijo T, et al. Expanding the clinical and molecular heterogeneity of nonsyndromic inherited retinal dystrophies. *J Mol Diagn*. 2020;22:532–543.

34. Hu X, Lu Z, Yu S, et al. CERKL regulates autophagy via the NAD-dependent deacetylase SIRT1. *Autophagy*. 2019;15:453–465.

35. Yu S, Li C, Biswas L, et al. *CERKL* gene knockout disturbs photoreceptor outer segment phagocytosis and causes rod-cone dystrophy in zebrafish. *Hum Mol Genet*. 2017;26:2335–2345.

36. Roche SL, Ruiz-Lopez AM, Moloney JN, Byrne AM, Cotter TG. Microglial-induced Müller cell gliosis is attenuated by progesterone in a mouse model of retinitis pigmentosa. *Glia*. 2018;66:295–310.

Supplementary table 1. List of primers used for testing gene editing in potential off-target regions.

Name	Primers (5'→3')	Region
Cerkl 53 DR274F	taggCCTTATATGAGGGGGTGGTC	5'
Cerkl 53 pX330F	caccCCTTATATGAGGGGGTGGTC	5'
Cerkl 53 R	aaacGACCACCCCCTCATATAAGG	5'
Cerkl 54 DR274F	taggCCTGACCACCCCCTCATATA	5'
Cerkl 54 pX330F	caccCCTGACCACCCCCTCATATA	5'
Cerkl 54 R	aaacTATATGAGGGGGTGGTCAGG	5'
Cerkl 33 DR274F	taggATCTTCTGCTTGGGCTTAGG	3'
Cerkl 33 pX330F	caccATCTTCTGCTTGGGCTTAGG	3'
Cerkl 33R	aaacCCTAAGCCCAAGCAGAAGAT	3'
Cerkl 34 DR274F	taggACAAACCTGAGCATTTATGC	3'
Cerkl 34 pX330F	caccACAAACCTGAGCATTTATGC	3'
Cerkl 34R	aaacGCATAAATGCTCAGGTTTGT	3'

Supplementary Table 2. List of reported *CERKL* mutations in human patients, classifed by their molecular effect, indicating the nucleotide and amino acid change, if reported in homo- or hetero-zygosis, and the associated clinical retinal phenotype (references at the end).

CERKL non-synonymous mutations (non-sense and missense)				
Mutation	**Localization**	**Aminoacid change**	**Zygosis**	**Retinal dystrophy**
GAG-TAG	c.193G>T	p.E65*	HM [1] HT [2]	RCD, MD
CGT-TGT	c.316C>T	p.R106C	HT [1]	arRP
CGT-AGT	c.316C>A	p.R106S	HM [3]	arRP
GGT-GAT	c.356G>A	p.G119D	HT [4]	CRD
CTC-CGC	c.365T>G	p.L122R	HM [5]	RP
TGC-TGG	c.375C>G	p.C125W	HM [6]	CRD
CTA-CCA	c.398T>C	p.L133P	HT [7]	RP
TGG-GGG	c.451T>G	p.W151G	HT [8]	RD
CCG-CTG	c.497C>T	p.P166L	HT [9]	MD
AAA-TAA	c.598A>T	p.K200*	HT [10]	RP
CAG-TAG	c.664C>T	p.Q222*	HT [11]	arRP
GAT-GTT	c.674A>T	p.D225V	HT [12]	RP
GGA-AGA	c.772G>A	p.G258R	HT [13]	CRD
CTG-CCG	c.812T>C	p.L271P	HM [14]	RP
CGA-TGA	c.847C>T	p.R283*	HM [15] HT [2]	RP, CRD
ATA-ACA	c.890T>C	p.I297T	HM [16]	RP, RCD
TGC-TGA	c.999C>A	p.C333*	HM [17]	CRD
CGA-TGA	c.1090C>T	p.R364*	HM [18]	CD, CRD
TGT-TGA	c.1164T>A	p.C388*	HT [19]	RD
CAG-TAG	c.1270C>T	p.Q424*	HM [20]	RP
CGA-TGA	c.1381C>T	p.R461*	HT [21]	RP
AGC-TGC	c.1651A>T	p.S551C	HT [22]	MD, CD, CRD

CERKL splicing mutations			
Mutation	**Localization**	**Zygosis**	**Retinal dystrophy**
IVS1 ds G-A +1	c.238+1G>A	HM [23]	RD
IVS2 ds T-G +2	c.481+2T>G	HM [20]	CRD
IVS9 as T-A -3	c.1212-3T>A	HT [24]	RP
IVS11 as C-G -3	c.1347-3C>G	HT [25]	RD
IVS1 ds T-C +2	c.238+2T>C	HT [26]	RP, CRD

Small *CERKL* deletions				
Mutation	**Localization**	**Aminoacid change**	**Zygosis**	**Retinal dystrophy**
CACTT^139 GATCTtATTAATTTAA	c.420delT	p.(Ile141 Leufs*3)	HT [10]	RP
ACTGT^149 GACATAtGGTTTAGACA	c.450_451 delAT	p.(Ile150 Metfs*3)	HM [27]	CRD
GTA^204ACAA_EI_ GTAagTAATTTTCAG	c.613+4_613+5 delAG		HT [25]	RP
TA^204ACAA_EI_ GTAAgtaaTTTTCAGAAT	c.613+5_613+8 delGTAA		HM [28]	RP

Mutation	Localization	Aminoacid change	Zygosis	Retinal dystrophy
TTTTCTAG_IE_ TGtT^254GTCTGTGTT	c.759delT	p.(Val254 Serfs*12)	HT [29]	RD
AATGCT^278 GGGAtGGAAACAGAC	c.836delT	p.(Met279 Argfs*7)	HT [30]	RP
GAATC^285 CTGACtCCTGTCAGAG	c.858delT	p.(Pro287 Leufs*10)	HT [10]	RP
ATTGCAC^322 ATTatAATGG_EI_GTAAG	c.968_969delTA	p.(Ile323 Asnfs*46)	HM [31]	
GTTCTCA^34 8GCCatGTTTGGCTTT	c.1045_1046 delAT	p.(Met349 Valfs*20)	HM [2]	RD
AAA^383CTTAA_EI_ GTaagtCTTTTTCTTA	c.1151+3_1151+6 delAAGT		HM [25]	RP
GCAGAA^387 GACTgtGAAATATCAT	c.1164_1165 delTG	p.(Cys388*)	HT [32]	
CTGTT^493 GAGGAaGTAAAAGTTC	c.1482delA	p.(Val495*)	HM [33]	RD

Small *CERKL* insertions

Mutation	Localization	Aminoacid change	Zygosis	Retinal dystrophy
GGGCATC^52 TTCtGAGATCGGGA	c.156_157insT	p.(Glu53*)	HM [30]	RP
GCGAG^66CGAGC gagcACTGCGGTGG	c.197_200dup GAGC	p.(Leu68 Serfs*15)	HT [24]	MD, CD, CRD
TGAGACT^490 TACttacACTGTTGAGG	c.1467_1470 dupTTAC	p.(Thr491 Leufs*4)	HM [34]	RP
ATCAGT^547 CTTTctttATGGAGGAAG	c.1639_1642 dupCTTT	p.(Tyr548 Serfs*19)	HT [7]	RP

Large *CERKL* deletions

Mutation	Localization	Zygosis	Retinal dystrophy
gDNA	Exon 1-2	HT [35]	RD
gDNA	Exon 2	HT [24]	RP
gDNA	Exon 2	HT [25]	MD, CD, CRD
gDNA	Exon 1	HT [26]	RP, CRD
gDNA	Exon 2	HT [26]	RP, CRD

ar: Autosomic recessive. **HM**: Homozygosis. **HT**: Heterozygosis. **RD**: Retinal Dystrophy. **RP**: Retinitis Pigmentosa. **CD**: Cone Dystrophy. **CRD**: Cone-Rod Dystrophy. **MD**: Macular degeneration.

(Mutations listed on *Human Gene Mutation Database* (HGMD) http://www.hgmd.cf.ac.uk/ac/index.php).

REFERENCES

[1] K. Avela, E. M. Sankila, S. Seitsonen, *et al.*, "A founder mutation in CERKL is a major cause of retinal dystrophy in Finland," *Acta Ophthalmol.*, 2018, vol. 96, no. 2, pp. 183–191.

[2] J. M. Ellingford, S. Barton, S. Bashkar, *et al.*, "Molecular findings from 537 individuals with inherited retinal disease," *J. Med. Genet.*, 2016, vol. 53, no. 11, pp. 761–767.

[3] M. Ali, V. L. Ramprasad, N. Soumittra, *et al.*, "A missense mutation in the nuclear localization signal sequence of CERKL (p . R106S) causes autosomal recessive retinal degeneration," *Mol. Vis.* 2008, vol. 14, pp. 1960–1964.

[4] M. Ezquerra-Inchausti, A. Anasagasti, O. Barandika, *et al.*, "A new approach based on targeted pooled DNA sequencing identifies novel mutations in patients with Inherited Retinal Dystrophies," *Sci. Rep.*, 2018, vol. 8, no. 1, pp. 1–12.

[5] L. Roberts, R. Ratnapriya, V. Chaitankar, *et al.*, "Molecular Diagnosis of Inherited Retinal Diseases in Indigenous African Populations by Whole-Exome Sequencing." *Investig. Ophthalmol. Vis. Sci.*, 2016, vol. 57, no. 14, pp. 6374–6381.

[6] K. W. Littink, R.K. Koenekoop, L.I. van den Born, *et al.*, "Homozygosity mapping in patients with cone-rod dystrophy: Novel mutations and clinical characterizations", *Investig. Ophthalmol. Vis. Sci.*, 2010, vol. 51, no. 11, pp. 5943–5951.

[7] Y. Xu, L. Guan, T. Shen *et al.*, "Mutations of 60 known causative genes in 157 families with retinitis pigmentosa based on exome sequencing.," *Hum. Genet.*, 2014, vol. 133, no. 10, pp. 1255–1271.

[8] X. F. Huang, F. Huang, K. Wu, *et al.*, "Genotype-phenotype correlation and mutation spectrum in a large cohort of patients with inherited retinal dystrophy revealed by next-generation sequencing," *Genet. Med.*, 2015, vol. 17, no. 4, pp. 271–278.

[9] P. Wang, S. Li, W. Sun, *et al.*, "An ophthalmic targeted exome sequencing panel as a powerful tool to identify causative mutations in patients suspected of hereditary eye diseases," *Transl. Vis. Sci. Technol.*, 2019, vol. 8, no. 2, pp. 21.

[10] K. M. Nishiguchi, R. G. Tearle, Y. P. Liu, *et al.*, "Whole genome sequencing in patients with retinitis pigmentosa reveals pathogenic DNA structural changes and NEK2 as a new disease gene," *Proc. Natl. Acad. Sci. U. S. A.*, 2013, vol. 110, no. 40, pp. 16139–16144.

[11] R. Perez-Carro, M. Corton, I. Sánchez-Navarro, *et al.*, "Panel-based NGS Reveals Novel Pathogenic Mutations in Autosomal Recessive Retinitis Pigmentosa," *Sci. Rep.*, 2016, vol. 6, no. 19531.

[12] S. Kantarci, J. L. Deignan, N. Dorrani, *et al.*, "Clinical Exome Sequencing for Genetic Identification of Rare Mendelian Disorders," *JAMA,* 2014, *vol.* 312, no. 18, pp. 1880–1887.

[13] C. Jespersgaard, M. Fang, M. Bertelsen, *et al.*, "Molecular genetic analysis using targeted NGS analysis of 677 individuals with retinal dystrophy," *Sci. Rep.*, 2019, vol. 9, no. 1, pp. 1–7.

[14] J. Wang, V. W. Zhang, Y. Feng, *et al.*, "Dependable and efficient clinical utility of target capture-based deep sequencing in molecular diagnosis of retinitis pigmentosa," *Investig. Ophthalmol. Vis. Sci.*, 2014, vol. 55, no. 10, pp. 6213–6223.

[15] M. Tuson, G. Marfany, and R. Gonzàlez, "Mutation of CERKL , a Novel Human Ceramide Kinase Gene , Causes Autosomal Recessive Retinitis Pigmentosa (RP26)," *Am. J. Hum. Genet.*, 2004, vol. 74, no. 1, pp. 128–138.

[16] N. Patel, N. A. Aldahmesh, H. Alkuraya, *et al.*, "Expanding the clinical, allelic, and locus heterogeneity of retinal dystrophies," *Genet. Med.*, 2016, vol. 18, no. 6, pp. 554–562.

[17] A. O. Khan and L. Abu-Safieh, "Rod-Cone Dystrophy with Initially Preserved Visual Acuity Despite Early Macular Involvement Suggests Recessive CERKL Mutations," *Ophthalmic Genet.*, 2015, vol. 36, no. 4, pp. 369–372.

[18] E. Boulanger-Scemama, S. El Shamieh, V. Démontant, *et al.*, "Next-generation sequencing applied to a large French cone and cone-rod dystrophy cohort: Mutation spectrum and new genotype-phenotype correlation," *Orphanet J. Rare Dis.*, 2015, vol. 10, no. 1.

[19] R. Matsui, A. V. Cideciyan, S. B. Schwartz, *et al.*, "Molecular heterogeneity within the clinical diagnosis of pericentral retinal degeneration," *Investig. Ophthalmol. Vis. Sci.*, 2015, vol. 56, no. 10, pp. 6007–6018.

[20] N. Glöckle, S. Kohl, J. Mohr, *et al.*, "Panel-based next generation sequencing as

a reliable and efficient technique to detect mutations in unselected patients with retinal dystrophies," *Eur J Hum Genet.,* 2014, vol. 22, no. 1, pp. 99–104.

[21]   E. M. Stone, J. L. Androf, S. S. Whitmore, *et al.,* "Clinically Focused Molecular Investigation of 1000 Consecutive Families with Inherited Retinal Disease," *Ophtalmology.*, 2017, vol. 124, no. 9, pp. 1314-1331.

[22]   J. Birtel, T. Eisenberger, M. Gliem, *et al.*, "Clinical and genetic characteristics of 251 consecutive patients with macular and cone/cone-rod dystrophy," *Sci. Rep.*, 2018, vol. 8, no. 1, pp. 1–11.

[23]   N. Auslender, D. Sharon, A. H. Abbasi, *et al.*, "A common founder mutation of CERKL underlies autosomal recessive retinal degeneration with early macular involvement among Yemenite Jews," *Investig. Ophthalmol. Vis. Sci.*, 2007, vol. 48, no. 12, pp. 5431–5438.

[24]   J. Birtel, M. Gliem, E. Mangold *et al.*, "Next-generation sequencing identifies unexpected genotype-phenotype correlations in patients with retinitis pigmentosa," *PLoS One*, 2018, vol. 13, no. 12, pp. 1–18.

[25]   K. Carss, G. Arno, M. Erwood, *et al.*, "Comprehensive Rare Variant Analysis via Whole-Genome Sequencing to Determine the Molecular Pathology of Inherited Retinal Disease," *Am. J. Hum. Genet.*, 2017, vol. 100, no. 1, pp. 75–90.

[26]   J. M. Ellingford, B. Horn, C. Campbel, *et al.*, "Assessment of the incorporation of CNV surveillance into gene panel next-generation sequencing testing for inherited retinal diseases," *J. Med. Genet.*, 2018, vol. 55, no. 2, pp. 114–121.

[27]   B. Azab, R. Barham, D. Ali, *et al.*, "Novel CERKL variant in consanguineous Jordanian pedigrees with inherited retinal dystrophies," *Cananian J. Ophtalmol.*, 2019, vol. 54, no. 1, pp. 51–59.

[28]   M. De Castro-Miró, R. Tonda, P. Escudero-Ferruz, *et al.*, "Novel candidate genes and a wide spectrum of structural and point mutations responsible for inherited retinal dystrophies revealed by exome sequencing," *PLoS One*, 2016, vol. 11, no. 12, pp. 1–19.

[29]   X. Huang, F. Huang, K. Wu, *et al.*, "Open Genotype – phenotype correlation and mutation spectrum in a large cohort of patients with inherited retinal dystrophy revealed by next-generation sequencing," *Genetics in Medicine,* 2015, vol. 17, no. 4, pp. 271–278.

[30]   Z. Tang, Z. Wang, Z. Wang, *et al.*, "Novel Compound Heterozygous Mutations in

CERKL Cause Autosomal Recessive Retinitis Pigmentosa in a Nonconsanguineous Chinese Family," *Arch Ophthalmol*, 2009, vol. 127, no. 8, pp. 1077.

[31]   P. Biswas, J. L. Duncan, B. Maranhao, *et al.*, "Genetic analysis of 10 pedigrees with inherited retinal degeneration by exome sequencing and phenotype-genotype association," *Physiol. Genomica.*, 2017, vol. 49, pp. 216–229.

[32]   T. S. Aleman, N. Soumittra, A. V. Cideciyan, *et al.*, "CERKL mutations cause an autosomal recessive cone-rod dystrophy with inner retinopathy," *Investig. Ophthalmol. Vis. Sci.*, 2009, vol. 50, no. 12, pp. 5944–5954.

[33]   Q. Fu, F. Wang, H. Wang, *et al.*, "Next-Generation sequencing-based molecular diagnosis of a Chinese patient cohort with autosomal recessive retinitis pigmentosa," *Investig. Ophthalmol. Vis. Sci.*, 2013, vol. 54, no. 6, pp. 4158–4166.

[34]   L. Wang, J. Zhang, N. Chen, *et al.*, "Application of whole exome and targeted panel sequencing in the clinical molecular diagnosis of 319 Chinese families with inherited retinal dystrophy and comparison study," *Genes.*, 2018, vol. 9, no. 7, pp. 1–11.

[35]   J. M. Ellingford, C. Campbel, S. Barton, *et al.*, "Validation of copy number variation analysis for next-generation sequencing diagnostics," *Eur. J. Hum. Genet.*, 2017, vol. 25, no. 6, pp. 719–724.

Figure S1. CRISPR/Cas9 guide position. To perform *Cerkl* gene edition we used four guides, two guides at 5' **(A)**, and two guides at 3' **(B)**.

A) Whole region

PCR whole deletion (Primers: Cerkl UF – Cerkl DR)
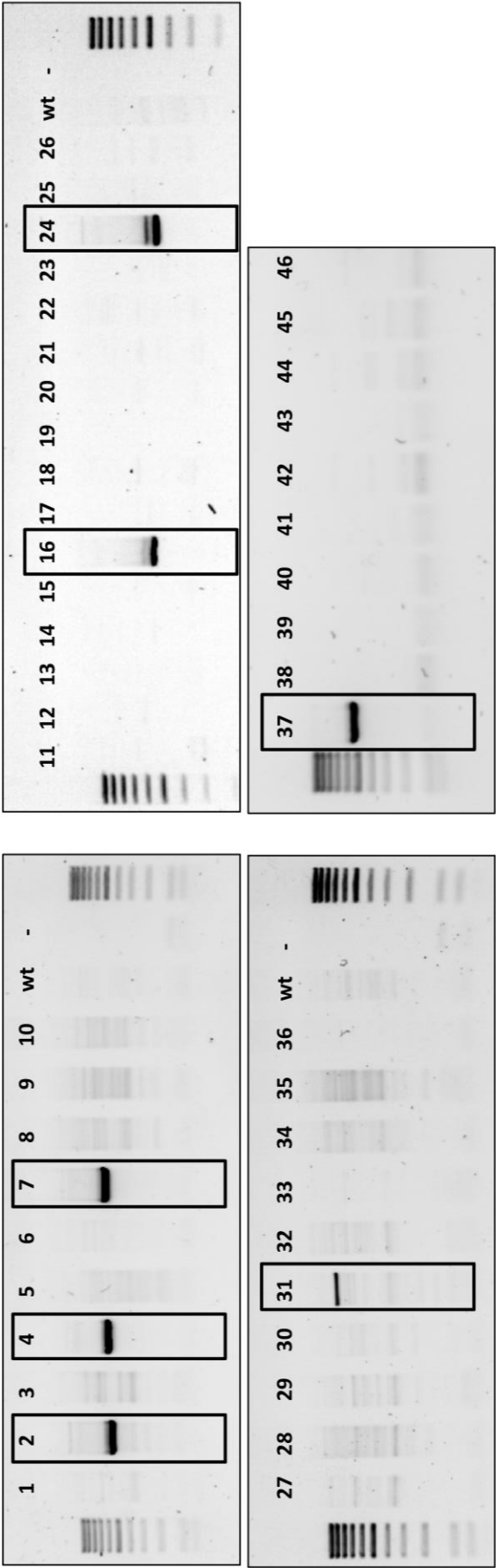
(guides underlined) (small insertions) (small deletions)

```
wt 5'       tagtacagaaacccagtttaaatcacccttcaatgctgaccacccctcataaggacttcacaaa
wt 3'       GGCGTTCTGCCTCCTAAGCCCAAGCCAGAGATTAAAAGCCAGAAGTTAGCACATTGTATAAATACATATGCACCACCTGTGATAAATACAAACCTGAGCATTTATGCTGGCATTGCAAACATTATTTGT

mouse 02    tagtacagaaacccagtttaaatcacccttcaatgctgaccacccctcat...                                 ...TGCAAACATTATTTTGT

mouse 04    tagtacagaaacccagtttaaatcacccttcaatgctgaccacccctcattcat...                            ...TGCTGGCATTGCAAACATTATTTTGT

mouse 07    tagtacagaaacccagtttaaatcacccttcaatgctgaccacccctcacaatgctcaggtttgtatttata...          ...ATGCTGGCATTGCAAACATTATTTTGT

mouse 16    tagtacagaaacccagtttaaatcacccttcaatgctgaccacccctcaggac...                             ...TGCTGGCATTGCAAACATTATTTTGT

mouse 24    tagtacagaaacccagtttaaatcacccttcaatgctgaccacccctc...                                  ...AAACATTATTTTGT

mouse 37    tagtacagaaacccagtttaaatcacccttcaatgctgaccacccctc...                                  ...ATTATTTTGT
```

B) 5' or upstream region

PCR 5' or upstream (Primers: Cerkl UF2 – Cerkl UR)

```
11 12 13 14 15 16 17 18 19 20 21 22 23 24 25 26 wt -
38 39 40 41 42 43 44 45 46
37
1 2 3 4 5 6 7 8 9 10 wt -
27 28 29 30 31 32 33 34 35 36 wt -
```

```
wt 5'           tagtacagaaacccagtttttaaatcacccttcaatgctgacaccccctcatataaggacttcacaaa
mouse 02 (11/11) tagtacagaaacccagtttttaaatcacccttcaatgctgacaccccctca-----------caaa
mouse 04a (10/12) tagtacagaaacccagtttttaaatcacccttcaatgctgacaccccctcataataaggacttcacaaa
mouse 04b (2/12)  tagtacagaaacccagtttttaaatcacccttcaatgctgacaccccctca------------aaa
mouse 07 (6/12)   tagtacagaaacccagtttttaaatcacccttcaatgctgacaccccctca-----------caaa
mouse 16a (5/10)  tagtacagaaacccagtttttaaatcacccttcaatgctgacc--ccctcatataaggacttcacaaa
mouse 16b (4/10)  tagtacagaaacccagtttttaaatcacccttcaatgctgacaccccctc-------ttcacaa
mouse 16c (1/10)  tagtacagaaacccagtttttaaatcacccttcaatgcc---cgacccctcataaggacttcacaaa
mouse 24a (3/14)  tagtacagaaacccagtttttaaatcacccttcaatgcagaggtggtgcatatgtgttatttatacaatgtgctaactttctgcttggcattgaaggacttcacaaa
mouse 24b (9/14)  tagtacagaaacccagtttttaaatcacccttcaatgctgaccac--------taaggacttcacaaa
mouse 24c (2/14)  tagtacagaaacccagtttttaaatcacccttcaatgctgacaccccctcataataaggacttcacaaa
mouse 37 (1/12)   tagtacagaaacccagtttttaaatcaccctcaatgctgacaccccctcattataaggacttcacaaa
```

C) 3' or downstream region (mice 7 & 37 wild type)

PCR 3' or downstream (Primers: Cerkl DF – Cerkl DR)
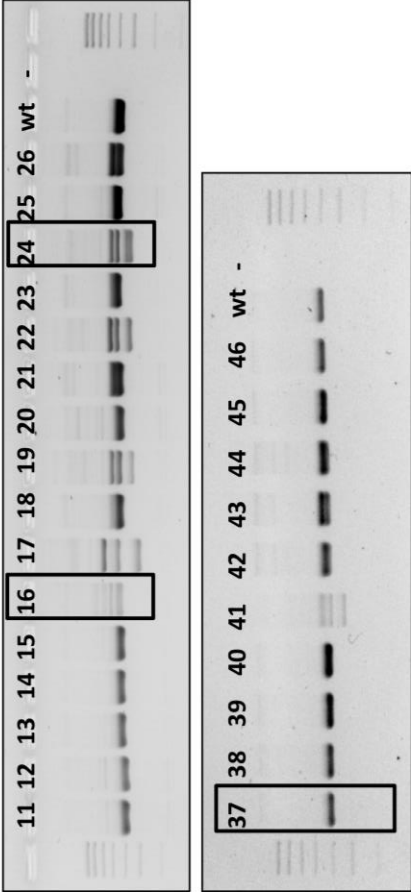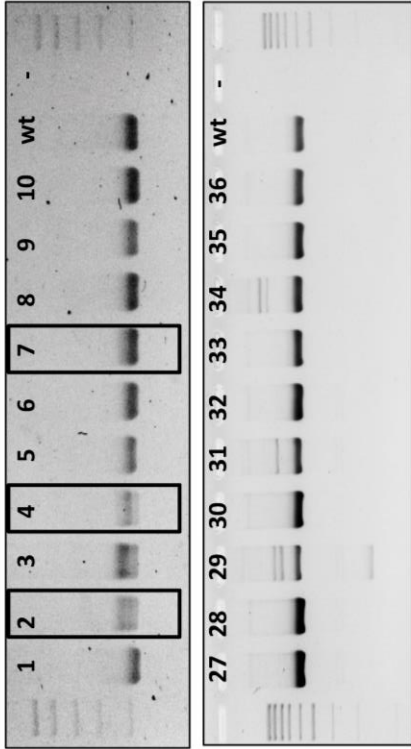

```
wt 3'            GGCGTTCTGCCTCCTAAGCCAGAGAGAGATTAGCACATTGTATAAATACACATTAGCACATTGTATAAATACAGAAAGCCAGAGAGATTAAAAGCCAGCACCTCTCAATAAATACAAACCTGAGCATTATGTGGCATTGCAAACATTATTTGT

mouse 02a (7/11) GGCGTTCTGCCTCCTAAGCCAGAGAGAGATTAGCACATTGTATAAATACACATTAGCACATTGTATAAATACAGAAAGCCAGAGAGATTAAAAGCCAGCACCTCTCAATAAATACAAACCTGAGCATTATTGCTGGCATTGCAAACATTATTTGT

mouse 02b (4/11) GGCGTTCTGCCTCCTAAGCCCAAGCAGAGAGATTAGCACATTGTATAAATACACATTAGCACATTGTATAAATACAGAAAGCCAGAGAGATTAAAAGCCAGCACCTCTCAATAAT--------------GCTGGCATTGCAAACATTATTTGT

mouse 04  (6/9)  GGCGTTCTGCCTCC-AAGCCCAAGCAGAGAGATTAGCACATTGTATAAATACACATTAGCACATTGTATAAATACAGAAAGCCAGAGAGATTAAAAGCCAGCACCTCTCAATAAATACAAACCTGA--------------GATTGCAAACATTATTTGT

mouse 16a (2/9)  GCGTTCTGCCTC---------AAGCAGAGAGATTAAAAGCCAGAGAGATTAAAAGCCAGCACCTCTCAATAAATACAAACCTG--------------GCATTGCAAACATTATTTGT

mouse 24a (3/8)  GGCGTTCTGC---------------------------TGGCATTGCAAACATTATTTGT

mouse 24b (3/8)  GGCGTTCTGC-----------------------------------AAACATTATTTGT

mouse 24c (2/8)  GGCGTTCTGCCT-----GCCCAAGCAGAGAGATTAAAAGCCAGAGAGATTAAAAGCCAGCACCTCTCAATAAATACAAACCTG--------------CTGGGCATTGCAAACATTATTTGT

wt (16b reference)
GAAAACCTGGGGCTATCTGGTTAAAGTTTCAAAGCTATAAAGATGTCAGAATGATGATGAAACTTAATTCTAATAGGGCGACCACCATGAAGCTGAAAGATGCTTTTTTTTTTTTTGTTTTTTTTTTTTTTTTGTTATATTTAGTTCAATTTCCCTTTGTG
GAGACTTATATCATTGAAGAAGTAAAAATTCACCCAAAGAGTAATAGCAATGAATGATACAGCCCAGGAGGGTGAAACCATACAACTGCTTCAGAACACGGGTTCCGTGGAATGGTAGTGGACTTAATGTGGCTTCATCGAGAGGTTCACCATTA
GGTAAGCCCAACTATTTTATGACTTTCTGTGCAGAATACACTATTAATAATAAGGGCGTTCTGTGGAAGTTAGCACATTGTATAAATACATATGCAGCTGTATAAATACAAA
CCTGAGCATTTATGCTGGCATTGCAAACATTATTTGTATAAATGATCAGAACATGTTGCAAATTTTGTCTTTGCATATTCTTAAAGTTTATAAGGTTAATGTAGTGCCATACTCTCTAGCCCTGCTCCC

mouse 16b  (7/9)
GAAAACCTGGGGCTATCTGGTTAAAGTTTCAAAGCTATAAAGATGTCAGAATGATGATGAAACTTAATTCTAATAGGGCGACCACCATGAAGCATC----CTTTTGTGAA
GCTGGCATTGCAAACATTATTTGTATAAATGATCAGAACATGTTGACAATTTACATTGTTTGTCTTTGAGGATATTCTTAAAGTTTATAAGGTTAATGTAGTGCCATACTCTCTAGCCCTGCTCCCA
```

Figure S2. Genotyping PCRs for CRISPR-edited alleles in mosaic pups, and sequences gene-edited alleles per mice. A) Specific PCRs for the whole *Cerkl* locus deletion allele with primers flanking the PAM sites for the Cas9 D10A nickase at 5' and 3' sequences, allowed to detect the pups (out of 46 born alive) carrying the full locus deletion. **B)** Specific primers for gene-editing in the upstream *Cerkl* region allowed to detect mosaic pups carrying alleles where Cas9 D10A nickase only cut at the 5' sites. **C)** Specific primers for gene-editing in the downstream *Cerkl* region allowed to detect mosaic pups carrying alleles where Cas9 D10A nickase only cut at the 3' sites. Per each specific primer pair, PCRs from animals carrying gene-edited alleles are highlighted. Bands were excised, cloned and sequenced. Very few alleles were present per animal (indicated by a and b sequences) and sequences are indicated below. Small indels at the edited sites were detected in some cases (blue nucleotides indicate small insertions and red nucleotides, small deletions). Mouse 16 b allele (gene-editing occurred only at the 3' *Cerkl* region carried a relatively larger deletion). Mouse 2 carrying the full locus deletion was chosen as a founder for our colony (highlighted in yellow).
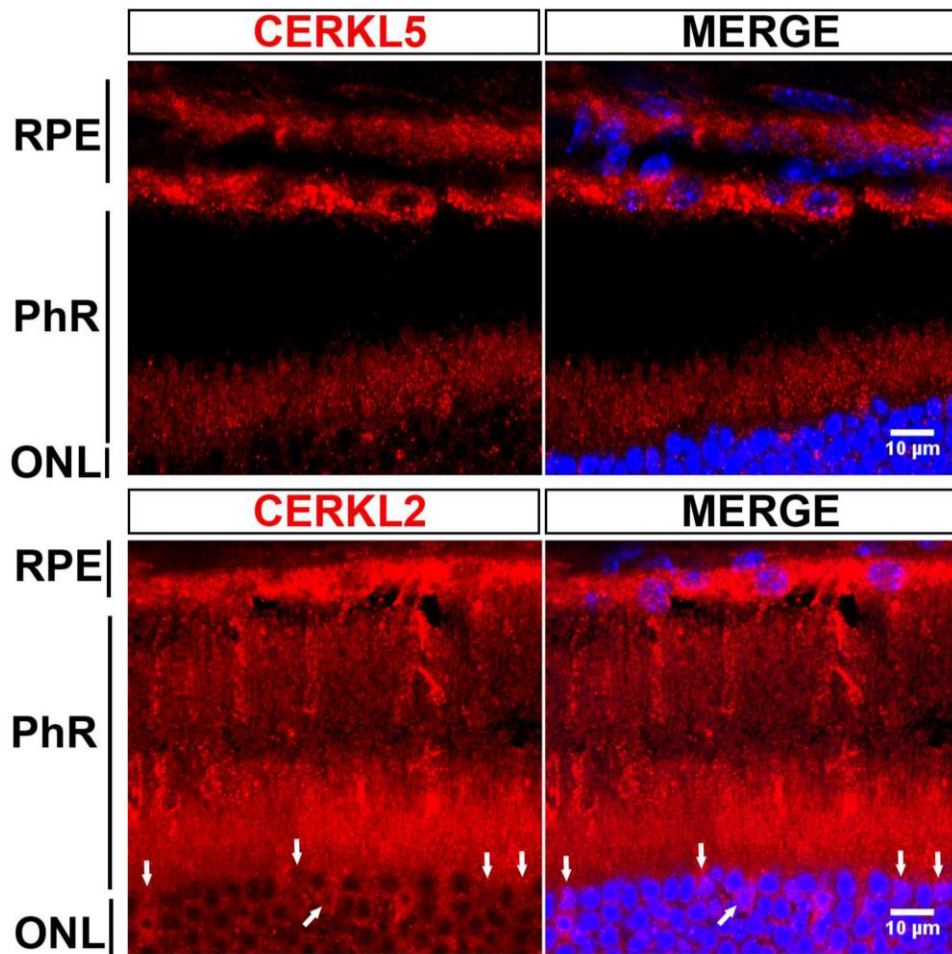
Figure S3. CERKL (in red) is highly expressed in the Retinal Pigment Epithelium (RPE) cells, as detected using two anti-CERKL antibodies recognizing different protein isoforms. Nuclei are counterstained with DAPI (blue). Note that some CERKL isoforms (detected with anti-CERKL2) are also localized in the nuclei of RPE cells and some cones (white arrows) (see main text). **PhR-** Photoreceptor layer (include the outer and inner segments of photoreceptors). **ONL-** Outer nuclear layer.
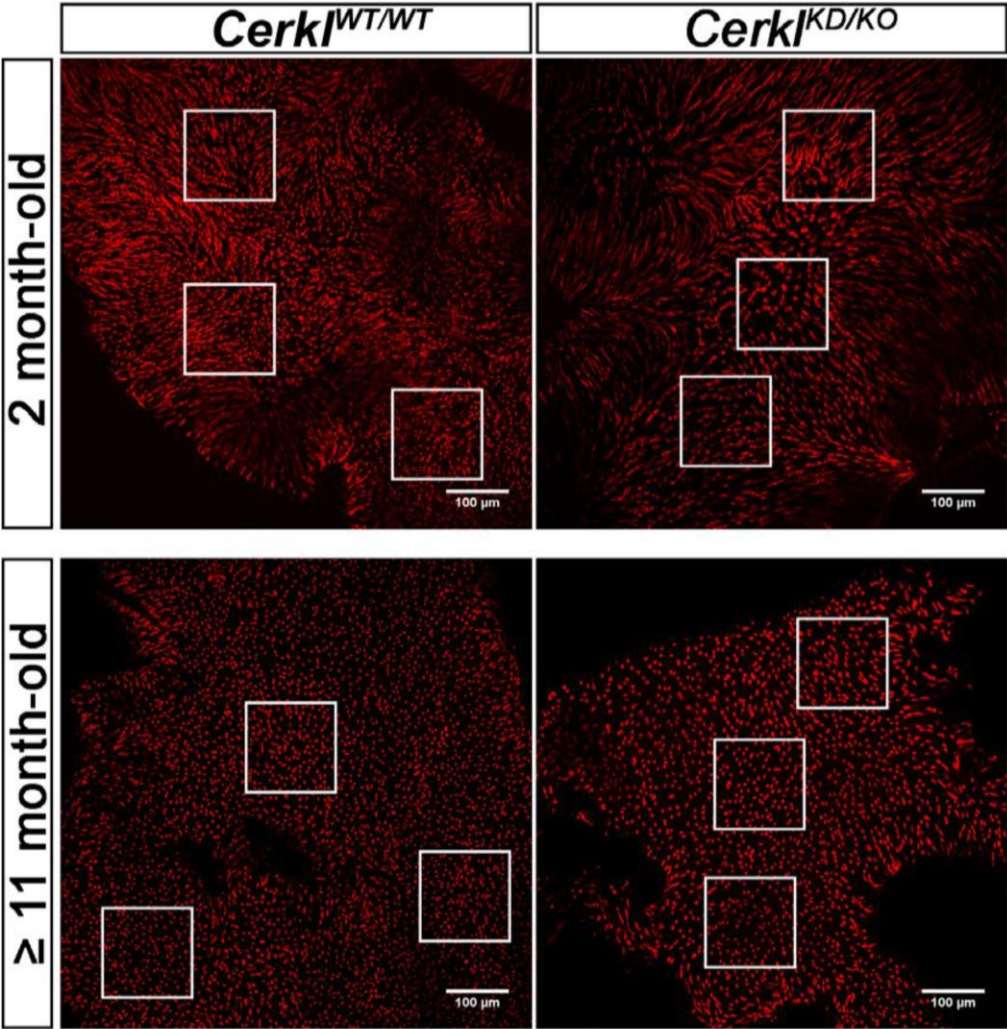
Figure S4. Representative positioning of the ROIs (regions of interest) in a retinal whole mount. The number of cones were counted on three ROIs per image and a minimum of 12 images per retina.
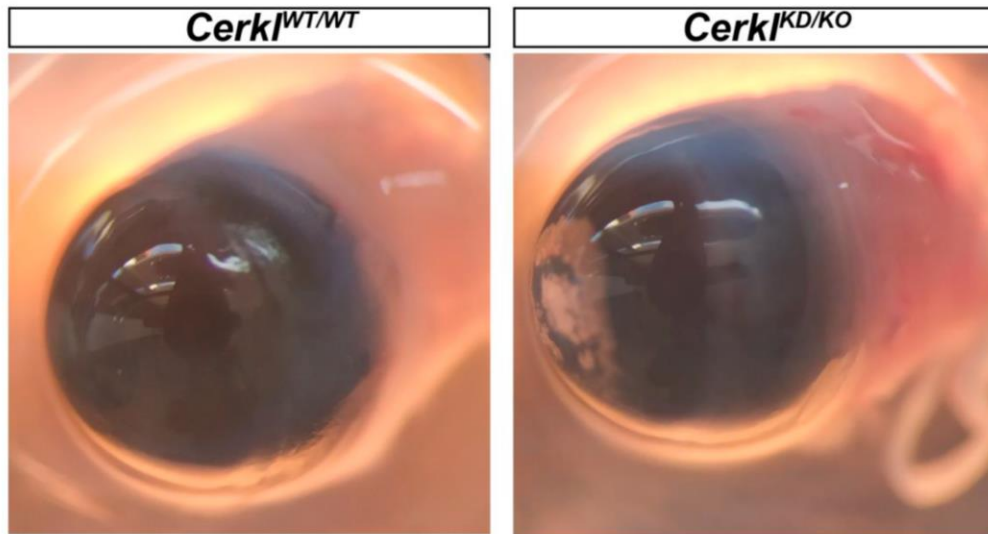
Figure S5. Corneal aggregates in aged *Cerkl*^{KD/KO} mice (≥18 months of age).
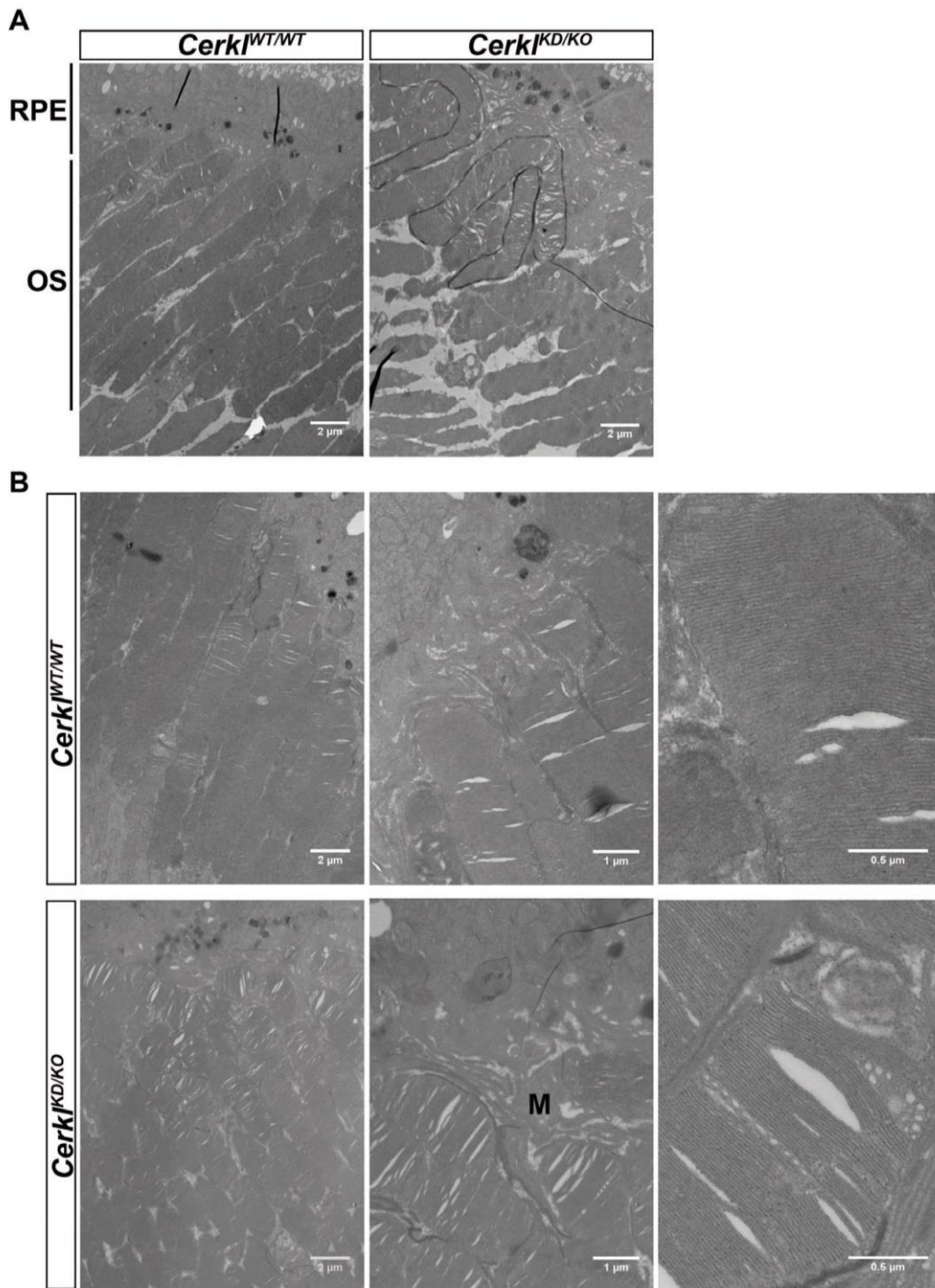
Figure S6. Transmission electron microscopy image showing the ultrastructure of retinal photoreceptors. A) *Cerkl*^{KD/KO} photoreceptors show loose stacking of the membraneous disks and disarrayed bent outer segments (outlined in black) and disorganized microvilli (M). B) Additional images from different *Cerkl*^{KD/KO} and *Cerkl*^{WT/WT} mice to show the consistency of the phenotype. Magnifications were taken at 5000x, 12000x and 40000x. Scale bars 2 μm, 1 μm and 0.5 μm respectively.

Review

The Alter Retina: Alternative Splicing of Retinal Genes in Health and Disease

Izarbe Aísa-Marín [1,2] , Rocío García-Arroyo [1,3] , Serena Mirra [1,2] and Gemma Marfany [1,2,3,*]

[1] Departament of Genetics, Microbiology and Statistics, Avda. Diagonal 643, Universitat de Barcelona, 08028 Barcelona, Spain; iaisa@ub.edu (I.A.-M.); rociogarciaarroyo@ub.edu (R.G.-A.); serena.mirra@ub.edu (S.M.)
[2] Centro de Investigación Biomédica en Red Enfermedades Raras (CIBERER), Instituto de Salud Carlos III (ISCIII), Universitat de Barcelona, 08028 Barcelona, Spain
[3] Institute of Biomedicine (IBUB, IBUB-IRSJD), Universitat de Barcelona, 08028 Barcelona, Spain
* Correspondence: gmarfany@ub.edu

Abstract: Alternative splicing of mRNA is an essential mechanism to regulate and increase the diversity of the transcriptome and proteome. Alternative splicing frequently occurs in a tissue- or time-specific manner, contributing to differential gene expression between cell types during development. Neural tissues present extremely complex splicing programs and display the highest number of alternative splicing events. As an extension of the central nervous system, the retina constitutes an excellent system to illustrate the high diversity of neural transcripts. The retina expresses retinal specific splicing factors and produces a large number of alternative transcripts, including exclusive tissue-specific exons, which require an exquisite regulation. In fact, a current challenge in the genetic diagnosis of inherited retinal diseases stems from the lack of information regarding alternative splicing of retinal genes, as a considerable percentage of mutations alter splicing or the relative production of alternative transcripts. Modulation of alternative splicing in the retina is also instrumental in the design of novel therapeutic approaches for retinal dystrophies, since it enables precision medicine for specific mutations.

Keywords: retina; alternative splicing; inherited retinal dystrophies; splicing factors; non-canonical splice site variants; deep intronic variants; microexons

1. Introduction

The human genome is estimated to contain ~30,000 genes, which represent about 1% of the total genome [1,2]. Although the number of genes is not much higher than in invertebrates, a higher molecular complexity can be attained by the production of multiple mRNA isoforms from a single gene, generated by alternative splicing (AS) and leading to a huge diversification of the proteome [3]. Alternative splicing events (ASEs) of pre-mRNA transcripts strongly contribute to the cellular regulatory landscape, protein diversity, and therefore, to organismal complexity, together with other related mechanisms such as the use of alternative promoters, transcription start sites and polyadenylation sites.

AS consists in the selective removal or retention of introns and exons giving rise to different rearranged patterns of mature mRNA products. In the classical view, AS may occur via different patterns of binary events involving two exons or two splice sites in the same exon. Binary AS includes exon skipping, mutually exclusive exons, alternative donor (5′) and receptor (3′) splice sites, and intron retention. However, this vision does not take account of complex splicing events [4]. The proper recognition of pre-mRNA regions during splicing is mediated by cis-acting regulatory elements, whose location on the pre-mRNA spatially orchestrates the splicing event. Cis splicing elements include the splice donor site (SDS), the splice acceptor site (SAS), the branch-site (BS) and the polypyrimidine tract (Py) upstream of the 3′ splice site. In addition, cis-regulatory sequences can interact with trans-acting regulatory elements to promote or repress splicing [5]. Splicing activators include

serine- and arginine-rich (SR) proteins, while splicing repressors include hnRNPs [6,7]. A number of other splicing activators or repressors have been identified, and the combinatory binding of these elements in a time- and space-specific manner originates high specific isoform patterns characteristic of each cell-type. Moreover, chromatin organization can also change or determine splicing patterns. The spliceosome catalyzes splicing in a two-step trans-esterification reaction that joins each donor site to the correspondent acceptor site [8].

Deep transcriptome sequencing of the human genome showed that the frequency of AS increases with species complexity, with almost all multi-exon human genes being alternatively spliced in humans [9,10]. AS occurs in all tissues and is subject to cell-specific and developmental-specific regulation [11]. Moreover, recent advances in genomic technologies and computational tools employed in genome-wide studies allowed us to shed light on the wide range of alternative splice isoforms generated in the context of homeostatic adaptation and diseases [12].

The most common occurrence of ASEs is observed in the central nervous system (CNS) of vertebrates [13], where it plays pivotal roles in processes such as neurogenesis, cell migration, synaptogenesis, synaptic function or neuronal network function and plasticity [14]. Remarkably, the CNS needs to rapidly adapt its physiology to dynamic environmental changes. Tissue- and cell-specific modulation of the AS patterns provides a brilliant solution to this high demand of plastic adaptation, guarantying an efficient adjustment of network dynamics. Indeed, it allows to produce several mRNA isoforms with specific regulatory features, such as stability or translational efficiency. Additionally, the set of protein isoforms arising from ASEs can vary with respect to their subcellular localization, protein or metabolite interactome and functional features.

The retina, the light sensing tissue of the eye, is a highly specialized tissue belonging to the CNS. Remarkably, high levels of ASEs occur in the retina where precise gene regulation is required for neuronal development and function. The importance of alternative splicing in retina is highlighted by numerous examples where splicing alterations underly retinal disorders and disease, such as cone-rod dystrophy, Usher syndrome (USH) and retinitis pigmentosa (RP). Notably, splicing mutations account for 9% of all disease-causing mutations reported in the Human Gene Mutation Database (HGMD) [15,16]. They include both mutations in gene sequence (exons or introns) compromising the precision of intron removal during the AS (e.g. generating a reading frame shift resulting in a dysfunctional protein) and mutations in proteins directly involved in splicing mechanisms. Then, they can be grouped in cis-acting mutations and trans-acting mutations respectively. Of note, cis-acting mutations located in the exons may impair the splicing pattern without altering the coding sequence [17]. These mutations are hard to identify and are often miscategorized as missense, nonsense, or silent, although they should be considered as splicing mutations.

In this review we will focus on the retinal specific mechanisms leading to the exquisitely regulated execution of the alternative splicing program in the mammalian retina. Moreover, we will pay attention on one of the most challenging aspects of the inherited retinal genetic diagnosis: the identification of mutations altering splicing process or the production of alternative splicing products. Finally, we will summarize the current therapeutic approaches to modulate splicing events in retinal disorders.

2. Alternative Splicing of Retinal Genes

2.1. Alternative Splicing in the Retina

In the retina, AS represents a crucial regulatory step of gene expression during development and homeostasis. Over 95% of human multiexon genes undergo AS, resulting in mRNA splice variants that are variably expressed between different cell and tissue types [9,18]. Many different types of AS have been identified in the retina, including cassette exons [19], exon skipping [20] and intron retention events [21], mutually exclusive exons [22], alternative splice sites [23,24], alternative promoters [25,26] and alternative polyadenylation (polyA) sites [27] (Figure 1A).

Mechanisms generating different transcripts from a single locus serve to diversify mRNA sequences, and allow to display a range of protein isoforms that often differ in their function. Interestingly, a specialized type of splicing leading to incorporation of alternative microexons (exons that are ≤30 nt) has been shown to impact neuronal differentiation and function [28]. Even though they represent only 1% of all AS, microexons are the most highly conserved component of developmental alternative splicing regulation. Furthermore, they are enriched for lengths that are multiple of 3 nucleotides and are thus likely to produce alternative protein isoforms [29]. Microexons impact on specific protein regulatory domains, are associated with late neurogenesis and appear altered in neurological disorders [29–33] (Figure 1B).

Some splicing errors can cause frameshift and premature protein truncation, thus resulting in transcripts that are recognized by the cellular mRNA control machinery and are degraded by nonsense-mediated decay (NMD). Therefore, NMD can serve both as a mechanism to target non-functional mRNAs as well as to fine-tune gene expression by regulating the abundance of multiple transcript isoforms from a single gene locus [34].
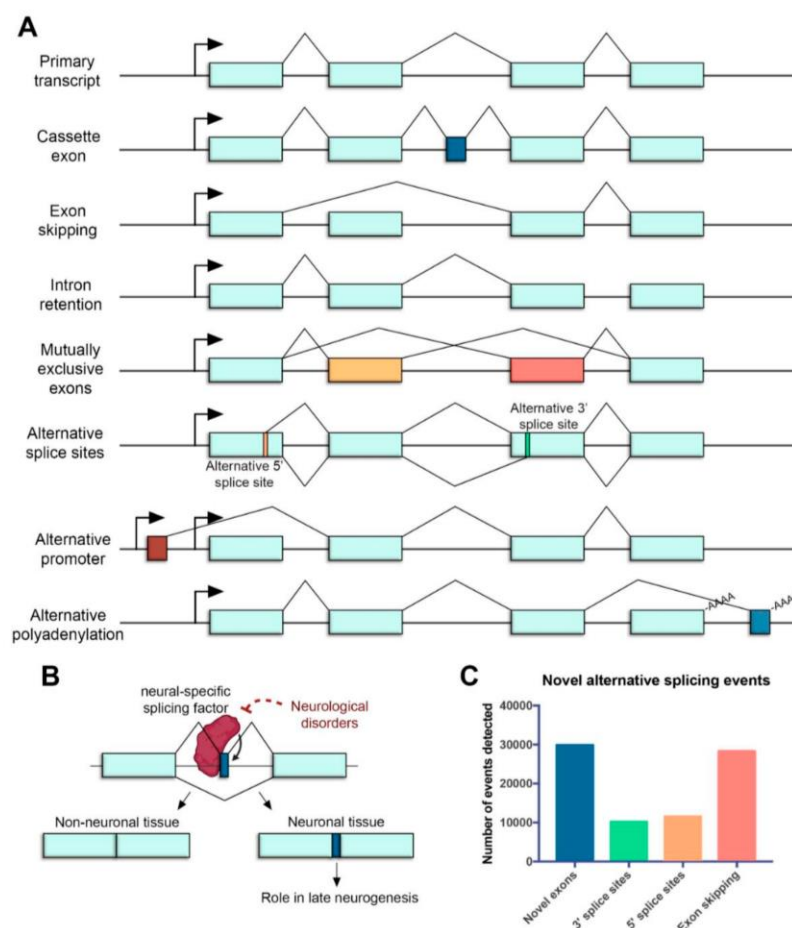
Figure 1. Alternative splicing in the neural retina. (**A**) Common mechanisms of alternative splicing in the retina. Boxes represent exons, lines represent introns, promoters are represented with arrows and polyadenylation sites are indicated with -AAAA. Exon regions included in the alternative transcript are colored. (**B**) Microexons have a role in late neurogenesis and are relevant in neurological disorders. The reduced expression of neural-specific splicing factors that regulate the inclusion of microexons is linked to the altered splicing of microexons in patients with neurological disorders. (**C**) Novel alternative splicing events in the human retina detected by RNA sequencing (data from [35]).

Some of these ASEs are particularly important in the retina. More than 7000 cassette exons (included only in some transcripts, Figure 1A) that showed differential AS patterns associated with distinct cell types and developmental stages have been reported [19]. Many of the cassette exons belong to retina-specific genes required for homeostasis maintenance in the adult retina, thus indicating that adult genes produce unique isoforms at certain stages, which may play a role in the differentiation maintenance rather than in development. Stage-specific alternative polyA sites have also been reported during retina development [27]. Alternative polyA generates transcript variants that may present different coding regions or 3′ untranslated regions (UTRs) (Figure 1A), whose variability can affect stability, localization, transport and translational properties of the mRNA. Authors found embryonic-specific polyA sites associated with genes involved in cell cycle and cytoskeleton, consistent with the high abundance of dividing progenitor cells. On the contrary, during the early postnatal period (when photoreceptors differentiate and mature), polyA sites were associated with genes involved in phototransduction and visual function [27]. These findings highlight the precise temporal and spatial regulation of AS and its importance controlling gene expression in the retina.

2.2. Novel Approaches to Detect Alternative Splicing Events

Next-generation sequencing (NGS) transcriptomic technologies have led to an explosion of new ASE findings in the retina. Authors have detected almost 80,000 novel ASEs, identifying of around 30,000 novel exons, 28,000 exon skipping events and 22,000 novel alternative splice sites (Figure 1C) [35]. Approximately 25% of these events maintained the open reading frame (ORF), encoding novel protein-coding transcript isoforms which may be critical for the retinal function. Most recent examples of new ASE findings in the retina producing protein-coding transcripts include Dp71 isoforms, which have been described to be differentially expressed in the mouse brain and retina [36]. Isl1 alternative splicing also produces two different isoforms in the mouse retina [37] and an alternative splicing product of Otx2, which plays critical roles in retina development, has been detected in neural retinal and retinal pigmented epithelial cells [38].

However, new emergent technologies suggest that the number of ASEs generating transcript diversity is even higher than expected. Typical RNA-seq read lengths are <200 bp, and such short reads are often unable to resolve the full-length sequence of RNA transcripts and determine specific isoforms [39]. In contrast, long-read sequencing is exceptionally useful in comprehensive characterization of RNA isoforms [40].

This technology, as provided by PacBio (Menlo Park, CA, USA) and Oxford Nanopore (Oxford, UK), is able to detect and quantify isoforms by sequencing molecules end to end from 3′ polyA to 5′ cap, thereby allowing the full-length transcript identification. A single long read covering a full-length transcript can then accurately define its transcription start site, all splice sites and the polyA site [41].

Long-read sequencing has already been proved useful to detect a previously unannotated isoform of the retinal degeneration gene CRB1. Mutations in CRB1 can cause a spectrum of inherited retinal dystrophies (IRDs), including RP and Leber Congenital Amaurosis (LCA). Using long-read sequencing, it was revealed that the most abundant retinal CRB1 isoform, CRB1-B, was a previously unknown variant containing unconventional 5′ and 3′ exons [42]. In mice, Crb1-A and -B isoforms have different promoters that drive their expression in Müller glia and photoreceptors, respectively. CRB1 is required for integrity of outer limiting membrane (OLM) junctions between Müller glia and photoreceptors [43]. In contrast to deletion of Crb1-A, which does not alter retinal function [44], deletion of Crb1-B causes retinal degeneration, recapitulating the human phenotype [42].

2.3. Implications of Retinal Alternative Splicing in Functional Analyses of IRD Genes

The complexity of the retinal alternative splicing system has a great impact in the diagnosis of IRDs. Many sequencing studies can readily identify the first but fail to identify the second mutant allele, which may be located within an exon of an as yet unidentified

transcript. Unannotated isoforms can encode uncharacterized protein-coding sequences or represent unknown expression patterns, overall causing disease-causative mutations to be either misinterpreted or completely missed out.

Experiment design and interpretation to understand gene function is also impaired by lack of comprehensive isoform sequence information. Unless transcript sequences are known, it is difficult to be certain that a "knockout" mouse allele fully eliminates expression of all isoforms. This was the situation encountered when generating a mouse model for the retinal dystrophy Cerkl gene, whose mutations can cause RP and Cone-Rod Dystrophy. The CERKL locus exhibits an incredibly high transcriptional complexity in human and mouse with alternative first exons, alternatively spliced exons, intron retention and additional splice sites [45]. To approach the function of the gene, the authors decided to create a knockout mouse model by deleting the Cerkl first exon and proximal promoter [46]. However, unreported alternative promoters directed basal expression of Cerkl in the retina, resulting in a knockdown model. Subsequently, the authors generated another Cerkl model using CRISPR/Cas9 [47]. The main message being that the comprehension of ASEs in the retina is essential to increase the genetic diagnosis of IRDs as well as to analyze gene regulation and function.

2.4. Splicing Factors Involved in the Processing of Retinal Transcripts

The splicing process is carried out by a dynamic ribonucleoprotein (RNP) machinery, the spliceosome, which is characterized by the orchestrated assembly and disassembly of several small nuclear RNPs (snRNPs) and associated protein co-factors. Fundamentally, the spliceosomal core is comprised of five different snRNPs named U1, U2, U4, U5 and U6 after the small nuclear RNAs (snRNAs) that compose them [48].

The assembly of the spliceosome system is a stepwise process in which the formation of different complexes between snRNPs and other proteins in pre-mRNA occurs. First, U1 snRNP recognizes the 5′ splice donor site (SDS) of the intron through base pairing of the U1 snRNA with the pre-mRNA. In addition, U1C, a protein from U1 snRNP, stabilizes this interaction [49]. Next, intronic 3′ splice acceptor site (SAS) is identified by U2 snRNP, SF1 and U2AF (U2 snRNP associated factors) [50]. These steps lead to the formation of complex E (Figure 2A).

Subsequently, U2 snRNA recognizes pre-mRNA sequences around the adenosine at the BS by base pairing and engages there generating the complex A (Figure 1B) [51]. U2 snRNP interacts with U1 snRNP to define intron boundaries forming the intron definition complex [52]. Afterwards, U5 and U4/U6 snRNPs are joined together as U4/U6·U5 tri-snRNP and recruited to the spliceosome to conform the complex B (Figure 2C), which is catalytically inactive [53]. Then, complex B becomes active (complex B*) throughout a sequence of compositional and conformational rearrangements. As a consequence of the release of U4 and U1 snRNPs from the spliceosome, U6 snRNP replaces U1 snRNP in the SDS [54]. These rearrangements lead to the interaction between U2 and U6 snRNP which will catalyse the splicing reaction [55].

Thereupon, complex B* (the active form of complex B) undergoes the first catalytic step of splicing, constituting the complex C (Figure 2D). Then, a set of conformational rearrangements occur in complex C. After the second catalytic step of splicing, 5′ and 3′ exons are ligated, intronic pre-mRNA is released in form of RNP and spliceosomal snRNPs (U2, U5 and U6) dissociate to be recycled for next splicing reactions (Figure 2E) [56].

Among all ubiquitously expressed splicing factors, some are of special relevance for the processing of retinal transcripts since mutations in them cause retinal dystrophies (this will be discussed in detail in Section 3.1). Interestingly, most of these factors are essential for the interaction between U4/U6 and U5 snRNPs and the stabilization of the U4/U6·U5 tri-snRNP, such as PRPF3, PRPF4, PRPF6, PRPF8 and PRPF31. Other examples include SNRNP200 and DHX38, RNA helicases that mediate different rearrangements of the spliceosome. PAP1, whose specific function in splicing is not well determined, is also involved in retinal dystrophies (reviewed in [57]). Finally, mutations in the spliceosomal

component *CWC27* (which interacts with human PRPF8 homolog in yeast [58]) cause a range of clinical phenotypes, including retinal degeneration [59]. Therefore, proper splicing of retinal transcripts is an important process for accurate retinal function and homeostasis, making the retina particularly sensitive to splicing alterations.
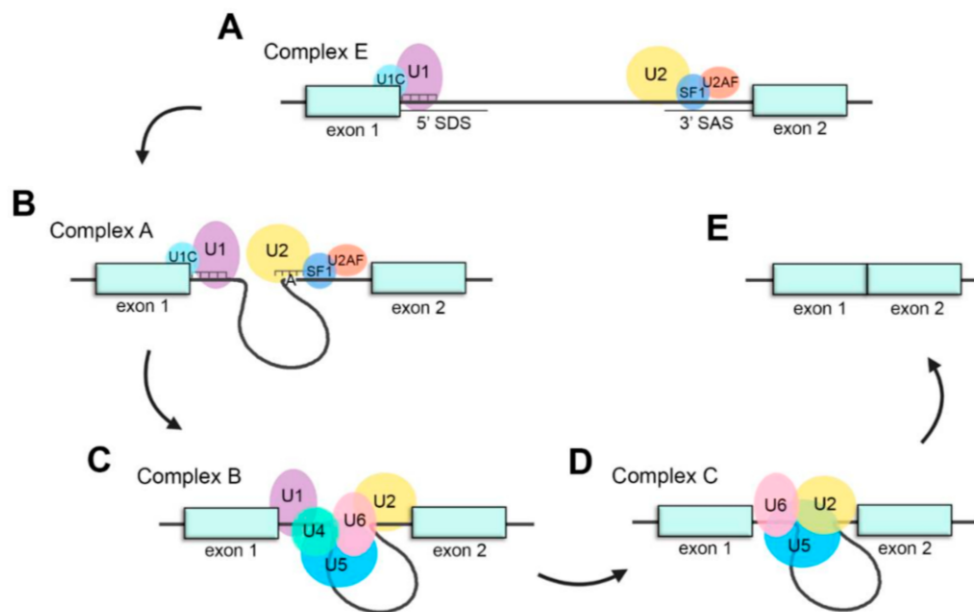
Figure 2. Schematic representation of the splicing process. (**A**) Assembly of the spliceosome: U1 snRNP recognizes the splice donor site (SDS) and U2 snRNP recognizes the splice acceptor site (SAS) to generate complex E. (**B**) U2 recognizes the adenosine at the branch-site and forms complex A. (**C**) The U4/U6·U5 tri-snRNP joins the spliceosome to form complex B. (**D**) U4 and U1 are released, U6 replaces U1 recognizing the SDS and interacts with U2, generating complex C and catalyzing the splicing reaction. (**E**) Exons are ligated, and intronic pre-mRNA and spliceosomal snRNPs are liberated.

2.5. Regulation of the Splicing

AS can be further modulated through cis-regulatory elements and trans-acting splicing factors, which are tissue-specific and contribute to the generation of tissue-specific isoforms. Cis-acting regulatory elements, also known as splicing regulatory elements (SREs), are specific sequences in the pre-mRNA located near the splice site that can enhance or silence splicing. Trans-acting regulatory proteins are recruited by enhancer or silencer SREs in order to steady or destabilize spliceosome assembly, hence controlling the inclusion or omission of differentially spliced exons. Therefore, spliceosome assembly represents a key control point in deciding between constitutive and alternative splicing [60,61].

2.5.1. Trans-Regulatory Elements: RNA-Binding Proteins

Processing of retinal transcripts is deeply regulated by means of a host of trans-acting specific regulatory proteins depending on the retinal cell type. These splicing regulatory proteins bind pre-mRNA to induce or supress different steps of the splicing machinery assembly and, concomitantly, activate or repress the inclusion of alternative exons. Depending on their function, we will distinguish between splicing activators and repressors [61].

In the retina, the splicing repressor PTBP1 is downregulated in photoreceptors and retinal neurons, whereas its homolog PTBP2, which regulates the inclusion of neuron-specific exons, is present in these cell types [62]. In fact, these splicing regulators act antagonistically, and downregulation of PTBP1 leads to the upregulation of PTBP2 [63].

Interestingly, some splicing regulators, such as RBFOX and NOVA1, are specific for some retinal neurons but not expressed in others, e.g., photoreceptors [62]. Typically, RB-FOX protein family has been described to be related to synaptogenesis and neurogenesis in CNS neurons. Lately, RBFOX1, RBFOX2 and RBFOX3 have been also reported to contribute to splicing of retinal transcripts in amacrine, horizontal and ganglion cells. RBFOX1 and RBFOX2 may be important for visual function, particularly for depth perception, while RBFOX3 is not [64–66]. In contrast, photoreceptors present specific factors that differ from those typically found in neurons. A well-studied example is the Musashi protein family (MSI1 and MSI2). These splicing factors are expressed in neuronal tissues in which they control stem-cell renewal and supress cell differentiation. However, and specifically concerning the retina, MS1 and MS2 regulate the splicing of photoreceptor-differentially spliced exons and are essential for photoreceptor function and homeostasis [62,67]. In addition, the upregulation of MS1 synergically interacts with the downregulation of PTBP1 in order to process photoreceptor-specific transcripts [68]. Summarizing, splicing regulators are differentially expressed depending on the retinal cell type and interact with each other to regulate all cell-specific splicing programs.

2.5.2. Cis-Regulatory Elements: Enhancers and Silencers

SREs, located in exons or introns, are able to promote (enhancers) or inhibit (silencers) splicing from neighboring splice sites [5]. There are at least four major types of cis-regulatory elements depending on their location and associated effect on splicing: exonic splicing enhancer (ESE), exonic splicing silencer (ESS), intronic splicing enhancer (ISE) and intronic splicing silencer (ISS). AS is often regulated by the combination of general and tissue-specific regulators. Furthermore, several disease-causing mutations that disrupt the cis-regulatory elements for splicing have been identified [69], indicating that they are critical for the function of the retina.

ESEs promote the recognition of exons with weak splice sites by assisting in the recruitment of splicing factors to the adjacent intron [70,71]. As an example concerning a relevant retinal gene, an ESE located in the *Nr2e3* gene has been recently reported [21]. NR2E3 is a transcription factor necessary for retinal development and homeostasis. Mutations in this gene can cause either RP or Enhanced S-cone Syndrome. The *NR2E3* locus produces two different protein coding isoforms: the full-length isoform, containing the 8 exons of the gene, and a shorter isoform, which lacks exon 8 and the functional domains encoded in this exon. Both isoforms have been detected in the retina, but the proportion of each transcript may vary depending on the developmental stage. The predicted ESE, located in exon 8 of *Nr2e3*, most probably promotes the splicing between exons 7 and 8, thus facilitating the production of the full-length isoform. A deletion of the ESE causes an increase of intron 7 retention, producing an imbalance between the two isoforms that may be associated with retinal disease [21].

3. The Role of Alternative Splicing in Retinal Disease

Around 9% of all disease-causing mutations are estimated to alter pre-mRNA splicing [15,16]. These mutations can disrupt or alter cis-regulatory sequences, or the binding of trans-acting splicing factors. Mutations affecting cis-acting splice sites or regulatory sequences can lead to inappropriate exon skipping, intron inclusion, exon inclusion or activation of cryptic splice sites (some of them in deep intronic positions), usually leading to frameshifts and premature termination. Mutations causing IRDs can also affect unannotated isoforms, which may cause misinterpretation of the genetic diagnosis. Indeed, most of the genes causing IRDs undergo alternative splicing (Table 1 compiles alternative splicing events of IRD genes). Around 90% of the IRD genes produce more than one transcript (Figure 3A), and for most of them (54%), between two to 10 alternatively spliced transcripts have been reported. Indeed, the multiplicity of transcripts also impacts on the multiplicity of encoded proteins, and at least 85% of the IRD genes display several protein isoforms (Figure 3B). Most of the genes produce between two and five distinct coding transcripts,

but 9% of them are able to generate more than 10 singular coding transcripts that translate into proteins that most probably carry out differential functions. Therefore, understanding AS and isoform sequence information is fundamental to comprehend both normal gene function and the phenotypic consequences of gene mutations.
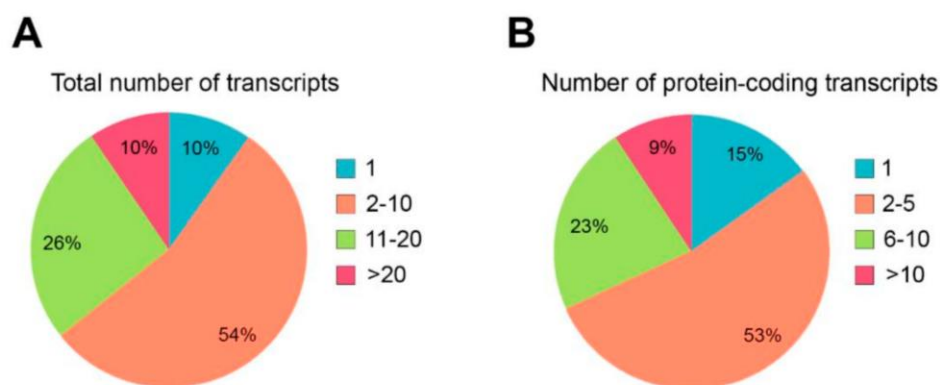
Figure 3. Quantification of alternative splicing events described in genes causing IRDs. (**A**) Percentage of IRD genes presenting alternative splicing events. Only 10% of the IRD genes produces a unique transcript, and most genes (54%) generate between 2 and 10 transcripts. (**B**) Percentage of IRD genes showing diverse protein-coding transcripts. Only 15% of the IRD genes produce one protein isoform. Most of the genes (53%) produce between 2 and 5 diverse protein isoforms. The list of genes was obtained from https://sph.uth.edu/retnet/ (accessed on 20 January 2021). Information about the number and type of the transcripts was obtained from https://www.ensembl.org/ (accessed on 20 January 2021).

Table 1. List of genes causative of IRDs (https://sph.uth.edu/retnet/ (accessed on 20 January 2021)) showing location, associated disease, number of splice variants and coding transcripts. Genes mentioned in the main text are indicated in bold.

Gene	Location	Associated Disease	Splice Variants	Coding Transcripts
ABCA4	**1p22.1**	**Recessive Stargardt disease, juvenile and late onset; recessive macular dystrophy; recessive retinitis pigmentosa; recessive fundus flavimaculatus; recessive cone-rod dystrophy**	8	3
ABCC6	16p13.11	Recessive pseudoxanthoma elasticum; dominant pseudoxanthoma elasticum	9	4
ABHD12	20p11.21	Recessive syndromic PHARC; recessive Usher syndrome, type 3-like	24	17
ACBD5	10p12.1	Recessive cone-rod dystrophy with psychomotor delay	8	7
ACO2	22q13.2	Recessive optic atrophy; recessive cerebellar degeneration with optic atrophy	7	2
ADAM9	8p11.23	Recessive cone-rod dystrophy	9	3
ADAMTS18	16q23.1	Recessive Knobloch syndrome; recessive retinal dystrophy, early onset	9	3
ADGRA3	4p15.2	Recessive retinitis pigmentosa	13	4
ADGRV1	5q14.3	Recessive Usher syndrome, type 2; dominant/recessive febrile convulsions	37	10
ADIPOR1	1q32.1	Recessive retinitis pigmentosa, syndromic, Bardet-Biedl like; dominant retinitis pigmentosa	5	4
AFG3L2	18p11.21	Dominant optic atrophy, non-syndromic; dominant spinocerebellar ataxia; recessive spastic ataxia	4	2
AGBL5	2p23.3	Recessive retinitis pigmentosa	10	7

Table 1. *Cont.*

Gene	Location	Associated Disease	Splice Variants	Coding Transcripts
AHI1	6q23.3	Recessive Joubert syndrome	17	10
AHR	7p21.1	Recessive retinitis pigmentosa	7	2
AIPL1	17p13.2	Recessive Leber congenital amaurosis; dominant cone-rod dystrophy	11	10
ALMS1	2p13.1	Recessive Alström syndrome	12	4
ARHGEF18	19p13.2	Recessive retinitis pigmentosa	6	5
ARL2BP	16q13.3	Recessive retinitis pigmentosa	4	3
ARL3	10q24.32	Dominant retinitis pigmentosa	1	1
ARL6	3q11.2	Recessive Bardet-Biedl syndrome; recessive retinitis pigmentosa	9	6
ARMS2	10q26.13	Age-related macular degeneration, complex etiology	1	1
ARSG	17q24.2	Recessive Usher syndrome, atypical	9	4
ASRGL1	11q12.3	Recessive retinal degeneration	11	6
ATF6	1q23.3	Recessive achromatopsia	2	1
ATOH7	10q21	Recessive nonsyndromal congenital retinal nonattachment	1	1
ATXN7	3p14.1	Dominant spinocerebellar ataxia w/ macular dystrophy or retinal degeneration	20	7
BBIP1	10q25.2	Recessive Bardet-Biedl syndrome	15	10
BBS1	11q13	Recessive Bardet-Biedl syndrome; recessive retinitis pigmentosa	25	7
BBS10	12q21.2	Recessive Bardet-Biedl syndrome	1	1
BBS12	4q27	Recessive Bardet-Biedl syndrome	3	3
BBS2	16q13	Recessive Bardet-Biedl syndrome; recessive retinitis pigmentosa	21	5
BBS4	15q24.1	Recessive Bardet-Biedl syndrome	18	5
BBS5	2q31.1	Recessive Bardet-Biedl syndrome	6	2
BBS7	4q27	Recessive Bardet Biedl syndrome	6	3
BBS8	**14q31.3**	**Recessive Bardet Biedl syndrome**	**13**	**7**
BBS9	7p14.3	Recessive Bardet Biedl syndrome	29	14
BEST1	11q12.3	Dominant macular dystrophy, Best type; dominant vitreoretinochoroidopathy; recessive bestrophinopathy; recessive retinitis pigmentosa; dominant retinitis pigmentosa	8	4
C12orf65	12q24.31	Recessive spastic paraplegia, neuropathy and optic atrophy	8	6
C1QTNF5	11q23.3	Dominant macular dystrophy, late onset; dominant macular dystrophy with lens zonules	4	3
C2	6p21.32	Age-related macular degeneration, complex etiology	17	11
C3	19p13.3	Age-related macular degeneration, complex etiology	18	5
C8orf37	8q22.1	Recessive cone-rod dystrophy; recessive retinitis pigmentosa with early macular involvement; recessive Bardet-Biedl syndrome	1	1
CA4	17q23.2	Dominant retinitis pigmentosa	6	4
CABP4	11q13.1	Recessive congenital stationary night blindness; recessive congenital cone-rod synaptic disease; recessive Leber congenital amaurosis	7	2
CACNA1F	Xp11.23	X-linked congenital stationary night blindness, incomplete; AIED-like disease; severe congenital stationary night blindness; X-linked progressive cone-rod dystrophy	6	4
CACNA2D4	12p13.33	Recessive cone dystrophy	26	9
CAPN5	11q13.5	Dominant neovascular inflammatory vitreoretinopathy	8	5

Table 1. *Cont.*

Gene	Location	Associated Disease	Splice Variants	Coding Transcripts
CC2D2A	4p15.33	Recessive retinitis pigmentosa and mental retardation; recessive Joubert syndrome	23	13
CCT2	12q15	Recessive Leber congenital amaurosis	14	3
CDH23	10q22.1	Recessive Usher syndrome, type 1d; recessive deafness without retinitis pigmentosa; digenic Usher syndrome with PCDH15	19	14
CDH3	16q22.1	Recessive macular dystrophy, juvenile with hypotrichosis	10	4
CDHR1	10q23.1	Recessive cone-rod dystrophy	7	4
CEP164	11q23.3	Recessive nephronophthisis with retinal degeneration	14	7
CEP19	3q29	Recessive Bardet-Biedl syndrome	2	2
CEP250	20q11.22	Recessive Usher syndrome, atypical	14	8
CEP290	**12q21.32**	**Recessive Senior-Loken syndrome; recessive Joubert syndrome; recessive Leber congenital amaurosis; recessive Meckel syndrome**	**34**	**13**
CEP78	9q21.2	Recessive cone-rod dystrophy with hearing loss; recessive Usher syndrome, atypical	24	14
CERKL	**2q31.3**	**Recessive retinitis pigmentosa; recessive cone-rod dystrophy with inner retinopathy**	**14**	**5**
CFAP410	21q22.3	Recessive cone-rod dystrophy	7	3
CFB	6p21.32	Age-related macular degeneration, complex etiology	14	4
CFH	1q31.3	Age-related macular degeneration, complex etiology; recessive drusen, early-onset	6	3
CHM	**Xq21.2**	**Choroideremia**	**5**	**2**
CIB2	15q25.1	Recessive Usher syndrome, type 1J	10	7
CISD2	4q22-q24	Recessive Wolfram syndrome	5	2
CLCC1	1p13.3	Recessive retinitis pigmentosa, severe	30	21
CLN3	16p11.2	Recessive Batten disease (ceroid-lipofuscinosis, neuronal 3), juvenile	62	20
CLRN1	3q25.1	Recessive Usher syndrome, type 3; recessive retinitis pigmentosa	8	4
CLUAP1	16p13.3	Recessive Leber congenital amaurosis	12	7
CNGA1	4p12	Recessive retinitis pigmentosa	7	6
CNGA3	2q11.2	Recessive achromatopsia; recessive cone-rod dystrophy; protein: cone photoreceptor cgmp-gated cation channel alpha subunit [Gene]	4	2
CNGB1	16q21	Recessive retinitis pigmentosa	9	6
CNGB3	8q21.3	Recessive achromatopsia Pingelapese; recessive progressive cone dystrophy	3	2
CNNM4	2q11.2	Recessive cone-rod dystrophy and amelogenesis imperfecta syndrome	4	1
COL11A1	1p21.1	Dominant Stickler syndrome, type II; dominant Marshall syndrome	14	10
COL2A1	12q13.11	Dominant Stickler syndrome, type I; dominant bone dysplasias, developmental disorders, osteoarthritic diseases, and syndromic disorders	9	2
COL9A1	6q13	Recessive Stickler syndrome; dominant multiple epiphyseal dysplasia (MED)	11	3
CRB1	**1q31.3**	**Recessive retinitis pigmentosa with para-arteriolar preservation of the RPE (PPRPE); recessive retinitis pigmentosa; recessive Leber congenital amaurosis; dominant pigmented paravenous chorioretinal atrophy**	**11**	**7**

<div align="center">**Table 1.** *Cont.*</div>

Gene	Location	Associated Disease	Splice Variants	Coding Transcripts
CRX	19q13.32	Dominant cone-rod dystrophy; recessive, dominant and de novo Leber congenital amaurosis; dominant retinitis pigmentosa	7	4
CSPP1	8q13.1-q13.2	Recessive Jobert syndrome	16	8
CTNNA1	5q31.2	Dominant macular dystrophy, butterfly-shaped	44	27
CWC27	**5q12.3**	**Retinitis pigmentosa with or without skeletal anomalies**	**5**	**2**
CYP4V2	4q35.2	Recessive Bietti crystalline corneoretinal dystrophy; recessive retinitis pigmentosa	4	1
DHDDS	1p36.11	Recessive retinitis pigmentosa	25	16
DHX38	**16q22.2**	**Recessive retinitis pigmentosa, early onset with macular coloboma**	**14**	**6**
DMD	Xp21.2-p21.1	Oregon eye disease (probably)	32	20
DNM1L	22q12.1-q13.1	Dominant optic atrophy	30	11
DRAM2	1p13.3	Recessive macular dystrophy, early adult onset	11	2
DTHD1	4p14	Recessive Leber congenital amaurosis with myopathy	6	4
DYNC2H1	**11q22.3**	**Syndromic and non syndromic retinal degeneration**	**11**	**5**
EFEMP1	2p16.1	Dominant radial, macular drusen; dominant Doyne honeycomb retinal degeneration (Malattia Leventinese)	14	10
ELOVL1	1p34.2	Dominant optic atrophy, deafness, ichthyosis and neuronal disorders	16	3
ELOVL4	6q14.1	Dominant macular dystrophy, Stargardt-like; recessive spinocerebellar ataxia; recessive ichthyosis, quadriplegia and retardation	1	1
EMC1	1p36.13	Recessive retinitis pigmentosa	13	5
ERCC6	10q11.23	Age-related macular degeneration, complex etiology; Cockayne syndrome, recessive	12	4
ESPN	1p36.31	Recessive Usher syndrome	17	14
EXOSC2	9q34.12	Recessive retinitis pigmentosa with hearing loss and additional disabilities	11	6
EYS	6q12	Recessive retinitis pigmentosa	11	5
FAM161A	2p15	Recessive retinitis pigmentosa	7	2
FBLN5	14q32.12	Familial macular dystrophy, age-related	9	4
FLVCR1	1q32.3	Recessive retinitis pigmentosa with posterior column ataxia (PCARP)	5	2
FSCN2	17q25.3	Dominant retinitis pigmentosa; dominant macular dystrophy	3	2
FZD4	11p13-p12	Dominant familial exudative vitreoretinopathy	1	1
FZD4	11q14.2	Dominant familial exudative vitreoretinopathy	1	1
GDF6	8q22.1	Recessive Leber congenital amaurosis; dominant Klippel-Feil syndrome; dominant microphthalmia	3	3
GNAT1	3p21.31	Dominant congenital stationary night blindness, Nougaret type; recessive congenital stationary night blindness	5	3
GNAT2	1p13.3	Recessive achromatopsia	2	2
GNB3	12p13.31	Recessive congenital stationary night blindness	10	6
GNPTG	16p13.3	Recessive retinitis pigmentosa and skeletal abnormalities; recessive mucolipidosis III gamma	9	3
GPR179	17q12	Recessive complete congenital stationary night blindness	1	1
GRK1	13q34	Recessive congenital stationary night blindness, Oguchi type	3	1
GRM6	5q35.3	Recessive congenital stationary night blindness	6	3

Table 1. *Cont.*

Gene	Location	Associated Disease	Splice Variants	Coding Transcripts
GUCA1A	6p21.1	Dominant cone dystrophy; dominant cone-rod dystrophy	2	2
GUCA1B	6p21.1	Dominant retinitis pigmentosa; dominant macular dystrophy	1	1
GUCY2D	17p13	Dominant central areolar choroidal dystrophy	2	1
GUCY2D	17p13.1	Recessive Leber congenital amaurosis; dominant cone-rod dystrophy	2	1
HARS1	5q31.3	Recessive Usher syndrome	30	13
HGSNAT	8p11.21-p11.1	Recessive retinitis pigmentosa, non-syndromic; recessive mucopolysaccharidosis	10	4
HK1	10q22.1	Dominant retinitis pigmentosa; recessive nonspherocytic hemolytic anemia; recessive hereditary neuropathy (Russe type)	18	10
HMCN1	1q25.3-q31.1	Dominant macular dystrophy, age-related	5	2
HMX1	4p16.1	Recessive oculoauricular syndrome	2	2
HTRA1	10q26.13	Age-related macular degeneration, complex etiology	3	3
IDH3B	20p13	Recessive retinitis pigmentosa	12	4
IFT140	16p13.3	Recessive Mainzer-Saldino syndrome; recessive retinitis pigmentosa; recessive Leber congenital amaurosis	11	5
IFT172	2p33.3	Recessive Bardet-Biedl syndrome; recessive retinitis pigmentosa	34	6
IFT27	22q12.3	Recessive Bardet-Biedl syndrome	12	5
IFT81	12q24.11	Recessive cone-rod dystrophy; recessive spectrum of ciliopathies including retinal dystrophy	9	4
IMPDH1	7q32.1	Dominant retinitis pigmentosa; dominant Leber congenital amaurosis	18	11
IMPG1	6q14.1	Dominant macular dystrophy, vitelliform; recessive macular dystrophy, vitelliform; dominant retinitis pigmentosa	4	4
IMPG2	3q12.3	Recessive retinitis pigmentosa	1	1
INPP5E	9q34.3	Recessive Joubert syndrome; recessive MORM syndrome	6	3
INVS	9q31.1	Recessive Senior-Loken syndrome; recessive nephronophthisis	7	3
IQCB1	3q13.33	Recessive Senior-Loken syndrome; recessive Leber congenital amaurosis	7	5
ITM2B	13q14.2	Dominant retinal dystrophy; dominant dementia, familial	11	4
JAG1	20p12.2	Dominant Alagille syndrome	9	2
KCNJ13	2q37.1	Dominant vitreoretinal degeneration, snowflake; recessive Leber congenital amaurosis	5	5
KCNV2	9p24.2	Recessive cone dystrophy with supernormal rod electroretinogram	1	1
KIAA1549	7q34	Recessive retinitis pigmentosa; protein: KIAA1549 protein	2	2
KIF11	10q23.33	Dominant microcephaly, lymphedema and chorioretinopathy	1	1
KIZ	20p11.23	Recessive retinitis pigmentosa	15	8
KLHL7	7p15.3	Dominant retinitis pigmentosa	13	5
LAMA1	18p11.31-p11.23	Recessive retinal dystrophy and cerebellar dysplasia	9	2
LCA5	6q14.1	Recessive Leber congenital amaurosis	3	3
LRAT	4q32.1	Recessive retinitis pigmentosa, severe early-onset; recessive Leber congenital amaurosis	8	3
LRIT3	4q25	Recessive congenital stationary night blindness	2	2
LRP5	11q13.2	Dominant familial exudative vitreoretinopathy; dominant high bone mass trait; recessive osteoporosis-pseudoglioma syndrome; recessive familial exudative vitreoretinopathy	7	2

Table 1. *Cont.*

Gene	Location	Associated Disease	Splice Variants	Coding Transcripts
LZTFL1	3p21.31	Recessive Bardet-Biedl syndrome with developmental anomalies	16	5
MAK	6p24.2	Recessive retinits pigmentosa	7	5
MAPKAPK3	3p21.2	Dominant Martinique retinal dystrophy and retinitis pigmentosa	8	6
MERTK	2q13	Recessive retinitis pigmentosa; recessive rod-cone dystrophy, early onset	7	5
MFN2	1p36.22	Dominant optic atrophy with neuropathy and myopathy; dominant Charcot-Marie-Tooth disease	33	17
MFRP	11q23.3	Recessive microphthalmos and retinal disease syndrome; recessive nanophthalmos	6	3
MFSD8	4q28.2	Recessive macular dystrophy	62	24
MKKS	20p12.2	Recessive Bardet-Biedl syndrome	4	3
MKS1	17q22	Recessive Bardet-Biedl syndrome; recessive Meckel syndrome	13	7
MMP19	12q13.13-q14.3	Dominant cavitary optic disc anomalies	9	3
MT-ATP6	mitochondrion	Retinitis pigmentosa with developmental and neurological abnormalities; Leigh syndrome; Leber hereditary optic neuropathy	1	1
MT-TH	mitochondrion	Pigmentary retinopathy and sensorineural hearing loss	1	-
MT-TL1	mitochondrion	Macular pattern dystrophy with type II diabetes and deafness	1	-
MT-TP	mitochondrion	Retinitis pigmentosa with deafness and neurological abnormalities	1	-
MT-TS2	mitochondrion	Retinitis pigmentosa with progressive sensorineural hearing loss	1	-
MTTP	4q23	Recessive abetalipoproteinemia	11	5
MVK	12q24.11	Recessive retinitis pigmentosa; recessive mevalonic aciduria; recessive hyper-igd syndrome	17	10
MYO7A	11q13.5	Recessive Usher syndrome, type 1b; recessive congenital deafness without retinitis pigmentosa; recessive atypical Usher syndrome (USH3-like)	14	8
NBAS	2p24.3	Recessive optic atrophy and retinal dystrophy, syndromic;	9	7
NDP	Xp11.3	Norrie disease; familial exudative vitreoretinopathy; Coats disease	3	2
NEK2	1q32.3	Recessive retinitis pigmentosa; protein: NIMA (never in mitosis gene A)-related kinase 2 [Gene]	5	3
NEUROD1	2q31.3	Recessive retinitis pigmentosa	2	1
NMNAT1	1p36.22	Recessive Leber congenital amaurosis	5	3
NPHP1	2q13	Recessive Senior-Loken syndrome; recessive nephronophthisis, juvenile; recessive Joubert syndrome; recessive Bardet-Biedl syndrome	22	12
NPHP3	3q22.1	Recessive Senior-Loken syndrome; recessive nephronophthisis, adolescent	11	3
NPHP4	1p36.31	Recessive Senior-Loken syndrome, recessive nephronophthisis	11	2
NR2E3	**15q23**	**Recessive enhanced S-cone syndrome (ESCS); recessive retinitis pigmentosa in Portuguese Crypto Jews; recessive Goldmann-Favre syndrome; dominant retinitis pigmentosa; combined dominant and recessive retinopathy**	**4**	**3**
NR2F1	5q15	Dominant optic atrophy with intellectual disability and developmental delay	6	3
NRL	14q11.2	Dominant retinitis pigmentosa; recessive retinitis pigmentosa	6	6
NYX	Xp11.4	X-linked congenital stationary night blindness	3	2
OAT	10q26.13	Recessive gyrate atrophy	8	2

Table 1. *Cont.*

Gene	Location	Associated Disease	Splice Variants	Coding Transcripts
OFD1	Xp22.2	Jobert syndrome; orofaciodigital syndrome 1, Simpson-Golabi-Behmel syndrome 2; X-linked retinitis pigmentosa, severe	9	4
OPA1	**3q29**	**Dominant optic atrophy, Kjer type; dominant optic atrophy with sensorineural hearing loss**	**32**	**14**
OPA3	19q13.32	Recessive optic atrophy with ataxia and 3-methylglutaconic aciduria; dominant optic atrophy with cataract, ataxia and areflexia	3	3
OPN1LW	Xq28	Deuteranopia and rare macular dystrophy in blue cone monochromacy with loss of locus control element	3	2
OPN1MW	Xq28	Protanopia and rare macular dystrophy in blue cone monochromacy with loss of locus control element	3	2
OPN1SW	7q32.1	Dominant tritanopia	1	1
OTX2	14q22.3	Dominant Leber congenital amaurosis and pituitary dysfunction; recessive microphthalmia; dominant pattern dystrophy	11	11
PANK2	20p13	Recessive HARP (hypoprebetalipoproteinemia, acanthocytosis, retinitis pigmentosa, and palladial degeneration); recessive Hallervorden-Spatz syndrome	12	6
PAX2	10q24.31	Dominant renal-coloboma syndrome	9	6
PCARE	2p23.2	Recessive retinitis pigmentosa	2	1
PCDH15	10q21.1	Recessive Usher syndrome, type 1f; recessive deafness without retinitis pigmentosa; digenic Usher syndrome with CDH23	36	31
PCYT1A	3q29	Recessive cone-rod dystrophy with skeletal disease	16	9
PDE6A	5q33.1	Recessive retinitis pigmentosa	5	3
PDE6B	4p16.3	Recessive retinitis pigmentosa; dominant congenital stationary night blindness	12	8
PDE6C	10q23.33	Recessive cone dystrophy, early onset; recessive complete and incomplete achromatopsia	2	1
PDE6G	17q25.3	Recessive retinitis pigmentosa	5	3
PDE6H	12p12.3	Recessive achromatopsia, incomplete	1	1
PDZD7	10q24.31	Recessive non-syndromic deafness	9	7
PEX1	7q21.2	Recessive Refsum disease, infantile form	10	3
PEX2	8q21.13	Recessive Refsum disease, infantile form	6	5
PEX7	6q23.3	Recessive Refsum disease, adult form	3	3
PGK1	Xq21.1	Retinitis pigmentosa with myopathy	6	2
PHYH	10p13	Recessive Refsum disease, adult form	7	5
PITPNM3	17p13.2	Dominant cone-rod dystrophy	5	3
PLA2G5	1p36.13-p36.12	Recessive benign fleck retina	8	1
PLK4	4q28.2	Recessive microcephaly, growth failure and retinopathy	11	6
PNPLA6	19p13.2	Recessive Boucher-Neuhauser syndrome with chorioretinal dystrophy	25	14
POC1B	12q21.33	Recessive cone-rod dystrophy; recessive Joubert syndrome	14	4
POC5	5q13.3	Recessive syndromic disease with retinitis pigmentosa	14	7
POMGNT1	1p34.1	Recessive retinitis pigmentosa	10	3
PRCD	17q25.1	Recessive retinitis pigmentosa	13	2
PRDM13	6q16.2	Dominant macular dystrophy, North Carolina type; dominant progressive bifocal chorioretinal atrophy	2	1

Table 1. *Cont.*

Gene	Location	Associated Disease	Splice Variants	Coding Transcripts
PROM1	4p15.32	Recessive retinitis pigmentosa with macular degeneration; dominant Stargardt-like macular dystrophy; dominant macular dystrophy, bull's-eye; dominant cone-rod dystrophy	22	11
PRPF3	**1q21.2**	**Dominant retinitis pigmentosa**	**7**	**1**
PRPF31	**19q13.42**	**Dominant retinitis pigmentosa**	**9**	**6**
PRPF4	**9q32**	**Dominant retinitis pigmentosa**	**3**	**2**
PRPF6	**20q13.33**	**Dominant retinits pigmentosa**	**1**	**1**
PRPF8	**17p13.3**	**Dominant retinitis pigmentosa**	**16**	**5**
PRPH2	6p21.1	Dominant retinitis pigmentosa; dominant macular dystrophy; digenic RP with ROM1; dominant adult vitelliform macular dystrophy; dominant cone-rod dystrophy; dominant central areolar choroidal dystrophy; recessive LCA	1	1
PRPS1	Xq22.3	Neuropathy, optic atrophy, deafness and retinitis pigmentosa	25	10
RAB28	4p15.33	Recessive cone-rod dystrophy	8	7
RAX2	19p13.3	Cone-rod dystrophy, isolated; age-related macular degeneration, isolated	2	2
RB1	13q14.2	Dominant germline or somatic retinoblastoma; benign retinoma; pinealoma; osteogenic sarcoma	9	4
RBP3	10q11.22	Recessive retinitis pigmentosa	1	1
RBP4	10q23.33	Recessive RPE degeneration	4	4
RCBTB1	13q14.2	Recessive syndromic and non-syndromic retinal dystrophy; dominant familial exudative vitreoretinopathy and Coats disease	4	2
RD3	1q32.3	Recessive Leber congenital amaurosis	2	1
RDH11	14q24.1	Recessive retinitis pigmentosa, syndromicxd	11	6
RDH12	14q24.1	Recessive Leber congenital amaurosis with severe childhood retinal dystrophy; dominant retinitis pigmentosaxd	4	2
RDH5	12q13.2	Recessive fundus albipunctatus; recessive cone dystrophy, late onset	11	4
REEP6	19p13.3	Recessive retinitis pigmentosa	4	2
RGR	10q23.1	Recessive retinitis pigmentosa; dominant choroidal sclerosis	18	9
RGS9	17q24.1	Recessive delayed cone adaptation	12	4
RGS9BP	19q13.12	Recessive delayed cone adaptation	1	1
RHO	**3q22.1**	**Dominant retinitis pigmentosa; dominant congenital stationary night blindness; recessive retinitis pigmentosa**	**1**	**1**
RIMS1	6q13	Dominant cone-rod dystrophy	20	16
RLBP1	15q26.1	Recessive retinitis pigmentosa; recessive Bothnia dystrophy; recessive retinitis punctata albescens; recessive Newfoundland rod-cone dystrophy	4	2
ROM1	11q12.3	Dominant retinitis pigmentosa; digenic retinitis pigmentosa with PRPH2	5	4
RP1	8q12.1	Dominant retinitis pigmentosa; recessive retinitis pigmentosa	8	3
RP1L1	8p23.1	Dominant occult macular dystrophy; recessive retinitis pigmentosa	2	1
RP2	Xp11.23	X-linked retinitis pigmentosa; X-linked retinitis pigmentosa, dominant	1	1
RP9	7p14.3	Dominant retinitis pigmentosa	4	2
RPE65	1p31.2	Recessive Leber congenital amaurosis; recessive retinitis pigmentosa; dominant retinitis pigmentosa with choroidal involvement	1	1

ANNEX

Table 1. *Cont.*

Gene	Location	Associated Disease	Splice Variants	Coding Transcripts
RPGR	**Xp11.4**	**X-linked retinitis pigmentosa, recessive; X-linked retinitis pigmentosa, dominant; X-linked cone dystrophy 1; X-linked atrophic macular dystrophy, recessive**	**10**	**9**
RPGRIP1	14q11.2	Recessive Leber congenital amaurosis; recessive cone-rod dystrophy	13	8
RPGRIP1L	16q12.2	Recessive Joubert syndrome; recesssive Meckel syndrome	12	10
RS1	Xp22.13	Retinoschisis	2	1
RTN4IP1	6q21	Recessive optic atrophy, non-syndromic and syndromic	4	2
SAG	2q37.1	Recessive Oguchi disease; recessive retinitis pigmentosa; dominant retinitis pigmentosa	16	3
SAMD11	1p36.33	Recessive retinitis pigmentosa	17	13
SDCCAG8	1q43	Recessive nephronophthisis, ciliopathy-related; recessive Bardet-Biedl syndrome	11	3
SEMA4A	1q22	Dominant retinitis pigmentosa; dominant cone-rod dystrophy	16	9
SLC24A1	15q22.31	Recessive congenital stationary night blindness	12	7
SLC25A46	5q22.1	Recessive syndromic optic atrophy; protein	8	5
SLC38A8	16q23.2-q24.2	Recessive foveal hypoplasia and anterior segment dysgenesis	4	3
SLC7A14	3q26.2	Recessive retinitis pigmentosa	2	1
SNRNP200	**2q11.2**	**Dominant retinitis pigmentosa**	**9**	**2**
SPATA7	14q31.3	Recessive Leber congenital amaurosis; recessive RP, juvenile	22	8
SPP2	2q37.1	Dominant retinitis pigmentosa	4	3
TEAD1	11p15.3	Dominant atrophia areata	6	5
TIMM8A	Xq22.1	Optic atrophy with deafness-dystonia syndrome	4	2
TIMP3	22q12.3	Dominant Sorsby's fundus dystrophy	1	1
TLR3	4q35.1	Age-related macular degeneration, complex etiology	5	3
TLR4	9q33.1	Age-related macular degeneration, complex etiology	4	3
TMEM126A	11q14.1	Recessive non-syndromic optic atrophy	6	3
TMEM216	11q12.2	Recessive Joubert syndrome; recessive Meckel syndrome	5	2
TMEM237	2q33.1	Recessive Jobert syndrome	13	3
TOPORS	9p21.1	Dominant retinitis pigmentosa	2	2
TREX1	3p21.31	Dominant retinal vasculopathy with cerebral leukodystrophy; dominant Aicardi-Goutiere syndrome 1, dominant chilblain lupus	6	6
TRIM32	9q33.1	Recessive Bardet-Biedl syndrome; recessive limb-girdle muscular dystrophy	3	3
TRNT1	3p26.2	Recessive retinitis pigmentosa with erythrocytic microcytosis; recessive retinitis pigmentosa, non-syndromic	20	7
TRPM1	15q13.3	Recessive congenital stationary night blindness, complete	12	7
TSPAN12	7q31.31	Dominant familial exudative vitreoretinopathy	7	6
TTC8	14q32.11	Recessive Bardet-Biedl syndrome; recessive retinitis pigmentosa	13	7
TTLL5	14q24.3	Recessive cone and cone-rod dystrophy	22	7
TTPA	8q12.3	Recessive retinitis pigmentosa and/or recessive or dominant ataxia	2	1
TUB	11p15.4	Recessive retinal dystrophy and obesity	3	3
TUBGCP4	15q15.3	Recessive chorioretinopathy and microcephaly	12	4

Table 1. *Cont.*

Gene	Location	Associated Disease	Splice Variants	Coding Transcripts
TUBGCP6	22q13.33	Recessive microcephaly with chorioretinopathy	8	4
TULP1	6p21.31	Recessive retinitis pigmentosa; recessive Leber congenital amaurosis	8	4
UNC119	17q11.2	Dominant cone-rod dystrophy	8	6
USH1C	11p15.1	Recessive Usher syndrome, Acadian; recessive deafness without retinitis pigmentosa	11	5
USH1G	17q25.1	Recessive Usher syndrome	2	1
USH2A	**1q41**	**Recessive Usher syndrome, type 2a; recessive retinitis pigmentosa**	**5**	**2**
VCAN	5q14.3	Dominant Wagner disease and erosive vitreoretinopathy	12	7
WDPCP	2p15	Recessive Bardet-Biedl syndrome	17	7
WDR19	4p14	Recessive renal, skeletal and retinal anomalies; recessive Senior-Loken syndrome	18	4
WFS1	4p16.1	Recessive Wolfram syndrome; dominant low frequency sensorineural hearing loss	9	6
WHRN	9q32	Recessive Usher syndrome, type 2; recessive deafness without retinitis pigmentosa	8	5
ZNF408	11p11.2	Dominant familial exudative vitreoretinopathy; recessive retinitis pigmentosa with vitreal alterations	5	1
ZNF423	16q12.1	Recessive Jobert syndrome; recessive nephronophthisis	8	8
ZNF513	2p23.3	Recessive retinitis pigmentosa	4	3

3.1. Trans-Acting Mutations in Splicing Factors: PRPF31

Although non-syndromic IRDs show a phenotype restricted to the eye, not all of the disease-causing genes (compiled in Table 1) are exclusively expressed in the retina. Mutations in the genes encoding splicing factors that are ubiquitously expressed and are important for the general process of pre-mRNA splicing–including PRPF3, PRPF4, PRPF6, PRPF8, PRPF31, SNRNP2000, PAP1, DHX38 and *CWC27* [57,59]—have been identified as causative of IRDs [69,72]. In fact, they represent the second most common cause for autosomal dominant RP (adRP), after mutations in the rhodopsin gene (RHO) [73]. It is unclear why mutations in these factors cause a phenotype restricted to the retina while being tolerated by other tissues. However, some of these factors are more highly expressed in the retina than in other tissues [74], which suggest higher splicing requirements for the retina. Moreover, photoreceptors exhibit a specific splicing program driven by the MS1 factor, which initiates during the development and affects transcripts encoding components of primary cilia and outer segments required for phototransduction [62]. Although the specific disease mechanisms are mostly unknown, some possible explanations have been proposed to account for the retina being highly sensitive to mutations that disturb the spliceosome assembly and function [75]. The reduced levels of splicing factors most probably lead to transcriptional dysregulation of specific retinal genes [57]. Furthermore, mutations in splicing factors induce protein-folding defects, which cause aggregation of misfolded mutant proteins [76]. Photoreceptor cells do not regenerate and thus, aggregates will accumulate over time resulting in increased probability of cell death. Alternatively, aggregates will activate the unfolded protein response (already detected in a RP model [77]), which will create long-lasting stress after constant detection of mis-folded proteins, ultimately triggering apoptosis [57].

PRPF31, an essential protein involved in the assembly and stability of the U4/U6·U5 tri-snRNP, illustrates the difficulty in studying splicing factors causing IRDs. Heterozygous mutations in PRPF31 gene have been determined as cause for adRP [78–81]. However,

modifier loci can prevent disease development and thus, adRP due to PRPF31 mutations shows incomplete penetrance, resulting in individuals carrying PRPF31 mutations that do not present RP symptoms, even in the same family [82,83]. Although amino acid substitutions are the main mutation type found in splicing factor genes, most mutations in PRPF31 are deletions, frameshifts or mutations that alter splicing, leading to the introduction of premature stop codons and resulting in reduced PRPF31 levels [57]. In contrast, the PRPF31 Ala216Pro variant, presents a dominant negative effect, as the mutant protein shows a stronger interaction with PRPF6, which results in the inhibition of the protein-RNA movements and subsequent impairment of spliceosome activation and recycling of the proteins for future splicing events [84]. Interestingly, over-expression of PRPF6 rescues the mutant phenotype and, consequently, PRPF6 expression may represent an additional factor accounting for some cases of PRPF31 adRP incomplete penetrance [85]. Regarding the retinal phenotype, studies using induced pluripotent stem cell (iPSC)-derived organoids, revealed that impaired splicing is restricted to retinal cells only and it affects genes involved in RNA processing as well as genes involved in phototransduction and ciliogenesis, which have been associated with progressive degeneration and cellular stress [86,87]. In fact, mis-splicing of ciliary genes was associated with severe defects in the retinal pigmented epithelium (RPE) cells, which are typically affected (together with photoreceptors) in the RP disease [87].

3.2. Cis-Acting Mutations Altering the Splicing

Splice-site mutations have been identified in patients with RP, USH or Stargardt disease, among other IRDs. Mutations can either disrupt a consensus splice site sequence causing exon skipping, shift the splicing acceptor or donor splices sites, or promote the usage of cryptic deep intronic sequences that result in different exon size, intron retention, or novel exon inclusion. One of the current challenges in the genetic diagnosis of IRDs is the detection and functional validation of variants that have not been previously reported and whose functional significance remains unclear. New cis-acting mutations causing retina-specific splicing defects are usually tested in HEK293T cells using in vitro mini- and midi-genes splice assays because IRD genes are not commonly expressed in accessible human tissues [88–90]. However, HEK293T cells do not reproduce retinal cell conditions since they do not express retina-specific splicing factors and adjuvant proteins. For this reason, variants showing no effect on splicing in these assays may still be proven to be pathogenic when assessed in induced iPSC-derived photoreceptor precursors [91]. Cis-acting variants are commonly hypomorphic variants, which reduce the range of correct splicing and lead to splicing alterations while retaining considerable productive transcript [92,93]. The severity of these variants is evaluated according to the percentage of the wildtype (WT) remaining product (the higher the percentage of the WT allele, the lower the severity of the variant). Many of these hypomorphic variants are identified in ciliary genes that when bearing a more severe mutation cause syndromic ciliopathies.

3.2.1. Non-Canonical Splice Site Variants (NCSS): ABCA4

Canonical splice sequences are located at the AG-receptor (−1 and −2) and GT-donor (+1 and +2) nucleotides, affecting directly the primary sequence of the receptor and donor sites, respectively. NCSS variants are instead located either at the first and last three nucleotides of an exon, or else at the −3 to −14 nucleotides from the acceptor site and +3 to +6 nucleotides from the donor site, altering the splicing motif recognition by the splicing factors. NCSS variants can lead to partial or entire exon skipping, producing partial in-frame deletions or open reading frame disruptions that cause frameshifts and lead to prematurely truncated proteins.

Stargardt disease is the most prevalent inherited macular dystrophy, usually presented as an autosomal recessive condition caused by mutations in the *ABCA4* gene. *ABCA4* is a large, highly polymorphic gene, consisting of 50 exons, which presents over 1200 disease-associated variants [94]. A recent study reported that 18% likely pathogenic variants present

a significant splice site alteration, including NCSS and deep intronic variants [95,96]. The identification of splicing variants in a highly polymorphic gene such as *ABCA4* is not unusual, however, the prediction and confirmation of pathogenicity has proven difficult [97]. Several sequencing studies only find one pathogenic allele and fail to identify the second and, as a consequence, 15% of the cases remain "unsolved" [94]. Some authors propose that hypomorphic splice variants account for some of these *ABCA4* missing pathogenic alleles [92,93].

The NCSS variant c.161G>A, which has been previously associated with Stargardt disease [98], demonstrates the complexity of the *ABCA4* genetic analysis. The c.161G>A variant is located in the first nucleotide of exon 3, a coding region of *ABCA4*. Exon 3 shows a weak natural exon skipping in 14% of the WT transcripts [96]. Notably, the variant c.161G>A has two different effects: it causes exon 3 skipping in around 50% of the transcripts (p.Cys54Serfs*14) but it is also a missense mutation that alters the amino acid sequence of ABCA4 protein (p.Cys54Tyr) (Figure 4A). Therefore, both events are contributing to the pathogenicity of the variant. Surprisingly, this variant has also been observed in the "control" population database [96]. Common hypomorphic variants at the *ABCA4* locus alter risk properties and they can be pathogenic only when in trans with a loss-of-function *ABCA4* allele [93,99]. Therefore, occasionally, they result in disease expression, particularly in those patients who carry only a pathogenic allele, thus explaining why some variants are found to be pathogenic in some individuals but not in others. Another example is the NCSS variant c.4849-8C>G, which has also been proved to be pathogenic since it lowers the value of the Pyrimidine tract upstream of the 3' splice site of intron 34, thus producing transcripts with intron retention that leads to premature protein truncation (Figure 4B) [88].

3.2.2. Deep Intronic Variants: ABCA4, CEP290 and USH2A

Deep intronic variants are located more than 100 bp away from exon-intron junctions, which usually lead to pseudo-exon inclusion due to activation of novel splice sites. The introduction of a pseudo-exon (PE) commonly alters the reading frame introducing a premature stop codon, which targets the mutant mRNA for degradation by NMD [100].

LCA is an IRD that results in severe visual loss in early childhood. One of the most common causative LCA genes is *CEP290*, encoding a centrosomal protein, which has also been associated with syndromic ciliopathies [101]. The most common *CEP290* mutation is the deep intronic c.2991+1655A>G variant, which is found in the majority of the *CEP290* LCA patients (86%) [102]. The mutation creates a strong splice donor site (SDS) that induces the inclusion of a cryptic exon between exons 26 and 27. This cryptic exon encodes a premature stop codon (p.Cys998Stop) (Figure 4C) [103]. Remarkably, 50% of the product is still spliced correctly, which may be sufficient for its function in other organs but not in photoreceptors [102,103], thereby highlighting the importance of splicing in the retina and explaining the retina-only phenotype of this particular mutation.

USH2A is the most commonly mutated gene in USH type 2, characterized by congenital hearing impairment and RP. The deep intronic variant c.7595-2144A>G is the second most common cause of USH type 2A [104,105]. This variant creates a novel SD site in intron 40, leading to the insertion of a PE into the mature transcript. This PE encodes a premature termination of translation (p.Lys2532Thrfs*56) (Figure 4D) [104,105]. In contrast to the case of the deep intronic variant c.1938-619A>G of the *ABCA4* gene, which created a novel splice site, this mutation in *USH2A* strengthens a cryptic splicing site, probably by increasing the strength of ESE motifs that induce the inclusion of the PE (Figure 4E) [96].

—385—
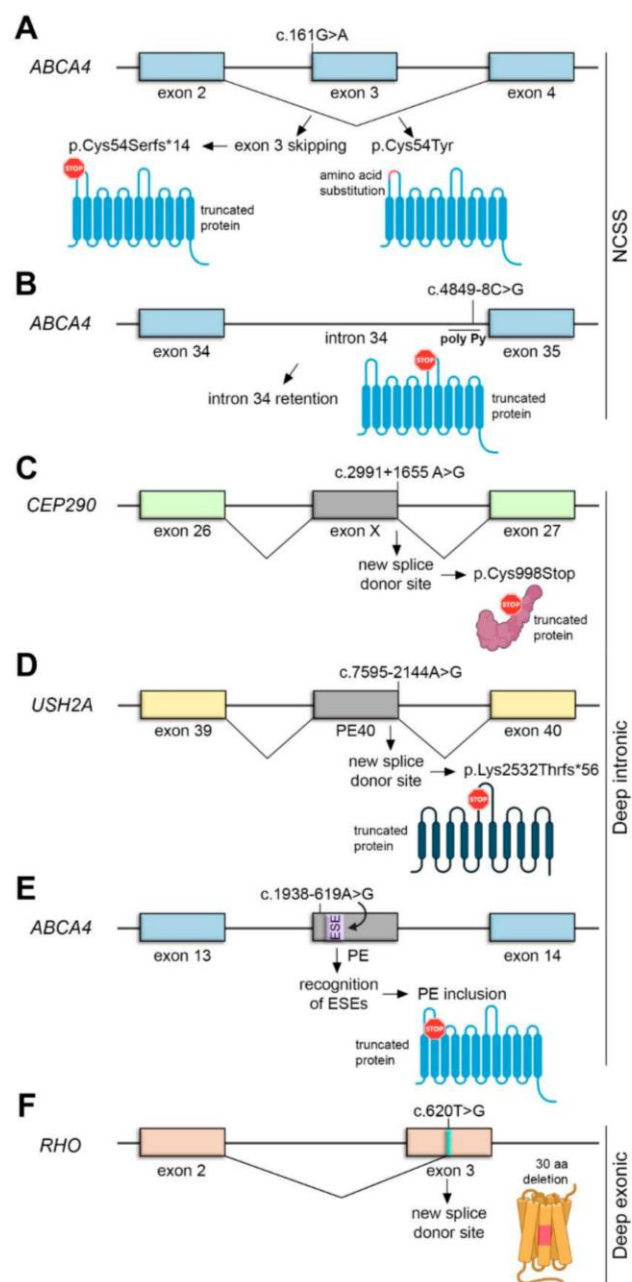
Figure 4. Overview of cis acting mutations altering splicing: NCSS (**A**,**B**), deep intronic (**C–E**) and deep exonic variants (**F**). (**A**) *ABCA4* exon 3 shows a weak natural exon skipping. The c.161G>A mutation increase exon 3 skipping (producing a truncated ABCA4 protein) and the p.Cys54Tyr amino acid substitution. (**B**) The *ABCA4* c.4849-8C>G mutation lowers the value of the poly-Py tract, thus causing intron 34 retention and production of a truncated protein. (**C**) The *CEP290* c.2991+1655A>G mutation creates a new SDS, that induce inclusion of a cryptic exon (exon X) encoding a premature stop codon. (**D**) The *USH2A* c.7595-2144A>G mutation creates a new SDS that causes pseudoexon inclusion (PE40) and introduces a premature stop codon. (**E**) The *ABCA4* c.1938-619A>G mutation, located in a cryptic pseudoexon (PE), leads to the recognition of ESEs that promote PE inclusion, leading to the truncation of the protein. (**F**) The *RHO* c.620T>G mutation creates a strong splice donor site that results in a 30 amino acid in-frame deletion.

3.2.3. Deep Exonic Variants: RHO

Interestingly, mutations located in the middle of an exon can also affect splicing, as it occurs with the c.620T>G variant in rhodopsin, a light-sensitive receptor involved in rod visual phototransduction. Mutations in *RHO* are the most common cause for adRP [106]. Among them, the c.620T>G variant, located in exon 3, was first classified as a missense mutation (Met207Arg) causing severe early-onset adRP [107,108]. The number of altered amino acids in mutations affecting Met207 and surrounding residues usually correlates with the severity of the adRP phenotype. However, another variant affecting the same nucleotide, the c.620T>A (Met207Lys), was associated with a mild late-onset adRP [109]. Researchers have recently discovered that the initial c.620T>G variant (previously classified as missense) is in fact a splicing mutation which generates a particularly strong splice acceptor that results in a 90 bp in-frame deletion and subsequent mislocalization of rhodopsin in photoreceptors [110], thus explaining the severe phenotype found in individuals carrying this mutation (Figure 4F). This finding suggest that point mutations located in exons should be routinely evaluated in silico and subsequently tested for their potential disruptive effect in mRNA splicing in order to avoid misinterpretation of the variants and understand genotype-phenotype correlations, disease mechanisms and ultimately predict the disease course.

3.3. Mutations in Retina-Specific Exons and Microexons: BBS8, RPGR and DYNC2H1

As discussed before, some mutations in widely expressed genes (e.g. in splicing factor genes or CEP290) result in primarily ocular disease. That is also the case of mutations that affect the prevalence of retina-specific transcripts or mutations in retina-specific exons [69]. Identifying retina-specific transcripts is thus essential to increase the genetic diagnosis yield in IRDs as well as to design specific therapeutic approaches.

Mutations in the RPGR gene, which encodes a ciliary protein, have been identified as the cause of over 70% of X-linked RP (XLRP). RPGR undergoes extensive splicing (Table 1) and several transcripts for this gene have been identified [111–113], among them the constitutive transcript, that contains exons 1 to 19, and a retina-specific transcript, which contains constitutive 1–14 exons plus an alternative 3′ terminal exon known as ORF15 [113]. All documented RPGR mutations responsible for XLRP affect the RPGR[ORF15] transcript, and 80% of these mutations occur in exon ORF15, which has been identified as a mutational hotspot [113]. The expression of both the constitutive and the retina-specific isoforms is regulated during retinal development and, interestingly, overexpression of the constitutive isoform causes retinal degeneration in mouse, suggesting that the balance between both isoforms is necessary for correct retinal function [114].

Some genes causing syndromic diseases can also contribute to the development of a retinal disease. Such is the case of BBS8, mutated in several ciliopathies, which presents an alternative 30 bp microexon, exon 2a, that results in a 10 amino acid longer protein whose expression is exclusively restricted to photoreceptors. The inclusion of this microexon is due to specific ISEs exclusively recognized by splicing factors of photoreceptor cells [115,116]. Surprisingly, the A>G substitution (IVS1-2AG), located in the canonical 3′ AG-acceptor of exon 2a, forces the use of a cryptic splice site located 7 nt downstream of the mutated site, which probably results in premature termination of the BBS8 reading frame and elimination of the protein in photoreceptors [116]. Cell types other than photoreceptors do not recognize exon 2a and are not affected therefore by the IVS1-2AG mutation, explaining the RP-restricted phenotype.

A similar case occurs in the DYNC2H1 gene and has been recently associated with severe ciliopathies. DYNC2H1 contains a microexon of 21 bp that is predominant in retinal transcripts [35,117]. Authors hypothesize that the isoform containing the microexon could be the major isoform expressed in photoreceptors because its expression in retinal organoids increase as photoreceptors differentiate, becoming the dominant transcript when photoreceptors are mature [117]. The DYNC2H1 c.9836C>G mutation is predicted to introduce a premature stop codon in the microexon, possibly resulting in a severely truncated protein.

As in previous cases, this variant causes nonsyndromic retinal degeneration, which suggest that the canonical isoform, expressed in all the other tissues, remains unaffected [117]. All these cases strongly indicate that AS is the main mechanism through which mutated syndromic ciliopathy genes lead to non-syndromic IRDs and highlight the importance of identifying retina-specific transcripts that are undeniably important for visual function.

4. Therapeutic Strategies to Modulate Aberrant Splicing

The eye is an ideal target organ for therapeutic interventions due to its easy accessibility and the presence of a blood-retina barrier that prevents exchange of the therapeutic molecules with other organs, thus reducing side effects and undesirable immune responses. Splicing modulation has been a key target for new therapeutic strategies to treat IRDs.

As aforementioned, U1 splice factor binds complementarily with nucleotides at the exon-intron border, promoting the recognition of splice donor site (SDS) and initiation of the splice process [118]. Aberrant splicing in IRDs is often the result of disturbed U1 binding to mutated SDS. Therefore, mutation-adapted U1 can be designed to match all nucleotide of patient SDS (including the mutation), leading to correction of splice defects. This strategy has been proven useful for RHO [119] and RPGR mutations [120]. The main advantage of the U1 technique is that it corrects the endogenously expressed transcript and reduces the amount of mutated protein, which is especially important for the treatment of dominant diseases with gain of function mutations [120].

Spliceosomal-mediated RNA trans-splicing (SMaRT) has also been considered for therapeutic approaches [121,122]. Unlike cis-splicing, trans-splicing naturally joins exons from two independent pre-mRNA molecules and results in a final mRNA consisting of the 5′ part of the first pre-mRNA and the 3′ part of the second pre-mRNA [123]. SMaRT requires the introduction of an exogenous pre-mRNA trans-splicing molecule (PTM), which consist of a binding domain to target the endogenous mutated pre-mRNA, an artificial intron containing the elements necessary for splicing and the cDNA gene sequence to be repaired. SMaRT technology producing hybrid mRNAs has been used as a therapeutic tool for correcting RHO [124] and CEP290 [125] mutations. As expected, the replacement of the mutated sequence decreases the mutant protein synthesis, which is important in cases of dominant IRDs (RHO) and increases the level of correct protein levels in recessive mutations (CEP290).

RNA therapeutic strategies for treating IRDs have been recently reviewed [126]. In this context, the use of siRNA and shRNA agents is worth nothing. siRNAs have shown potential in patients with age-related macular dystrophy (AMD) [127], however, noninternalized siRNAs may stimulate the immune system via Toll-like receptor activation in the RPE, thus inducing retinal degeneration [128,129]. On the other hand, shRNAs have been proven particularly beneficial in the treatment of autosomal dominant disorders, such as those caused by RHO mutations [130] as well as in silencing VEGF production in AMD mouse models [131]. One of the most promising therapeutic agents are antisense oligonucleotides (AONs), small RNA molecules that bind complementarily to the pre-mRNA to correct aberrant splicing caused by the activation of cryptic splice sites [132–134]. AON-based therapies have shown promising results for mutations in CEP290 [135–137], OPA1 [138], CHM [139], USH2A [105] and ABCA4 [91,140], and are now being tested in clinical trials with patients.

Finally, gene editing techniques allow direct correction of the pathogenic allele in the genomic DNA. CRISPR-Cas9 has been successfully used to correct the splicing effect of the deep intronic CEP290 c.2991 + 1655A > G mutation in vivo, first in mouse and now already in human clinical trials [137]. This approach could be useful to correct aberrant splicing caused by deep intronic mutations in other IRD genes.

5. Conclusions

The retina, as an extension of the nervous system, exhibits an exceptional transcript diversity that require an exquisite regulation performed by general and specific splicing

factors. Some retinal cells, such as post-synaptic neurons and photoreceptors, express different splicing factors and, interestingly, mutations in splicing factors ubiquitously expressed and important for the general process of pre-mRNA splicing can cause a retina-restricted phenotype.

Among all the alternative splicing events identified in the retina, incorporation of cassette exons and microexons strongly contributes to development and homeostasis. The retina is one of the tissues that present a higher number of ASEs. In fact, identification of these events has been increasingly growing as massive parallel sequencing and other emergent technologies are developed and implemented in routine genetic diagnosis.

Around 90% of IRD genes present more than one transcript and a considerable percentage of mutations alter splicing or are located in unidentified transcripts exclusively expressed in the retina. Therefore, lack of information regarding AS may cause misinterpretation of IRD diagnosis. One of the current challenges is the detection of variants that have not been previously reported, including hypomorphic variants that are also found in the general population and whose functional significance remains unclear. Functional analysis of mutations causing retina-specific splicing defects should be tested in retinal cell-like environments, such as organoids or iPSC-derived photoreceptor precursors, since some of the splicing factors required are only expressed in the retina. In specialized organs and tissues such as the retina, comprehensive isoform information is fundamental to increase genetic diagnosis yield and comprehend both normal gene function and phenotypic consequences of mutations.

Modulation of alternative splicing in the retina is also crucial to develop novel therapeutic approaches. In fact, siRNAs and AONs are mutation-specific therapies that represent a promising tool to treat retinal dystrophies in a patient-focused personalized medicine.

Conflicts of Interest: The authors declare no conflict of interest.

References

1. Patrushev, L.I.; Kovalenko, T.F. Functions of noncoding sequences in mammalian genomes. *Biochemistry* **2014**, *79*, 1442–1469. [CrossRef]
2. Lee, H.; Zhang, Z.; Krause, H.M. Long Noncoding RNAs and Repetitive Elements: Junk or Intimate Evolutionary Partners? *Trends Genet.* **2019**, *35*, 892–902. [CrossRef]
3. Liu, Y.; Gonzàlez-Porta, M.; Santos, S.; Brazma, A.; Marioni, J.C.; Aebersold, R.; Venkitaraman, A.R.; Wickramasinghe, V.O. Impact of Alternative Splicing on the Human Proteome. *Cell Rep.* **2017**, *20*, 1229–1241. [CrossRef]
4. Vaquero-Garcia, J.; Barrera, A.; Gazzara, M.R.; Gonzalez-Vallinas, J.; Lahens, N.F.; Hogenesch, J.B.; Lynch, K.W.; Barash, Y. A new view of transcriptome complexity and regulation through the lens of local splicing variations. *Elife* **2016**, *5*. [CrossRef]
5. Lee, Y.; Rio, D.C. Mechanisms and regulation of alternative Pre-mRNA splicing. *Annu. Rev. Biochem.* **2015**, *84*, 291–323. [CrossRef] [PubMed]
6. Geuens, T.; Bouhy, D.; Timmerman, V. The hnRNP family: Insights into their role in health and disease. *Hum. Genet.* **2016**, *135*, 851–867. [CrossRef] [PubMed]
7. Jeong, S. SR proteins: Binders, regulators, and connectors of RNA. *Mol. Cells* **2017**, *40*, 1–9. [CrossRef]
8. Tellier, M.; Maudlin, I.; Murphy, S. Transcription and splicing: A two-way street. *Wiley Interdiscip. Rev. RNA* **2020**, *11*. [CrossRef]
9. Pan, Q.; Shai, O.; Lee, L.J.; Frey, B.J.; Blencowe, B.J. Deep surveying of alternative splicing complexity in the human transcriptome by high-throughput sequencing. *Nat. Genet.* **2008**, *40*, 1413–1415. [CrossRef]

ANNEX

10. Merkin, J.; Russell, C.; Chen, P.; Burge, C.B. Evolutionary dynamics of gene and isoform regulation in mammalian tissues. *Science* **2012**, *338*, 1593–1599. [CrossRef] [PubMed]

11. Baralle, F.E.; Giudice, J. Alternative splicing as a regulator of development and tissue identity. *Nat. Rev. Mol. Cell Biol.* **2017**, *18*, 437–451. [CrossRef]

12. Kim, H.K.; Pham, M.H.C.; Ko, K.S.; Rhee, B.D.; Han, J. Alternative splicing isoforms in health and disease. *Pflugers Arch. Eur. J. Physiol.* **2018**, *470*, 995–1016. [CrossRef]

13. Furlanis, E.; Scheiffele, P. Regulation of Neuronal Differentiation, Function, and Plasticity by Alternative Splicing. *Annu. Rev. Cell Dev. Biol.* **2018**, *34*, 451–469. [CrossRef]

14. Hermey, G.; Blüthgen, N.; Kuhl, D. Neuronal activity-regulated alternative mRNA splicing. *Int. J. Biochem. Cell Biol.* **2017**, *91*, 184–193. [CrossRef]

15. Anna, A.; Monika, G. Splicing mutations in human genetic disorders: Examples, detection, and confirmation. *J. Appl. Genet.* **2018**, *59*, 253–268. [CrossRef]

16. Bergsma, A.J.; van der Wal, E.; Broeders, M.; van der Ploeg, A.T.; Pim Pijnappel, W.W.M. Alternative Splicing in Genetic Diseases: Improved Diagnosis and Novel Treatment Options. *Int. Rev. Cell Mol. Biol.* **2018**, *335*, 85–141. [PubMed]

17. Sterne-Weiler, T.; Howard, J.; Mort, M.; Cooper, D.N.; Sanford, J.R. Loss of exon identity is a common mechanism of human inherited disease. *Genome Res.* **2011**, *21*, 1563–1571. [CrossRef] [PubMed]

18. Wang, E.T.; Sandberg, R.; Luo, S.; Khrebtukova, I.; Zhang, L.; Mayr, C.; Kingsmore, S.F.; Schroth, G.P.; Burge, C.B. Alternative isoform regulation in human tissue transcriptomes. *Nature* **2008**, *456*, 470–476. [CrossRef]

19. Wan, J.; Masuda, T.; Hackler, L.; Torres, K.M.; Merbs, S.L.; Zack, D.J.; Qian, J. Dynamic usage of alternative splicing exons during mouse retina development. *Nucleic Acids Res.* **2011**, *39*, 7920–7930. [CrossRef] [PubMed]

20. Fong, H.K.W.; Lin, M.Y.; Pandey, S. Exon-skipping variant of RGR opsin in human retina and pigment epithelium. *Exp. Eye Res.* **2006**, *83*, 133–140. [CrossRef] [PubMed]

21. Aísa-Marín, I.; López-Iniesta, M.J.; Milla, S.; Lillo, J.; Navarro, G.; de la Villa, P.; Marfany, G. Nr2e3 functional domain ablation by CRISPR-Cas9D10Aidentifies a new isoform and generates retinitis pigmentosa and enhanced S-cone syndrome models. *Neurobiol. Dis.* **2020**, *146*. [CrossRef]

22. Mellough, C.B.; Bauer, R.; Collin, J.; Dorgau, B.; Zerti, D.; Dolan, D.W.P.; Jones, C.M.; Izuogu, O.G.; Yu, M.; Hallam, D.; et al. An integrated transcriptional analysis of the developing human retina. *Development* **2019**, *146*. [CrossRef] [PubMed]

23. Stojic, J.; Stöhr, H.; Weber, B.H.F. Three novel ABCC5 splice variants in human retina and their role as regulators of ABCC5 gene expression. *BMC Mol. Biol.* **2007**, *8*. [CrossRef]

24. Yang, D.; Swaminathan, A.; Zhang, X.; Hughes, B.A. Expression of Kir7.1 and a novel Kir7.1 splice variant in native human retinal pigment epithelium. *Exp. Eye Res.* **2008**, *86*, 81–91. [CrossRef] [PubMed]

25. Campla, C.K.; Mast, H.; Dong, L.; Lei, J.; Halford, S.; Sekaran, S.; Swaroop, A. Targeted deletion of an NRL- and CRX-regulated alternative promoter specifically silences FERM and PDZ domain containing 1 (Frmpd1) in rod photoreceptors. *Hum. Mol. Genet.* **2019**, *28*, 804–817. [CrossRef] [PubMed]

26. Hao, H.; Tummala, P.; Guzman, E.; Mali, R.S.; Gregorski, J.; Swaroop, A.; Mitton, K.P. The transcription factor Neural Retina Leucine Zipper (NRL) controls photoreceptor-specific expression of myocyte enhancer factor Mef2c from an alternative promoter. *J. Biol. Chem.* **2011**, *286*, 34893–34902. [CrossRef]

27. Hu, W.; Li, S.; Park, J.Y.; Boppana, S.; Ni, T.; Li, M.; Zhu, J.; Xie, Z.; Xiang, M. Dynamic landscape of alternative polyadenylation during retinal development HHS Public Access. *Cell Mol. Life Sci.* **2017**, *74*, 1721–1739. [CrossRef]

28. Yang, L.; Chen, L.L. Microexons go big. *Cell* **2014**, *159*, 1488–1489. [CrossRef]

29. Irimia, M.; Weatheritt, R.J.; Ellis, J.D.; Parikshak, N.N.; Gonatopoulos-Pournatzis, T.; Babor, M.; Quesnel-Vallières, M.; Tapial, J.; Raj, B.; O'Hanlon, D.; et al. A highly conserved program of neuronal microexons is misregulated in autistic brains. *Cell* **2014**, *159*, 1511–1523. [CrossRef]

30. Li, Y.I.; Sanchez-Pulido, L.; Haerty, W.; Ponting, C.P. RBFOX and PTBP1 proteins regulate the alternative splicing of micro-exons in human brain transcripts. *Genome Res.* **2015**, *25*, 1–13. [CrossRef]

31. Capponi, S.; Stöffler, N.; Irimia, M.; Van Schaik, F.M.A.; Ondik, M.M.; Biniossek, M.L.; Lehmann, L.; Mitschke, J.; Vermunt, M.W.; Creyghton, M.P.; et al. Neuronal-specific microexon splicing of TAF1 mRNA is directly regulated by SRRM4/nSR100. *RNA Biol.* **2020**, *17*, 62–74. [CrossRef]

32. Gonatopoulos-Pournatzis, T.; Blencowe, B.J. Microexons: At the nexus of nervous system development, behaviour and autism spectrum disorder. *Curr. Opin. Genet. Dev.* **2020**, *65*, 22–33. [CrossRef]

33. Porter, R.S.; Jaamour, F.; Iwase, S. Neuron-specific alternative splicing of transcriptional machineries: Implications for neurodevelopmental disorders. *Mol. Cell. Neurosci.* **2018**, *87*, 35–45. [CrossRef]

34. da Costa, P.J.; Menezes, J.; Romão, L. The role of alternative splicing coupled to nonsense-mediated mRNA decay in human disease. *Int. J. Biochem. Cell Biol.* **2017**, *91*, 168–175. [CrossRef] [PubMed]

35. Farkas, M.H.; Grant, G.R.; White, J.A.; Sousa, M.E.; Consugar, M.B.; Pierce, E.A. Transcriptome analyses of the human retina identify unprecedented transcript diversity and 3.5 Mb of novel transcribed sequence via significant alternative splicing and novel genes. *BMC Genom.* **2013**, *14*. [CrossRef]

36. Aragón, J.; González-Reyes, M.; Romo-Yáñez, J.; Vacca, O.; Aguilar-González, G.; Rendón, A.; Vaillend, C.; Montañez, C. Dystrophin Dp71 Isoforms Are Differentially Expressed in the Mouse Brain and Retina: Report of New Alternative Splicing and a Novel Nomenclature for Dp71 Isoforms. *Mol. Neurobiol.* **2018**, *55*, 1376–1386. [CrossRef] [PubMed]

37. Whitney, I.E.; Kautzman, A.G.; Reese, B.E. Alternative splicing of the LIM-homeodomain transcription factor Isl1 in the mouse retina. *Mol. Cell. Neurosci.* **2015**, *65*, 102–113. [CrossRef]

38. Kole, C.; Berdugo, N.; Silva, C.D.; Aït-Ali, N.; Millet-Puel, G.; Pagan, D.; Blond, F.; Poidevin, L.; Ripp, R.; Fontaine, V.; et al. Identification of an alternative splicing product of the OtX2 gene expressed in the neural retina and retinal pigmented epithelial cells. *PLoS ONE* **2016**, *11*. [CrossRef] [PubMed]

39. Bayega, A.; Wang, Y.C.; Oikonomopoulos, S.; Djambazian, H.; Fahiminiya, S.; Ragoussis, J. Transcript Profiling Using Long-Read Sequencing Technologies. *Methods Mol. Biol.* **2018**, *1783*, 121–147.

40. Midha, M.K.; Wu, M.; Chiu, K.P. Long-read sequencing in deciphering human genetics to a greater depth. *Hum. Genet.* **2019**, *138*, 1201–1215. [CrossRef] [PubMed]

41. Byrne, A.; Cole, C.; Volden, R.; Vollmers, C. Realizing the potential of full-length transcriptome sequencing. *Philos. Trans. R. Soc. B Biol. Sci.* **2019**, *374*. [CrossRef] [PubMed]

42. Ray, T.A.; Cochran, K.; Kozlowski, C.; Wang, J.; Alexander, G.; Cady, M.A.; Spencer, W.J.; Ruzycki, P.A.; Clark, B.S.; Laeremans, A.; et al. Comprehensive identification of mRNA isoforms reveals the diversity of neural cell-surface molecules with roles in retinal development and disease. *Nat. Commun.* **2020**, *11*. [CrossRef] [PubMed]

43. Quinn, P.M.; Pellissier, L.P.; Wijnholds, J. The CRB1 complex: Following the trail of crumbs to a feasible gene therapy strategy. *Front. Neurosci.* **2017**, *11*. [CrossRef]

44. van de Pavert, S.A.; Kantardzhieva, A.; Malysheva, A.; Meuleman, J.; Versteeg, I.; Levelt, C.; Klooster, J.; Geiger, S.; Seeliger, M.W.; Rashbass, P.; et al. Crumbs homologue 1 is required for maintenance of photoreceptor cell polarization and adhesion during light exposure. *J. Cell Sci.* **2004**, *117*, 4169–4177. [CrossRef]

45. Garanto, A.; Riera, M.; Pomares, E.; Permanyer, J.; de Castro-Miró, M.; Sava, F.; Abril, J.F.; Marfany, G.; Gonzàlez-Duarte, R. High transcriptional complexity of the retinitis pigmentosa CERKL gene in human and mouse. *Investig. Ophthalmol. Vis. Sci.* **2011**, *52*, 5202–5214. [CrossRef]

46. Garanto, A.; Vicente-Tejedor, J.; Riera, M.; De la Villa, P.; Gonzàlez-Duarte, R.; Blanco, R.; Marfany, G. Targeted knockdown of Cerkl, a retinal dystrophy gene, causes mild affectation of the retinal ganglion cell layer. *Biochim. Biophys. Acta Mol. Basis Dis.* **2012**, *1822*, 1258–1269. [CrossRef] [PubMed]

47. Domènech, E.B.; Andres, R.; López-Iniesta, M.J.; Mirra, S.; Arroyo, R.G.; Milla, S.; Sava, F.; Andilla, J.; Alvarez, P.L.; De La Villa, P.; et al. A New cerkl mouse model generated by crispr-cas9 shows progressive retinal degeneration and altered morphological and electrophysiological phenotype. *Investig. Ophthalmol. Vis. Sci.* **2020**, *61*, 14. [CrossRef]

48. Wilkinson, M.E.; Charenton, C.; Nagai, K. RNA Splicing by the Spliceosome. *Annu. Rev. Biochem.* **2020**, *89*, 359–388. [CrossRef] [PubMed]

49. Kondo, Y.; Oubridge, C.; van Roon, A.M.M.; Nagai, K. Crystal structure of human U1 snRNP, a small nuclear ribonucleoprotein particle, reveals the mechanism of 5′ splice site recognition. *Elife* **2015**, *4*. [CrossRef]

50. Sickmier, E.A.; Frato, K.E.; Shen, H.; Paranawithana, S.R.; Green, M.R.; Kielkopf, C.L. Structural Basis for Polypyrimidine Tract Recognition by the Essential Pre-mRNA Splicing Factor U2AF65. *Mol. Cell* **2006**, *23*, 49–59. [CrossRef]

51. Wu, J.; Manley, J.L. Mammalian pre-mRNA branch site selection by U2 snRNP involves base pairing. *Genes Dev.* **1989**, *3*, 1553–1561. [CrossRef]

52. Sterner, D.A.; Carlo, T.; Berget, S.M. Architectural limits on split genes. *Proc. Natl. Acad. Sci. USA* **1996**, *93*, 15081–15085. [CrossRef]

53. Wan, R.; Yan, C.; Bai, R.; Wang, L.; Huang, M.; Wong, C.C.L.; Shi, Y. The 3.8 Å structure of the U4/U6.U5 tri-snRNP: Insights into spliceosome assembly and catalysis. *Science* **2016**, *351*, 466–475. [CrossRef] [PubMed]

54. Raghunathan, P.L.; Guthrie, C. RNA unwinding in U4/U6 snRNPs requires ATP hydrolysis and the DEIH-box splicing factor Brr2. *Curr. Biol.* **1998**, *8*, 847–855. [CrossRef]

55. Sun, J.S.; Manley, J.L. A novel U2-U6 snRNA structure is necessary for mammalian mRNA splicing. *Genes Dev.* **1995**, *9*, 843–854. [CrossRef] [PubMed]

56. Fourmann, J.B.; Schmitzová, J.; Christian, H.; Urlaub, H.; Ficner, R.; Boon, K.L.; Fabrizio, P.; Lührmann, R. Dissection of the factor requirements for spliceosome disassembly and the elucidation of its dissociation products using a purified splicing system. *Genes Dev.* **2013**, *27*, 413–428. [CrossRef] [PubMed]

57. Růžičková, Š.; Staněk, D. Mutations in spliceosomal proteins and retina degeneration. *RNA Biol.* **2017**, *14*, 544–552. [CrossRef] [PubMed]

58. Yan, C.; Wan, R.; Bai, R.; Huang, G.; Shi, Y. Structure of a yeast activated spliceosome at 3.5 Å resolution. *Science* **2016**, *353*, 904–912. [CrossRef]

59. Xu, M.; Xie, Y.; Abouzeid, H.; Gordon, C.T.; Fiorentino, A.; Sun, Z.; Lehman, A.; Osman, I.S.; Dharmat, R.; Riveiro-Alvarez, R.; et al. Mutations in the Spliceosome Component CWC27 Cause Retinal Degeneration with or without Additional Developmental Anomalies. *Am. J. Hum. Genet.* **2017**, *100*, 592–604. [CrossRef] [PubMed]

60. Matera, A.G.; Wang, Z. A day in the life of the spliceosome. *Nat. Rev. Mol. Cell Biol.* **2014**, *15*, 108–121. [CrossRef]

61. Shenasa, H.; Hertel, K.J. Combinatorial regulation of alternative splicing. *Biochim. Biophys. Acta Gene Regul. Mech.* **2019**, *1862*. [CrossRef]

62. Murphy, D.; Cieply, B.; Carstens, R.; Ramamurthy, V.; Stoilov, P. The Musashi 1 Controls the Splicing of Photoreceptor-Specific Exons in the Vertebrate Retina. *PLoS Genet.* **2016**, *12*. [CrossRef] [PubMed]

63. Qi, X. The role of miR-9 during neuron differentiation of mouse retinal stem cells. *Artif. Cells Nanomed. Biotechnol.* **2016**, *44*, 1883–1890. [CrossRef] [PubMed]

64. Gu, L.; Bok, D.; Yu, F.; Caprioli, J.; Piri, N. Downregulation of splicing regulator RBFOX1 compromises visual depth perception. *PLoS ONE* **2018**, *13*. [CrossRef]

65. Lin, Y.S.; Kuo, K.T.; Chen, S.K.; Huang, H.S. RBFOX3/NeuN is dispensable for visual function. *PLoS ONE* **2018**, *13*. [CrossRef]

66. Gu, L.; Kawaguchi, R.; Caprioli, J.; Piri, N. The effect of Rbfox2 modulation on retinal transcriptome and visual function. *Sci. Rep.* **2020**, *10*. [CrossRef] [PubMed]

67. Sundar, J.; Matalkah, F.; Jeong, B.; Stoilov, P.; Ramamurthy, V. The Musashi proteins MSI1 and MSI2 are required for photoreceptor morphogenesis and vision in mice. *J. Biol. Chem.* **2020**, 100048. [CrossRef] [PubMed]

68. Ling, J.P.; Wilks, C.; Charles, R.; Leavey, P.J.; Ghosh, D.; Jiang, L.; Santiago, C.P.; Pang, B.; Venkataraman, A.; Clark, B.S.; et al. ASCOT identifies key regulators of neuronal subtype-specific splicing. *Nat. Commun.* **2020**, *11*. [CrossRef] [PubMed]

69. Liu, M.M.; Zack, D.J. Alternative splicing and retinal degeneration. *Clin. Genet.* **2013**, *84*, 142–149. [CrossRef]

70. Buvoli, M.; Buvoli, A.; Leinwand, L.A. Interplay between exonic splicing enhancers, mRNA processing, and mRNA surveillance in the dystrophic Mdx mouse. *PLoS ONE* **2007**, *2*. [CrossRef]

71. Lam, B.J.; Hertel, K.J. A general role for splicing enhancers in exon definition. *RNA* **2002**, *8*, 1233–1241. [CrossRef] [PubMed]

72. Wheway, G.; Lord, J.; Baralle, D. Splicing in the pathogenesis, diagnosis and treatment of ciliopathies. *Biochim. Biophys. Acta Gene Regul. Mech.* **2019**, *1862*. [CrossRef]

73. Van Cauwenbergh, C.; Coppieters, F.; Roels, D.; De Jaegere, S.; Flipts, H.; De Zaeytijd, J.; Walraedt, S.; Claes, C.; Fransen, E.; Van Camp, G.; et al. Mutations in Splicing Factor Genes Are a Major Cause of Autosomal Dominant Retinitis Pigmentosa in Belgian Families. *PLoS ONE* **2017**, *12*, e0170038. [CrossRef] [PubMed]

74. Cao, H.; Wu, J.; Lam, S.; Duan, R.; Newnham, C.; Molday, R.S.; Graziotto, J.J.; Pierce, E.A.; Hu, J. Temporal and Tissue Specific Regulation of RP-Associated Splicing Factor Genes PRPF3, PRPF31 and PRPC8—Implications in the Pathogenesis of RP. *PLoS ONE* **2011**, *6*, e15860. [CrossRef]

75. Tanackovic, G.; Ransijn, A.; Thibault, P.; Elela, S.A.; Klinck, R.; Berson, E.L.; Chabot, B.; Rivolta, C. PRPF mutations are associated with generalized defects in spliceosome formation and pre-mRNA splicing in patients with retinitis pigmentosa. *Hum. Mol. Genet.* **2011**, *20*, 2116–2130. [CrossRef]

76. Comitato, A.; Spampanato, C.; Chakarova, C.; Sanges, D.; Bhattacharya, S.S.; Marigo, V. Mutations in splicing factor PRPF3, causing retinal degeneration, form detrimental aggregates in photoreceptor cells. *Hum. Mol. Genet.* **2007**, *16*, 1699–1707. [CrossRef]

77. Shinde, V.; Kotla, P.; Strang, C.; Gorbatyuk, M. Unfolded protein response-induced dysregulation of calcium homeostasis promotes retinal degeneration in rat models of autosomal dominant retinitis pigmentosa. *Cell Death Dis.* **2016**, *7*. [CrossRef] [PubMed]

78. Vithana, E.N.; Abu-Safieh, L.; Allen, M.J.; Carey, A.; Papaioannou, M.; Chakarova, C.; Al-Maghtheh, M.; Ebenezer, N.D.; Willis, C.; Moore, A.T.; et al. A human homolog of yeast pre-mRNA splicing gene, PRP31, underlies autosomal dominant retinitis pigmentosa on chromosome 19q13.4 (RP11). *Mol. Cell* **2001**, *8*, 375–381. [CrossRef]

79. Sato, H.; Wada, Y.; Itabashi, T.; Nakamura, M.; Kawamura, M.; Tamai, M. Mutations in the pre-mRNA splicing gene, PRPF31, in Japanese families with autosomal dominant retinitis pigmentosa. *Am. J. Ophthalmol.* **2005**, *140*, 537–540. [CrossRef] [PubMed]

80. Wang, L.; Ribaudo, M.; Zhao, K.; Yu, N.; Chen, Q.; Sun, Q.; Wang, L.; Wang, Q. Novel deletion in the pre-mRNA splicing gene PRPF31 causes autosomal dominant retinitis pigmentosa in a large Chinese family. *Am. J. Med. Genet.* **2003**, *121 A*, 235–239. [CrossRef]

81. Sullivan, L.S.; Bowne, S.J.; Seaman, C.R.; Blanton, S.H.; Lewis, R.A.; Heckenlively, J.R.; Birch, D.G.; Hughbanks-Wheaton, D.; Daiger, S.P. Genomic rearrangements of the PRPF31 gene account for 2.5% of autosomal dominant retinitis pigmentosa. *Investig. Ophthalmol. Vis. Sci.* **2006**, *47*, 4579–4588. [CrossRef]

82. Vithana, E.N.; Abu-Safieh, L.; Pelosini, L.; Winchester, E.; Hornan, D.; Bird, A.C.; Hunt, D.M.; Bustin, S.A.; Bhattacharya, S.S. Expression of PRPF31 mRNA in patients with autosomal dominant retinitis pigmentosa: A molecular clue for incomplete penetrance? *Investig. Ophthalmol. Vis. Sci.* **2003**, *44*, 4204–4209. [CrossRef] [PubMed]

83. Rose, A.M.; Shah, A.Z.; Venturini, G.; Krishna, A.; Chakravarti, A.; Rivolta, C.; Bhattacharya, S.S. Transcriptional regulation of PRPF31 gene expression by MSR1 repeat elements causes incomplete penetrance in retinitis pigmentosa. *Sci. Rep.* **2016**, *6*. [CrossRef]

84. Wilkie, S.E.; Vaclavik, V.; Wu, H.; Bujakowska, K.; Chakarova, C.F.; Bhattacharya, S.S.; Warren, M.J.; Hunt, D.M. Disease mechanism for retinitis pigmentosa (RP11) caused by missense mutations in the splicing factor gene PRPF31. *Mol. Vis.* **2008**, *14*, 683–690. [PubMed]

85. Huranová, M.; Hnilicová, J.; Fleischer, B.; Cvačková, Z.; Staněk, D. A mutation linked to retinitis pigmentosa in HPRP31 causes protein instability and impairs its interactions with spliceosomal snRNPs. *Hum. Mol. Genet.* **2009**, *18*, 2014–2023. [CrossRef] [PubMed]

86. Azizzadeh Pormehr, L.; Ahmadian, S.; Daftarian, N.; Mousavi, S.A.; Shafiezadeh, M. PRPF31 reduction causes mis-splicing of the phototransduction genes in human organotypic retinal culture. *Eur. J. Hum. Genet.* **2020**, *28*, 491–498. [CrossRef]

87. Buskin, A.; Zhu, L.; Chichagova, V.; Basu, B.; Mozaffari-Jovin, S.; Dolan, D.; Droop, A.; Collin, J.; Bronstein, R.; Mehrotra, S.; et al. Disrupted alternative splicing for genes implicated in splicing and ciliogenesis causes PRPF31 retinitis pigmentosa. *Nat. Commun.* **2018**, *9*. [CrossRef] [PubMed]

88. Toulis, V.; Cortés-González, V.; de Castro-Miró, M.; Sallum, J.F.; Català-Mora, J.; Villanueva-Mendoza, C.; Ciccioli, M.; Gonzàlez-Duarte, R.; Valero, R.; Marfany, G. Increasing the genetic diagnosis yield in inherited retinal dystrophies: Assigning pathogenicity to novel non-canonical splice site variants. *Genes* **2020**, *11*, 378. [CrossRef]

89. Sangermano, R.; Bax, N.M.; Bauwens, M.; Van Den Born, L.I.; De Baere, E.; Garanto, A.; Collin, R.W.J.; Goercharn-Ramlal, A.S.A.; Den Engelsman-Van Dijk, A.H.A.; Rohrschneider, K.; et al. Photoreceptor Progenitor mRNA Analysis Reveals Exon Skipping Resulting from the ABCA4 c.5461-10T→C Mutation in Stargardt Disease. *Ophthalmology* **2016**, *123*, 1375–1385. [CrossRef]

90. Sangermano, R.; Khan, M.; Cornelis, S.S.; Richelle, V.; Albert, S.; Garanto, A.; Elmelik, D.; Qamar, R.; Lugtenberg, D.; Ingeborgh van den Born, L.; et al. ABCA4 midigenes reveal the full splice spectrum of all reported noncanonical splice site variants in Stargardt disease. *Genome Res.* **2018**, *28*, 100–110. [CrossRef]

91. Albert, S.; Garanto, A.; Sangermano, R.; Khan, M.; Bax, N.M.; Hoyng, C.B.; Zernant, J.; Lee, W.; Allikmets, R.; Collin, R.W.J.; et al. Identification and Rescue of Splice Defects Caused by Two Neighboring Deep-Intronic ABCA4 Mutations Underlying Stargardt Disease. *Am. J. Hum. Genet.* **2018**, *102*, 517–527. [CrossRef]

92. Zernant, J.; Lee, W.; Nagasaki, T.; Collison, F.T.; Fishman, G.A.; Bertelsen, M.; Rosenberg, T.; Gouras, P.; Tsang, S.H.; Allikmets, R. Extremely hypomorphic and severe deep intronic variants in the ABCA4 locus result in varying Stargardt disease phenotypes. *Cold Spring Harb. Mol. Case Stud.* **2018**, *4*. [CrossRef]

93. Zernant, J.; Lee, W.; Collison, F.T.; Fishman, G.A.; Sergeev, Y.V.; Schuerch, K.; Sparrow, J.R.; Tsang, S.H.; Allikmets, R. Frequent hypomorphic alleles account for a significant fraction of ABCA4 disease and distinguish it from age-related macular degeneration. *J. Med. Genet.* **2017**, *54*, 404–412. [CrossRef] [PubMed]

94. Cremers, F.P.M.; Lee, W.; Collin, R.W.J.; Allikmets, R. Clinical spectrum, genetic complexity and therapeutic approaches for retinal disease caused by ABCA4 mutations. *Prog. Retin. Eye Res.* **2020**, *79*, 100861. [CrossRef] [PubMed]

95. Fujinami, K.; Strauss, R.W.; Chiang, J.; Audo, I.S.; Bernstein, P.S.; Birch, D.G.; Bomotti, S.M.; Cideciyan, A.V.; Ervin, A.M.; Marino, M.J.; et al. Detailed genetic characteristics of an international large cohort of patients with Stargardt disease: ProgStar study report 8. *Br. J. Ophthalmol.* **2019**, *103*, 390–397. [CrossRef]

96. Fadaie, Z.; Khan, M.; Del Pozo-Valero, M.; Cornelis, S.S.; Ayuso, C.; Cremers, F.P.M.; Roosing, S.; The ABCA4 Study Group. Identification of splice defects due to noncanonical splice site or deep-intronic variants in ABCA4. *Hum. Mutat.* **2019**, *40*, 2365–2376. [CrossRef]

97. Chiang, J.P.W.; Trzupek, K. The current status of molecular diagnosis of inherited retinal dystrophies. *Curr. Opin. Ophthalmol.* **2015**, *26*, 346–351. [CrossRef] [PubMed]

98. Lee, W.; Xie, Y.; Zernant, J.; Yuan, B.; Bearelly, S.; Tsang, S.H.; Lupski, J.R.; Allikmets, R. Complex inheritance of ABCA4 disease: Four mutations in a family with multiple macular phenotypes. *Hum. Genet.* **2016**, *135*, 9–19. [CrossRef] [PubMed]

99. Schulz, H.L.; Grassmann, F.; Kellner, U.; Spital, G.; Rüther, K.; Jägle, H.; Hufendiek, K.; Rating, P.; Huchzermeyer, C.; Baier, M.J.; et al. Mutation spectrum of the ABCA4 gene in 335 stargardt disease patients from a multicenter German cohort—impact of selected deep intronic variants and common SNPs. *Investig. Ophthalmol. Vis. Sci.* **2017**, *58*, 394–403. [CrossRef] [PubMed]

100. Vaz-Drago, R.; Custódio, N.; Carmo-Fonseca, M. Deep intronic mutations and human disease. *Hum. Genet.* **2017**, *136*, 1093–1111. [CrossRef] [PubMed]

101. Coppieters, F.; Lefever, S.; Leroy, B.P.; De Baere, E. CEP290, a gene with many faces: Mutation overview and presentation of CEP290base. *Hum. Mutat.* **2010**, *31*, 1097–1108. [CrossRef] [PubMed]

102. Drivas, T.G.; Wojno, A.P.; Tucker, B.A.; Stone, E.M.; Bennett, J. Basal exon skipping and genetic pleiotropy: A predictive model of disease pathogenesis. *Sci. Transl. Med.* **2015**, *7*. [CrossRef] [PubMed]

103. Den Hollander, A.I.; Koenekoop, R.K.; Yzer, S.; Lopez, I.; Arends, M.L.; Voesenek, K.E.J.; Zonneveld, M.N.; Strom, T.M.; Meitinger, T.; Brunner, H.G.; et al. Mutations in the CEP290 (NPHP6) gene are a frequent cause of leber congenital amaurosis. *Am. J. Hum. Genet.* **2006**, *79*, 556–561. [CrossRef]

104. Vaché, C.; Besnard, T.; le Berre, P.; García-García, G.; Baux, D.; Larrieu, L.; Abadie, C.; Blanchet, C.; Bolz, H.J.; Millan, J.; et al. Usher syndrome type 2 caused by activation of an USH2A pseudoexon: Implications for diagnosis and therapy. *Hum. Mutat.* **2012**, *33*, 104–108. [CrossRef]

105. Slijkerman, R.W.; Vaché, C.; Dona, M.; García-García, G.; Claustres, M.; Hetterschijt, L.; Peters, T.A.; Hartel, B.P.; Pennings, R.J.; Millan, J.M.; et al. Antisense Oligonucleotide-based Splice Correction for USH2A-associated Retinal Degeneration Caused by a Frequent Deep-intronic Mutation. *Mol. Ther. Nucleic Acids* **2016**, *5*, e381. [CrossRef] [PubMed]

106. Athanasiou, D.; Aguila, M.; Bellingham, J.; Li, W.; McCulley, C.; Reeves, P.J.; Cheetham, M.E. The molecular and cellular basis of rhodopsin retinitis pigmentosa reveals potential strategies for therapy. *Prog. Retin. Eye Res.* **2018**, *62*, 1–23. [CrossRef] [PubMed]

107. Farrar, G.J.; Findlay, J.B.C.; Kumar-singh, R.; Kenna, P.; Humphries, M.M.; Sharpe, E.; Humphries, P. Autosomal dominant retinitis pigmentosa: A novel mutation in the rhodopsin gene in the original 3q linked family. *Hum. Mol. Genet.* **1992**, *1*, 769–771. [CrossRef] [PubMed]

108. McWilliam, P.; Farrar, G.J.; Kenna, P.; Bradley, D.G.; Humphries, M.M.; Sharp, E.M.; McConnell, D.J.; Lawler, M.; Sheils, D.; Ryan, C.; et al. Autosomal dominant retinitis pigmentosa (ADRP): Localization of an ADRP gene to the long arm of chromosome 3. *Genomics* **1989**, *5*, 619–622. [CrossRef]

109. Audo, I.; Friedrich, A.; Mohand-Saïd, S.; Lancelot, M.E.; Antonio, A.; Moskova-Doumanova, V.; Poch, O.; Bhattacharya, S.; Sahel, J.A.; Zeitz, C. An unusual retinal phenotype associated with a novel mutation in RHO. *Arch. Ophthalmol.* **2010**, *128*, 1036–1045. [CrossRef] [PubMed]

110. Riedmayr, L.M.; Böhm, S.; Biel, M.; Becirovic, E. Enigmatic rhodopsin mutation creates an exceptionally strong splice acceptor site. *Hum. Mol. Genet.* **2020**, *29*, 295–304. [CrossRef]

111. Schmid, F.; Glaus, E.; Cremers, F.P.M.; Kloeckener-Gruissem, B.; Berger, W.; Neidhardt, J. Mutation- and tissue-specific alterations of RPGR transcripts. *Investig. Ophthalmol. Vis. Sci.* **2010**, *51*, 1628–1635. [CrossRef]

112. Neidhardt, J.; Glaus, E.; Barthelmes, D.; Zeitz, C.; Fleischhauer, J.; Berger, W. Identification and characterization of a novel RPGR isoform in human retina. *Hum. Mutat.* **2007**, *28*, 797–807. [CrossRef]

113. Vervoort, R.; Lennon, A.; Bird, A.C.; Tulloch, B.; Axton, R.; Miano, M.G.; Meindl, A.; Meitinger, T.; Ciccodicola, A.; Wright, A.F. Mutational hot spot within a new RPGR exon in X-linked retinitis pigmentosa. *Nat. Genet.* **2000**, *25*, 462–466. [CrossRef]

114. Wright, R.N.; Hong, D.H.; Perkins, B. Misexpression of the Constitutive Rpgr ex1-19 Variant Leads to Severe Photoreceptor Degeneration. *Investig. Ophthalmol. Vis. Sci.* **2011**, *52*, 5189–5201. [CrossRef]

115. Riazuddin, S.A.; Iqbal, M.; Wang, Y.; Masuda, T.; Chen, Y.; Bowne, S.; Sullivan, L.S.; Waseem, N.H.; Bhattacharya, S.; Daiger, S.P.; et al. A Splice-Site Mutation in a Retina-Specific Exon of BBS8 Causes Nonsyndromic Retinitis Pigmentosa. *Am. J. Hum. Genet.* **2010**, *86*, 805–812. [CrossRef] [PubMed]

116. Murphy, D.; Singh, R.; Kolandaivelu, S.; Ramamurthy, V.; Stoilov, P. Alternative Splicing Shapes the Phenotype of a Mutation in BBS8 To Cause Nonsyndromic Retinitis Pigmentosa. *Mol. Cell. Biol.* **2015**, *35*, 1860–1870. [CrossRef] [PubMed]

117. Vig, A.; Poulter, J.A.; Ottaviani, D.; Tavares, E.; Toropova, K.; Tracewska, A.M.; Mollica, A.; Kang, J.; Kehelwathugoda, O.; Paton, T.; et al. DYNC2H1 hypomorphic or retina-predominant variants cause nonsyndromic retinal degeneration. *Genet. Med.* **2020**, *22*. [CrossRef]

118. Wahl, M.C.; Will, C.L.; Lührmann, R. The Spliceosome: Design Principles of a Dynamic RNP Machine. *Cell* **2009**, *136*, 701–718. [CrossRef] [PubMed]

119. Tanner, G.; Glaus, E.; Barthelmes, D.; Ader, M.; Fleischhauer, J.; Pagani, F.; Berger, W.; Neidhardt, J. Therapeutic strategy to rescue mutation-induced exon skipping in rhodopsin by adaptation of U1 snRNA. *Hum. Mutat.* **2009**, *30*, 255–263. [CrossRef]

120. Glaus, E.; Schmid, F.; Da Costa, R.; Berger, W.; Neidhardt, J. Gene therapeutic approach using mutation-adapted U1 snRNA to correct a RPGR Splice defect in patient-derived cells. *Mol. Ther.* **2011**, *19*, 936–941. [CrossRef]

121. Puttaraju, M.; Jamison, S.F.; Mansfield, S.G.; Garcia-Blanco, M.A.; Mitchell, L.G. Spliceosome-mediated RNA trans-splicing as a tool for gene therapy. *Nat. Biotechnol.* **1999**, *17*, 246–252. [CrossRef]

122. Finta, C.; Zaphiropoulos, P.G. Intergenic mRNA molecules resulting from trans-splicing. *J. Biol. Chem.* **2002**, *277*, 5882–5890. [CrossRef]

123. Wu, C.S.; Yu, C.Y.; Chuang, C.Y.; Hsiao, M.; Kao, C.F.; Kuo, H.C.; Chuang, T.J. Integrative transcriptome sequencing identifies trans-splicing events with important roles in human embryonic stem cell pluripotency. *Genome Res.* **2014**, *24*, 25–36. [CrossRef] [PubMed]

124. Berger, A.; Lorain, S.; Joséphine, C.; Desrosiers, M.; Peccate, C.; Voit, T.; Garcia, L.; Sahel, J.A.; Bemelmans, A.P. Repair of rhodopsin mRNA by spliceosome-mediated RNA trans-splicing: A new approach for autosomal dominant retinitis pigmentosa. *Mol. Ther.* **2015**, *23*, 918–930. [CrossRef] [PubMed]

125. Dooley, S.J.; McDougald, D.S.; Fisher, K.J.; Bennicelli, J.L.; Mitchell, L.G.; Bennett, J. Spliceosome-Mediated Pre-mRNA trans-Splicing Can Repair CEP290 mRNA. *Mol. Ther. Nucleic Acids* **2018**, *12*, 294–308. [CrossRef] [PubMed]

126. Gemayel, M.C.; Bhatwadekar, A.D.; Ciulla, T. RNA therapeutics for retinal diseases. *Expert Opin. Biol. Ther.* **2020**. [CrossRef]

127. Jiang, J.; Zhang, X.; Tang, Y.; Li, S.; Chen, J. Progress on ocular siRNA gene-silencing therapy and drug delivery systems. *Fundam. Clin. Pharmacol.* **2020**. fcp.12561. [CrossRef]

128. Kleinman, M.E.; Kaneko, H.; Cho, W.G.; Dridi, S.; Fowler, B.J.; Blandford, A.D.; Albuquerque, R.J.C.; Hirano, Y.; Terasaki, H.; Kondo, M.; et al. Short-interfering RNAs induce retinal degeneration via TLR3 and IRF3. *Mol. Ther.* **2012**, *20*, 101–108. [CrossRef] [PubMed]

129. Ramsay, E.; Raviña, M.; Sarkhel, S.; Hehir, S.; Cameron, N.R.; Ilmarinen, T.; Skottman, H.; Kjems, J.; Urtti, A.; Ruponen, M.; et al. Avoiding the pitfalls of siRNA delivery to the retinal pigment epithelium with physiologically relevant cell models. *Pharmaceutics* **2020**, *12*, 667. [CrossRef]

130. Cideciyan, A.V.; Sudharsan, R.; Dufour, V.L.; Massengill, M.T.; Iwabe, S.; Swider, M.; Lisi, B.; Sumaroka, A.; Marinho, L.F.; Appelbaum, T.; et al. Mutation-independent rhodopsin gene therapy by knockdown and replacement with a single AAV vector. *Proc. Natl. Acad. Sci. USA* **2018**, *115*, E8547–E8556. [CrossRef]

131. Askou, A.L.; Pournaras, J.A.C.; Pihlmann, M.; Svalgaard, J.D.; Arsenijevic, Y.; Kostic, C.; Bek, T.; Dagnæs-Hansen, F.; Mikkelsen, J.G.; Jensen, T.G.; et al. Reduction of choroidal neovascularization in mice by adeno-associated virus-delivered anti-vascular endothelial growth factor short hairpin RNA. *J. Gene Med.* **2012**, *14*, 632–641. [CrossRef] [PubMed]

132. Gerard, X.; Garanto, A.; Rozet, J.M.; Collin, R.W.J. Antisense oligonucleotide therapy for inherited retinal dystrophies. *Adv. Exp. Med. Biol.* **2016**, *854*, 517–524.

133. Garanto, A. RNA-Based Therapeutic Strategies for Inherited Retinal Dystrophies. *Adv. Exp. Med. Biol.* **2019**, *1185*, 71–77. [PubMed]
134. Vázquez-Domínguez, I.; Garanto, A.; Collin, R.W.J. Molecular Therapies for Inherited Retinal Diseases—Current Standing, Opportunities and Challenges. *Genes* **2019**, *10*, 654. [CrossRef]
135. Collin, R.W.; Den Hollander, A.I.; Der Velde-Visser, S.D.V.; Bennicelli, J.; Bennett, J.; Cremers, F.P. Antisense oligonucleotide (AON)-based therapy for leber congenital amaurosis caused by a frequent mutation in CEP290. *Mol. Ther. Nucleic Acids* **2012**, *1*, e14. [CrossRef] [PubMed]
136. Gerard, X.; Perrault, I.; Hanein, S.; Silva, E.; Bigot, K.; Defoort-Delhemmes, S.; Rio, M.; Munnich, A.; Scherman, D.; Kaplan, J.; et al. AON-mediated exon skipping restores ciliation in fibroblasts harboring the common leber congenital amaurosis CEP290 mutation. *Mol. Ther. Nucleic Acids* **2012**, *1*, e29. [CrossRef]
137. Cideciyan, A.V.; Jacobson, S.G.; Drack, A.V.; Ho, A.C.; Charng, J.; Garafalo, A.V.; Roman, A.J.; Sumaroka, A.; Han, I.C.; Hochstedler, M.D.; et al. Effect of an intravitreal antisense oligonucleotide on vision in Leber congenital amaurosis due to a photoreceptor cilium defect. *Nat. Med.* **2019**, *25*, 225–228. [CrossRef] [PubMed]
138. Bonifert, T.; Gonzalez Menendez, I.; Battke, F.; Theurer, Y.; Synofzik, M.; Schöls, L.; Wissinger, B. Antisense Oligonucleotide Mediated Splice Correction of a Deep Intronic Mutation in OPA1. *Mol. Ther. Nucleic Acids* **2016**, *5*, e390. [CrossRef]
139. Garanto, A.; van der Velde-Visser, S.D.; Cremers, F.P.M.; Collin, R.W.J. Antisense oligonucleotide-based splice correction of a deep-intronic mutation in CHM underlying choroideremia. *Adv. Exp. Med. Biol.* **2018**, *1074*, 83–89. [PubMed]
140. Sangermano, R.; Garanto, A.; Khan, M.; Runhart, E.H.; Bauwens, M.; Bax, N.M.; van den Born, L.I.; Khan, M.I.; Cornelis, S.S.; Verheij, J.B.G.M.; et al. Deep-intronic ABCA4 variants explain missing heritability in Stargardt disease and allow correction of splice defects by antisense oligonucleotides. *Genet. Med.* **2019**, *21*, 1751–1760. [CrossRef]